Achieving Na-ion Battery Advancements Through Decoding Degradation Pathways and Electrolyte Engineering

Parth Desai

▶ **To cite this version:**

Parth Desai. Achieving Na-ion Battery Advancements Through Decoding Degradation Pathways and Electrolyte Engineering. Material chemistry. Sorbonne Université, 2023. English. NNT : 2023SORUS681 . tel-04543545

HAL Id: tel-04543545
https://theses.hal.science/tel-04543545

Submitted on 12 Apr 2024

HAL is a multi-disciplinary open access archive for the deposit and dissemination of scientific research documents, whether they are published or not. The documents may come from teaching and research institutions in France or abroad, or from public or private research centers.

L'archive ouverte pluridisciplinaire **HAL**, est destinée au dépôt et à la diffusion de documents scientifiques de niveau recherche, publiés ou non, émanant des établissements d'enseignement et de recherche français ou étrangers, des laboratoires publics ou privés.

Sorbonne Université

Ecole doctorale - ED 397 - Physique et Chimie des Matériaux

Collège de France

Laboratoire – Chaire de Chimie du Solide et de l'Energie

Achieving Na-ion Battery Advancements Through Decoding Degradation Pathways and Electrolyte Engineering

Parth DESAI

Doctoral thesis in Materials Science / Chemistry

Supervised by Sathiya Mariyappan and Jean-Marie Tarascon

Presented and defended publicly on October 2nd 2023, in front of the jury:

Mathieu Morcrette	Director of LRCS, HDR, Amiens	Referee
Valérie Pralong	Research director of CNRS, CRISMAT	Referee
Kang Xu	ARL Fellow and team leader of the Extreme Electrochemistry Team at USA Army Research Lab	Examiner
Michael Metzger	Assistant Professor, Dalhousie University	Examiner
Sathiya Mariyappan	CNRS Researcher, Collège de France	Co-supervisor
Jean-Marie Tarascon	Professor, Collège de France	Director

Except where otherwise noted, this work is licensed under
http://creativecommons.org/licenses/by-nc-nd/3.0/

योगस्थः कुरु कर्माणि सङ्गं त्यक्त्वा धनञ्जय।
सिद्ध्यसिद्ध्योः समो भूत्वा समत्वं योग उच्यते॥

-Bhagvad Gita 2.48

"Perform your duties equipoised, O Arjuna, abandoning all attachment to success or failure. Such equanimity is called yoga."

Dedicated to my parents,

Aai (Medha DESAI) and Baba (Prasad DESAI).

Acknowledgements

I was fortunate enough to begin my journey under the discerning gaze of Prof. Jean-Marie Tarascon at Collège de France. Working in a state-of-the-art lab with global exposure, Jean-Marie's passion and commitment to scientific depth was palpable in every interaction. His guidance was invaluable, and our many discussions further shaped my research. Similarly, my heartfelt gratitude goes to Dr. Sathiya Mariyappan, whose relentless supervision, planning, and guidance ensured I stayed on track and delved deep into my research.

Engaging in scientific discussions was a significant portion of my growth, and for that, I owe Biao, Jiaqiang, Ezzoubair, and Juan from the lab. I must also express my profound appreciation for Manoj, Animesh, and Saurabh, my friends from IIT Bombay, who were ever-present to brainstorm and share their insights regarding the research.

Collaborations add depth to any research, and I am immensely grateful to the team from Tiamat, especially John, Hervé, and Mathieu. Their invaluable contributions, from providing electrodes to 18650 type cells, enriched my work. Hussein's screening of the Gen-3 additive combination significantly enhanced this thesis. Special thanks to Jiaqiang (optical sensing), Juan (CVs), Valentin (ICP measurements), Tuncay (SEM measurements), Ronan (SEM measurements), Gwenaëlle (XRD refinements), Artem (TEM measurements), Damien (MS measurements) and Michaël (NMR measurements) for their respective experiments and analyses. A note of gratitude also goes out to the 11BM open access facility for their assistance with synchrotron XRD. My sincere appreciation goes to the RS2E research network (LabEX STORE-EX) in France for their financial support towards my thesis.

I sincerely thank my jury members, Kang Xu, Michael Metzger, Mathieu Morcrette, and Valérie Pralong, for their meticulous evaluation of my thesis.

The camaraderie and insightful exchanges in the office were an integral part of my experience. Thanks to Biao, Tuncay, Aleksandra, Léa, Anshuman, Wei, Clémence, Elisabeth, and Yassin. Their spirited discussions, both scientific and casual, made every day a learning experience. Additionally, my journey at Collège de France was made even more memorable by

my colleagues Ezzoubair, Jiaqiang, Zhenying, Elisabeth, Elisa, Jacques, Ronan, Damien, Ivette, Fu, Benjamin, Valentin, and Laura.

Paris, with its unique charm, became a lot more like home due to friends from Cité Universitaire such as Patrick, the vibrant Tunisian group (Zayneb, Takwa, Oumayma, and Hadhami), Razane, Humna, Ranjith, Mahraz, Maria, Clément, Sandy, and Marouane. A warm thanks to Razane for her steadfast support during my thesis writing, both in nurturing my spirit and in practical assistance with the formatting.

Even miles away from India, my friends Anuja, Mayank, Anand, Saurabh, Piyush, Pawan, Pooja Di, Pawan sir, Chithra, Raghav, Aman, Tushar, and Gaurav kept the connection alive, their virtual presence reminding me of the warmth and camaraderie of home. On a personal note, I'd like to extend deep thanks to Anuja for standing by me and offering unwavering support through both my highs and lows.

Lastly, this journey would be incomplete without mentioning my pillars of strength: Aai (Medha), Baba (Prasad), Pranav, and Swapnali. Your faith in me, your encouragement, and your unwavering love was the true fuel behind my every achievement.

Table of Contents

Acknowledgements iii

Table of Contents v

Broader context and thesis outline 1

1. Climate change and battery technology 2

2. Thesis Outline 5

Chapter 1 | Na-ion batteries: Development and challenges from its origins until today. 7

1. Historical perspective: From Volta's cell to rechargeable Na-ion cell 8

2. Working principle of Na-ion battery 12

3. Electrode materials: A comprehensive summary 17

3.1. Negative electrode materials 17

3.2. Positive electrode materials 21

3.2.1 Insight into layered oxides, polyanionic compounds, and Prussian blue analogues 21

3.2.2 Evaluating key matrices of different cell chemistries 25

3.2.2.1 Comparing Energy Density 25

3.2.2.2 Exploring Cyclic Stability: Comparative Analysis at Ambient and High Temperatures 25

3.2.2.3 Choosing cell chemistry after overall comparison 29

4. Electrode electrolyte Interphase: Key to make superior cells 30

4.1 Passivation of electrodes: formation of Interphases 30

4.2 Electrolyte components 32

4.3 Decomposition reactions and (C)SEI components 34

4.4 Interphases of Li-ion vs. Na-ion batteries 38

4.4.1 Solvation behavior 38

4.4.2 SEI components and solubility 39

4.4.3 Importance of CSEI 41

5. Conclusions of the chapter 42

Chapter 2 | Introducing battery diagnosis toolbox and exploring $Na_3V_2(PO_4)_2F_3$|HC electrochemistry. 45

1. Transferrable knowledge from Li-ion to Na-ion battery system for evaluating the cell degradation 46

2. Cell degradation analysis toolkit 48

2.1 Electrochemical analysis from the full cell 48

2.1.1 Understanding cycling curves 48

2.1.2 First cycle or formation cycle 49

2.1.3 Coulombic efficiency and capacity retention 50
2.1.4 Cell polarization (ΔV) 52
2.1.5 Electrochemical impedance spectroscopy 55
2.1.6 Introducing simulated positive and negative electrodes 58
2.1.7 Effect of mass loss during cycling 59
2.1.8 Electrode slippage: Consequence of parasitic reactions 60
2.1.9 Differential capacity ($dQdV$) analysis 62
2.1.10 Differential voltage ($dVdQ$) analysis 64
2.1.11 Endpoint slippages 66
2.2 Additional electrochemical measurement tools 67
2.2.1 Three electrode cyclic voltammetry 67
2.2.2 Symmetric cells 70
2.3 Postmortem analysis on aged cells 72
3. Chemistry and development of Na3V2(PO4)2F3 | hard carbon cells 74
4. Conclusions of the Chapter 78
Chapter 3 | Unraveling the Interplay between Electrodes and Electrolytes in $Na_3V_2(PO_4)_2F_3$ Full Cells: Synergistic Degradation Pathways and Enhanced Performance Solutions." 81
1. Background and Motivation 82
2. Results and Discussion 83
2.1 Decoding Degradation: Post-Mortem Analysis of NVPF-HC Cell 83
2.2 Quantifying vanadium dissolution 85
2.3 Structural transformations of NVPF induced by parasitic reactions 88
2.4 Microscopic analysis of NVPF leached by parasitic reactions 93
2.5 Mechanism of self-discharge, electrolyte oxidation, and NVPF deterioration 98
2.6 Impact of dissolved vanadium on the degradation of NVPF-HC cells 101
2.6.1 dQ/dV fingerprint and Δ(dQ/dV) analysis 101
2.6.2 Electrolyte destabilization 105
2.6.3 Electrode degradations 107
2.7 Partially suppressing V dissolution 108
2.7.1 NaTFSI based electrolytes 108
2.7.2 Efficient carbon coating of NVPF 110
3. Conclusions of the chapter 111
Chapter 4 | Enhancing Electrode-Electrolyte Interphase Chemistry through Combination of Effective Electrolyte Additives. 113

1. Background and Motivation 114
2. Results and discussions 117
2.1 Heat Evolution during Formation Cycle for “Control Electrolyte” 117
2.2 Impact of Additives on Heat Evolution during the Formation Cycle 120
2.3 Electrochemical analysis of NVPF|HC full cells 124
2.4 Unraveling the role of additives from symmetric cells 129
2.5 Gen-3 electrolyte: Vanadium Dissolution and Gassing in the cells 132
2.6 Evaluating the Feasibility of the Gen-3 Electrolyte for Real-World Applications 136
2.7 Limitation of Gen-3 electrolyte 138
3. Conclusions of the Chapter 138
Chapter 5 | Harnessing High Power and Low Temperature Performance Using Methyl Acetate Cosolvent." 141
1. Background and Motivation 142
2. Results and discussions 144
2.1 Improvement in electrolyte conductivity with ester cosolvents 144
2.2 Electrochemical stability with inclusion of ester cosolvents at elevated temperature 146
2.3 Long term cycling at ambient temperature 148
2.4 Cosolvents in action: Low temperature behavior 150
2.5 Charge transfer identification 151
2.6 Commercial implementation in 18650 cells: Power performance and High temperature stability 155
2.7 Limitations of the MA containing electrolyte 158
3. Conclusions for the Chapter 160
Chapter 6 | A special case interphase degradation: Zero-volt storage of Na-ion cells. " 161
1. Background and Motivation 162
2. Results and Discussion 164
2.1 Benchmarking the Li-ion system 164
2.2 Na-ion cells at 0V: Exploring the degradation mechanism 167
2.2.1 SEI decomposition and regrowth 167
2.2.2 Impedance tracking: Supplementary “SEI decomposition and regrowth” 169
2.2.3 XPS analysis: Supplementary “SEI decomposition and regrowth” 171
2.2.4 Operando optical calorimetry tracking SEI evolutions due to 0V storage 174
2.3 Cell chemistry optimization to improve 0V stability of Na-ion cells 176
2.3.1 Manipulating electrolyte formulation 176

2.3.2 Manipulating positive electrode material 178
3. Conclusions of the Chapter 181
General conclusions and perspectives 183
- General conclusion 184
- Perspective and Future Directions 186

Appendix 191
S-1 Supplementary Information for Chapter 1 192
- Supplementary Figures 192

S-2 Supplementary Information for Chapter 2 199
- Supplementary Figures 199

S-3 Supplementary Information for Chapter 3 216
- Methods 216
- Supplementary Figures 222

S-4 Supplementary Information for Chapter 4 239
- Methods 239
- Supplementary Figures 243

S-5 Supplementary Information for Chapter 5 256
- Methods 256
- Supplementary Figures 257

S-6 Supplementary Information for Chapter 6 263
- Methods 263
- Supplementary Figures 265

References 277

Broader context and thesis outline

1. Climate change and battery technology

Propelled by the surge in population and the fervor for automation, global energy consumption has undergone remarkable expansion since the 19th century, the dawn of the industrial era. Despite the recent disruptive impact of health crises (COVID-19) on the global economy and geopolitics, current projections persist in indicating an approximate 10% uptick in global energy demand by 2030 compared to pre-crisis levels[1]. This surge is predominantly steered by the economic and demographic growth across Asia and Africa. Concurrently, the planet grapples with a rise in atmospheric concentrations of greenhouse gases (GHGs), mainly released during the conversion of primary energy sources (CO_2 emissions from combustion processes)[2,3]. These heightened concentrations contribute to an escalation in Earth's surface temperatures on a global scale (**Fig. 1**). In the quest to meet this voracious energy appetite while constraining GHG emissions, an urgent imperative emerges: to reduce the carbon intensity inherent in our energy conversion systems.

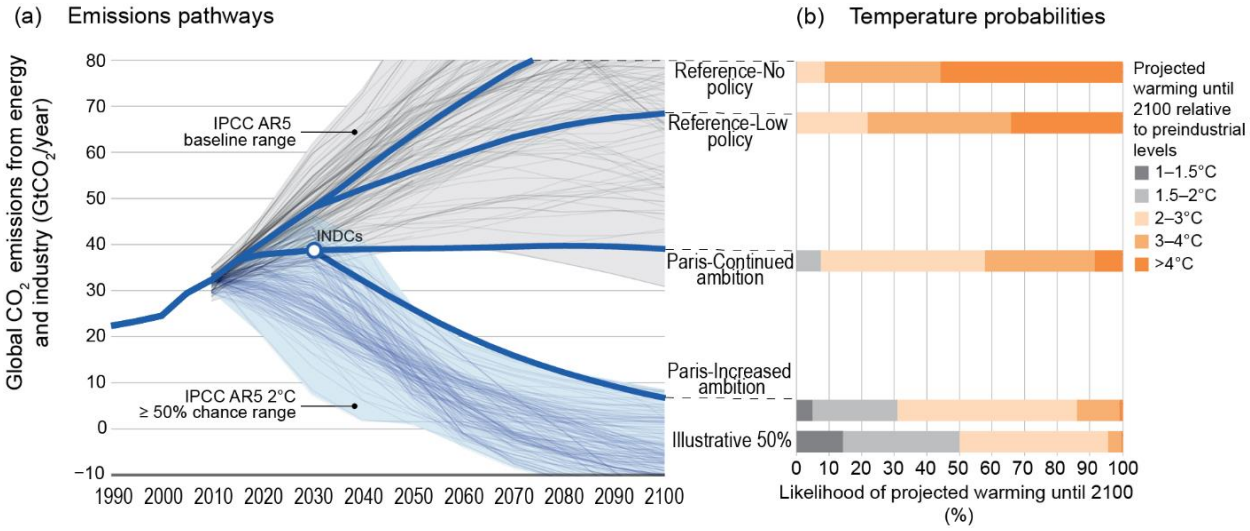

Fig. 1 | Impact of GHG emissions and pro-climate policies on temperature increase. Global CO_2 emissions and probabilistic temperature outcomes of policy announcements associated with the lead-up to the Paris climate conference. (a) Global CO_2 emissions from energy and industry for emissions pathways following no policy, current policy, meeting the announcements with constant country decarbonization rates past 2030, and meeting the announcements with higher rates of decarbonization past 2030. (b) Likelihoods of different levels of increase in global mean surface temperature during the 21st century relative to preindustrial levels for the four scenarios. Although (a) shows only CO_2 emissions from energy and industry, temperature outcomes are based on the full suite

of GHG, aerosol, and short-lived species emissions across the full set of human activities and physical Earth systems. IPCC AR5 is The Fifth Assessment Report of the United Nations Intergovernmental Panel on Climate Change. INDCs refer to Intended Nationally Determined Contributions, which is the term used for the announced actions in the lead-up to Paris. The figure is adapted from Chapter 14 of the Climate science special report.[3]

In this context, the Paris Agreement[4] adopted unanimously by 195 nations on December 12, 2015, marks a milestone in climate change action. Its objective is to fortify the global response against the looming threat of climate change, aiming to restrain the 21st-century temperature escalation to well below 2 °C (2 °C above pre-industrial levels – a time dating back to the mid-19th century). The forecasted effect of the implementation of different climate policies suggested by the Intergovernmental Panel on Climate Change (IPCC)[5] on projected global warming is presented in **Fig. 1**.

Energy storage technologies (ESTs) are pivotal in realizing these objectives. The effective integration of renewable sources such as solar and wind, characterized by their intermittent nature and unpredictable behavior, hinges on concurrent advancements in ESTs.[6,7] Additionally, ESTs offer adaptability to energy systems, enabling improved optimization and efficiency gains. The acceleration of electrifying the transportation and electric power sector is contingent upon achieving competitive costs for ESTs. These technologies are classified into categories encompassing electrical, electrochemical, thermal, and mechanical domains, with varying scales and degrees of decentralization. Among these, electrochemical innovations like batteries, fuel cells, and supercapacitors have undergone remarkable research and innovation acceleration recently[8,9]. Noteworthy is the substantial progress of lithium-based batteries, which have surpassed their predecessors, namely lead-acid and nickel metal hydride batteries.[7,10–12] These lithium-based batteries currently dominate the portable electronics sector and are well on their way to widespread adoption for electric transportation, extending even to large-scale grid applications.[13–15] An impactful report from the World Economic Forum (WEF) asserts that the successful integration of batteries, coupled with the implementation of a circular value chain (involving repair, refurbishment, and recycling) in both transportation and the electric power sector, holds the potential to curtail greenhouse gas emissions[16], thereby assisting in keeping the global temperature increase below 2°C (**Fig. 2**).

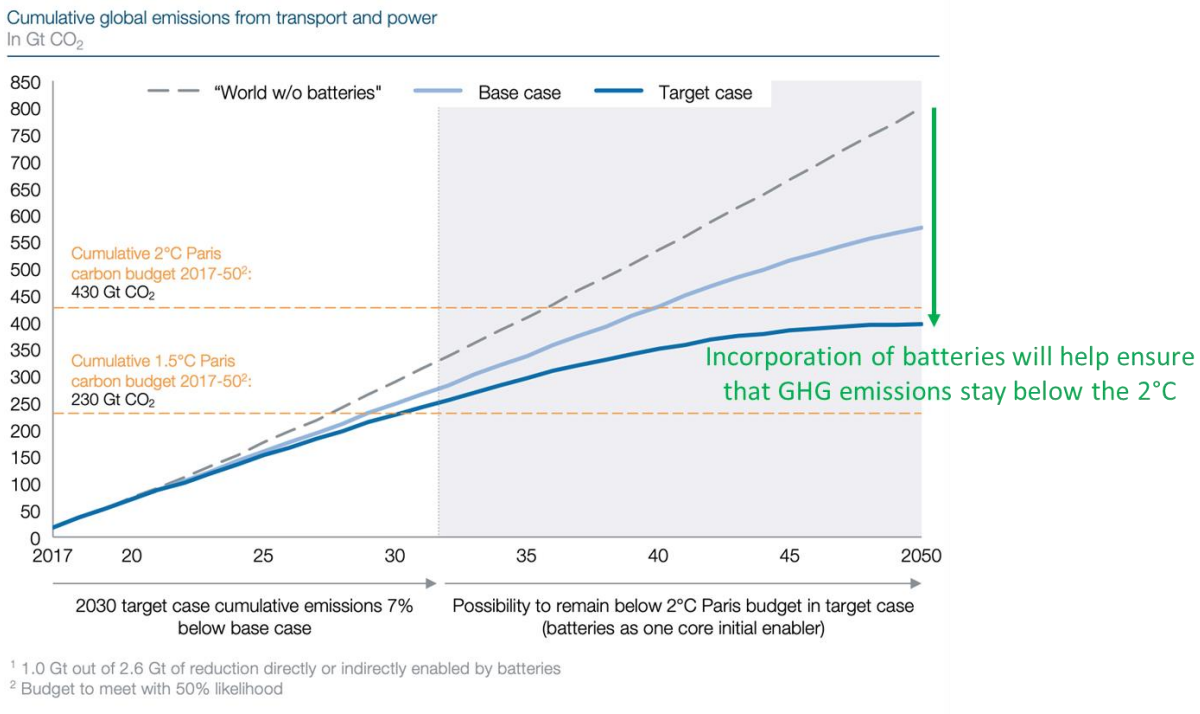

Fig. 2 | Target state of transport and power sector emissions to stay below the Paris Agreement goal. Batteries help to ensure that GHG emissions stay below the 2°C Paris carbon budget in 2050. Note that only the transport and power sectors are considered. Figure is adapted from World economic forum report[16].

While lithium-ion batteries have revolutionized portable electronics and electric vehicles, they come with limitations in terms of finite lithium resources[17–19]. Alternatively, there is a potential for other emerging battery concepts to gain traction during this period. Advanced lithium-ion (solid-state batteries, lithium-sulfur batteries, etc.) and beyond lithium-ion battery technology (Na-ion, Mg-ion, Al-ion, Zn-ion batteries, etc.)[20,21] hold immense importance in our pursuit of sustainable and efficient energy storage solutions. Beyond lithium-ion battery technologies promises sustainable electric transition but also addresses environmental and geopolitical concerns related to lithium extraction. The development of beyond lithium-ion batteries heralds a new era of innovation, enabling us to transit towards cleaner energy ecosystems and drive forward the electrification of various sectors while reducing our carbon footprint and ensuring a more sustainable future[22].

2. Thesis Outline

This thesis aims to contribute to the development of 'beyond lithium-ion batteries' and, more specifically, sodium-ion batteries (NIBs). With an overarching ambition, this thesis targets to enhance the longevity and performance of NIBs. Different chapters of the thesis focus on particular aspects of the NIB chemistry studied with the knowledge of solid-state chemistry, optical sensing, electrochemical measurements, and analysis.

It is structured into the following seven chapters:

Chapter 1 begins with a brief introduction to lithium-ion batteries (LIBs) and the comparative development of sodium-ion batteries (NIBs). The working principle of sodium-ion batteries and the importance of electrodes and electrolytes is discussed. The study pivots toward a comprehensive analysis of full cells featuring layered oxide, Prussian blue, and polyanionic materials, culminating in the selection of the **$Na_3V_2(PO_4)_2F_3$ |hard carbon chemistry** as the principal system of investigation. An exposition of the formation and intricacies of interphases in the NIB system serves as a fitting prelude to the subsequent chapters.

Chapter 2 is divided into two parts. The first part explores the different **electrochemical measurements and their analysis**. These range from the intuitive scrutiny of charge-discharge curves to the intricate dissection of impedance measurements, effectively uncovering valuable insights into cell degradation. Additionally, the electrochemical analysis can be confirmed with the postmortem of the cells. This investigation is complemented by a **synoptic review of studies pertaining to $Na_3V_2(PO_4)_2F_3$|hard carbon cells**, encapsulating their notable achievements and limitations. This review prepares the intellectual terrain for the central theme of the thesis.

Chapter 3 undertakes an exhaustive inquiry into the degradation intrinsic to the $Na_3V_2(PO_4)_2F_3$ material. **High potential induced surface degradation, vanadium dissolution,** and its dependence on salt are explored. Progressing in complexity, the study unveils the **fingerprint** of vanadium dissolution manifested within electrochemical curves. Subsequently, strategies for attenuating vanadium dissolution and simultaneously realizing cell longevity and performance are meticulously presented.

Chapter 4 deals with the practical challenge of designing the electrolyte tailored to the $Na_3V_2(PO_4)_2F_3$|hard carbon cells that can be implemented in commercial cell formats. A novel **electrolyte composition featuring additives** takes center stage, forming a robust interphase and adeptly suppressing parasitic reactions to mitigate excessive gas generation. Thus, the suggested electrolyte shows remarkable elevated and ambient temperature performance in terms of calendar and cycle life.

Chapter 5 is dedicated to **overcoming an impedance-related limitation** inherent to the electrolyte elucidated in **Chapter 4**. The meticulous incorporation of a low-viscosity ester, specifically **methyl acetate**, into the electrolytic blend unveils an effective remedy for surmounting the impedance barrier. This strategic intervention is helpful in low-temperature operations and fast-charging applications, signifying a marked advancement in the electrolyte architecture.

Chapter 6 focuses on a very specific application of **'Zero-volt storage'**. As compared to LIBs, NIBs are being claimed as chemistries to sustain the overdischarge and storage at 0V. Thus, this chapter deals with the **degradation mechanism related to the 0V**. A distinctive focus is cast upon the solid electrolyte interphase (SEI) decomposition, catalyzed by the potential shoot-up of hard carbon during 0V storage. The intricate interplay between electrolyte compositions and their influence on cell stability in 0V conditions is meticulously examined. Concluding this exploration, a suite of strategies is discussed to circumvent the hard carbon potential shoot-up.

The concluding **Chapter 7** summarizes this thesis's fundamental and practical achievements along with the remaining questions. This is immediately followed by the opening of two future directions for further expanding the designing space of sodium-ion batteries by manipulating either electrodes and electrolytes. In concluding the thesis, I finalize by sharing my optimistic personal viewpoint regarding the practical feasibility of sodium-ion batteries in real-world scenarios.

Chapter 1 | Na-ion batteries: Development and challenges from its origins until today.

1. Historical perspective: From Volta's cell to rechargeable Na-ion cell

The journey of battery development began with Alessandro Volta's invention[23] of the "cell" in 1799, which sparked the creation of modern batteries. This journey saw the evolution from the Daniell cell (1836) to the Leclanché cell (1866) and eventually to Union Carbide's alkaline small dry cell in 1949[24]. The advent of rechargeable batteries started with Gaston Planté's lead acid battery (1859), followed by nickel-cadmium (1899) and nickel-metal hydride batteries (mid-1980s).[25] On another front, realizing the high electroactive nature of Li, exploration of non-aqueous lithium-based batteries began in the 1960s, leading to various chemistries like sulfur dioxide (Li|SO_2), polycarbon monofluoride (Li|$(CF_x)_n$), manganese oxide (Li|MnO_2), and copper oxide (Li|CuO).[26,27] The Li|MnO_2 batteries were even used in calculators in 1975 by Sanyo Company.[28,29] Batteries based on polyvinyl-pyridine electrode, Li/LiI/Li_2PVP batteries are being used in cardiac pacemakers from 1972 until today.[30,31]

The game-changer was the commercialization of a "**rechargeable**" lithium-ion battery (LIB) by Sony in 1991, which was based on the reversible intercalation of lithium ions in the host electrodes (Li_xCoO_2 and carbon).[32] This invention was the culmination of years of research, including the first-ever TiS_2|Li rechargeable LIB[33] (Whittingham et al. in 1974) with an output voltage of 2V, the seminal discovery of reversible intercalation of Li in Li_xCoO_2 increasing cell voltage[34] to 4V (Goodenough et al. in 1979), and the replacement of problematic Li metal electrodes with petroleum coke[35] (Yoshino et al. in 1985). The development of LIBs was further boosted with the discovery of spinel[36] $LiMn_2O_4$ (Thackeray et al. in 1983), olivine[37] $LiFePO_4$ (Padhi et al. in 1997), $LiNi_xMn_yCo_{1-x-y}O_2$ (known as NMC[38,39], Dahn et al. and Ohzuku et al. in 2001) and later with attractive Ni-rich NMCs. In recognition of the immense impact of the discovery and advancement of rechargeable Li-ion cells, the Nobel Prize in Chemistry 2019 was awarded to John B. Goodenough, M. Stanley Whittingham, and Akira Yoshino.[40]

During the 1980s, alongside research into Li^+ intercalation (refer to **Fig. 1.1**), investigations into the reversible intercalation of Na^+ and phase diagrams of Na_xMO_2 (M = Co, Cr, Ni, Ti, Mn, Mo, and Fe)[41–52] were conducted with the aim of developing sodium-ion batteries (NIBs). In the

1980s, a few US and Japanese companies[53–55] (**Fig. 1.1**) developed prototype cells containing P2-Na_xCoO_2 and Na-Pb alloy as electrodes which showed 300 cycles with an average voltage of 2.9V.

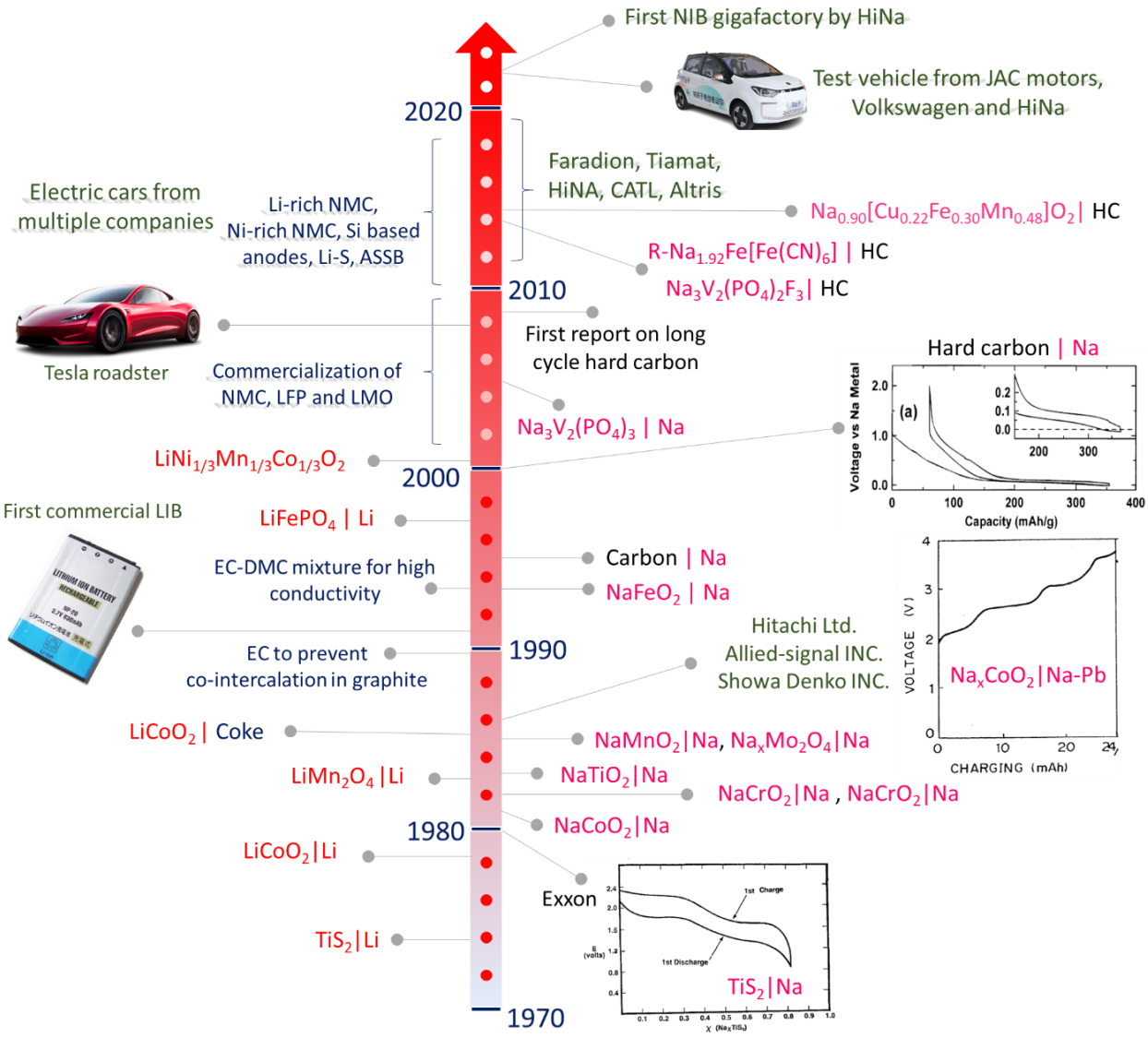

Fig. 1.1 | Timeline of critical developments in NIBs. The timeline illustrates significant discoveries and advancements in the development of sodium-ion batteries, along with a comparative timeline for lithium-ion batteries. The presented information is derived from the mentioned references.[41–58]

However, by the 1990s, after commercialization by Sony, LIBs had demonstrated significant potential, resulting in decreased interest in NIBs. This was primarily attributed to the lower energy density of NIBs compared to LIBs, a consequence of sodium's greater mass (22.99 g/mol versus 6.94 g/mol for lithium) and higher standard electrode potential (-2.71 V versus SHE as

compared to -3.02 V versus SHE for lithium).[59,60] Another critical reason was the lack of suitable negative electrodes. Before the discovery of hard carbon electrodes[61,62] (Dahn et al.) in 2000, there was no suitable negative electrode from the commercial prospect in terms of cost, capacity, voltage, and stability. In 2010, Komaba et al. achieved stable long cycling of hard carbon.[53,63] Apart from these few works, the NIB research field remained dead for two decades (refer to **Fig. 1.2**) after the commercialization of LIBs in 1991.

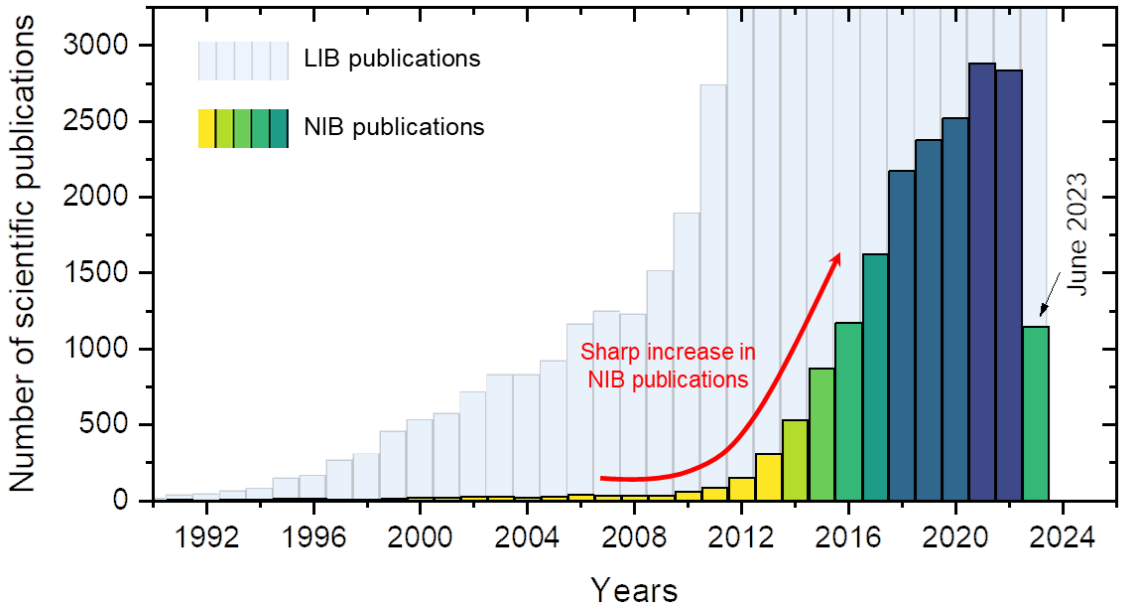

Fig. 1.2 | Resurgence of interest in NIBs after 2010. Yearly number of original papers on NIBs compared with that of LIBs. Data is accessed from the Web of Knowledge accessed on June 24, 2023.

The early 2011s saw a resurgence of interest in NIBs (as reflected in **Fig. 1.2**) spurred by factors summarized below.

- Increasing global demand for LIBs has raised concerns about the sufficiency of available lithium resources. Therefore, a burden on Li precursors' supply chain triggered research on beyond LIB or a complementary NIB technology.[17,18,21]
- The positive electrodes of high-performing LIBs contain rare, expensive, and geographically limited metals such as Li, Co, and Ni. Conversely, sodium sources are abundantly available, cheap, and widely distributed globally. If other earth-abundant and cheap elements are

used to design electrode materials, it will make NIBs a more economically feasible and geo-politically neutral technology.[64]

- Unlike Li, Na does not form alloys with aluminum, making it possible to use aluminum as a current collector instead of the more expensive copper.[55,65]
- As the world transitions to renewable energy sources like wind and solar, there's a need for reliable energy storage devices. Due to Li scarcity, NIBs are seen as a sustainable or greener alternative to LIBs.

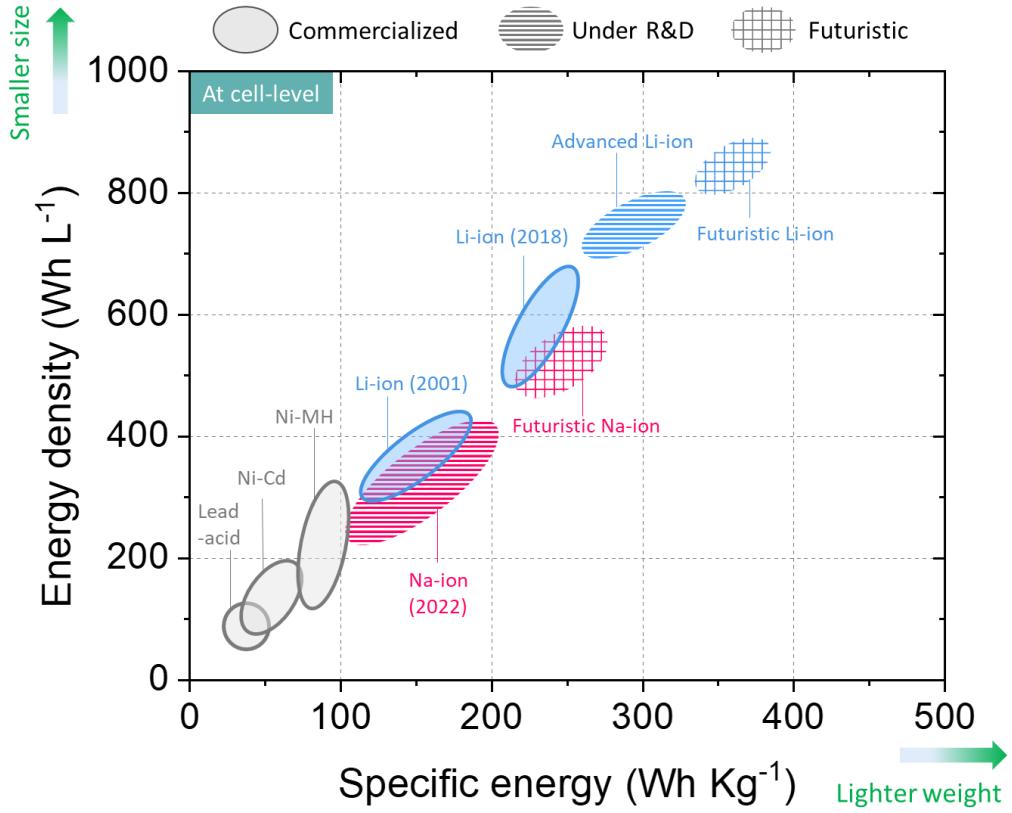

Fig. 1.3 | Roadmap of different battery technologies in terms of energy density and specific energy. Such trends, originally reported in 2001 by Tarascon and Armand[7], have been extended here to show today's status and future likelihoods based on a survey of the literature.[66–69] Among R&D technologies, only those with fully demonstrated prototype cells have been included. Futuristic technologies are included based on the predictions.[68,70]

To compare commercially attractive battery chemistries, certain metrics are used. The amount of storable electrical energy can be measured either per unit of weight (Wh/kg) as specific energy or per unit of volume (Wh/L) as energy density. Specific energy depends on the cell potential (V) and capacity (Ah/kg), which are directly linked to the system's chemistry.[10,71]

Fig. 1.3 provides a development roadmap of battery technologies over the years. Note that this development is triggered with the intention to store more energy in smaller and lighter packages. In this context, Na-ion battery technology (as of 2022) acts as a bridge between Li-ion (as of 2018) and previous rechargeable battery chemistries like lead-acid, Ni-Cd, and Ni-MH. Further commercial optimization and supply chain development for NIBs will increase their energy density, reduce the cost, and eventually reduce our exclusive reliance on LIBs for various applications.

Realizing this potential, numerous startups worldwide, including Tiamat Energy (France), HiNa (China), Faradion Limited (UK), and Altris (Sweden), have introduced NIB cell prototypes with varied chemistries.[68] In December 2022, HiNa celebrated the first GWh-class NIB production line roll-out, utilizing layered oxide as the positive electrode.[72] HiNa, JAC motors, and Volkswagen[72] collaborated on a test vehicle equipped with NIBs, boasting a range of 252 km and an energy density of 120-140 $Wh.kg^{-1}$. With a commanding 37% market share, leading LIB manufacturer CATL aims to institute a significant sodium-ion battery production chain by late 2023, dedicated to powering Chery's electric vehicle model.[73] Tiamat has initiated preliminary tests on a 48V battery pack for hybrid electric vehicles and a 3.6V screwdriver, focusing on high-power applications based on $Na_3V_2(PO_4)_2F_3$ (a polyanionic compound) as the positive electrode.[74,75] Altris, a startup specializing in Prussian Blue analogues (PBAs), has announced plans for an industrial-scale production facility.[76] This facility aims to manufacture 1000 metric tons of PBAs, facilitating the annual production of 1GWh worth of NIBs. Thus, after discussing the commercial interest in NIBs, the next session will delve into the fundamentals of NIB chemistry, different positive and negative electrode materials, and comprehensive comparisons of potential chemistries in terms of key performance parameters, advantages, and limitations.

2. Working principle of Na-ion battery

Fig. 1.4a-b illustrates typical half cells, which by definition contain Na metal as one of the electrodes. Another electrode consists of Na^+ host materials. The electrolyte is an ionic conductor but an electronic insulator, while the electrodes are ionic and electronic conductors. The current collectors provide electronic conductivity and mechanical support to the electrodes but do not

participate in electrochemical reactions.[77] As the potential of Na/Na^+ redox couple on Na metal electrode roughly stays the same (acting as a reference electrode), half cells are used to study the behavior of the working electrode. By definition, the positive electrode denotes the electrode possessing a higher electric potential, while conversely, the negative electrode signifies the electrode characterized by a lower electric potential. Generally, the positive electrode (e.g., Na_xMO_2) consists of the active Na^+ ions, which can be reversibly extracted during the charge (**Fig. 1.4a**), and the negative electrode (e.g., hard carbon) can reversibly host the Na^+ ions during the discharge(**Fig. 1.4b**) in the respective half cells.

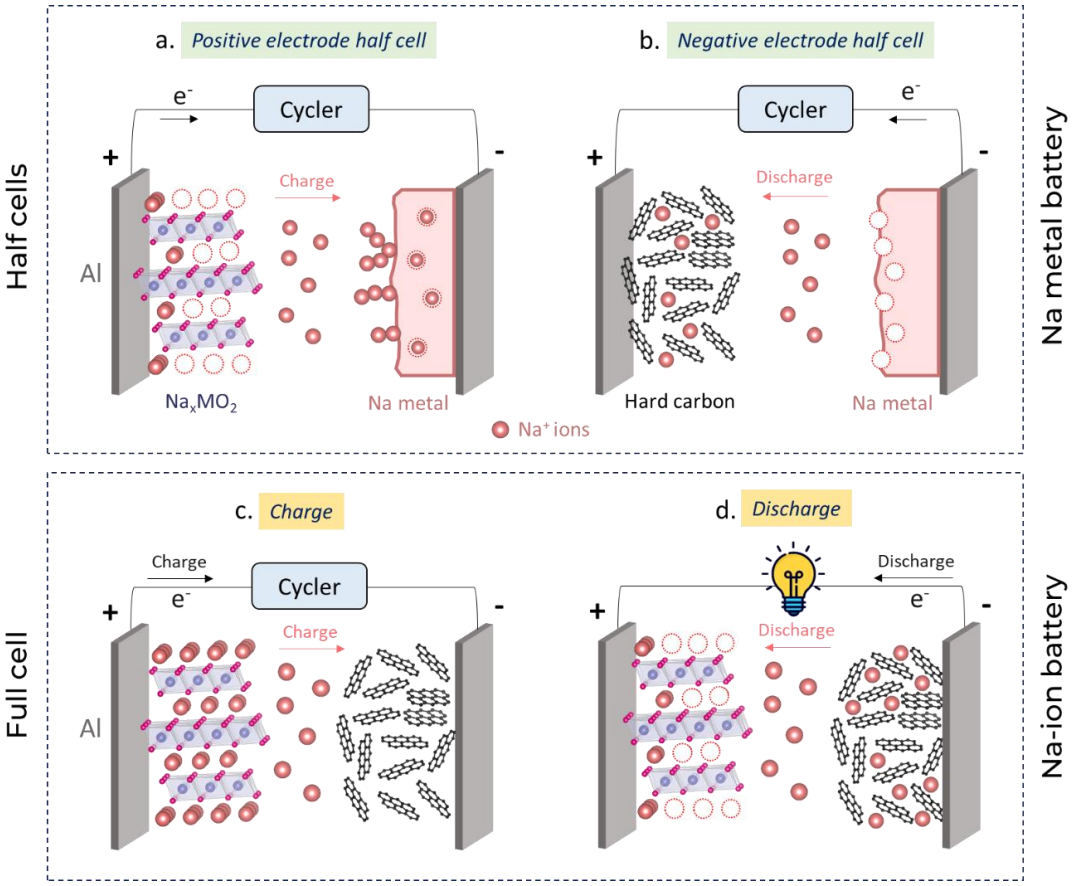

Fig. 1.4 | Schematic representation of half cells and full cells. Representative scheme for (a) Charging of Na metal half-cell of positive electrode Na_xMO_2. Na^+ ions from the electrolyte are being removed from Na_xMO_2 and plated on top of the Na metal. (b) Discharging of Na metal half-cell of negative electrode hard carbon. Na^+ ions are being stripped from Na metal and being inserted into hard carbon. (c) Charging of Na_xMO_2|HC full cell. (d) Discharging of Na_xMO_2|HC full cell. **Note that from electrochemistry terminology, in half cells, the negative electrode will always be Na metal, here, negative electrode half cell terminology is used to represent the negative electrode used in full cell, in this case, hard carbon.**

Using Na metal half cells is not commercially viable due to safety concerns related to the highly reactive nature of Na metal and the formation of dendrites, which can lead to internal short circuits and explosions.[78] To address these issues, a full cell configuration is employed where the positive (e.g., Na_xMO_2) and negative electrodes (e.g., hard carbon) are combined into a single cell (**Fig. 1.4c-d**), making it suitable for practical applications. To gain a better understanding of the charging and discharging processes, as well as the movement of Na^+ ions and electrons at a fundamental level, refer to **Fig. 1.4c-d** while correlating it to **Fig. 1.5**.

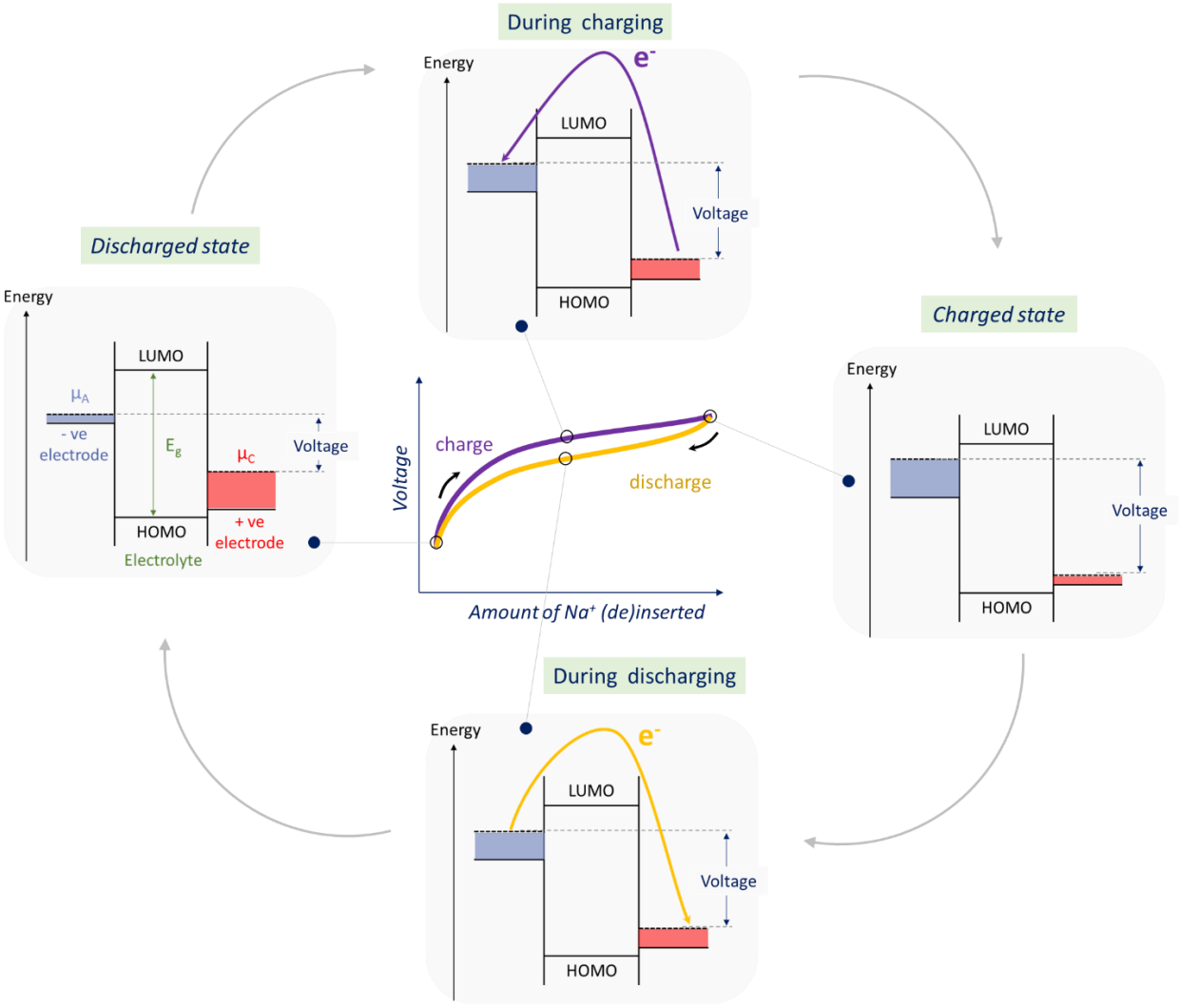

Fig. 1.5 | Schematic representation of energy levels of positive and negative electrodes during battery functioning. The middle part shows the electrochemical profile of the NIB during charge/discharge and is represented as cell voltage as a function of Na-removal. The left part shows the energy levels of electrodes and electrolytes when the cell is assembled. μ_+ and μ_- are the chemical potentials of the positive and negative electrode, while electrolyte

energy levels are marked by HOMO and LUMO. Note that when the cell is charged, the electron goes from the positive electrode to the negative electrode, increasing the cell voltage. The exact reverse process happens during the discharge of the cell. Generally, for high-energy electrodes, the chemical potential while the cell is operational exists beyond the HOMO and LUMO levels of the electrolyte leading to electrolyte decompositions and interphase formation, as discussed in **Section 4.1** of this chapter.

In insertion based systems such as NIBs, electrochemical reactions are driven by the difference in the sodium chemical potential (μ) between two electrodes (Note μ_+ and μ_- in **Fig. 1.5**)[10,71]. Energy levels of electrolyte are defined by the highest occupied molecular orbitals (HOMO) and lowest unoccupied molecular orbital (LUMO) and shown in **Fig. 1.5**. During charging, the positive electrode material, which has a low sodium chemical potential, is oxidized by removal of Na^+ ions from the structure and releasing electrons (**Fig. 1.4c**) to the external circuit. Concurrently, the negative electrode material, which has a high sodium chemical potential, is reduced by accepting electrons from the external circuit (**Fig. 1.4c**) and accepting Na^+ ions in the structure from the electrolyte. Note that during charging (**Fig. 1.5**) electrons are effectively transferred from the energy band of positive electrode to the negative electrode and thus lead to increase in cell voltage (difference between sodium chemical potential of two electrodes) as Na^+ ions are being transferred (charging curve in **Fig. 1.5**). This process is reversed when the battery is being discharged (refer to **Fig. 1.4d** and discharge process in **Fig. 1.5**) providing electric current to the external circuit that can be utilized to perform works[10,71], such as powering an electronic device.

At this point, some of the important terminologies related to cell chemistry and performance will be defined, which will be of critical importance throughout the thesis. As discussed, the difference in chemical potentials of the sodium-ion in each electrode is related to the open circuit voltage of the battery by the Nernst equation[10].

$$V = -\frac{\mu_+^{Na} - \mu_-^{Na}}{e} \qquad \text{Equation 1.1}$$

Where μ_+^{Na} is the Na chemical potential of the positive electrode, and μ_-^{Na} is the Na chemical potential of the negative electrode. Note that high cell voltage can be realized with low μ_+^{Na} and high μ_-^{Na}. However, the operating voltage of a battery is functionally limited by electrolyte

stability (HOMO and LUMO), and the so-called "electrochemical stability window" represented by E_g in **Fig. 1.5**, which will be discussed in **Section 4.1-4.4** of this chapter.

The cell voltage is the energy that is stored or returned by one working ion moving across the electrolyte. Complimentary to this, capacity (Q) is the amount of working ions that are transported between electrodes across the electrolyte[10,77]. The specific capacity of an electrode active material, in units of mAh/g, is

$$Q = \frac{96485 * n(Na^+)}{3600 * \mathrm{M}} \qquad \text{Equation 1.2}$$

Where $n(Na^+)$ is number of Na^+ ions, and M is the molecular weight of the electrode material.

Gravimetric energy density is the product of the specific capacity and average cell voltage. It can be expressed either as

$$E_{gravimetric}\ (Wh/kg) = Q\ (Ah/kg)\ .\ V_{avg}\ (V) \qquad \text{Equation 1.3}$$

Gravimetric energy density is related to volumetric energy density (Wh/L) by the active material's density.

Rate capability is the ability of a battery to charge and discharge quickly while still holding a significant amount of energy. This is crucial for batteries used in high-power applications like power tools and fast-charging electric vehicles. In order for a battery to have good rate capability, its electrodes must possess high electronic and ionic conductivity and electrolyte must have high ionic conductivity.[66]

Cycle life refers to a battery's capacity to maintain its energy storage capability after repeated charging and discharging cycles. Commercial batteries need to operate at the highest percentage of their initial performance over their lifetime, especially in electric vehicles and stationary grid storage that require a service life of at least ten years and need to retain their capacity for more than 10,000 cycles.[79]

Battery safety is of utmost importance and is often prioritized over performance. Safety concerns prevent the use of Na metal (or Li metal) as a negative electrode despite its potential

for higher energy densities.[80] One critical safety property is positive electrode safety, which refers to a material's tendency to decompose at high voltages, leading to oxygen gas evolution. This decomposition, combined with the exothermic reaction between the battery electrolyte[81–85] and oxygen gas, can cause thermal runaway and pose a significant fire hazard.

3. Electrode materials: A comprehensive summary

An ideal electrode material should possess the following properties[71,86] for practicability: 1) can host a large amount of Na-ions (high specific capacity); 2) shows high redox potential; 3) maintains structural integrity during cycling (long life span); 4) has a large diffusion coefficient for Na^+ ions and high electronic conductivity (good rate performance); 5) has high chemical and thermal stability (good cycle life), and is highly compatible with electrolytes (good safety); 6) is easily accessible, environmentally friendly, and cost-effective.

3.1. Negative electrode materials

In a full cell, a negative electrode is defined as an electrode with higher sodium chemical potential, μ_- in the energy diagram (**Fig. 1.5**) or lower voltage as compared to other (or positive) electrode. In order to achieve high voltages in a full cell, it is crucial to minimize the potential of the negative electrode, making it as low as possible. **Supplementary Fig. S1.1a** provides an overview of different types of electrode reactions, such as insertion, alloying, and conversion. On the other hand, **Supplementary Fig. S1.1b** summarizes the specific capacity and working voltage of various negative electrodes reported for NIBs. The insertion type includes carbonaceous materials and titanium-based oxides ($Na_2Ti_3O_7$, TiO_2, etc.), while transition metal oxides (Fe_2O_3, Fe_3O_4, Co_3O_4, etc.) or transition metal sulfides (CoS_x, ZnS, etc.) undergo conversion reactions.[55] Additionally, alloying compounds of group 14 or 15 elements with sodium, such as Na-M (M = Sn, Ge, Sb, P, SnSb), are being considered as potential candidate materials.[87]

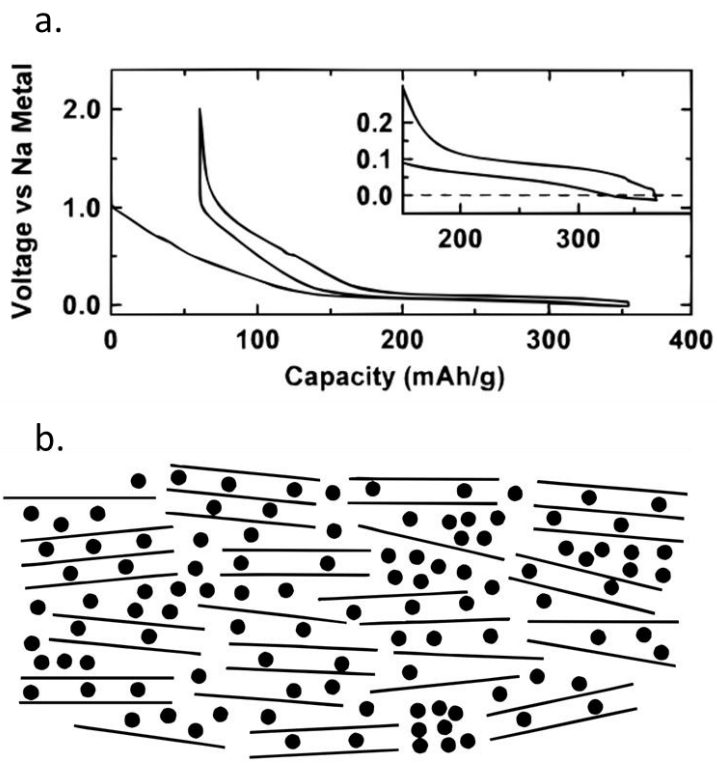

Fig. 1.6 | First report on hard carbon as negative electrode and its storage mechanism. (a) Voltage vs. capacity profile of hard carbon electrode. (b) Na storage mechanism is explained using the house of card model. Parallel lines represent graphitic regions in the hard carbon, and non-parallel lines indicate non-graphitic regions. Na-ion segregated at one place indicates the existence of pores. Reproduced from Dahn et al. paper.[62]

In the category of carbonaceous materials, graphite which is commonly used in LIBs, exhibits a significant limitation as it fails to intercalate sodium in carbonate solvents[88,89]. However, the first report[61,62] in the year 2000 showed that disordered non-graphitizable hard carbon (HC) can reversibly insert Na^{+}, giving a capacity of 300 mAh/g (**Fig. 1.6a**). Note that the voltage-capacity curve shows two regions, a sloppy region in the initial and a flat region in the later stages of insertion. This behavior was explained by a simple "house of cards" model[62] (**Fig. 1.6b**), where Na^{+} initially goes into the parallel layers of graphene sheets (graphitic region), and later it goes into the nanoscale porosity leading to a flat potential region. Recently, Grey et al. used a more rigorous atomic model for hard carbon[90] considering the defects, curvature, and sp^3-hybridized carbons. The model was supported by experimental PDF and NMR measurements. This model affirms the main claims of the house of cards model with the observance of Na clusters (13–15 Å diameter) at pores in the low voltage flat region. Komaba et al., using Density

Functional Theory (DFT), confirmed the formation of Na clusters[91] and asserted that the observed 478 mAh/g capacity in MgO template[92] HC is achieved by enhancing the ability to form nanoclusters of Na. Nevertheless, it remains unclear how small Na metal clusters can form at positive potentials and what is the nature of the Na in those clusters.

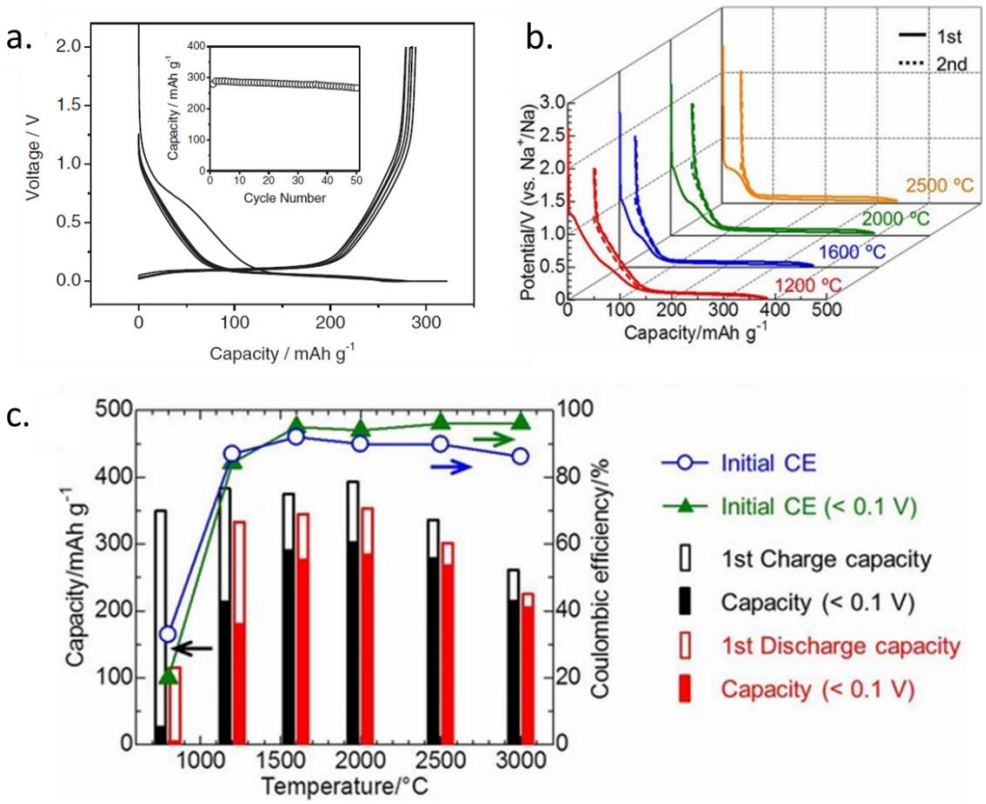

Fig. 1.7 | Choosing the right hard carbon and other cell parameters. (a)First stable cycling of HC half cell reported by Komaba et al. (b) Effect of synthesis temperature on the capacity and first cycle irreversibility. (c) Bar chart summary of capacity and irreversibility as a function of synthesis temperature. Reproduced from Komaba et al. and Abe et al.'s paper.[54,63,93]

Regrettably, performance-wise, the initially reported hard carbon in 2000 exhibited suboptimal cyclic stability with only two cycles reported (**Fig. 1.6a**). Only in 2010 Komaba and team demonstrated the stable cyclic performance[53,63] (**Fig. 1.7a**) of hard carbon by optimizing HC synthesis and other cell conditions like a binder, purity, water content of solvents and salts, etc. Notably, the reversible capacity, capacity from the sloppy and flat region, and first-cycle capacity loss are greatly influenced by synthesis temperature (**Fig. 1.7b-c**). Currently, with synthesis optimization, the HC with first cycle irreversibility as low as 5% and a reversible capacity of 350

mAh/g can be achieved[93] (HC synthesized at 2000°C in **Fig. 1.7c**). Therefore, choosing the right precursor and synthesis conditions to make hard carbon, binder to make electrodes, and purity of the salts and solvents is essential to make state-of-the-art HC electrodes and cells.

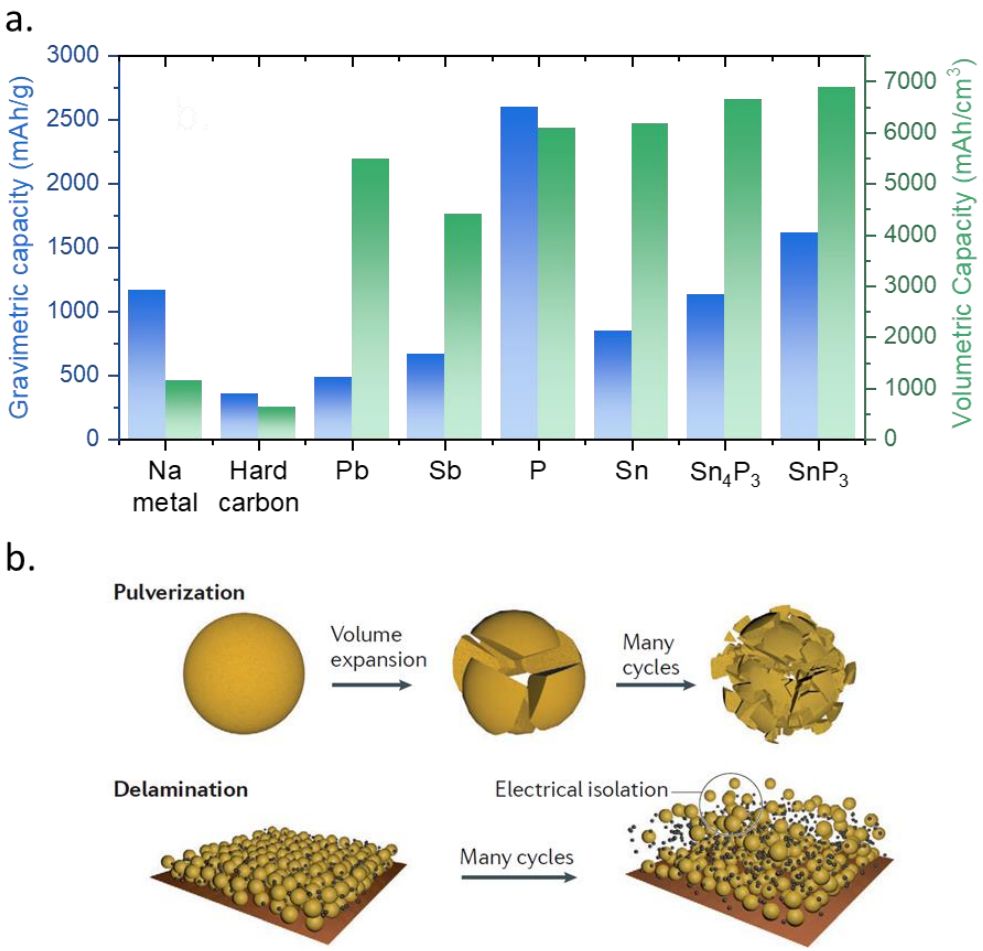

Fig. 1.8 | Next-generation negative electrodes for NIBs. (a) Tabulated gravimetric and volumetric capacity of the potential negative electrodes for NIBs. (b) Problems of particle pulverization and delamination in alloy-type negative electrodes. Part (b) is reproduced from Aurbach et al.'s work.[19]

HC is currently irreplaceable as a negative electrode due to its low cost, easy synthesis, and high stability, achieved through extensive research in the past decade. To increase the energy density of sodium-ion batteries (as shown in **Fig. 1.3**), it is important to explore alloying and conversion electrodes with high capacity (**Fig. 1.8a**). However, these electrodes suffer from poor cyclic stability due to volume expansion, self-pulverization, and delamination of particles (**Fig. 1.8b**)[19,87]. While stabilizing them is crucial for future technology, they are not yet ready for practical use compared to HC.

3.2. Positive electrode materials

3.2.1 Insight into layered oxides, polyanionic compounds, and Prussian blue analogues

The determination of energy density in NIBs heavily relies on the positive electrode material, as it contains the active Na-ion inventory and exhibits a high voltage during Na^+ (de)insertion. The positive electrode material encompasses a variety of materials, which can be categorized into layered oxides, polyanionic compounds, and Prussian blue analogues (PBAs), as shown in the general structure and representative chemical formula[94,95] in **Fig. 1.9**. Experimental observations of capacity and average voltages for different materials are depicted in **Fig. 1.10**. By examining **Fig. 1.10**, a general comparative trend can be observed: layered oxides demonstrate higher capacity but lower voltages (represented by orange dots), polyanionic compounds exhibit high voltages but lower capacity (represented by blue dots), and PBAs display moderate capacity and voltage (represented by green dots).

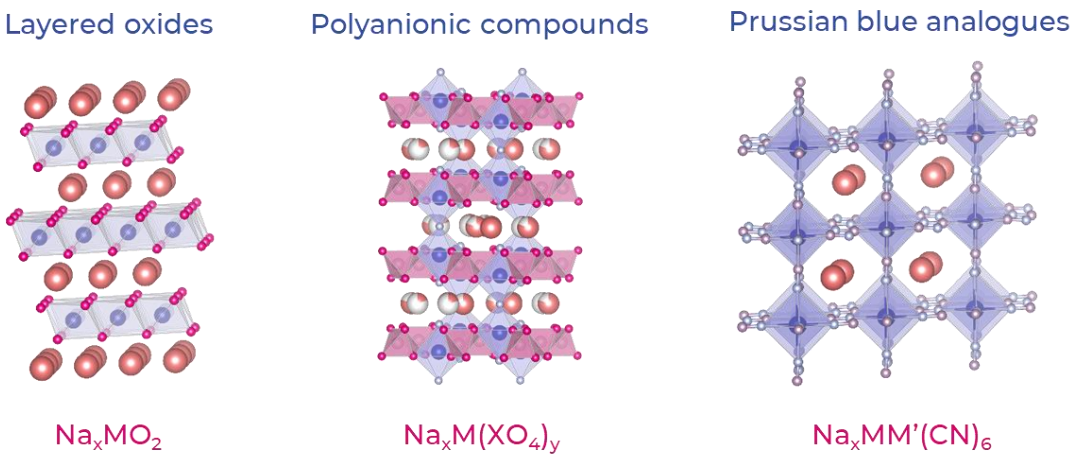

Fig. 1.9 | General molecular formula and structural representation of Layered oxides, Polyanionic compounds, and Prussian blue analogues. Note that depending on the transition metal M and cationic/anionic doping will finally decide the molecular formula and crystal structure.

Layered oxides can be classified into P2, P3, O2, or O3 type based on the crystal structure[43] (**supplementary Fig. S1.2**). The letter P and O denotes prismatic or octahedral coordination of Na ion, and the number represents the minimum number of MO_2 slabs required to reproduce the oxygen stacking sequence. Sodium layered oxides (Na_xMO_2) with x>0.9,

generally crystallize in O3 structure, thus offering high capacity, which is attractive for practical applications. As seen from **Fig. 1.10**, most of the layered oxide contains Ni as a redox center. Additionally, Na_xMO_2 compounds are typically more prone to Na^+-driven phase transitions compared to their Li analogs due to larger Na^+ size and Na^+-vacancy ordering[96,97]. Moreover, generally, O3 type Na_xMO_2 are highly sensitive to atmospheric moisture and result in the formation of insulating NaOH, Na_2CO_3, and $Na_2CO_3.H_2O$, which degrades the electrode performances[53,98]. Due to above discussed reasons, multiple transition metal ions are doped to manipulate the phase transitions, air stability, and voltage in these compounds.

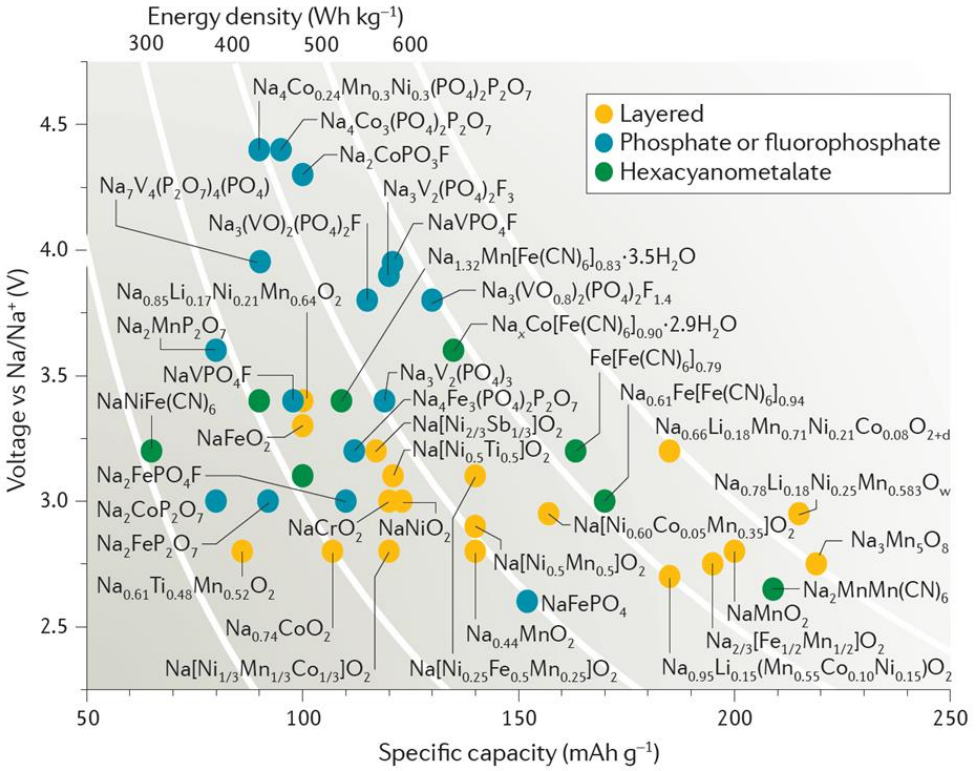

Fig. 1.10 | Research progress of cathode materials for NIBs presenting average charge voltage and discharge capacity. Reproduced from Aurbach et al.'s review paper.[19]

Polyanion-type electrode materials are compounds that consist of a series of tetrahedral anionic units $(XO_4)^{n-}$ or their derivatives $(X_mO_{3m+1})^{n-}$ (where X represents elements such as S, P, Si, As, Mo, or W) connected by strong covalent-bonded MO_x polyhedra (with M representing a transition metal).[10,71,99] Goodenough et al. systematically demonstrated that replacing oxygen with polyanionic units increases the redox voltage of the transition metal due to the inductive

effect. For example, the redox potential of Fe^{3+}/Fe^{2+} can be effectively increased from 2.4 eV to 3.9 eV just by incorporating polyanionic groups (**Fig. 1.11a**).

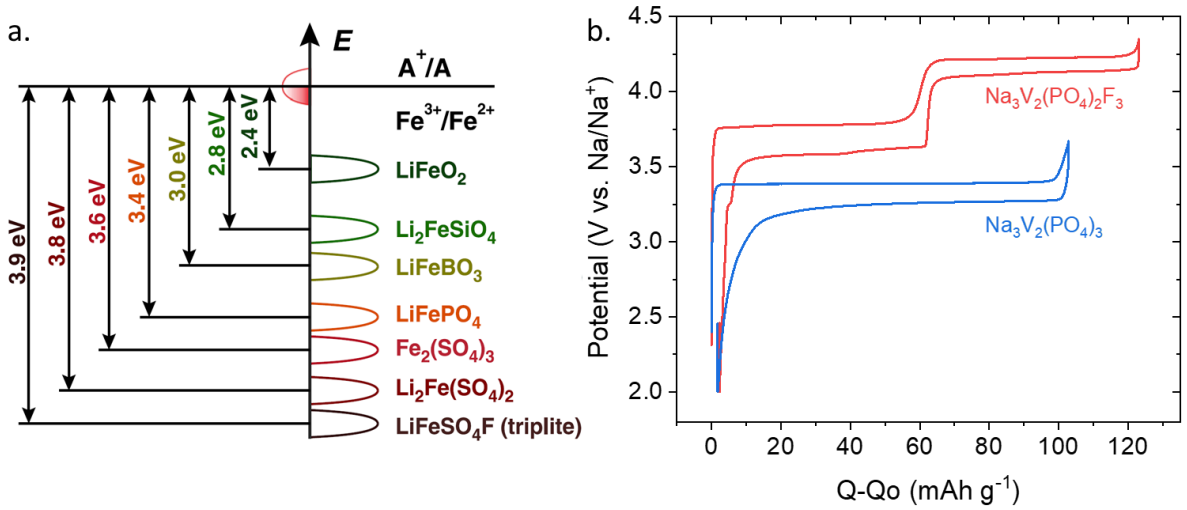

Fig. 1.11 | Effect of polyanionic group on voltage. (a) Effective redox voltage of Fe^{2+}/Fe^{3+} for different Li based polyanionc compunds as presented by Goodenough et al. Reproduced from the review paper[100] of Abakumov et al. (b) Potential vs. cumulative capacity profile of NVP and NVPF electrodes in Na metal half cell.

Phosphates are among the most common polyanion compounds and are typically based on the $(PO_4)^{3-}$ anion.[99,101] $Na_3V_2(PO_4)_3$ (NVP) is a well-known positive electrode material that crystallizes in the NASICON structure (monoclinic, space group: C/2c). It exhibits a flat plateau at 3.35 V and a reversible capacity of 107 mAh/g (**Fig. 1.11b**).[102] By replacing one $(PO_4)^{3-}$ with three F^- ions, $Na_3V_2(PO_4)_2F_3$ (NVPF) is obtained. NVPF crystallizes in the orthogonal system (Amam) [103,104], and the inductive effect of F^- significantly increases the overall redox potential of V (**Fig. 1.11b**), resulting in an average voltage of 3.9 V and a reversible capacity of 120 mAh/g[105]. The charging profile of NVPF exhibits two flat plateaus corresponding to the removal of two sodium ions per formula unit. NVPF possesses a high Na-ion diffusivity due to its open structure, resulting in excellent power performance (**supplementary Fig. S1.3**). Note that various compounds with $Na_3V_2(PO_4)_2F_xO_y$ are possible[106], but among them, NVPF is the most attractive due to its higher voltages. Interestingly, both NVP and NVPF are stable in water,[107] making their handling and processing highly convenient. One limitation of NVPF is its low electronic conductivity, which can be addressed by carbon coating[108] of NVPF particles. The discussed properties of NVPF make it a promising candidate for a commercial application.

The Prussian blue analogues (PBAs)[109] represents a family of metal organic framework that could be represented as $Na_xM_1[M_2(CN)_6]_y \cdot zH_2O$. Here, M_1 and M_2 typically are transition metals bonded by −C≡N− bonds to form a 3D open structure with the capability to host sodium inside the crystal structure. Water exists in three kinds of forms in the PBA framework, namely the adsorbed water on the surface, the zeolitic water in the interstitial sites, and the coordinated water that is chemically bonded with the metal ions.[110,111] **Fig. 1.12a** shows an example of a structurally flawless PBA, $Na_2M[Fe(CN)_6]$, while **Fig. 1.12b** presents an ideal defective PBA, $NaM[Fe(CN)_6]_{0.75}\bullet\square_{0.25}$, in which 25% of the $Fe(CN)_6$ sites are vacant, and a neighboring M atom is coordinated with a water molecule.[112] Depending on the synthesis route, an experimentally obtained PBA compound would fall between these two ideal crystal structures, and tuning defect chemistry is critical for optimal performance. The partially dehydrated PBAs exhibit better performance but are highly susceptible to moisture. Moreover, PBAs exhibit low electronic conductivity. Thus, optimizing synthesis conditions, handling conditions (due to moisture sensitivity), and conductive coating can lead to good electrochemical performance.

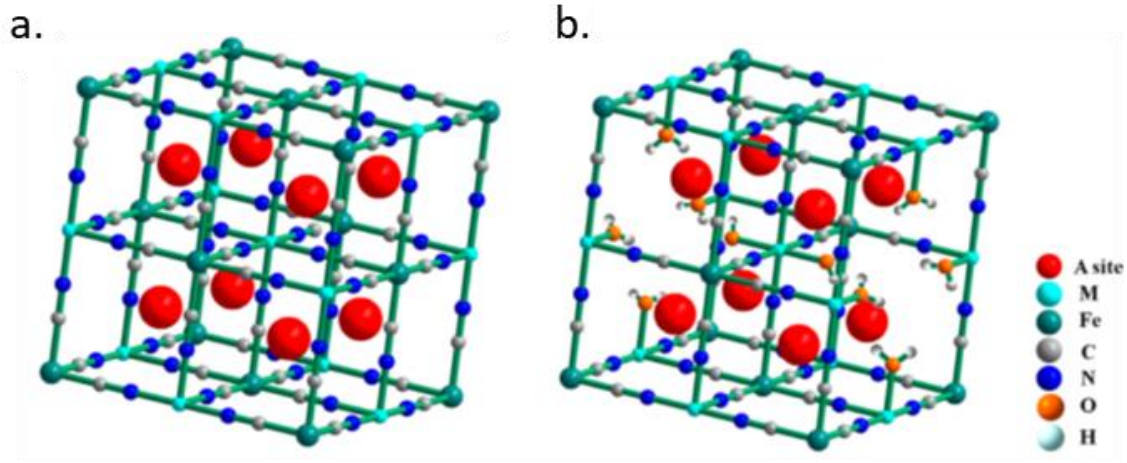

Fig. 1.12 | Generation of vacancies and coordinated water in PBAs (a) A structurally flawless $Na_2M[Fe(CN)_6]$ framework is presented, with M ions being six-fold coordinated to the nitrogen atoms of the CN ligands and Fe ions being octahedrally neighbored with the carbon atoms of the CN ligands. This results in the formation of a three-dimensional polymeric framework with large interstitial spaces, where the guests (Na^+ ions and zeolitic water molecules) occupy the interstitial "A" sites located at the center of every eight sub-cubes. For clarity, the zeolitic water molecules are not included in the framework. (b) An ideally defective $NaM[Fe(CN)_6]_{0.75}\bullet\square_{0.25}$ framework is present, where 25% of the $Fe(CN)_6$ sites are vacant in each unit cell. In this case, the M ions neighboring to the vacancies are coordinated by water molecules, with the total number of water molecules in the unit being six. Reproduced from Yang et al.'s paper.[112]

Based on the previous discussion, it is evident that positive electrodes can be categorized into three types: layered oxides, PBAs, and polyanionic compounds. Each category has its own set of advantages and disadvantages. To make the right choice for a specific purpose, it is important to compare these key matrices. In the next session, we will discuss the cyclic stability of these three chemistries.

3.2.2 Evaluating key matrices of different cell chemistries

3.2.2.1 Comparing Energy Density

In order to identify the best suitable cell chemistry, it is important to compare different parameters. The first parameter is the specific energy of the material. **Fig. 1.13** depicts the development of different commercial prototype cells in terms of energy density over the years.[68] Note that layered oxides (Faradion and HiNa) and PBAs (CATL and Altris) show higher energy density prototypes than polyanionic NVPF based cells (Tiamat). Interestingly, these NIBs are approaching the energy density of $LiFePO_4$ (LFP)-based LIBs (**Fig. 1.13**). The next section will focus on the cyclic stability of different chemistries.

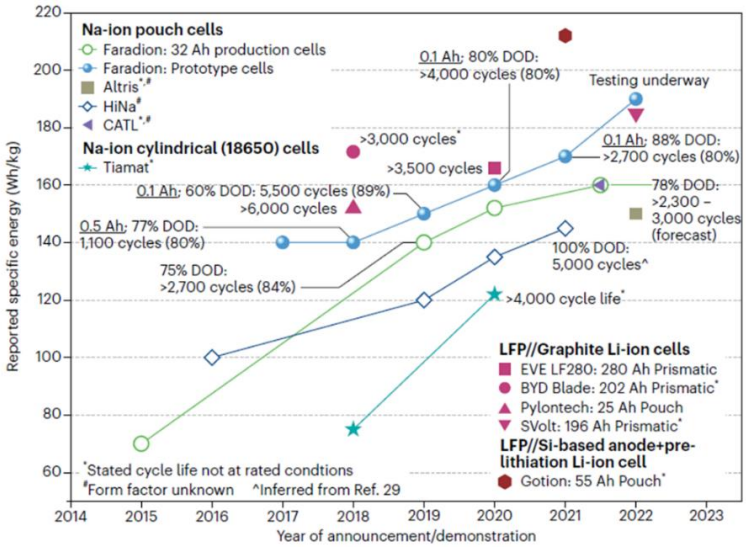

Fig. 1.13 | State-of-the-art energy densities and cycle lives of the Na-ion technology. Reproduced from reference.[68]

3.2.2.2 Exploring Cyclic Stability: Comparative Analysis at Ambient and High Temperatures

Beyond the previously discussed parameters like voltage and capacity, another critical aspect is the cycle and calendar life of batteries. Capacity retention offers insights into battery

cycle life, where electrode and electrolyte degradation play determining roles. This section explores the optimal stability observed across distinct NIB chemistries in existing literature, spanning both ambient and elevated temperature conditions.

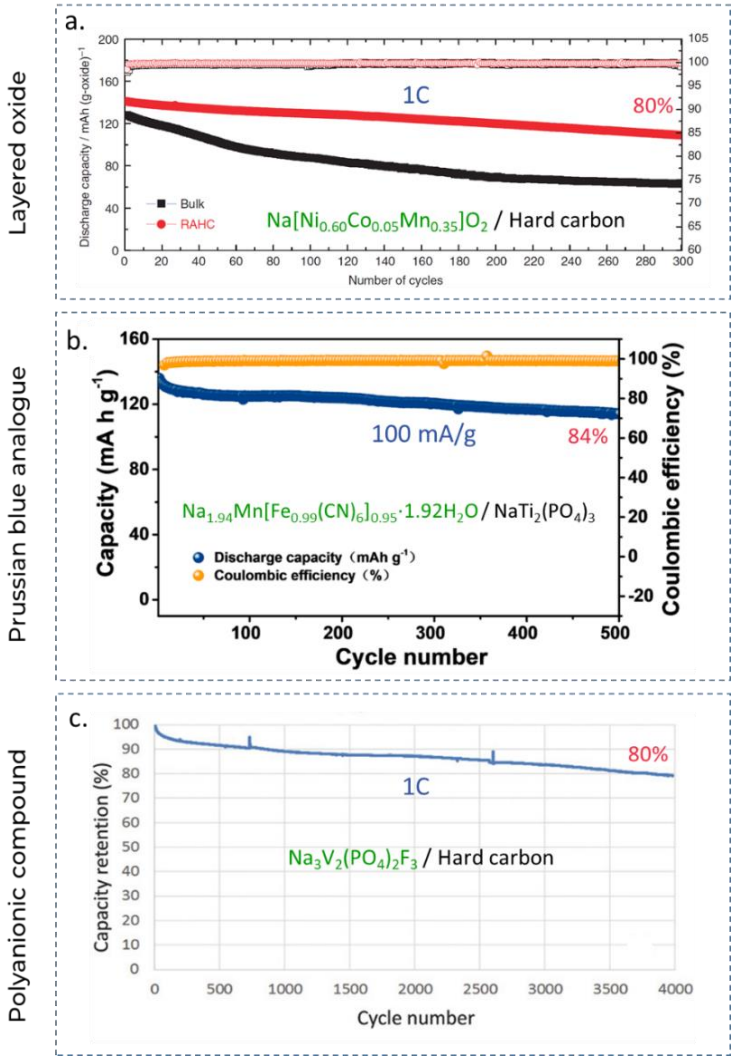

Fig. 1.14 | Notable cyclic stability performances for full cells. (a) Layered oxide synthesized with core-shell strategy $Na[Ni_{0.60}Co_{0.05}Mn_{0.35}]O_2$ cycled against HC negative electrode. Reproduced from Soon et al.'s paper.[113] (b) $Na_{1.94}Mn[Fe_{0.99}(CN)_6]_{0.95}\cdot 1.92H_2O$ synthesized using mechanochemical route cycled against $NaTi_2(PO_4)_3$ negative electrode. Reproduced from Hu et al.'s paper.[114] (c) Carbon coated NVPF cycled against hard carbon electrode. Reproduced from Masquelier et al.'s paper.[108]

In **Fig. 1.14**, various full cells are evaluated for their discharge capacity retention, showcasing notable performances from the literature. $Na[Ni_{0.60}Co_{0.05}Mn_{0.35}]O_2$ synthesized using the concentration gradient strategy demonstrates 80% capacity retention after 300 cycles at 1C

(**Fig. 1.14a**) when paired with hard carbon negative electrode.[113] $Na_{1.94}Mn[Fe_{0.99}(CN)_6]_{0.95}\cdot\square_{0.05}$ $1.92H_2O$, synthesized through mechanochemical means with optimal composition, exhibits a high capacity retention of 84% after 500 cycles (**Fig. 1.14b**) when assembled with $NaTi_2(PO_4)_3$ as the negative electrode.[114] Additionally, carbon-coated NVPF|HC cells display superior stability, retaining 80% of their capacity even after cycling for 4000 cycles at 1C (**Fig. 1.14c**).[108]

Supplementary Table S1.1-1.2 provides a summary of remarkable performances for both half cells and full cells for different layered oxides and PBAs. Analyzing the available literature data suggests that NVPF|HC cells exhibit superior cycling stability compared to full cells utilizing PBAs or layered oxides as positive electrode materials. This superiority is likely attributed to the structural stability of the NVPF polyanionic framework.

The aforementioned results are for electrochemical performances at room temperature. However, high-temperature (>55°C) cycling data and discussions on the degradation mechanisms of Na-ion full cells are lacking in the NIB literature. Testing full cells at high temperatures leads to exponential degradation, rapid capacity loss, and potential cell failure.[115–119] This lack of data may be due to the poorer stability of NIBs compared to LIBs, which commonly undergo high-temperature testing for screening purposes and ensuring safety. Nonetheless, there have been few reported performances of NIB full cells at 55°C.

In a recent study (2023), Metzger et al. improved the 40°C cyclic stability (**Fig. 1.15a left)** of $NaCa_{0.03}[Mn_{0.39}Fe_{0.31}Ni_{0.22}Zn_{0.08}]O_2$|HC cells with manipulating electrolyte.[120] Soon et al. synthesized hierarchically formed columnar structured spheres of O3 type $Na[Ni_{0.60}Co_{0.05}Mn_{0.35}]O_2$ with a concentration gradient of Mn and Ni within the spherical particles[113], as depicted in **Fig. 1.15a right**. When cycled with an HC negative electrode at 55°C and C/2, this material exhibited remarkable capacity retention of 83% after 100 cycles. Similarly, Younesi et al. developed $Na_{1.82}Fe[Fe(CN)_6]\cdot 1.92H_2O$ full cells (**Fig. 1.15b**) with an electrolyte containing NaBOB salt in NMP solvent[121], which showed 69% capacity retention after 100 cycles at 55°C. Furthermore, Tarascon et al. demonstrated that NVPF|HC cells, optimized with appropriate electrolyte additives (**Fig. 1.15c**), experienced 1% capacity loss after 60 cycles at 55°C, exhibiting superior high temperature stability.[122,123]

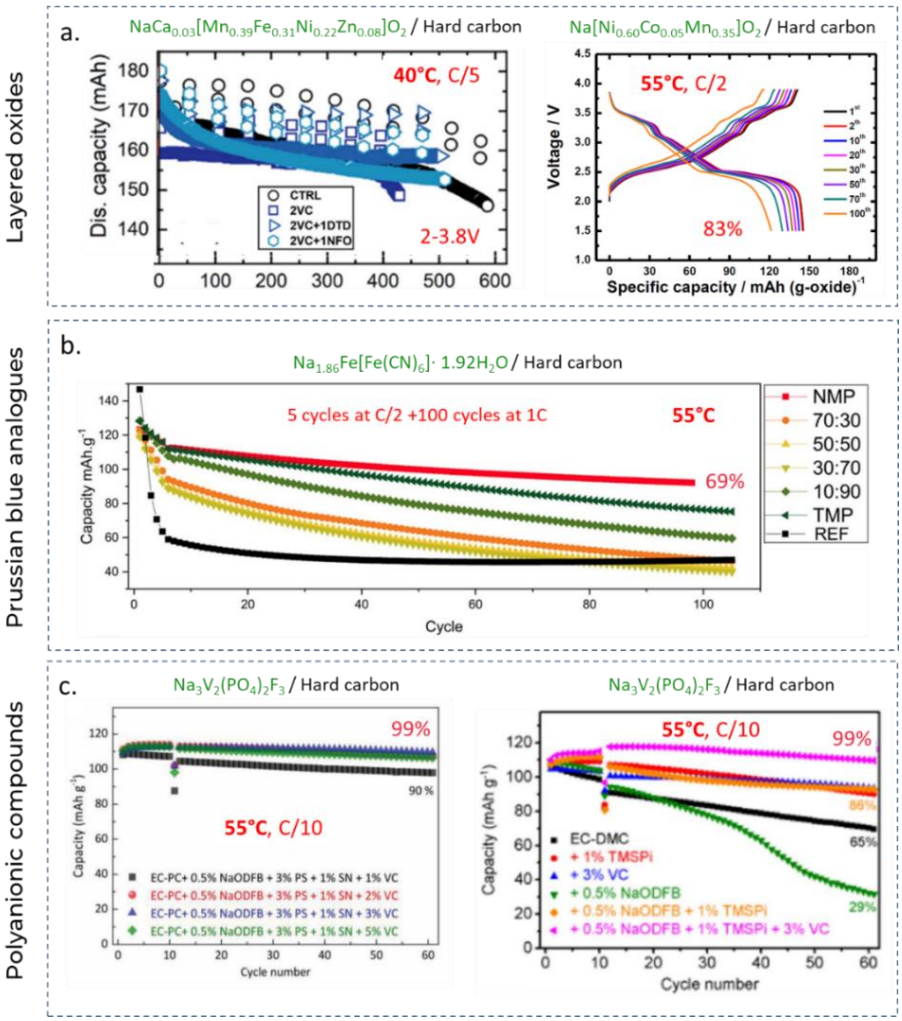

Fig. 1.15 | High temperature (55°C) cycling of full cells (a) Layered oxide and hard carbon full cell cycled with different electrolytes (left), Reproduced from Metzger et al.'s paper.[120] Layered oxide synthesized with core-shell strategy $Na[Ni_{0.60}Co_{0.05}Mn_{0.35}]O_2$ cycled against HC negative electrode (right), Reproduced from Soon et al.'s paper.[113] (b) Prussian white compound from Altris, $Na_{1.82}Fe[Fe(CN)_6]\cdot 1.92H_2O$ cycled against HC negative electrode. Reproduced from Younesi et al.'s paper.[121] (c) Carbon-coated NVPF cycled against hard carbon electrodes with different electrolyte formulations. Reproduced from Tarascon et al.'s paper.[122,123]

To the best of my knowledge, at the starting of this Ph.D. thesis, the available reports on the long cycling of Na-ion full cells are limited, especially at high temperatures. However, the data available indicated that polyanionic NVPF, thanks to its structural stability, exhibits superior cyclic stability compared to layered oxides and PBAs. In the next session, we will compare the key parameters that have been discussed thus far with respect to later developed prototypes, in order to have an overview of this topic.

3.2.2.3 Choosing cell chemistry after overall comparison

As per the specific energy comparison, the layered oxide chemistry is at the top, with the added advantage of the ability to fine tune the composition and structure as required. However, there are other key matrices that also need to be fulfilled for real-life applications, which we tried to compare for the three different chemistries discussed in the radar plot in **Fig. 1.16**. We considered Ni-based O3 type layered oxides, NVPF polyanionic compound, and PBAs based on Fe-Fe and Fe-Mn. Each class has advantages and tradeoffs. O3-type layered oxides excel in energy density and environmental friendliness, but they are sensitive to moisture, that creates difficulties in storing and handling the electrode active materials. In addition, the cycle life and power rate capabilities are limited compared to polyanionic compounds. On the other hand, PBAs are affordable, use abundant elements, and exhibit good rate capability. However, they pose difficulties in removing the crystalline water from the structure to prepare dehydrated materials with the best electrochemical performances. In addition, the thermal stability of the material is still debatable as recent reports claim poor thermal stability of PBAs and the formation of toxic gases during thermal runaway.[124] Finally, NVPF demonstrates fast charging capability, easy handling (stable in water), and potential stability during cycling at room temperature and 55°C. The main disadvantages of NVPF are the use of vanadium in the material and the comparatively lower energy density than the sodium layered oxides.

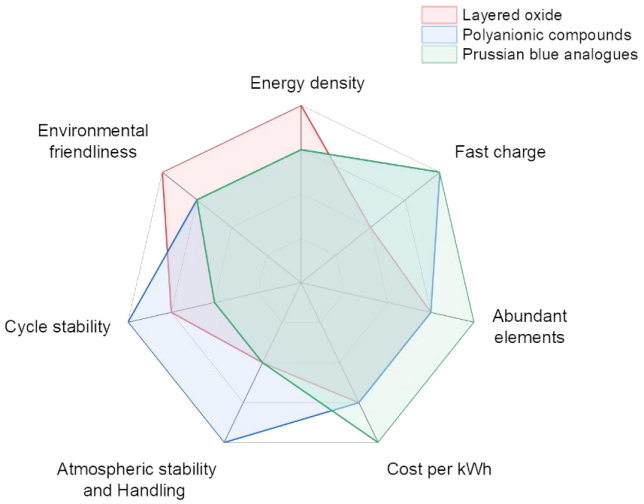

Fig. 1.16 | Tentative comparison of all critical key parameters for O3 type layered oxides containing Ni, Polyanionic compound mainly NVPF and PBAs based on Fe-Fe/Fe-Mn system. The information has been derived from the references. [59,68,125]

However, due to the favorable characteristics exhibited by NVPF, particularly its remarkable resistance to degradation when exposed to air and water, its notable power capabilities, and its stable cyclic performance, the prototype cell developments were much faster, and the first 18650 cells of Na-ion batteries were demonstrated by CNRS and CEA researchers in the year 2015.[126] Following, the start-up TIAMAT has been created to bring the NVPF|HC technology from prototype to real-life applications. However, there were a few challenges, which will be discussed in **Table 2.2** of **Chapter 2**, with respect to calendar life and cycling stability at room/high temperatures. The issues are associated with poor interphase stability, which is intrinsic to Na-ion chemistry. Considering these factors, the current thesis is centered on advancing the NVPF|HC chemistry to enhance both its operational lifespan and performance. Thanks to TIAMAT energy, the NVPF and HC electrodes used for this study are provided by them, and are processed on the industrial scale, reducing the number of variables that can change throughout the study. In addition, TIAMAT has also provided the cylindrical 18650 dry cells to test the developed electrolyte from lab scale to industrial scale.

In order to follow the developments made with the NVPF-HC chemistry during this period, it is essential to discuss the fundamental issues and challenges we had with respect to designing an optimized electrolyte for NVPF|HC based Na-ion batteries. Before going into that in **Section 3** of **Chapter 2**, the following section will discuss the fundamental properties and roles of electrolytes. This exploration is crucial, as a well-designed electrolyte holds the potential to provide superior cells.

4. Electrode electrolyte Interphase: Key to make superior cells

Introducing interphases in the context of the LIB domain holds crucial significance, given the extensive research on this topic. The subsequent section will compare interphases in both NIBs and LIBs. Leveraging over five decades of LIB studies, these comparisons will profoundly contribute to the progress of NIB technology.

4.1 Passivation of electrodes: formation of Interphases

For the electrolyte to exhibit thermodynamic stability, it is necessary for the sodium chemical potentials (μ_+ and μ-) of the electrode to lie within the stability window of the

electrolyte, as shown in **Fig. 1.5**. However, commonly used electrolytes with organic liquid solvents are not electrochemically stable upon oxidation or reduction within the operating potentials of the positive and negative electrodes.[80] This is illustrated in **Fig. 1.17**, where E_g represents the electrochemical stability window, which is the difference between the highest occupied molecular orbital (HOMO) and lowest unoccupied molecular orbital (LUMO) of the electrolyte.

After the cell is assembled and charged for the first time, during the initial charge cycle (indicated by the purple arrow in **Fig. 1.17**), μ_- crosses the LUMO energy level of electrons, causing the transfer of an electron to the electrolyte and reducing it. This reduction of the electrolyte leads to the formation of a solid phase known as solid electrolyte interphase (SEI) on the surface of the negative electrode.[127–129] Similarly, at a certain point during the first charge cycle (also indicated by the purple arrow in **Fig. 1.17**), μ_+ reaches lower energy levels than the HOMO of the electrolyte. This results in the transfer of an electron from the electrolyte to the positive electrode, leading to the oxidation of the electrolyte and the formation of a cathode solid electrolyte interphase (CSEI).[130–132] These terminologies of SEI (on negative electrode) and CSEI (on positive electrode) will be used throughout the thesis. These interphases provide kinetic stability by forming a barrier between the electrode and the electrolyte (marked by a yellow area in **Fig. 1.17**). However, this comes at the expense of a loss of capacity and an increase in impedance, as discussed in **section 2.1.2** of **Chapter 2**.

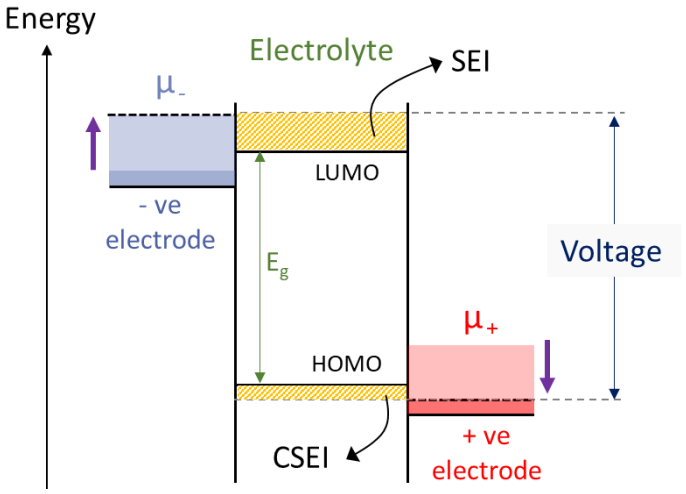

Fig. 1.17 | Energy diagram explaining the formation of SEI and CSEI. μ is the chemical potential, HOMO is the highest occupied molecular orbital, LUMO is the lowest unoccupied molecular orbital, and E_g is the electrochemical stability

window or difference between HOMO and LUMO. The purple arrow indicates the shift in sodium chemical potential at the end of the charge.

To ensure the smooth functioning of the cell, the SEI (or CSEI) should have the following properties:[80,133,134]

1. Electronically insulating: preventing further electrolyte decomposition and (C)SEI growth.
2. Facile ion transfer: Allow easy Na^+ ion transfer between electrolyte and electrode.
3. Insolubility in electrolyte: Stable and non-soluble in the liquid electrolyte at operating temperatures to prevent depletion.
4. Mechanical stability: Withstands volume changes in the electrode during cycling, maintaining mechanical integrity and preventing cracking.
5. Chemical and electrochemical stability: Endures reactions with electrolyte, active materials, and other species, ensuring long-term stability and functionality.

By possessing these properties, the SEI (or CSEI) enhances the overall performance, stability, and efficiency of the cell. The solid-electrolyte-interphase indicates the nature of the layer formed on electrodes, as it functions as a solid electrolyte, which is a phase between electrode and electrolyte.

As SEI and CSEI is formed from the decomposition of electrolyte it is crucial to introduce the chemical composition of the electrolyte before discussing the components of SEI.

4.2 Electrolyte components

The most commonly used electrolyte salts and solvents with their structure and properties are presented in **Table 1.1**. Ideal electrolyte salts should meet minimal requirements:[80] (1) It should be able to dissolve and dissociate. (2) Salt anion should be stable against oxidative decomposition. (3) Salt anion should be inert to solvent and cell components. Due to impressive SEI forming abilities, high ionic conductivity, stability against Al current collector and safety, PF_6-based salts are commonly used in practical cells.

a.

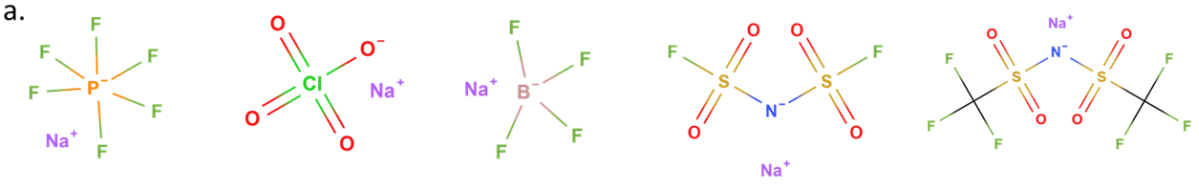

$NaPF_6$ $NaClO_4$ $NaBF_4$ NaFSI NaTFSI

b.

Common name	Chemical structure	Boiling point (°C)	Melting point (°C)	Melting point (cP)	Dielectric constant	Donor number
Ethyl carbonate (EC)	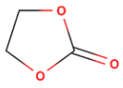	248	36.4	1.86 (40°C)	89.6 (40°C)	16.4
Propylene carbonate (PC)	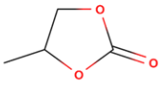	242	-48	2.5	64.9	15
Dimethyl carbonate (DMC)	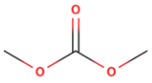	90	4.6	0.59	3.12	8.7
Diethyl carbonate (DEC)	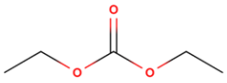	126	-74	0.75	2.82	8
Ethyl methyl carbonate (EMC)	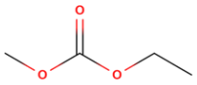	109	-55	0.65	2.9	6.5

Table 1.1 | Chemical components of salts and solvents used for the electrolyte. (a) Na based salts and (b) Linear and cyclic ester solvents and their physiochemical properties. Information is derived from Linden's handbook of batteries.[135]

As mentioned earlier (**Fig. 1.17**), for good stability, electrolyte solvents should have a high electrochemical stability window, and esters are considered the most suitable options. **Table 1.1** provides a summary of commonly used linear and cyclic esters. The electrolyte solvent plays a crucial role in solvating the Na^+ ions, thereby controlling their transport and migration. To ensure good ionic conductivity, the electrolyte solvent should have a high dielectric constant (which aids in salt dissociation) and low viscosity (which facilitates Na^+ transport).[80] Achieving this combination is challenging with a single solvent, leading to the introduction of a mixture of cyclic carbonates (with a high dielectric constant) and linear carbonates (with low viscosity), as

proposed by Tarascon et al.[136] in 1994. This strategy of solvent blends containing both cyclic and linear carbonates is still employed in current LIBs and NIBs.

4.3 Decomposition reactions and (C)SEI components

With the knowledge about salts and solvents that are optimal for NIBs, now it is time to discuss their decomposition products. **Fig. 1.18** gives a complete picture of the main decomposition products categorized into inorganic compounds, gases and organic compounds, along with their respective states of matter (solid, liquid, or gas).[80,133,134,137–141] Please note that the state of these components is approximately established, and there will be a certain degree of solubility of one component within the others. The solid components highlighted in purple are typically found in the SEI, some of which are also present in the CSEI. Soluble species and liquids are indicated by the color red, while gases are labeled in blue. Text in bold within **Fig. 1.18** signifies the significant quantities of specific chemical components compared to other byproducts within the cell. The sodium-based compounds formed during these processes exhibit certain solubility in carbonate solvents. It is important to note that these decomposition products and SEI/CSEI have been confirmed through various analytical techniques such as FTIR, NMR, XPS, TEM, GC-MS, and ESI-HRMS. However, despite 50 years of research, our understanding of interphase formation and its functionality remains incomplete.

To provide an overview of the degradation processes, the following text will discuss the three main steps: degradation of salt, reductive decomposition of the electrolyte, and oxidative decomposition of the electrolyte.

1. $NaPF_6$ (or $LiPF_6$ in LIBs) salt is irreplaceable in NIBs due to its optimal properties. However, $NaPF_6$ is chemically and thermally very sensitive. Even at room temperature, the following equilibrium exists:[80,142]

$$NaPF_6(s) \rightleftharpoons NaF(s) + PF_5(g)$$

Generation of the gaseous product, PF_5, drives the equilibrium to the right, and this process is favored at elevated temperatures.

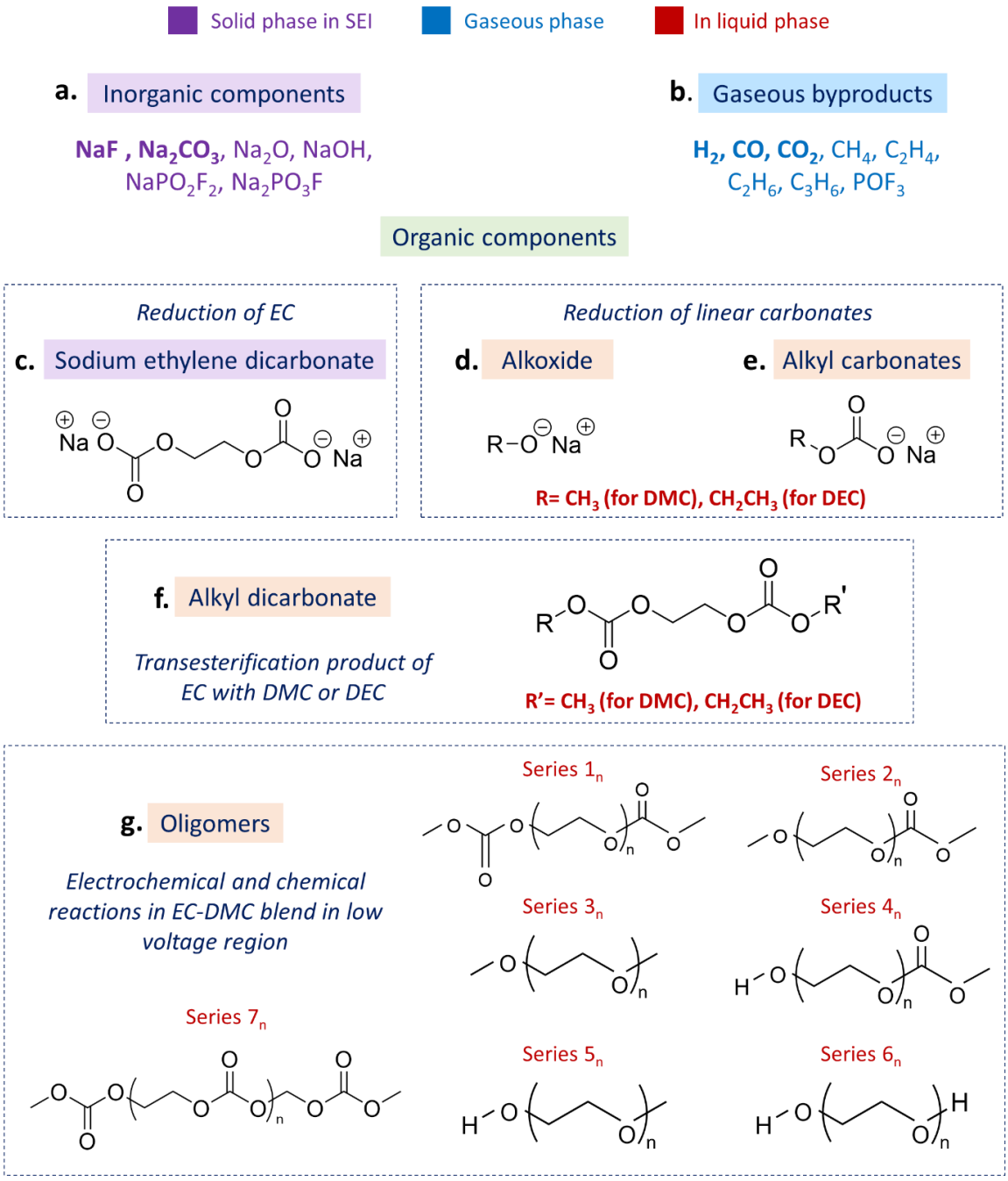

Fig. 1.18 | Summary of major byproducts formed in-situ during parasitic reactions in a full cell. (a) Inorganic components. (b) Gaseous byproducts. (c) Formation of sodium ethylene dicarbonate by EC reduction. (d) Formation of alkoxide and (e) alkyl carbonate by reduction of linear carbonate. (f) Alkyl dicarbonate as a transesterification byproduct as a cross-talk reaction between linear and cyclic carbonate. (g) Oligomers formed as a chemical and electrochemical reaction between linear and cyclic carbonate. Note that alkoxides, alkyl carbonates, and alkyl dicarbonates are solid salts but exhibit solubility in the electrolyte, thus illustrated as being in a liquid phase. The information has been summarized from the collection of references.[80,133,134,137–141,143]

The presence of strong Lewis acid PF_5 tends to initiate a series of reactions such as ring-opening polymerization or cleavages of ester linkages[80] shown below:

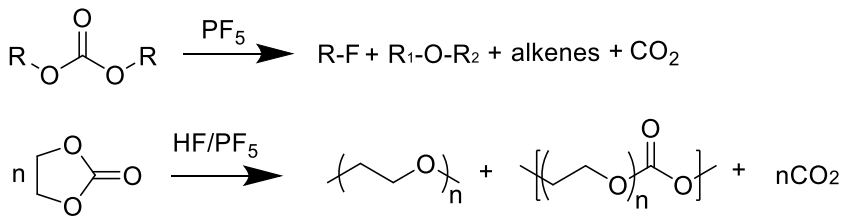

On the other hand, P-F bond is rather labile towards hydrolysis, even trace amounts of moisture in non-aqueous solvents produce a series of corrosive products[80,142] such as HF and POF_3.

$$NaPF_6(sol.) + H_2O \rightarrow NaF(s) + 2HF(sol.) + POF_3(sol.)$$

$$PF_5(sol.) + H_2O \rightarrow 2HF(sol.) + POF_3(sol.)$$

The corrosive HF and POF_3 create cascaded reactions, which are omitted here for the sake of simplicity.

2. An additional set of significant reactions occur during the reduction of cyclic carbonate (EC) and linear carbonate (DMC or DEC) solvents in the presence of $NaPF_6$ at the negative electrode. These reactions result in the formation of the SEI and other byproducts. **Fig. 1.18a-b** illustrates the inorganic compounds and gaseous products that are generated. In a mixture of EC-DMC, it has been observed that EC is susceptible to reduction before DMC.[80,133,144] The reduction of EC yields sodium ethylene dicarbonate (**Fig. 1.18c**) and Na_2CO_3, both of which are solid components critical to the SEI.[145] Furthermore, the reduction of linear carbonates leads to the formation of alkoxides (R-ONa) (**Fig. 1.18d**) and alkyl carbonates (R-O-COONa) (**Fig. 1.18e**).[146] EC and DMC can undergo cross-reactions, resulting in the production of alkyl dicarbonates (**Fig. 1.18f**) through a process known as "trans-esterification."[147] This trans-esterification product chemically reacts with the alkoxides (R-ONa), leading to the formation of various oligomeric species (**Fig. 1.18g**).[139] For comparison, the evolution of our knowledge about SEI is summarized[148] in **Supplementary Fig. S1.4**. It is important to note that while this

provides a simplified explanation of the major products, there are numerous side products and reactions involved.[134] The mechanism of these reactions remains a highly debated topic in the field. Some of these parasitic reactions contribute to the degradation of cell health.

3. Studying the chemical or electrochemical oxidation of the electrolyte on the positive electrode poses certain challenges. This is primarily because some of the reduced products formed on the negative electrode, such as alkoxides and alkyl carbonates, are prone to oxidation even before the pure electrolyte. For instance, Zhang et al. reported that Na_2CO_3, a residual impurity on the positive electrode material, can decompose before the electrolyte, generating CO_2 gas.[149] Similarly, Guochun et al. discovered that cycling NVPF|HC cells using electrolytes containing only linear carbonates (DMC, EMC, or DEC) resulted in overcharging in the first cycle and cell failure within five cycles due to parasitic oxidation of "sodium alkoxide" on positive electrode formed by the reduction of linear carbonates on negative eletrode[146] (refer to **Fig. 1.18g**). This is discussed in detail in **section 3** of **chapter 2**. In order to investigate the electrolyte oxidation process, Grey et al. conducted experiments where the $LiPF_6$ in EC-DMC electrolyte was oxidized on a Pt electrode in an H-type cell, where the positive and negative electrode compartments were separated. They observed a variety of oxidation products, including CO_2, lithium methyl carbonates, methanol, formaldehyde, glycolic acid, VC, FEC, and other products[150] (summarized in **Supplementary Fig. S1.5**).
4. The understanding of the CSEI on the positive electrode is even more limited compared to the SEI. Surprisingly, the CSEI layers formed on the positive electrode primarily consist of decomposition products of solvents and salts, which are similar to those found on the negative electrode.[134] It has been proposed that cross-talk reactions or migration of byproducts from the anode contribute to this phenomenon. The CSEI primarily contains inorganic and organic species, with key components including NaF, $Na_xPO_yF_z$, and Na_2CO_3, as well as some polycarbonates and alkyl carbonates, among others. For comparison, the investigation and development of the CSEI for lithium-ion batteries is summarized in **Supplementary Fig. S1.6**.[148]

4.4 Interphases of Li-ion vs. Na-ion batteries

Even though the same carbonate ester solvents and PF_6-based salts are used in LIBs and NIBs, the difference in the behavior is observed because of the physiochemical differences (ionic size, cationic solvation, reactivity, etc.) between Li^+ and Na^+. These differences are studied in this section.

4.4.1 Solvation behavior

Na^+ has a larger radius (102 pm) than Li^+ (76 pm), resulting in lower charge density and weaker Lewis acidity. This leads to a different coordination behavior with other atoms/molecules in the solution. DFT simulations show Li^+ having a well-defined first solvation shell with coordination number ~4 in carbonate solvents, while larger Na^+ exhibits more flexible solvation structures with coordination number ~5.7 (**Fig. 1.19a-d**).[151] Xu et al.'s combined IR and Raman measurements also support similar solvation behavior.[152]

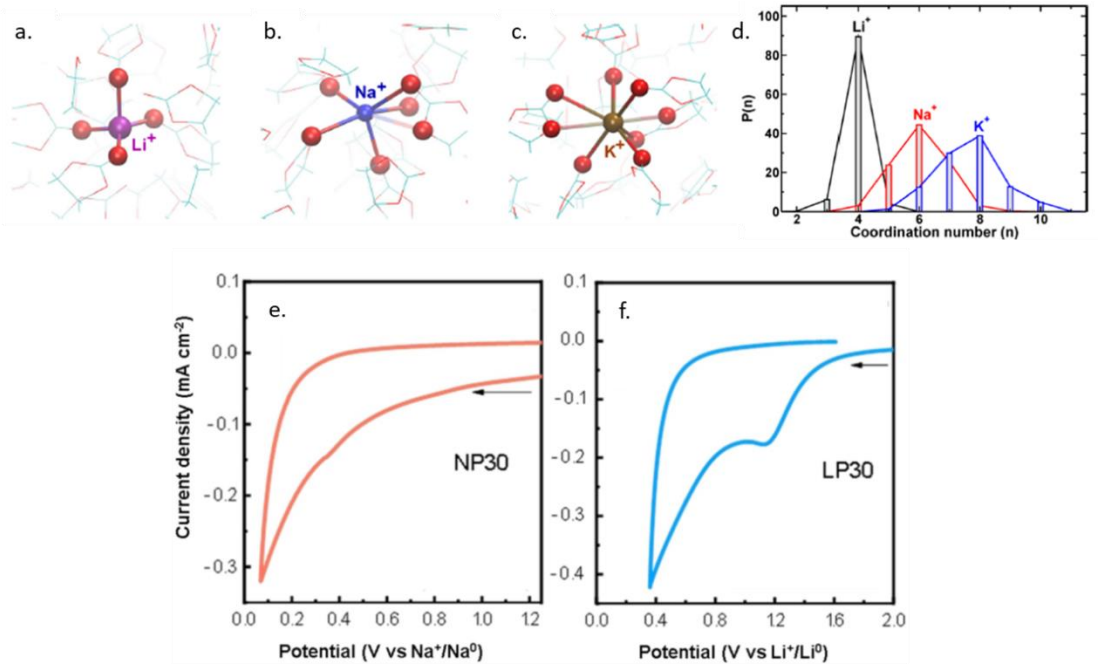

Fig. 1.19 | Effect of solvation structure on electrolyte reduction. Scheme representing the solvation structures of a) Li^+ and b) Na^+ c) K^+ derived from molecular dynamic simulations showing tetrahedral (CN=4) and trigonal bipyramidal/square pyramidal (CN=6) coordination for Li^+ and Na^+ respectively in EC solvent. d) Histograms of the coordination number in the first solvation shell. Cyclic voltammetry at a rate of 0.1 V/s for (e) NP30 and (f) LP30 electrolytes, a glassy carbon disk working electrode, and a Pt counter electrode are used. The reference electrode

potential (Ag/Ag+) is converted to Na^+/Na^0 or Li^+/Li^0 based on the open circuit potential (OCP) measured against Na or Li metal. Reproduced from our review paper.[153]

Due to the stronger coordination of Li^+ to EC compared to Na^+, the carbonyl group in EC of LP30 (1M $LiPF_6$ in EC-DMC) will be more electron deficient than in NP30 (1M $NaPF_6$ in EC-DMC). This makes EC more prone to electrochemical reduction in LP30 than in NP30. Sathiya et al. confirmed this with cyclic voltammetry (CV) of LP30 and NP30 at the same reduction potential vs. SHE. LP30 showed a distinct peak (**Fig. 1.19f**) corresponding to EC reduction, while NP30 showed no well-defined peak (**Fig. 1.19e**), indicating a lesser extent of EC reduction.[153] Thus, the SEI components will differ significantly between NP30 and its Li^+ counterpart.

4.4.2 SEI components and solubility

The nature of the SEI in NIBs is influenced by factors other than just their different solvation behaviors. One such factor is the variation in the reduction potentials of Na and Li (-2.71 V vs. SHE compared to -3.02 V vs. SHE for lithium). In carbonate solvents (EC/DEC mixture), most of the reduced products occur at <0.2 V vs. Li/Li^+ (<-0.1 V vs. Na/Na^+), which cannot happen in NIBs. Komaba et al. investigated the differences in SEI between Li and Na-HC cells with perchlorate electrolyte using X-ray photoelectron spectroscopy (XPS) and time-of-flight secondary ion mass spectrometry (TOF-SIMS).[63] Note the multiple peaks in the TOF-SIMS results (**Fig. 1.20**) for Li-based SEI and very few peaks in Na-based SEI. SEI layer in the Na cells consisted mainly of inorganic compounds (NaOH, NaF, NaCl, Na_2O, Na_2CO_3), while the SEI layer in the HC from the Li cell contained a mix of inorganic and various organic compounds such as alkoxide, alkyl carbonate, and polymers. Additionally, the SEI layer in NIBs was found to be thinner and less homogeneous than in LIBs.

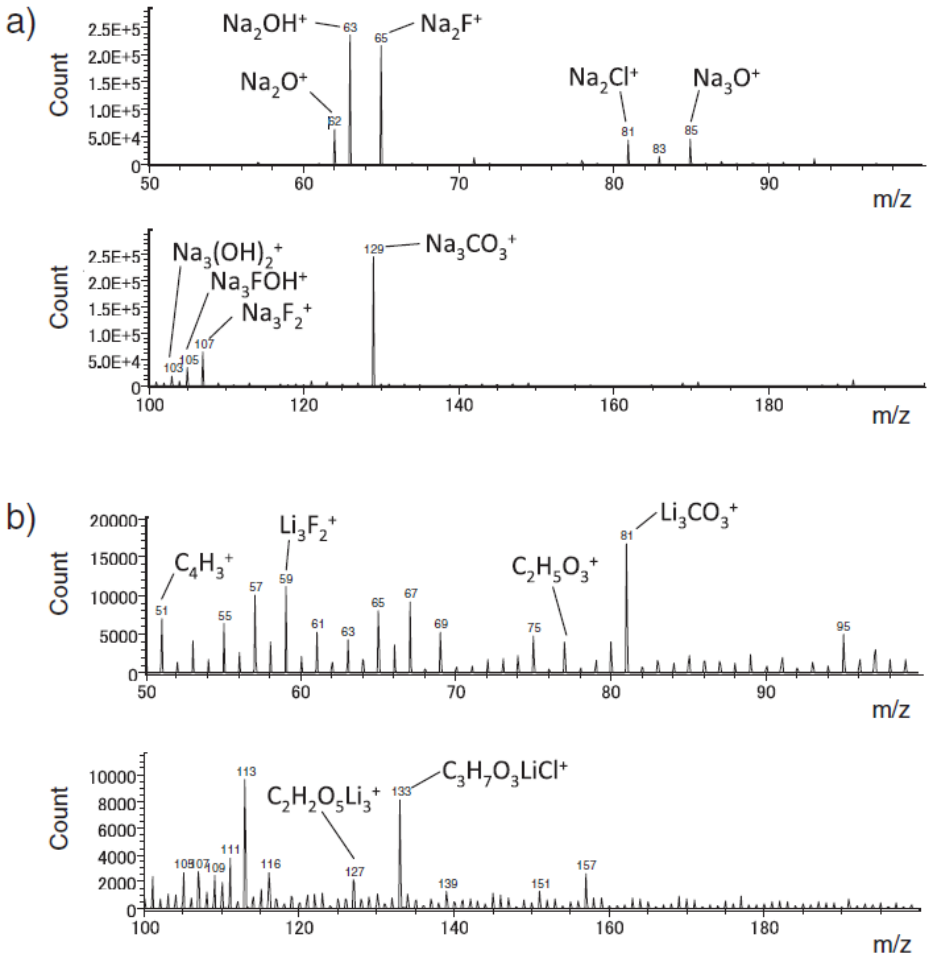

Fig. 1.20 | Difference between chemical components of Na vs Li-based SEI. TOF-SIMS profiles of cycled HC electrodes in (a) Na and (b) Li cells in perchlorate based electrolyte. Multiple peaks corresponding to multiple SEI species are observed when HC is cycled in a Li-based electrolyte as opposed to Na Na-based electrolyte. Reproduced from Komaba et al.'s paper.[63]

Supporting similar behavior, Younesi et al. studied the solubility of SEI in Na electrolytes and found differences compared to Li-based SEI in terms of columbic efficiency and self-discharge rate.[154] **Fig. 1.21a-b** illustrates the charge-discharge capacity of HC electrodes in Li and Na cells after pausing for different periods. Na cells experienced a larger capacity loss than Li cells, with large voltage rise in **Fig. 1.21c-d** attributed to the pronounced SEI dissolution of Na-based SEI. HAXPES measurement supported the SEI thickening during the next charges. Recent solubility measurements (**Supplementary Table S1.3**) by Ma et al.[155] further confirm the high solubility of

NaF and Na_2CO_3 as compared to LiF and Li_2CO_3. To conclude, Na-based SEI is more fragile than Li-based SEI in terms of chemical nature and solubility.

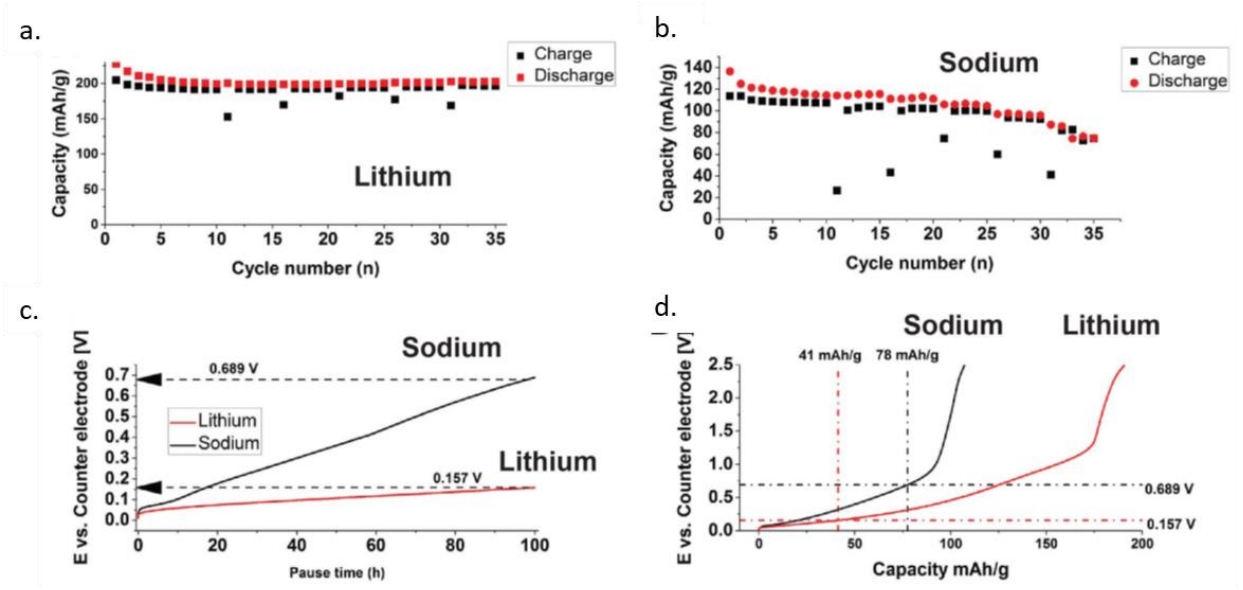

Fig. 1.21 | Effect of SEI solubility on electrochemical performance. a) Cycling performance of Li cells and b) Na cells with different pausing times during cycling. c) Comparison of Na and Li cell voltage profiles at different pausing times. d) Comparison of capacity loss after 100 h pausing. Reproduced from Younesi et al.'s paper.[154]

4.4.3 Importance of CSEI

As components of CSEI are similar to those of SEI, therefore based on the discussion in the last section, Na-based CSEI will be more soluble than Li-based CSEI. Additionally, due to the 0.33V difference in reduction potential of Na and Li (represented in **Fig. 1.22a**), electrolyte facing Na-based positive electrode at (x)V vs. Na/Na^+ will be equivalently at (x+0.33)V vs. Li/Li^+. **Fig. 1.22b** shows the profile of NVPF and NVP in NIBs with the reference electrode potential of Na/Na^+ on the left axis and equivalent converted Li/Li^+ potential on the right axis. The NVPF electrode going to 4.35V vs. Na/Na^+ (in **Fig. 1.22b)** is equivalently at 4.68V vs. Li/Li^+. From our knowledge of LIBs, it is well known that electrolyte oxidation starts as low as 4V vs. Li/Li^+. Thus, such high potential will lead to severe electrolyte oxidation[80,156]. Therefore, engineering a good CSEI on NVPF is going to be a crucial challenge, especially at high temperatures.

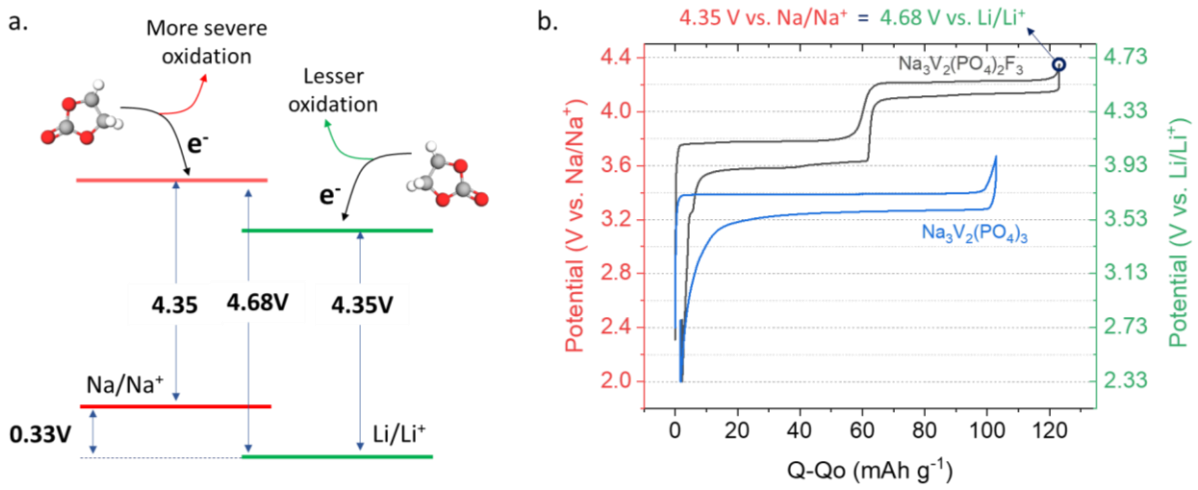

Fig. 1.22 | Sever oxidation in case of NIBs. (a) Difference of redox voltage between Na/Na^+ and Li/Li^+. More electrolyte oxidation will happen at the positive electrode with the same half cell potential in NIBs and LIBs. (b) The electrochemical profile of NVPF and NVP in NIBs is shown with the additional equivalent axis of Li/Li^+ potentials on the right.

5. Conclusions of the chapter

The first chapter of this study aimed to elucidate the crucial steps involved in the evolution of the modern-day status of NIBs, which were significantly influenced by the development of LIBs. Although the research on LIBs and NIBs was initiated around the same period, the commercial potential of NIBs was overshadowed by the lower energy density of NIB electrodes and the absence of a suitable negative electrode until 2000. In contrast, LIBs became an indispensable part of electronic devices, and their prices decreased annually until they reached saturation. The surge in demand for energy storage, the limited availability of lithium resources, the associated supply chain challenges, and the less sustainable nature of LIBs led to renewed interest in NIB research after 2010.

The commercial viability of NIB technology hinges on the selection of the appropriate negative electrode, positive electrode, and electrolyte. The current chapter expounds upon several potential negative electrode materials, but it highlights the practical readiness and attractive features (cost, stability, energy density, etc.) of hard carbon (HC), thanks to the research done over the previous decades. For the positive electrode material, layered oxides, Prussian blue analogues (PBAs), and polyanionic compounds are three promising options. A

critical comparison of Layered oxides, PBAs, and polyanionic compounds is presented, showing the advantages and limitations of each. The NVPF|HC, with its superior rate capability, long cycling stability at ambient and high temperatures, and easy handling of raw materials, seems to be more appropriate for the first generation of NIBs than layered oxides and PBAs. After meticulous analysis, the NVPF|HC cell system is chosen as the central point of study for the thesis. Although, the previous work on electrolyte achieve high stability in coin cells, those electrolytes were not transferable to practical 18650 type cells. Therefore, this thesis focuses on enhancing high-temperature performance in practical 18650 cells, as well as improving the overall longevity and performance of NVPF|HC cells.

Cell lifetime and performance can be significantly improved by electrolyte manipulation. Thus, the last section of this chapter discusses the properties of electrolytes and introduces the concept of the interphase, specifically solid electrolyte interface (SEI) on negative electrode and cathode solid electrolyte interface (CSEI) on positive electrode, and its enigmatic nature. Although NIBs use similar salts and solvents as LIBs, the interphase varies significantly due to the different chemical properties of Li^+ and Na^+ and the compounds formed from them. The high solubility of SEI and CSEI components produces less passivating interphases in NIBs, presenting a significant challenge. Hence, the strategies employed for LIBs may not necessarily translate to NIBs. After understanding the essentials of Na-ion cell chemistry, the next chapter will introduce techniques to analyze cell (or electrode, electrolyte, and interphase) degradation and then summarize previously done degradation studies on NVPF|HC chemistry.

Chapter 2 | Introducing battery diagnosis toolbox and exploring $Na_3V_2(PO_4)_2F_3$|HC electrochemistry.

1. Transferrable knowledge from Li-ion to Na-ion battery system for evaluating the cell degradation

As explicated in the preceding Chapter, the battery functions as an electrochemical device employed for the storage of energy. The measure of storable energy (E) within a battery can be expressed as the product of its capacity (Q) and the average voltage (V_{av}). However, the presence of undesired parasitic reactions within the cell contributes to the gradual deterioration of either capacity, voltage, or both, leading to a decline in the overall storable energy.[157] Furthermore, this reduction in storable energy is accompanied by a simultaneous degradation of various performance parameters, such as rapid charging capabilities, self-discharge rates, operability across diverse climatic conditions, and safety aspects.[157–159]

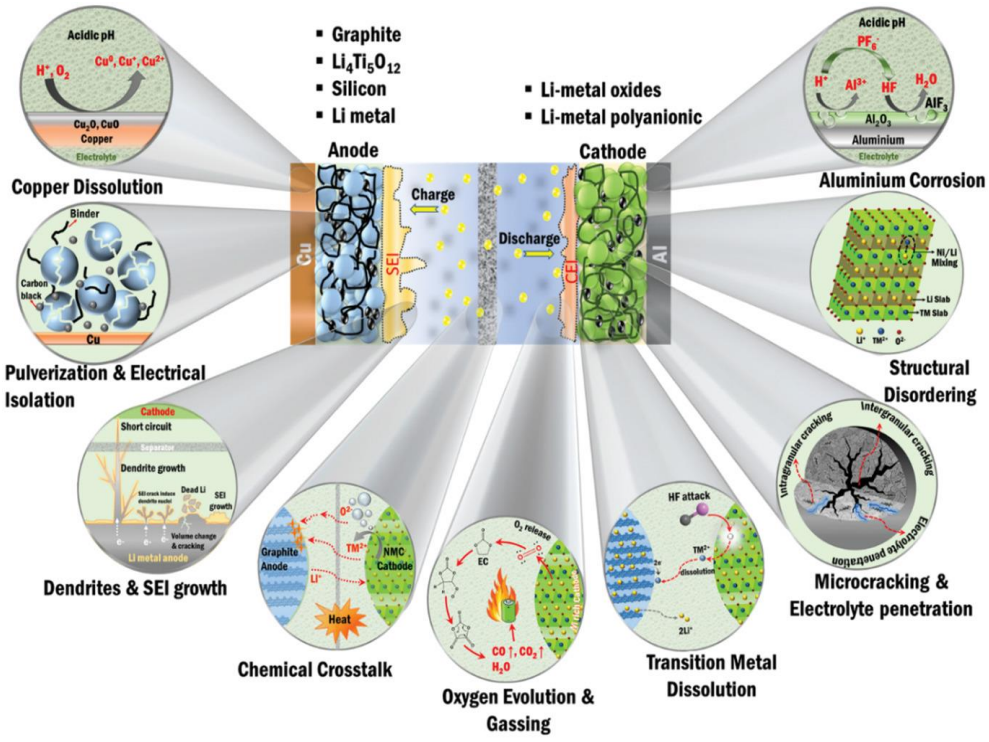

Fig. 2.1 | Overview of the major degradation mechanisms in Li-ion batteries. Reproduced from Dominko et al.'s paper.[160]

Extensive research on lithium-ion batteries (LIBs) has identified degradation modes that can be categorized into several categories (**Fig. 2.1**). These categories[157–159] include active material degradation (e.g., particle cracking, pulverization, structural disordering, transition metal dissolution, oxygen evolution), electrolyte decomposition (e.g., electrolyte oxidation and

reduction, (electro)chemical cross-talk), interphase dissolution/growth, and other cell component degradation (e.g., aluminum/steel corrosion, separator contamination, binder/carbon black oxidation, etc.). The interconnected nature of the electrochemical cell often results in the degradation of one component, triggering the degradation of others. For instance, particle cracking induces increased electrolyte oxidation, forming a new interphase on the particle, while transition metal dissolution contaminates the solid-electrolyte interphase (SEI) and enhances electrolyte instability. Notably, certain degradations like copper (Cu) dissolution are not applicable to sodium-ion batteries (NIBs) as Cu is not used as an anode current collector, this will be discussed in detail in **Chapter 6**.

The cell degradation pathways extensively studied in LIBs cannot be directly applied to NIBs for two reasons. Firstly, the different chemistry of Na^+ leads to issues like poor SEI solubility and aggressive electrolyte oxidation (discussed in **Chapter 1, section 4.4**). Secondly, the dominant mode of cell degradation is highly sensitive to the system and can change when a component or its nature is altered. However, the most critical electrochemical methodologies and approaches utilized to analyze cell degradation can be learned from a vast database of LIB studies and effectively applied to NIBs, as summarized in **Fig. 2.2**.

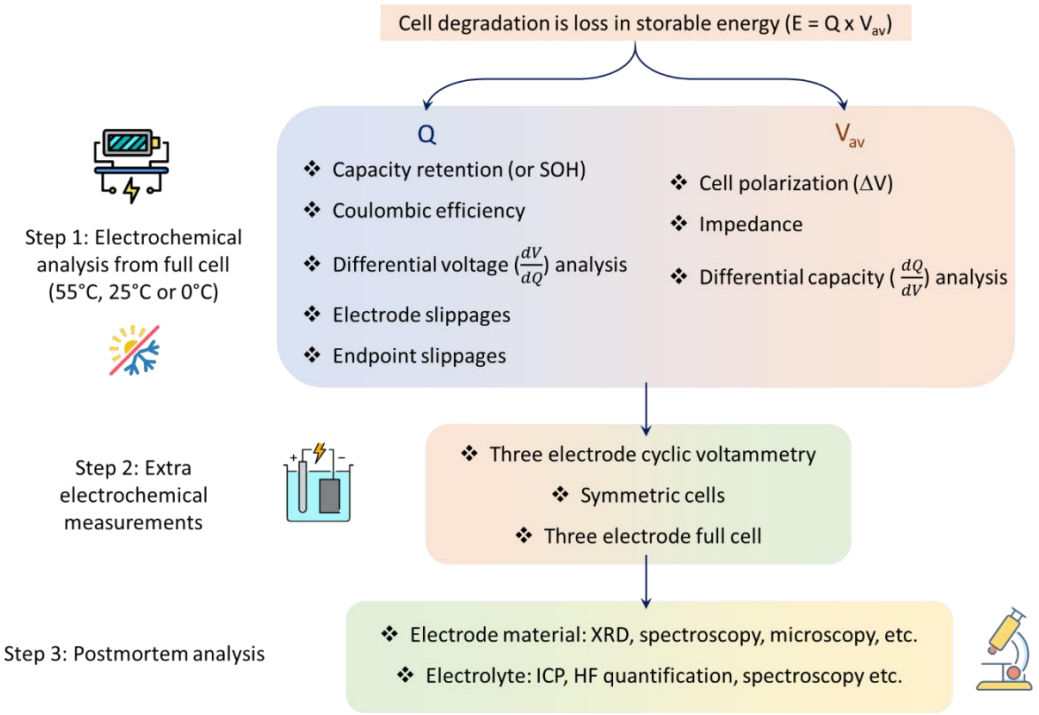

Fig. 2.2 | Workflow of different electrochemical measurements and analysis to understand cell degradation.

Thus, the present Chapter applies a "bottom-up" approach[161], looking at how degradation at positive (+ve) and negative (-ve) electrodes will affect the full cell curves. Schematics are used throughout the Chapter to visualize the impact of degradation on the full cell profile. The complementary "top-down" approach[161] that starts from the tracking of full cell curves and connects the changes there to the degradation of +ve and -ve electrodes is discussed together with the related examples from literature provided in **Supplementary Information** of **Chapter 2**.

2. Cell degradation analysis toolkit

2.1 Electrochemical analysis from the full cell

2.1.1 Understanding cycling curves

The most common technique to (dis)charge the battery is galvanostatic cycling with potential limitation (GCPL).[162] In the GCPL (refer to **Fig 2.3a**), the constant current I is applied to charge a cell till the voltage V_2, then the cell is discharged with negative current $-I$ till the voltage limit of V_1. Voltage-time response (in **Fig 2.3b**) full cell is measured using a galvanostat giving typical charge/discharge curves.

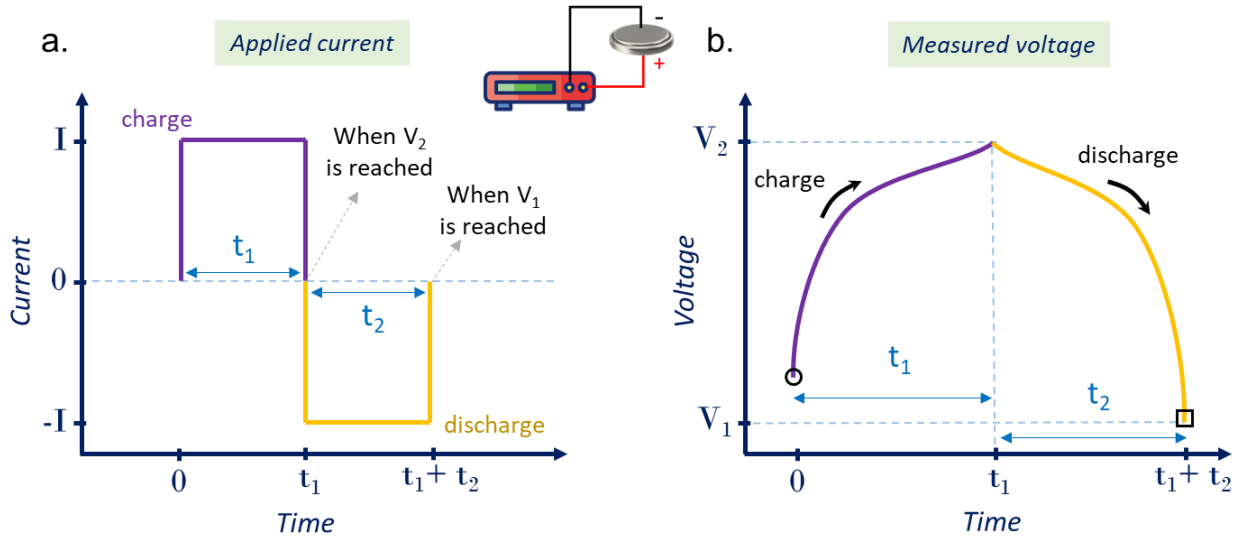

Fig. 2.3 | Galvanostatic cycling of a cell. Schematic representation of (a) Current vs. time profile for a GCPL method. (b) Corresponding voltage vs. time response of the typical cell when the GCPL technique is applied.

The voltage-time (**Fig 2.3b**) response can be converted to voltage-capacity curves (**Fig 2.4a**) by linearly converting the time scale into the capacity scale (as Q = I x time). The amount

of capacity achieved during charge and discharge is Q_2 and Q_2-Q_1, respectively. In reality, the observed full cell voltage response is the difference between positive and negative electrode potentials ($V_{full\ cell} = V_+ - V_-$), as shown in **Fig. 2.4b**. It is important to note that, in practical commercial cells, we only measure the full cell curves when we cycle a cell. However, the following sections will discuss how we can still get information about both the +ve and -ve electrodes from these full cell curves.

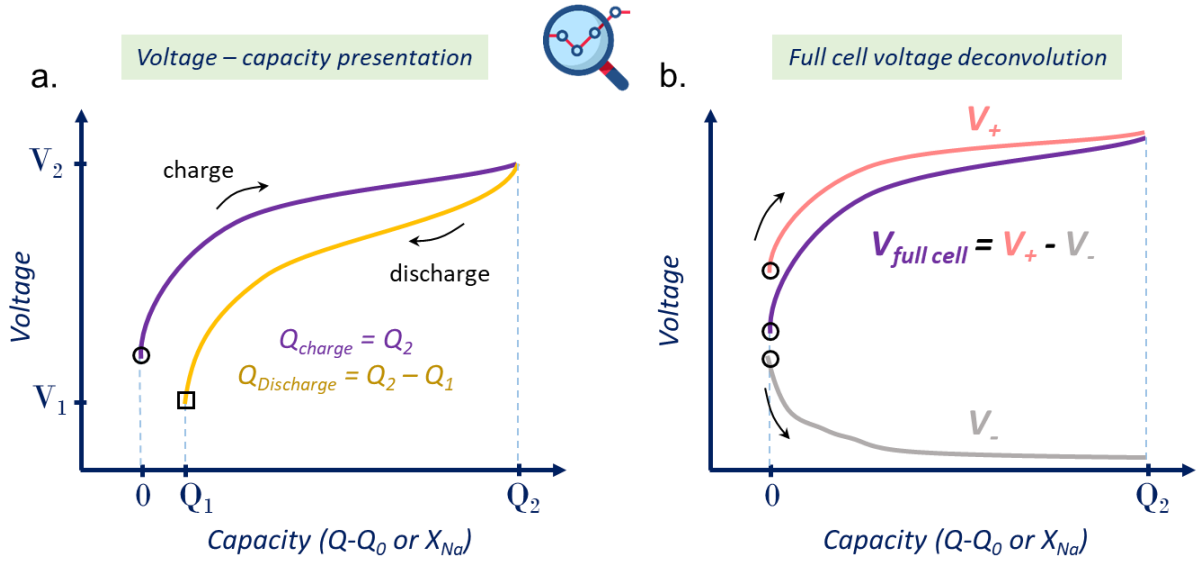

Fig. 2.4 | Understanding voltage vs. capacity curves. Schematic representation of V-Q curves. (a) Voltage vs. capacity of a typical full cell curve. (b) Voltage vs. capacity of full cell with the deconvolution of +ve and -ve electrode profiles.

2.1.2 First cycle or formation cycle

When the assembled cell is cycled for the first time (also known as the formation cycle), the interphases are formed on the electrodes. In an ideal cell (**Fig. 2.5a**), there will be no capacity loss during the first and the consequent cycles ($Q_{charge} = Q_{discharge}$). However, in an actual cell (**Fig. 2.5b**), there is irreversible capacity loss (or $Q_{charge} > Q_{discharge}$) due to interphase formation and loss of active inventory in terms of Na-based compounds in SEI. The cycling curves for the real cell (**Fig. 2.5b**) are deconvoluted in terms of +ve and -ve electrode potentials (**Fig. 2.5c**).

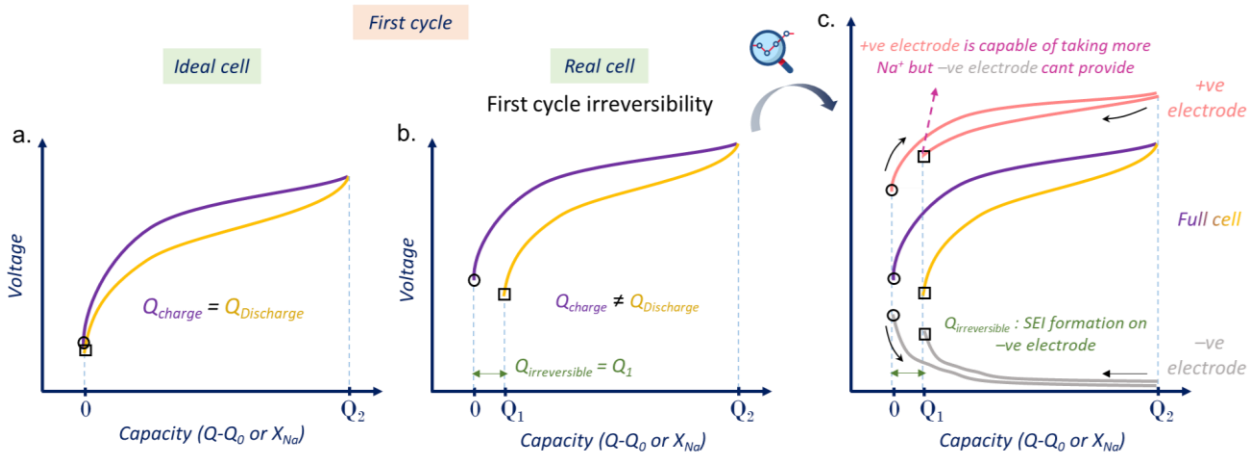

Fig. 2.5 | Visualizing first cycle capacity loss in practical cells. Schematic representation of first cycle capacity loss. (a) Voltage vs. capacity representation of an ideal full cell for the first cycle. (b) Voltage vs. capacity representation of a real full cell for the first cycle. (c) Voltage vs. capacity representation of a real full cell for the first cycle with the deconvolution of +ve and -ve electrode profiles. Note that the battery capacity is limited by cathode capacity.

Few reports suggest that there is an irreversible loss of Na^+ (or Li) inventory for the positive electrode (**Supplementary Fig. S2.1**), which can be divided into recoverable (kinetically hindered) and irreversible (electrolyte decompositions) parts.[163] **Supplementary Fig. S2.2** shows that most of the capacity loss of the first cycle for well-known positive electrodes like LFP, LCO, LNMO, and NMC half cell is recoverable and not due to parasitic reactions.[163] On the contrary, it is well established that the first cycle capacity loss on the negative electrode is irreversible and is caused by electrolyte reduction and forming SEI layer by consuming active Na^+ inventory in terms of Na_2CO_3, NaF, NaOR, etc. or irreversible Na^+ trapping in pores.[62,164] To summarize (see text on **Fig. 2.5c**), in a well-balanced practical cell (with N/P ratio=1.05-1.15), the irreversible capacity loss is mainly caused by SEI formation on the negative electrode, not by parasitic reactions on the positive electrode.

2.1.3 Coulombic efficiency and capacity retention

The irreversible capacity loss during any "***single cycle***" is better represented by the term known as coulombic efficiency (CE).[165,166] CE is the ratio of charge by discharge capacity and is defined as

$$CE\ (\%) = \frac{Q_n^{dis}}{Q_n^{ch}} \times 100 \qquad \text{Equation 2.1}$$

Where Q_n^{dis} and Q_n^{ch} represents the discharge and charge capacity of the nth cycle, respectively.

Another important term that tracks the capacity loss over "***multiple cycles***" is capacity retention (CR), also known as the state of health (SOH)[165–167] and defined as

$$CR\ (\%) = \frac{Q_n^{dis}}{Q_1^{dis}} \times 100 \qquad \text{Equation 2.2}$$

Where Q_n^{dis} and Q_1^{dis} represents the discharge capacity in the nth and 1st cycles, respectively.

Fig. 2.6 shows CE and CR development of typical cells as a function of cycle number. The first cycle CE is low due to capacity loss due to SEI formation. Note that the variations of CE and CR can be divided into two regions. In Region-I, CE rapidly increases, and CR rapidly decreases due to more Na^+ inventory loss required for forming stable interphases and/or electrode degradations (particle cracking, precursor impurities, absorbed moisture, etc.). In Region-II, the CR decreases at a slower rate, and CE stabilizes to a particular value. These behaviors can be observed throughout the literature (refer to **Supplementary Fig. S2.3-S2.6**). Additionally, as CE/CR parameter reflects Na (or Li) inventory loss, it is naturally highly sensitive to the nature of electrodes, electrolyte, C-rate, potential window, and the operational temperature (Supplementary **Fig. S2.7-S2.8**).[165,166]

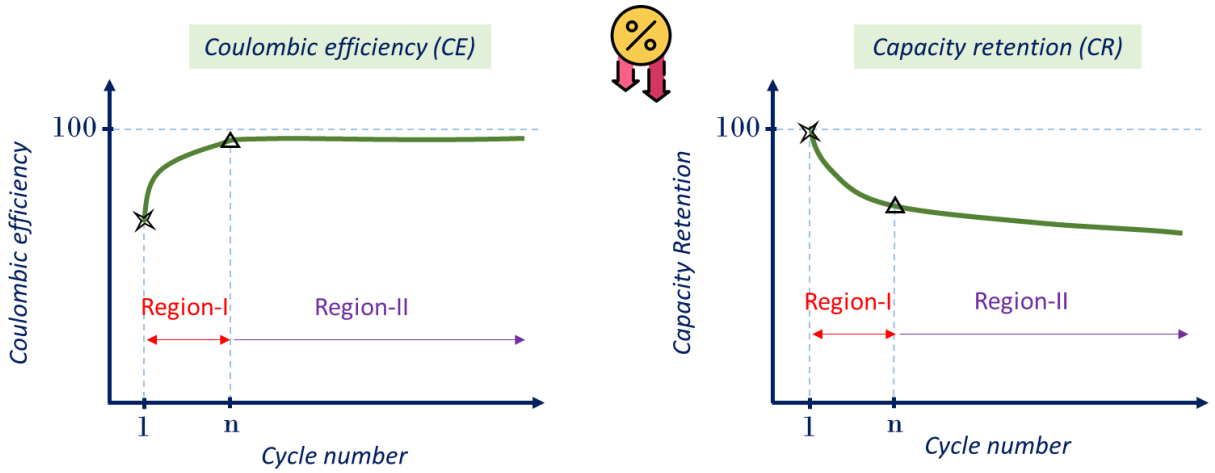

Region-I : CE rapidly increases and CR rapidly decrease. SEI formation and stabilization in initial n cycles.

Region-II : CE stabilizes and CR decreases at slower rate. SEI stabilizes with other active degradation modes.

Fig. 2.6 | CE and CR variation in typical cells. Schematic representation of (a) Coulombic efficiency (%) vs. cycle number for a typical full cell. (b) Capacity retention (%) vs. cycle number for the same cell shown in (a).

Intuitively, **Fig 2.6** gives the impression that CE (irreversibility in a single cycle) and CR (capacity loss over multiple cycles) can be related. This is calculated using the conventional method[168–170] (**Equation 2.3**), where n is the cycle number.

$$\left(\frac{CR}{100}\right) = \left(\frac{CE}{100}\right)^{n} \qquad \text{Equation 2.3}$$

For example, in order to achieve 500 stable cycles with over 80% capacity retention, the *average* CE would need to exceed 99.95%, as shown in **Fig. 2.7**. This idea was exploited by Smith et al. by designing high precision charger (HPC)[171,172] which measures CE on the scale of at least ± 0.01%. These HPC measurements can predict the battery's lifetime in weeks instead of years[173] of cycling trials (**Supplementary Fig. S2.9**).

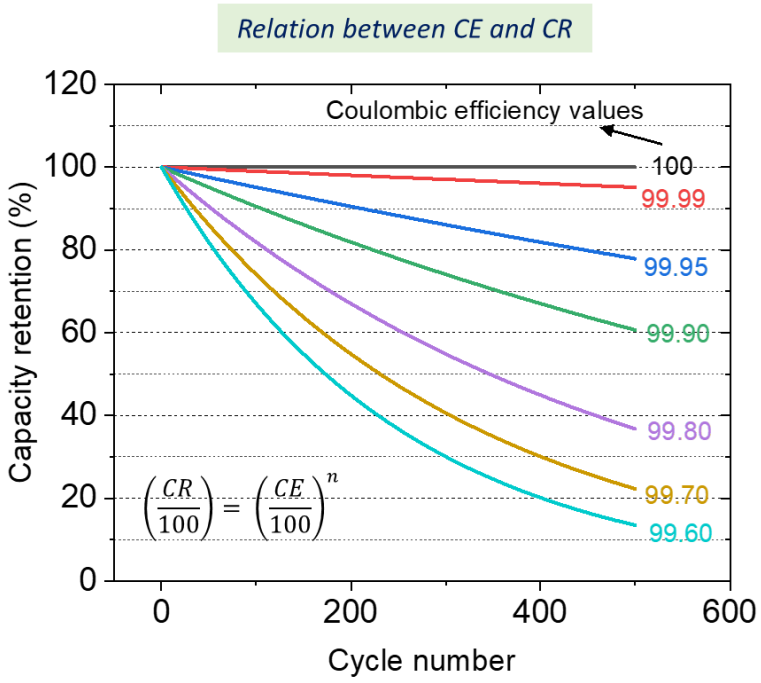

Fig. 2.7 | Relationship between CR and CE represented by the classic equation in the figure.

2.1.4 Cell polarization (ΔV)

When the current is applied to a cell, the voltage of the cell moves away from the open-circuit voltage (OCV) due to polarization arising from activation polarization, concentration polarization, and internal resistance of the cell (discussed in **Supplementary Fig. S2.10**).[174] When the cell degrades, this polarizations and mainly polarization due to the internal resistance

changes, which can be effectively tracked by calculating average voltage from V-Q profiles. The average voltage is capacity-weighted[175] and can be calculated by the equation below:

$$V_{av} = \frac{1}{Q_T} \int_0^{Q_T} V.dq \qquad \text{Equation 2.4}$$

Where V_{av} is the average voltage, Q_T is the total capacity, and the integral is the area under the V-Q curve of the full cell. The method is discussed systematically with a visual guide to grasp its importance from electrochemical curves.

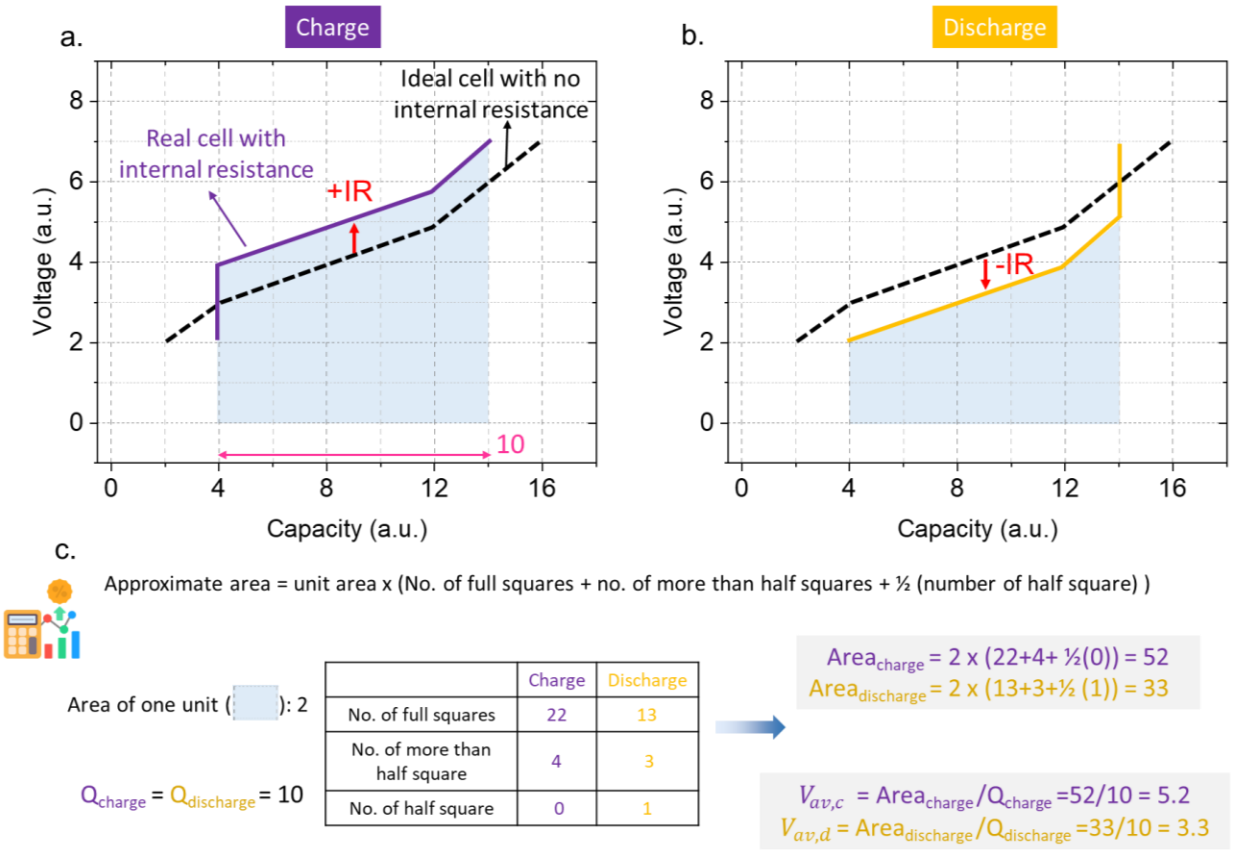

Fig. 2.8 | Schematic representation of internal resistance and average voltage calculations. (a) Charging curve of ideal cell and real cell with internal resistance. (b) Discharging curve of ideal cell and real cell with internal resistance. The area under the curve is highlighted (c) Method to calculate the shaded area in (a) and (b) by counting the small areal units.

Fig. 2.8a shows an ideal cell with no resistance and a real cell with internal resistance R, causing the curve to shift upwards due to ohmic polarization of IR during charge, similarly for discharge in **Fig. 2.8b**. The area under the curve divided by the capacity is V_{av}. Capacity is 10 units

for both charge and discharge (refer to **Fig. 2.8a**). The area is calculated by the classical method of unit counting on graph paper, as described in **Fig. 2.8c.** Thus, the area of charge and discharge comes out to 52 and 33, respectively. Consequently, $V_{av,c}$ and $V_{av,d}$ comes out as 5.2 and 3.3 for charge and discharge, respectively. Note that the average voltage values lie in the middle of the voltage-capacity curve. It is worth noting that the area beneath the curve indicates energy. For charging, it represents the energy given by the potentiostat, while for discharging, it shows the energy provided by the battery. Therefore, the area trapped inside the charge-discharge curve gives the energy lost as heat.

In **Fig. 2.9a**, when the ohmic overvoltage (or IR) is intentionally increased, as a first consequence, the capacity is reduced from 10 (green) to 9.1 (blue) to 8.2 (pink) because the voltage endpoints are reached sooner. $V_{av,c}$ and $V_{av,d}$ are calculated as described (in **Fig. 2.8**) and tabulated in **Fig. 2.9b**. Secondly, $V_{av,c}$ increases, $V_{av,d}$ decreases and, as a consequence, the cell polarization parameter (defined as $\Delta V = V_{av,c} - V_{av,d}$) increases from 1.9 (green) to 3.1 (blue) to 4.1 (pink) (**Fig. 2.9b**). Note that the area encapsulated inside the V-Q curve increases with an increase in internal resistance, indicating more energy is lost as heat, decreasing the overall energy efficiency of the cell.

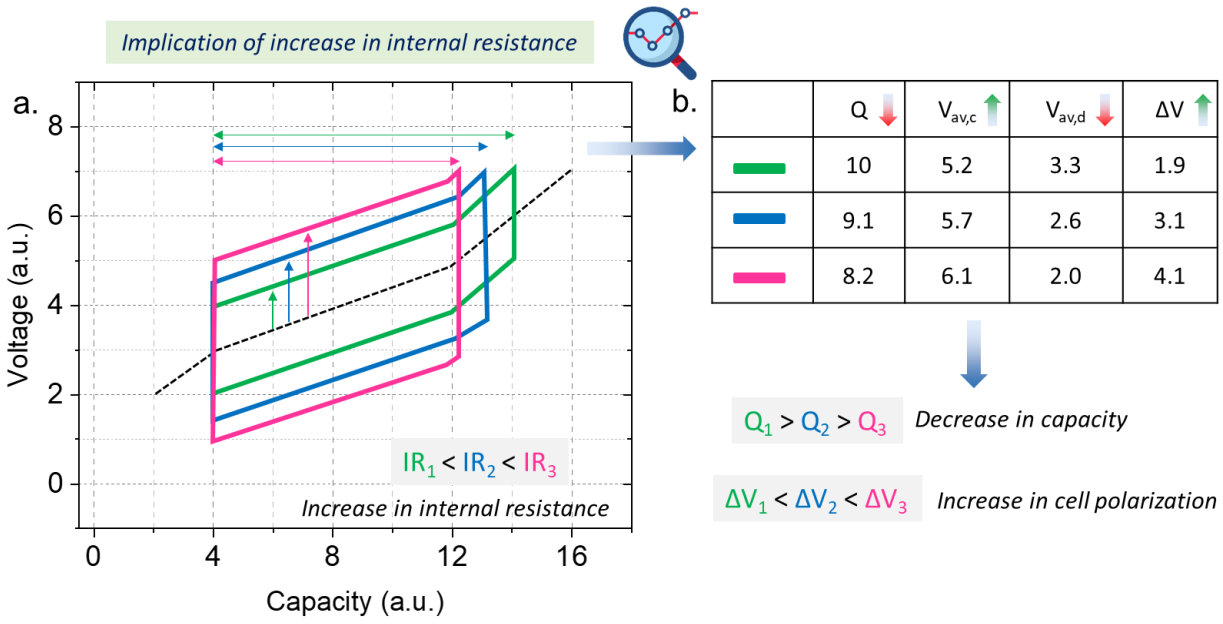

Fig. 2.9 | Illustration depicting the impact of escalating internal resistance within the cell. (a) Internal resistance is intentionally increased for three cells from green to blue to pink curves to understand its consequences. (b) Capacity, average voltages and polarization is tabulated for all three cells showing the trend in various parameters.

The trends in Q, V_{av}, ΔV discussed here is observed for most of the cells in literature. **Supplementary Fig. S2.11-13** discusses the average voltage and cell polarization development for different cell chemistries. Remarkably, by utilizing ΔV from charge-discharge curves alone without any additional measurements, it is possible to track the increase in cell impedance. Thus ΔV analysis is used in **Chapter 3** (**Fig. 3.15** and **Fig. 3.16**), **Chapter 4** (**Fig. 4.6**), **Chapter 5** (**Fig. 5.3-5**), **Chapter 6** (**Fig. 6.4, Fig. 6.9** and **Fig. 6.11**) of the main text of the thesis. However, ΔV cannot provide insight into the specific reasons behind the impedance increase, which can be better elucidated through techniques such as electrochemical impedance spectroscopy, as discussed in the subsequent section.

2.1.5 Electrochemical impedance spectroscopy

The importance of electrochemical impedance spectroscopy (EIS) lies in its ability to discriminate and provide a wealth of information for various electrical, electrochemical, and physical processes taking place in a real electrochemical system.[176] EIS does it by using perturbation signals of varying frequency and is systematically explained in subsequent text.

Fig. 2.10a illustrates the time-dependent input voltage perturbation signal, spanning from high to low frequency with time. The corresponding electrochemical current response is depicted as I vs. V in **Fig. 2.10b**. It is important to emphasize that EIS operates as a transfer function, thus requiring a linear relationship between the output current response and the input voltage perturbations[177]. **Fig. 2.10b** demonstrates that applying small-amplitude voltage perturbations is necessary to ensure this linearity. The transfer function defines the electrochemical impedance (Z = input v(t)/output i(t)), which is presented in the form of complex numbers in **Fig. 2.10c**. Electrochemical impedance is commonly depicted using a Nyquist plot ($-Z_i$ vs. Z_r), exhibiting characteristic semicircular features,[176,177] as depicted in **Fig. 2.10d**. Each feature corresponds to specific processes, allowing for the probing of fast processes in the high-frequency region and slow processes in the low-frequency region,[176,177] as demonstrated in **Fig. 2.10d**. EIS measurements are fitted using equivalent circuits with a combination of resistors, capacitors, inductors, etc. Fitting EIS spectra with analog circuits reveals crucial information about resistances, capacitance, and time constants (τ) corresponding to the different cell processes.[176,177]

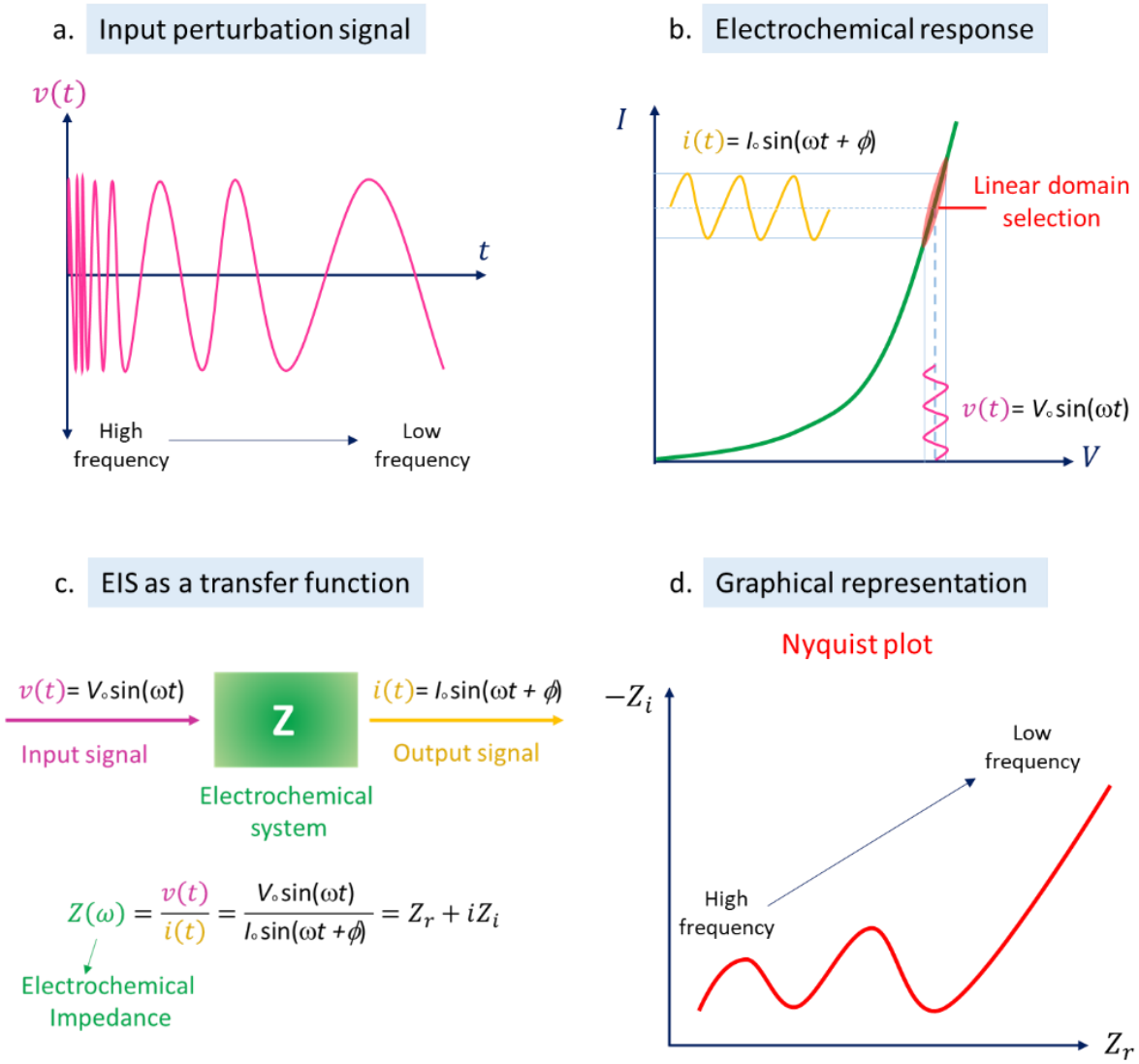

Fig. 2.10 | Basics of an EIS measurement. a) Input voltage perturbation as a function of time (b) Output current signal from the electrochemical system, which is carefully adjusted to linear region by using small voltage perturbations. (c) Mathematical treatment of the input and output signals as a transfer function or electrochemical impedance. (d) Nyquist plot representation of electrochemical impedance with marked high to low frequency region.

Although EIS contains transport information related to all the processes happening in the cell, the signals of a few processes are often merged together[176] as shown in **Supplementary Fig. S2.14**. Thus, transport properties of electrolyte, separator, and electrode have to be extracted from designing different types of experiments. For example, changing cell components from steel to aluminum to identify the position of contact impedances semicircle[178] (**Supplementary Fig. S2.15**), comparing blocking vs. non-blocking electrode configuration to identify the location of

charge transfer semicircle[178] (**Supplementary Fig. S2.16**), taking impedance at various temperatures to separate charge transfer[178] (**Supplementary Fig. S2.17**), assembling symmetric cells to separate +ve and –ve electrode impedance evolution[179–181] (**Supplementary Fig. S2.17**). Therefore, after correctly relating all the semicircular peaks in the Nyquist plot to cell processes, the evolution of the peaks over the cycling period will give crucial information about the degradation mode (example of LCO|graphite cell in **Supplementary Fig. S2.18**), which was not possible by calculating only cell polarization ΔV.

Table 2.1 outlines the influence of various degradation modes that can contribute to the degradation of electrical and ionic transport. EIS is a valuable tool for monitoring electronic and ionic transport, enabling a comprehensive investigation of the effects of these degradation modes on impedance and other kinetic transport properties.[182] In conclusion, by careful simplification, EIS can be a valuable tool for analyzing basic transport properties and identifying the causes of cell degradation. Both of which are critical in ensuring optimal performance and superior cell life. Thus, EIS analysis is effectively utilized in **Chapter 5, Section 2.5,** and **Chapter 6, Section 2.2.2**.

Cause	Effect
Electrolyte decomposition	○ Loss of alkali metal
Interphase formation and growth	○ Loss of alkali metal
Binder decomposition	○ Loss of alkali metal ○ Loss of active electrode material
Particle contact loss	○ Loss of active electrode material
Changes in electrode porosity	○ Increasing resistance for Na^+ movement
Changes in separator porosity	○ Increasing resistance for Na^+ movement
Current collector corrosion	○ Loss of electric and mechanical contacts

Table 2.1. | Different cell degradation modes and their effects will lead to deterioration of ionic and electric transports.

2.1.6 Introducing simulated positive and negative electrodes

Until this point in the Chapter, schematic curves are used to discuss different phenomena. However, for better visualization of certain phenomena like mass loss, electrode slippages, dQ/dV, and dV/dQ analysis, the simulated electrode curves are being introduced. **Fig. 2.11a** shows the simulated half cell curves of the +ve electrode (Q =183 mAh/g) and –ve electrode (Q =202 mAh/g). These curves are randomly created such that when assembling full cell, with equal mass loading of +ve and –ve electrode active material, an N/P ratio[183,184] of 1.1 is achieved. Full cell profile from the defined +ve and –ve electrode with equal mass loading can be visualized in **Fig. 2.11b** ($V_{full\ cell} = V_+ - V_-$), and the final generated full cell curves are shown in **Fig. 2.11c**.

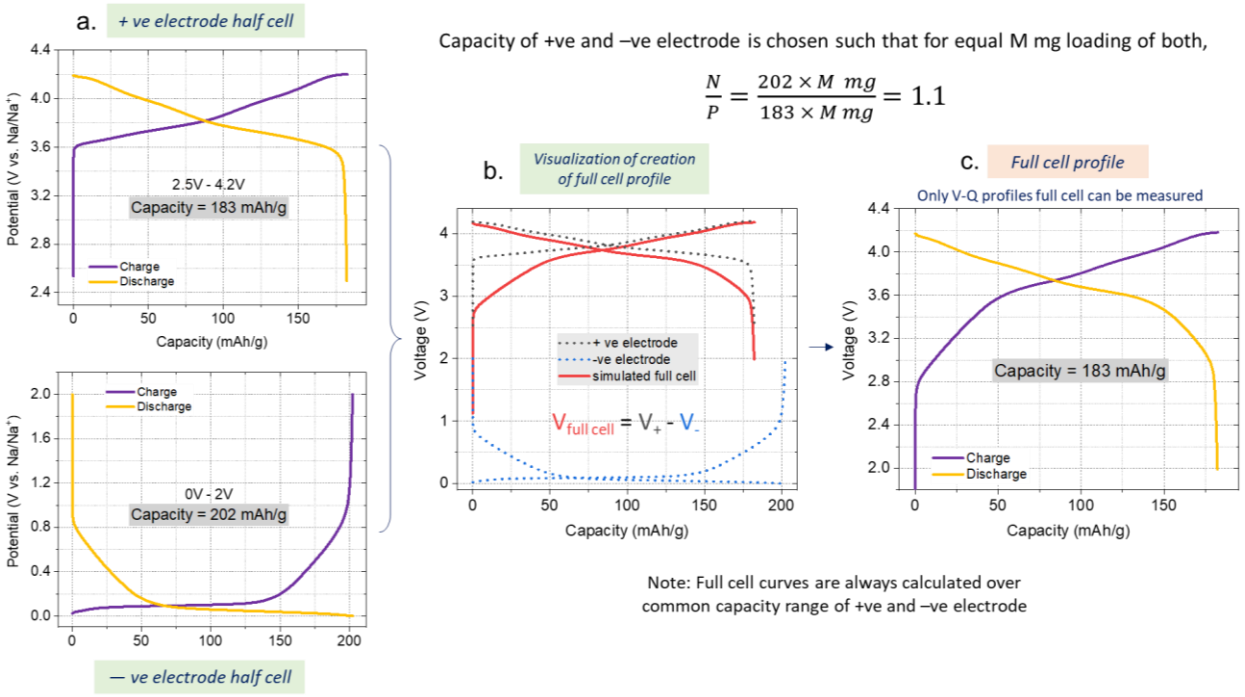

Fig. 2.11 | Simulated +ve and –ve electrode half cells and a full cell profiles. (a) Simulated half-cell profiles of +ve electrode (top) and –ve electrode (bottom). (b) Visualization of full cell curve generation from the introduced half-cell curves in (a). (c) Generated full cell profile

Generally, most of the major degradation modes (**Fig. 2.1**) will lead to either mass loss of active material or capacity loss due to parasitic reaction[166]. They influence the electrode curves in a certain way, which can be analyzed by examining full cell data. These methods are discussed in the next sections.

2.1.7 Effect of mass loss during cycling

During the cycling of a full cell, the electrode can lose mass due to different reasons like particle delamination, loss of electric contact, etc. (**Fig.2.12a**). The impact of mass loss is systematically explained in **Fig.2.12b**. **Step 1** shows the original V-Q profiles of +ve and –ve electrodes and generated full cell. Note that the generated full cell profile is created using the equation $V_{full\ cell} = V_+ - V_-$, applied only on the common capacity range of +ve and –ve electrodes. In **step 2**, the case of positive electrode mass loss is considered. As a consequence of mass loss at the positive electrode, the V-Q profile will shrink. This can be understood with a simple analogy. For example, if initially, all the material was giving the capacity and half of the positive electrode material is lost, the same cell will show half of the initial capacity. Finally, **Step 3** shows the new electrodes and full cell profiles after mass loss and compares them to the old ones. Effectively, mass loss at the +ve electrode can lead to cell capacity loss without any changes in the -ve electrode profile.

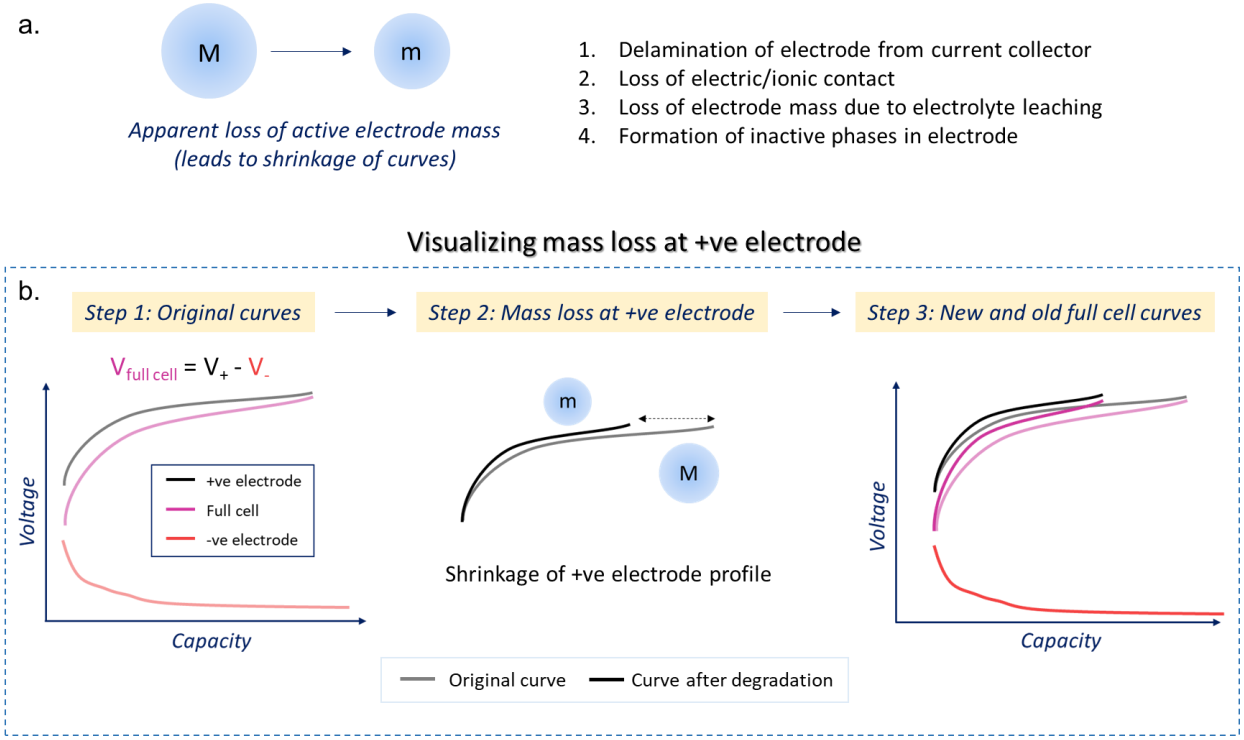

Fig. 2.12 | Apparent mass loss in electrodes. (a) Schematic explaining the apparent mass loss during the cycling of the electrode and its reasons. (b) Schematic representation to visualize the impact of +ve electrode mass loss on the full cell curve. The original curves are faint, and the ones after degradation are dark.

Three cases of mass loss (**Fig 2.13**), namely at only +ve electrode, only -ve electrode, and both electrodes are simulated using the predefined electrodes in **Section 2.1.6**. Mass loss at +ve electrode can lead to capacity loss (**Fig 2.13a**), at –ve electrode can lead to plating (**Fig 2.13b** bottom panel), and at both the electrodes can lead to capacity loss shown in **Fig 2.13c**. In reality, full cell profiles are measured by galvanostat, however, with the help of dQ/dV or dV/dQ fitting (discussed in the upcoming section), the +ve and –ve electrode curves are accessed, and mass loss can be identified.

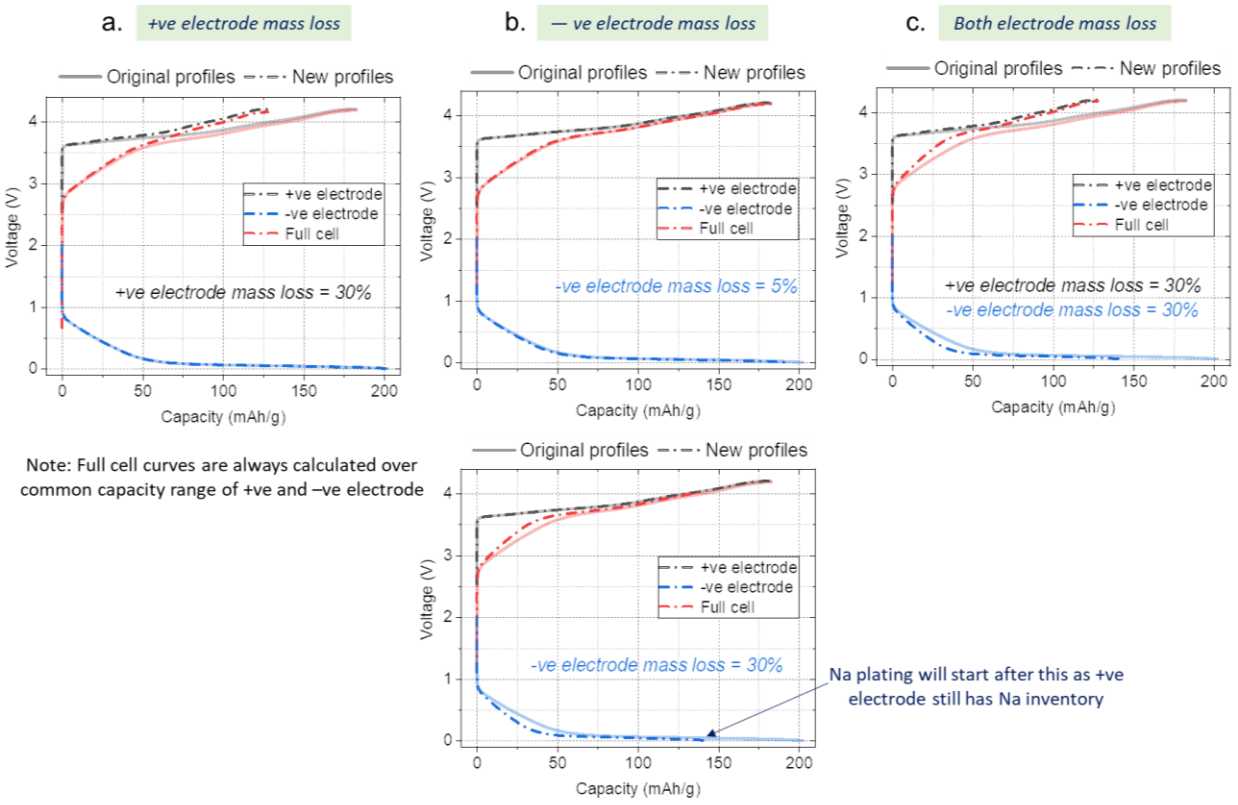

Fig. 2.13 | Effect of electrode mass loss on full cell profile. Simulations representing impact of electrode mass loss on full cell curves. (a) 30% mass loss of +ve electrode (b) 5% mass loss of -ve electrode (top panel) and 30% mass loss –ve electrode (bottom panel). (c) 30 % mass loss of both +ve and –ve electrode.

2.1.8 Electrode slippage: Consequence of parasitic reactions

Parasitic reactions occurring on the electrodes lead to the slipping of one of the electrodes relative to the other, which is known as "**electrode slippage**".[185–188] The reactions occurring on the –ve electrode consume active Na^+ inventory, which leads to capacity loss. The origin of

slippage is explained by taking the case of SEI formation or growth (**Fig. 2.14a**). Virtually pause the cell when SOC of the electrodes lies on the vertical blue line in **Step 1** of **Fig. 2.14b**. Imagine the parasitic reaction at this moment will lead to Na^+ loss and consequent increase in –ve electrode potential (see black arrow and circle in **Step 2** in **Fig. 2.14b**) while +ve electrode potential will stay the same. When the reaction is finished, to balance both electrode potentials on a single vertical line, the **–ve electrode curve has to be shifted** to the right by the same amount as the Na^+ lost to side reactions (**Step 3** in **Fig. 2.14b**). Finally, **Step 4** in **Fig. 2.14b** shows the new curves after slippage (dark) and original curves (faint) for comparison with **no change in +ve electrode curves**. It is visually clear that the new full cell curve has less capacity than the original curves.

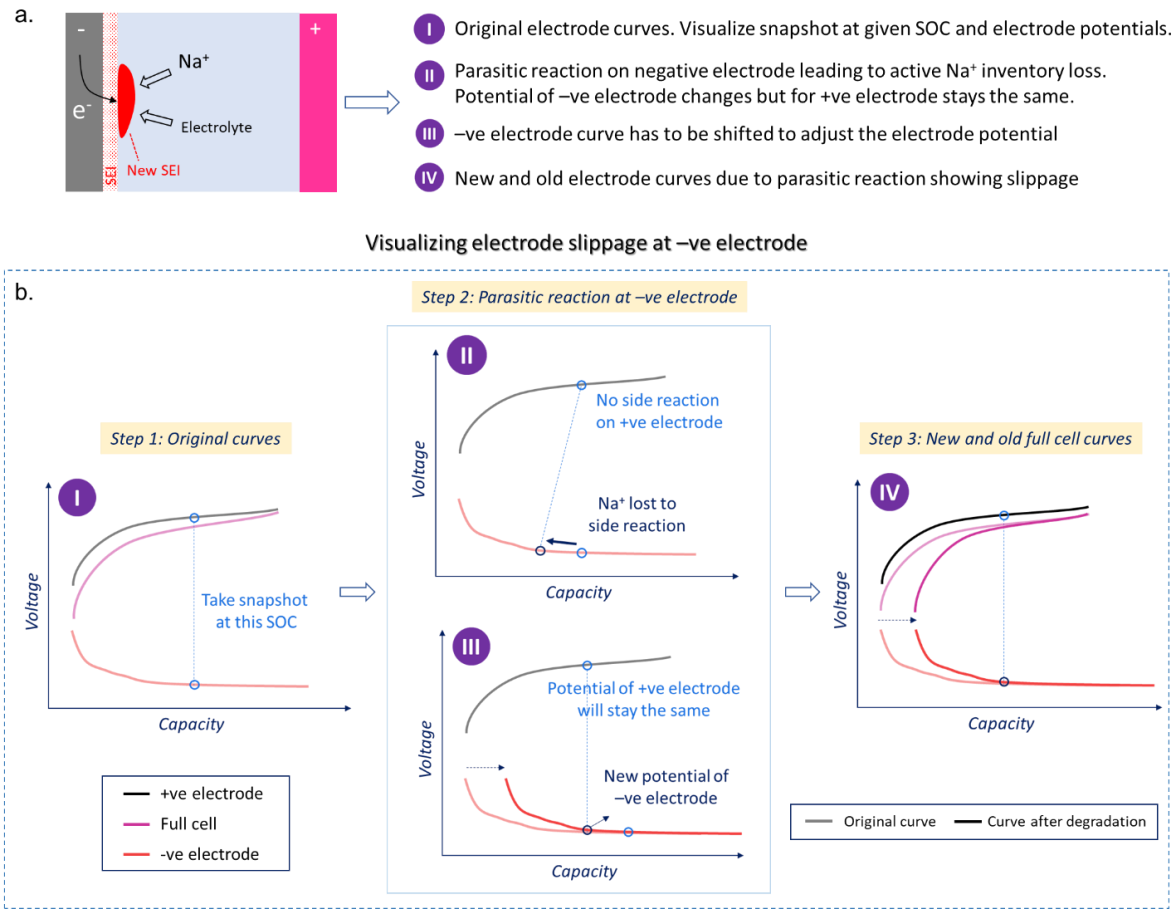

Fig. 2.14 | Schematic explanation of the impact of electrolyte reduction and SEI formation/growth on electrode slippages. (a) Scheme showing the electrolyte reduction and slippage visualization steps mentioned in (b). (b) Snapshot method to visualize slippage at –ve electrode affecting the full cell curve. It is divided into several steps with the details mentioned in the scheme.

Fig. 2.15 shows slippages caused by parasitic reactions on +ve and –ve electrodes using simulation of the predefined electrodes (in **Section 2.1.6**). Electrolyte reduction leads to Na^+ loss with –ve electrode slippage leading to capacity loss (red curve in **Fig. 2.15a**). Electrolyte oxidation can lead to +ve electrode slippage (red curve in **Fig. 2.15b**). When parasitic reactions occur at both electrodes, slippage occurs at both electrodes, leading to capacity loss (red curve in **Fig. 2.15b**). Note that slippage can occur in the right or left direction on the basis of intake or loss of Na inventory by the electrode. After dQ/dV or dV/dQ fitting (discussed in the next section), the +ve and –ve electrode slippages can be accessed.

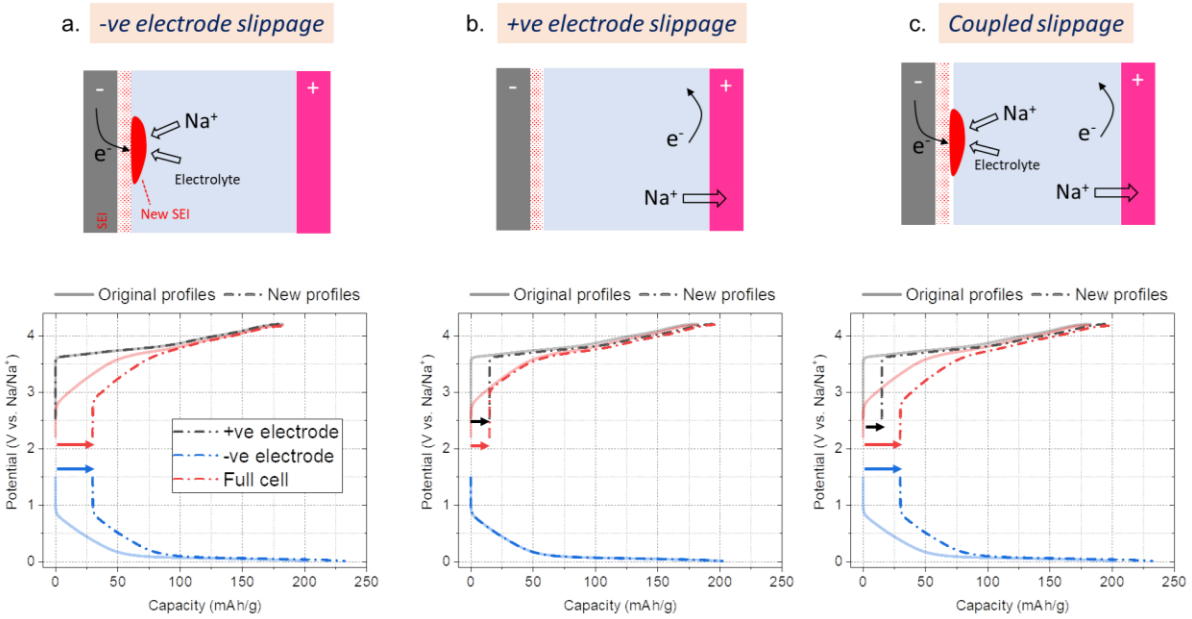

Fig. 2.15 | Simulations representing the impact of parasitic reaction on full cell curves. (a) Electrolyte reduction. (b) Electrolyte oxidation (c) both electrolyte oxidation and reduction.

2.1.9 Differential capacity ($\frac{dQ}{dV}$) analysis

Differential (or incremental) capacity is defined as the derivative of capacity with voltage vs. voltage (dQ/dV vs. V). Differential of a function highlights the minute changes in slope in terms of peaks (**Fig. 2.16**), these peaks can be assigned to different electrochemical processes.[189] The simulated electrodes introduced in **section 2.1.6** are used here. For half cells of +ve and –ve electrodes, the peak highlights the specific redox processes corresponding to phase transformation in the material[190–194] (**Fig. 2.16b**). While the dQ/dV profile of full cell contains

overlapped redox processes of both +ve and –ve electrode as shown in the right panel of **Fig. 2.16b**.

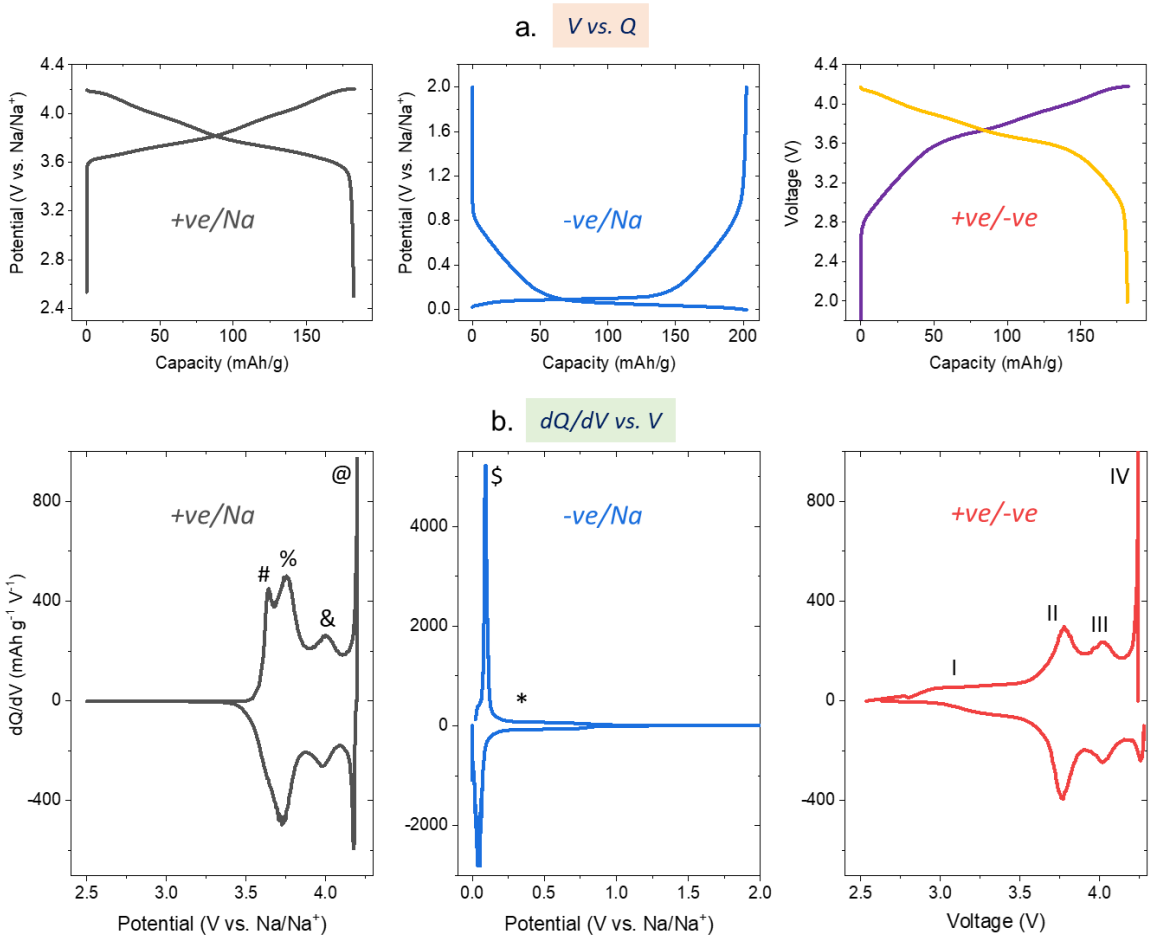

Fig. 2.16 | Simulations showing the dQ/dV profiles. (a) voltage vs. capacity profiles for +ve electrode, -ve electrode and full cell introduced in **Section 2.1.6**. (b) dQ/dV vs. voltage curves for +ve electrode, -ve electrode and full cell shown in (a). Different peaks are marked with different symbols.

The area under the dQ/dV vs. V curve corresponds to the capacity, thus decrease in the area implies capacity loss. The cell degradation using differential voltage analysis can be divided into two types (**Fig. 2.17**). In the **type 1** analysis shown in **Fig. 2.17a**, the evolution of the peaks is tracked as a function of cycle number, apart from the decrease in area and increase in polarization, more information regarding the loss of redox peak corresponding to +ve and –ve electrode can be identified.[190–194] This technique was introduced by Bloom et al. in 2005, who studied the degradation of different LIB chemistries.[189] A more critical analysis is **type 2**, shown in **Fig. 2.17b**, where the experimental full cell curve is fitted with the half cell curves of the +ve

and –ve electrodes. After the fitting, V-Q profiles of +ve and –ve electrodes for the observed degradation are retrieved. For example, Korte et al. retrieved the slippage information from $LiNi_{0.5}Mn_{1.5}O_4$ | $Li_4Ti_5O_{12}$ and concluded the rapid capacity fade is caused by parasitic reactions and slippage of $Li_4Ti_5O_{12}$ electrodes[195] (**Supplementary Fig. S2.19**). Additionally, Dahn et al. fitted experimental $LiMn_2O_4$ |graphite curves for initial 20 cycles and identified the mass loss of $LiMn_2O_4$ as the main reason for capacity fade[196] (**Supplementary Fig. S2.20**).

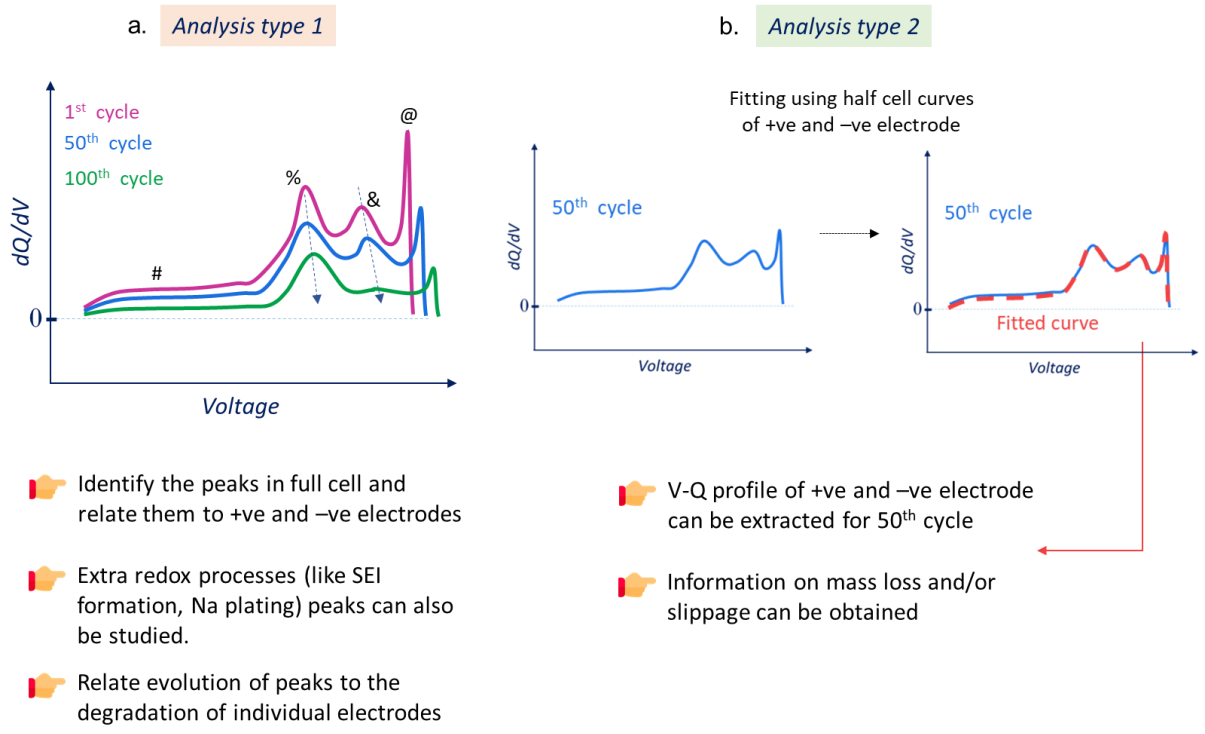

Fig. 2.17 |Schematic representation of two types of analysis performed in the literature. (a) Type 1: Identifying the peaks in full cell DCA curves to the individual electrodes and tracking them with cycling. (b) Type 2:Fitting the experimental curve with the half cell curves of +ve and –ve electrodes and get their V-Q profile after degradation.

In summary, DCA can provide distinct features for different redox processes, and by monitoring changes in these features during cycling, valuable insights into cell health can be obtained.[197] Thus, DCA is used for analyzing NVPF|HC degradation path in **Fig. 3.10** of **Chapter 3**.

2.1.10 Differential voltage ($\frac{dV}{dQ}$) analysis

Differential voltage analysis (DVA) is defined as the derivative of voltage with capacity vs. capacity (dV/dQ vs. Q). This allows the features in the voltage vs. capacity data to be seen more

clearly[185,188,189,192,198,199] as shown in **Fig. 2.18**. Top panel in **Fig. 2.18** shows the voltage vs. capacity curves for simulated +ve and –ve electrode and full cell (introduced in **Section 2.1.6**) and bottom panel shows the corresponding dV/dQ vs. Q curves.

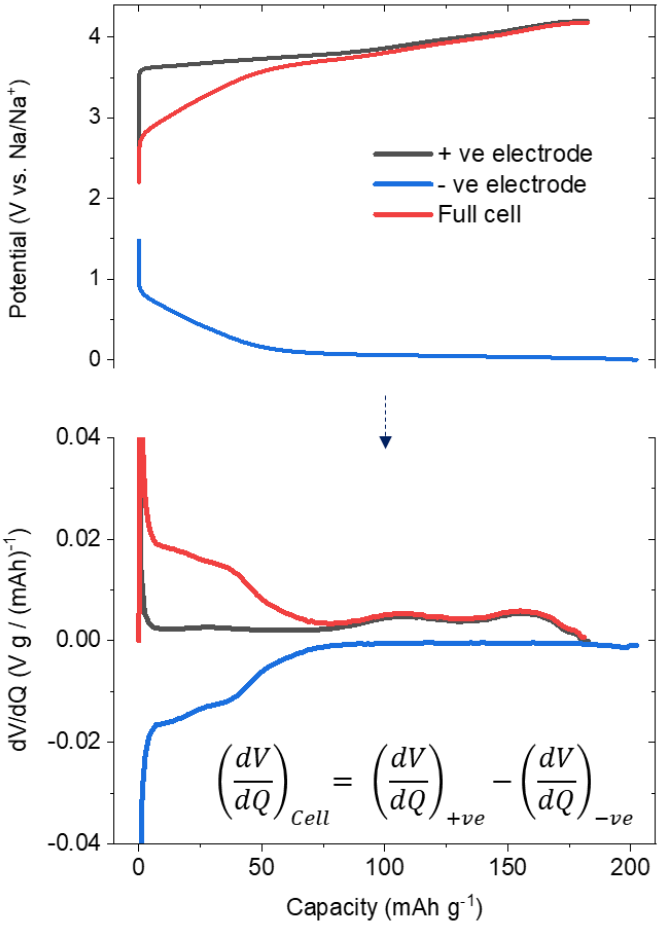

Fig. 2.18 | Simulations showing the dV/dQ profiles. (a) voltage vs. capacity profiles for +ve electrode, -ve electrode and full cell introduced in **Section 2.1.6** (b) Corresponding dV/dQ profiles on the same scale.

To compare, DCA (dQ/dV) is more sensitive to changes in voltage (thus redox peaks) while DVA (dV/dQ) is more sensitive to changes in the capacity. For example, dV/dQ is more sensitive to mass loss and slippage as it highly affects the capacity, thus fitting of dV/dQ curve is more relevant (than dQ/dV) to get relevant information. The dV/dQ technique was introduced by bloom et al. in 2005 who defined two modes of analysis discussed before, namely mass loss and slippage[189]. As discussed before in **Fig. 2.16**, same two types of analysis can be done with dV/dQ. **First type** is analyzing the changes in peak and relating it to the individual electrodes. Bloom et

al. studied the degradation of $LiNi_{0.8}Co_{0.1}Al_{0.1}O_2$|graphite 18650 cells using dV/dQ and related the peaks to +ve and –ve electrodes using half-cell curves (**Supplementary Fig. S2.21**).[200] To make the analysis more critical, Dahn et al. developed the dV/dQ fitting software,[185] which can accurately identify the mass loss and slippages of +ve and –ve electrodes with the case study presented for LCO|graphite 18650 cell[187] (**Supplementary Fig. S2.22**).

To conclude, the highest value of DVA lies in the fitting and deconvolution of +ve and –ve electrode V-Q profiles without the use of a third electrode.[185] The obtained V-Q profile of electrodes gives information regarding electrolyte parasitic reactions and active material loss. This analysis is used in **Chapter 4** (**Fig. 4.7** and **Fig. 4.8**) and **Chapter 5** (**Fig. 5.3** and **Fig. 5.4**) of the thesis. Evaluating both DCA (dQ/dV) and DVA (dV/dQ) will help understand the degradation modes of the system.

2.1.11 Endpoint slippages

The final critical term in the toolbox to diagnose cell health is endpoint slippages. The schematic in **Fig. 2.19** illustrates this idea. In the V vs. ($Q-Q_0$) plot, the slipping of the charge endpoint is marked by charge endpoint slippage (Δ_C), and the slipping of the discharge endpoint is marked by discharge endpoint slippage (Δ_D). The mathematical significance of Δ_C and Δ_D are rigorously derived by Dahn et al. using the lithium inventory model.[166]

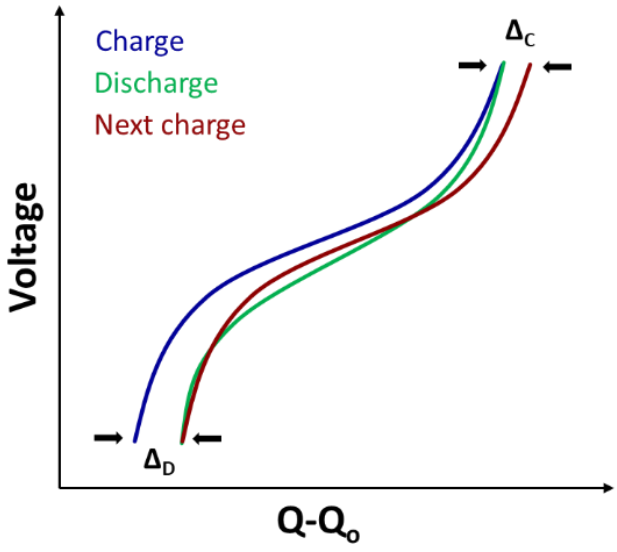

Fig. 2.19 | An illustration depicting the discharge endpoint slippage (Δ_D) and charge endpoint slippage (Δ_C) of a full cell.

Those conclusions from the lithium inventory model can be easily understood just by a simple analysis of the curve. In an ideal cell with no capacity loss, the discharge (green) curve should meet the charge (blue) curve at the end of discharge in **Fig. 2.19**. But if there is a capacity loss, there will be quantifiable Δ_D, indicating coulombic inefficiency. Next, for a non-degrading cell, the discharge (green) curve and next charge (brown) curve should meet at the end of the charge with $\Delta_C = 0$. Note that Δ_C captures how much capacity is wasted on processes (generally electrolyte oxidation) that do not necessarily cause capacity fade but cause more capacity to be measured during charge compared to discharge. In summary, with some assumptions Δ_D and Δ_C signify the coulombic inefficiency and electrolyte oxidation, respectively. The assumptions lie in their mathematical equations[166] presented below.

$$\Delta_D = (1 - CE)Q_0 \qquad \text{Equation 2.8}$$

$$\text{and } \Delta_C = q_{ox} - 2q_p \qquad \text{Equation 2.9}$$

Where CE and Q_0 represent coulombic efficiency in fraction and cell capacity, respectively. Moreover, q_{ox} and q_p represent the average oxidation charge and charge of Li trapped in the electrode, respectively.

This method is used in literature to easily capture the electrolyte oxidation effects. Meunier et al. used the endpoint slippage to identify the severe electrolyte oxidation taking place in 5M LiFSI DMC electrolyte as compared to LP57 electrolyte for NMC811|graphite cells[201,202] (**Supplementary Fig. S2.23**). Dahn et al. used LFP dried at 100°C with and without VC in LFP graphite cells. Cell without VC showed huge charge endpoint slippage[203] due to the formation of lithium alkoxides in the presence of trace water (**Supplementary Fig. S2.24**). Endpoint slippage analysis is used in **Chapter 4** (**Supplementary Fig. S4.10**) and **Chapter 5** (**Fig. 5.3** and **Fig. 5.4**) of the thesis.

2.2 Additional electrochemical measurement tools

2.2.1 Three electrode cyclic voltammetry

Cyclic voltammetry (CV) is a potentiodynamic technique where the potential of the working electrode (WE) is ramped with respect to the reference electrode (RE) linearly with time.[77] This ramping of potential induces a redox process at the WE, which is balanced by a

corresponding redox reaction at the counter electrode (CE), resulting in a net current. The current passed vs. potential of WE is plotted to give cyclic voltammogram trace[77,204] (**Fig. 2.20**). In the typical setup illustrated in **Fig. 2.20a**, the WE, CE, and RE are commonly made of glassy carbon, platinum mesh, and an Ag/Ag^+ organic reference couple, respectively.[123] The objective of these experiments is to investigate the reduction or oxidation of the electrolyte, leading to the formation of an interphase on the electrode surface, and subsequently evaluate the stability of the interphase or electrolyte. Cometto et al. claimed that when the glassy carbon (GC) working electrode is scanned at high sweeping rates, no Na ions are intercalated, indicating that only the redox reaction in electrolyte will occur.[123] Additionally, nature of passivating film formed on GC was found to be similar to one formed on hard carbon in same electrolyte.[123]

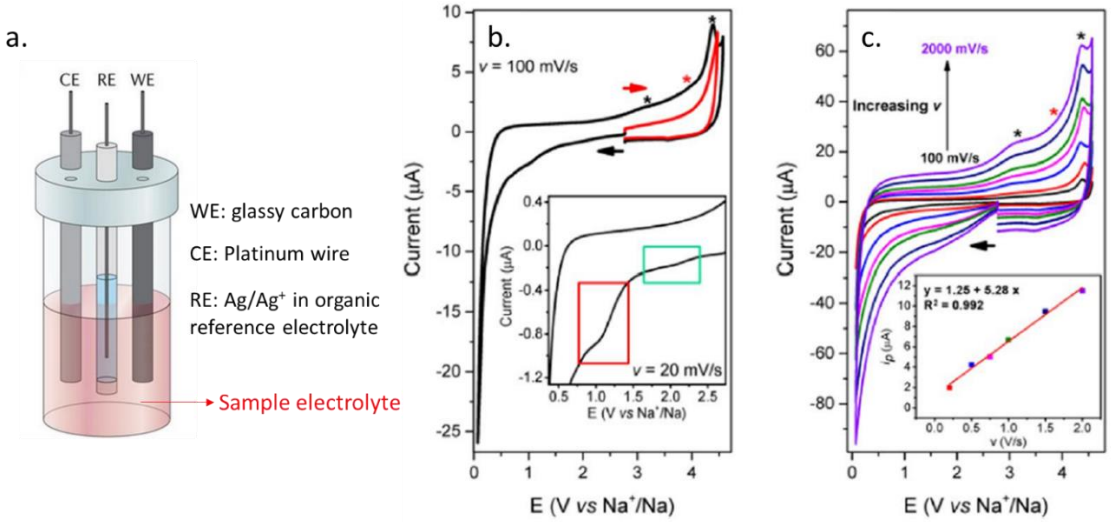

Fig. 2.20 | a) Schematic of typical three electrode CV setup used b) CVs of a 1M $NaPF_6$ in EC-DMC (1:1 by volume) solution at 100 mV/s and 25°C. Sweeping toward low potentials (black) and high potential values (red). Both CVs correspond to the first scan after electrode polishing. The inset shows a zoom of the reduction waves at 20 mV/s. c) CVs of the same solution at 100 mV/s (black), 200 mV/s (red), 500 mV/s (blue), 750 mV/s (magenta), 1000 mV/s (green), 1500 mV/s (navy) and 2000 mV/s (violet). The inset shows the ip vs v plot for the oxidation peak at 3.2 V vs Na^+/Na. A glassy carbon (3 mm diameter) was used as the working electrode. The figure is adapted from Cometto et al.'s work.[123]

Fig. 2.20b shows CV traces of 1M $NaPF_6$ in EC-DMC (1:1 by volume) electrolyte starting with reduction. The inset shows two reduction waves (**Fig. 2.20b**) followed by steep increase in reduction current. When the potential is reversed, several unresolved oxidation peaks emerge at

3.2V, 3.9V and 4.2V marked by *. They are related to the oxidation of species produced by the electrolyte reductive decomposition, as confirmed by the absence of intense peaks in the simple oxidation scan of the solvent (red trace in **Fig. 2.20b**). The 3.2V peak is attributed to oxidation of alkoxide, and linear relation (inset of **Fig. 2.20c**) between peak current (i_p) vs. scan rate (v) suggest the adsorption (or precipitation) of the oxidized species. Conversely, the peak at 4.4V followed linear relation for i_p vs. $v^{1/2}$ indicating oxidation of unknown species that is likely diffusive.[123]

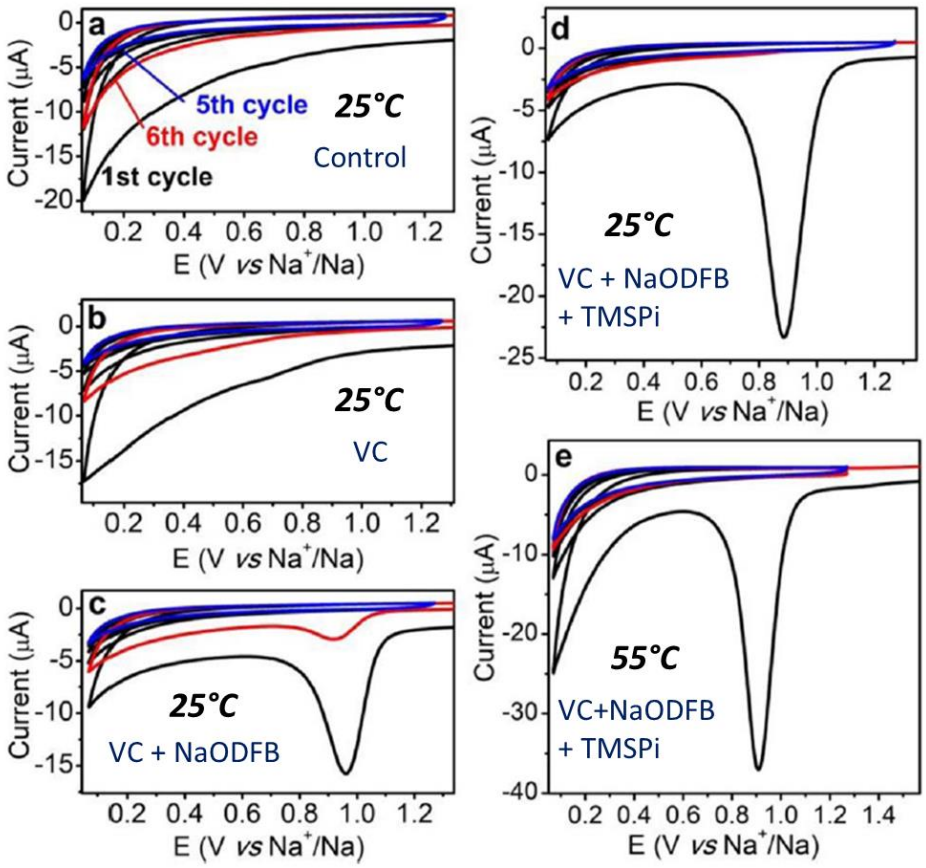

Fig. 2.21 | Five potential cycles to produce the SEI (black) and following CV after five minutes resting (red). v = 100 mV/s. For a) Control at 25°C, b) Control +VC at 25°C, c) Control + VC + NaODFB at 25°C, d) Control + VC + NaODFB + TMSPi at 25°C, and e) Control + VC + NaODFB + TMSPi at 55°C. Where control is 1M $NaPF_6$ in EC-DMC (1:1 by volume) and concentration of VC is 3%, NaODFB is 0.5% and TMSPi is 1% in the electrolyte formulations. The electrode was polished before the experiment for all the electrolyte compositions. Figure is adapted from Cometto et al.'s work.[123]

Moreover, Cometto et al. also studied the stability of the SEI formed with the electrolyte with or without presence of additives[123] (**Fig. 2.21**). Specific protocol was followed which contains 5 cycles in the low voltage region to form the SEI and passivate the electrode, subsequently the

GC electrode is kept at rest for 5 min before performing the 6th cycle. Note the **Fig. 2.21a-c** for control, VC and VC+NaODFB electrolyte, the sixth cycle (red curve) has a higher reduction current than 5th cycle (blue curve), indicating the instability of the formed passivation. Only after the addition of all three additives, namely VC + NaODFB + TMSPi, the 6th cycles almost overlaps 5th cycle (**Fig 2.21d**). Moreover, the same stability of the SEI formed on the GC electrode with all three additives is observed at 55°C (**Fig 2.21e**).

In conclusion, CV with GC electrode can simplify the system by preventing the insertion of Na-ions and only electrochemically reacting with the electrolyte. Thus the stability of the test electrolyte and the interphase formed can be assessed as discussed here.[205–207] The oxidative stability of the SEI is studied using this technique in **Chapter 6** (**supplementary Fig. S6.4**).

2.2.2 Symmetric cells

Symmetric cells are assembled using two identical host materials containing different Na content.[179,208] This is achieved by incorporating one electrode in a charged state and another in a discharged state, as described in **Fig 2.22**. For example, an NVPF symmetric cell is built by charging NVPF in half cell, recovering the electrode, and reassembling it with the fresh NVPF electrode (**Fig 2.22)**. Similarly, an HC symmetric cell can be built, as shown in **Fig. 2.22**.

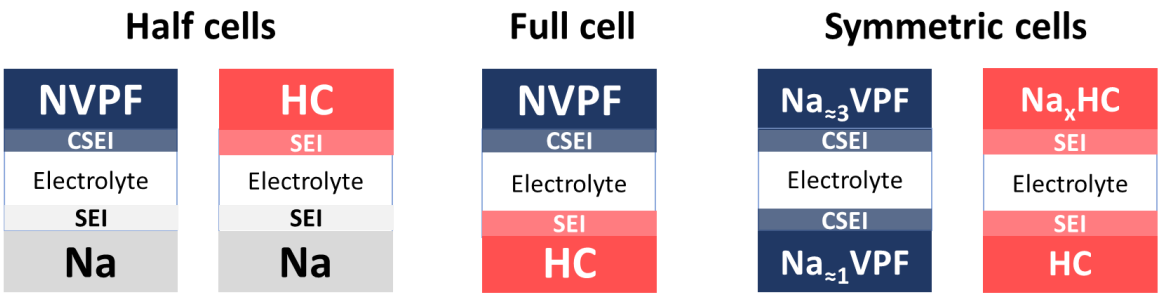

Pros:	1. Gives V vs Q of the material 2. Information on nature of redox, phase transformation etc.	1. Practical system for study	1. Same host material same interphase for both the electrodes 2. Same nature of parasitic reactions on both the electrode
Cons:	1. Cannot predict the stability in the full cell system 2. Unlimited source of Na^+ 3. Reactive Na metal	1. Cannot differentiate between parasitic reactions taking place at NVPF and HC	1. Cannot predict the parasitic reactions caused by cross-talk between NVPF and HC

Fig. 2.22 | Introducing and comparing half cell, full cell and symmetric cell design and properties.

The advantages of using a symmetric cell configuration are highlighted in the context of NVPF and HC symmetric cells as follows:

1. Both electrodes operate within the same voltage range. For instance, in an NVPF symmetric cell, both NVPF electrodes will undergo cycling between 3V and 4.3V.
2. Since both electrodes are the same material, there is only a single material degradation pathway to consider.
3. The interphase formed on both electrodes is identical. For instance, in NVPF symmetric cells, the cathode solid electrolyte interphase (CSEI) is on both electrodes.
4. The dominant mode of electrolyte degradation is unique. Either electrolyte oxidation based degradation in the case of NVPF symmetric cells or electrolyte reduction-based degradation in case of graphite symmetric cells.
5. Finally by making symmetric cells of NVPF and HC, respectively. The material and electrolyte degradation routes of NMC and graphite can be systematically separated.

The concept of symmetric cell cycling was first introduced by Dahn et al. in 2011, initially for graphite symmetric cells[208], which was later extended to NMC symmetric cells[209] to investigate degradation pathways. Dahn et al.'s approach, involves monitoring the degradation of individual electrodes within symmetric cells through dV/dQ fitting.[210] This method is exemplified with NMC532 and graphite symmetric cells in **Fig. 2.23**. **Fig. 2.23a** demonstrates the complete cell charging curve (blue) and the deconvoluted curves for NMC532 (red) and graphite (yellow) electrodes, obtained via dV/dQ fitting, as elucidated in **Section 2.1.10** of this Chapter. In **Fig. 2.23b**, the discharge curve (blue) for the NMC symmetric cell post-assembly is displayed. Notably, dV/dQ fitting enables the extraction of deconvoluted V-Q profiles (red and yellow curves in **Fig. 2.23b**) for each NMC electrode. Similarly, **Fig. 2.23c** portrays the charge curve of the graphite symmetric cell and the corresponding deconvoluted V-Q profiles for both graphite electrodes. These profiles can be monitored as symmetric cell cycling progresses and the cell undergoes degradation. Inspired by this analytical approach, an in-depth investigation of NVPF and HC symmetric cells is undertaken in **Chapter 4**, **Section 2.4**.

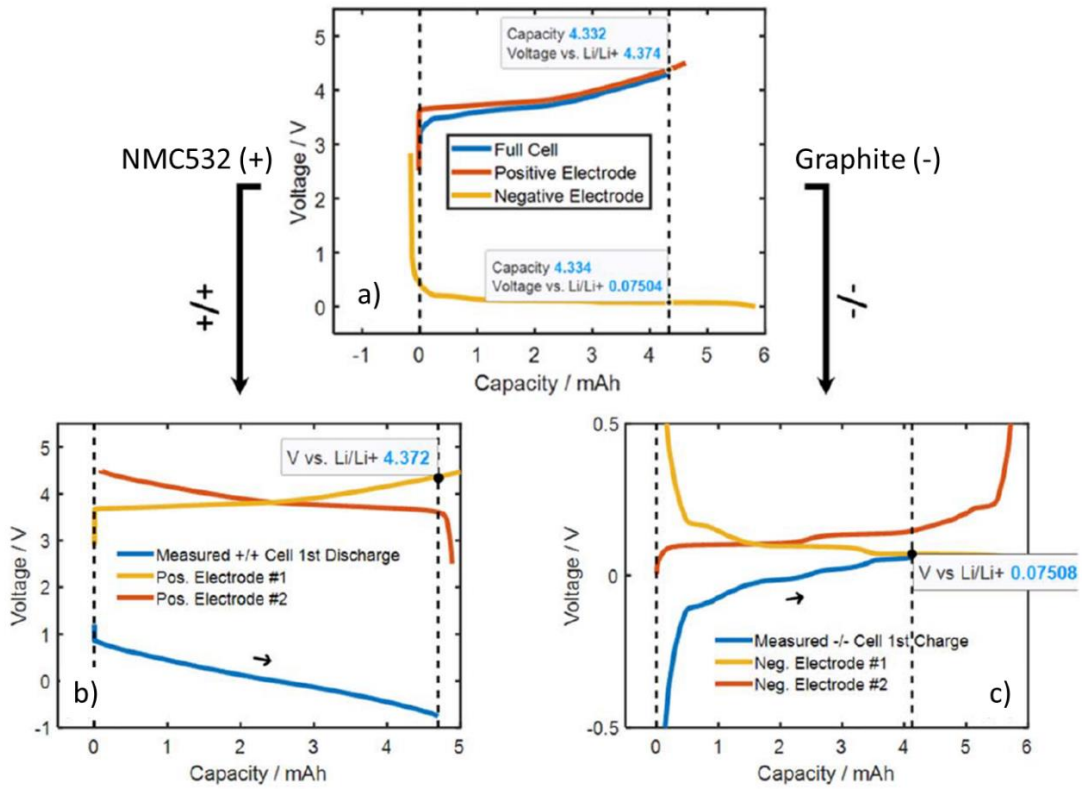

Fig. 2.23 | Separating two full coin cell into NMC|NMC and graphite | graphite symmetric cells. a) Full coin cell operates between 3 and 4.3 V. b) 1st discharge for NMC symmetric cell cycled between ± 0.76 V. d) 1st charge for graphite symmetric cell cycled between ± 0.61 mV. Tests were done at 40°C. Figure is adapted from Dahn et al.'s work.[210]

Symmetric cells of positive and negative electrode materials can be cycled to separate and identify the dominant degradation mode as studied in the literature.[208–210] Additionally, symmetric cells can also be used to separate the impedance contribution of positive and negative electrodes.[178–181]

2.3 Postmortem analysis on aged cells

The electrochemical methods and analysis previously discussed in this Chapter are essential in tracking the different degradation routes in the cell, but none of these analyses provide chemical insight into the origin of those degradations. Disassembly and so-called "**postmortem analysis**" of the recovered cell components, including anode, cathode, electrolyte, separator, current collector, cell casing, etc., is a must to pinpoint the reason for observed behavior in electrochemical analysis.

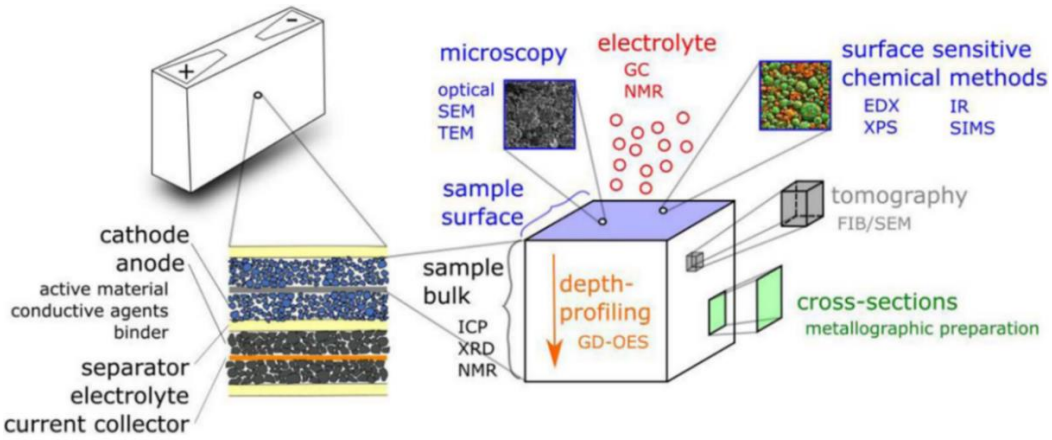

Fig. 2.24 | Overview of components inside a battery and physico-chemical methods for characterization after post-mortem analysis. The figure is adapted from Waldmann et al.'s work.[211]

Postmortem analysis, depicted in **Fig. 2.24**, involves opening the aged electrochemical cell in an inert environment (Ar or N_2) to recover the electrodes, electrolyte, and other components. These recovered electrodes can then be used to create half cells, full cells, and symmetric cells, providing insights into cell failure. A thorough analysis of the recovered electrodes using advanced characterization techniques, including surface, bulk, cross-section, and tomography examination, reveals information about particle cracks, changes at the particle's surface/bulk, films on particles, clogging of pores, loss of adhesion, and dissolution of transition metals.[119,211] Physio-chemical analysis of the electrolyte uncovers parasitic reactions like electrolyte oxidation/reduction, salt decomposition, SEI dissolution, and dissolved transition metals.

Disassembly of batteries is mandatory to collect samples for determination of aging mechanisms and improvement of materials, including step-by-step improvement of state-of-the-art materials as well as the development of new material generations.[212]

Until this point in the Chapter, we have examined cell degradation measurement and analysis techniques. To proficiently apply these methods to NVPF|HC cell chemistry, a comprehensive understanding of the NVPF half cell, HC half cell, and NVPF|HC full cell profiles is essential. Additionally, familiarity with prior degradation studies on NVPF|HC chemistry is pivotal, setting the groundwork for the research conducted in this thesis. Thus, the subsequent section delves into the specifics of NVPF|HC cell chemistry and reported degradation studies.

3. Chemistry and development of Na3V2(PO4)2F3 | hard carbon cells

Before embarking on the degradation analysis studies in upcoming Chapters, it is worth pointing out the critical behavior and developments made in the NVPF|HC cell system. The NVPF and HC electrodes employed in **Fig. 2.25** and throughout the thesis were provided by Tiamat. **Fig. 2.25a** shows the V-Q profile of NVPF|Na half cell, indicating the reversible capacity of ~115 mAh/g with two distinct plateaus for reversible (de)insertion of two sodium ions from the formula unit, respectively. **Fig. 2.25b** presents the HC|Na half cell with a reversible capacity of ~270mAh/g and two distinct regions, namely sloppy and plateau regions. For full cell the NVPF and HC mass loading in the electrodes is balanced with an active mass of NVPF roughly twice that of HC (N/P ratio of 1.17).

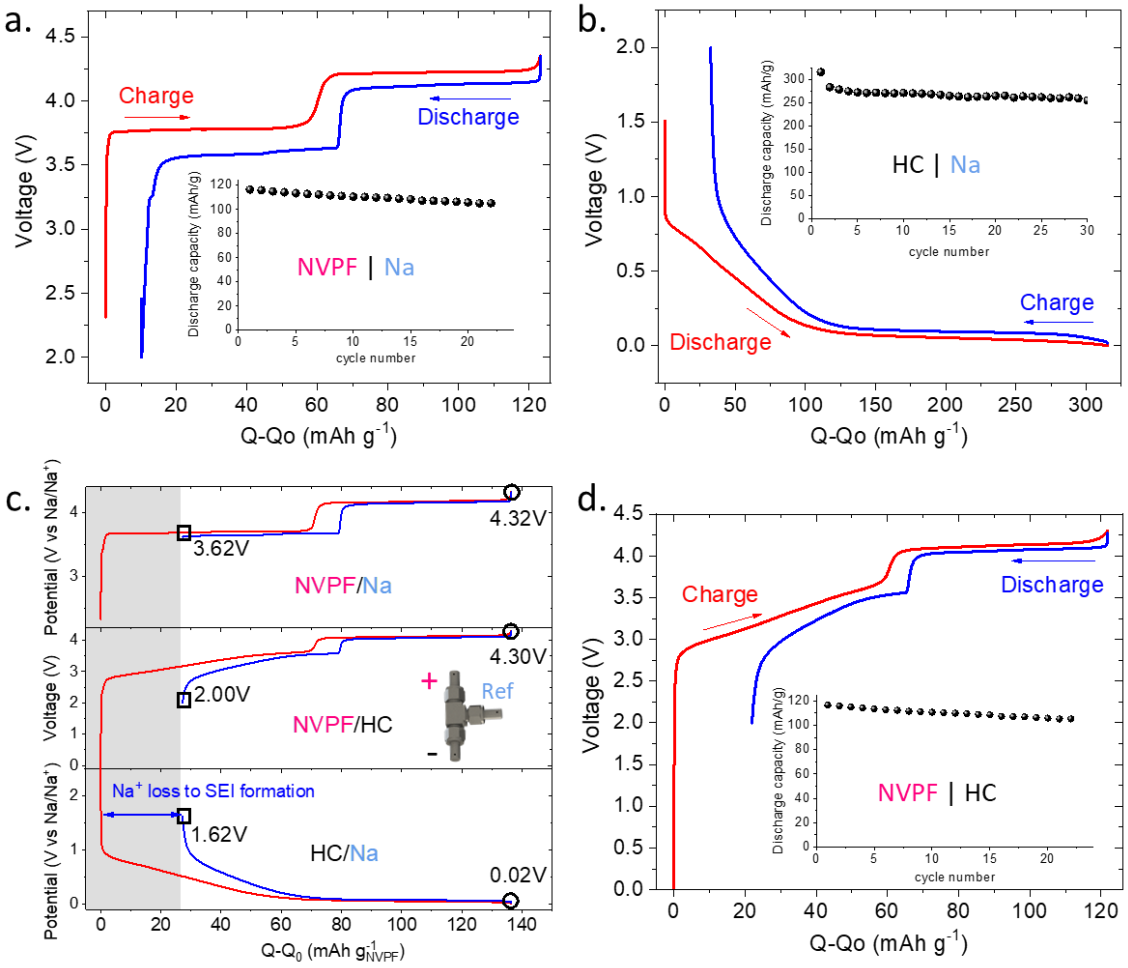

Fig. 2.25 | Behavior of NVPF and HC in half cell, full cell and three electrode cell. voltage vs. potential for a) NVPF|Na half cell with capacity retention as inset and b) HC|Na half cell with capacity retention as inset. c) Three electrode

NVPF|HC cell with Na metal as a reference electrode to visualize the capacity balancing and redox processes of NVPF and HC electrodes. d) Voltage vs. capacity profile for NVPF|HC full cell with capacity retention as inset.

The first cycle of three-electrode cells with the balanced NVPF and HC electrodes is shown in **Fig. 2.25c** with measured individual potential variation of NVPF (top panel) and HC (bottom panel). Note that the irreversible capacity loss in the first cycle is mainly from HC since it cannot provide Na at the end of discharge, while NVPF can take more Na. The origin of this loss is primarily from the loss of Na inventory for SEI formation. Still, the contribution from other factors like irreversible Na trapping in HC pores, apparent extra capacity from parasitic reactions at NVPF, etc. cannot be neglected. Finally, **Fig. 2.25d** shows NVPF|HC full cell with ~105mAh/g of reversible capacity and mixed features (as $V_{cell} = V_{NVPF} - V_{HC}$) from both NVPF and HC curves apparent in **Fig. 2.25c**.

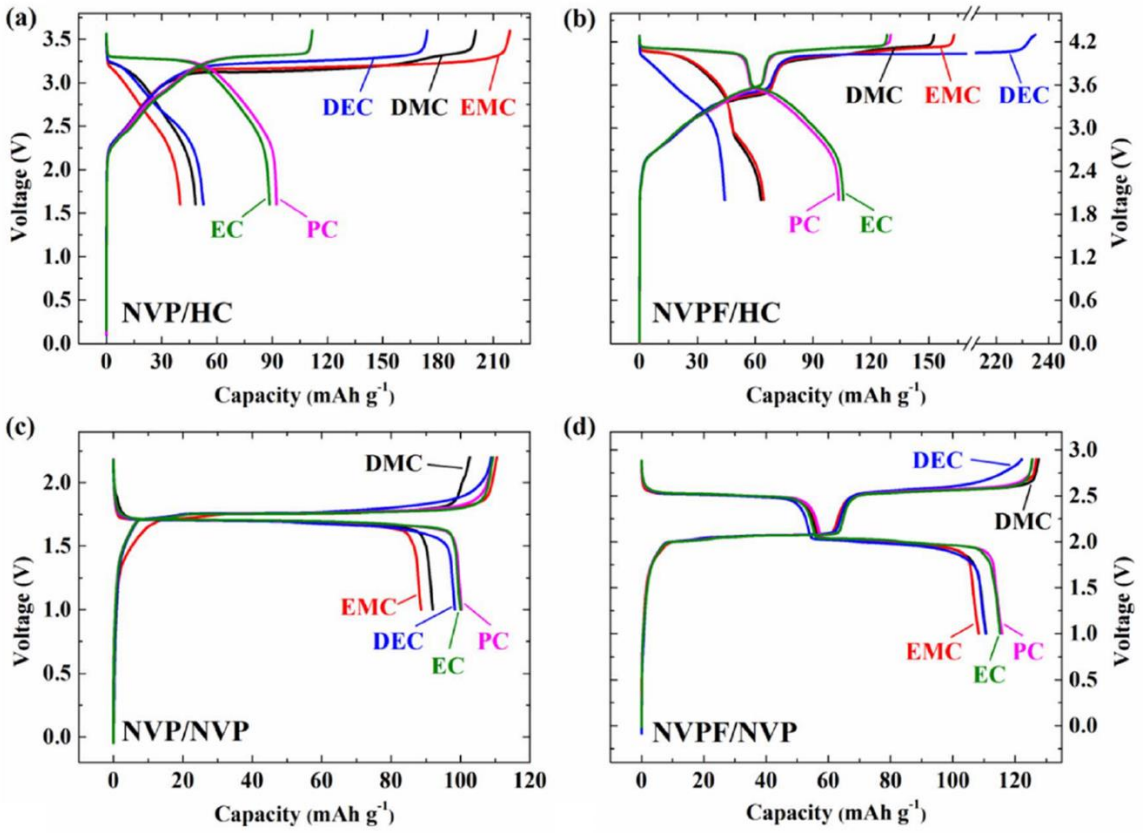

Fig. 2.26 | Instabilities for linear carbonates. The first charge-discharge curves of 1M $NaPF_6$ with DMC, EMC, DEC, PC, and EC electrolyte in NVP|HC (a), NVPF|HC (b), NVP|NVP (c) and NVPF|NVP (d) full cells at C/10 under room temperature.

One of the important studies on NVPF|HC includes accessing the stability of carbonate solvents by Guochun et al., which is discussed here.[146] Four different kinds of cells were assembled: NVP |HC, NVPF|HC, NVP|NVP, and NVPF|NVP, where $Na_3V_2(PO_4)_3$ is NVP. This was possible because NVP can take one more sodium (at ~1.5V vs. Na/Na^+) or give away two sodium (at ~3.4V vs. Na/Na^+). 1M $NaPF_6$ in a single solvent, either linear carbonates DMC, EMC and DEC or cyclic carbonates EC and PC. Note that NVP|HC cells (**Fig.2.26a**) and NVPF|HC cells (**Fig.2.26b**) containing DMC, EMC, or DEC show huge overcharge during the first charge and less capacity in discharge than EC or PC electrolytes. Surprisingly this overcharge is not present when NVP|NVP (**Fig.2.26c**) and NVP|NVPF (**Fig.2.26d**) cells are cycled using linear or cyclic carbonate electrolytes. Thus, the observed overcharge in NVP|HC and NVPF|HC stems from the shuttling mechanism caused by the reduction of linear carbonates on the HC electrode and the formation of sodium alkyl oxides and sodium alkyl carbonates (as claimed by authors) and subsequent oxidation of those species on NVPF electrode giving overcharge plateau. To conclude, when used alone, linear carbonates are disastrous as their reduction can lead to parasitic overcharge and huge capacity loss.

Year	Motivation of the study	Key points	Limitations / missing points	Reference
2012	Electrolyte development: 1M $NaPF_6$ in EC-PC	Comparative study of diverse electrolyte systems with salts ($NaPF_6$, $NaClO_4$, and NaTFSI) and solvents (EC, PC,DMC, DME, DEC, THF and triglyme). Different electrolytes' ionic conductivity, viscosity, electrochemical stability, and thermal stability are compared. Half cells and full cells were cycled with different electrolytes.	Storage studies for calendar life are missing. High-temperature cycling and low-temperature impedance are missing.	Ponrouch et al.[213]
2013	Electrolyte development: 1M $NaPF_6$ or $NaClO_4$ in EC:PC:DMC	High ionic conductivity, low degree of ion-pairing, low viscosity. Stable room temperature cycling and 70mAh/g at 5C and	Low loading of electrodes ($2mg/cm^2$). Storage studies for calendar life are missing. High temperature cycling and low temperature impedance are missing.	Ponrouch et al.[214]

2018	Electrolyte development: 1M $NaPF_6$ in Diglyme	Stable in half-cell and full cells. Similar ionic conductivity with 1M NaPF6 EC-DMC solution.	NVPF|NVP cell shows stable cycling but not NVPF|HC cell. Storage studies for calendar life are missing. High temperature cycling and low temperature impedance are missing.	Westman et al.[215]
2018	Accessing electrolyte stability of 1M $NaPF_6$ with single solvent EC,PC, DMC, DEC, EMC	Successfully identified the instabilities in the presence of linear carbonates caused by the shuttling of reduced products to NVPF electrode causing parasitic overcharge. Sodium alkyl oxides and sodium alkyl carbonates. Year-long cycling data of NVPF|HC cells with 1M NaPF6 in EC or PC	Storage studies for calendar life are missing. High temperature cycling and low temperature impedance are missing.	Guochun et al.[146]
2018	Analyzing degradation: Using dV/dQ and high temperature cycling and storage of full cells	dV/dQ analysis of full cell is presented. High temperature (40C and 55C) cycling of 10 cycles with 160h of storage at 100% SOC is presented for 1M NaPF6 in EC-DMC, PC-DMC, PC-DEC, PC-EMC electrolytes	High temperature instabilities and high self-discharge. Low temperature impedance is missing.	Guochun et al.[216]
2019	Electrolyte development: 1M $NaPF_6$ in EC-PC with four additives namely 0.5% NaODFB + 3% PS + 1% SN + 3% VC	High temperature cycling and storage is presented for varieties of electrolyte formulations. Capacity retention, polarization development and impedance is analyzed. Provided highly stable electrolyte at high temperature.	Highly viscous EC-PC solvent with low wettability may not be practical in large format cells. Low temperature (<10°C) cycling/impedance is missing.	Guochun et al.[122]
2019	Electrolyte development: 1M $NaPF_6$ in EC-DMC with three additives namely 0.5% NaODFB + 3% VC + 1% TMSPi	High temperature cycling and storage is presented for a variety of electrolyte formulations. The stability of the interphase formed is studied with CV. An electrolyte with low viscosity and high-temperature stability is formulated.	High charge endpoint slippage (or increase in capacity) during cycling. Probable gassing issues. Low temperature (<10°C) cycling/impedance is missing.	Cometto et al.[123]

Table 2.2 | Summary of important studies on NVPF|HC full cell system.

Table 2.2 summarizes significant advancements made in the past decade regarding the NVPF|HC cells. These advancements range from foundational investigations to comprehensive studies aimed at checking the performance characteristics of NVPF|HC cells. Notably, the

development of electrolytes capable of withstanding extremely high temperatures during cycling and storage has been achieved. Nevertheless, **Table 2.2** highlights certain challenges associated with these electrolytes. For example, high viscosity and low temperatures issues of EC-PC based electrolyte (+ 4 additives) developed by Guochun et al. and high charge endpoint slippage may lead to oxidative gassing in the EC-DMC electrolyte (+3 additives) developed by Cometto et al. Furthermore, while electrolytes capable of sustaining high temperatures have been developed, the underlying factors contributing to their instability remain unresolved questions. The subsequent Chapter will delve into these issues and propose potential solutions.

4. Conclusions of the Chapter

This Chapter begins by unraveling different degradation pathways based on the deterioration of electrode material, the decomposition of electrolyte, the dissolution or growth of interphase, and the degradation of cell components. The meticulous study of these specific cell degradation details for LIBs is highlighted, though these cannot be directly inferred for NIBs due to the high specificity of cell chemistry, encompassing the anode, cathode, and electrolyte. However, the tools used to assess cell health are readily transferable from LIBs to NIBs.

The Chapter subsequently delves into an extensive exposition of various tools used to monitor cell degradation. This degradation is explained as a decline in the cell's storable energy ($E = Q \times V_{av}$), attributable to a loss in capacity (Q) or average voltage (V_{av}). Several parameters and measurements to track these losses are examined, including capacity retention (CR) or state-of-health (SOH), coulombic efficiency (CE), cell polarization (ΔV), electrochemical impedance spectroscopy (EIS), mass loss, electrode slippage, dQ/dV analysis (DCA), dV/dQ analysis (DVA), electrode slippages, and endpoint slippages. Extensive schematic representations, simulated profiles, and supporting examples from the literature are provided to make the study complete. The Chapter introduces two specific electrochemical techniques: three-electrode cyclic voltammetry and symmetric cell measurements. It's crucial to highlight that while the discussed analysis sheds light on the causes of cell degradation, it does not delve into the chemical origins of this process. To support this analysis, additional chemical and structural characterizations performed on postmortem components of aged cell are undoubtedly necessary.

The concluding section focuses on the electrochemical behavior of NVPF|HC. Prior research discovered that linear carbonates (DMC, DEC, and EMC) are highly unstable in NVPF|HC cells, surviving only a few cycles when used alone. This instability stems from the reduction of linear carbonates into sodium alkoxide, which oxidizes on high-voltage NVPF electrodes. This instability escalates at high temperatures. As a next step in the development, previously various electrolyte formulations have been suggested to stabilize the NVPF|HC cell at elevated temperatures, but they have their own limitations. Nevertheless, the inherent nature of this high temperature instability has not been thoroughly explored. The upcoming Chapter will center its attention on the inherent instabilities that emerge due to the interaction between NVPF material and the electrolyte at elevated temperatures.

Chapter 3 | Unraveling the Interplay between Electrodes and Electrolytes in $Na_3V_2(PO_4)_2F_3$ Full Cells: Synergistic Degradation Pathways and Enhanced Performance Solutions."

" This Chapter is based on the following research article that I co-authored: Desai, P., Forero-Saboya, J., Meunier, V., Rousse, G., Deschamps, M., Abakumov, A.M., Tarascon, J.-M., and Mariyappan, S. (2023). Mastering the synergy between $Na_3V_2(PO_4)_2F_3$ electrode and electrolyte: A must for Na-ion cells. Energy Storage Materials 57, 102–117. 10.1016/j.ensm.2023.02.004.

1. Background and Motivation

In this thesis, **Chapter 1** discussed the Na-ion batteries with issues and challenges associated with different chemistries available for NIBs currently. Among the different chemistries in the trial, the $Na_3V_2(PO_4)_2F_3$ (NVPF)| hard carbon (HC) chemistry has emerged as a promising option for the initial commercialization of Na-ion batteries (NIBs) due to its high voltage, fast charging capabilities, and favorable handling and processing characteristics, including water/air stability. However, the challenges associated with optimizing electrolyte for NIBs are huge and requires various analyses based on electrochemical as well as analytical techniques that were discussed in **Chapter 2**. At this stage, it is essential to understand the root cause of the problems associated, in particular to NVPF|HC chemistry, in order to identify potential solutions and effectively enhance the cell performance and lifetime. This chapter's focus and research direction are motivated by several key factors, which will be discussed below.

One of the critical aspects that warrants attention is the notable high potential plateau of NVPF, as illustrated in **Fig. 2.25a** of **Chapter 2**. This plateau manifests at approximately 4.20 V vs. Na/Na^+ (or 4.53 V vs. Li/Li^+ as discussed in **Fig. 1.22** of **chapter 1**). In the realm of lithium-ion batteries (LIBs), it is widely acknowledged that electrolytes containing carbonate solvents begin to undergo oxidation at voltages as low as 4V vs. Li/Li^+.[150,156] Once the positive electrode potential surpasses this threshold in LIBs, undesired electrolyte oxidation takes place at the electrode surface. This detrimental process inflicts harm upon the electrode surface, cathode solid electrolyte interphase (CSEI), and liquid electrolyte, resulting in capacity loss and an elevation in impedance.[131,217,218] Moreover, these detrimental parasitic reactions become significantly exacerbated under elevated temperatures, further shortening the overall lifespan of the cell.

Additionally, the dissolution of transition metals (TM) from the positive electrode host has emerged as a significant contributor to cell deterioration in LIBs.[219–221] This phenomenon affects well-known positive electrodes such as $LiNi_xMn_yCo_zO_2$, $LiMn_2O_4$, and even low voltage electrodes like $LiFePO_4$ (with an average potential of ~3.4V vs. Li/Li^+), particularly under high temperatures.[217,221–226] The dissolution and subsequent migration of TM from the positive electrode, leading to deposition on the negative electrode, are recognized as one of the primary

causes of capacity degradation.[220,222] Therefore, comprehending the interplay between parasitic oxidation reactions and vanadium dissolution becomes crucial in unraveling the behavior of the NVPF electrode.

The current study commences by investigating the causes behind the failure of 18650-type NVPF|HC cells cycled at 55 °C. The analysis centers on the degradation mechanism of 18650 cells, with a primary focus on the NVPF material. Experimental details regarding synthesis of NVPF material, cell assembly, electrochemical testing, leaching procedure, ICP-MS measurements, XRD measurements, TEM measurements, SEM measurements, FTIR measurements, Mass spectroscopy measurements, NMR spectroscopy measurements are explained in **Methods section** of **Supplementary information** for **chapter 3**.

2. Results and Discussion

2.1 Decoding Degradation: Post-Mortem Analysis of NVPF-HC Cell

The empty 18650 NVPF-HC cells from TIAMAT Energy were dried and subsequently filled with a 1M $NaPF_6$ in EC-PC-DMC (1:1:1 by volume) electrolyte. Cell formation and cycling took place at a temperature of 55 °C, employing a cycling rate of C/5 (1C = 128 mAh/g). **Fig. 3.1a** illustrates the capacity retention plot, indicating that the cell retains 93% of its original capacity after 28 cycles. Although the cell does not exhibit a significant capacity loss, the current interruption device (CID) broke after approximately 10 days (28 cycles) at 55 °C. This CID failure is indicative of a substantial increase in internal pressure (approximately 15 bars) within the cell, attributed to the generation of gaseous by-products resulting from parasitic reactions with the electrolyte.

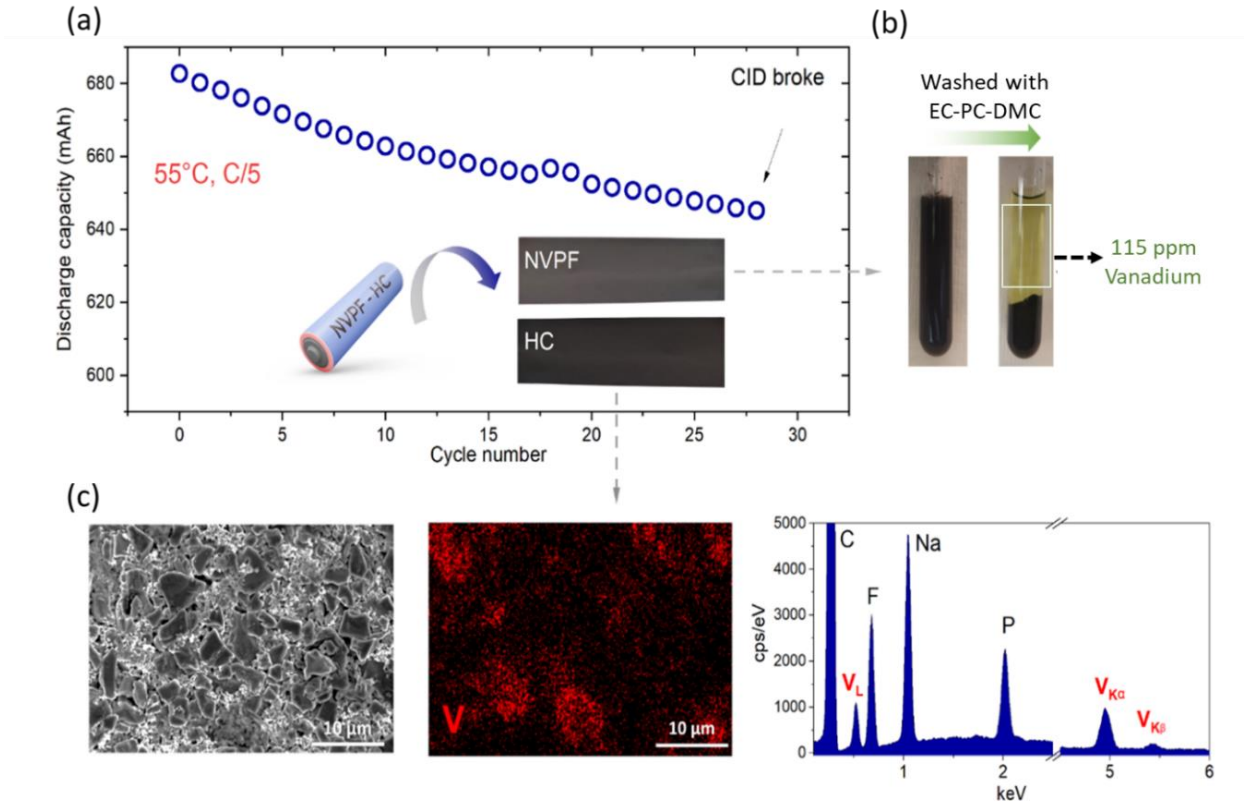

Fig. 3.1 | Electrochemical cycling of cylindrical 18650 Type NVPF|HC cell at 55 °C and postmortem analysis. (a) Plot of Discharge Capacity Retention for NVPF|HC Cells at 55 °C. Formation cycle data is excluded for clarity. The inset depicts the NVPF and HC electrodes after the CID break. (b) Solution Color and Dissolved Vanadium Content obtained from Washing 360 mg of Cycled NVPF Electrode with 3 mL of EC-PC-DMC. The solution exhibited a green/yellow color, and ICP analysis revealed 115 ppm of dissolved vanadium. (c) SEM/EDX Analysis of Recovered HC, featuring a SEM image (left), EDX elemental mapping of vanadium (middle), and EDX spectra (right).

Following the CID break, the cell was opened, and individual electrodes were recovered for further analysis. The NVPF electrode, upon washing with EC-PC-DMC solvent, exhibited a release of yellow/slight green coloration into the solvent, as depicted in **Fig. 3.1b**. This coloration indicates the presence of soluble vanadium containing species on the NVPF electrode, as confirmed by inductively coupled plasma-mass spectroscopy (ICP-MS). Interestingly, the pristine NVPF electrode did not exhibit any dissolution in this solvent mixture. Moreover, SEM-EDX analysis revealed the presence of deposited vanadium on the surface of the recovered HC electrode, as shown in **Fig. 3.1c**. These findings unambiguously confirm the occurrence of

vanadium dissolution in the cycled NVPF/HC cell, with a portion of the soluble vanadium species migrating into the electrolyte and subsequently depositing onto the surface of the hard carbon negative electrode. The next session will focus on quantifying V dissolution and studying the various factors it depends on.

2.2 Quantifying vanadium dissolution

To quantify vanadium dissolution, experiments were conducted in coin cells using fresh NVPF and HC electrodes, along with glass fiber separators soaked in 1M $NaPF_6$ in EC-PC-DMC electrolyte. Full cells were cycled to a specific state of charge (SOC) and maintained at that potential for 24 hours or 1 week before disassembly. Experiments were performed at 25°C and 55°C. The aim was to measure vanadium dissolution under different cycling conditions and temperature regimes.

The HC electrode, along with one separator adjacent to it, was recovered from the cells. These components were digested separately or together using 2% HNO_3. It is worth noting that the separator next to the NVPF electrode was not used due to the presence of attached NVPF particles, which would have affected the accuracy of our measurements (refer to **Supplementary Fig. S3.1**). The resulting solutions were filtered and analyzed using ICP-MS to determine the vanadium content. The detected amounts are presented in **Fig. 3.2a**. Importantly, the sum of the vanadium detected from the carbon electrode (~0.1%) and separator (~0.44%) alone is nearly equal to the experimental value obtained (~0.6%) when both are analyzed together. Hence, for meaningful comparisons, we report the total amount of vanadium combined in both the HC electrode and separator. Using this protocol, we demonstrate in **Fig. 3.2b** that vanadium dissolution increases with the oxidation potential/SOC of the NVPF electrode, with the maximum dissolution observed at 100% state of charge (4.3 V). Additionally, increasing the resting period at a high potential (4.3V) or the cycling temperature promotes vanadium dissolution, as shown in **Fig. 3.2c**. Moreover, **Fig. 3.2d** illustrates that the amount of dissolved vanadium continues to increase with cycling, albeit at a slower rate with increasing cycle numbers.

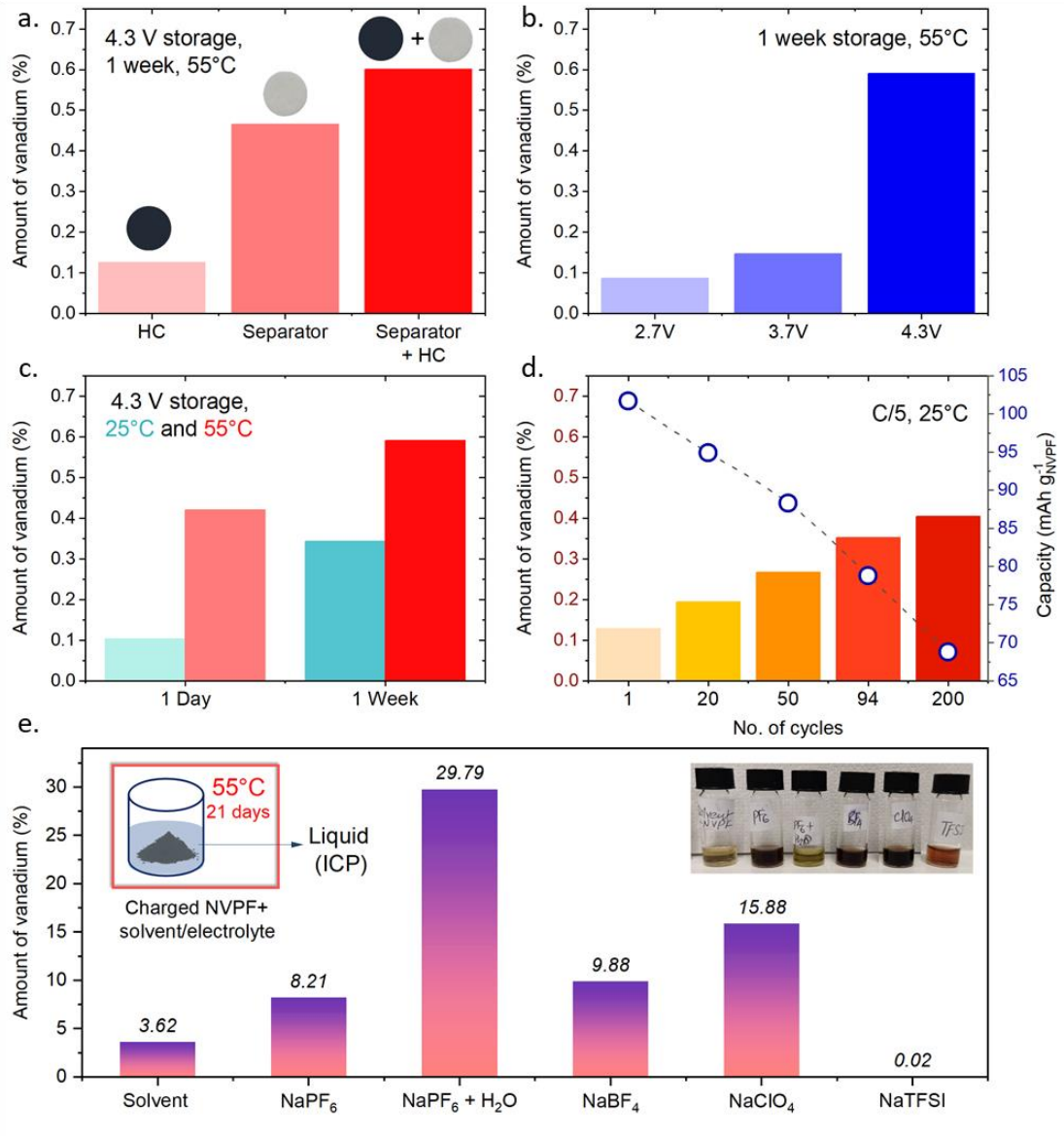

Fig. 3.2 | Factors Affecting Vanadium Dissolution. The figure presents the amount of vanadium dissolved from NVPF detected by ICP-MS. To facilitate comparison, the measured ppm values are converted to %V, where the dissolved vanadium is normalized relative to the total vanadium content in the NVPF electrode used in the experiment. (a) %V detected from the hard carbon electrode, separator, and their combination recovered from NVPF-HC coin cells stored for 1 week at 4.3 V and 55 °C. (b) %V detected from the combination of hard carbon and separator recovered from cells cycled to different upper cutoff voltages (2.7 V, 3.7 V, and 4.3 V) and stored for 1 week at 55 °C. (c) %V detected from the combination of hard carbon and separator recovered from cells charged to 4.3 V and stored at 25 °C and 55 °C for 1 day and 1 week. (d) Amount of dissolved vanadium and discharge capacity plotted against cycle number for NVPF|HC coin cells cycled at 25 °C. The electrolyte used in all experiments (a-d) is 1M NaPF6 in EC-PC-DMC. (e) Amount of vanadium dissolved from charged NVPF (or $Na_1V_2(PO_4)_2F_3$) powder leached in EC-PC-DMC with or without different Na-salts at 55 °C for 21 days.

To investigate whether vanadium dissolution is limited to $NaPF_6$-based electrolytes, we conducted experiments to study the effect of different electrolyte formulations. In these experiments, the nature of the salt in the electrolyte was changed while keeping the solvent constant. The fully charged NVPF powders (to the potential of 4.3 V vs. Na/Na^+) with a composition of $Na_1V_2(PO_4)_2F_3$ (or Na_1VPF), and the studied electrolytes were mixed together, sealed in Al bags, and then stored at 55 °C for 21 days (refer to **Supplementary Fig. S3.2**). After the designated period, the liquid supernatants and solid products were separated using centrifugation and filtration. The liquid supernatants were then analyzed using ICP-MS to determine their vanadium content, while the solids were analyzed by XRD analysis to identify any structural changes. For clarity, the charged material leached with EC-PC-DMC solvents (without any salt) is referred to as SL-NVPF (Solvent Leached-NVPF). The samples leached with electrolytes containing specific salts are denoted by the salt anion, such as PF_6-NVPF (for $NaPF_6$), TFSI-NVPF, ClO_4-NVPF, and so on.

The results regarding the amounts of dissolved vanadium are presented in **Fig. 3.2e**. As expected, the electrolyte containing 200 ppm of water shows the highest amount of dissolved vanadium. This is attributed to the hydrolysis of PF_6^- in the presence of water, leading to the liberation of HF, which triggers significant dissolution of the active material. Similar behavior has been reported[203,218,223,224,227] for $LiFePO_4$, $LiNi_xMn_yCo_zO_2$ and $LiMn_2O_4$. On the other hand, other electrolytes also exhibit a significant but lower amount of dissolved vanadium, following the order: $NaPF_6$+H_2O > $NaClO_4$ > $NaBF_4$ > $NaPF_6$ > solvent > NaTFSI. Interestingly, the NaTFSI-based electrolyte, known for its lower tendency for HF formation,[228–230] shows the least amount of vanadium dissolution from the 'charged NVPF' material, almost negligible. This observation is consistent with the results obtained with NaFSI-based electrolyte as well (see **Supplementary Figure S3.3**). These findings suggest that the formation of acidic by-products resulting from electrolyte oxidation may contribute to the observed sequence of vanadium dissolution. However, it is not the sole cause, as $NaClO_4$ and $NaBF_4$ electrolytes, which generate fewer acidic species, exhibit more vanadium dissolution than $NaPF_6$ electrolyte.[224,231,232] This suggests that the salt anion or its oxidized by-products likely play a role in vanadium dissolution. Surprisingly, we also observed some vanadium dissolution when using a pure solvent mixture (EC-PC-DMC). This

dissolution cannot be explained by the presence of acidic impurities or oxidized salt anion species. It indicates a significant reactivity between the oxidized NVPF material and the carbonate solvent itself, resulting in vanadium losses. This further complicates the mechanism of vanadium dissolution in this system.

The findings of our study reveal a substantial dissolution of vanadium from the NVPF material into the electrolyte, especially when the material is fully charged ($Na_1V_2(PO_4)_2F_3$). In the subsequent sections, we will delve into the consequences of this dissolution on the NVPF material itself and the overall aging of NVPF | HC cells during cycling.

2.3 Structural transformations of NVPF induced by parasitic reactions

To assess the impact of vanadium dissolution on electrochemical performance, NVPF|Na half cells were prepared using leached NVPF materials as positive electrodes and 1M $NaPF_6$ in PC as the electrolyte. Cycling was initiated with charging, as shown in **Fig. 3.3a**. Additionally, the as-charged $Na_1V_2(PO_4)_2F_3$ material stored in an argon atmosphere without solvent/electrolyte treatment was included for comparison. Except for the as-charged NVPF cell (no leaching), all other cells exhibited a starting potential (OCV) within the low voltage plateau (<3.9 V), indicating sodium uptake during the leaching process with simultaneous electrolyte oxidation. This effect was more pronounced with NaTFSI. Notably, the solvent-treated NVPF (SL-NVPF), which did not have additional sodium for uptake in the EC-PC-DMC blend, also displayed some oxidation during the initial charge.

In the subsequent cycle, the charge and discharge curves (**Fig. 3.3b**) exhibit stair-case profiles similar to those of NVPF, although this is less pronounced for SL-NVPF, which displays a profile resembling that of the oxygen-substituted NVPF phase (**Supplementary Figure S3.4**).[106] Moreover, except for SL-NVPF, PF_6-H_2O-NVPF, and TFSI-NVPF samples, the measured reversible capacity is significantly lower than the typical capacity of NVPF (~120 mAh/g). The reduction in capacity is not solely attributed to vanadium removal during leaching, as evidenced by the fact that the observed capacity loss (in the half cell **Fig. 3.3b**) does not correlate with the calculated capacity loss due to V dissolution (calculated from ICP measurements in **Supplementary Figure S3.5**). This indicates that NVPF undergoes decomposition, forming one electrochemically active

phase and one or more inactive phases responsible for the reduced capacity and electrochemical dead weight.

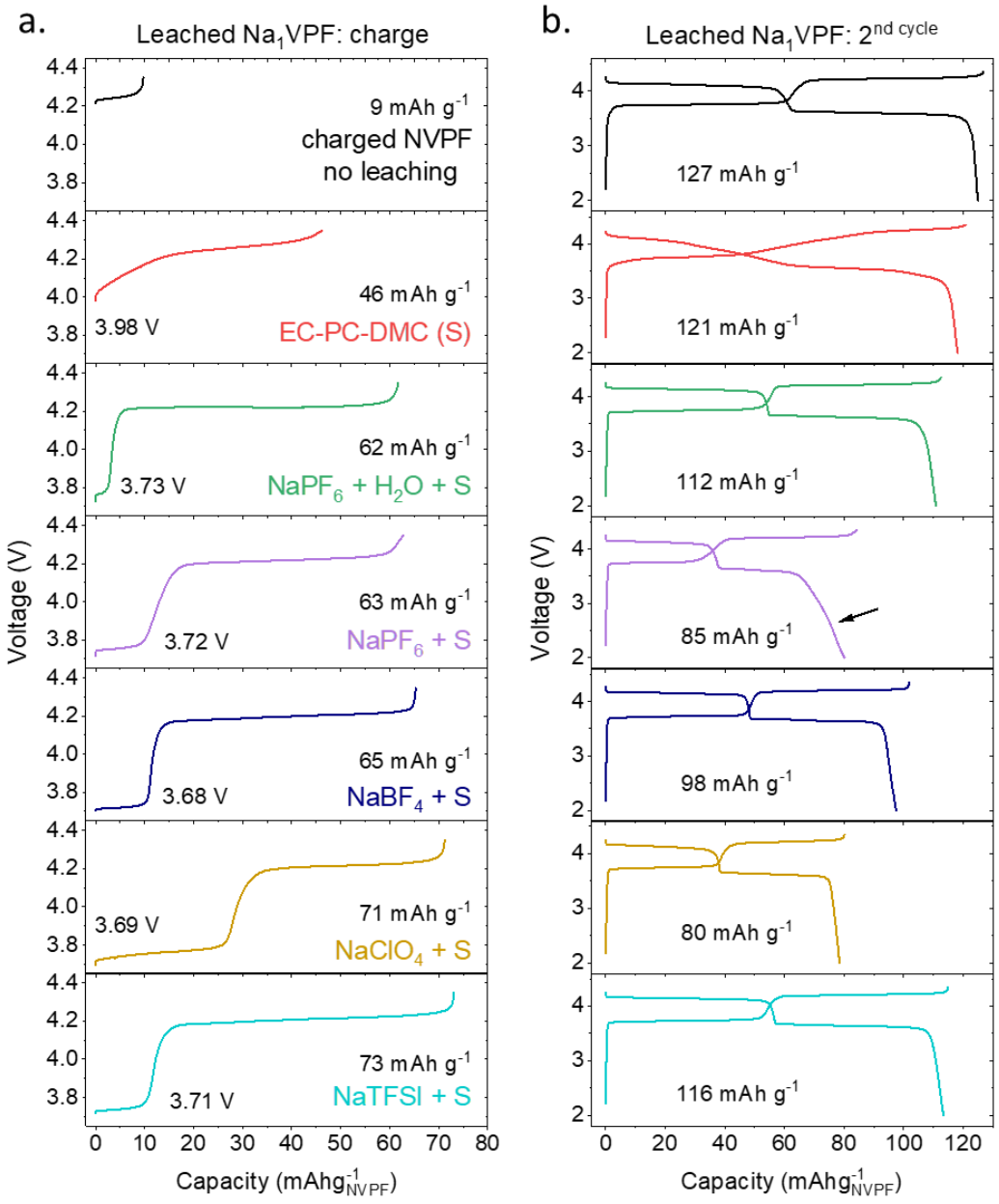

Fig. 3.3 | Electrochemical Performance of Leached/Unleached Na_1VPF in Na-Half Cells (a) First charging curve, depicting the open circuit voltage (OCV) after cell assembly and the observed charge capacity. The OCV and charge capacity values are specified in the figure. Leaching experiments were conducted at 55 °C for 21 days using the indicated electrolyte or solvents. The specific salt used is mentioned in Figure 3a, while 'S' denotes a mixture of solvents, namely EC-PC-DMC. (b) The second cycle, illustrating the electrochemical behavior of the Na_1VPF electrode

in leached and unleached conditions. The abovementioned experiments involved leaching at 55 °C for 21 days using the electrolyte or solvents explained in **Supplementary Fig. S3.2.**

Based on the open circuit voltage (OCV) of the leached samples in **Fig. 3.3a**, it is possible to hypothesize that the structure consists of a mixture of $Na_2V_2(PO_4)_2F_3$ and $Na_{2+x}V_2(PO_4)_2F_3$ phases. To validate this hypothesis, synchrotron XRD patterns were obtained for all the leached samples and compared with the XRD patterns of $Na_1V_2(PO_4)_2F_3$, $Na_2V_2(PO_4)_2F_3$ and $Na_3V_2(PO_4)_2F_3$, and the lab-scale operando XRD measurements, as depicted in **Fig. 3.4a**. For clarity, only the 2θ range of [4.6-8.5°] of leached NVPF samples is plotted (refer to **Supplementary Fig. S3.6** for whole range), which is highly sensitive to the sodium-vacancy ordering and sodium content (x).[108,233]

Interestingly, the PF_6-H_2O-NVPF sample exhibits a single-phase XRD pattern resembling $Na_2V_2(PO_4)_2F_3$ (**Fig. 3.4a**). However, both patterns are slightly different from the previously reported XRD pattern of $Na_2V_2(PO_4)_2F_3$ indexed in the *I 4/m m m* space group with a≈6.30 Å and c≈10.81 Å by Bianchini et al.[233] Our synchrotron patterns for the PF_6-H_2O-NVPF sample and for $Na_2V_2(PO_4)_2F_3$ cannot be indexed using this tetragonal cell, as the (2 0 0) peak splits into two peaks (**Fig. 3.5**) at 2θ ≈ 8.335°. Therefore, we proceeded with the structural resolution of this phase. The XRD pattern of the PF_6-H_2O-NVPF sample can be indexed using a body-centered orthorhombic unit cell with space group *I m m m* and lattice parameters a = 6.311646(6) Å, b = 6.318539(6) Å, and c = 10.817618(11) Å, which represents a distortion of the tetragonal *I 4/m m m* cell. The Rietveld refinement of PF_6-H_2O-NVPF is presented in **Fig. 3.5**, and the sodium content was refined to 0.489(12), indicating a $Na_2V_2(PO_4)_2F_3$ composition (refined structural parameters are in **Supplementary Table S3.1**). This phase is referred to as 'P' hereafter, and blue dotted lines are used to emphasize its prominent Bragg peaks in **Fig. 3.4a**.

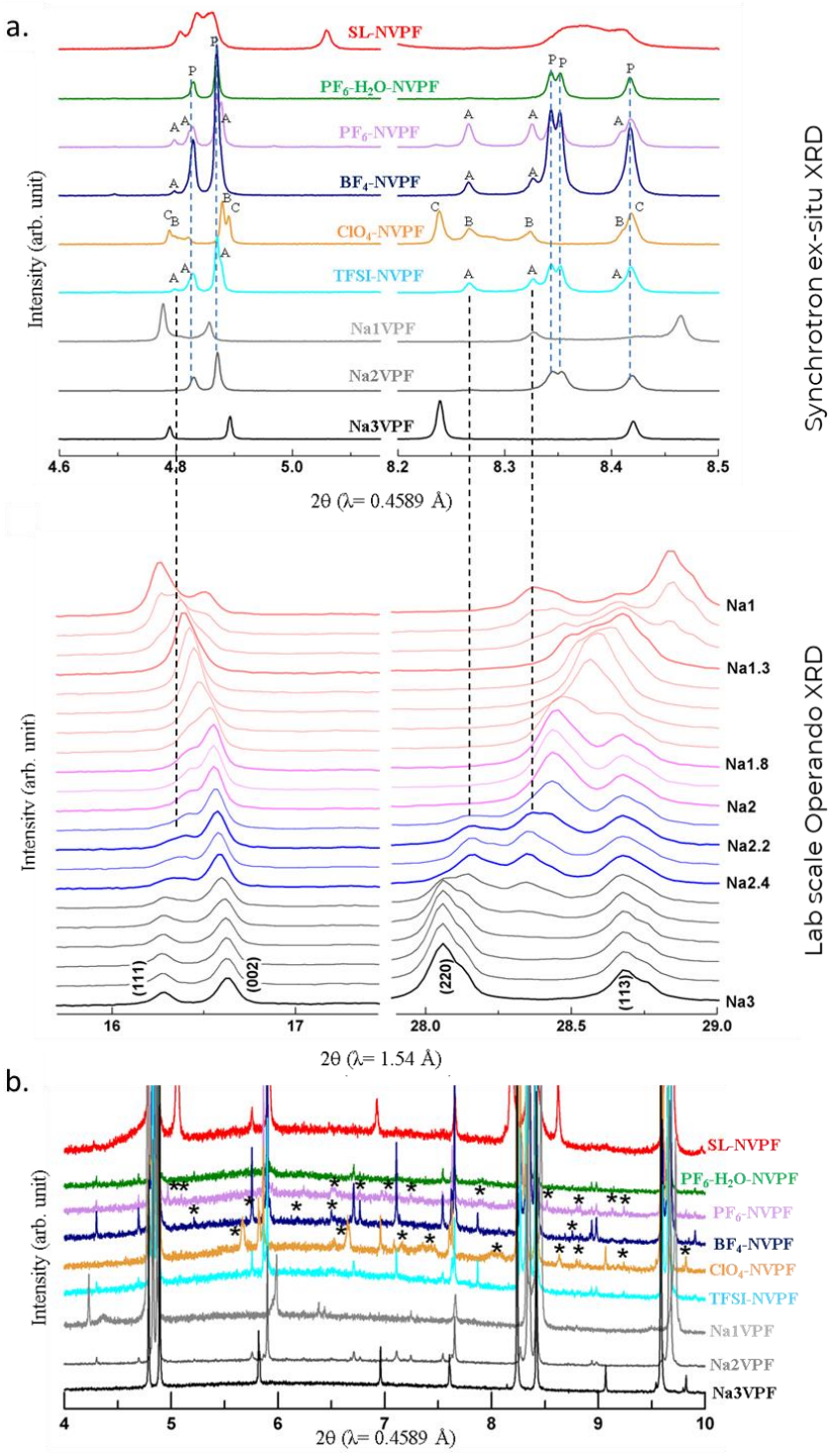

Fig. 3.4 | X-ray Diffraction Pattern of Leached Na_1VPF. (a) The synchrotron powder XRD pattern obtained from the recovered Na1VPF powder after the leaching treatment in the specified electrolyte at 55 °C for 21 days. For comparison, synchrotron patterns of pristine $Na_1V_2(PO_4)_2F_3$, $Na_2V_2(PO_4)_2F_3$, and $Na_3V_2(PO_4)_2F_3$ are also presented. (b) Zoomed-in image (y-axis) of **Fig. 3.4a**, highlighting additional peaks that are not accounted for by the NVPF structure. These peaks are likely attributed to the decomposed products of NVPF during the leaching process.

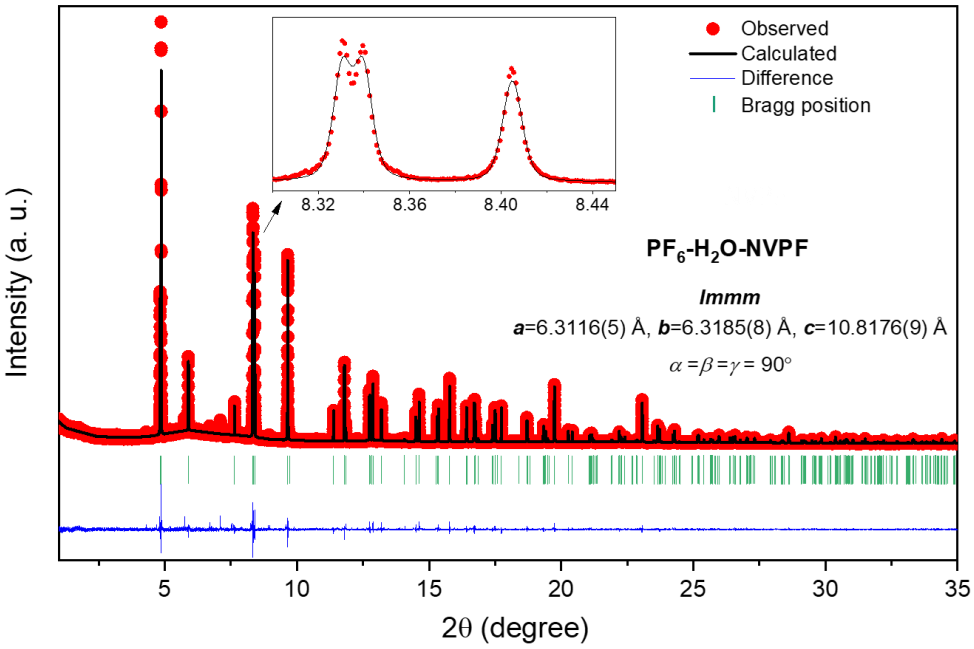

Fig. 3.5 | Refined structure for PF_6-H_2O-NVPF. Rietveld refinement of the PF_6-H_2O-NVPF sample, where the observed, calculated, and difference patterns are denoted by red circles, black lines, and blue lines, respectively. The vertical tick marks represent Bragg reflections in the orthorhombic *I m m m* cell (refer to the text for details).

In the BF_4-, TFSI-, and PF_6-NVPF samples, the 'P' phase coexists with another phase labeled 'A'. However, in the ClO_4-NVPF sample, the 'P' phase is absent, and the majority is comprised of the 'B' and 'C' phases. By comparing with the operando XRD of NVPF (see **Fig. 3.4a** bottom part), the 'A' and 'B' phases can be closely matched to $Na_{\sim 2.2}V_2(PO_4)_2F_3$ with slight variations in sodium stoichiometry, while the 'C' phase corresponds to $Na_{\sim 3}V_2(PO_4)_2F_3$ (**Fig. 3.4a**). The major peaks in all the electrolyte-leached samples can be indexed with the NVPF structure, with variations in sodium content. It is worth noting that attempts at Rietveld refinement for the collected XRD pattern of SL-NVPF were unsuccessful, as the peaks were too broad, indicating structural disorder resulting from the leaching process. It is important to note that this is the extractable information from the XRD with available data, more sophisticated techniques may shed more light on the nature of phases 'A', 'B', and 'C'.

By zooming in on the XRD patterns of **Fig. 3.4a** (presented in **Fig. 3.4b**), it is observed that most of the leached samples, except for PF_6-H_2O- and TFSI-NVPF, exhibit additional peaks that cannot be indexed with the NVPF structure. These extra peaks likely correspond to the electrochemically inactive phases observed during cycling, which contribute to the dead weight

and reduce the observed capacity of the material, as previously mentioned. The absence of these extra peaks in the PF_6-H_2O-NVPF sample throughout the leaching process is surprising, considering that the presence of H_2O in the presence of PF_6^- typically leads to the formation of HF, which would provoke partial dissolution. However, the lack of these extra peaks suggests that the formed HF dissolves the electrochemically inactive phases, leaving only the electroactive NVPF material behind. This observation is further supported by the closely matching capacity of the PF_6-H_2O-NVPF sample to the expected capacity of NVPF. It is important to note that the leaching experiments were performed ex-situ, by placing charged NVPF powder in the electrolyte rather than in an electrochemical cell.

The Na uptake reaction appears to be the only significant reaction occurring for TFSI-NVPF, as it remains structurally unaffected with minimal capacity loss (**Fig. 3.3b**). In contrast, PF_6-NVPF, ClO_4-NVPF, and BF_4-NVPF exhibit significant capacity loss, which can be attributed to structural deterioration or the presence of impurity phases indicated by the extra peaks in the XRD patterns (**Fig. 3.4b**). Collectively, the XRD and cycling results indicate that all the leached samples undergo self-discharge through the uptake of Na ions and simultaneously oxidize the electrolyte. With the exception of SL-NVPF, the samples maintain the NVPF structure, with or without the presence of extra impurity phases resulting from NVPF decomposition during the leaching process.

2.4 Microscopic analysis of NVPF leached by parasitic reactions

To gain further insights into the competing degradation and dissolution reactions, transmission electron microscopy (TEM) was employed, focusing specifically on the SL-NVPF and PF_6-NVPF samples where the XRD analysis could not identify the present phases. High-angle annular dark-field scanning transmission electron microscopy (HAADF-STEM) images of the SL-NVPF crystals (see **Supplementary Fig. S3.7**) reveal numerous elongated pits and cracks, confirming the occurrence of the leaching process. Moreover, STEM-EDX maps and EDX spectra (**Fig. 3.6a**, **Supplementary Fig. S3.8**) indicate a core-shell structure, with a sodium-rich core ($Na_{1.9(2)}$: $V_{1.999(8)}$: $P_{2.001(8)}$ as quantified from integrated EDX spectra) and a shell that contains virtually no sodium and fluorine ($Na_{0.4(2)}$: $V_{2.00(1)}$: $P_{2.00(1)}$). The difference between the core and

shell is also reflected in the electron energy-loss spectroscopy (EELS) spectra (**Fig. 3.6b**) of the V-$L_{2,3}$ and O-K edges. In the EELS spectra from the core area, there is a clear splitting of the V-L_3 and V-L_2 peaks, indicating the coexistence of V^{3+} (V-L_3 at ~518.1 eV) and V^{5+} (V-L_3 peak at ~519.6 eV). On the other hand, the V-$L_{2,3}$ edge for the shell consists of two broad peaks centered at ~519.3 eV and 525.9 eV, which fall between the energy losses characteristic of V^{4+} and V^{5+}. Notably, the V cations in both the core and shell are significantly more oxidized than vanadium in the pristine NVPF, which exists exclusively in the +3 oxidation state (see **Supplementary Fig. S3.9**).

The electron energy loss spectrum (EELS) analysis of the O-K edge provides insight into the chemical nature of oxygen (**Fig. 3.6b**). The onset of a pre-peak at ~531 eV indicates the presence of "free" oxide ions (O^{2-}) that are not bonded to the PO_4 group[234], resulting from the O2p-V3d hybridization. On the other hand, the intense peak at 539.4 eV arises from mixed O2p and P3sp states, corresponding to O^{2-} within the PO_4 group. The strong pre-peak at 531 eV in the shell region suggests the presence of a significant amount of oxygen that does not belong to the PO_4 groups. In contrast, the core region exhibits a low intensity of the pre-peak at 531 eV, in agreement with the $Na_{3-x}V_2(PO_4)_2F_3$ formula, considering that the core spectrum includes contributions from the shell. Additionally, the low fluorine content in the shell further supports the suggestion that the chemical formula for the shell phase is $Na_{0.4}V_2O_y(PO_4)_2F_z$. The presence of a vanadyl bond in the SL-NVPF sample was also confirmed by NMR and IR analyses (see **Supplementary Fig. S3.10**). Therefore, the SL-NVPF sample can be viewed as consisting of a core that is more reduced with a higher sodium content than the expected 1Na for "charged NVPF" ($Na_{1.9}V_2(PO_4)_2F_3$), and a surface that is more oxidized, desodiated, and enriched in oxygen, with a chemical composition of $Na_{0.4}V_2O_y(PO_4)_2F_z$.

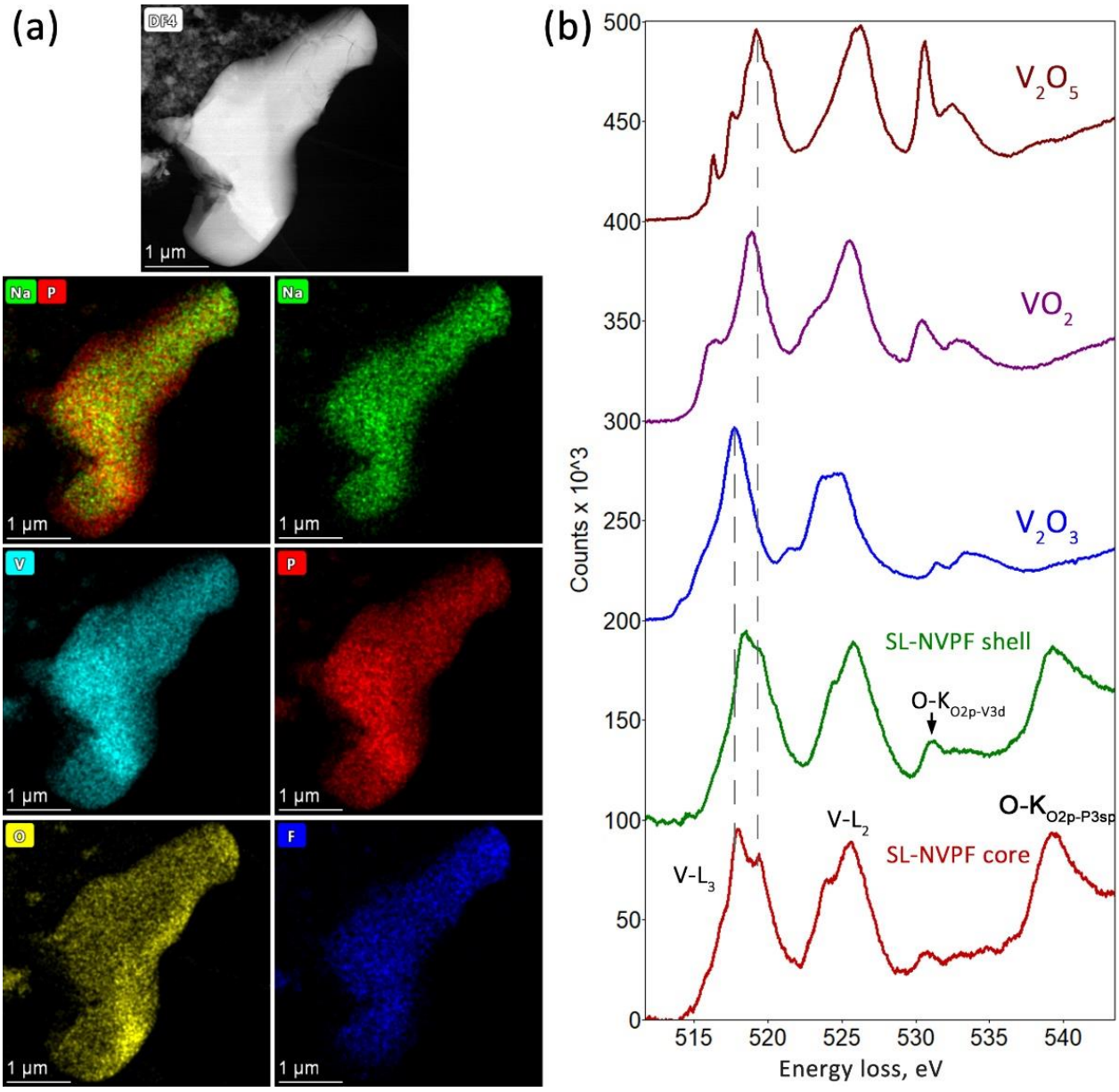

Fig. 3.6 | Identification of Chemical Changes in Solvent-Leached SL-NVPF using TEM. (a) High-Angle Annular Dark-Field Scanning Transmission Electron Microscopy (HAADF-STEM) image accompanied by Energy-Dispersive X-ray (EDX) compositional maps, highlighting the Na-depleted core (appearing red in the mixed Na/P map) of SL-NVPF. (b) Electron Energy Loss Spectroscopy (EELS) spectra of the shell and core regions in SL-NVPF, alongside characteristic spectra of vanadium oxides.

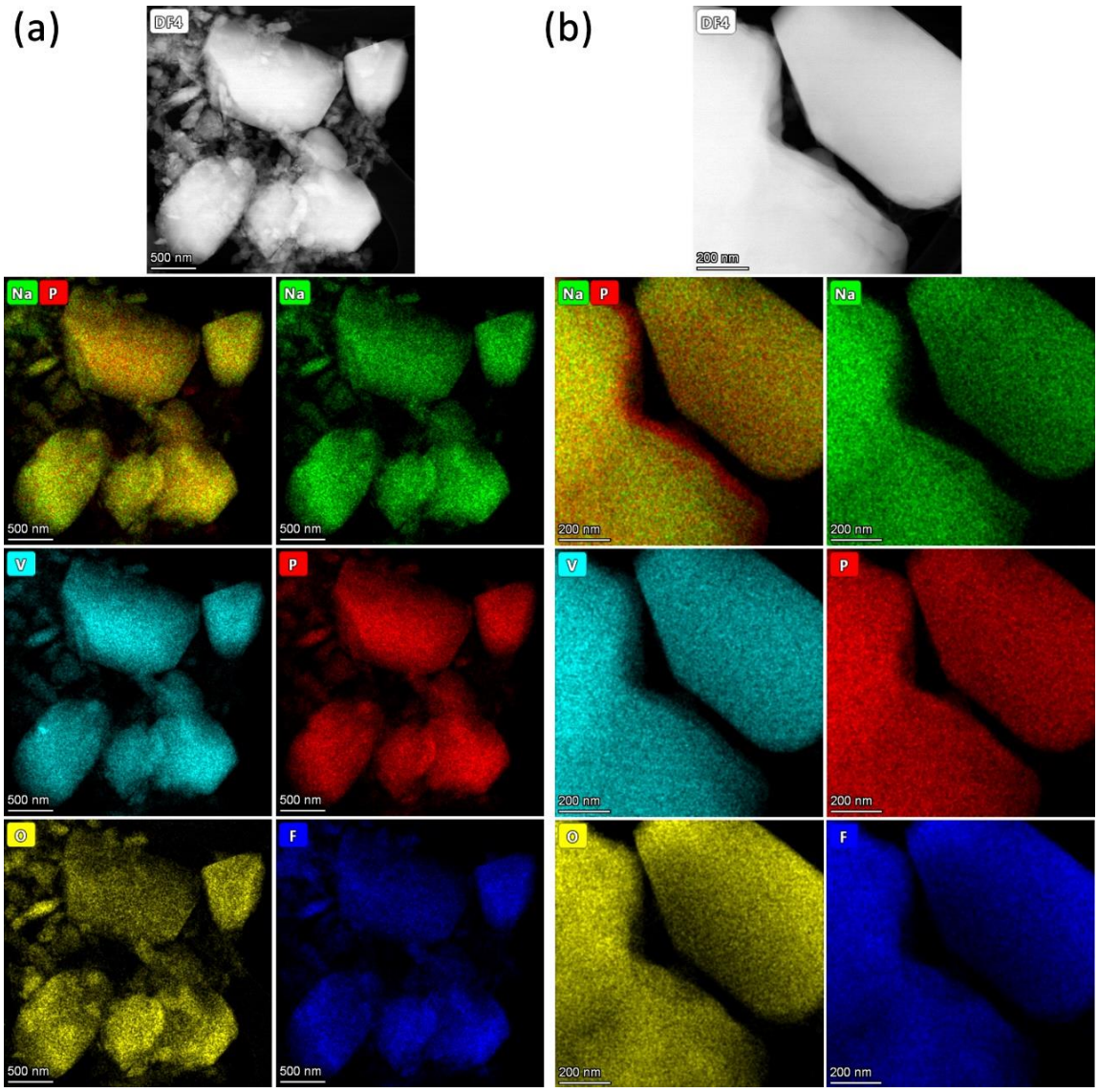

Fig. 3.7 | Identifying Chemical Changes in PF_6-Leached NVPF using TEM. (a) HAADF-STEM image and EDX compositional maps of crystallites exhibiting different Na content, distinguished by the mixed Na/P map showing varying combinations of green and red colors. (b) HAADF-STEM image and EDX compositional maps of a crystallite revealing a Na-depleted shell, indicated by the red color in the mixed Na/P map.

Moving to the more practical system containing $NaPF_6$ salt in the solvent, the crystallites of the PF_6-NVPF sample appear largely disintegrated, forming numerous small, shapeless particles (**Fig. 3.7a**). EDX analyses on different particles reveal the presence of at least two different types, exhibiting distinct sodium stoichiometry corresponding to $Na_{1.7(3)} : V_{2.00(2)} : P_{2.00(2)}$ and $Na_{2.4(2)} : V_{2.00(1)} : P_{2.00(1)}$ formulas (**Fig. 3.7a** and **Supplementary Fig. S3.11a-b**). Furthermore, a core-shell structure is observed, with the surface layer containing minimal sodium (**Fig. 3.7b**)

and a significantly different V:P ≈ 1:2 ratio ($Na_{0.09(2)}$: $V_{1.00(2)}$: $P_{2.00(1)}$, **Supplementary Fig. S3.11c**), indicating highly depleted vanadium regions. This suggests the occurrence of non-homogeneous vanadium dissolution in the PF_6-NVPF material. Additionally, the EELS spectra taken over the V-depleted shell regions (**Supplementary Fig. S3.12**) demonstrate a predominance of the V^{3+} signal over V^{5+}, indicating that the shell is predominantly leached.

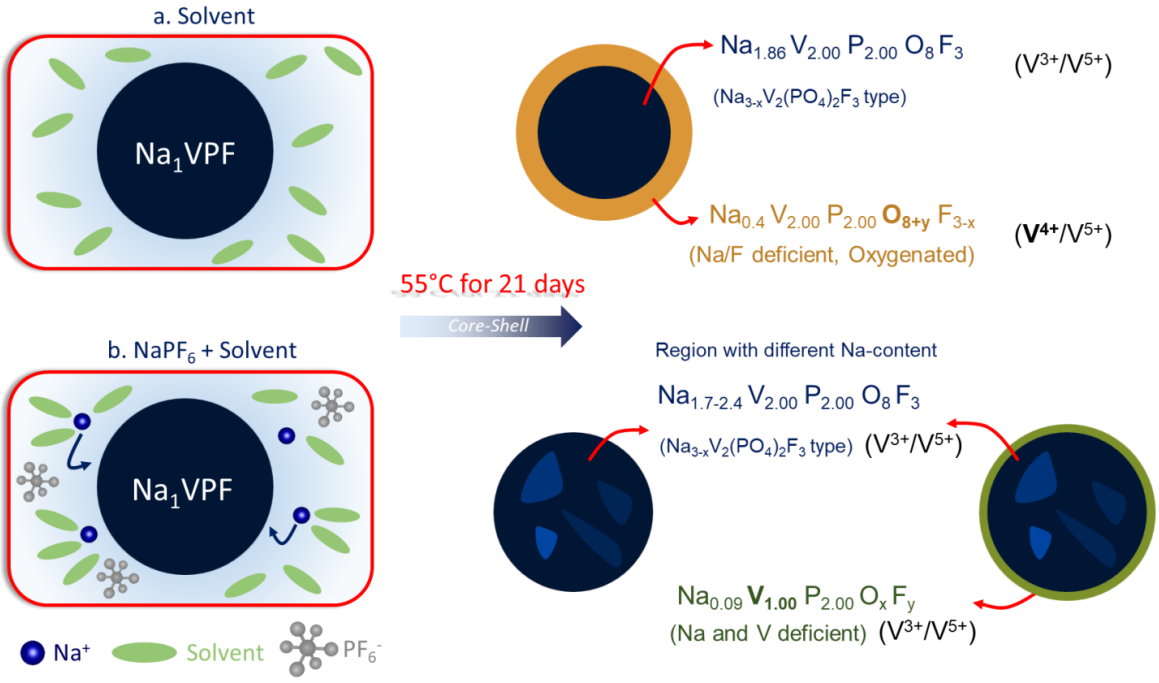

Fig. 3.8 | Schematic of Structural Degradation in SL- and PF_6-NVPF. (a) Solvent-leached NVPF results in a core-shell type structure, where the core remains intact while a thick shell forms, consisting of oxygenated material. (b) Electrolyte (1M NaPF6 in EC-PC-DMC) leaching of NVPF leads to a core-shell type structure, where the shell becomes thin and depleted in vanadium.

As shown in **Fig. 3.8**, both the SL-NVPF and PF_6-NVPF samples exhibit a core-shell structure. The core region of the SL-NVPF sample is richer in Na compared to the starting Na_1VPF phase. In the presence of a Na^+-free solvent, the observed excess Na in the SL-NVPF core is likely the result of Na diffusion from the surface to the core, which is consistent with the Na-deficient surface/shell observed by TEM. This explains the higher oxidation state of vanadium (V^{4+} and V^{5+}) in the surface region compared to the core region (V^{3+} and V^{5+}), as well as the observed capacity of approximately 50 mAh/g in the first charge for SL-NVPF (**Fig. 3.3a**), attributed to the formation

of Na-rich core. It is important to note that the charge capacity for SL-NVPF is the lowest among the leached samples in **Fig. 3.3a** since the capacity is achieved from the Na^+ migrated to the core.

A surprising finding with the SL-NVPF sample is the presence of a vanadyl (V=O) bond in the shell of the particles. The oxygen required for this vanadyl bond formation does not originate from the solvent molecules, as even O-free solvents like acetonitrile show similar results (**Supplementary Fig. S3.13**). Therefore, we suspect that the NVPF material itself is involved in a process that involves the breaking of O-PO_3 bonds, releasing phosphate anions into the solvent, and forming the vanadyl bond while sodium migrates from the surface to the bulk of NVPF. This explanation is supported by NMR studies that reveal the presence of phosphate anions in the recovered solvents from the leaching reaction leading to SL-NVPF. In contrast, no phosphate species were detected in the recovered solvents from the leaching reaction leading to PF_6-NVPF (**Supplementary Fig. S3.14**).

In summary, our observations indicate distinct leaching mechanisms depending on the solvent or $NaPF_6$ electrolyte used. In the case of SL-NVPF, the leaching process is homogeneous, resulting in particles undergoing internal redox reactions and leaving behind a vanadyl-rich shell with reduced sodium content. It is important to note that in real electrochemical cells, the electrolyte salt is always present along with the solvent for ionic conduction. On the other hand, for PF_6-NVPF, the leaching process is non-homogeneous and leads to the formation of vanadium-deficient shells, which can account for the presence of inactive phases observed previously by XRD and during electrochemical cycling.

2.5 Mechanism of self-discharge, electrolyte oxidation, and NVPF deterioration

The proposed reaction scheme in **Fig. 3.9** accounts for the formation of PF_6-NVPF, TFSI-NVPF, and SL-NVPF samples based on parasitic reactions occurring on its surface. A self-discharge phenomenon is evident in all cases from the capacity recorded during the first charge after recovering the materials (**Fig. 3.3a**). However, as explained below, the reducing agent that donates the required electrons for the self-discharge process differs in each case, leading to different reaction pathways.

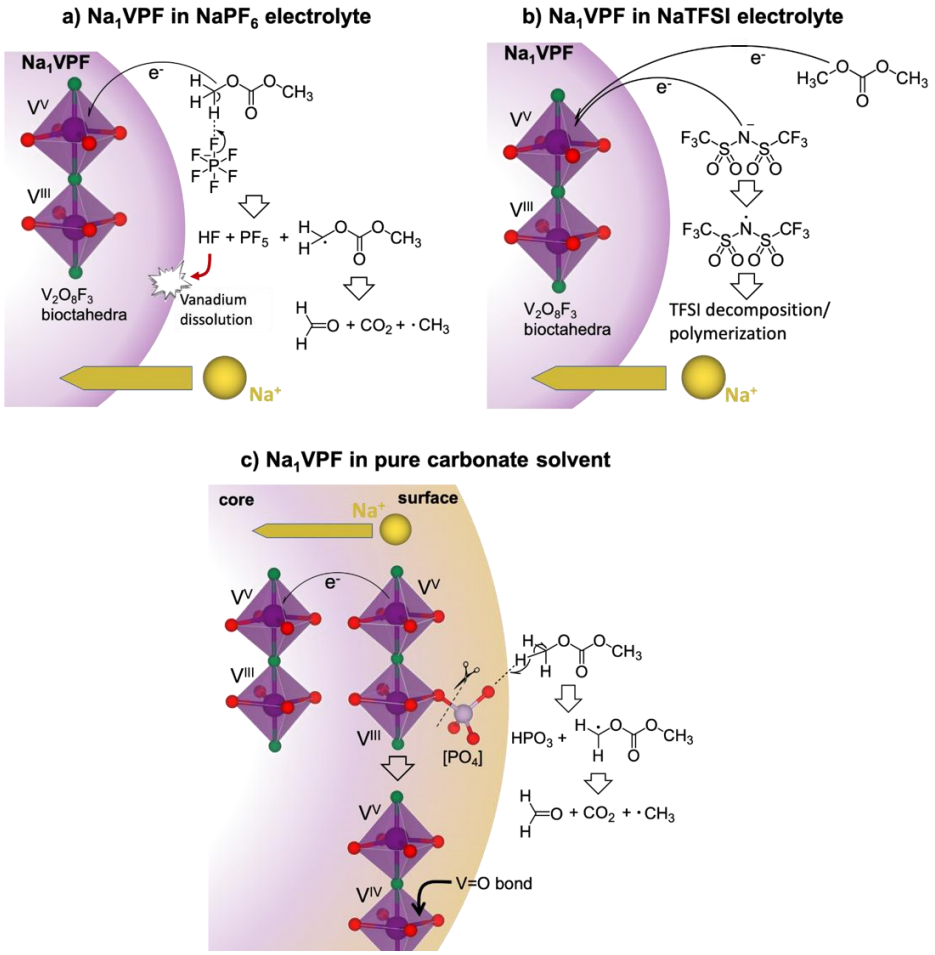

Fig. 3.9 | The proposed mechanism illustrates the structural degradation of Na_1VPF in $NaPF_6$, NaTFSI, and pure carbonate solvent. (a) In the case of $NaPF_6$-based electrolyte, simultaneous oxidation of DMC (dimethyl carbonate) and Na+ insertion in Na_1VPF occur, resulting in the formation of HF. The generated HF attacks the surface of Na_1VPF particles, leading to structural degradation. (b) In the case of NaTFSI-based electrolyte, Na^+ insertion in Na_1VPF particles occurs along with the oxidation of $TFSI^-$ anion. This oxidation process leads to the decomposition of the TFSI anion. (c) In the case of the interaction between Na_1VPF and the carbonate solvent, internal phase separation takes place within Na_1VPF particles. Simultaneously, the solvent undergoes oxidation, represented here by the oxidation of DMC as an example. In reality, other carbonate solvents like EC (ethylene carbonate) and PC (propylene carbonate) could also undergo similar oxidation pathways.

In the presence of $NaPF_6$ electrolyte (**Fig. 3.9a**), Na^+ cations are inserted into Na_1VPF, while the carbonate solvent (EC/PC/DMC) undergoes oxidation.[213,235–237] This oxidation is facilitated by the interaction with PF_6^- anions[80], leading to the formation of PF_5 and HF. The presence of HF is responsible for the observed vanadium dissolution, as confirmed by 19F-NMR

analysis (**Supplementary Fig. S3.15**). Additionally, the dehydrogenated solvent can form an organic radical that subsequently decomposes into formaldehyde, CO_2, and a methyl radical. This methyl radical can react with other electrolyte components, as supported by mass spectrometry analysis (**Supplementary Fig. S3.16** and **Table S3.2**).

A different scenario arises with the NaTFSI electrolyte, where the $TFSI^-$ anions undergo oxidation along with the solvent[80], without the formation of HF. This absence of HF formation is confirmed by NMR analysis (**Supplementary Fig. S3.17**), explaining the minimal observed vanadium dissolution. The radical formed from the oxidation of $TFSI^-$ is stabilized due to the high charge delocalization of the anion, although it may eventually decompose or polymerize, with or without the evolution of gaseous by-products. The lack of HF release in this anion decomposition accounts for the negligible V-dissolution observed. However, it should be noted that the charged NVPF in this electrolyte still exhibits significant self-discharge, which is associated with electrolyte oxidation. This issue needs to be addressed before utilizing NaTFSI-based electrolytes for Na-ion cells.

The SL-NVPF sample exhibits more pronounced structural changes, characterized by the reduction of the core of the particles by acting as a reductant (as observed in EELS data, **Fig. 3.6b**). This redox process affects the homogeneous distribution of V^{3+}-V^{5+} bi-octahedra in the Na_1VPF material, with the core evolving towards V^{3+}-V^{4+} (which eventually disproportionate back to V^{3+}-V^{5+}), while the surface changes to V^{4+}-V^{5+}. Since V^{4+} is not stable in this coordination environment, the ligands must reorganize, resulting in the dissolution of either PO_3^- groups (confirmed by 31P NMR analysis of the collected leached solvent shown in **Supplementary Fig. S3.14**) or F^-, along with a small amount of vanadium. These findings support the proposed reaction scheme (**Fig. 3.9c**) to explain the formation of vanadyl bonds (V=O) in the SL-NVPF material. Further detailed investigation through operando measurements using sophisticated techniques is required to elucidate the complete reaction mechanism.

Up to this point, the deterioration of NVPF particles has been studied by ex-situ and post mortem analyses. In the next section, we try to correlate the findings with the observed changes

in electrochemical performances of NVPF|HC cells during cycling. Starting with dQ/dV analysis discussed in **Chapter 2** is used to understand the NVPF|HC cell degradation mechanism.

2.6 Impact of dissolved vanadium on the degradation of NVPF-HC cells.

2.6.1 dQ/dV fingerprint and Δ(dQ/dV) analysis

The dQ/dV plot of the 18650 cell cycled at 55°C (from **Fig. 3.1**), is visually represented in **Fig. 3.10a-b**. The evolution of the curve is highlighted by arrow and denoted with roman numerals from 'I to V' to signify the occurring processes. Notably, observable changes include peak shifts, peak attenuation, and the emergence of new peaks. For better visualization of NVPF|HC full cell peaks, dQ/dV for half cells of NVPF and HC are presented in **Supplementary Fig. S3.18.**

To visualize the changes clearly Δ(dQ/dV) for few cycles is introduced[238] for the charge (**Fig. 3.10c-d**) and discharge (**Fig. 3.10e-f**) separately and defined as:

$$\Delta\left(\frac{dQ}{dV}\right)_n = \left(\frac{dQ}{dV}\right)_n - \left(\frac{dQ}{dV}\right)_2$$

Where $(dQ/dV)_n$ and $(dQ/dV)_2$ is for n^{th} and 2^{nd} cycle, respectively. Following is the summary of the processes happening analyzed with Δ(dQ/dV):

1. Except process 'I', all the processes occurring in the charge has corresponding processes in the discharge in the mirror image fashion marked by the roman numbers (**Fig. 3.10c-f**) indicating their reversibility.
2. Note and compare the evolution of Δ(dQ/dV) peaks in charge vs. discharge. As cycling proceeds (**Fig. 3.10c-f**), hysteresis for processes 'II' decreases but it increases for process 'III' and 'IV'.
3. The peaks corresponding to 'II, III and IV' have sharper peaks in charge and broader peaks in the discharge.

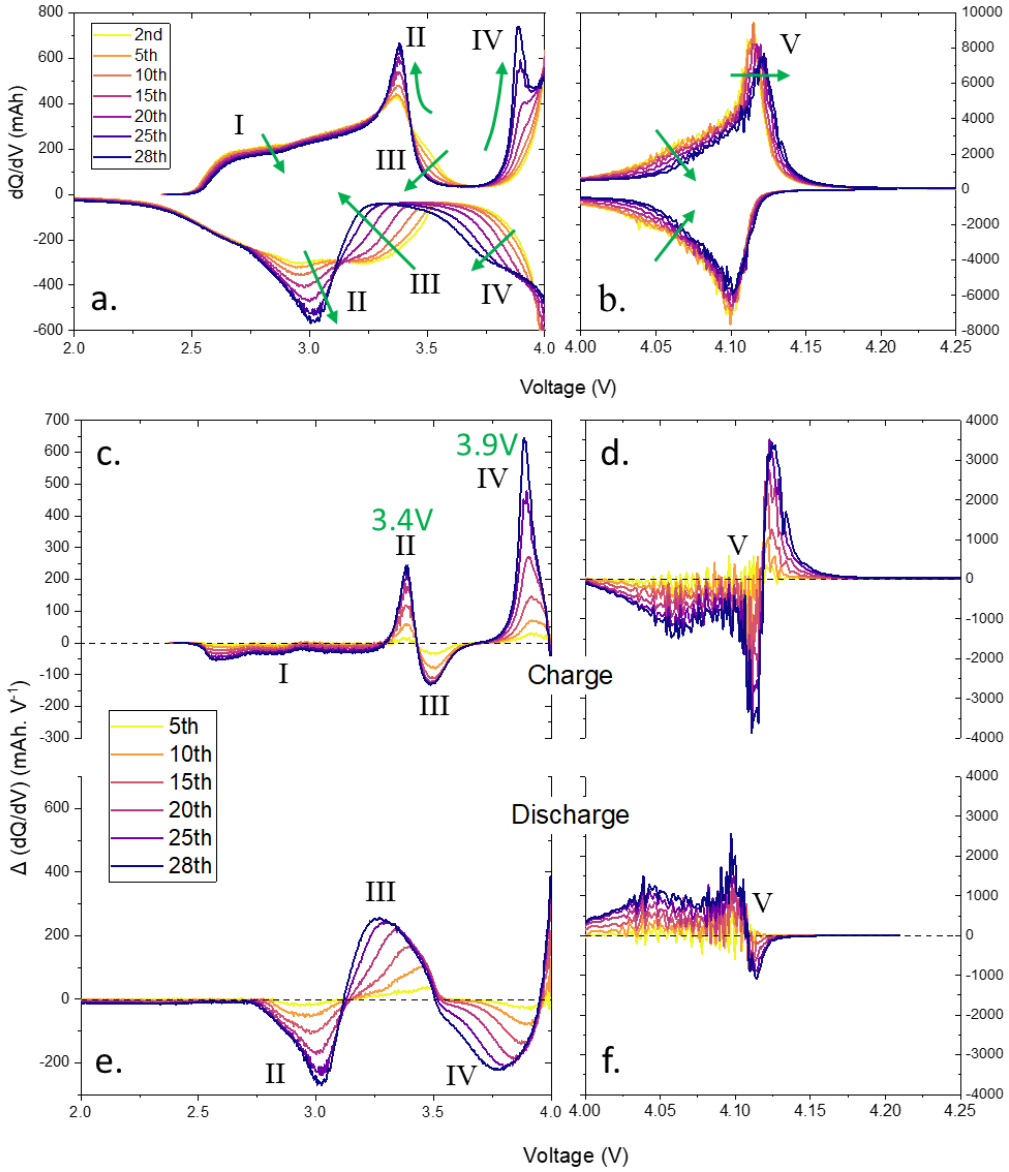

Fig. 3.10 | dQ/dV and Δ(dQ/dV) analysis for ageing of 18650 type NVPF-HC cell. (a) and (b) dQ/dV profile for selected cycles of 18650 cell. (c) and (d) Δ(dQ/dV) profile for selected charging curves. (e) and (f) Δ(dQ/dV) profile for selected discharging curves.

In order to delve deeper into these processes and understand their origins, a simple formulation is presented in **Fig. 3.11**. For simplicity, the discussion focuses on the dQ/dV corresponding to charge curves, which can also be extended to discharge curves. Changes in the dQ/dV curve can be visualized as variations in peak intensity or shifts of peaks, or a combination of both. **Fig. 3.11a** illustrates the peak attenuation in dQ/dV, resulting in a negative increase in peak intensity for Δ(dQ/dV). This attenuation can occur if there is an apparent mass loss from the

electrodes (refer to **Fig. 2.12** of **Chapter 2**). Conversely, if a new peak emerges at a specific voltage, it will exhibit a positive Δ(dQ/dV) as in the case of peak 'IV' in **Fig. 3.10c**. The simulation in **Fig. 3.11b** demonstrates how a shift in the dQ/dV peak leads to a bimodal curve in Δ(dQ/dV). A rightward shift produces a down-up type bimodal curve (as shown in **Fig. 3.11b**), while a leftward shift results in an up-down bimodal curve. Peak shifts can be caused by factors such as slippage, material transformation, or polarization, as discussed earlier in **Chapter 2**. Polarization, specifically, shifts the entire dQ/dV profile to the right (as depicted in **Fig. 3.11c**), leading to the formation of repetitive down-up type bimodal curves in Δ(dQ/dV).

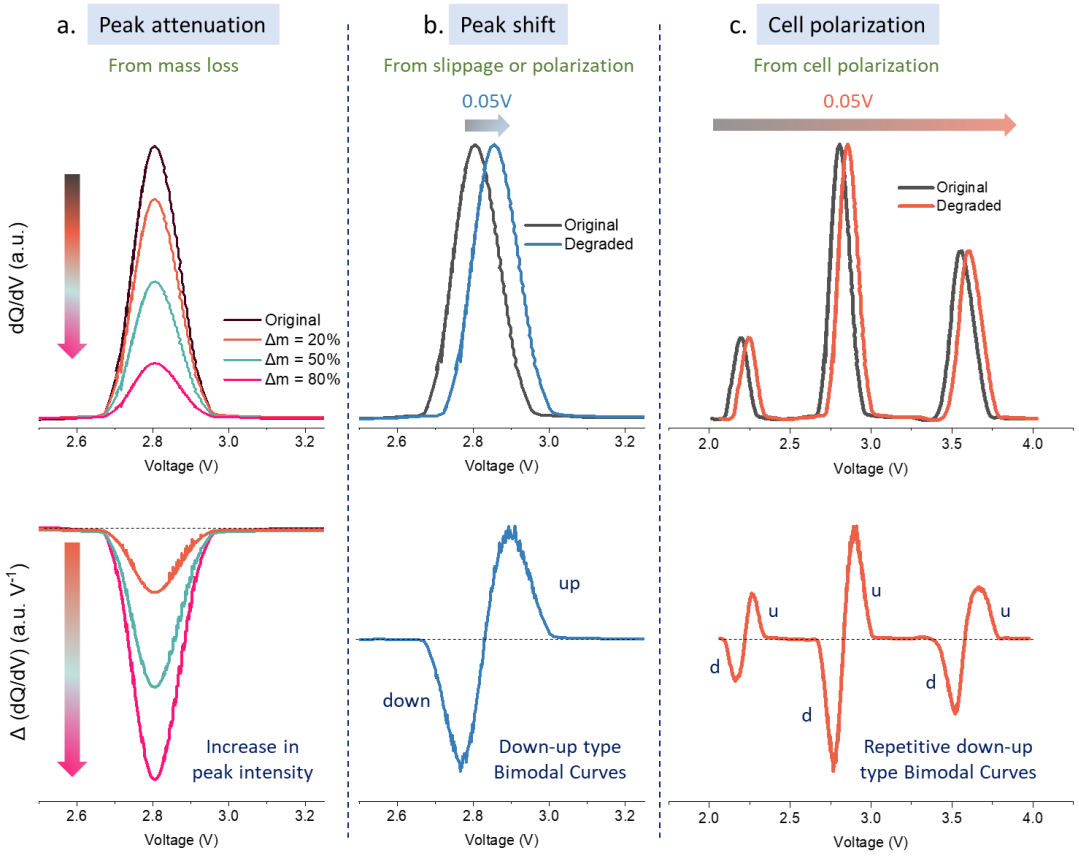

Fig. 3.11 | Simulated profile to formalize Δ(dQ/dV). (a) Effect of peak attenuation on Δ(dQ/dV). (b) Effect of rightward peak shift by 0.05V on Δ(dQ/dV). (c) Effect of cell polarization by 0.05V on Δ(dQ/dV).

Upon revisiting and analyzing the processes depicted in **Fig. 3.10**, it becomes apparent that the bimodal peaks observed in **Fig. 3.10c-d** do not exhibit the repetitive down-up pattern, indicating the absence of significant polarization effects on the dQ/dV curve. Process 'I' may be attributed to apparent mass loss, while processes 'II' and 'III' could result from a leftward shift of

the dQ/dV peak due to slippage. Process 'IV' represents a completely new process, and processes 'V' could arise from a rightward shift of the dQ/dV peak due to slippage. However, further analysis is required to confirm the hypothesis regarding processes 'II', 'III', and 'V' and the influence of slippage. To investigate further, **Fig. 3.12** presents simulated results illustrating the impact of HC slippage on the dQ/dV and Δ(dQ/dV) profiles of the full cell. In the event that the HC curve slips to the right (**Fig. 3.12a**) as a consequence of parasitic reactions, it predominantly affects processes 'I', 'III', and 'V' in the dQ/dV curve (**Fig. 3.12b**), which is clearly evident from the corresponding Δ(dQ/dV) profiles (**Fig. 3.12c-d**).

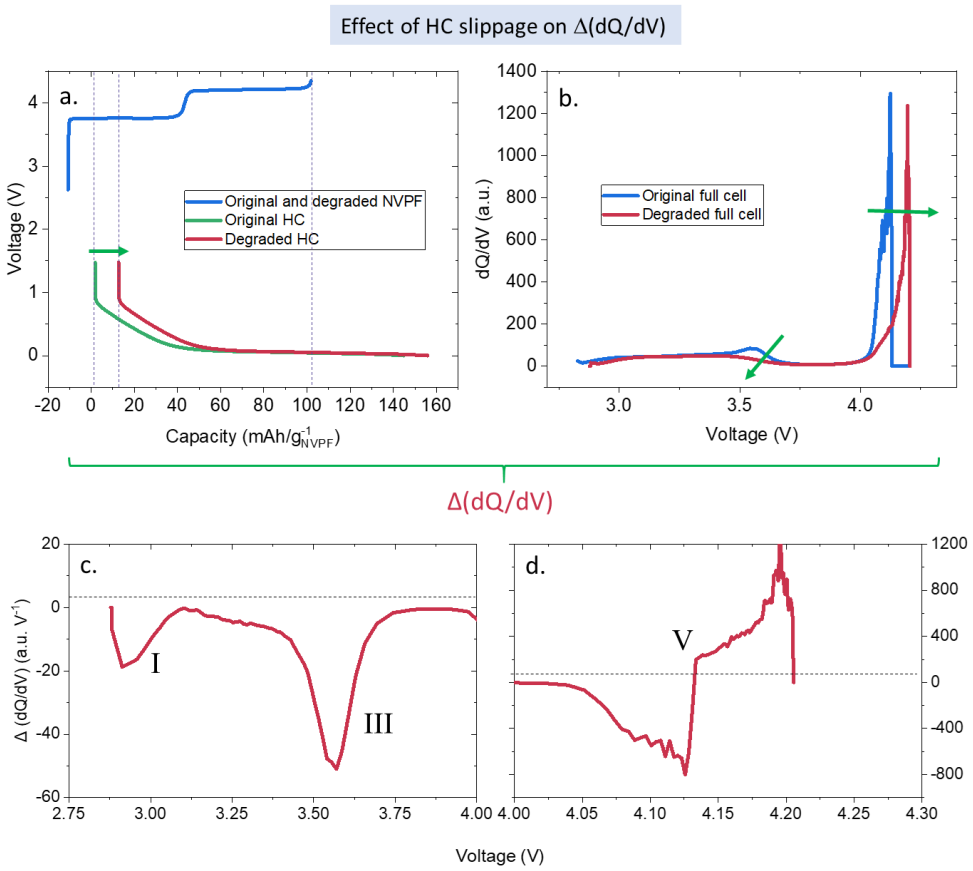

Fig. 3.12 | Effect of HC slippage on dQ/dV and Δ(dQ/dV). (a)Leftwards slippage of HC relative to the NVPF, the dotted lines are presented to show the common area between NVPF and HC curves. (b) Effect of the HC slippage shown in (a) on the dQ/dV profile of full cell. (c) and (d) Δ(dQ/dV) due to only HC slippage.

Following is the conclusion after analyzing all the Δ(dQ/dV) peaks using mass loss and slippage:

1. Processes or peaks at I, III and V are attributed to parasitic reactions leading to HC slippage.

2. Peaks II (~3.4V) and IV (~3.9V) appear to be completely new reversible redox processes occurring within the electrodes. These peaks indicate structural modifications or transformations taking place during the operation of the cell.
3. Slight mass loss of NVPF (processes 'I') and leftwards slippage of HC relative to NVPF (processes 'I, III and V') due to electrolyte reduction is primary cause for the capacity loss.

The emergence of new reversible redox peaks at 3.4V and 3.9V serves as an indication of structural modifications occurring in the NVPF electrode. These peaks act as unique fingerprints and can be utilized effectively to monitor the health of the NVPF electrode, particularly in response to parasitic electrolyte attack at high temperatures, which leads to vanadium dissolution and structural/surface alterations. The upcoming section delves further into the destabilization of the electrolyte and provides more information about distinctive fingerprint peaks.

2.6.2 Electrolyte destabilization

To assess the reactivity of the V-containing electrolyte, two experiments were conducted as depicted in **Fig. 3.13**. Three-electrode cyclic voltammetry (CV), explained in **Fig. 2.20** and **Fig. 2.21** of **Chapter 2**, was performed. In **Fig. 3.13a**, the aged 18650 cell, following a current interrupt device (CID) break as shown in **Fig. 3.1**, was meticulously recovered, washed with EC-PC-DMC, and filtered. This process yielded a green solution containing soluble V species derived from the NVPF electrode. Subsequently, 1M $NaPF_6$ was added to this green solvent blend, creating the V-containing electrolyte referred to as the "green electrolyte." The CV results displayed visible peaks around ~3.4V and ~3.9V. Notably, new reversible peaks named 'II' (at 3.4V) and 'IV' (at 3.9V) appeared in the dQ/dV profile of NVPF|HC full cell (**Fig. 3.10**), confirming that these peaks were caused by the formation of a new phase on the NVPF surface or partial dissolution of this phase in the electrolyte. As this phase exhibited partial solubility in the EC-PC-DMC, thereby exhibiting similar redox behavior in the electrolyte. Furthermore, it was observed that the NVPF|HC cell exhibited a faster rate of degradation when the green electrolyte was used compared to the pristine electrolyte (**Supplementary Figure S3.19**).

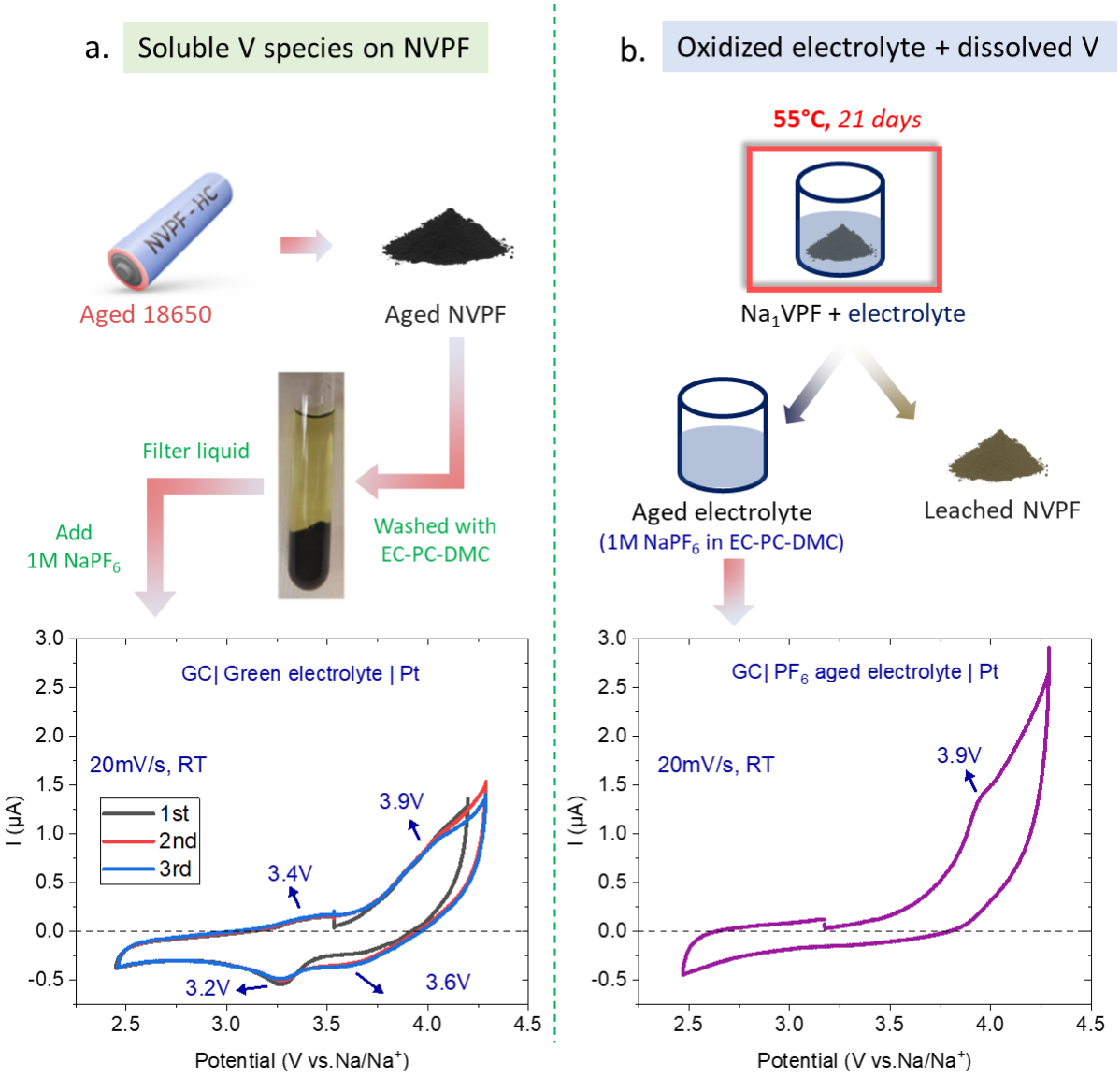

Fig. 3.13 | Electrolyte destabilization due to dissolved V and electrolyte oxidation. (a)Process of getting V containing green electrolyte and its three electrode CV. (b) Aging of $NaPF_6$ electrolyte in contact with charged Na_1VPF at 55°C and its three electrode CV.

In contrast, charged Na_1VPF underwent leaching with 1M $NaPF_6$ in EC-PC-DMC (**Fig. 3.13b**) at 55°C for 21 days. During this process, both the solvent and/or salt were oxidized and decomposed, in addition to V dissolution. The resulting aged electrolyte is referred to as the "PF_6-aged electrolyte." The CV of the PF_6-aged electrolyte (**Fig. 3.13b**) revealed a peak at around ~3.9V, which could be from dissolved V as **Fig. 3.13a** or from the presence of oxide (or sodium methoxide) as observed by Cometto et al. Furthermore, the nature of vanadium present in the

$NaPF_6$ based electrolyte after the leaching process was analyzed. The resulting PF_6-aged electrolyte, as shown in the 51V-liquid NMR result in **Supplementary Fig. S3.20**, exhibited the absence of an NMR signal. This suggests that vanadium is present in either the +2, +3, or +4 oxidation states within the PF_6-aged electrolyte. Additionally, when the PF_6-aged electrolyte cathodically reduced on glassy carbon, it gave a distinctive peak with a high reduction current at ~1.6V (**Supplementary Fig. S3.21**), showing high redox activity of V containing electrolyte.

Comparing the current values of cyclic voltammograms (CVs) at room temperature for the green electrolyte and the PF_6-aged electrolyte reveals their potential electrochemical activity, which will be even more enhanced at high temperatures. These electrolytes can act as redox shuttles on both the NVPF and HC electrodes, which operate at different potentials (between 3-4.3V and 2-0.0V vs. Na^+/Na^0, respectively) in the NVFP|HC full cell. This kind of redox shuttle activity can result in self-discharge and rapid cell degradation, as described elsewhere. Moreover, the vanadium-based species present in the electrolyte have the potential to deposit on the HC electrode, leading to electrode poisoning. This, in turn, can cause the dissolution and growth of interphases (such as SEI and CEI), resulting in increased impedance, pore-clogging, and other detrimental effects. It is worth noting that acidic impurities (such as HF, HPO_2F_2, etc.) formed during the oxidation of the electrolyte, as mentioned in previous reports,[80,142,239,240] can also contribute to the dissolution and formation of interphases (SEI, CEI). This not only leads to a loss of Na-inventory but also increases the overall cell impedance. Thus, the impact of V dissolution on both the electrodes is analyzed in the subsequent section.

2.6.3 Electrode degradations

NVPF and HC electrodes were recovered from the aged 18650 cells (shown in **Fig. 3.1**), washed with DMC, and assembled into half cells after drying (**Supplementary Fig. S3.22**). NVPF and HC show a loss of capacity and an increase in polarization from the degradation of the material. To identify the limited electrode causing the capacity loss among NVPF and HC, full cells with a combination of pristine and aged electrodes were assembled and cycled at 55°C (shown in **Fig. 3.15**). Pristine NVPF|Aged HC showed rapid capacity loss as compared to Aged

NVPF|Pristine HC indicating that the capacity loss is mainly due to degradation of HC and SEI poisoning from vanadium during the aging.

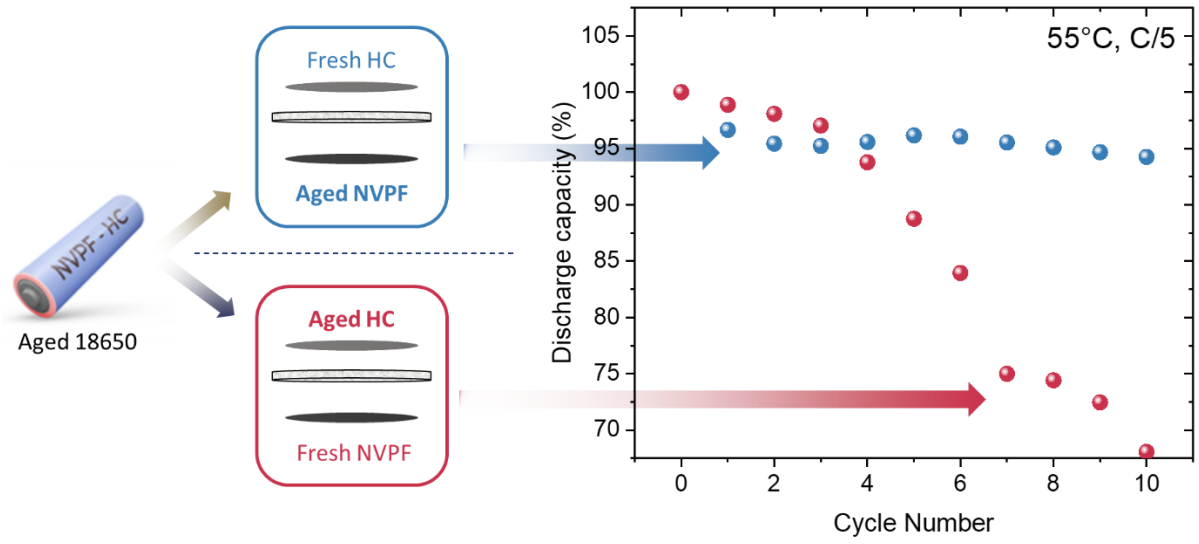

Fig. 3.14 | Identification of limited electrode in between NVPF and HC due to V dissolution and cell aging. Process of making full cell with a combination of Aged NVPF|Fesh HC and Fresh NVPF|Aged HC and their cyclic stability at 55°C.

After understanding the mechanism of vanadium dissolution and its impact on cell electrochemistry, mainly the formation of new redox processes with the fingerprint at ~3.4V and 3.9V, redox shuttle formation, and poisoning of the hard carbon electrode, a few strategies could be introduced to alleviate this issues. The next session discusses two of the strategies that will suppress V dissolution, thus improving the cell performance.

2.7 Partially suppressing V dissolution

2.7.1 NaTFSI based electrolytes

In our first strategy, we investigated the use of NaTFSI as the electrolyte salt to prevent V-dissolution into the electrolyte. However, NaTFSI alone corrodes the Al current collector at high potentials (above ~4V vs. Li/Li^+),[241] so a mixture of $NaPF_6$ and NaTFSI was used. Comparative analysis (**Fig. 3.15a**) between 1M $NaPF_6$ and 0.7M $NaPF_6$ - 0.3M NaTFSI electrolytes in a 1:1:2 mixture of EC-PC-DMC at 55°C revealed similar capacity loss during self-discharge (**Fig. 3.15b**). However, the subsequent cycle showed higher capacity recovery and retention, as well as fewer

changes in cell polarization, with the NaTFSI-containing electrolyte (**Fig. 3.15a** and **3.15c**). ICP analysis of the electrodes and separator after 850 hours of cycling (**Fig. 3.15d**) indicated lower vanadium dissolution (2.17%) for the $NaPF_6$:NaTFSI mixed electrolyte compared to the 1M $NaPF_6$ electrolyte (5.45%). Although self-discharge loss of 25% was still observed in both cells, further measures are being explored to address electrolyte oxidation. These findings show promising results, highlighting the potential of using NaTFSI-containing electrolytes with improved performance and reduced V-dissolution.

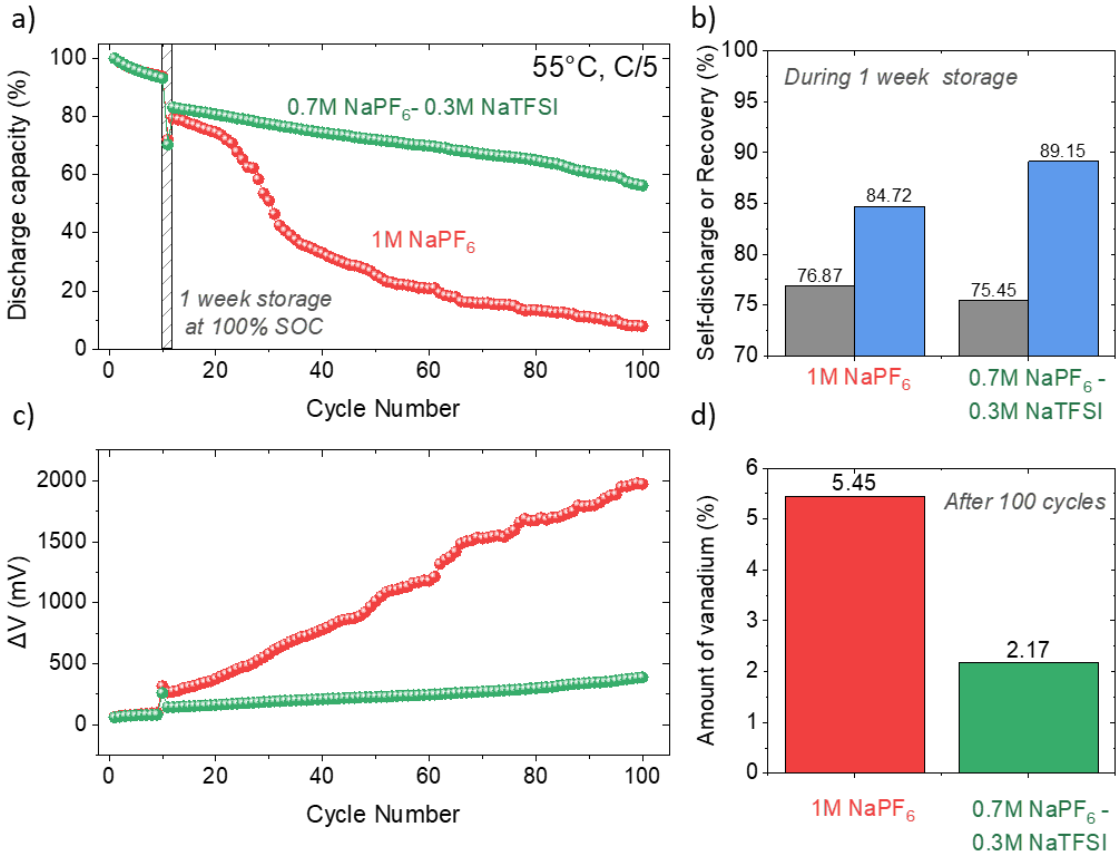

Fig. 3.15 | Impact of NaTFSI on the protection of the NVPF surface. NVPF-HC coin cells were cycled at a C/5 rate and 55 °C, using either 1M $NaPF_6$ or 0.7M $NaPF_6$-0.3M NaTFSI in EC-PC-DMC (1:1:2) as the electrolyte. The figure presents the following information: (a) Discharge capacity retention. (b) Self-discharge (Q_9/Q_{10}) and recovery (Q_{11}/Q_{10}) processes during the storage period. (c) Polarization evolution in terms of ΔV, which is the average charge voltage minus the average discharge voltage. (d) The amount of vanadium in the coin cells after 100 cycles, was measured using ICP-MS.

2.7.2 Efficient carbon coating of NVPF

The second strategy involved exploring the coating of NVPF particles, and two batches of NVPF with different amounts of carbon coating were prepared as confirmed by TGA analyses (**Fig. 3.16a**). Batch 1 exhibited a carbon content of approximately 7%, while Batch 2 had a carbon content of around 3%. EDX mapping indicated a more uniform carbon coating for Batch 1 (**Supplementary Fig. S3.23**). To evaluate vanadium dissolution, both batches were tested in coin cells with 1M $NaPF_6$ in EC-PC-DMC as the electrolyte. The cells were stored at 100% state of charge (SOC) for one week at 55 °C. The results (**Fig. 3.16b**) revealed a higher level of vanadium dissolution for Batch 2, which had a lower amount of coated carbon.

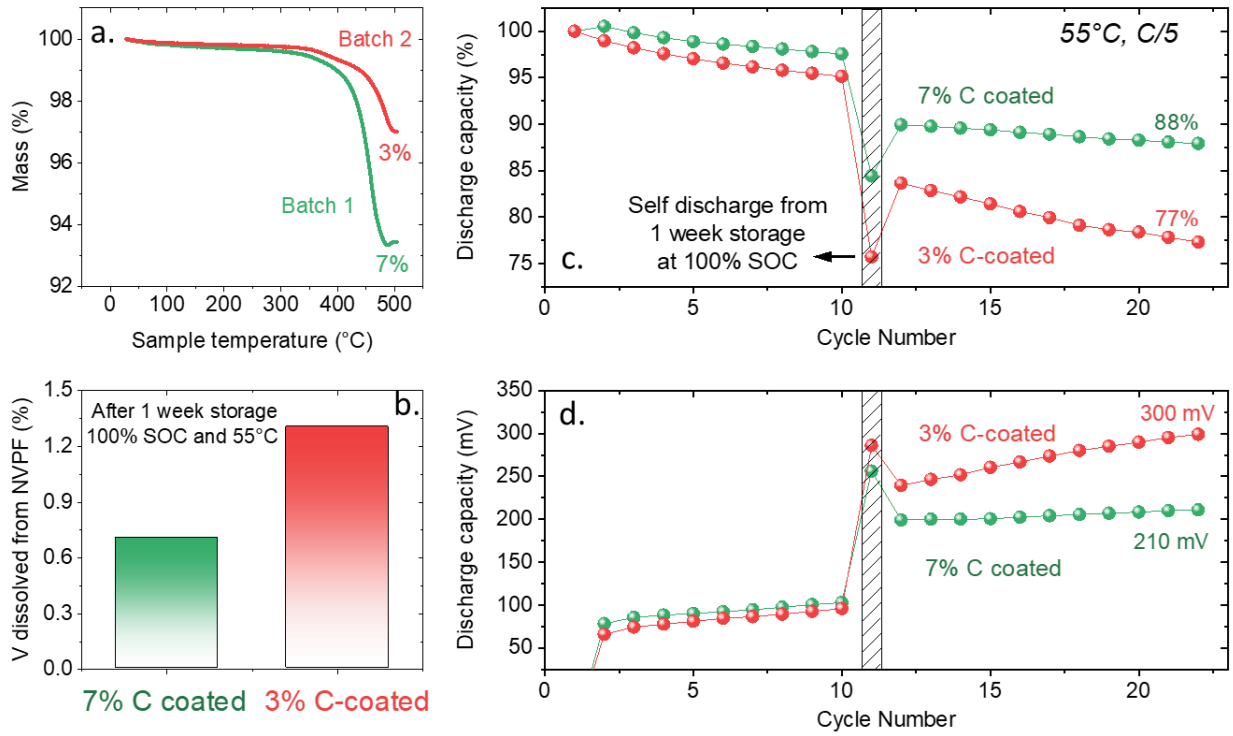

Fig. 3.16 | Effect of carbon coating on vanadium dissolution and cell electrochemistry. The figure includes the following details: (a) TGA analysis comparing the amount of carbon coating in Batch-1 and Batch-2. (b) The amount of vanadium dissolved from NVPF for 7% and 3% carbon-coated NVPF when NVPF-HC cells were stored at 55 °C for 1 week. (c) Discharge capacity retention of 7% and 3% carbon-coated NVPF in NVPF-HC full cell mode at 55 °C with a C/5 rate. (d) Corresponding cell polarization represented in terms of ΔV, which is calculated as the average charge voltage minus the average discharge voltage.

In addition, coin cells utilizing both batches as the positive electrode, along with 1M $NaPF_6$ in EC-PC-DMC electrolyte, were cycled at 55 °C. The capacity retention (**Fig. 3.16c**) and polarization evolution (**Fig. 3.16d**) during cycling demonstrated that NVPF with a higher carbon coating (7%) exhibited less self-discharge loss during rest periods (1 week) and lower polarization after the self-discharge process, compared to NVPF with only 3% carbon coating. Overall, these results confirm the positive impact of carbon coating in reducing vanadium dissolution during rest periods at 100% SOC.

In summary, the carbon coating and electrolyte optimization on NVPF demonstrates positive effects in reducing reactivity at the NVPF electrolyte interface. However, an increase in carbon content, leading to thicker coating, has a negative impact on the specific energy and potentially the power rate capability of the material. Therefore, it is essential to carefully tune the surface coating, choose the electrolyte formulation wisely, and establish an optimized formation cycle to minimize V-dissolution to achieve high performance in NVPF|HC Na-ion cells at an industrial level.

3. Conclusions of the chapter

Transition metal dissolution presents a significant challenge in various battery technologies, including well-established LIBs. This study unveils that the dissolution of 3d metals poses an equally significant issue in NIBs, especially for the NVPF|HC chemistry, as the redox potential of NVPF (~4.2 V vs. Na/Na^+) surpasses the thermodynamic stability of conventional electrolytes. The extent of V dissolution was found to be influenced by several factors, including the formulation of the electrolyte. Different electrolyte salts exhibited varying effects on the degradation of NVPF. Interestingly, when charged NVPF interacts with the bare solvent, and Na and F deficient and oxygen-rich shell is formed, characterized by vanadyl (V=O) bonds, surrounding a core resembling NVPF. During this process, Na^+ ions migrate from the shell to the core. In practical $NaPF_6$-based electrolytes, a different kind of core-shell type degradation mechanism occurs, with the shell containing almost no sodium and half the vanadium content of the original NVPF formula, while the core retains its structural integrity.

During the aging of the NVPF|HC cell, in addition to NVPF mass loss and HC slippage, distinctive fingerprint peaks emerge at around ~3.4V and ~3.9V vs. Na/Na^+. These peaks indicate surface transformations of NVPF and the formation of a secondary phase resulting from parasitic electrolyte oxidation and vanadium dissolution. This phase exhibits partial solubility and demonstrates redox activity in the electrolyte. Furthermore, the aged $NaPF_6$ electrolyte containing dissolved vanadium exhibits high redox activity in both oxidation and reduction processes. Consequently, the aged electrolyte, with the presence of vanadium, forms redox shuttles within the cell. These shuttles can contribute to self-discharge, capacity fade, and increased cell polarization. Finally, the degraded electrodes were analyzed to determine the primary source of capacity loss. By combining degraded electrodes against fresh electrodes in full cell, it was identified that HC is most impacted by the V dissolution which was also realized as HC slippage from Δ(dQ/dV) analysis.

Finally, efforts were made to prevent V-dissolution in NVPF|HC cells. Firstly, it was demonstrated that a NaTFSI-based electrolyte prevents this process, although it undergoes oxidation at high potentials. Secondly, it was shown that coating NVPF particles with carbon provide an attractive approach to reduce vanadium dissolution and protect the cell's surfaces. Both the approaches lead to better cell lifetime at elevated temperatures. Overall, the study highlights the importance of optimizing the synergy between electrode and electrolyte to achieve optimal performance in NVPF/HC Na-ion cells. From a fundamental perspective, this study offers valuable insights into the mechanisms of transition metal dissolution, its relationship with different salts, and the role of dissolved transition metals in altering the electrochemical performance of the cell.

The chapter commenced with cycling aging of an 18650 type NVPF|HC cell at 55°C, utilizing a 1M $NaPF_6$ in EC-PC-DMC blend. The cell underwent 28 cycles before experiencing a current interrupt device failure caused by significant pressure build-up inside the cell. This pressure was a result of gas generation during the parasitic reaction of the electrolyte, primarily stemming from electrolyte oxidation. Addressing this issue and achieving a stabilized electrolyte and interphase will be the focus of the next chapter, aiming to enable realistic utilization of the NVPF|HC cell chemistry.

Chapter 4 | Enhancing Electrode-Electrolyte Interphase Chemistry through Combination of Effective Electrolyte Additives.

" This Chapter is based on the following research article that I co-authored : Desai, P., Huang, J., Hijazi, H., Zhang, L., Mariyappan, S., and Tarascon, J. (2021). Deciphering Interfacial Reactions via Optical Sensing to Tune the Interphase Chemistry for Optimized Na-Ion Electrolyte Formulation. Adv. Energy Mater., 2101490. 10.1002/aenm.202101490.

1. Background and Motivation

As discussed in the previous Chapter, the use of the control electrolyte, namely 1M $NaPF_6$ in EC-PC-DMC, leads to a significant pressure buildup and breakage of the current interrupt device in commercial 18650 type $Na_3V_2(PO_4)_2F_3$ (NVPF) | hard carbon (HC) cells when cycled at 55°C (**Fig. 3.1** in **Chapter 3**). First, it leads to poor cycling performance of the NVPF- HC cells at high temperatures. Further, irrespective of the origin of such gassing, the LIB literature often report, the general gas composition found primarily includes H_2, CO, CO_2, and hydrocarbons (Refer to **Supplementary Fig. 4.1**).[141] This gas mixture is flammable, and in cases of significant pressure buildup, it can cause a rupture in the cell casing, leading to various safety-related accidents.[242,243] Therefore, it is crucial to understand the source of gas generation and take measures to prevent it.

The gases formed in the battery are byproducts of parasitic reactions triggered by electrolyte decompositions on desodiated NVPF (high potential) and sodiated HC (low potential) when the full cell is at a high state of charge (SOC). These reactions involve the oxidation and reduction of the electrolyte, leading to the release of different gases, as studied by Zhang et al. for various Na-ion chemistries.[149] Guochun et al. previously found that cross-talk reactions, primarily the reduction of linear carbonates to form sodium alkoxide (R-ONa) and sodium alkyl carbonates (R-O-CO-ONa), and their subsequent oxidation on NVPF lead to overcharge[146] when only linear carbonate solvent is used (**Fig. 2.26b** of **Chapter 2**). Further studies by Cometto et al. using three-electrode cyclic voltammetry (CV) experiments revealed that reduced byproducts in CV create species that are susceptible to oxidation[123] (**Fig. 2.20b** of **Chapter 2**).

These electrolyte redox instabilities and parasitic currents can be further promoted from the presence of dissolved vanadium, as discussed in the previous Chapter. Thus, the parasitic currents causing electrolyte degradation and capacity loss are responsible for the gassing.[149,232] **Fig. 4.1** illustrates the rapid capacity fade observed when NVPF|HC cells are cycled at 55°C compared to room temperature, thus intensifying the cell degradation and/or gassing. To ensure good cycling stability and minimize gas generation at elevated temperatures, suppressing these parasitic reactions is of utmost importance, thus improving the overall performance and safety

of the battery system. Additionally, NVPF|HC cells are intended for high-power applications, and during 5C cycling, cell temperatures increased to around 50°C, as noted by Huang et al. This emphasizes the crucial need for high temperature stability in extremely high-power cells.[244]

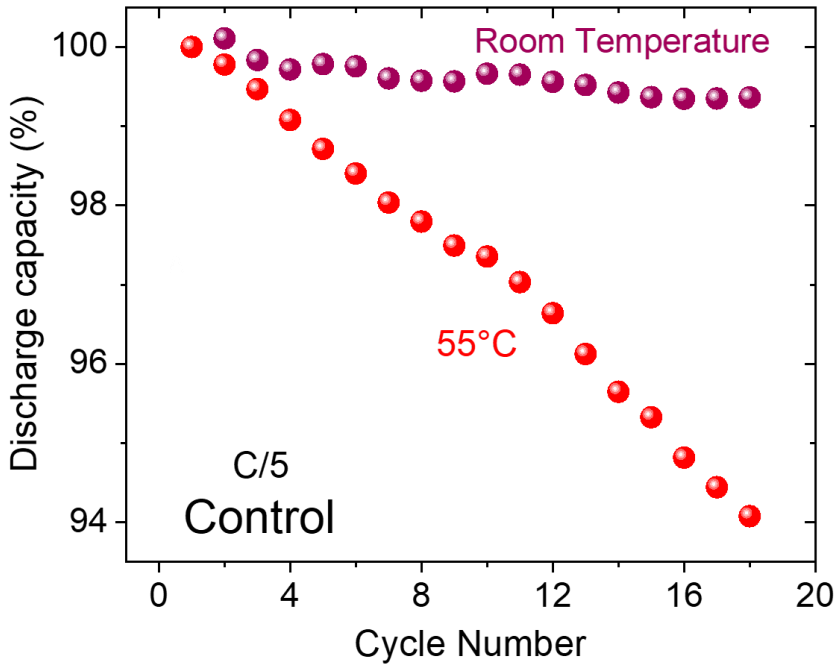

Fig. 4.1 | High temperature instabilities in NVPF-HC cell. Discharge capacity retention plot of NVPF|HC cell containing control electrolyte cycled at 55°C and C/5.

Electrolyte additives[112,245–248] have proven to be the most effective and efficient solution to suppress the parasitic currents discussed earlier. The addition of a very small quantity (0.1-10 wt%) of these chemical components to the electrolyte can completely mitigate the undesired reactions. These additives achieve this by forming a passivating interphase, generally through preferential (electro)chemical oxidation or reduction during the first few cycles of cell formation. **Fig. 4.2** summarizes the development of electrolyte engineering done for NVPF|HC cells in our group over the previous years with their advantages and limitations.

Guochun et al. screened a variety of electrolyte additives[122] from the knowledge of a huge Li-ion database and formulated electrolyte securing high temperature stability: 1M $NaPF_6$ in EC-PC with four additives, namely sodium difluoro(oxalate)borate (NaODFB), Succinonitrile (SN), vinylene carbonate(VC) and 1,3-propane sultone (PS). We will call this electrolyte "**Gen-1**

electrolyte" (**Fig. 4.2**) for the sake of simplicity. Although it exhibited remarkable stability, the electrolyte contained only cyclic carbonates (EC and PC), leading to its impracticality in commercial cells with celgard separator due to its high viscosity and poor wettability. Additionally, this high viscosity due to the absence of linear carbonates (DMC, EMC and DEC) will lead to limited power performance, inability to cycle at low temperatures and high chances of sodium plating on HC.

To tackle this issue, Claudio et al. incorporated DMC in the electrolyte blend and came up with the new electrolyte formation[123]: 1M $NaPF_6$ in EC-DMC with three additives, namely NaODFB, SN, Tris(trimethylsilyl) Phosphite (TMSPi), also named as "**Gen-2 electrolyte**" (**Fig. 4.2**). This electrolyte could be implemented in real commercial cells as it can wet the celgard separator. However, the observed increase in the discharge capacity, and associated charge endpoint slippage indicated parasitic electrolyte oxidation, as discussed in **Table 2.2** of **Chapter 2**, and when implemented in 18650 cylindrical cells led to gassing followed by CID break at high temperatures (55 °C).

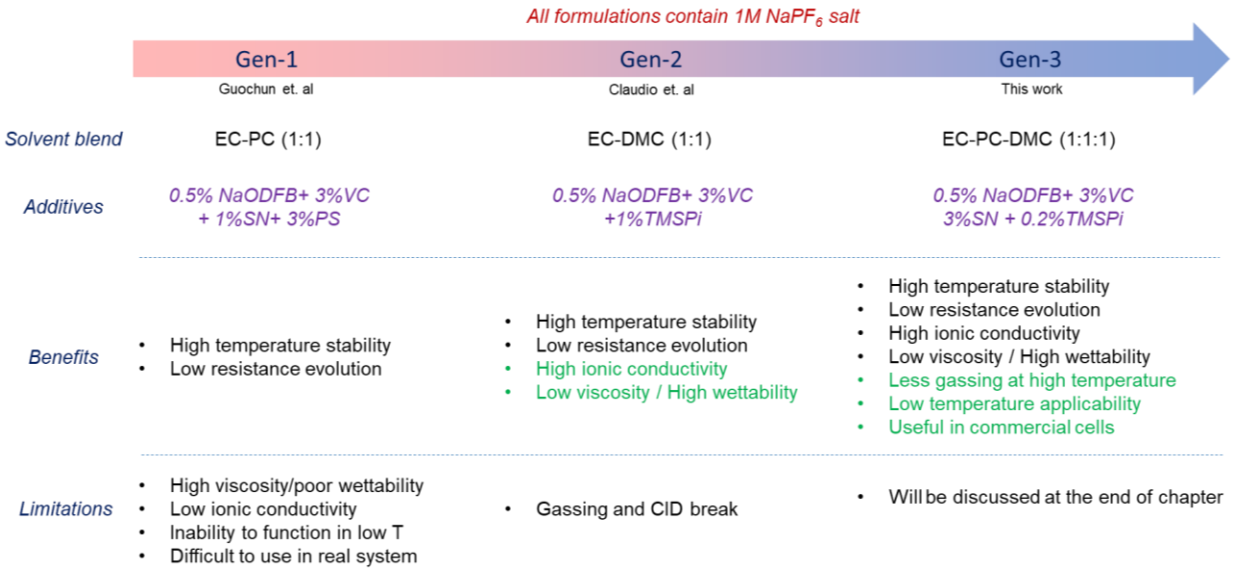

Fig. 4.2 | Electrolyte development flowchart for NVPF|HC. Electrolyte developments containing different additives is summarized. Starting with Gen-1 electrolyte by Guochun et al. to Gen-2 electrolyte by Claudio et al. and Gen-3 electrolyte presented in this work. All of the electrolytes possess certain advantages and limitations but with newer generation electrolytes limitations were minimized.

To tackle the issue of gassing "**Gen-3 electrolyte**" consisting 1M $NaPF_6$ in EC-PC-DMC (1:1:1 by vol%) with 0.5%NaODFB + 3%VC + 3%SN + 0.2% TMSPi was invented. This constitutes the main topic of discussion in this Chapter. In the starting stages of the chapter, optical sensing on commercial 18650 type NVPF-HC cells was used to track the parasitic heat release during formation and initial cycles. Then, the role of additives and their performance was further rationalized with electrochemical tests. More information about optical sensing calorimetry and other experimental details can be found in the **Methods section** of this chapter.

2. Results and discussions

2.1 Heat Evolution during Formation Cycle for "Control Electrolyte"

For the base or control electrolyte, we carefully selected 1M $NaPF_6$ dissolved in a mixture of EC–PC–DMC (volume ratio of 1:1:1) based on its favorable chemical and electrochemical reactivity and overall performance[122,123,146] at room temperature and high temperature (**Fig. 4.1**). EC was chosen for its role in SEI formation[164], DMC for reducing electrolyte viscosity and increasing conductivity/wettability[80,249], and PC for reducing the freezing point.[249–251] Before use, all solvents were dried with molecular sieves and tested for water content (<10 ppm) by Karl Fischer titration. The resulting electrolyte exhibits ionic conductivities of 6.07, 11.14, and 15.9 mS cm^{-1} at 0, 25, and 55 °C, respectively. The cells were mainly tested at 55 °C for accelerated testing.[115] This additive-free mother electrolyte 1M $NaPF_6$ in EC-PC-DMC is referred to as the "control," and other electrolyte formulations with additives are named based on their specific identities.

The chemical/electrochemical stability of the control electrolyte was tested using a recently developed calorimetry technique based on optical sensors by our group.[244] More details about this technique are given in the **Methods section** of this Chapter and in recent articles.[244,252,253] Dry NVPF|HC 18650 cells were obtained from TIAMAT (France), allowing us to add different electrolyte combinations while keeping other parameters constant. The cells were pierced to one end with the hole that was used to fill the electrolyte of our choice and also to inject the optical fiber Bragg grating (FBG) sensor prior to being sealed by epoxy. Two other FBG sensors were placed at the cell surface and in its surrounding ambient to perform reliable calorimetry

measurements. The cells, along with the FBGs, were placed in an oven at a fixed temperature of 55 °C and cycled at C/10 rate for 3 charge-discharge cycles. Charge curves for the first three cycles of the cell with the control electrolyte are shown in **Fig. 4.3a**.

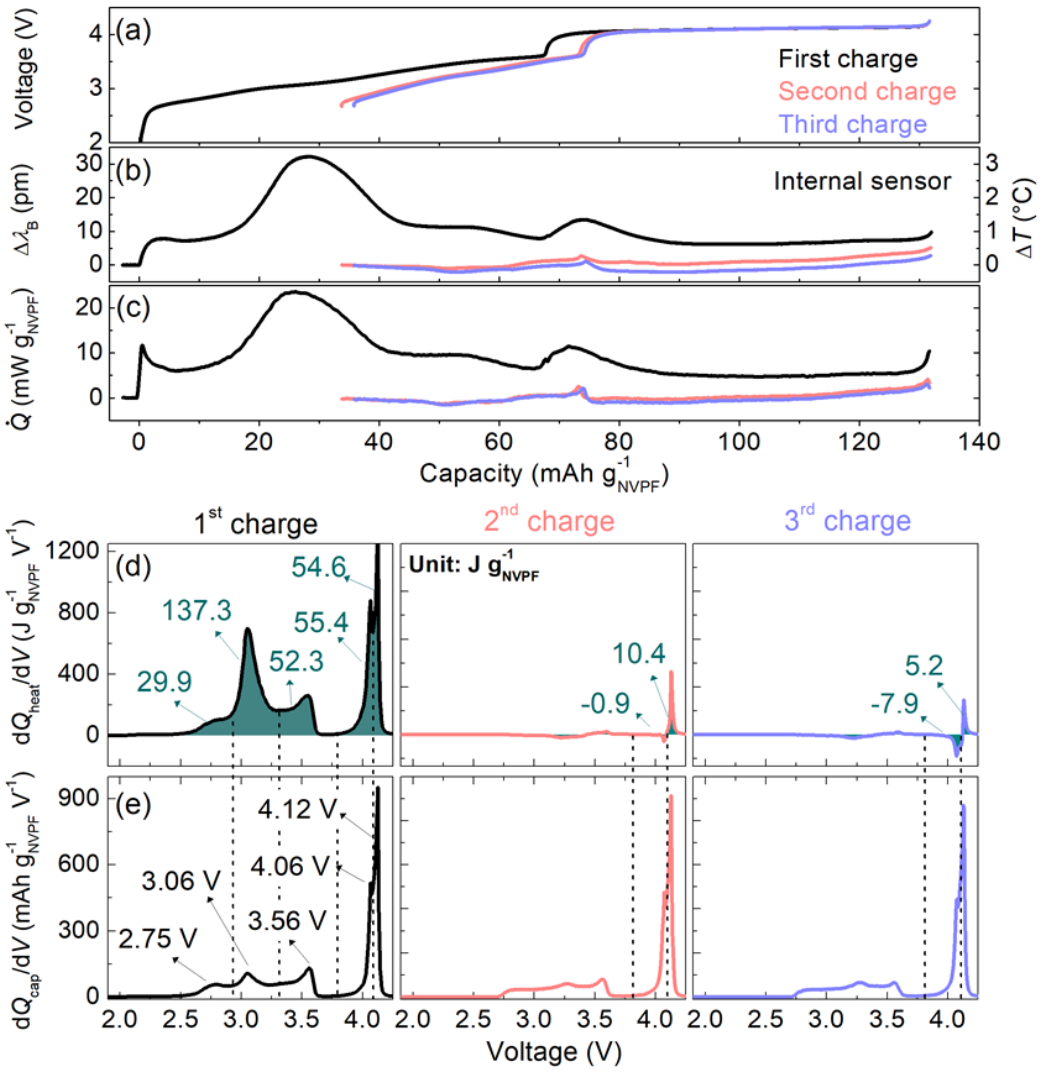

Fig. 4.3 | Sensing calorimetry studies conducted on 18650 type NVPF/HC cells using a control electrolyte. The figure includes the following plots: a) Capacity versus voltage plot. b) Change in Bragg wavelength ($\Delta\lambda_B$) measured by Fiber Bragg Gratings (FBGs), which is converted to the equivalent temperature change (ΔT) and displayed on the right y-axis, as a function of capacity. c) Heat rate ($\dot{Q}$) as a function of capacity, providing insights into the heat generation rate during the charge and discharge cycles. d) Derivative of heat evolution (dQ_{heat}/dV) with values indicating integrated heat in J/g_{NVPF} for regions separated by a dashed line. e) Derivative of capacity (dQ_{cap}/dV) as a function of cell voltage for the 1st, 2nd, and 3rd charges, with voltage values corresponding to the peaks labeled in the figure. The experiment was conducted with two cells having the exact configuration, and identical results were

observed in both cells. The cells were cycled at 55 °C, with a voltage range from 2 - 4.25 V at a C/10 rate (1C = 128 $mAh.g^{-1}$).

The FBGs were connected with the optical interrogator to analyze the shift in Bragg wavelength ($\Delta\lambda_B$) that was converted to temperature variations (ΔT) with high resolutions (1 s and 0.1 °C) as shown in **Fig. 4.3b** (check the left axis for $\Delta\lambda_B$ and right axis for ΔT). The ΔT, in turn, was used to calculate the heat rate ($\dot{Q}$ in **Fig. 4.3c**) using a simplified 0D thermal model whose intrinsic parameters must be defined for each cell prior to conducting the measurements (**Supplementary Fig. S4.2**). The heat derivative as a function of voltage was calculated as dQ_{heat}/dV (in **Fig. 4.3d**) and compared with the capacity derivative dQ_{cap}/dV (in **Fig. 4.3e**). From **Fig. 4.3d-e**, it can be seen that, while minimal change in shape is observed in capacity derivative (dQ_{cap}/dV) among the first three charges, however a huge change is observed in heat derivatives (dQ_{heat}/dV) where the heat evolution is maximum for the first charge and reduced drastically for the second and third ones.

As Q_{heat} is differentiated with respect to voltage, dQ_{heat}/dV and dQ_{cap}/dV may give peaks at similar voltage positions because both are differentiated with the same term. This is because variations of capacity, voltage, and heat flow are ultimately related to time and thus are interrelated to each other by time. In our dQ_{heat}/dV analysis, our interest lies explicitly in the area under the curve (and not the shape of the curve) for the specific regions (marked by vertical lines in Fig. 4.3d) where dQ_{cap}/dV shows a peak, this area gives us the heat corresponding to the processes leading to a peak in dQ_{cap}/dV. These findings demonstrate the viability of using heat evolution, as determined by FBGs, as a tool to follow the interfacial reactions between electrodes and electrolytes within NPVF|HC cells.

The heat changes we observed can be attributed to two main factors: parasitic redox reactions occurring in the electrolyte and phase transitions or diffusion-limited kinetics[244] within the electrode material. However, considering that the contributions from electrode materials are anticipated to remain consistent across subsequent cycles (2^{nd} and 3^{rd} cycle in **Fig. 4.3d**), the irreversible heat evolutions observed during the initial charging primarily stem from the electrolyte redox process and mainly interphase formation.

By comparing the potentials of the individual NVPF and HC electrodes (refer to **Supplementary Fig. S4.3**), we observed that the region spanning from the Open Circuit Voltage (OCV) to 3.8 V corresponds to the sloppy region of HC. Consequently, the exothermic peaks observed at 2.75, 3.06, and 3.56 V (as shown in **Fig. 4.3e**) are mainly associated with the formation of the SEI, which stabilizes after the initial cycle. In contrast, the other two exothermic peaks (at 4.06 and 4.12 V) occurring beyond 50% of the cell's charging capacity take place during the high voltage plateau of NVPF and flat potential plateau of HC. This includes the heat of reaction related to the phase transition from $Na_2V_2(PO_4)_2F_3$ to $Na_1V_2(PO_4)_2F_3$, as well as diffusion-limited kinetics at the end of charge, along with the electrolyte oxidation and reduction. Furthermore, we noted that the process at 4.06 V becomes endothermic during the 2nd and 3rd charges, indicating that the exothermic heat observed during the 1st charge primarily originates from electrolyte oxidation on NVPF or reduction on HC. However, for the process at 4.12 V, only a decrease in exothermicity is observed when moving from the 1st to the 2nd and 3rd charges, indicating the observed heat is a mixture of both exothermic electrolyte oxidation/reduction and the endothermic phase transition and diffusion-limited kinetics at the end of the charge from the material.

2.2 Impact of Additives on Heat Evolution during the Formation Cycle

Subsequently, we delved into the evolution of heat events during the charging process by introducing various chemical additives. To achieve this, we carefully incorporated NaODFB, VC, SN, and TMSPi into the mother electrolyte in specific ratios, starting with 0.5 wt.% NaODFB, 3 wt.% VC, 3 wt.% SN, and 0.2 wt.% TMSPi. These additives were chosen due to their widespread use in LIBs and their previous investigation in NIBs.[122,123,254] To ensure the reliability of our findings, each electrolyte formulation underwent measurement twice, ensuring reproducibility. In total, we examined five different electrolyte formulations: control, NaODFB, NaODFB+VC, NaODFB+VC+SN, and NaODFB+VC+SN+TMSPi. The cycling curves and their corresponding dQ_{cap}/dV plots for each formulation can be found in **Supplementary Fig. S4.4 and S4.5**.

The ΔT measured from FBGs serves as the basis for deriving the dQ_{heat}/dV plots, as demonstrated for the control electrolyte. The 1st charge data is depicted in **Fig. 4.4a-e**, while the data for the 2nd and 3rd charges can be found in **Supplementary Fig. S4.6**.

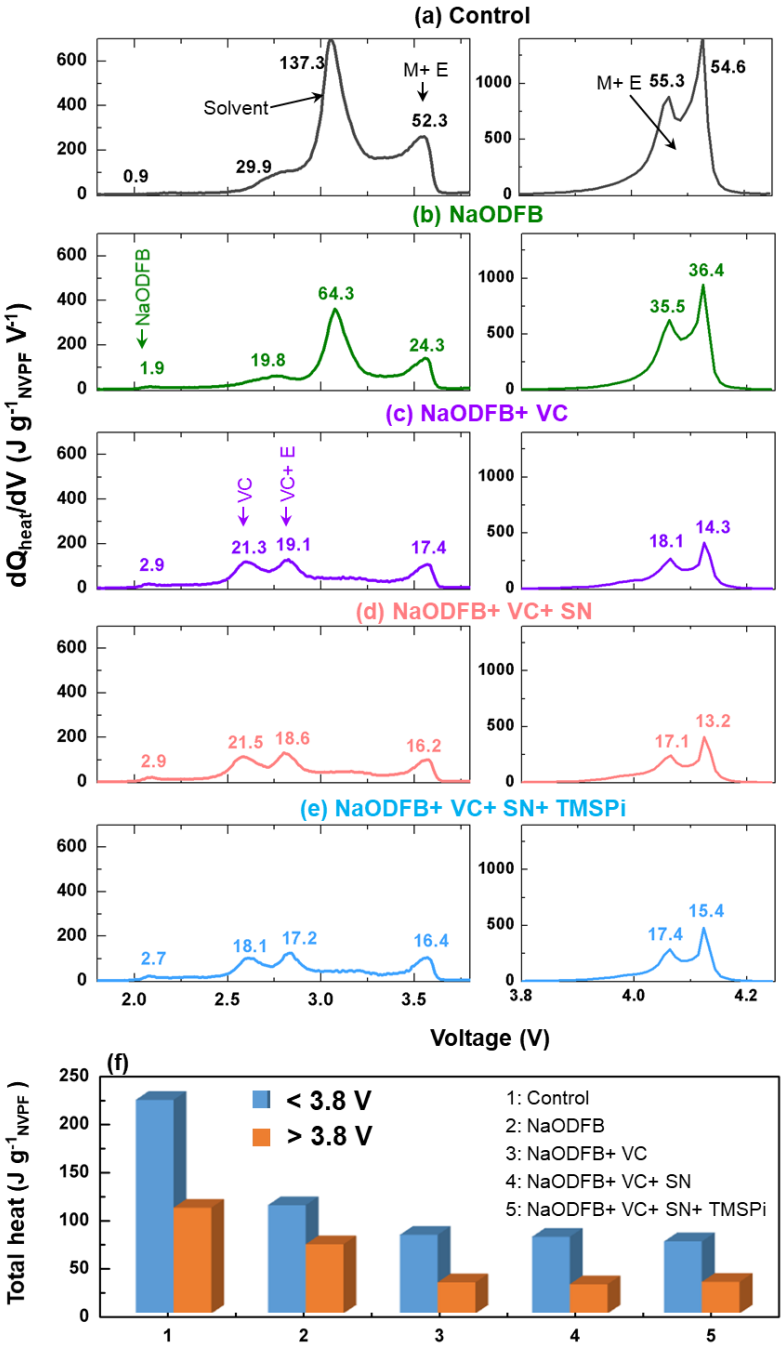

Fig. 4.4 | Heat evolutions due to incorporation of additives in the electrolyte. a–e) The derivatives of heat with respect to voltage (dQheat/dV) of NVPF/HC cylindrical 18650 cells cycled at C/10 in an oven maintained at 55 °C. The cells were tested using different electrolyte formulations: (a) no additives - control, and with the additives (b) 0.5

wt.% NaODFB, (c) 0.5 wt.% NaODFB + 3 wt.% VC, (d) 0.5 wt.% NaODFB + 3 wt.% VC + 3 wt.% SN, and (e) 0.5 wt.% NaODFB + 3 wt.% VC + 3 wt.% SN + 0.2 wt.% TMSPi. The figures on the left show the voltage window from open circuit voltage (OCV) to 3.8 V, and the right ones show the voltage window from 3.8 to 4.25 V. The integrated heats (in joules per gram of NVPF) of SEI/CSEI formation peaks were labeled, and the arrow marks serve as a guide to show the redox process of NaODFB, VC, electrolyte solvent (E), and heat evolution due to sodium (de-)insertion in the material (M). f) The total heat observed at < 3.8 V and >3.8 V is shown as a function of electrolyte formulation.

To ensure clarity, we presented the data in two panels: one for the heat events occurring below 3.8 V (left) and the other for those above 3.8 V (right). This separation allows us to analyze the impact of the additives on the SEI formation and other processes discussed before (mainly exothermic electrolyte oxidation/reduction and endothermic material phase transformation). Note that the onset potential of the new thermal events compared to the control electrolyte, together with their amplitudes is a response to the additive used. The total evolved heat in both of these voltage regions (<3.8 V and >3.8 V) for each electrolyte formulation is plotted in **Fig. 4.4f**. Strikingly, there is an abrupt decrease in the cumulated heat in the two voltage regions with the addition of electrolyte additive(s) (**Fig. 4.4f**), implying the additives assist the formation of SEI and CSEI that reduce the unwanted parasitic reactions with the electrolyte solvents.

The addition of just a single additive, NaODFB (**Fig. 4.4b**), leads to a remarkable 50% reduction in the evolved heat, highlighting the reactivity of NaODFB or its derived product in both the negative and positive electrodes. At around 2V, the heat due to NaODFB reduction is considerably low, approximately 2 J/g_{NVPF}, which indicates its effectiveness in safeguarding the electrode surface without releasing excessive heat. Nevertheless, peaks associated with solvent reduction at 2.75, 3.06, and 3.56 V still persist, indicating that NaODFB alone may not be sufficient in completely preventing excessive solvent reduction but lower it to some extent.

However, when VC is added along with NaODFB (**Fig. 4.4c**), a nearly complete reduction in the heat associated with solvent reduction at 3V is observed. Instead, the heat profile shows two new exothermic processes at 2.6 and 2.8 V. The 2.8 V process coincides with the solvent reduction observed in the control electrolyte (2.75 V). Interestingly, the peak at 2.6 V corresponds to ~1.0 V in HC versus Na^+/Na^0, closely matching the reported ~1.4 V versus Li^+/Li^0 for VC reduction.[255] Upon closer examination using dQ_{cap}/dV with dQ_{heat}/dV plots

(**Supplementary Fig S4.7**), we find that both the 2.6 and 2.8 V redox processes exhibit nearly similar heat evolution (21 and 19 J per gram of NVPF, respectively). However, the 2.6 V reduction involves only 0.065 electrons (0.065 Na^+ removal from NVPF) compared to 0.22 electrons at 2.8 V reduction. This result suggests that VC reduction at 2.6 V is either highly exothermic or associated with a parallel chemical reaction that releases a significant amount of heat. This aligns well with the reported VC redox mechanism in the literature, where VC undergoes a 1 or 2 electron redox process,[256–258] leading to an exothermic peak at 2.6 V. The products of VC reduction then react with EC (peak at 2.8 V) and polymerize, releasing CO_2. The evolved heat at 2.6 V is relatively higher when VC is used alone (**Supplementary Fig. S4.8**) as the available HC surface is higher without passivation by NaODFB. In the high voltage region (3.8–4.25 V), the addition of VC reduces the overall heat, and relatively fewer changes in the heat of the reaction are observed in the second and third charges (**Supplementary Fig. S4.6**), indicating possible passivation and stabilization of the positive electrode as well.

Next, we tested the additive SN, known for its effectiveness in protecting the positive electrode.[259–261] When added to NaODFB+VC, SN further reduced the heat associated with the high-voltage region (>3.8 V) process, indicating a relatively less severe electrolyte oxidation in the positive electrode. This suggests a synergetic effect of SN in combination with VC, resulting in efficient protection of the positive electrode (**Fig. 4.4d**). However, we did not observe any new specific feature that could suggest the oxidation or adsorption of SN on the electrode surface.

Similarly, the addition of TMSPi (0.2 wt.%) also did not reveal any new features in the heat derivative plot, except for a reduction in the evolved heat during the low-voltage processes (<3.8 V; **Fig. 4.4e**). TMSPi is known in the literature as an effective acid/O_2 scavenger,[262,263] and this property could be responsible for the observed decrease in heat during the low-voltage processes. On the other hand, a slight increase in heat is observed at high voltages, which we associate with the oxidation of TMSPi (calculated oxidation potential is 4.29 V vs Li^+/Li^0)[262] or one of its reduction products on the positive electrode. This behavior warrants further investigation to understand the specific mechanisms involved in the high voltage region.

In summary, the calorimetry measurements revealed that the studied electrolyte additives displayed reactivity both at the NVPF and HC electrodes, except for SN, which showed activity solely on the NVPF electrode. The additive mixture of NaODFB with VC actively participated in the formation of SEI and probably CSEI. Moreover, SN and TMSPi appeared to fine-tune these processes further, as they led to a reduction in the heat of the reaction. The most significant reduction in heat was observed when all four additives were combined in the mother electrolyte. While these findings provided valuable guidance, they were not sufficient to determine the best suitable electrolyte for the NVPF/HC chemistry. To gain further insights, we conducted electrochemical analyses using the same combinations of additive blends in NVPF/HC Na-ion full cells.

2.3 Electrochemical analysis of NVPF|HC full cells

The experimental protocol involved assembling coin-type 2032 cells and cycling them at 55°C within the voltage range of 2-4.3 V. To ensure data robustness, a minimum of 2 coin cells was used for each electrolyte formulation. Initially, the cells underwent 10 cycles at a rate of C/5 to establish a stable interphase. Subsequently, a self-discharge test was conducted (refer to **Fig. 4.5a**) by placing the cells at rest at 100% state of charge (4.3 V) for 1 week at 55°C.

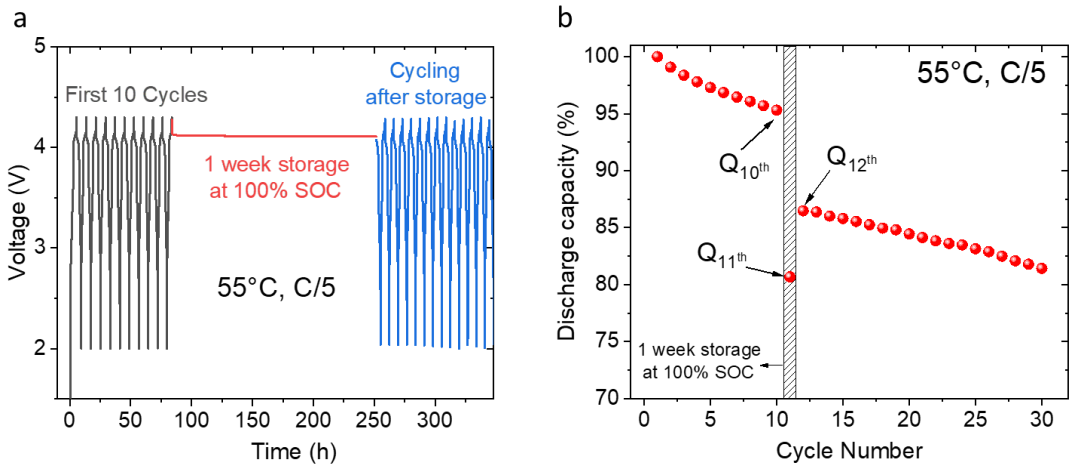

Fig. 4.5 | Protocol to access high temperature cycle life and calendar life. a) Voltage vs. time plot for the cycling and storage protocol. b) The capacity loss and recovery during the storage period and defining SD and RE parameters.

After this self-discharge period, the cycling resumed, and the two parameters SD (Resistance to self-discharge = Q_{11th}/Q_{10th} x 100) and RE (recovery= Q_{12th}/Q_{10th} x 100) are defined presented in

the **Fig. 4.5b**. Note that continuous cycling gives an indication of cycle life, and 1 week of storage gives an indication of calendar life.[264–266] For better calendar life, both SD and RE values should be high. Thus, capacity retention, SD, and RE will give overall life indication of different electrolyte formulations.

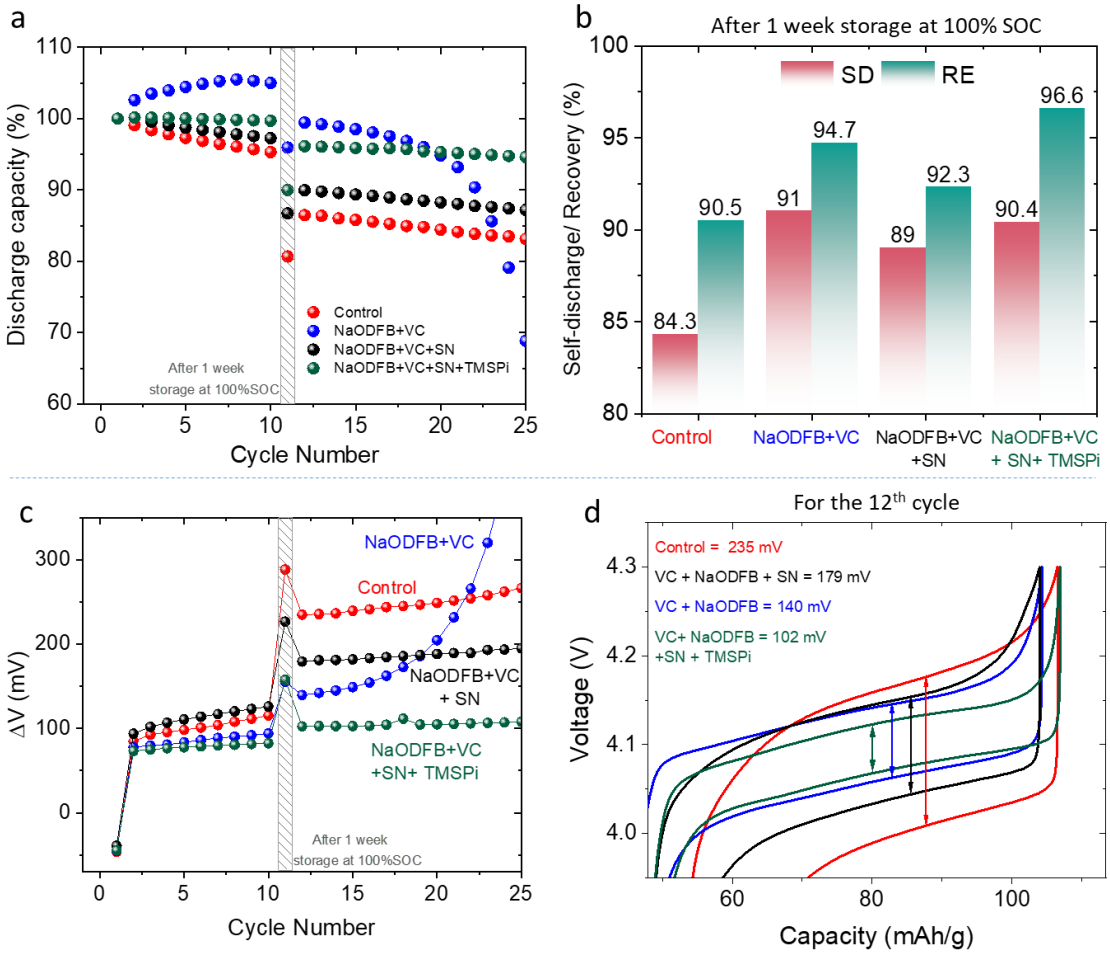

Fig. 4.6 | Electrochemical performance of the chosen additive combinations. a) Discharge capacity vs. cycle number. b) SD and RE values for the storage period c) ΔV vs. cycle number. d) Zoomed in part of voltage vs. capacity plot for 12th cycle to indicate the developed polarization.

Fig. 4.6a shows capacity retention for the chosen electrolyte combinations before and after self-discharge periods with their charging profiles in **Supplementary Fig. S4.9**. Note that electrolyte with all 4 additives, NaODFB+VC+SN+TMSPi, shows 95% capacity retention after 25 cycles and 1 week of storage at 100% SOC. Similarly, it shows the highest SD and RE values (**Fig. 4.6b**), showing high resistance to self-discharge and high recovery values. All the electrolytes

containing additives demonstrated only a 9–10% capacity loss during the 1-week storage at 55°C. In contrast, the control electrolyte exhibited a 16% loss with only 90% recovery (**Fig. 4.6b**). This highlights the effectiveness of the electrolyte additives in enhancing the cell's stability during the self-discharge process.

Polarization development corresponding to cycling is shown in **Fig. 4.6c**. As cycling proceeds, the polarization increases for all the cells with sharp steps after the storage period. Polarization development is slower for the cell with NaODFB+VC+SN+TMSPi as compared to other combinations. The upper plateau region of full cell for the 12^{th} cycle was zoomed in to show this polarization development after the storage period in **Fig. 4.6d**, indicating the least polarization for NaODFB+VC+SN+TMSPi electrolyte. This indicates the suppression of impedance buildup due to interphase degradation and growth.

The incorporation of additives shows impressive performance at 55°C, but the above analysis (capacity retention, SD, RE, and ΔV) of different additive combinations did not give a clear indication of their role in stabilizing the capacity. Additionally, studying charge and discharge endpoint slippages (**Supplementary Fig. S4.10**) did not provide any solid support to spot the role of each additive. Thus, electrode slippages and mass loss are analyzed next to identify the role of each additive in stabilizing the interphase.

It was discussed in **Chapter 2 Section 2.1.6** about the ability of dV/dQ analysis to identify the parasitic reactions taking place via quantifying electrode slippages and mass loss.[185,187–189] The processes include fitting the experimental $(dV/dQ)_{exp}$ with the half cell profile of positive electrode $(dV/dQ)_{+}$ and negative electrode $(dV/dQ)_{-}$ with the help of electrode slippages and mass loss. For the particular NVPF|HC system, NVPF has only one sharp distinguishable feature, and HC has a small feature (refer to **Supplementary Fig. S4.11**), which makes the fitting less reliable, and only two parameters can be fitted safely. One is NVPF mass loss (due to apparent mass loss at NVPF electrode), and the other parameter is HC slippage (due to parasitic reactions at HC), which can be easily identified from the discharge curves without the dV/dQ fitting.

Fig. 4.7a shows the full cell discharge curves with deconvoluted NVPF and HC profiles in V vs. Q and dV/dQ vs. Q format. Note that in the full cell, the step feature corresponds to NVPF

phase change, and the end of discharge corresponds to HC potential shoot-up (refer to **Supplementary Fig. S4.11** and **Fig. 4.7a**). Thus, the shift in the phase change step and end of discharge is tracked as a function of cycling (refer to **Fig. 4.7b**) and named NVPF slippage and HC slippage. Note that to compare our analysis with classical fittings done by Dahn et al.,[185] our NVPF slippage term corresponds to apparent mass loss at the NVPF electrode, and the HC slippage term is due to parasitic reaction at HC interphase causing SEI growth and capacity loss.

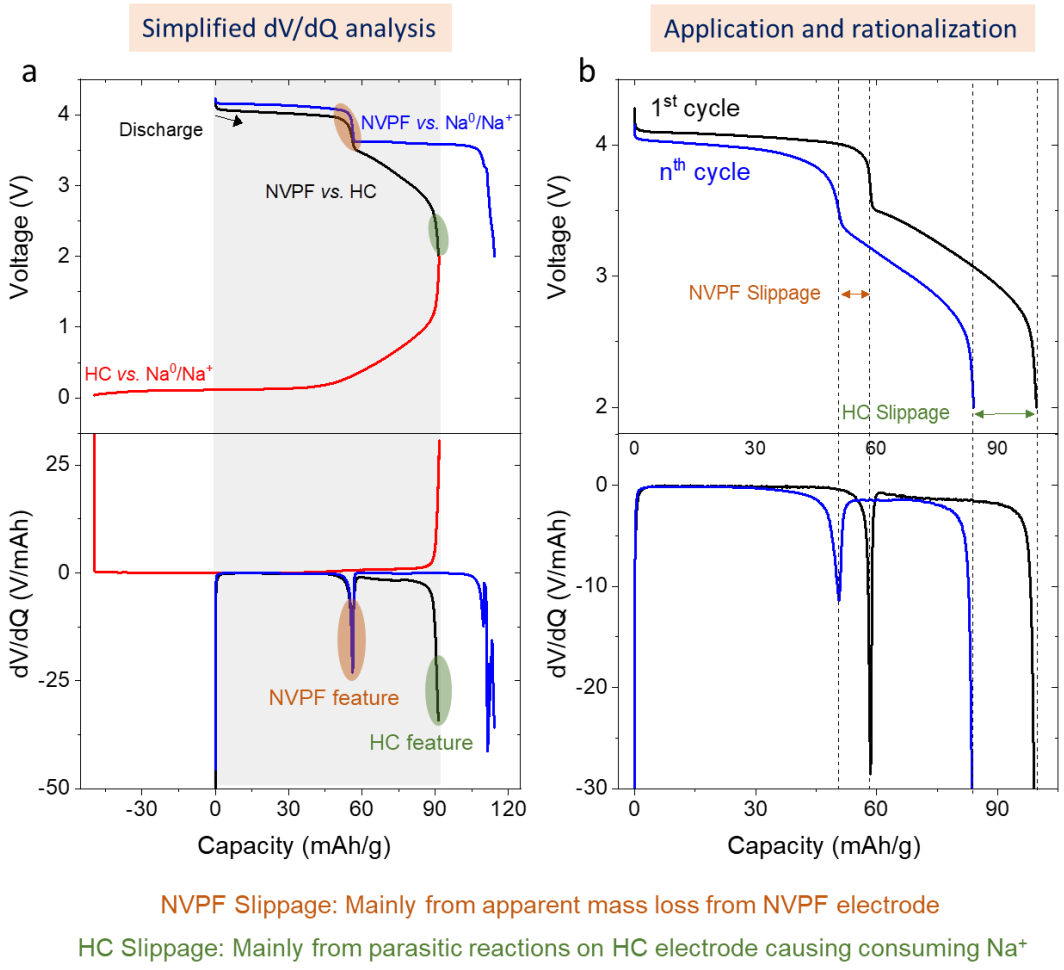

Fig. 4.7 | Simplified dV/dQ analysis for NVPF|HC system. a) Voltage vs. capacity (top) and dV/dQ vs. capacity (bottom) for discharge curve(in black) of NVPF|HC cell. The deconvoluted NVPF (in blue) and HC (in red) curves are shown. Significant NVPF and HC features are marked with orange and green shade, respectively. b) Voltage vs. capacity (top) and dV/dQ vs. capacity (bottom) for discharge curve of 1st and nth cycle with change in NVPF and HC feature marked as slippage.

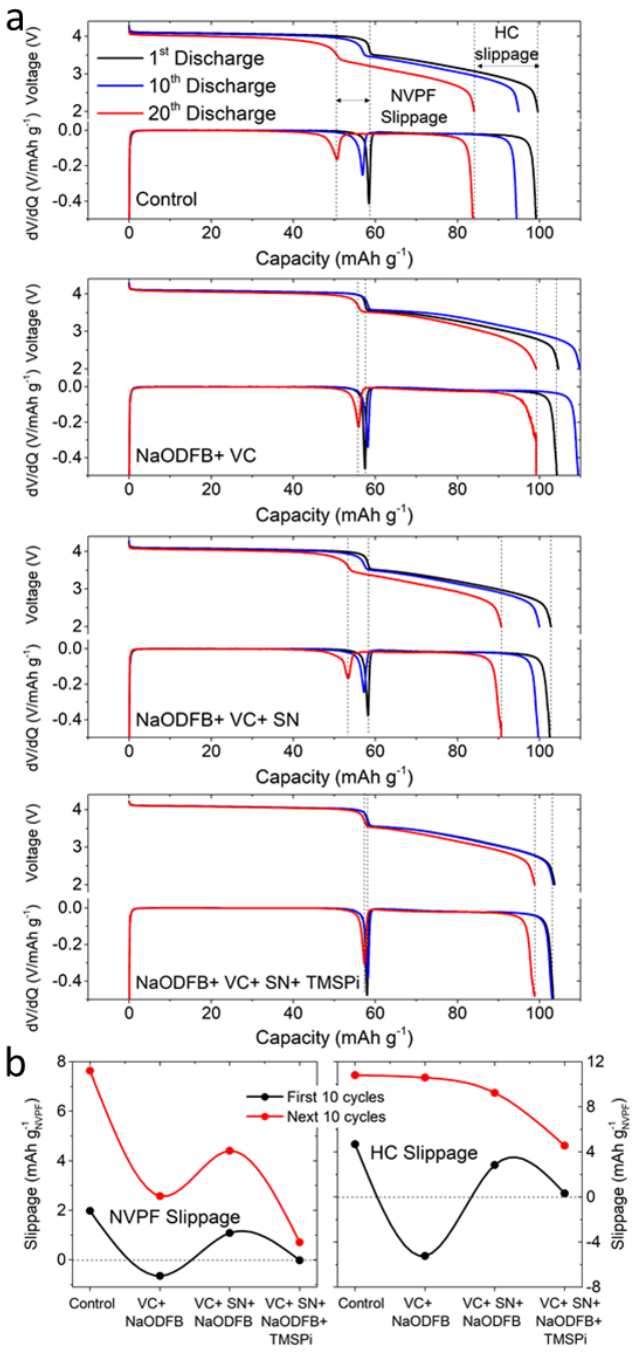

Fig. 4.8 | dV/dQ analysis for NVPF|HC cells. (a) The discharge voltage versus capacity plots of the 1st, 10th, and 20th cycles are shown together with the differential voltage (dV/dQ) for NVPF/HC cells with different electrolyte formulations. The cells were tested with the control electrolyte and with the following additives: 0.5 wt% NaODFB, 0.5 wt% NaODFB + 3 wt% VC, 0.5 wt% NaODFB + 3 wt% VC + 3 wt% SN, and 0.5 wt% NaODFB + 3 wt% VC + 3 wt% SN + 0.2 wt% TMSPi. The original data for these curves can be found in Figure S9 of the Supplementary Information. (b) The electrode slippage in the positive electrode (NVPF) and negative electrode (HC) is calculated from the discharge voltage versus capacity plots (a).

Fig. 4.8a demonstrates the dV_{cell}/dQ profiles for 1st, 10th, and 20th discharge cycles in different electrolytes, and **Fig. 4.8b** summarizes NVPF and HC slippage for the first ten and next ten cycles. Control electrolyte shows huge electrode slippage. As NaODFB+VC is added, both the NVPF and HC slippage becomes negative for the first ten cycles (**Fig. 4.8b**) this is due to extra Na^+-inventory gain from the electrolyte oxidation, thus increasing capacity in initial cycles (**Fig. 4.6a**) but then leading to rapid capacity loss after 20 cycles. When NaODFB+VC+SN is added to the control electrolyte, the slippages become positive but less than the control electrolyte (**Fig. 4.8b**). When TMSPi was added to NaODFB+VC+SN, it showed the least NVPF and HC slippages (**Fig. 4.8b**), indicating negligible NVPF mass loss and suppressed parasitic reactions at HC electrode.

The dV/dQ or slippage analysis provided additional information relating to the effectiveness of additives in passivating interphase and relating the observed capacity loss to NVPF mass loss and SEI growth. However, the role of each additive remains unclear. For this reason NVPF and HC symmetric cells with the same electrolyte combinations were investigated.

2.4 Unraveling the role of additives from symmetric cells

Symmetric cells contain the same host material as positive and negative electrodes, the same interphase, and both the electrodes run in the same potential window as discussed in **section 2.2.2** of **Chapter 2**. These cells were designed with configurations of $Na_{\approx 1}V_2(PO_4)_2F_3|Na_{\approx 3}V_2(PO_4)_2F_3$ and desodiated HC|sodiated HC, respectively. The electrodes were prepared and recovered following the protocol described in the Experimental Section and **Supplementary Note S4.1**.

The cycling curves for NVPF and HC symmetric cells with electrolyte is shown in **Fig. 4.9a-b**. The charging curves for the first cycle were fitted using dV/dQ fitting software developed by Dahn et al.[185] and individual electrode curves were accessed as shown in **Fig. 4.9c-d**. The changes observed in the cycling curves are associated with the specific degradation mode, and these are shown in **Supplementary Fig. S4.12**, along with additional details in **Supplementary Notes S4.2 and S4.3** in the Supplementary Information. It is important to mention that the dominant mechanism for the degradation of NVPF and HC symmetric cells is electrolyte oxidation and electrolyte reduction, respectively. NVPF degrades by electrolyte oxidation with the consequence

of gaining extra Na inventory and cell capacity reaches zero when both the electrode concentration become $Na_{\approx 3}V_2(PO_4)_2F_3$, confirmed with the slippage analysis and half-cells of recovered electrodes from symmetric cell (**Supplementary Fig. S4.12c**). On the contrary HC cell degrades by loss of Na inventory due to continuous electrolyte reduction (**Supplementary Fig. S4.12d**).

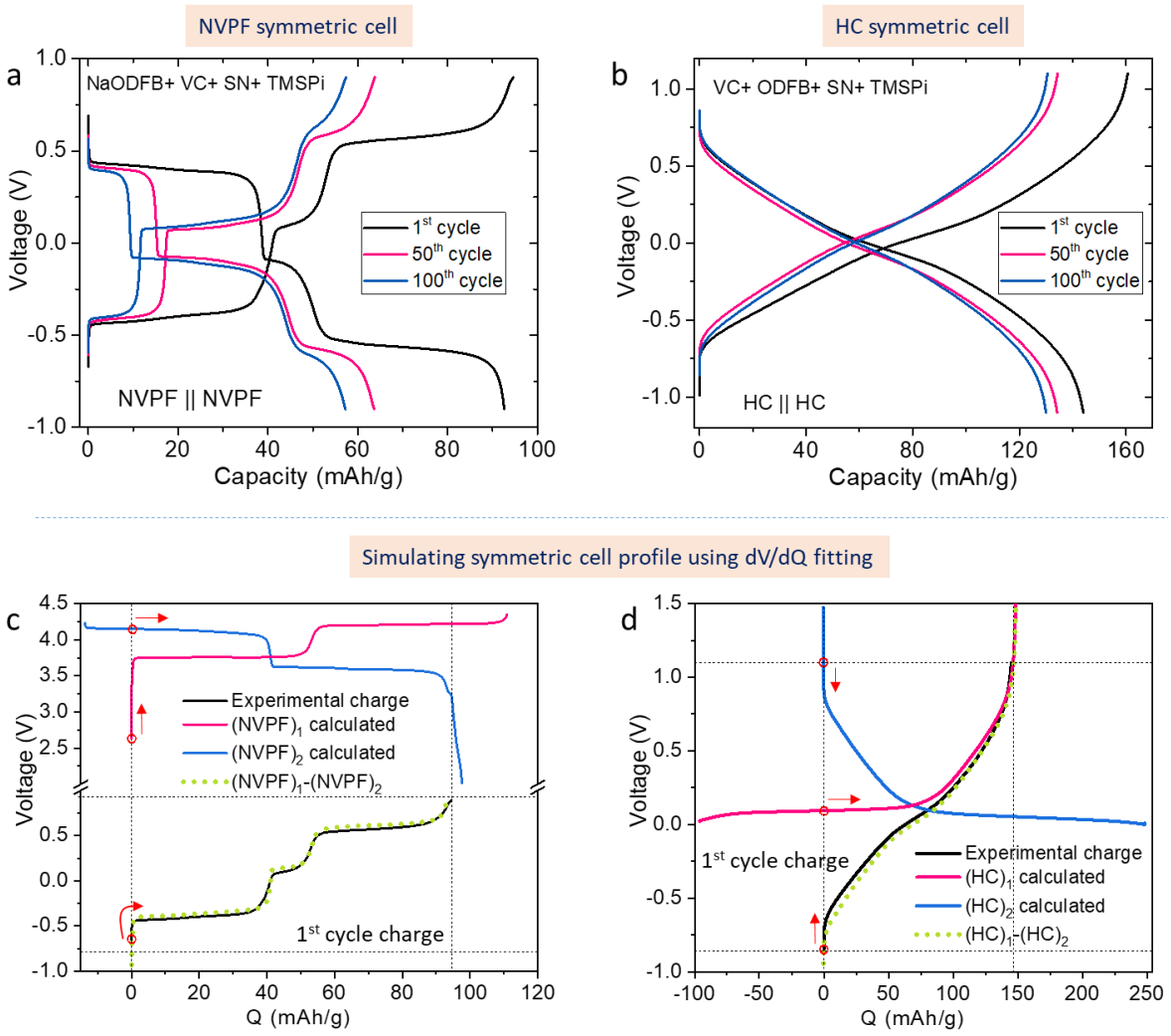

Fig. 4.9 | Symmetric cell profile and its deconvolution in individual electrodes for NVPF and HC. Voltage vs. capacity profiles for 1st,50th, 100th cycle a)NVPF symmetric cells and b)HC symmetric cells with NaODFB+VC+SN+TMSPi electrolyte. Deconvoluted profile of individual electrodes (pink and blue) with charging curve (black) and calculated charging curve (green dots) for c) NVPF symmetric cell and d)HC symmetric cell.

The cumulated capacity retention plots of both NVPF and HC symmetric cells for chosen additive combinations are shown in **Fig. 4.10**, providing insights into the capacity retention

behavior over cycling. In the case of NVPF symmetric cells, the lowest capacity retention is observed for the control electrolyte. The addition of NaODFB+VC does not affect capacity retention (**Fig. 4.10a**), implying its inability to effectively passivate NVPF from electrolyte oxidation. Notably, the capacity decay is quite evident right from the initial cycles. However, the addition of SN leads to a significant improvement in electrolyte stability. SN acts as a protective agent for the NVPF electrode and enhances the oxidative stability of the electrolyte. On the other hand, the addition of TMSPi to NaODFB+VC+SN further enhances the capacity retention (**Fig. 4.10a**) of NVPF cells by a slight amount. Degradation analysis by dV/dQ fitting for the discussed electrolytes is shown in **Supplementary Fig. S4.13**.

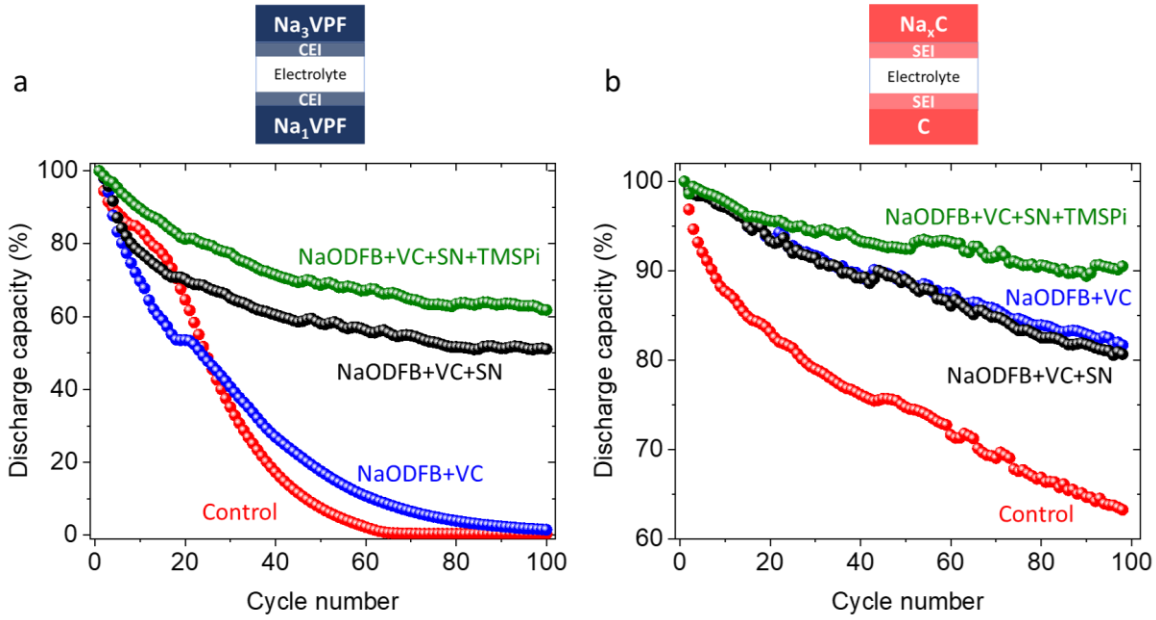

Fig. 4.10 | Cycling stability of symmetric cells unraveling the role of additives. Discharge capacity as a function of cycle number for NVPF and HC symmetric cells cycled at 25 °C with a C/5 rate using different electrolyte formulations. The plots include the control electrolyte and electrolytes containing the following additives: 0.5 wt.% NaODFB, 0.5 wt.% NaODFB+ 3 wt.% VC, 0.5 wt.% NaODFB+ 3 wt.% VC+ 3 wt.% SN, and 0.5 wt.% NaODFB+ 3 wt.% VC+ 3 wt.% SN+ 0.2 wt.% TMSPi.

In contrast to NVPF symmetric cells, the HC symmetric cells retain 62% of their capacity after 100 cycles (**Fig. 4.10b**) with the control electrolyte alone. With the inclusion of additives, approximately 80–90% of the initial capacity is retained even after 100 cycles in HC symmetric cells. HC symmetric cells demonstrate stable performance with NaODFB+VC additives alone, and

an improvement in stability is achieved with NaODFB+VC+SN+TMSPi additives (**Fig. 4.10b**). The stable performance in HC symmetric cell cycling indicates the formation of a good SEI, which prevents further electrolyte reduction and SEI growth.

Overall, NaODFB+VC is sufficient in creating a good SEI, but the NVPF/HC full cell still shows capacity decay due to the poor oxidative stability of the electrolyte. However, with the addition of SN, the NVPF surface is protected, leading to a suppression of electrolyte oxidation. The additive TMSPi further enhances the stability of the SEI by protecting SEI through acid-scavenging properties. As a result, the electrolyte with NaODFB+VC+SN+TMSPi exhibits the best stability, addressing both the SEI and CSEI, thus providing superior full cell stability (**Fig. 4.6a**). After achieving stable interphases with Gen-3 additives, the subsequent task involves examining the impact of these additives on V dissolution and gassing, as discussed in **Chapter 3.**

2.5 Gen-3 electrolyte: Vanadium Dissolution and Gassing in the cells

To further understand the impact of additives, control and Gen-3 electrolyte (with NaODFB+VC+SN+TMSPi) are investigated for V dissolution. The apparent NVPF mass loss observed from the dV/dQ analysis hints towards the dissolution of some part of active material. This dissolution can further promote electrolyte decomposition, shuttling reactions, and gassing as discussed in **Section 2.6.2 of Chapter 3**.

Fig. 4.11a shows that the amount of dissolved vanadium after one week of storage of NVPF|HC coin cells at 55 °C in 100% state of charge (SOC) is reduced by nearly 50% in the presence of additives. Encouraged by these results, 18650 cylindrical cells loaded with this electrolyte were cycled at 55 °C for over four months (**Fig. 4.11b**). The cell with Gen-3 electrolyte exhibited better capacity retention without any CID break due to pressure buildup compared to the cell without any electrolyte additive, which failed after just 10 days. Interestingly, the derivative plot shows a barely noticeable 3.4 and 3.9 V peak (arrow in **Fig. 4.11c**, left) for the electrolyte containing additives, as opposed to a well-pronounced feature for the electrolyte without additives. As discussed in **Section 2.6.1 of Chapter 3**, these two peaks are an indicative fingerprint of V-dissolution and NVPF deterioration. This confirms that Gen-3 additives suppress the V dissolution, leading to low apparent NVPF mass loss, increase in capacity retention, and

reduction in the gassing in 18650 cells. Still, it is important to note that the additives do not fully eliminate vanadium dissolution, and further optimization from electrode and electrolyte is required to achieve the best interphase stability.

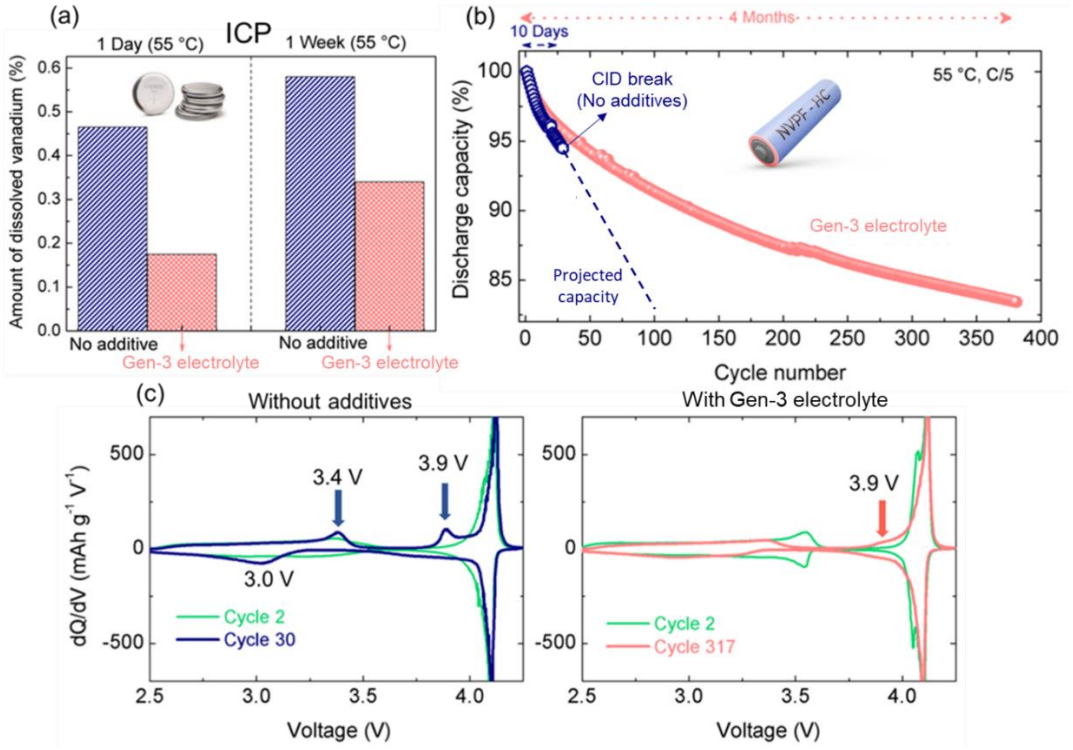

Fig. 4.11 | Protective effect of electrolyte additives on the NVPF surface. a) ICP analyses revealed that cells with electrolyte additives exhibit significantly reduced dissolved vanadium compared to cells without additives, indicating the additives' protective effect on NVPF. b) The 18650 cell with electrolyte additives demonstrates better capacity retention (pink circles) over four months compared to the cell without additives (blue circles). c) Derivative plots of the two cells' cycles indicate that the appearance of a new redox process around 3.9 V is less evident in cells with electrolyte additives even after four months of cycling at 55°C, in contrast to the cell without additives that exhibits the feature after just 10 days of cycling.

Another issue observed during high temperature cycling of NVPF-HC cells is the gassing where the gases formed from the deleterious parasitic reactions of electrolyte and/or dissolved vanadium. In order to understand the gassing phenomenon during formation and upon long cycling, we carried out online electrochemical mass spectroscopy (OEMS) studies and optical sensing studies that are discussed one by one next.

For OEMS studies, specially designed cells[267] were assembled using NVPF and HC electrodes. Since VC and TMSPi additives have been associated with gas generation,[268–270] with excessive VC causing CID breakage in 18650 cells during formation cycles, two compositions were selected: NaODFB+VC+SN and NaODFB+VC+SN+TMSPi. The cells were cycled at 55 °C using a C/10 rate, and the gases evolved during cycling were analyzed using a mass spectrometer. The signals corresponding to CO_2, H_2, and C_2H_4 gases were calibrated for quantification. Additionally, gases such as POF_3 and trimethyl-fluorosilane (TMSF), which are reported as side-products from $NaPF_6$ decomposition and TMSPi reaction with fluoride ions,[269] were also detected during the analysis, but their quantities were not quantified in this study.

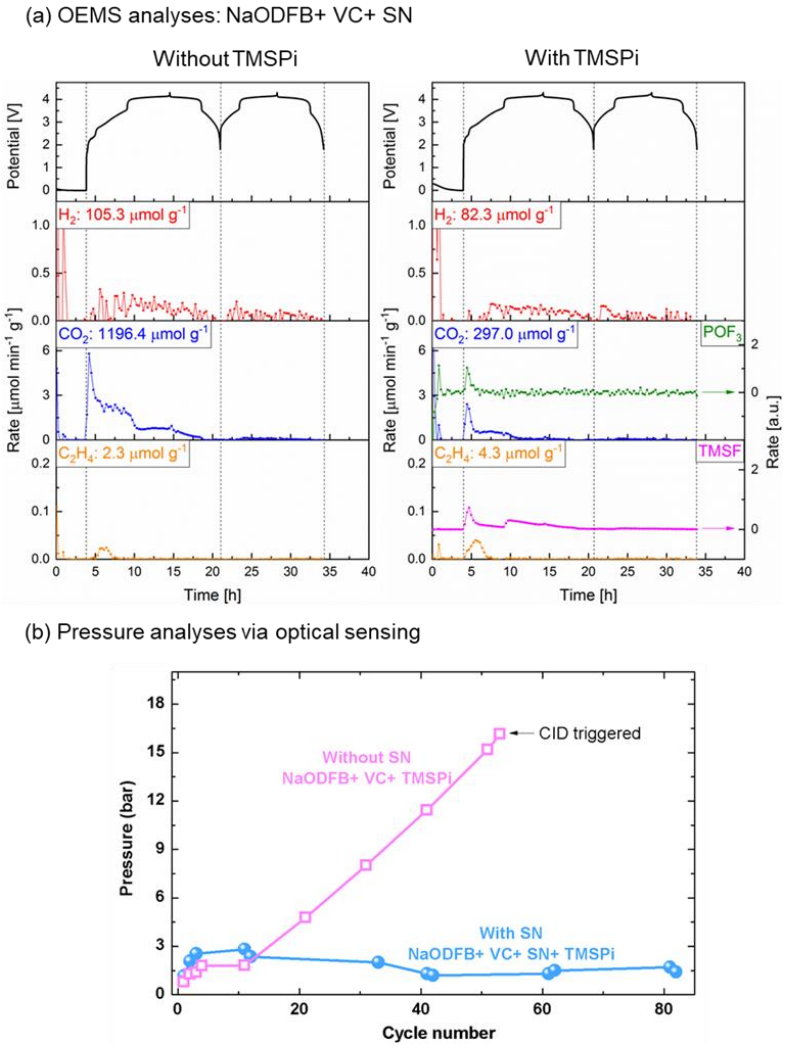

Fig. 4.12 Gassing analysis for electrolyte with additives. a) OEMS (Online Electrochemical Mass Spectrometry) analyses of NVPF/HC cells using 1 M $NaPF_6$ in EC: PC: DMC and electrolyte additives NaODFB+VC+SN, without (left) and with (right) TMSPi added to the electrolyte. The numbers in each panel represent the total amount of H_2, CO_2,

and C_2H_4 gases evolved from the cell during cycling. The gases POF_3 and TMSF were observed only when TMSPi was used in the electrolyte and were not quantified. b) The change in cell pressure (followed by FBGs - Fiber Bragg Gratings) of NVPF/HC cylindrical 18650 cells upon cycling at 55 °C using a C/10 rate. The electrolyte consists of 1 M $NaPF_6$ in a 1:1:1 EC:PC:DMC mixture, where the additives used are NaODFB+VC+TMSPi with (blue circles) and without SN (pink squares).

The results of OEMS are summarized in **Fig. 4.12a**. Small amounts of POF_3 and TMSF gases were detected only in electrolytes containing TMSPi during the first cycle, consistent with previous literature reporting that TMSPi induces PF_6^- decomposition. Additionally, we observed a similar amount of C_2H_4 gas produced, regardless of the presence or absence of TMSPi in the electrolyte. This is indicative of limited EC reduction, as the SEI mainly forms from the reduction of NaODFB and VC. However, the NVPF|HC cell containing the electrolyte with NaODFB+VC+SN is associated with a significant evolution of CO_2 gas during SEI formation (below 3.8 V). The amount of released CO_2 is reduced by nearly fivefold with the addition of TMSPi. On the other hand, the presence of TMSPi does not significantly affect the amount of H_2 gas produced, suggesting a separate process that is likely related to the reduction of protic species on the anode.[271] Overall, while TMSPi leads to a small amount of POF_3 and TMSF gases in the first cycle, it effectively reduces the amount of CO_2 produced during SEI formation. This reduction is likely due to the synergistic effects between TMSPi and the other electrolyte additives.

The gassing results mentioned above are quite surprising, considering that we previously observed vigorous gassing when using the electrolyte containing NaODFB+VC+TMSPi (Gen-2 electrolyte in **Fig. 4.2**) additives, as reported by our group earlier. It is worth noting that this vigorous gassing was mainly observed in 18650 cells, where the amount of active material used was much higher (approximately 8-11 g of NVPF) compared to the coin-type or OEMS cells (around 14-20 mg of NVPF). Additionally, the gassing was more prominent when the cells were cycled at 55 °C for extended periods. To overcome the challenges of performing long-term cycling with the OEMS cells, we once again used optical sensors to monitor the pressure evolution during long cycling. For this purpose, we integrated microstructured optical fiber (MOF-FBG) into the 18650 cells, which is sensitive to hydraulic pressure, along with single-mode optical fibers (SMF-FBG) that are less sensitive to pressure changes. By using these optical sensors, we aim to better

understand the gassing behavior and pressure variations during prolonged cycling in the OEMS cells.

The results were compared, and pressure changes were calculated based on the experimental methods (see experimental methods section). **Fig. 4.12b** presents the data comparing the change in pressure as a function of cycle number for two different electrolyte formulations: NaODFB+VC+TMSPi (Gen-2 electrolyte defined in **Fig. 4.2**) and NaODFB+VC+SN+TMSPi (Gen-3 electrolyte defined in **Fig. 4.2**), discussed in this chapter.

In cells without SN (with NaODFB+VC+TMSPi), a gradual increase in cell pressure was observed, leading to a critical internal pressure (CID) break when the pressure reached a maximum limit of approximately 16 bars inside the cell. On the other hand, the electrolyte containing SN in its formulation (NaODFB+VC+SN+TMSPi) showed much less change in pressure, indicating a significantly reduced amount of gassing with this electrolyte formulation. The key difference between the two studied electrolytes in **Fig. 4.12b** is the presence or absence of SN. The symmetric cell studies (**Fig. 4.10a**) also revealed that SN plays a protective role for the positive electrode. This suggests that the significant gassing observed in the absence of SN is due to electrolyte oxidation, resulting in an increase in built-in pressure and a deterioration in cell performance.

2.6 Evaluating the Feasibility of the Gen-3 Electrolyte for Real-World Applications

To complete the study, the practicality of the electrolyte formulation with additives NaODFB+VC+SN+TMSPi is discussed. First, the ionic conductivity measurements indicated slightly lower values than the control electrolyte, measuring 5.9, 10.49, and 15.8 mS cm^{-1} (6.07, 11.14, and 15.9 mS cm^{-1} for the control electrolyte) at 0, 25, and 55 °C, respectively, probably due to the addition of viscous components like VC and SN (solid at room temperature). Next, cycling experiments were conducted in 2032 coin cells at 0, 25, and 55 °C (**Fig. 4.13a-c**). At all temperatures, the electrolyte demonstrated excellent electrochemical performance, with only a 3% capacity loss and 100% recovery (**Fig. 4.13d**) at both 0 and 25 °C after self-discharge tests for 1 week at 100% state of charge (SOC) (4.3 V, after the removal of 2 Na from NVPF). At 55 °C, the cells exhibited nearly 10% capacity loss during the 1-week rest, with a 96% capacity recovery. The

capacity retention plots in **Fig. 4.13e** show stable capacity retention before and after self-discharge.

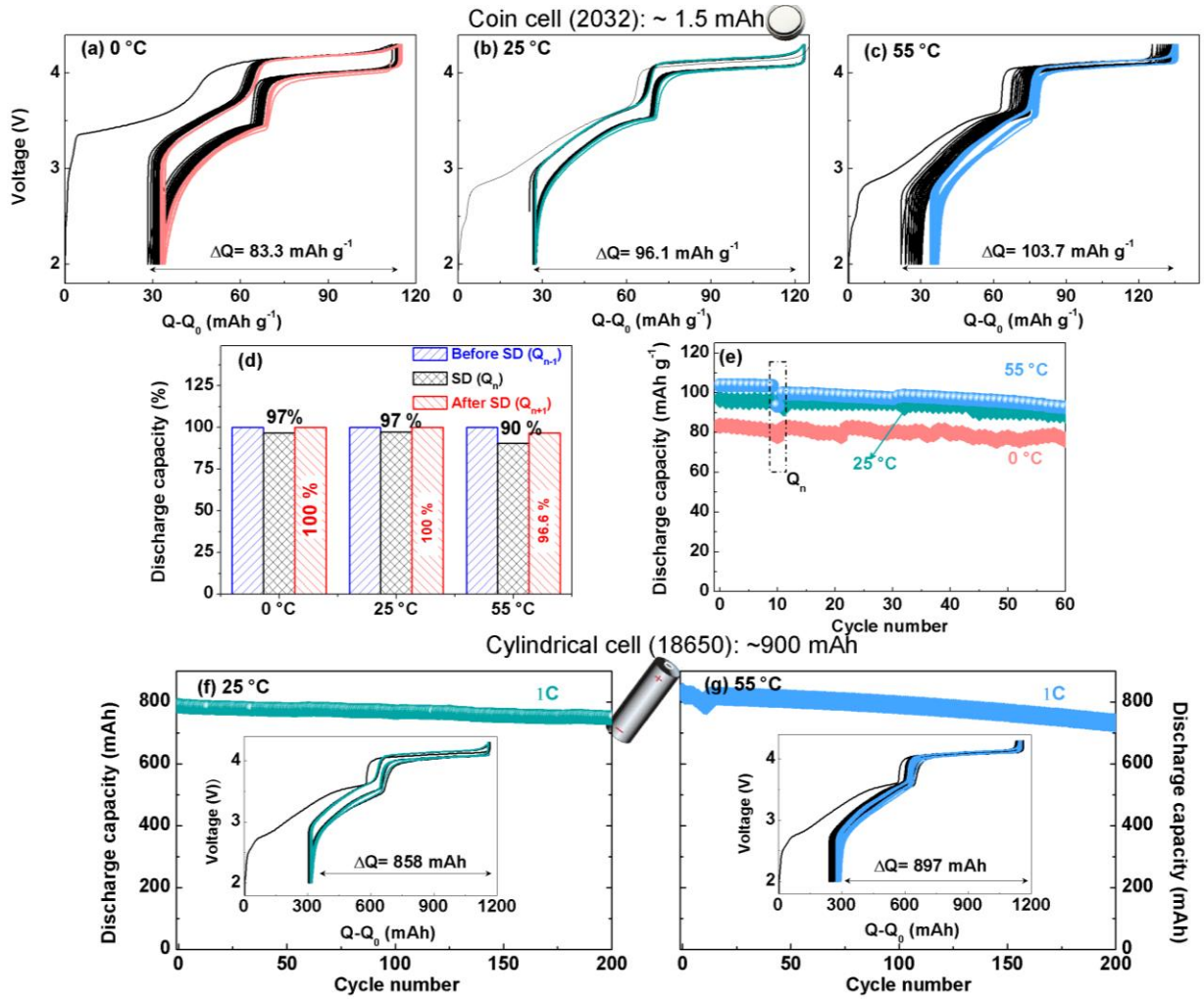

Fig. 4.13 The electrochemical performance of NVPF/HC cells using the electrolyte 1 m $NaPF_6$ in a 1:1:1 EC:PC:DMC mixture containing 0.5 wt.% NaODFB, 3 wt.% VC, 3 wt.% SN, and 0.2 wt.% TMSPi additives (Gen-3 electrolyte) was evaluated in different cell configurations: a–e) Data derived from testing in coin-type 2032 cells cycled at constant temperatures of (a) 0 °C, (b) 25 °C, and (c) 55 °C. (d) Comparison of discharge capacity observed before self-discharge test (Qn−1), during the self-discharge cycle (Qn), and after self-discharge test (Qn+1). (e) Capacity retention plot, where the 10th cycle capacity is due to the self-discharge test. f, g) Data derived from 18650 cells; Capacity retention at 1C of the cells cycled at (f) 25 °C and (g) 55 °C after the self-discharge test, where the cells were cycled for a minimum of 20 cycles and allowed to rest for 1 week at 100% SOC. The insets in each plot show the cycling profile for the formation cycle (black) and after the self-discharge test (green for 25 °C and blue for 55 °C), in which the cells were cycled at a C/5 rate.

To validate the knowledge transfer from coin cells to prototype cylindrical cells, we assembled 18650 cells using Gen-3 electrolyte. The cells were initially formatted at 55 °C by charging at a C/10 rate for one charge (4.3 V). Then cycled at C/5 for 10 cycles, followed by a self-discharge test for 1 week and recovery cycles using the same rate. The experiments were conducted at both 25 °C (**Fig. 4.13f**) and 55 °C (**Fig. 4.13g**), and similar results as in coin cells were obtained. The 18650 cells exhibited approximately 98% capacity recovery even at 55 °C after 1 week of rest at full SOC (4.3 V). The long cycling performance was tested at a 1C rate and is shown in **Fig. 4.13f-g**. Overall, the electrolyte formulation with additives NaODFB+VC+SN+TMSPi demonstrates promising practicality and stability, as indicated by the favorable electrochemical performance in both coin cells and prototype cylindrical cells.

2.7 Limitation of Gen-3 electrolyte

Although the formulated electrolyte with NaODFB+VC+SN+TMSPi (Gen-3) was impressive in terms of achieving stability at high temperatures, it has some limitations. The impedance of the Gen-3 electrolyte at ambient or low temperature is high as compared to the control electrolyte. This indicates the resistive nature of the formed interphase, which helps stabilize the cell at elevated temperatures. Some of the NVPF|HC coin cells containing Gen-3 electrolyte cycled at 0°C showed signs of plating. This limitation could hinder the use of the Gen-3 electrolyte at high rates or extremely low temperatures, which will be the focus of the next study.

3. Conclusions of the Chapter

The investigation presented in this study has demonstrated the effectiveness of a specific electrolyte formulation containing 1 M $NaPF_6$ in EC:PC:DMC with the addition of four electrolyte additives: 0.5 wt.% NaODFB, 3 wt.% VC, 3 wt.% SN, and 0.2 wt.% TMSPi. This electrolyte composition resulted in a stable SEI/CSEI formation, leading to improved electrochemical performance in NVPF|HC cells.

The first part of the study with optical sensing calorimetry gives an indication of suppression of solvent decomposition and rather additives decomposition leading to a decrease in exothermic heat. The optical sensing study guides us in the synergy of additives and their

interaction in the initial cycles. For further information, NVPF|HC coin cells were employed, and capacity retention, SD, RE, ΔV, NVPF mass loss, HC slippage, and (dis)charge endpoint slippage were evaluated.

Subsequent cycling of symmetric cells yielded essential insights into the individual contributions of each additive. It was observed that VC and NaODFB effectively passivate the HC electrode, while SN played a critical role in suppressing electrolyte oxidation, thereby reducing V dissolution and NVPF mass loss. Additionally, TMSPi served as an acid scavenger, contributing to the integrity of the formed interphases.

The optimized electrolyte formulation demonstrated several desirable characteristics, including long cycle life and calendar life, low vanadium dissolution, reduced NVPF mass loss, a slower rate of SEI growth, and minimal gassing. Most importantly, the electrolyte's practicality was demonstrated through its successful transfer to commercial 18650 type cells. Overall, the study highlights the importance of carefully selecting and fine-tuning electrolyte additives to achieve improved battery performance and stability. The combination of specific additives in the electrolyte played a crucial role in addressing various challenges associated with the NVPF/HC chemistry, resulting in a highly efficient and practical electrolyte for Na-ion batteries.

The drawback of the developed Gen-3 electrolyte is its higher interphase resistance at both ambient and low temperatures compared to the control electrolyte, which will impact low temperature and high power performance. This demands further engineering of the proposed electrolyte and will be the focus of the next Chapter.

Chapter 5 | Harnessing High Power and Low Temperature Performance Using Methyl Acetate Cosolvent."

" This Chapter is based on the following research article that I co-authored: Desai, P., Abou-Rjeily, J., Tarascon, J.- M., and Mariyappan, S. (2022). Practicality of methyl acetate as a co-solvent for fast charging Na-ion battery electrolytes. Electrochimica Acta 416, 140217. 10.1016/j.electacta.2022.140217.

1. Background and Motivation

The last Chapter provided a notable practical achievement by enhancing the lifetime of $Na_3V_2(PO_4)_2F_3$ (NVPF) | hard carbon (HC) based cells at both ambient and high temperatures. However, while designing the electrolyte, it should be kept in mind to optimize all the key parameters like ionic conductivity, self-discharge, gassing, fast charging, all-climate operation, etc.[153] Frequently, the enhancement of one parameter is accompanied by a deterioration in another parameter. For example, the incorporation of additives discussed in the previous chapter for better interphase stability leads to an increase in cell impedance and may impose fast charging and low-temperature cycling restrictions. Thus, this Chapter will focus on enhancing low temperature and high power behavior of NVPF|HC cells (which was ignored in the last Chapter), while keeping track of other crucial parameters like high-temperature stability.

Fast-charging (FC) is the new Holy Grail in battery technology. The US Department of Energy granted over $19 million to enable ultrafast charging (XFC) with the goal of 15-minute EV charging by 2028.[272] Na-ion batteries gain importance as some of the electrodes and electrolytes exhibit faster Na-ion diffusion kinetics than lithium counterparts. Positive electrodes like NVPF and PBA achieve a rapid 10C (full capacity in 6 minutes) sodium (de)insertion rate.[273,274] Moreover, the commonly used Na-ion negative electrode, HC, exhibits better rate capability to graphite due to its higher redox potential, facilitating faster Na-insertion without competing Na-plating.[62,275]

The electrolyte transport properties are as crucial as the positive and negative electrodes in determining how fast a cell can be charged. Particularly at low temperatures and/or high rates, the polarization across the electrolyte and electrode-electrolyte interphase can lead to limited deployable capacity, resulting in an early hitting of the cut-off voltage.[276,277] Fast charging has a more pronounced impact, causing a reduction in calendar/cycle lifetimes and, in extreme cases, rollover failure. In LIBs, rollover behavior is attributed to unwanted lithium plating on the negative electrode surface when large currents are applied.[278,279] The lifetime loss due to plating occurs through multiple routes.[280–282] Firstly, the plated metal consumes the cell's active metal ion (Li^+/ Na^+) inventory, leading to irreversible capacity loss. Secondly, the plated metal is not

chemically stable, reacting with the electrolyte, releasing byproduct gases, and forming a new SEI. Lastly, in some extreme cases, plated metal can form dendrites, causing shorts in the cell and raising safety concerns.

Regarding Na-ion electrolytes, they exhibit high Na-ion conductivity because of the weaker solvation of Na^+-ions in comparison to Li^+-ions.[273] However, the interphase formed in Na-ion batteries is often reported to be relatively unstable, requiring the use of electrolyte additives to stabilize interphase as seen in **Chapter 4** for Gen-3 electrolyte (with NaODFB+VC+SN+TMSPi). Unfortunately, in the case of our Gen-3 electrolyte, the additives lead to Na plating at low temperatures and or extremely high C-rates. Thus, achieving fast-charging Na-ion cells necessitates an electrolyte design that not only possesses high ionic conductivity but also forms highly conductive and stable interphases over a broad temperature range.

One approach reported with lithium-ion batteries (LIBs) to enable fast-charging (FC) is to engineer electrode materials with coatings or smaller particle sizes, enhancing electrical and Li^+ conductive transport within the material.[283–286] Another strategy involves the use of salts/additives,[287,288] such as Lithium bis(fluorosulfonyl)imide (LiFSI) and Lithium bis(trifluoromethanesulfonyl)imide (LiTFSI), which effectively reduce the interphase resistance. Additionally, to address polarization and plating issues and achieve FC, the ionic conductivity of the electrolyte can be improved by incorporating low-viscosity cosolvents.[235,289–294] For LIBs, ester-based cosolvents, such as methyl acetate (MA) and ethyl acetate (EA), have been found to decrease the depletion of Li^+ at the negative electrode surface during insertion, leading to reduced overpotential and prevention of associated metal plating under high currents.[235,295–297] However, these organic ester-based cosolvents suffer from poor electrochemical stability.

Table S5.1 compares the essential physiochemical properties of esters (MA and EA) with those of linear (DMC, DEC, and EMC) and cyclic (EC and PC) compounds. Esters have the advantage of low viscosity and high melting point, making them highly beneficial for high-power and low-temperature applications. However, their low boiling point and flash point present a significant challenge when incorporating them into practical cells.

	Viscosity	Dielectric constant	Donor Number	Melting Point (°C)	Boiling Point (°C)	Flash Point (°C)
EC	1.86 (40C)	89.6 (40°C)	16.4	36.4	248	143
PC	2.5	64.9	15.1	-48	242	116
DMC	0.59	3.12	8.7	4.6	90	16
DEC	0.75	2.82	8	-74	126	25
EMC	0.65	2.9	6.5	-55	109	23
MA	**0.385**	6.6	-	**-98**	**56.9**	**-13**
EA	**0.416**	5.99	-	**-83**	**77.1**	**-3**

Table S5.1 | Critical physiochemical properties of electrolyte solvents. The mentioned properties are collected from several references.[80,135,235,298] As EC is solid at room temperature, the viscosity is measured at 40°C.

In this study, we explored the impact of adding MA or EA to a Gen-3 electrolyte containing four additives NaODFB+VC+SN+TMSPi. These additives form a good passivation film and exhibit excellent performance at both ambient and high temperatures. In the initial stages of the study, conductivity improvement and electrochemical stability of EA/MA are explored. Subsequently, electrolyte formulations are engineered using this information, and their performance is assessed.

2. Results and discussions

2.1 Improvement in electrolyte conductivity with ester cosolvents

In our study, the control electrolyte was prepared as 1M $NaPF_6$ in EC-PC-DMC (1:1:2 by vol %). To investigate the effect of ester cosolvents on conductivity, 20% of the solvent blend was replaced with MA or EA, creating the blends 20% MA+Control and 20% EA+Control, respectively. The bulk ionic conductivity of the control electrolyte was measured at different temperatures and is presented in **Fig. 5.1**, with specific values given in **Supplementary Fig. S5.1**. At 25°C, the conductivity of the control electrolyte was observed to be 11.65 mS/cm, which decreased to 4.75 mS/cm at -10°C. Remarkably, the addition of 20% MA to the control electrolyte resulted in a significant increase in conductivity, reaching 13.65 mS/cm at 25°C and 7.07 mS/cm at -10°C. On the other hand, the blend with EA exhibited an intermediate conductivity between the MA-

containing and control electrolytes, likely due to the higher viscosity of EA (0.416 cP at 25°C) compared to that of MA (0.385 cP at 25°C).

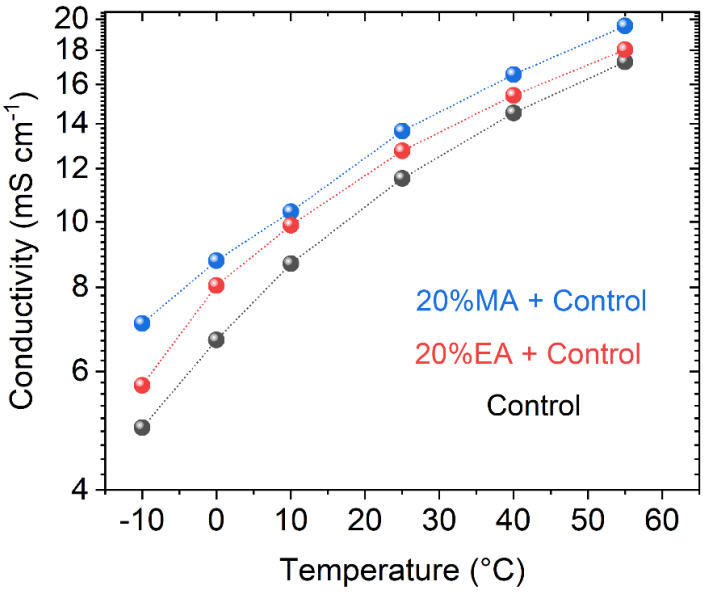

Fig.5.1 | Effect of ester based cosolvent on ionic conductivity of electrolyte. Ionic conductivity of the electrolyte blends Control (1M $NaPF_6$ in EC-PC-DMC 1:1:2 by vol %), 20%MA + Control (1M $NaPF_6$ in EC-PC-DMC-MA 1:1:2:1 by vol %) and 20%EA + Control (1M $NaPF_6$ in EC-PC-DMC-EA 1:1:2:1 by vol %) measured at -10°C, 0°C, 10°C, 25°C, 40°C and 55°C.

In general, cyclic carbonates (such as EC, PC, etc.) have high dielectric constants and high viscosity, while linear carbonates (like DMC, EMC, DEC, etc.) possess low dielectric constants and low viscosity.[80,299,300] Ideally, solvent blends that exhibit both high dielectric constants (more salt dissociation) and low viscosity (less drag force experienced by Na-ion) demonstrate high ionic conductivity. When the dielectric constant of the solvent blend decreases, ion association can occur, leading to reduced ionic conductivity. However, in our case, even though 60% of the solvents (40% DMC and 20% MA) have low dielectric constants, we observed an increase in ionic conductivity. This phenomenon can be explained by the work of Logan et al.,[301] who demonstrated that as low as 30% EC is sufficient to prevent ion association, even at high salt concentrations. In our study, we used nearly 40% cyclic carbonates (EC-PC), effectively separating the anions and cations. As a result, the bulk ionic conductivity of the electrolyte significantly increased simply by adding a small amount of low-viscosity cosolvent (MA/EA). In summary, the remarkable increase in ionic conductivity observed with the addition of MA/EA is attributed to

the low drag force experienced by ions during their migration, which were already well dissociated by EC and PC. In the upcoming session, the electrochemical stability of EA and MA will be examined in NVPF|HC cells, given their known instability at extreme potentials.

2.2 Electrochemical stability with inclusion of ester cosolvents at elevated temperature

The electrochemical stability of the electrolytes containing ester cosolvent was evaluated in NVPF|HC cells (**Fig. 5.2**). Initially, we tested the incorporation of as little as 4% MA/EA without any electrolyte additives at a high temperature of 55°C to assess potential degradation. The first cycle curves shown in **Fig. 5.2** demonstrate the behavior of the electrolytes with ester cosolvents alongside the control electrolyte. During the first cycle, we observed an increase in irreversibility with the addition of ester cosolvent, indicating a significant loss of Na^+ inventory during the formation of the interphases. Moreover, the 4% EA + Control electrolyte exhibited more irreversible loss than the 4% MA + Control electrolyte. This observation aligns with existing literature for lithium-ion batteries (LIBs), where EA and MA are known to have poor oxidative/reductive stabilities, likely contributing to the observed irreversibility and poor cyclability of the electrolytes containing ester cosolvents in NVPF-HC full cells (potential window 2- 4.3 V).

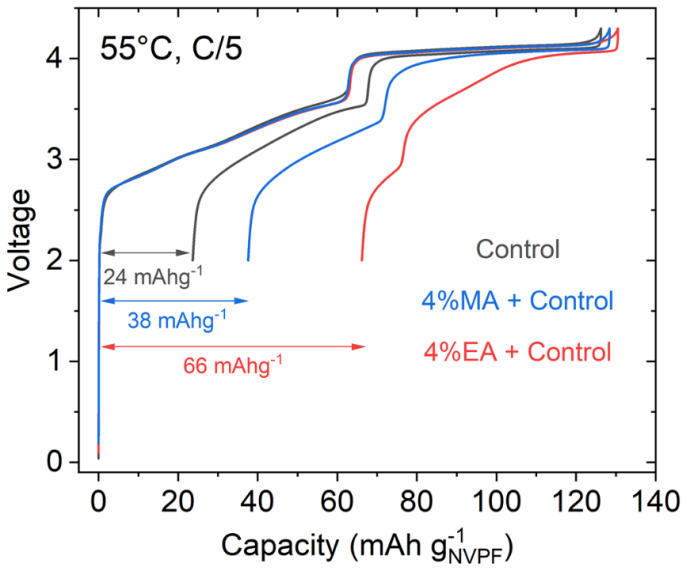

Fig. 5.2 | First cycle irreversibility with inclusion of 4%MA or EA in Control electrolyte. Voltage vs. Capacity profile for the first cycle of NVPF/HC coin cells using Control, 4%MA + Control and 4%EA + Control electrolyte blends. The arrow in the figure represent the irreversible capacity loss in the first cycle.

To enhance the electrochemical stability of the MA/EA-containing electrolyte, we added a mixture of Gen-3 additives, namely 0.5% NaODFB, 3% VC, 3% SN, and 0.2% TMSPi. For simplicity, we denote the resulting electrolyte formulations with these additives as 'MA/EA + Add' in their names. The testing protocol at 55°C (detailed in **Supplementary Fig. S5.2**) commenced with 10 cycles at C/5 followed by charging the cell to 4.3 V (100% state of charge) and storing it for 1 week at 55°C and then the cycling was resumed. The values of self-discharge (Q_{dis-11}/Q_{dis-10} x 100) and recovery (Q_{dis-12}/Q_{dis-10} x 100) provided quantification of parasitic reactions during storage, which can have a negative impact on the cell's calendar life (as described in **Supplementary Fig. S5.3**). Additionally, continuous cycling measured the capacity retention, giving insight into the cell's cycle life. Furthermore, the polarization of the cell (ΔV) was calculated as the average discharge voltage subtracted from the average charge voltage, indicating impedance growth within the cell (discussed in **Chapter 2**, **Section 2.1.4**). The slippage values of the NVPF and HC electrodes indicated any parasitic reactions or mass losses occurring at the respective electrodes, and the calculation method for this parameter is described in **Fig. 4.7 and Fig. 4.8** of **Chapter 4**.

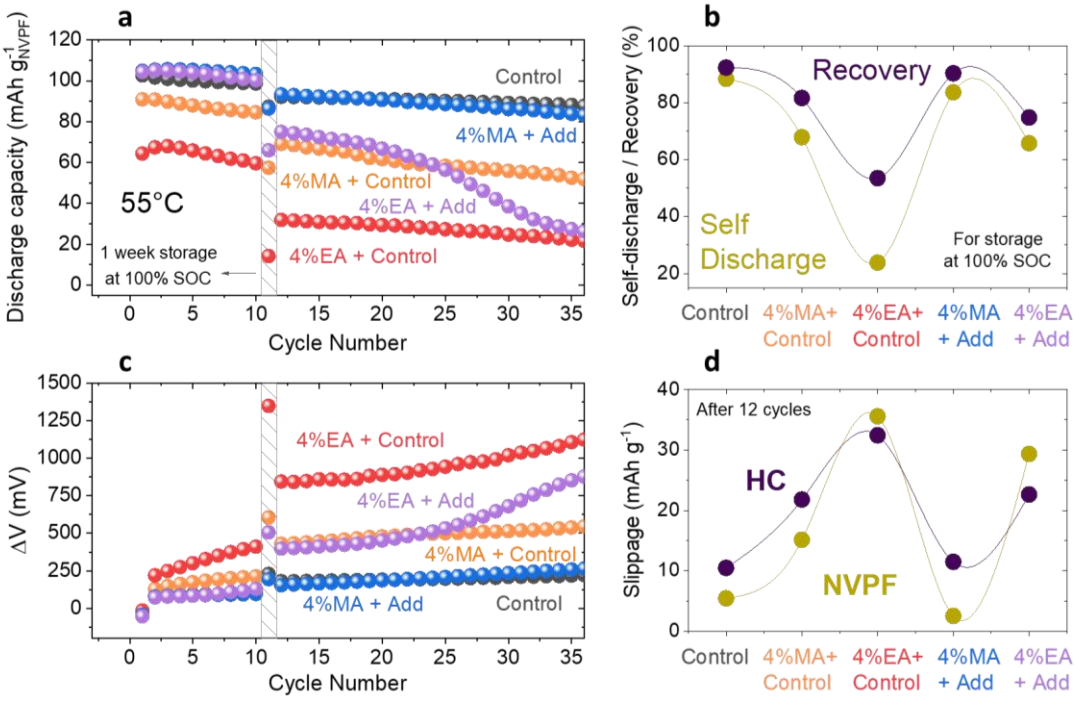

Fig. 5.3. | Stabilizing the EA/MA cosolvent with Gen-3 additives. Electrochemical performance of NVPF/HC coin cells of five different electrolyte blends, Control, 4%MA+Control, 4%EA+Control, 4%MA+Additives, 4%EA+Additives

cycled in 55°C oven at C/5 rate. (a) Discharge capacity (%) vs. cycle number for electrolytes. (b) Self-discharge (%) and recovery (%) of the cells with electrolytes during the one week storage at 100% SOC. (c) Polarization (ΔV) development as a function of cycle number for different electrolytes. (d) NVPF and HC slippage for electrolytes after 12 cycles.

In **Fig. 5.3a**, it is evident that the 4% MA+Add and 4% EA+Add electrolytes retained more capacity compared to their counterparts, 4% MA+Control and 4% EA+Control, respectively. The presence of additives led to reduced cell polarization (**Fig. 5.3c**), decreased capacity loss during self-discharge (**Fig. 5.3b**), and lower slippage amplitude of both NVPF and HC electrodes. These observations indicate that the additives effectively passivated the electrodes, preventing side reactions and resistance growth.

Interestingly, the behavior of 4% MA+Add closely resembled that of the Control electrolyte in terms of capacity retention, cell polarization, self-discharge, and slippage. Subsequently, we increased the MA concentration up to 20%, and similar stability at high-temperature cycling (55 °C) was observed, suggesting that the interphase stability is primarily controlled by the additives (**Supplementary Fig. S5.4**). As a result, we confirmed through 55 °C testing that MA is much more stable than EA, and its stability can be further enhanced by using the additives. Therefore, our subsequent studies focused solely on the MA cosolvent containing the Gen-3 additives. For the sake of comparison, it is worth noting that the same Gen-3 additives, when used in the electrolyte without organic esters (MA/EA), exhibited much better stability at 55 °C (**Supplementary Fig. S5.5**). This behavior suggests that the observed degradation might be associated with the possible degradation of MA at high temperatures. Next, the behavior at ambient temperature was studied to evaluate the same parameters.

2.3 Long term cycling at ambient temperature

The long-term cycling stability of the MA-containing electrolytes with the Gen-3 additives was tested at ambient temperature (~25°C) using the same cycling protocol described in **Supplementary Fig. S5.2**. **Fig. 5.4a** and **Fig. 5.4c** illustrate the discharge capacity and cell polarization evolution with cycles for the Control, 4% MA+Add, and 20% MA+Add electrolytes.

Notably, all cells containing additives displayed better capacity retention and less polarization compared to cells based on our Control electrolyte.

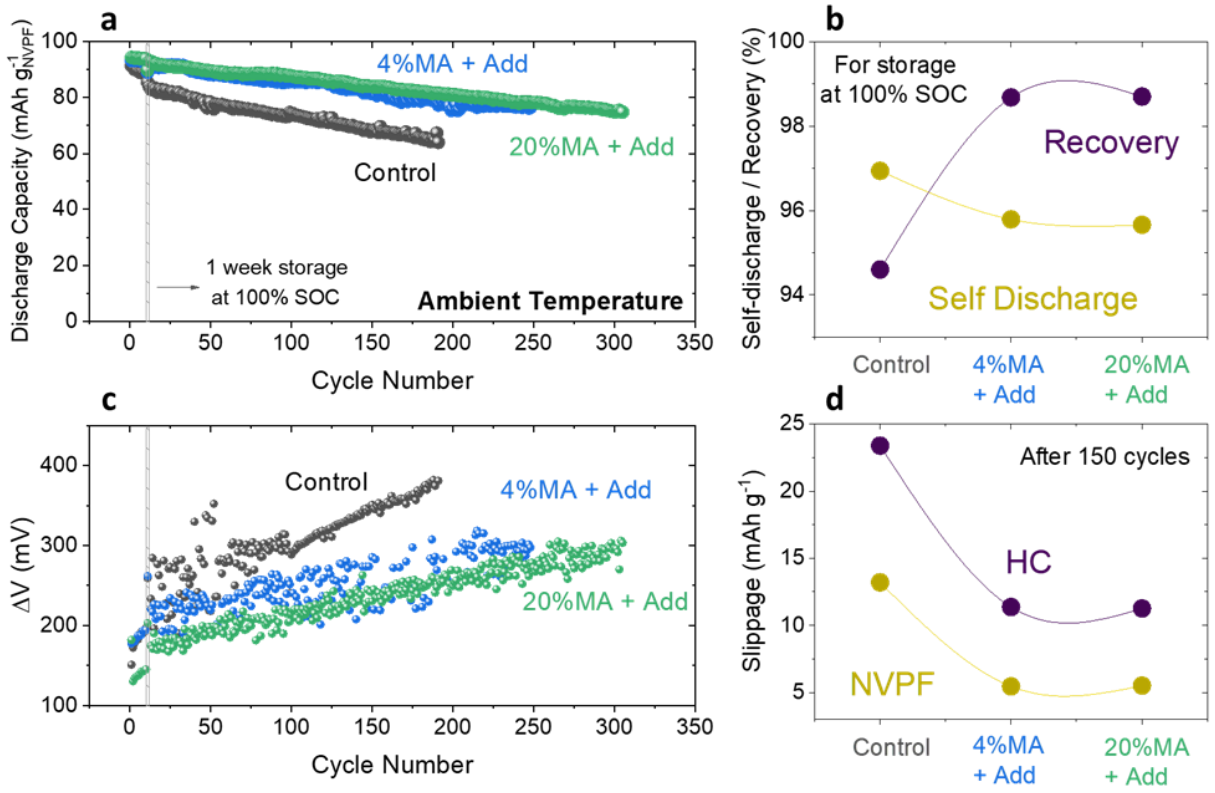

Fig. 5.4 | Ambient temperature cycling of electrolyte with MA + Gen-3 additives. Electrochemical performance of NVPF/HC coin cells of three different electrolyte blends, Control, 4%MA+Additives, 20%MA+Additives, cycled at ambient temperature with C/5 rate. (a) Discharge capacity (%) vs. cycle number for electrolytes. (b) Self-discharge (%) and recovery (%) of the cells with electrolytes during the one week storage at 100% SOC. (c) Polarization (ΔV) development as a function of cycle number for different electrolytes. (d) NVPF and HC slippage for electrolytes after 150 cycles.

After one week of storage, the recovery (**Fig. 5.4b**) was the lowest for the Control electrolyte, while it was comparable for the electrolytes with additives, regardless of the amount of MA. Additionally, the slippage of the NVPF and HC electrodes, plotted after 150 cycles (**Fig. 5.4d**), exhibited the same trend, and more slippage was observed for the electrolyte without additives. The recovery (after one-week storage at 100% state of charge) and slippage (calculated after 150 cycles) provide a qualitative comparison of the cell's calendar life and cycle life, respectively. Interestingly, there was a similar degradation for both 4% and 20% of MA, further confirming that the additives play a crucial role in forming the stable interphase.

At this stage, the role of additives has been predominantly observed, while the function of the MA cosolvent remains unclear. To gain more insights into this issue, the cycling behavior of the MA-containing electrolytes was tested at low temperatures to enhance the effect of electrolyte resistance.

2.4 Cosolvents in action: Low temperature behavior

Fig. 5.5a and **Fig. 5.5c** display the discharge capacity and polarization (ΔV) evolution for cells with different electrolyte formulations: Control, Add (with Gen-3 additives and no ester cosolvent), 4%MA+Add, and 20%MA+Add at 0°C. At a C/5, the capacity of all cells is comparable, but the trend for polarization is different, with the order being "Add > 4%MA+Add > 20%MA+Add > Control." **Fig. 5.5b** shows the charging profile of the cells, and the inset highlights the cell with Add electrolyte (red curve), which exhibits signs of sodium plating during charging and stripping during discharge. This is more evident in the dQ/dV charging profiles shown in **Fig. 5.5d**, which clearly display the signature of sodium plating and stripping.

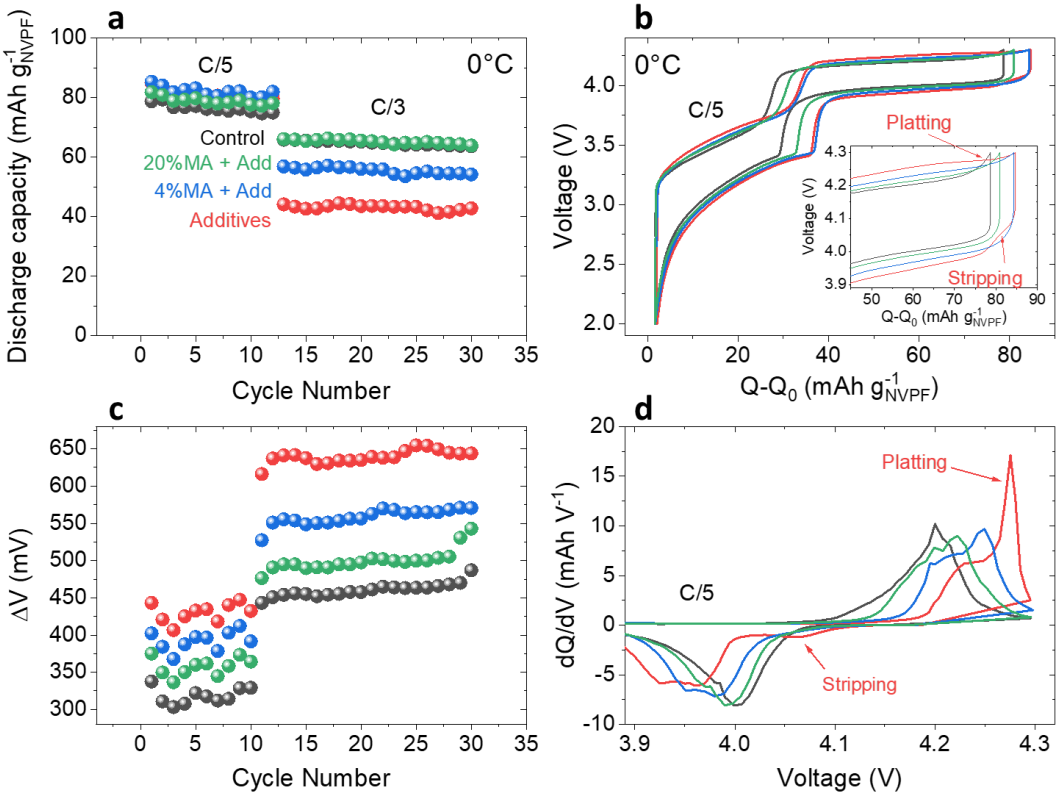

Fig. 5.5 | Low temperature behavior of MA based electrolyte. Electrochemical performance of NVPF/HC coin cells of four different electrolyte blends, Control, Additives, 4%MA+Additives, 20%MA+Additives, cycled at 0°C with C/5

and C/3 rate. (a) Discharge capacity (%) vs. cycle number for electrolytes. (b) Voltage vs. Q-Q_0 profile of the second cycle. (c) Polarization (ΔV) as a function of cycle number for different electrolytes. (d) dQ/dV vs. V of the second cycle represented in (b).

As the charging rate increases to C/3, the polarization trend (**Fig. 5.5c**) remains the same but with a higher magnitude. The cells with higher polarization result in less capacity due to an early hitting of the cut-off voltage, and the trend of capacity changes to "Control ~ 20%MA+Add > 4%MA+Add > Add." Notably, the 20% MA-containing electrolyte is very effective in reducing polarization and achieving higher capacity at C/3 without any signs of sodium plating, unlike the cells with only additives (Add).

Previously, in LIBs, it was claimed that the high conductivity coming from MA reduces the concentration polarization at the negative electrode interphase and, consequently, reduces the chances of metal plating. To investigate whether the same is true for NVPF|HC sodium-ion cells, we studied the impedance behavior of cells containing different electrolyte formulations, with or without MA cosolvent.

2.5 Charge transfer identification

A challenge in impedance analysis lies in accurately identifying the resistances associated with ionic/electronic transports, cell components, and electrode/current collector interfaces from the charge transfer resistance. To address this challenge, we employed the strategy of blocking and non-blocking electrode states, which has been reported elsewhere.[178] During Potentiostatic Electrochemical Impedance Spectroscopy (PEIS), in the blocking state, there is no sodium insertion/extraction from the electrodes, but sodium migration occurs in the electrolyte due to the voltage pulse.[302] Conversely, in the non-blocking state, there is sodium insertion/extraction in electrodes as well as sodium migration in the electrolyte. We designated the blocking state as 0% state of charge (SOC), and for convenience, the non-blocking state was chosen as 100% SOC.

Fig. 5.6a displays the impedance plot of the NVPF-HC cells in both blocking and non-blocking states at 25°C. Cells in the blocking state exhibit only one semi-circle at high frequencies, while cells in the non-blocking state show two semi-circles at both high and low frequencies. A

similar nature of impedance spectra has been observed in lithium-ion cells.[178] In this case, the low-frequency semi-circle in the non-blocking state corresponds to the charge transfer resistance, while the high-frequency semi-circle corresponds to all the other resistances. Notably, when the temperature is lowered to 0°C (**Fig. 5.6b**), the relation between blocking and non-blocking states remains the same, but there is a significant increase in the charge transfer semi-circle and a slight increase in the other resistances. This crucial information indicates that at low temperatures, the charge transfer impedance becomes the primary factor contributing to the overall cell impedance.

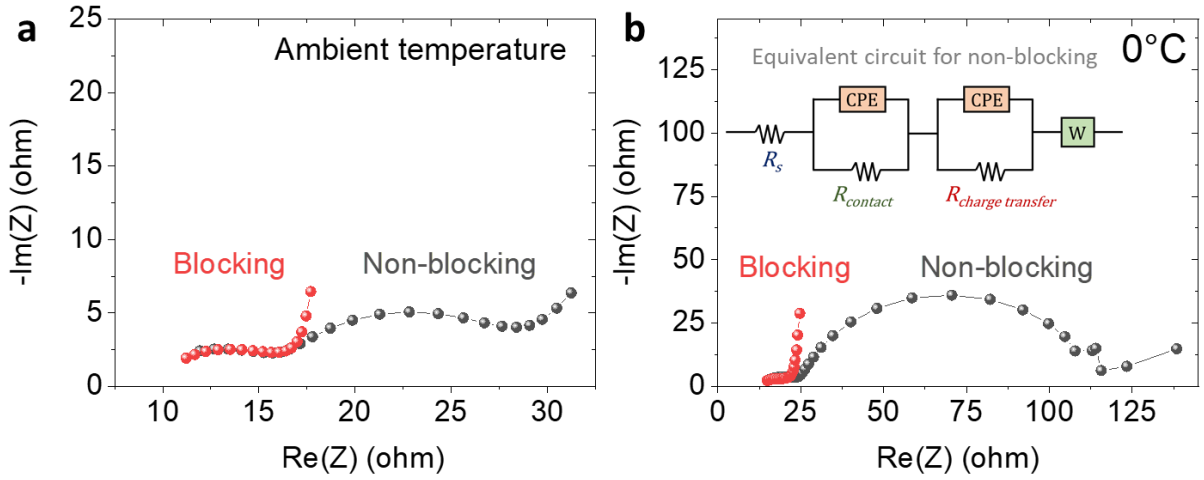

Fig. 5.6 | Separating charge transfer resistance. Electrochemical impedance spectroscopy in blocking and non-blocking configuration of the NVPF/HC cells containing electrolyte with additives at (a) ambient temperature and (b) 0°C with equivalent circuit model for non-blocking configuration. The scale of the X and Y-axis are in 1:1 ratio and the electrode area is 1.267 cm^2.

The impedance model and details of the corresponding resistances are provided in **Fig. 5.6b** inset and **Supplementary Fig. S5.6**. R_s (solution resistance) combines the electrode electronic resistance and the electrolyte ionic resistance. On the other hand, $R_{contact}$ cumulates all the coin cell contacts and the Constant Phase Element (CPE) parallel to it represents the imperfect capacitive behavior from the interfaces at those contacts. Lastly, the desolvation of Na^+, its travel across the interphase, and its entry into the electrode particle are denoted as $R_{charge\ transfer}$, while the CPE parallel to it represents the double layer capacitance at the electrode interface.

To compare the charge transfer resistance, we examined four electrolytes: Control, Add, 4%MA+Add, and 20%MA+Add. The impedance measurements were conducted using a protocol that involved two cycles at different temperatures: 55°C, 40°C, 25°C, and 10°C, respectively. During these cycles, Potentiostatic Electrochemical Impedance Spectroscopy (PEIS) was performed at 100% state of charge (SOC) for each electrolyte. **Fig. 5.7** displays the impedance curves at various temperatures for the different electrolytes. It is important to note that we began to observe the charge transfer resistance only at 25°C, marked by the rectangles in **Fig. 5.7**. For our system, temperatures higher than 25°C presented challenges in fitting the data and obtaining reliable charge transfer resistance values. Therefore, the impedance curve of the electrolytes at 25°C and 10°C was fitted, and the values of R_s (solution resistance), $R_{contact}$ (contact resistance), and $R_{charge\ transfer}$ (charge transfer resistance) are provided in **Supplementary Fig. S5.7**.

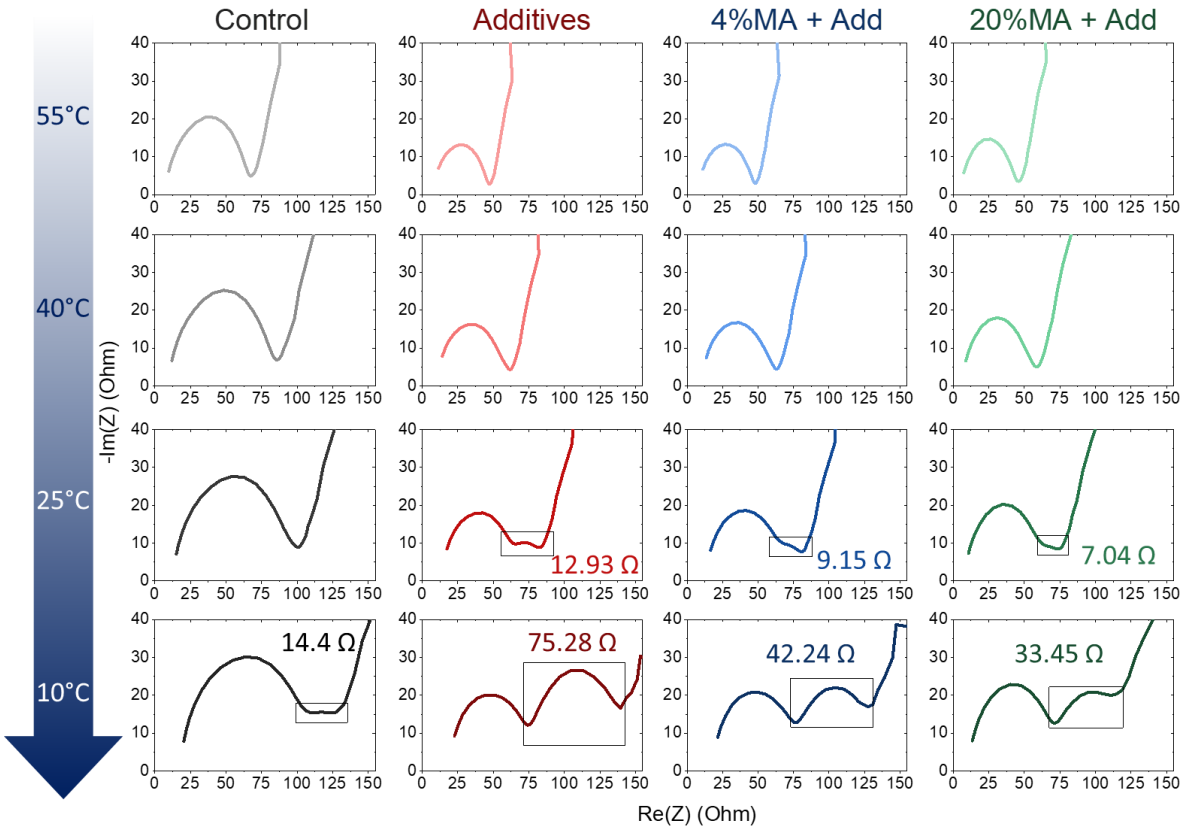

Fig. 5.7 | Charge transfer evolution with inclusion of additives and MA. Electrochemical impedance spectroscopy in non-blocking configuration and 100% SOC of the NVPF/HC cells containing four different electrolytes, namely Control, Additives, 4%MA+Additives, 20%MA+Additives at 55°C, 40°C, 25°C and 10°C. Scale of X and Y-axis are not in 1:1 ratio and electrode area is 1.267 cm^2.

At 10°C, the charge transfer resistance values in **Fig. 5.7** were as follows: Control (14.4 Ω, lowest), Add (75.28 Ω, highest), 4%MA+Add (42.24 Ω), and 20%MA+Add (33.45 Ω). The addition of MA cosolvent resulted in a decrease in charge transfer resistance to almost half the value (from 75.28Ω for Add to 33.45 Ω for 20%MA+Add). There are two possible reasons that could account for this decrease in charge transfer with MA. Firstly, MA increases the ionic conductivity of the electrolyte, leading to less depletion of sodium ions from electrode interphases during the 10mV voltage pulse of PEIS. This leads to fast sodium migration in electrolytes with MA compared to electrolytes without MA. Secondly, MA could participate in the primary/secondary solvation sheath of sodium, altering the (de)solvation energy during insertion/extraction.

Phenomena of decrease in drag force or increase in ionic conductivity (due to lowering of viscosity) and change in solvation shell are complex and intertwined, making it difficult to differentiate which of them is affecting the charge transfer and to what extent. Further investigation and analysis are required to gain a comprehensive understanding of the specific contributions of MA to the improved charge transfer in the electrolyte.

Conclusively, it seems here that Control electrolyte is the best choice for high power and low temperature commercial applications. However, the total cell resistance ($R_{charge\ transfer}$ + $R_{contact}$) for temperatures equal to or higher than the 25 °C is the largest for the Control electrolyte (**Fig. 5.7**). Also, the stability of the electrolyte at ambient temperatures is the least for Control electrolyte (**Fig. 5.4a**). Moreover, control electrolyte cannot be used as it can lead to unwanted parasitic reactions, excessive gas generation, and consequently, CID breaking when cycled at 55°C for just 28 cycles, as discussed in **Fig. 3.1** of **Chapter 3**. Finally, it was convenient to use additives that will increase the cell lifetime at ambient/high temperatures and reduce the impedance at low temperatures, as done in the case of MA cosolvent. This approach provides a good .compromise between high-power performance and stability under various operating conditions. On this note, next, we try to check the effect of MA on the power performance of commercial 18650 type NVPF|HC cells containing additives.

2.6 Commercial implementation in 18650 cells: Power performance and High temperature stability

As discussed before, MA cosolvent reduces the charge transfer resistance and increases the ionic conductivity, which enhances Na-ion conduction at low temperatures. However, at room/high temperatures and slower cycling rates (C/5), the improvement in electrolyte conductivity does not have a significant impact on performance (**Fig. 5.1-5.7**).

To further investigate the effect of MA on cycling performance, NVPF|HC-based dry 18650 cells from TIAMAT were filled with either a control electrolyte (with no additives) or 20% MA+Add electrolyte. Impedance analyses were carried out at 25°C at 100% SOC (**Fig. 5.8a**) and 50% SOC (**Supplementary Fig. S5.8**), showing relatively lower impedance for cells containing 20% MA+Add electrolyte, in line with the coin cell experiments at 25°C and 4.3 V (**Fig. 5.7**).

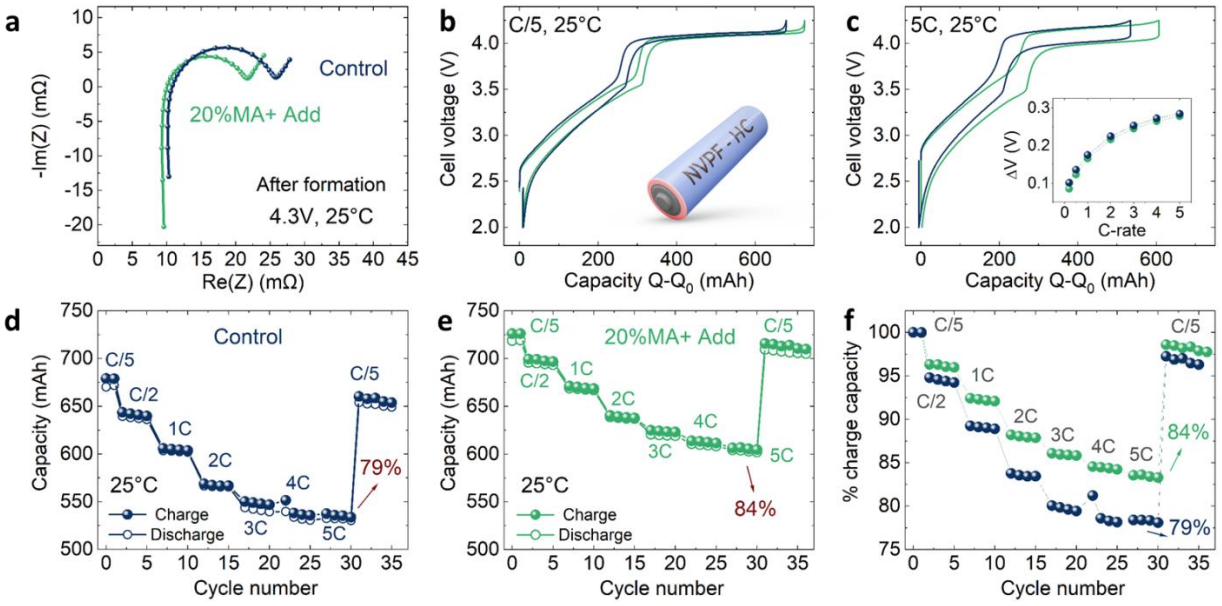

Fig. 5.8 | Power performance in NVPF|HC 18650 cells. The electrochemical performance of cylindrical 18650 NVPF/HC cells filled with Control or 20%MA+Add electrolytes (a) Impedance spectra taken at 100% SOC or 4.3V of the cell at 25 °C. (b) Charge profiles at C/5 and 25 °C. (c) Charge profiles at 5C and 25 °C with inset containing cell's average polarization at different rates. (d) Rate behavior of the Control electrolyte in absolute capacity vs. cycle number (e) Rate behavior of the 20%MA+Add electrolyte in absolute capacity vs. cycle number (f) Rate comparison of Control and 20%MA+Add electrolytes in terms of charge capacity(%) vs. cycle number.

Fig. 5.8b compares the initial cycles at C/5, and the 20% MA+Add electrolyte shows a higher reversible capacity than the Control, indicating less electrolyte decomposition during formation cycles. However, the cycling profile of the 20% MA+Add electrolyte exhibits an average polarization of about 85 mV, with a higher voltage gap observed in the low voltage region (<3.6 V) compared to the high voltage region (>3.6 V). As the cycling rates increase, the voltage gap between charge and discharge also increases (inset of **Fig. 5.8c**), reaching a maximum of about 270 mV at 5C rate for both Control and 20% MA+Add electrolytes. The cycling profile in **Fig. 5.8c** shows nearly similar polarization for both electrolytes, but with slightly less capacity for the Control, possibly due to the initial poor capacity after the formation.

In **Fig. 5.8d** and **Fig. 5.8e**, capacity retention for Control and 20% MA+Add electrolytes is shown at different rates. **Fig. 5.8f** illustrates charge capacity retention as a function of rate. Slow-rate cycling (C/5: D/5) was used to mitigate heat during fast cycles. Transitioning from C/5 to 3C showed a significant capacity difference between Control and 20% MA+Add. However, the difference reduced at 4C and 5C (**Fig. 5.8f**). At 5C, Control retained 79%, while 20% MA+Add retained up to 84%. Both exhibited good rate capabilities, around 80% retention at 5C. The 20% MA+Add electrolyte showed better cycling stability, recovering 98% at C/5, compared to Control's 96% (after the 31st cycle in **Fig. 5.8f**).

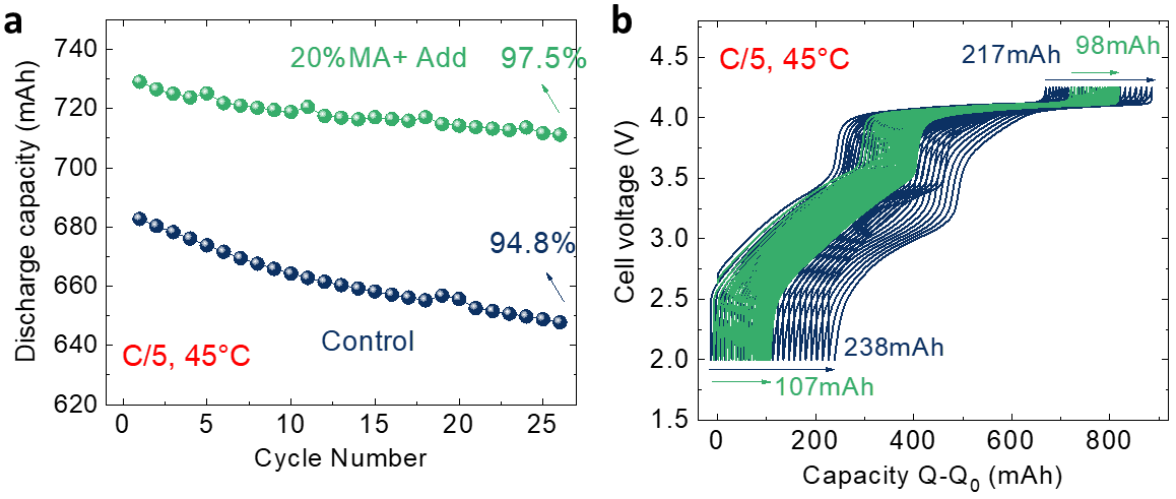

Fig. 5.9 | High temperature stability of NVPF|HC 18650 cells. a) Capacity retention of the cells containing Control and 20%MA+Add electrolytes at 45 °C with the b) corresponding cycling profiles for 1- 25 cycles

Furthermore, at high temperature (45°C), the 20% MA+Add electrolyte shows better stability, retaining 97.5% of its initial capacity after 25 cycles, compared to 94.8% retention for the Control electrolyte (**Fig. 5.9a**). The cycling profile at 45°C also reveals reduced charge/discharge endpoint slippage (**Fig. 5.9b**) for the 20% MA+Add electrolyte, indicating less parasitic reactions and better interphase stability. These points to an enhanced cycle life at high temperature. The long cycling performance at 25°C using fresh 18650 cells with 20% MA+Add electrolyte confirms its stability at ambient temperatures, as indicated in **Supplementary Fig. S5.10**. Overall, the 20% MA+Add electrolyte shows promising improvements in both rate capability and cycling stability, making it a viable option for enhancing the power performance and high temperature performance of NVPF-HC sodium-ion cells.

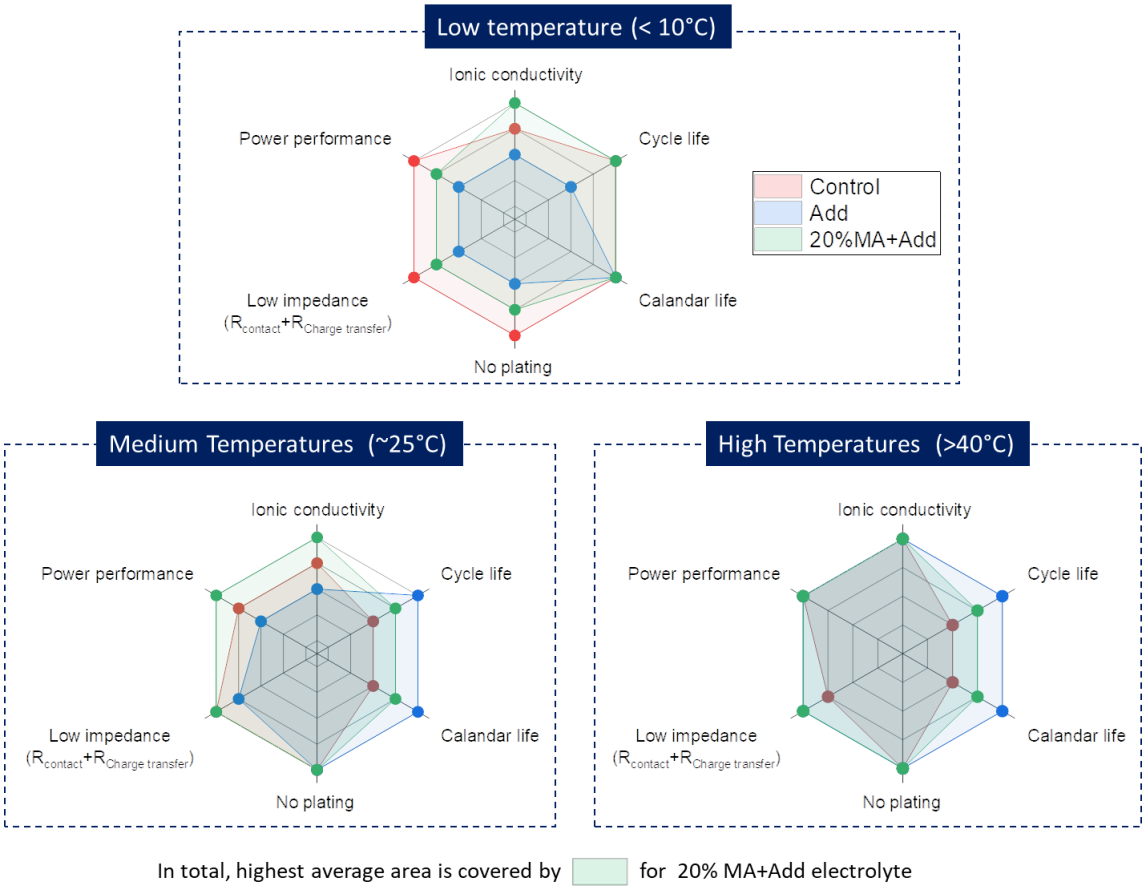

Fig. 5.10 | Summary of the relative comparison of the different observables that are the key for evaluating battery performance and safety. Control is the mother electrolyte, Add is the electrolyte containing Gen-3 additives and 20% MA+Add is the electrolyte containing both Gen-3 additives as well as MA cosolvent.

Fig. 5.10 summarizes the studied test parameters, comparing electrolyte properties at different temperatures for three types: Control, Additives (Add), and 20%MA cosolvent with additives (20%MA+Add). The Control electrolyte performs well at low temperatures and high power, but its cycling stability at medium/high temperatures is poor, making it less favored. The 'Add' electrolyte exhibits high cycling stability at medium/high temperatures, suitable for high-temperature applications, but its power performance and low-temperature applications are limited due to interphase resistance. The MA+Add electrolyte shows balanced properties with good low-temperature performance, relatively better power performance, and cycling stability. It demonstrates the suitability of the MA cosolvent for improved power and low-temperature applications, though high-temperature performance is a bit compromised.

Indeed, upon comparing the area occupied by the electrolyte at all temperatures, the 20% MA+Add stands out with the maximum area. This suggests that it is the most suitable electrolyte for all climate conditions, outperforming both the Control and Add electrolyte.

2.7 Limitations of the MA containing electrolyte

It is essential to note that MA has a very low flash point (-10°C) and boiling point (57.1°C), causing rapid evaporation even at ambient temperatures. At higher operating temperatures (40°C or 55°C), the partial pressure of MA inside the cell can increase, leading to an overall pressure rise. A detailed study on this aspect is still lacking.

Furthermore, the low flash point presents challenges during electrolyte filling in cells, as MA can evaporate at ambient temperature unless handled with care, particularly in automated cell assembly lines. An experiment with the 20% MA+Control electrolyte exposed to the glovebox atmosphere revealed a significant 60% weight loss of MA due to solvent evaporation in just one hour (**Fig. 5.11**). This indicates the care that has to be taken during filling of the electrolyte.

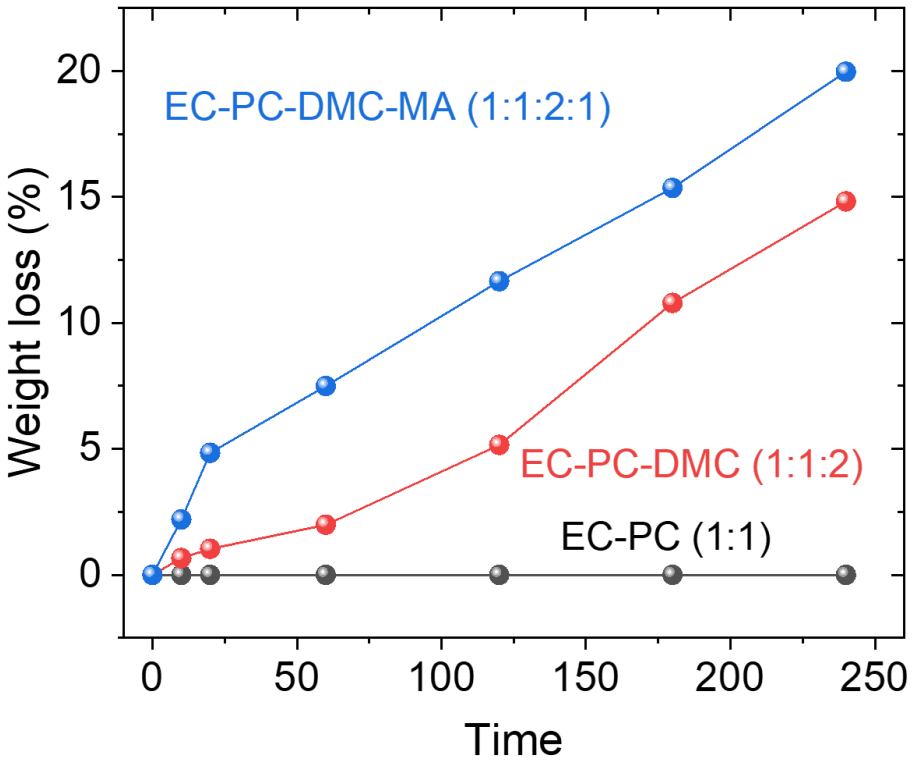

Fig. 5.11 Weight loss (%) of different electrolytes due to evaporation, which were exposed to glovebox environment. Electrolyte formulations were containing 1M $NaPF_6$ in different solvent, namely EC-PC 1:1 by vol %, EC-PC-DMC 1:1:2 by vol %, EC-PC-DMC-MA 1:1:2:1 by vol %. The difference in weight loss between EC-PC-DMC and EC-PC could be attributed to evaporation of DMC alone. Similarly, the difference in weight loss between EC-PC-DMC and EC-PC-DMC-MA can be attributed to evaporation of MA alone. Weight % of MA in the electrolyte is 12%.

These practical challenges necessitate meticulous consideration when employing the MA cosolvent at an industrial scale. To guarantee the secure and effective utilization of the MA cosolvent in real-world applications, appropriate safety protocols and handling procedures must be established. Alternative cosolvents, such as propionitrile and i-Butyronitrile, characterized by high flash points, could be investigated. These cosolvents demonstrate low viscosity and have been noted for their notable high-temperature stability.

3. Conclusions for the Chapter

The Chapter begins with the introduction of Methyl Acetate (MA) and Ethyl Acetate (EA) as potential cosolvents to enhance the performance of Gen-3 electrolyte, specifically in terms of low temperature and high power. The low viscosity and low melting point of MA/EA are attractive attributes. However, EA was found to be less stable than MA at high temperatures, and efforts to stabilize it were unsuccessful. Thus, the study continued with manipulating MA in the electrolyte, incorporating 4% and 20% MA. The ambient temperature performance of these formulations was found to be superior to the control electrolyte. However, the formulation with 20% MA plus additives showed less stability than the additive-only electrolyte.

At low temperatures, the inclusion of MA led to a decrease in polarization and realization of higher capacity than additive-only electrolyte. Notably, 20%MA+Add did not show any signs of plating, unlike the Add electrolyte. The impact of MA on charge transfer resistance was studied, with 20%MA+Add showing significantly less resistance at 10°C. The 18650 type cell format comparison revealed that 20%MA+Add showed less impedance, lesser polarization, high power performance, and high-temperature stability compared to the control electrolyte.

A radar plot presented in the last part of the Chapter compares all the analyzed parameters for low, medium, and high temperatures. While the control electrolyte has more benefits at low temperatures, the electrolyte with additives has clear advantages at ambient and high temperatures. With the inclusion of MA, a single electrolyte with the best average performance at all temperatures is achieved, especially superior power and low-temperature performance. The low boiling point and flash point of MA present challenges in practical systems, but these can be managed through efficient engineering.

This conclusion encapsulates the key findings and insights from the Chapter, highlighting the potential of MA as a cosolvent to enhance the performance of Gen-3 electrolyte across various temperature ranges and power requirements. The study demonstrates the feasibility of MA in practical systems, acknowledging the challenges and proposing engineering solutions.

Chapter 6 | A special case interphase degradation: Zero-volt storage of Na-ion cells. "

" This Chapter is based on the following research article that I co-authored : Desai, P., Huang, J., Foix, D., Tarascon, J.-M., and Mariyappan, S. (2022). Zero volt storage of Na-ion batteries: Performance dependence on cell chemistry! Journal of Power Sources 551, 232177. 10.1016/j.jpowsour.2022.232177.

1. Background and Motivation

The thesis has progressed through several Chapters, exploring cell deterioration pathways and solutions to improve stability and performance. **Chapter 1** and **Chapter 2** primarily introduced the Na-ion system, with a particular emphasis on the NVPF|HC chemistry, and highlighted strategies for analyzing cell degradation. **Chapter 3** focused on studying the stability of the positive electrode $Na_3V_2(PO_4)_2F_3$ (NVPF) in terms of vanadium dissolution, associated structural/microstructural changes, and SEI or hard carbon (HC) poisoning. In **Chapter 4**, an electrolyte formulation with Gen-3 additives was proposed to stabilize the interphase at both ambient and high temperatures. This led to the suppression of parasitic reactions, enabling the successful implementation of the proposed electrolyte in 18650 cells without gassing and CID break at 55°C. In **Chapter 5**, the issue of high impedance at low temperatures in the Gen-3 electrolyte was addressed by incorporating a methyl acetate co-solvent. This modification not only resolved the low-temperature impedance problem but also improved power performance. The current Chapter (**Chapter 6**) focuses on a specific type of SEI degradation caused by a high potential surge of the negative electrode during the specific application of 0V storage of the full cell. The following paragraphs introduce the importance of 0V storage or over-discharge protection.

Rechargeable Li-ion batteries (LIBs) have become indispensable in today's world due to their numerous advantages - affordability, high voltage, exceptional energy density, and long cycle/calendar life. As a result, they find wide-ranging applications, from powering portable electronics to driving electric vehicles and enabling smart grids. However, with their flammable liquid electrolytes posing safety risks, LIBs have been classified as "dangerous goods" by the International Civil Aviation Organization (ICAO) and the United Nations Economic Commission for Europe (UNECE).[303] Consequently, there are strict restrictions on their storage and transportation, with a recommended maximum state of charge (SOC) of 30% to ensure safe shipping.[82]

Over the past 15 years, despite extensive testing and safety regulations, there have been approximately 354 reported incidents[304] of fire, smoke, or explosion involving LIBs during cargo

or air transportation. Some of these incidents were triggered by unintentional external shorts of the battery cells. This external short circuit occurs when the cell's voltage drops to 0 V, causing the negative electrode to be pushed to high potentials to match the positive electrode's potential. During this process, the copper current collector in the negative electrode also reaches a high potential, leading to oxidation (**Fig. 6.1a**) and subsequent Cu-dissolution. This phenomenon can further lead to Cu plating, dendrites formation, and consequently, internal shorts in a practical full cell.[305,306] These internal shorts will lead to thermal runway and safety hazards.

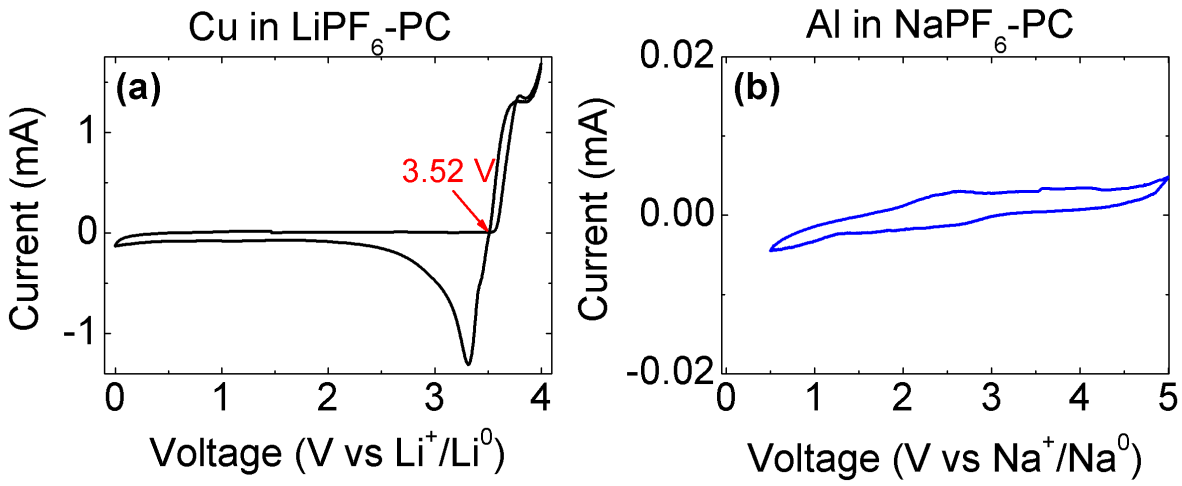

Fig. 6.1 | Oxidative stability of Cu and Al current collectors in Li and Na-electrolytes, respectively. The cyclic voltammogram were measured in Swagelok type three electrode cells for two different cell configurations namely, (a) Cu // 1M $LiPF_6$ in PC // Li with lithium metal as reference electrode and (b) Al // 1M $NaPF_6$ in PC // Na with sodium metal as reference electrode. The CV curves in the figure shows that the onset of Cu oxidation starts around ~3.5 V, whereas the Al foil in the sodium electrolyte is stable towards oxidation up to 4.5V or more.

From another perspective, in real-world scenarios, the effects of self-discharge can become significant, especially for applications like back-up energy storage or military use, where batteries might remain idle for extended periods, possibly years. Without proper management via battery management system (BMS), this situation could lead to over-discharge conditions, particularly at elevated temperatures.[307–309] A similar concern arises in electric vehicles parked with low State of Charge (SOC) levels for long durations, especially in high-temperature environments exceeding

40°C.[310] In such cases, the batteries can actually experience over-discharge, significantly impacting their overall lifespan. Ensuring adequate management and control of these factors is crucial in maintaining battery health and extending their operational life in various applications.

In contrast, Na-ion batteries (NIBs) utilize an aluminum (Al) current collector, which proves to be significantly more stable than Cu towards oxidation (**Fig. 6.1b**). This is because sodium does not form an alloy with aluminum, unlike lithium.[59,311] Therefore, research papers and a patent from Faradion Limited suggest that their NIBs, incorporating sodium transition metal layered oxide as the positive electrode and hard carbon as the negative electrode, can be safely transported in the shorted (0 V) state.[312,313] This promising feature potentially mitigates the safety concerns associated with short-circuit incidents during shipping and handling of batteries.

From fundamental point of view, few crucial questions arise: Is the stability of the current collector the sole determining factor for the 0 V stability of the cell? Additionally, apart from the layered oxide chemistry used by Faradion, what will be the behavior of NVPF|HC cells towards 0V storage? Moreover, it is necessary to compare the degradation rate of LIBs to that of NIBs when faced to 0V storage. Therefore, the next session starts with studying the consequence of 0V storage on well-known LIB chemistries.

2. Results and Discussion

2.1 Benchmarking the Li-ion system

To investigate the 0 V behavior of LIBs, we assembled coin-type cells using NMC811|graphite (2-4.2V) and LFP|graphite (2-4V) with Al and Cu serving as the positive and negative electrode current collectors, respectively. The cycling stability of these cells during 0 V hold was rigorously tested using a ***harsh cycling protocol*** (**Fig. 6.2**). This procedure entailed cycling the cells to 5 cycles within the standard voltage range for cycling, followed by discharging and maintaining it at 0 V for either 24 hours or 72 hours (referred to as 0 V hold). The process was then repeated every 5 cycles until the cell's capacity is exhausted. For fair comparison, cells without any 0 V hold were also tested.

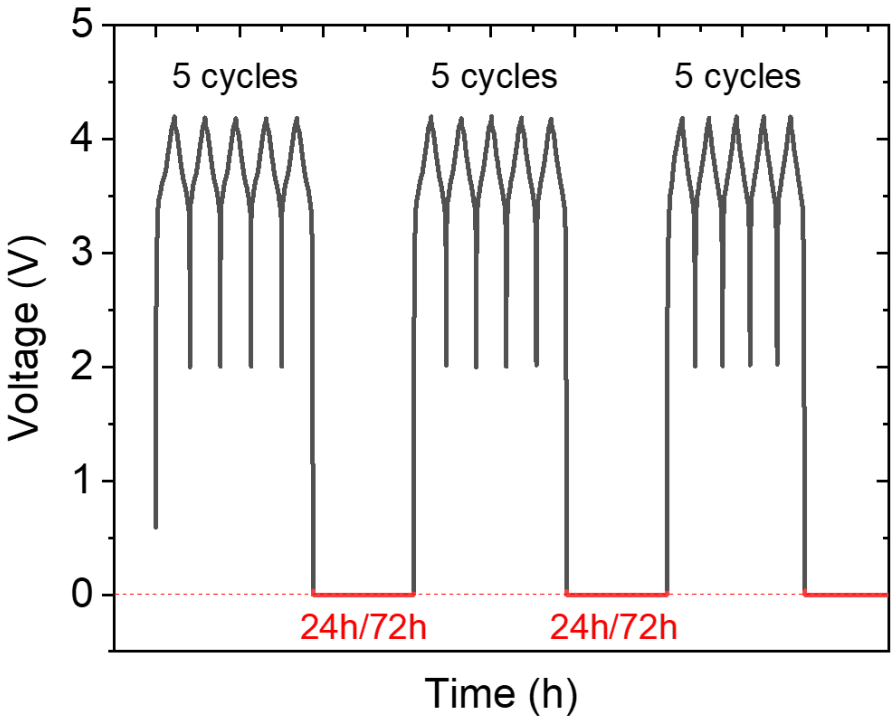

Fig. 6.2 | The testing protocol used for studying the 0V stability of Na-ion cells. The cell is cycled for 5 cycles to form a stable SEI and CSEI and then discharged to 0V and stored at 0V for 24h or 72h. The same protocol is repeated and the capacity retention with 0V hold is compared with cells that cycled between 2- 4.30 V without any 0V discharge. The testing protocol is quite harsh, however in real-life applications, the cells may not be undergoing repeated 0V discharge and storage as done here.

After applying the mentioned (**Fig. 6.2**) cycling protocol for NMC811|graphite and LFP|graphite cells, we observed a temporary gain in discharge capacity (for every 5th cycle of hold in **Fig. 6.3a** and **Fig. 6.3b**) during 0 V hold. However, upon subsequent cycling, the capacity gradually decreased, and the cells with 0 V holds exhibited a faster capacity decay compared to the cells without such holds. For NMC811-graphite cells, they rapidly failed after three 0 V holds, while LFP-graphite cells endured six 0 V holds before showing signs of deterioration. This indicates a relatively slower degradation rate for the LFP-based cells in comparison.

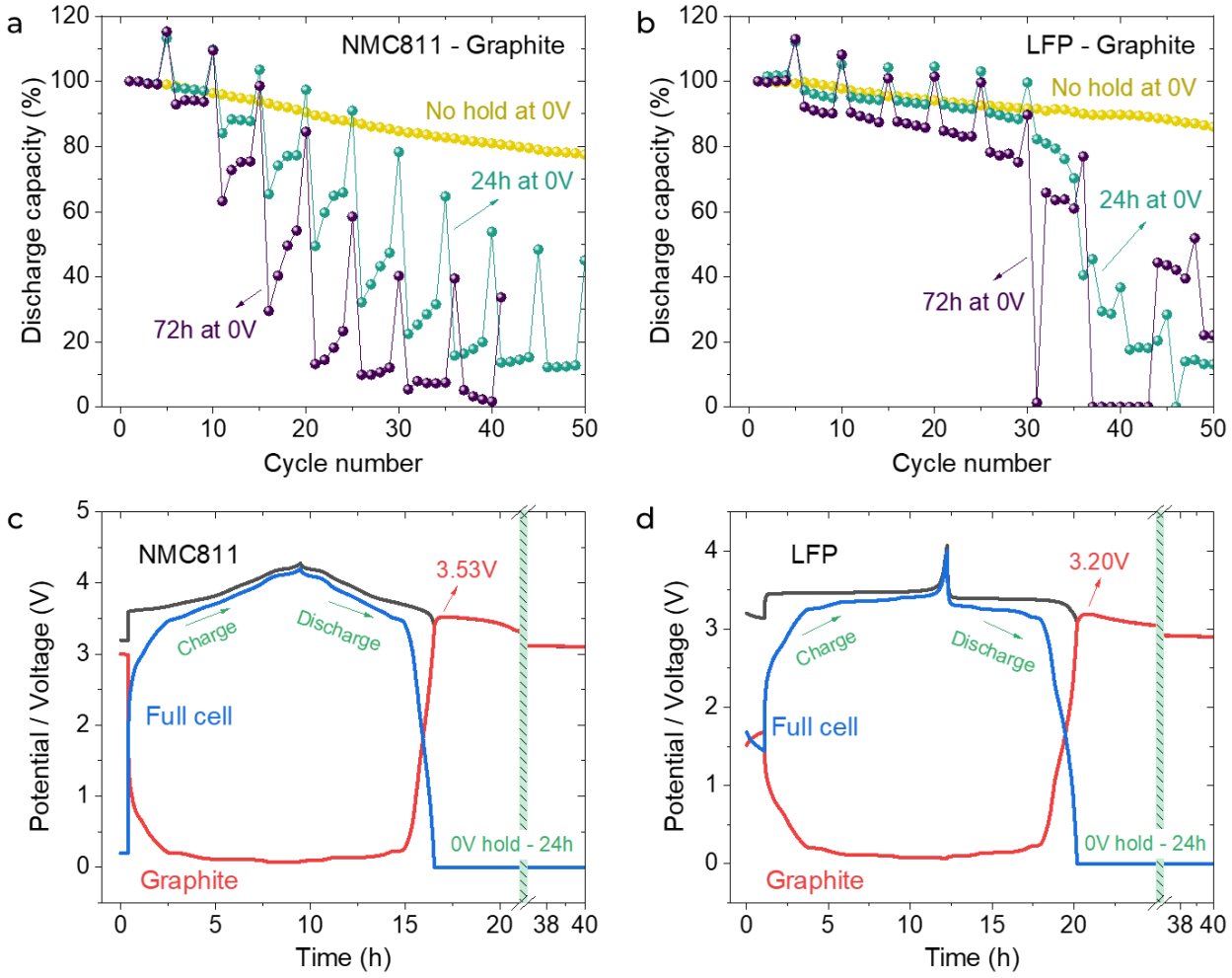

Fig. 6.3 | Stability of NMC811|graphite and LFP|graphite at zero volt. Discharge capacity vs. cycle number of (a) LiNMC811- Graphite cycled in 2-4.2V for normal cycling and (b) LFP- Graphite cells cycled in 2-4V for normal cycling. Three different cycling conditions were compared for cells cycled without any 0V holding, with 24h and 72h holding for every 5 cycles. Cycling profile of (c) LiNMC811- graphite and (d) LFP- graphite in three electrode cell assembly where lithium metal is used as the reference electrode.

To investigate this difference, we constructed three-electrode cells using Li-metal as the reference electrode, allowing us to monitor the cycling behavior of each electrode independently. Notably, during the cycling of the NMC811-graphite cell, the potential of the graphite electrode surged to 3.53 V vs. Li/Li^+ when cell voltage reached 0 V. This high potential triggered the oxidation-driven dissolution of copper, which was visually observed on the separator when the cell was disassembled (**Supplementary Fig. S6.1**). The dissolved copper could then undergo reduction/oxidation, resulting in metallic deposits on both the negative and

positive electrodes. These deposits have the potential to damage the electrode-electrolyte interphase, leading to rapid capacity loss and eventual cell failure. Moreover, in cases where multiple over-discharges to 0 V occur, the deposited copper can form dendrites, creating internal shorts[314] and potentially leading to thermal runaway, a critical safety concern.

In contrast, the graphite potential in LFP-graphite cells exhibits a lower value, approximately 3.2 V vs. Li/Li^+, during 0 V hold (as shown in **Fig. 6.3d**). Consequently, the initial degradation in LFP-graphite cells during 0 V holds is probably related to the degradation of the interphases. However, with repetitive 0 V storages, larger cell polarization occurs (**Fig. S6.3**), leading to a higher potential surge of the graphite electrode and subsequent copper dissolution, as mentioned earlier. In summary, both NMC811|graphite and LFP|graphite cells, utilizing Cu as a current collector for graphite, demonstrate a rollover-type failure (sudden cell death)[315–317] after a few 0 V holds and cycling. Next, we will delve into Na-ion system.

2.2 Na-ion cells at 0V: Exploring the degradation mechanism

2.2.1 SEI decomposition and regrowth

The NVPF|HC full cell cycling stability in 2032 coin-type cells, using the same 0V hold protocol as previously stated (**Fig. 6.2**), is presented in **Fig. 6.4a**, alongside a similar cell tested without 0 V hold. The normalized cell polarization evolution for all cells is depicted in **Fig. 6.4b**. The cells with 0 V hold exhibit faster capacity degradation (**Fig. 6.4a**) and an increase in cell polarization (**Fig. 6.4b**). However, it is important to note that there is no occurrence of a sudden cell death or rollover failure, as observed with Li-ion batteries (**Fig. 6.3**). This distinction indicates a different failure mechanism and behavior for NVPF|HC cells under these conditions.

Simultaneously, the three-electrode measurements using $Na_3V_2(PO_4)_3$ (NVP) at 50% SOC as the reference electrode in **Fig. 6.4c** reveal that the hard carbon potential rises to 3.67 V vs. Na/Na^+ (approximately 0.96 V vs. standard hydrogen electrode (SHE)) while discharging the NVPF|HC cell to 0 V (**Fig. 6.4c**). Notably, this potential is higher compared to the potential observed for NMC811|graphite cells (3.53 V vs. Li/Li^+, approximately 0.49 V vs. SHE). This observed stability of NVPF|HC cells with repeated 0 V holds, in contrast to Li-ion cells, could

potentially be attributed to the stability of the Al current collector, which remains stable up to 4.5 V vs. Na/Na^+ in PF_6^- based electrolytes (**Fig. 6.1b**).

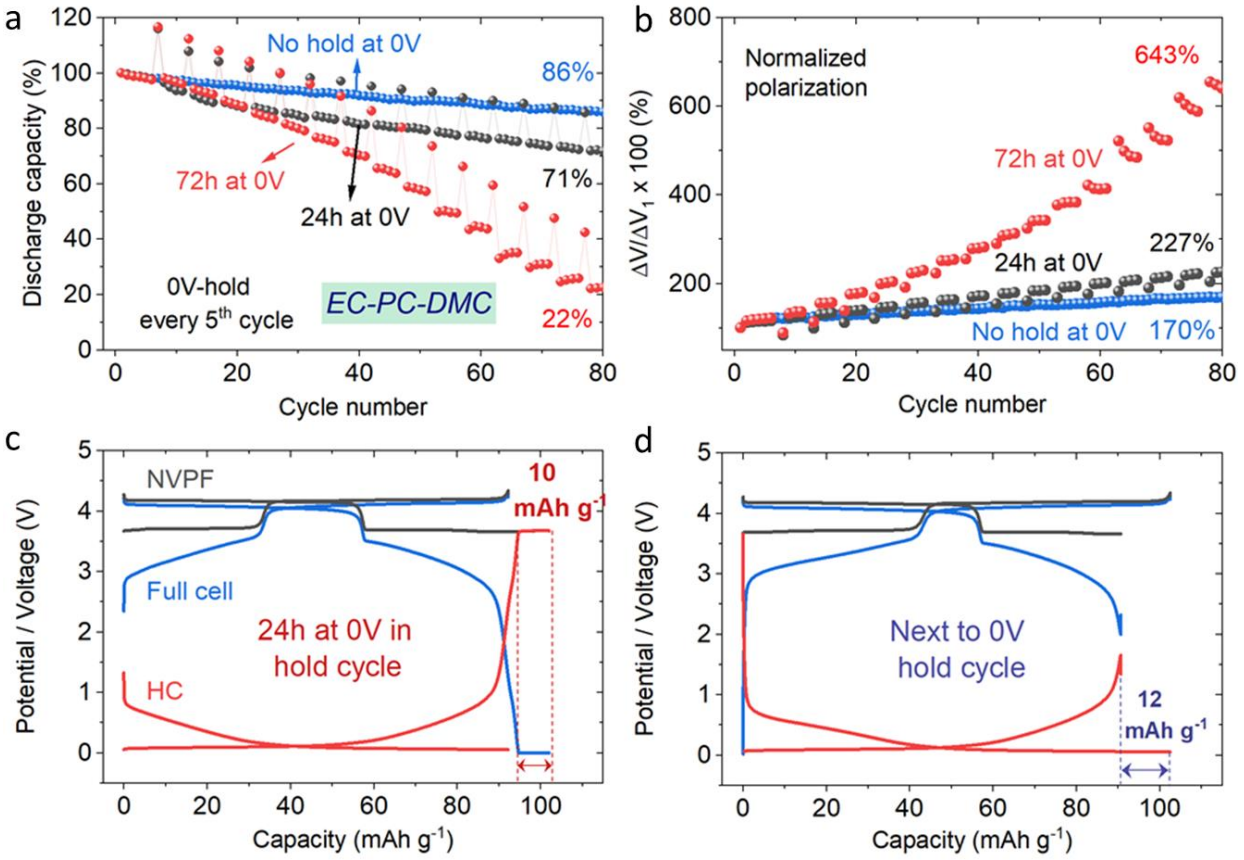

Fig. 6.4 | Stability of NVPF|HC cells at 0V. (a) Capacity retention (%) and (b) normalized polarization as a function of cycle number of NVPF-HC cells using 1M $NaPF_6$ in EC-PC-DMC electrolyte. Cell formation with two cycles was done at 55°C leading to 25% irreversible loss in the first cycle. (c-d) Cycling profile of NVPF-HC Na-ion cells in three electrode set-up using NVP at 50%SOC as reference electrode, (c) during 0V discharge with 24h holding at 0V and (d) on subsequent charge. The actual potentials were calculated vs NVP and converted vs Na/Na^+ using the conversion factor xV vs NVP= (x+ 3.37) V vs Na/Na^+, as NVP reference electrode is used at 3.37 vs Na/Na^+.

In **Fig. 6.4a**, we observe a notable increase in discharge capacity after each 0 V hold for 24 hours or 72 hours. This capacity increase during 0 V holding surpasses what we typically see for 2 V or 1 V holding (**Supplementary Fig. S6.2**). This indicates that the capacity rise during 0 V hold is not solely attributed to Na^+ diffusion kinetics. Surprisingly, holding the cells at -1 V leads to an even higher capacity increase, suggesting more Na-insertion into the NVPF structure (**Supplementary Fig. S6.3**). It's worth mentioning that the maximum capacity increase observed

is equivalent to the first cycle irreversibility of the NVPF|HC cells (the maximum amount of sodium re-inserted into the NVPF structure does not exceed 3). Since there is no extra Na-inventory in a full cell, we expect that the hard carbon is fully de-sodiated at this potential (full cell voltage of ~2 V or less) and the observed gain in capacity (Na^+ to insert into NVPF) must be related to the SEI decomposition. Additionally, our cyclic voltammetry studies (**Supplementary Fig. S6.4**) validate that the formed SEI exhibits poor oxidative stability and begins to oxidize above 2.5 V (vs. Na/Na^+). Upon recharge (**Fig. 6.4d**), the gained 12mAh/g is lost from the HC electrode as the SEI reforms, which is evident from the discharge curve of the HC electrode.

Indeed, the claims regarding SEI decomposition and regrowth, based on the observed extra capacity during 0 V hold and its subsequent loss in the next cycle, should be substantiated with additional experiments. These experiments will be discussed in detail in the subsequent section of our study.

2.2.2 Impedance tracking: Supplementary "SEI decomposition and regrowth"

Impedance spectroscopy was then employed to investigate the dynamics of the SEI during 0 V hold. The NVPF|HC cell with control electrolyte was cycled and impedance spectra were collected before each charge and discharge at 2 V with intermittent 0 V-hold for 24 h (**Fig. 6.5a**) repeating every cycle. Our focus was primarily on analyzing the impedance spectra obtained at 2 V to minimize the impact of charge transfer resistance and solely monitor changes related to the interphase film and contacts resistances (**Supplementary Fig. S6.5**).

To illustrate the dynamics of the SEI during 0 V hold, impedance spectra were recorded before and after each 0 V hold, as well as one cycle after the 0 V hold (**Fig. 6.5b**- Nyquist plot and **Supplementary Fig. S6.6** Bode plot). The semicircle part of the impedance spectra is crucial for tracking the SEI film resistance, which was fitted using the model shown in the inset of **Fig. 6.5b** (left) and represented by dots on the impedance curves. The measured resistances before 0V hold, after 0 V hold, and one cycle after 0 V hold, are defined as (R_B), (R_D), and (R_R), respectively.

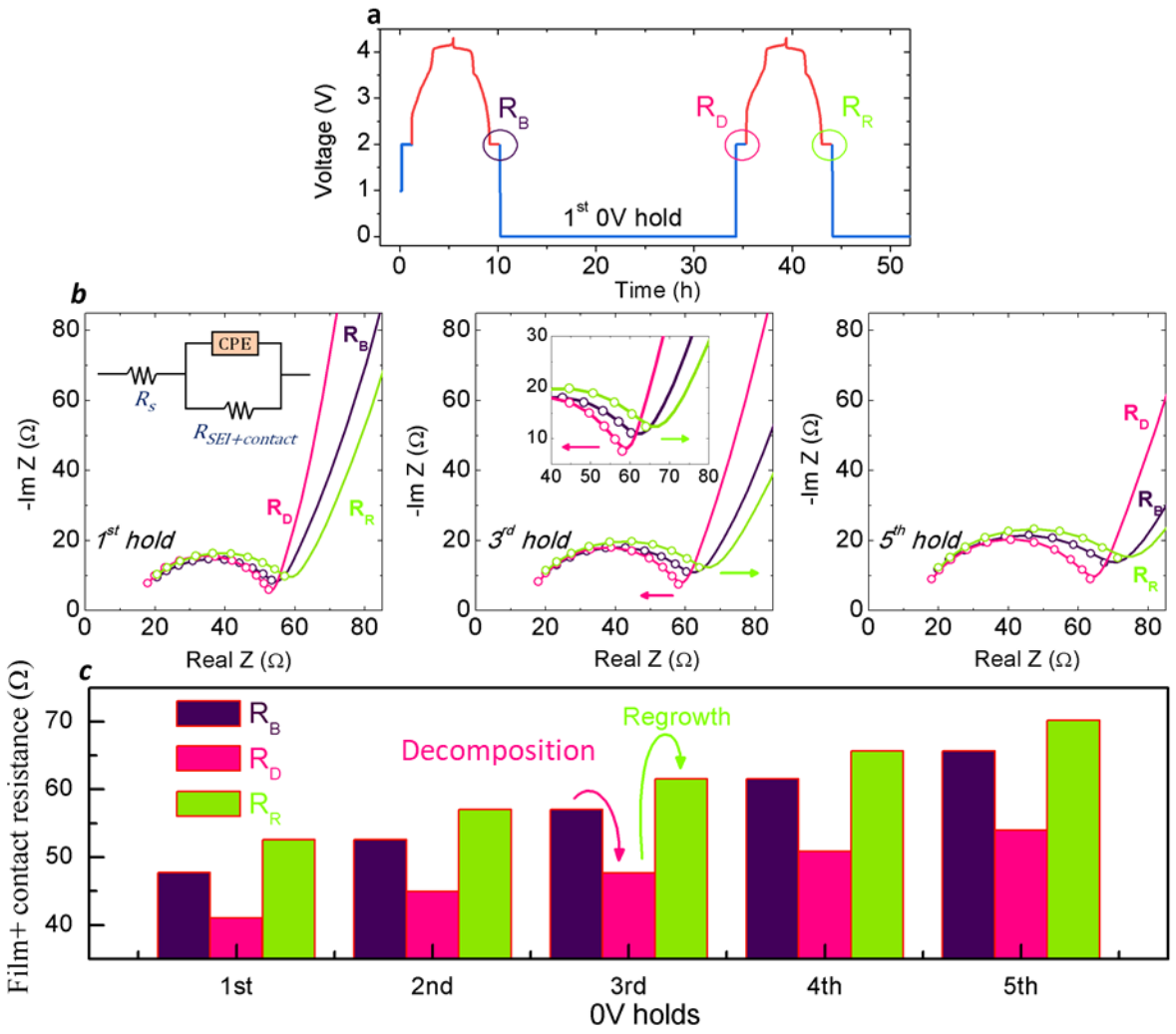

Fig. 6.5 | Impedance evolution in NVPF|HC cell during SEI decomposition and regrowth. (a) The cycling condition followed to study the impedance spectra where the impedance analysis was carried out at 2V before 0V hold (R_B), charge after 0V hold (R_D) and the next cycle (R_R). The spectra in (b) cumulate these impedance spectra after 1(left), 3(middle) and 5(right) holds at 0V for 24h. The equivalent circuit model is represented in inset of left figure in (b). The dots on the semicircle part of the impedance curves are from the fitted data while the solid line represents the experimental data. (c) The impedance value was obtained by fitting the spectra using the equivalent circuit shown in (b). In this regard, note that the R_R for n^{th} cycle becomes the R_B for the $(n+1)^{th}$ cycle and so on. The decrease in impedance during 0V hold is shown as 'dissolution' and the increasing impedance during SEI reformation is mentioned as 'regrowth' in the figure.

The interphase resistances, calculated using the equivalent circuit in **Fig. 6.5b** inset (left), are shown in **Fig. 6.5c** as a function of the number of 0 V hold cycles. During the 0 V holds, there is a decrease in interphase film resistance ($R_D < R_B$), indicating interphase degradation and

dissolution. After the subsequent cycle, the resistance increases ($R_B < R_R$), indicating interphase reformation. This observed trend $R_D < R_B < R_R$ throughout all the holds confirms the interphase dissolution-reformation mechanism, with resistance increasing during the reformation step.

However, this repeated sequence is detrimental to the cell's performance, leading to a significant impedance rise, approximately a 40% increase in resistance between the first and fifth 0 V hold. The analysis of the electrode materials (HC and NVPF) after impedance using XRD and SEM (**Supplementary Fig. S6.7** and **Fig. S6.8**) indicates less modification at the bulk material level. Therefore, the observed degradation mainly arises from interphase instability. Next, we tried to study these interphases using XPS technique.

2.2.3 XPS analysis: Supplementary "SEI decomposition and regrowth"

To investigate the evolution of the interphase during the 0 V hold process separately in the positive and negative electrodes, we conducted X-ray photoelectron spectroscopy (XPS) on the NVPF and HC electrodes. The XPS spectra of the NVPF pristine and cycled electrodes (**Supplementary Fig. S6.9**) at different stages of the 0 V hold process showed no significant changes, indicating the absence of major alterations in the cathode solid electrolyte interphase (CSEI) during the 0 V hold. This can be explained by the fact that the NVPF electrode is maintained at approximately 3.67 V (as shown in **Fig. 6.4c**) during the 0 V hold of the NVPF|HC cell, at which the CSEI is likely stable against oxidation/reduction.

In contrast, XPS analysis of the pristine HC electrode and cycled electrodes at different points indicated in **Fig. 6.6a** revealed substantial variations (**Fig. 6.6ab**). This demonstrates that the observed changes in the interphase during 0 V hold primarily stem from SEI decomposition and reformation. As the SEI is known to consist of organic and inorganic components,[318] XPS helps us to understand the evolution in the composition of the SEI throughout a cycle, shedding light on which components are involved in its decomposition and reformation processes.

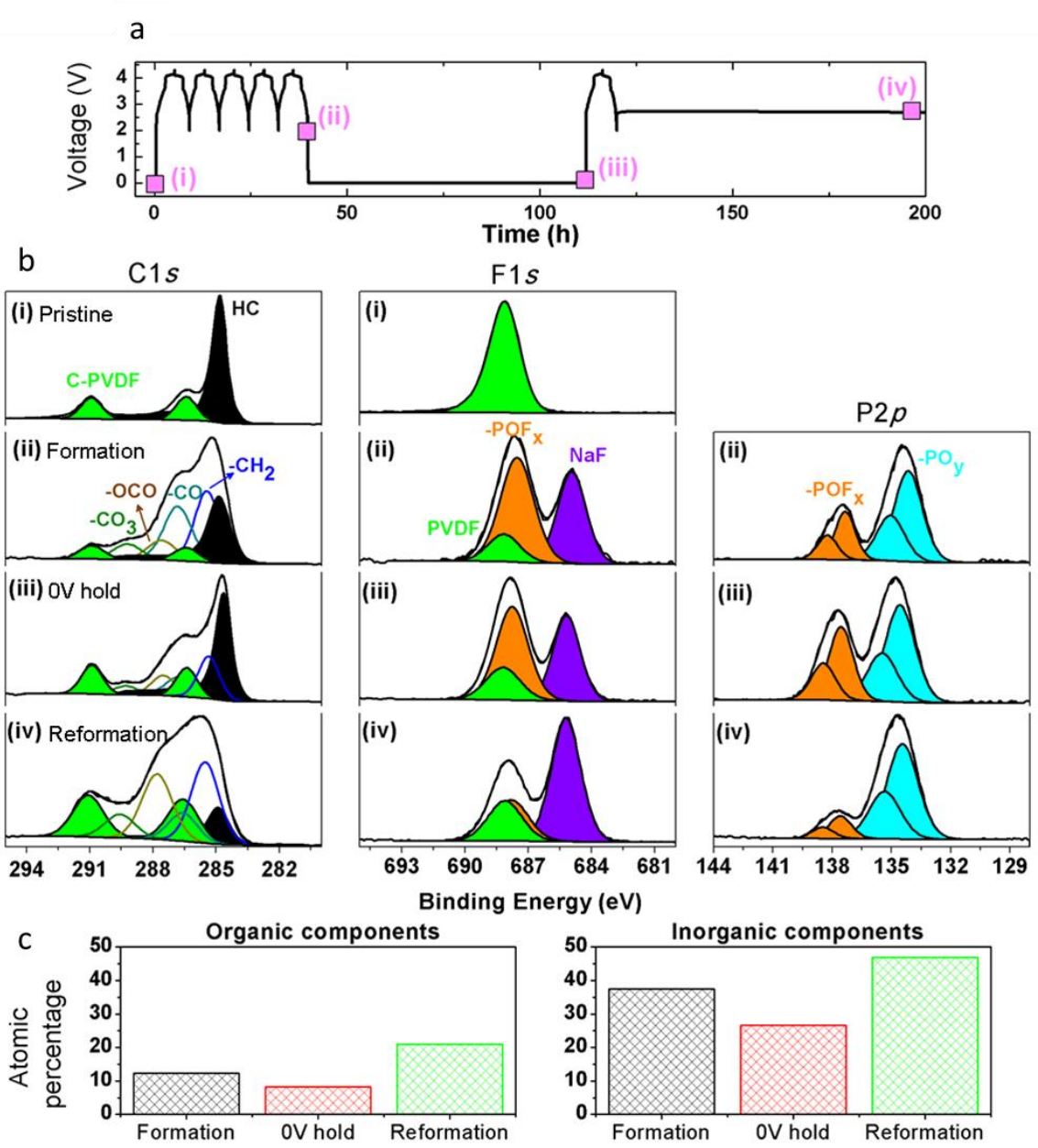

Fig. 6.6 | Interphase evolution in NVPF|HC cell during SEI decomposition and regrowth analyzed by XPS. XPS analyses of the HC electrodes recovered at different states of NVPF-HC cell cycling as per the points mentioned in (a). The C1s, F1s and P2p for all the electrodes are cumulated in (b). There is no P components in the pristine electrode and hence not included in this image. (c) Histogram showing the relative amount of organic and inorganic components of SEI during formation, degradation/dissolution (0V hold) and reformation (one cycle after 0V hold). Noteworthy, the intensity of HC spectrum is less seen whenever there is a SEI growth. Hence, the quantifications of SEI components were done by normalizing C1s peak area of HC as 10 in all the spectra (Table S1).

The XPS spectra of the pristine electrode shown in **Fig. 6.6b(i)** exhibit peaks corresponding to HC and PVDF binder (C and F). After the formation cycle **Fig. 6.6b(ii)**, additional peaks emerge due to C-O, $–CH_2$, and NaF, along with decomposed species of $NaPF_6$ ($-POF_x$ and $-PO_y$). These additional peaks indicate that the SEI is composed of both organic (C1s) and inorganic (F1s and P2p) components. In **Fig. 6.6b(iii)**) and the quantification results in **Fig. 6.6c** (**Supplementary Table S6.1**), it is evident that the SEI undergoes degradation and dissolution during the 0 V hold, affecting both the organic and inorganic components.[80,143] Upon the subsequent cycle (**Fig. 6.6b(iv)**), reformation of the SEI is observed, and **Fig. 6.6c** shows that the intensity of both organic and inorganic components is much higher compared to the initial SEI observed during the formation cycle. This confirms the thickening of the SEI layer during the reformation step.

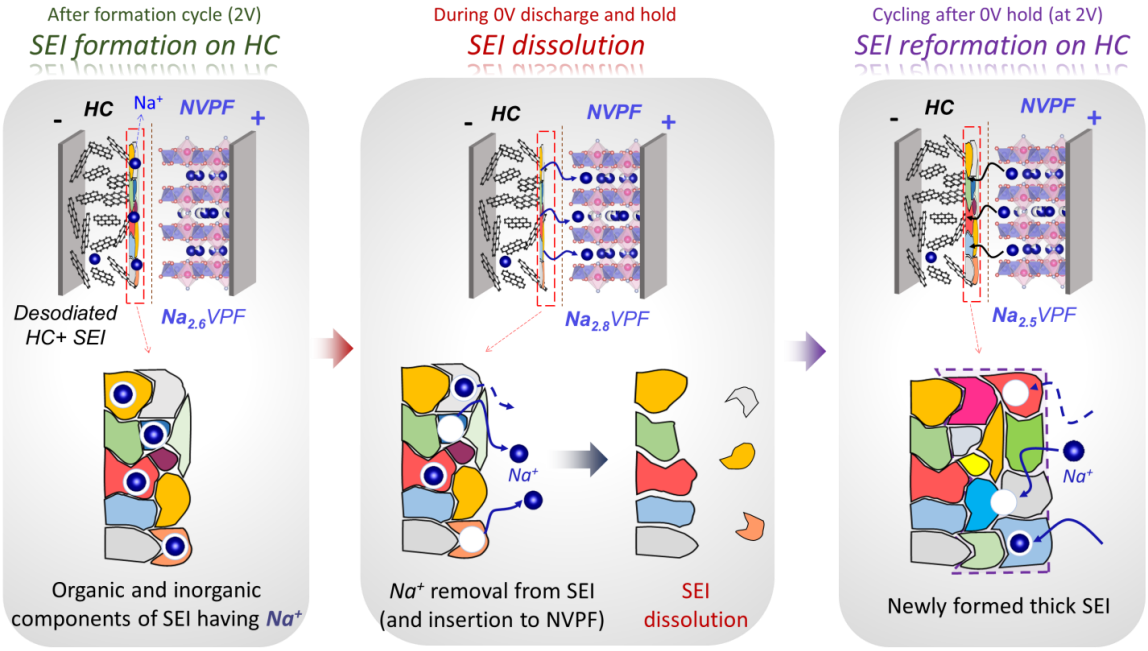

Fig. 6.7 | Schematic showing the SEI formation, decomposition during 0V hold, and reformation on subsequent cycle.

Based on all the observations presented, we propose the reaction scheme for the 0 V hold process, as shown in **Fig. 6.7**. During the 0 V hold, a portion of the SEI oxidizes, decomposes, and dissolves, simultaneously releasing Na^+ ions to insert into the NVPF structure. Upon subsequent charging after the 0 V hold, a portion of Na^+ from NVPF is utilized for SEI reformation, along with

additional electrolyte decomposition. As a result, the reformed SEI becomes thicker, leading to an increase in SEI resistance, which is reflected in larger cell polarization (**Fig. 6.4b**).

2.2.4 Operando optical calorimetry tracking SEI evolutions due to 0V storage

Previous studies, along with literature on calorimetry analyses,[244,252,253] indicate that both SEI formation and decomposition reactions are associated with heat changes. In order to address this, operando optical calorimetry is performed.

In this study, we performed optical calorimetry measurements using tilted fiber Bragg grating (TFBG) sensors inscribed on optical fibers, which were embedded into dry 18650 NVPF|HC cells obtained from TIAMAT. The cells were filled with a 1 M $NaPF_6$ in EC-PC-DMC electrolyte. Detailed information on the integration of TFBG sensors into the cells, along with their calibration, has been reported in our previous works and in **Supplementary methods**. The experiments were conducted at a temperature of 25 °C, employing a C/5 cycling rate in constant current mode. The TFBG sensors were used to monitor the shift in Bragg wavelength ($\Delta\lambda_B$), which was tracked using an optical interrogator. The measured $\Delta\lambda_B$ was then converted to temperature variations (ΔT) with high resolutions (1s and 0.1 °C, respectively). The obtained ΔT values were used to calculate the heat rate ($\dot{Q} = dQ_{heat}/dt$) and heat derivative (dQ_{heat}/dV) using a simplified 0D thermal model.[244] These thermal parameters provide valuable information on the heat generation and dissipation processes occurring within the NVPF|HC cells during the 0 V holding and cycling phases.

The capacity retention plot (**Supplementary Fig. S6.10**) confirms that the observed increase in capacity during 0 V hold, followed by deterioration in cycling performances, is reproducible in the cylindrical 18650 cells, similar to what was observed in the coin cells (**Fig. 6.4**). Moving on to the thermal analysis, the heat values derived from the TFBGs are shown in **Fig. 6.8a**, alongside the cell potential evolutions as a function of time. During SEI formation (first cycle charge) and each 0 V hold, an increase in heat is observed (**Fig. 6.8a**), indicating that both SEI (re)formation and decomposition are exothermic processes.

The exothermic heat observed during the first charge, associated with interfacial reactions decreases sharply after the formation of a stable SEI (charge 3 in **Fig. 6.8b**). When discharging to 0 V (**Fig. 6.8c**), a significant increase in heat is again observed, reaching its maximum when the cell reaches 0 V, and then it slowly decreases. Notably, the heat release never becomes zero during the entire 24-hour holding period at 0 V, suggesting continuous parasitic reactions during this time. Interestingly, for the charge after 0V, exothermic reactions of even greater intensities than during the formation cycle are observed (**Fig. 6.8d**). This larger heat release indicates that the reactions involved in the SEI reformation and/or electrolyte oxidation in the charge after 0 V holding likely differ from those during the initial formation cycle. This recurring interphase reformation leads to active Na-inventory loss, which is repeated after each 0 V hold (**Supplementary Fig. S6.11**). Consequently, this explains the rapid capacity decay observed throughout this cycling sequences.

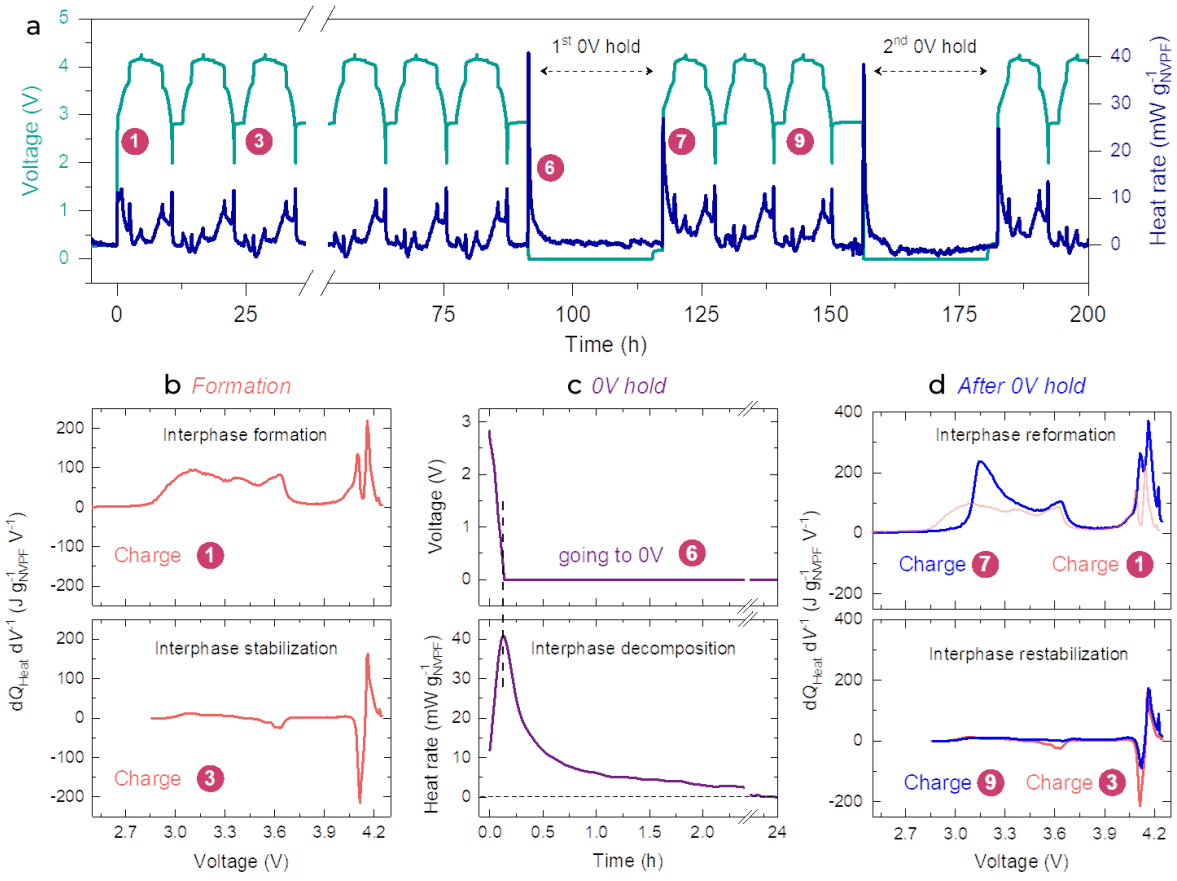

Fig. 6.8 | Optical sensing calorimetry for 18650 type NVPF|HC cell to track heat evolutions during 0V. (a) Heat evolutions for cylindrical 18650 NVPF-HC cells during formation cycle and 0V hold, subsequent cycles measured by

TFBGs, and the time where break appears in the graph were used for thermal calibration. The heat derivative from charges 1, 3, 6, 7, and 9 (marked in (a)) is shown in (b) formation cycles (c) during 0V hold and (d) SEI recreation after 0V hold.

In summary, despite the Al current collector being stable during 0 V discharge of Na-ion cells, the comprehensive studies conducted indicate that the SEI forming on hard carbon is not very stable at such high oxidation potentials (3.67 V in the case of NVPF|HC cells). Given this stability issue with the SEI, there is a clear need to explore and implement strategies to overcome it.

2.3 Cell chemistry optimization to improve 0V stability of Na-ion cells

At this juncture, it becomes crucial to explore the possibility of improving the 0V stability of Na-ion cells. As established in the literature, the stability of the SEI is closely linked to the formulation of the electrolyte, as the SEI is formed through the reduction of salts, solvents, and additives present in the electrolyte. Therefore, our primary approach is to focus on optimizing the electrolyte formulation to enhance the 0V storage capability of Na-ion cells.

2.3.1 Manipulating electrolyte formulation

The effect of changing the electrolyte solvent from EC-PC-DMC to various linear and cyclic carbonate combinations, as well as individual solvents, was thoroughly investigated in terms of 0V stability. Electrolytes with only linear carbonates are not chosen because of its known instability from the work of Guochun et. al.[146] The capacity retention plots for the studied electrolyte are presented in **Supplementary Fig. S6.12**, and the percentage capacity retention after 80 cycles (15 times of 0V hold for 24h intervals) is compared in **Fig. 6.9a**. Among the different electrolyte formulations studied, the PC electrolyte exhibited the best capacity retention (84% after 80 cycles). It also showed a minor increase in polarization (**Fig. 6.9b**) even when holding at 0V for 72 hours each time. On the other hand, the least stability was observed with DMC-based electrolytes (71% after 80 cycles).

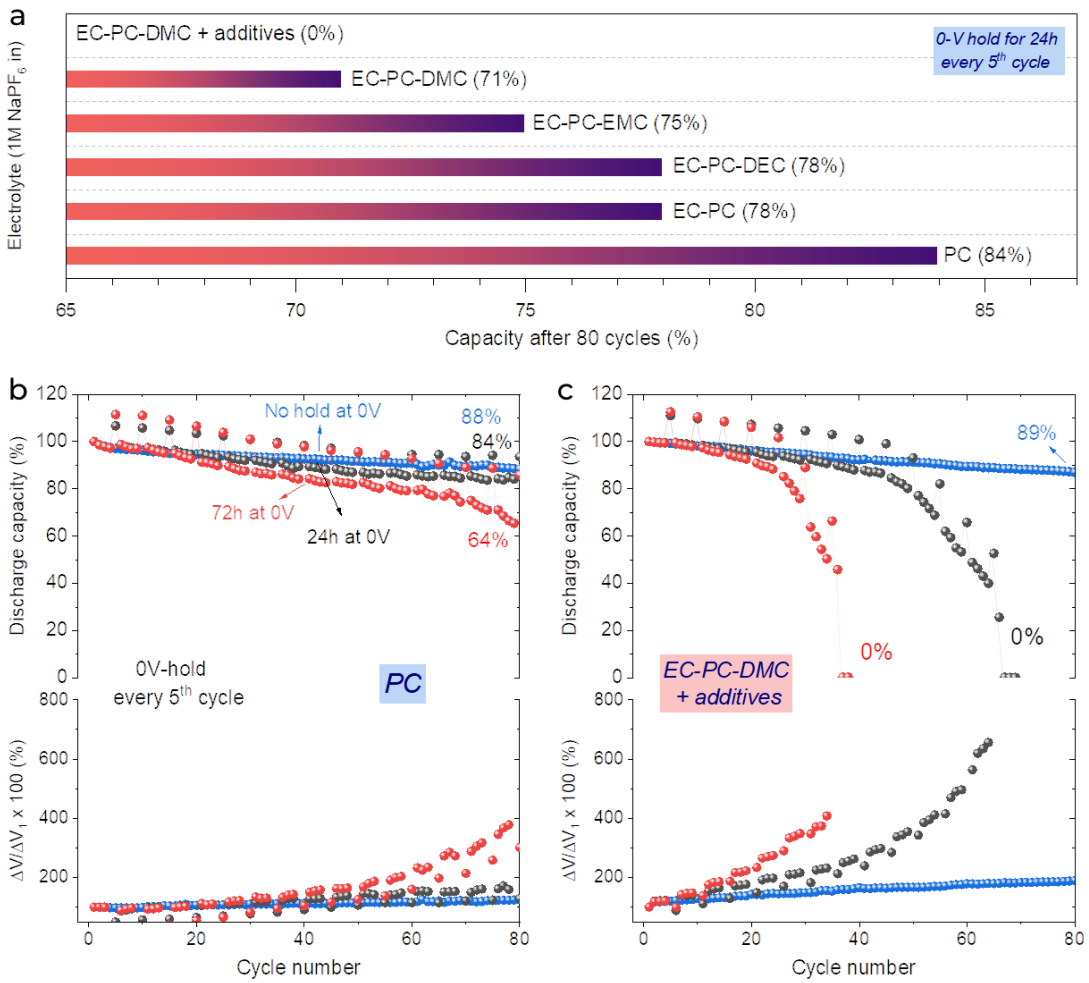

Fig. 6.9 | Stability of NVPF|HC cells at 0V with different solvent combinations. (a) Comparison of capacity retained in NVPF-HC cells using different electrolyte formulations, after 80 cycles. The cells were hold at 0V for 24h after each 5 cycles between 2- 4.25 V. The capacity retention plots are shown in **Supplementary Fig. S6.12**. (b and c) Capacity retention (top) and polarization changes (bottom) of the NVPF-HC cell containing (b) PC based electrolyte and (c) electrolyte having 4 additives.

As discussed in the previous section, the stability of cells under intermittent 0V storage is influenced by SEI decomposition, SEI reformation reactions, and subsequent cross talk interactions between both electrodes during the reoccurring 0V storages. Previous studies by our group[146] have indicated that the cross talk species formed after reduction of electrolyte at HC, in the presence of EC/PC (sodium ethyle dicarbonate, sodium carbonate etc.), are more stable than the DMC/EMC ones (sodium alkoxide and sodium alkyl carbonate). This is due to more soluble nature of sodium alkoxides and consequently parasitic oxidative tendency on NVPF. This

observation helps explain the superior stability of PC electrolyte. Despite its usefulness, PC alone cannot serve as an electrolyte solvent for batteries due to its high viscosity, impeding ion transport within the cell, and its inability to wet the commercial celgard separator, limiting its practical applicability.

In a subsequent trial, we used an electrolyte formulation composed of 1 M $NaPF_6$ in EC-PC-DMC with the addition of Gen-3 additives: 3 wt% succinonitrile (SN), 3wt% vinylene carbonate (VC), 0.5wt% sodium oxalatodifluoroborate (NaODFB), and 0.5 wt% tri-methylsilylphosphite (TMSPi). This electrolyte formulation had previously shown good calendar/cycle life at ambient and high temperatures as discussed in Chapter 4. Initially, an increase in cell capacity was observed upon 0 V holding, with similar capacity retention to cell with uninterrupted cycling in the early stages of 0 V holding for 24 h or 72 h (**Fig. 6.9c**). However, to our surprise, the cell deteriorated rapidly after a few cycles of 0 V holding, accompanied by a significant increase in impedance (**Fig. 6.9c**), ultimately leading to rollover failure of the cell.

Upon analyzing the 0 V degradation mechanism, it became evident that reoccurring reduction of additives and their by-products during repetitive 0 V storages significantly increased the cell's impedance, leading to the formation of a thick interphase and Na plating (**Supplementary Fig. S13**). The occurrence of Na plating was also observed in 18650 cells (**Supplementary Fig. S14**), indicating that this phenomenon is primarily triggered by the impedance increase resulting from 0 V storage. This outcome serves as a crucial reminder of the complexities involved in designing electrolytes that can deliver both high-temperature performance and 0 V stability. A more in-depth characterization of the SEI decomposition products during 0 V holding, combined with multiple experimental screenings and trials, is still necessary to design an optimized multi-purpose electrolyte additives for NVPF|HC Na-ion cells.

2.3.2 Manipulating positive electrode material

Another promising alternative to improve the 0 V stability is to control the shoot-up potential of HC when the full cell goes to 0V, as it directly influences the stability of the SEI. Previous research from our group has demonstrated that the 3rd Na in NVPF can be electrochemically activated,[319] resulting in a disordered structure with a relatively flat profile and

a low voltage plateau at around 1 V (**Fig. 6.10a**). This offers a solution to limit the HC potential shoot-up to approximately 1 V. This hypothesis has been experimentally verified, as NVPF|HC cells with activated 3rd Na displayed excellent capacity retention of 81% (compared to 71% retention with 2 Na removal) after 8 cycles with 24 hours of 0 V-hold every 5th cycle in EC-PC-DMC based electrolyte. This successful demonstration underscores the potential of this approach to improve the 0 V stability of Na-ion cells.

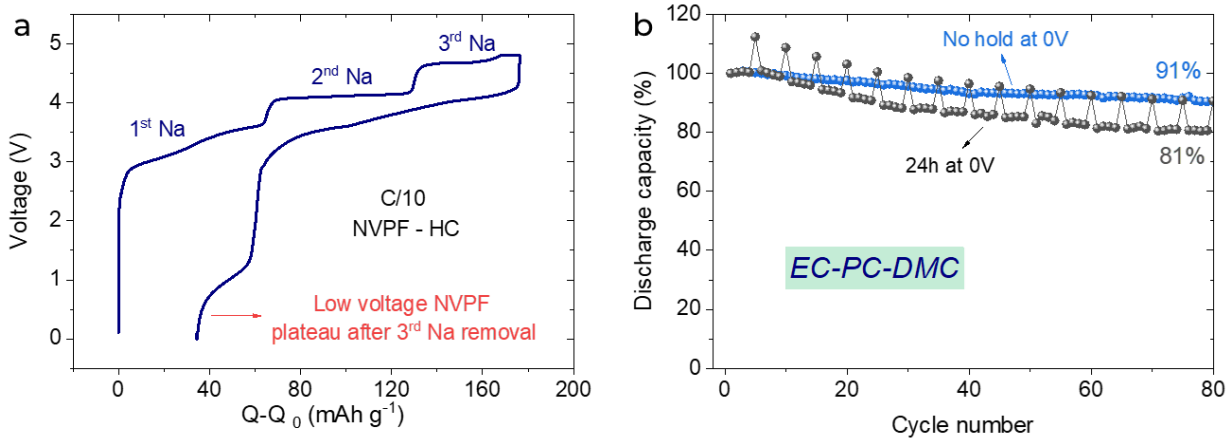

Fig. 6.10 | Activating 3rd Na from NVPF to improve 0V stability. (a) Cycling profile of NVPF- HC cells where the third soium from NVPF is extracted by oxidizing to high potentials of ~4.8 V. The removal of third sodium leads to structural changes in NVPF hence changing the cycling profile in the following discharge where a low voltage redox (~1V) is observed. (b) Capacity retention plots of NVPF-HC cells cycled using 3 Na, without any 0V hold/ interruptions and with 0V hold for 24h every 5cycles.

In a second approach, we explored the replacement of the NVPF positive electrode with a sodium layered oxide, specifically $NaNi_{0.45}Zn_{0.05}Mn_{0.35}Ti_{0.15}O_2$ (ZNMT).[320] ZNMT exhibits a lower voltage redox behavior compared to NVPF. On the other hand, the Prussian blue analogs, another family of positive electrodes, show biphasic cycling behavior with potential at the end of discharge close to ~3.4 V, similar to NVPF. However, ZNMT offers a distinct advantage with a larger voltage window ranging from 2.2-4.5 V, featuring different plateau and sloppy regions in cycling (**Supplementary Fig. S6.15**). In three-electrode cells using NVP with 50% SOC as a reference, we observed that the HC potential is raised only to 2.7 V (vs. Na/Na^+) when pushing the ZNMT|HC full cell to 0 V (**Fig. 6.11b**). Thus by coupling ZNMT with PC based electrolyte we

assembled ZNMT|HC cells(**Fig. 6.11b** and **6.11c**), showing excellent capacity retention (81% and 75% for 0 V-holds of 24 h and 72 h, respectively vs. 87% retention for no 0 V hold).

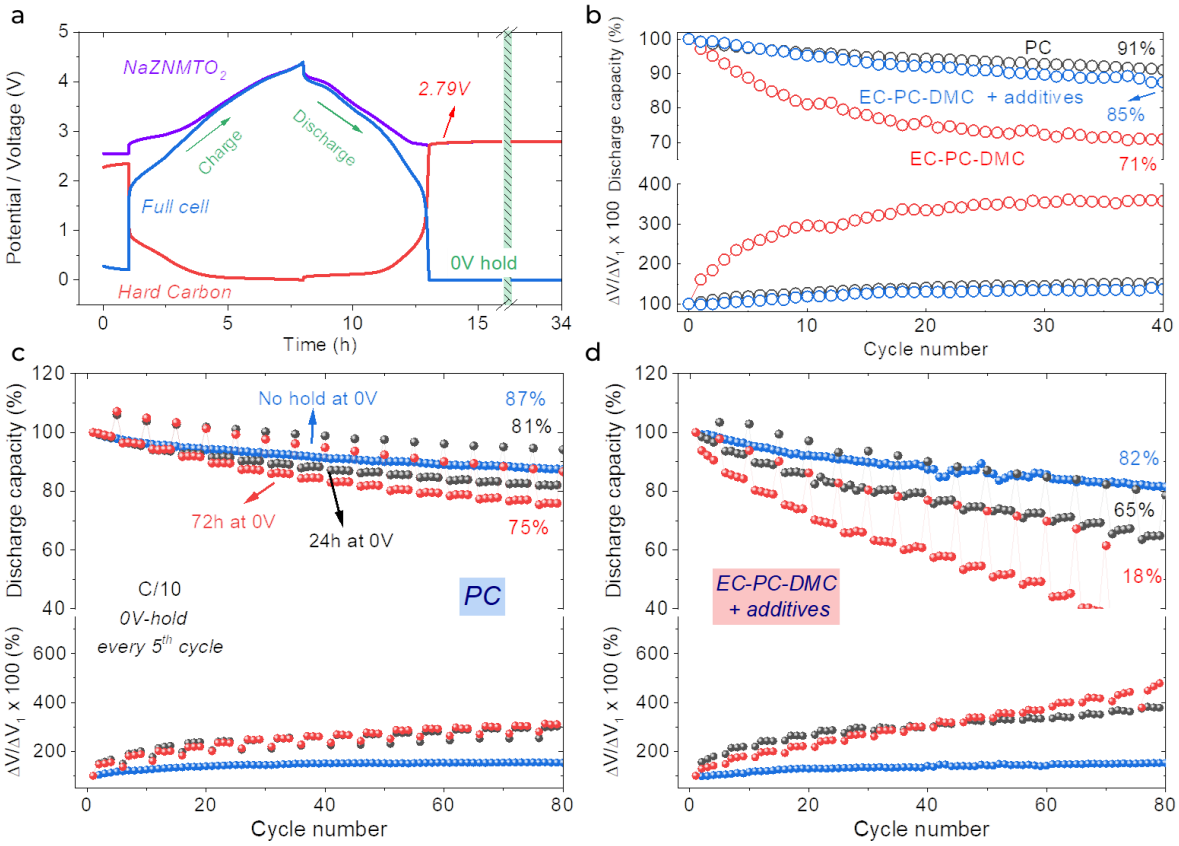

Fig. 6.11 | Layered oxide ZNMT and its 0V stability in a ZNMT|HC full cell. (a) Cycling profile of ZNMT-HC cell in three electrode set up where NVP s used as the reference electrode. (b) Capacity retention plot of ZNMT- HC coin cells using different electrolytes. Comparative capacity retention plots of ZNMT- HC coin cells using (c) 1M $NaPF_6$ in PC and (d) 1M $NaPF_6$ in EC-PC-DMC with additives as electrolytes respectively. In both cases, the cycling is compared with and without 0V hold.

The cycling stability of ZNMT|HC cells utilizing an electrolyte with linear carbonate exhibits suboptimal performance even in the absence of a 0 V hold. Nevertheless, this issue can be ameliorated by incorporating specific additives in the electrolyte, as indicated in **Fig. 6.11b**. In particular, when employing the electrolyte formulation featuring Gen-3 additives (SN, VC, NaODFB, and TMSPi) utilized in the NVPF study, the ZNMT|HC cells maintain 65% and 18% of their capacity after 80 cycles with 24 hours or 72 hours of 0 V-hold every 5th cycle, respectively. Conversely, under the same electrolyte conditions, the NVPF|HC cells suffer complete capacity

loss due to plating. The enhanced stability of ZNMT|HC cells with Gen-3 additives (as compared to NVPF|HC cells with Gen-3 additives) can be attributed to the lower propensity for HC shoot-up and consequent decrease in parasitic side reactions. In summary, sodium layered oxides demonstrating low voltage redox behavior that helps to exhibit superior 0 V stability when coupled with an appropriate electrolyte. However, this advantageous performance of layered oxides is accompanied by the drawback of positive electrodes being sensitive to moisture, and ZNMT|HC Na-ion cells exhibiting limited cycle life and power rate capability compared to NVPF|HC Na-ion cells.

3. Conclusions of the Chapter

We reported the 0 V stability of sodium ion systems with different positive electrodes or electrolytes summarized in **Fig. 6.12**. The best performances were observed when using either sodium layered oxides (with PC electrolyte) or NVPF (with PC electrolyte) or when activating the 3rd Na from NVPF with EC-PC-DMC based electrolyte, the latter showing the most attractive system performances in a practical sense. However, the presence of linear carbonate (DMC) in the electrolyte could hinder high-temperature performances, necessitating the use of suitable electrolyte additives to stabilize the SEI and CEI and improve practicality.

1M $NaPF_6$ in	*ZNMT - HC*	*NVPF - HC*	*3rd Na in NVPF - HC*
PC	😀	😀	-
EC-PC-DMC	😐	🙂	😀
EC-PC-DMC + additives	😐	☹	-

😀 Very good (>80%), 🙂 Good (>70%), 😐 Poor (>60%) ☹ Very bad(<60%)

Fig. 6.12 | Key parameters comparison for stable 0V cells. Comparison chart cumulating the various Na-ion systems (NVPF- HC and ZNMT- HC) studied using different electrolyte formulations. The mentioned percentage values refer to the retention after 80 cycles for 24h 0V-hold every 5 cycles protocol.

The final Chapter of the thesis delves into a unique type of SEI deterioration, specifically SEI oxidation. During the NVPF|HC full cell's transition to 0V, the HC potential rapidly increases to high values, around 3.6V, causing the SEI to decompose. However, it reforms during the subsequent charge of the full cell leading to Na-inventory loss, SEI thickening and impedance build-up. Enhancing the oxidative stability of the SEI poses a fresh challenge to investigate in the NIB system. Therefore, exploring additives, salts, or solvents that can form an oxidatively stable SEI becomes essential for optimizing the NVPF|HC system. This new approach opens up opportunities to optimize the electrolyte for 0V stability without compromising high/low-temperature stability. Another potential method to mitigate the issue of HC potential shoot-up is to opt for a positive electrode with a lower discharge voltage, such as ZNMT. However, this choice comes at the expense of energy density due to its reduced discharge voltage. In conclusion, the discussed results and strategies pave the way for further exploration in this field.

General conclusions and perspectives

○ General conclusion

Throughout this Ph.D. investigation, we've gained a deep understanding of how NVPF|HC cells degrade and proposed practical solutions by adjusting the electrolyte to form better interphases and engineering NVPF electrodes via uniform carbon coating. We tested these solutions in lab-scale cells and successfully applied them to commercial 18650-type cells. These solutions offer a good balance between cell lifespan, self-discharge, performance at different temperatures, fast charging, and safety.

First, we searched the reason for the high-temperature instabilities in the NVPF|HC cells. We identified through key experiments that the synergistic interaction of electrolyte and NVPF at high potentials leads to parasitic electrolyte oxidation and V dissolution, which is highly deleterious for cell health. Firstly, V dissolves from NVPF, leading to capacity decay caused by the electrochemically dead weight of phases associated with the loss of V. Secondly, owing to the notably reactive redox characteristics of V, it was observed that the dissolved V in the electrolyte experiences reciprocal redox-shuttle interactions on NVPF and HC. This phenomenon leads to capacity deterioration, self-discharge, and potential gas formation. Thirdly, V migrates to HC and poisons the interphase/electrode. This V poisoning of HC is the cause of destabilized SEI and causes capacity fade, which is a more critical reason than the prior two reasons. Curing strategies to mitigate V dissolution from NVPF involved the incorporation of NaTFSI or NaFSI co-salts in the electrolyte and homogeneous carbon coating of NVPF particles. Despite these remedies, while safeguarding the NVPF electrode against decay, complete prevention of electrolyte decompositions at elevated temperatures remains unattainable. As a next step, electrolyte additives are incorporated into the cell chemistry to suppress these decompositions.

At this stage, through an effective screening of additives, we designed a Gen-3 electrolyte (1M $NaPF_6$ in EC: PC: DMC in 1:1:1 vol% and NaODFB+VC+SN+TMSPi additives) which suppressed the parasitic electrolyte interactions. Utilizing optical sensing calorimetry, we observed a reduction in heat release due to solvent reduction upon the incorporation of these additives. When applied to the NVPF|HC cell, the Gen-3 electrolyte exhibited notable benefits, including enhanced capacity retention, minimal self-discharge, reduced cell polarization, diminished NVPF

mass loss, and limited HC slippage in comparison to the control electrolyte (1M $NaPF_6$ in EC: PC: DMC in 1:1:1 vol%). This efficacy of Gen-3 additive combination was rationalized with the assessment of NVPF and HC symmetric cells. NaODFB+VC is sufficient in building good SEI, suppressing further electrolyte reduction, yet it displayed limitations in preventing electrolyte oxidation on NVPF. Adding SN to NaODFB+VC effectively stops electrolyte oxidation. Furthermore, it was confirmed with operando pressure sensing using optical fibers that SN suppresses electrolyte oxidation, thus effectively suppressing electrolyte gassing at 55°C in 18650 cells. Moreover, it was found that Gen-3 electrolyte additives suppress V dissolution, thanks to oxidative stability imparted by SN and acid scavenging behavior of TMSPi.

Here, the practical implications of the Gen-3 electrolyte are assessed. Gen-1 (by Guochun et al.)[122] and Gen-2 (by Cometto et al.)[123] electrolytes previously proposed by our group, demonstrated promising performance in coin cells. However, these solutions could not be seamlessly transitioned to practical 18650 cells due to inherent challenges. Gen-1 faced limitations arising from its low wettability, while Gen-2 encountered significant gassing concerns when subjected to a temperature of 55°C. On a practical note, the significance of the Gen-3 electrolyte lies in its adaptability to 18650 cells, functioning effectively within a temperature range spanning from 10°C to 55°C. Nonetheless, it's important to acknowledge that the Gen-3 electrolyte experiences elevated charge transfer resistance due to the interphase established by the incorporated additives, especially at low temperatures. This resistance can limit low temperature and extremely high power applications.

As the next step, methyl acetate(MA), a low-viscosity cosolvent, is introduced to ameliorate the interphase resistance. The incorporation of MA lowers the solvent blend's viscosity, enhancing ionic conductivity. Up to 20% MA was introduced in the solvent blend without having a significant penalty at elevated temperatures while excelling in low-temp and fast-charging (84% charge in under 10 mins) performance. All this thanks to a decrease in the charge transfer resistance due to facile Na transfer within the electrode pores close to the particle surface. Adding MA addresses Gen-3 electrolyte limitations, offering an appealing choice for practical 18650 cells.

After studying the degradation modes and designing the electrolyte to improve cell lifetime and performance for NVPF|HC cells, the last part of the thesis deals with a very specific application: 0 V storage. It was observed that during the 0 V storage (or over-discharge), the HC potential shoots up to match the NVPF potential (~3.6V). Surprisingly, it was found that the SEI on the hard carbon is not stable at such high potential and decomposes by giving extra Na to NVPF (thus, excess capacity is achieved during the storage periods). In the charging cycle after the 0V storage period, the extra Na inventory acquired through NVPF and some additional Na inventory is subsequently utilized to regenerate a portion of the SEI. This SEI decomposition and reformation decreases the active Na-inventory (leads to capacity loss) and increases cell resistance. It was shown that 0V stability could be improved by engineering the electrolyte (with cyclic carbonate solvents like PC and EC-PC) or circumventing hard carbon shoot-up (activating 3rd Na in NVPF or changing the positive electrode to layered oxide). Overall, this study opens up the design space to engineer additives that can improve the oxidative stability of SEI.

In summary, our study shows that it is possible to identify the key factors contributing to cell degradation, optimizing electrolytes at the laboratory level, and seamlessly transitioning them to the commercial realm. A noteworthy accomplishment involves the application of our lab-designed Gen-3 electrolyte in Tiamat's 18650 NVPF|HC cells, which find utility in commercial high-power applications either in single-cell format or 48V battery pack.[74,75]

○ Perspective and Future Directions

Although our work has led to significant advances in the performances of Na-ion NVPF/C cells, there is still room for improvement to approach perfection. This section examines persistent challenges and outlines overarching pathways to be pursued at the component and cell levels.

The electrolyte, a critical determinant of interphase, influences the cell's lifetime and performance. Poor SEI stability at the negative electrode and excessive electrolyte oxidation on the positive electrode pose an added challenge in NIBs compared to classic LIB chemistries (LFP and NMC). Thus, as many as four additives were needed in NVPF|HC system as studied in this thesis (NaODFB+VS+SN+TMSPi) as compared to typical two additives combination (VC+DTD,

FEC+$LiPO_2F_2$, etc. in NMC|graphite cells) in LIBs. Addressing these intricacies necessitates a comprehensive combinatorial analysis of additives, spanning single, binary, and tertiary combinations, including vital additives like VC, DTD, SN, NaODFB, FEC, PES, $LiPO_2F_2$, $NaPO_2F_2$, NaBOB, TTSPi, TMSPi, MMDS, ethylene sulfate, etc.[245,246] Moreover, exploring novel organic and inorganic compounds for additives capable of forming stable interphases at high temperatures and exhibiting low impedance in colder conditions is crucial. This endeavor holds promise for reducing the number and concentration of additives in commercial-scale cells, but, unfortunately, this approach can only occur through trial and error despite the promise of robotics of AI to rapidly advance the discovery of new electrolytes.

Additionally, co-salts such as NaFSI, NaTFSI, NaFTFSI, etc.,[321,322] and low-viscosity co-solvents like methyl formate, n-propyl formate, propionitrile, and i-butyronitrile,[235] recognized for their ability to decrease charge transfer resistance and enhance electrolyte conductivity, should be integrated into the electrolyte in conjunction with the additives. Beyond their role in curbing transition metal dissolution, the imide-based salts also serve as acid scavengers, as recently claimed by Armand et al.,[323] thereby shielding interphases from acid attack due to HF generated through the hydrolysis of $NaPF_6$. The introduction of a significant proportion (10-40%) of co-salt can effectively inhibit $NaPF_6$ hydrolysis, thus preserving cell chemistry, decreasing cell resistance, enabling fast charging, and extending cell lifespan.

Numerous considerations exist for electrode-side development. In the context of well-established hard carbon, its porous nature can lead to pore clogging during SEI formation/growth and the irreversible entrapment of sodium within these pores, both contributing to capacity loss. Here, the enhancement of long-term stability through hard carbon engineering becomes a focal point. It's worth noting the significance of such factors; for instance, the prolonged cell lifespan demonstrated in the million-mile NMC|graphite cells by Dahn et al. was achieved via meticulous engineering of the graphite negative electrode.[324–326] Moreover, to augment cell stability, the application of protective coatings (such as Al_2O_3, AlF_3, etc.) onto active material particles emerges as a valuable strategy. This approach can mitigate electrolyte attacks on electrodes, thereby curtailing transition metal dissolution, safeguarding hard carbon electrode, mitigating SEI expansion, and averting pore clogging. However, the decomposition of the parasitic electrolyte

also depends on the nature of the positive and negative electrodes acting as catalysts, so the field will gain enormously from examining interfaces from the electrocatalyst's point of view. Two recent papers on Li-S batteries illustrate the benefits of such an approach.[327–329]

From a practical standpoint, elevating cell energy density necessitates the adoption of thick electrodes with substantial mass loading (approximately 25 mg/cm^2 for the positive electrode and around 15 mg/cm^2 for the negative electrode in energy-dense commercial LIBs).[66] However, The utilization of hard carbon as a negative electrode poses a bottleneck for achieving thick coatings. Firstly, due to its low material density (about 1.6 g/cm^3), achieving thick coatings proves arduous, impeding effective porosity reduction in electrodes.[184,330] Moreover, even if efforts were made to decrease porosity in hard carbon electrodes, it would lead to capacity loss as a considerable fraction of Na^+ ions are housed within their pores. One of the reports by Rudola et al. shows HC capacity reduction from 340 mAh/g to 290 mAh/g when mass loading increased from 5.9 mg/cm^2 to 8.8 mg/cm^2 while maintaining similar porosity values.[331] Consequently, a pivotal stride toward enhancing practical energy density in NIBs involves transitioning to pure or composite-based alloying-type negative electrodes (e.g., P, Sb, Sn) with higher capacity as well as material density.

On the other hand, utilizing high capacity and voltage of positive electrode is necessary for pushing energy density to its limit. One avenue involves unlocking the potential of the third sodium in NVPF, which can uplift the energy density[319] of NVPF|HC cells by 14%. However, attaining this requires developing a proficient electrolyte design to accommodate elevated potentials. Simultaneously, stabilizing the high capacity inherent in O3-type layered oxides is imperative and can be bolstered through adept doping, coating, and microstructural engineering techniques. Looking further ahead, envisaging these positive electrodes alongside with alloy-based (pure or composite) negative electrodes marks a strategic advancement. This transformative shift promises to enhance energy density significantly, outpacing even LFP-based LIBs. Pushing the boundaries of energy density can be further achieved by transitioning from liquid electrolytes to solid electrolytes, ultimately into the realm of solid-state batteries. Realizing these prospects could elevate the sodium-ion battery to an indispensable technology in our daily lives.

In summation, this thesis underscores the intricate nature of cell degradation and presents effective measures to mitigate these challenges while maintaining optimal cell performance. The strategies elucidated herein are poised to propel the advancement of NIBs, aligning their development with that of LFP-based LIBs. These insights illuminate a promising path forward for the evolution of next-generation energy storage technologies. As we close this thesis, let us remember that every discovery, every solution, and every hurdle overcome brings us closer to unlocking the boundless potential of the Na-ion technology.

Appendix

S-1 Supplementary Information for Chapter 1

○ Supplementary Figures

Supplementary Fig. S1.1

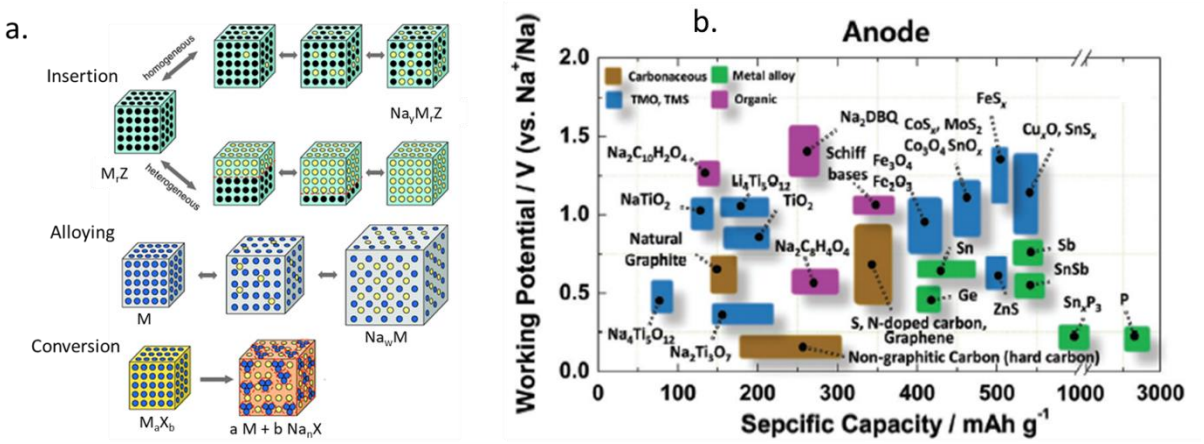

(a) A schematic representation of the different reaction mechanisms observed in electrode materials for lithium batteries. Black circles: voids in the crystal structure, blue circles: metal, yellow circles: sodium. Adopted and modified from reference with permission. (b) Research progress of anode materials for NIBs. Reproduced from the references.[55,332]

Supplementary Fig. S1.2

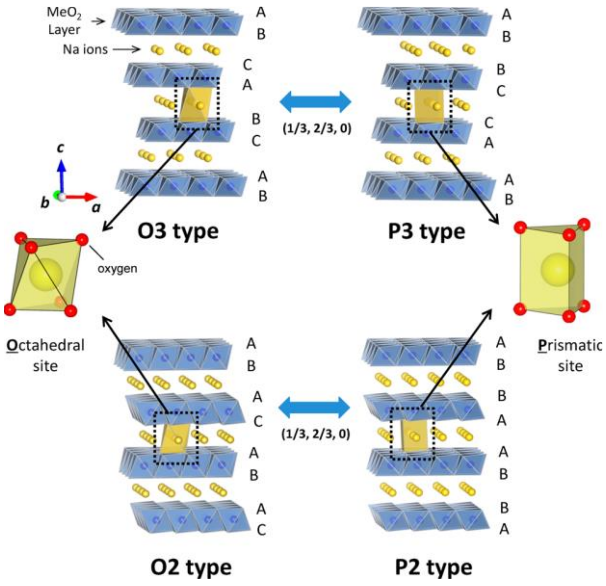

Classification of Na based transition metal oxides based on the Na environment and O stacking. Reproduced from the reference.[54]

Supplementary Fig. S1.3

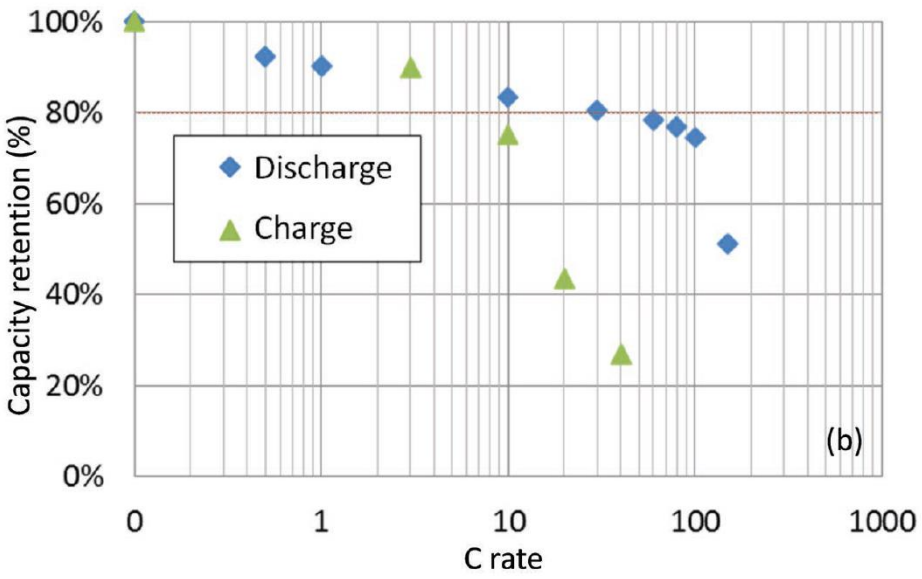

Performance obtained in 18650 NVPF|HC cells: rate capabilities for 55 Wh kg^{-1} prototypes. Reproduced from the reference.[108]

Supplementary Fig. S1.4

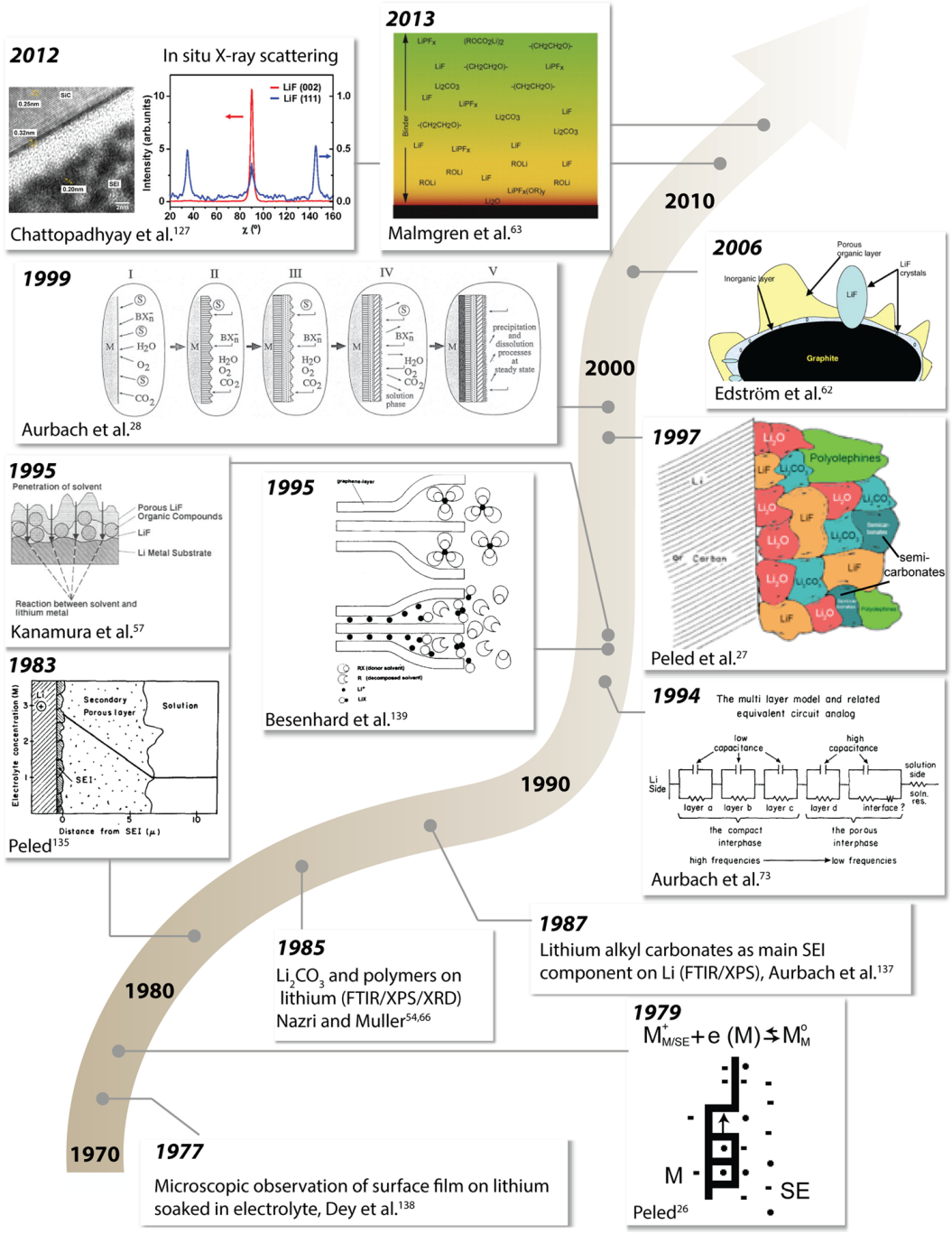

Evolution of knowledge and models of the SEI on negative electrodes in LIBs. Reproduced from the reference.[148]

Supplementary Fig. S1.5

species	pristine electrolyte	lithium metal		$LiCoO_2$ electrode		electrochemical electrolyte oxidation
		4.6 V	4.9 V	4.6 V	4.9 V	
H_2O	×	×	×	×	–	–
HF	×	–	–	–	×	×
lithium ethylene dicarbonate (LEDC)	–	×	×	–	–	–
lithium methyl carbonate (LMC)	–	×	×	×	×	×
lithium methoxide	–	×	×	×	–	–
lithium succinate	–	×	×	–	–	–
methanol	–	×	×	×	×	×
formic acid	–	–	×	–	×	–
formaldehyde	–	–	×	–	–	×
glycolic acid/lithium glycolate	–	–	–	–	×	×
glyoxal	–	–	–	–	–	×
vinylene carbonate (VC)	–	–	–	–	–	×
fluoroethylene carbonate (FEC)	–	–	–	–	–	×
acetals	–	–	–	–	–	×
$OPF_2(OH)$	–	–	–	–	×	×
$OPF_2(OCH_3)$	–	×	×	–	–	–
$PF_3(C_2O_4)$	–	–	–	–	–	×
SiF_x	–	–	×	–	×	–
BF_4^-	–	–	×	–	×	×
$OPF_2OH–BF_3$	–	–	–	–	×	–

[a]A "×" indicates that the species was present under that condition, whereas a "–" indicates that the species was not.

Summary of electrolyte decomposition products observed. As identified by solution NMR, and the conditions under which they are formed. Reproduced from the reference.[150]

Supplementary Fig. S1.6

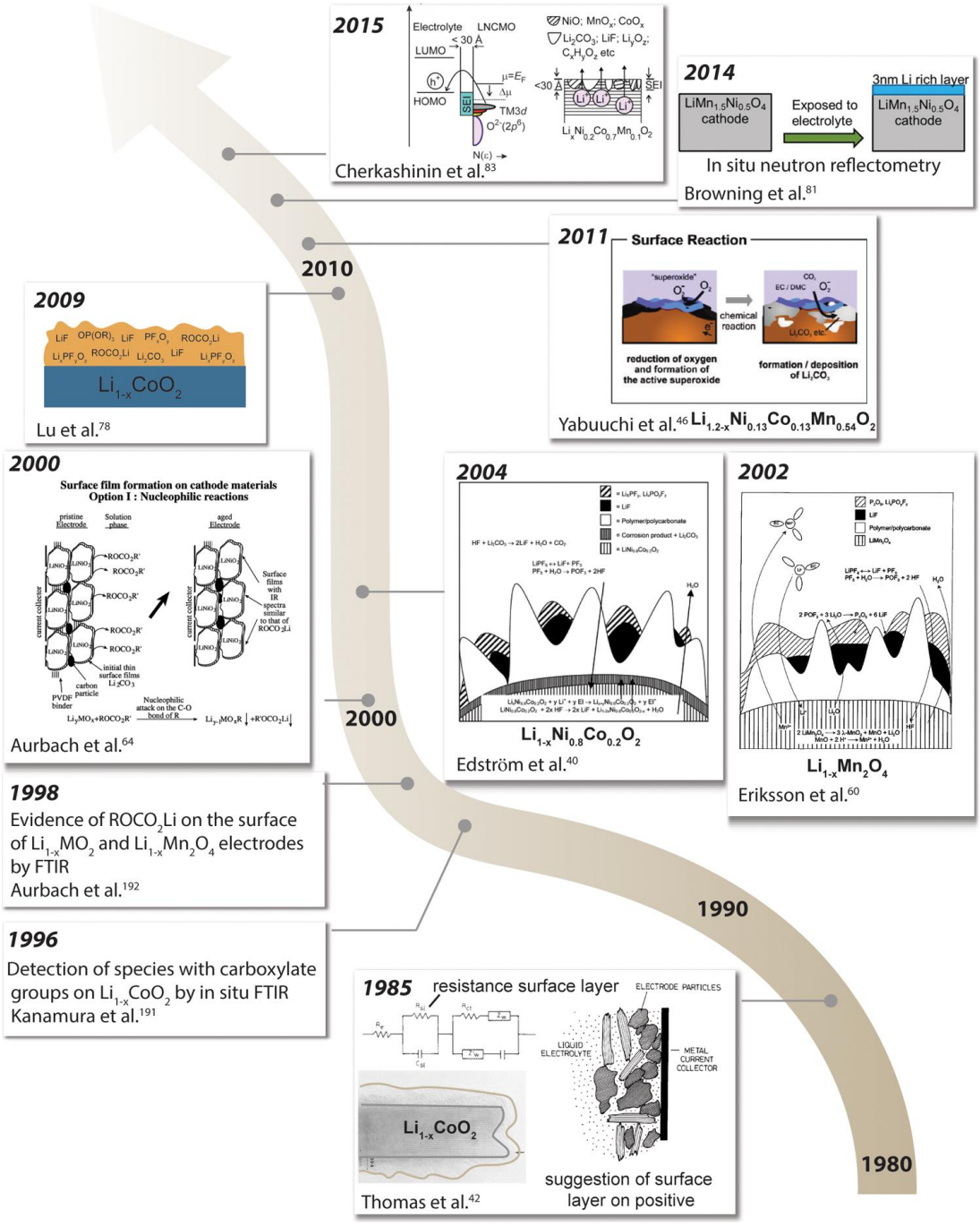

Investigation of the CSEI layers formed on positive electrodes in LIBs. Reproduced from the reference.[148]

Supplementary Table S1.1

Material composition	Type	1st cycle capacity (mAh/g)	Capacity retention (Half cell vs. Na)	Capacity retention (Full Cell vs. HC.)	Ref.
$Na[Ni_{0.5}Mn_{0.5}]O_2$	O3 layered	147	82% (100 cycles)	~79% energy ret. (100 cycles at C/10)	
$Na[Ni_{0.5}Mn_{0.3}Ti_{0.2}]O_2$	O3 layered	150	-	~83% energy ret. (100 cycles at C/10)	
$Na[Fe_{0.4}Cu_{0.2}Mn_{0.4}]O_2$	O3 layered	92	-	~87% energy ret. (100 cycles at C/10)	
$Na[Ni_{1/3}Fe_{1/3}Mn_{1/3}]O_2$	O3 layered	125	95% (10 cycles)	~82% (125 cycles at C/2)	
$Na[Ni_{0.6}Co_{0.2}Mn_{0.2}]O_2$	O3 layered (Al2O3 coated spherical particles)	151	90% (50 cycles)	75% (300 cycles at C/2)	
$Na[Ni_{0.6}Co_{0.05}Mn_{0.35}]O_2$	O3 layered (Spherical particles concentration gradient)	157	84% (100 cycles)	80% (300 cycles at C/2)	
$NaNi_{0.45}Zn_{0.05}Mn_{0.4}Ti_{0.1}O_2$	O3 layered	187	85% (100 cycles)	-	
$Na_{0.95}[Ni_{0.5}Mn_{0.5}]O_{1.95}F_{0.05}$	O3 layered (Spherical particles)	140	89% (100 cycles)	92% (500 cycle at C/2)	
$Na_{0.95}[Ni_{0.317}Mn_{0.317}Mg_{0.158}Ti_{0.208}]O_2$	O3 layered	155	-	80% (500 cycle at C/6)	
O3 - $Na_{0.95}[Ni_{0.317}Mn_{0.317}Mg_{0.158}Ti_{0.208}]O_2$ P2 - $Na_{0.667}[Ni_{0.300}Mn_{0.600}Mg_{0.033}Ti_{0.067}]O_2$	O3 - P2 mixed phase	158	-	80% (3000 cycles at 1C)	

Promising cathode compositions for sodium transition metal oxides and their corresponding performances that have been reported in the literature. Most notable performances are mark in red color. Reproduced from the mentioned references.[113,311,333]

S upplementary Table S1.2

Material composition	Avg. Voltage	1st cycle capacity	Rate capability	Capacity retention	Ref.
$Na_{0.61}Fe[Fe(CN)_6]_{0.94}.xH_2O$	2.8 V	170 mAh/g	70 mAh/g at 4 C	100% after 150 cycles at 0.2 C	67
$Na_{1.56}FeFe(CN)_6 \cdot 3.1H_2O$	2.8 V	103.6 mAh/g	90 mAh/g at 100 mA/g	97% after 400 cycles at 20 mA/g	87
$Na_{1.63}Fe[Fe(CN)_6]_{0.89} \cdot \square_{0.11}.xH_2O$	2.7 V	150 mAh/g	N.A.	90% after 200 cycles at 25 mA/g	64
$Na_{1.92}FeFe(CN)_6.xH_2O$	3.25 V	160 mAh/g	145 mAh/g at 10 C	80% after 750 cycles at 0.5C	38
$Na_{1.89}Mn[Fe(CN)_6]_{0.97}.xH_2O$	3.4 V	150 mAh/g	121 mAh/g at 20 C	75% after 500 cycles at 105 mA/g	70
$Na_{1.85}Co[Fe(CN)_6]_{0.99} \cdot 1.9H_2O$	3.5 V	153 mAh/g	60 mAh/g at 500 mA/g	90% after 200 cycles at 200 mA/g	48
$Na_{1.76}Ni_{0.12}Mn_{0.88}[Fe(CN)_6]_{0.98}.\square_{0.02}$	3.1 V	123.3 mAh/g	50.2 mAh/g at 600 mA/g	83.8% after 800 cycles at 100 mA/g	46

Promising cathode compositions for PBA and their corresponding performances that have been reported in the literature. Most notable performances are mark in red color. Reproduced from the reference. Reproduced from the mentioned references.[110,111,114,125,334]

Supplementary Table S1.3

	Solubility in H_2O (Ref)[35]	Solubility in PC (ICP-OES)	Solubility in EC:DEC (ICP-OES)
LiF	1.34 g/L	0.157 mg/L	0.066 mg/L
Li_2CO_3	13.0 g/L	0.160 mg/L	0.135 mg/L
NaF	41.3 g/L	8.617 mg/L	3.057 mg/L
Na_2CO_3	307 g/L	6.603 mg/L	3.648 mg/L

Reported solubility for main SEI components in LIBs and NIBs. Reproduced from the mentioned reference.[155]

S-2 Supplementary Information for Chapter 2

○ Supplementary Figures

Supplementary Fig. S2.1

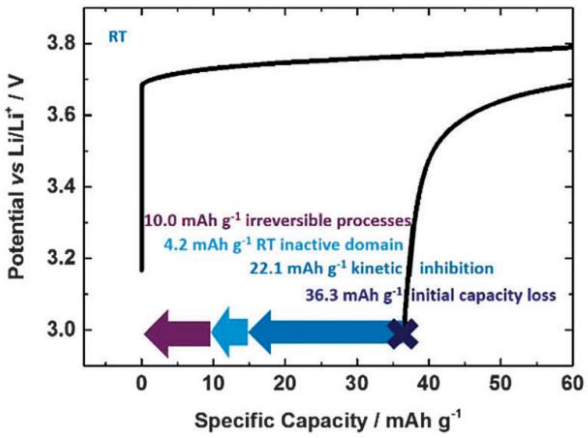

Magnification of the relevant region of the 1st cycle potential profile of a NCM/Li half cell with a charge cut-off potential of 4.6 V vs. Li/Li+ at a specific current of 30 mA/g at RT. Different impacts on the 1st cycle specific capacity loss are schematically highlighted. Reproduced from the mentioned reference.[163]

Supplementary Fig. S2.2

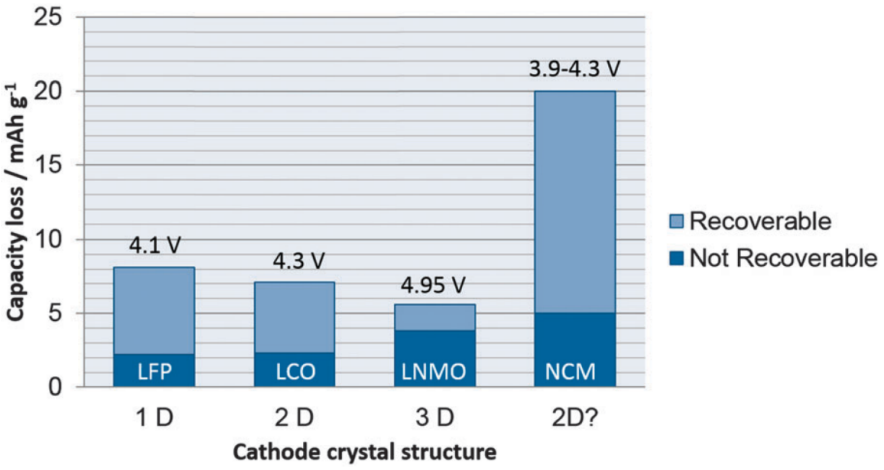

When comparing three different cathode types (olivine, layered, and spinel), the first cycle capacity loss can be categorized into recoverable and non-recoverable losses. This allows for a systematic and meaningful comparison based on the cathode's crystal structure (solid-state Li+ diffusion) and charge cut-off potential. The recoverable capacity loss, which is kinetically hindered and reversible, decreases as the dimension of solid-state Li+ diffusion increases (1D < 2D < 3D). On the other hand, the non-recoverable capacity loss increases with higher charge cut-off

potential. However, the NCM material behaves differently in terms of both recoverable and non-recoverable capacity losses. Reproduced from the mentioned reference.[163]

Supplementary Fig. S2.3

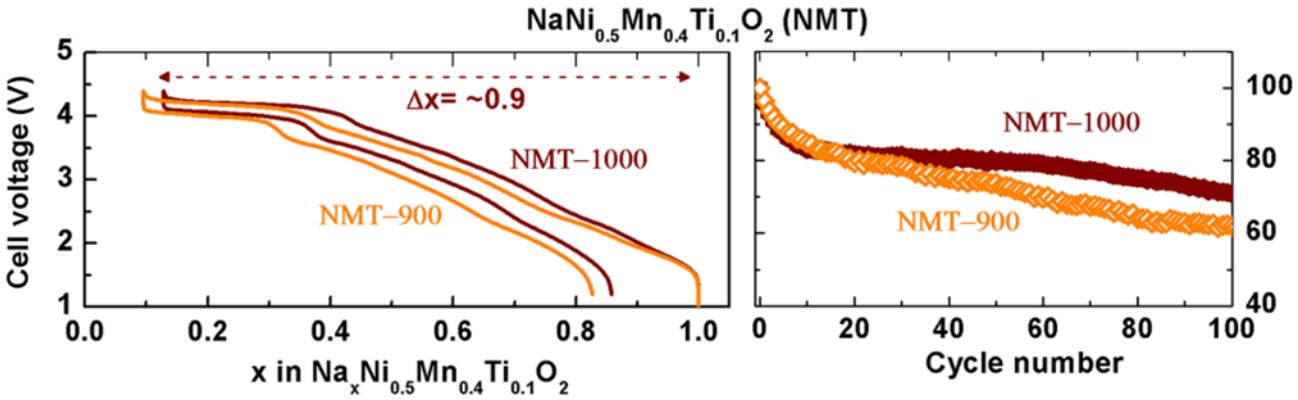

NMT materials synthesized at two different synthesis conditions (900 °C/24 h mentioned as 900 and re-annealed at 1000 °C/12 h mentioned as 1000) in Na-ion full cells using a hard carbon negative electrode and cycled at C/10 rate within a voltage window of 1.2–4.4 V and the corresponding capacity retention plots in the right. Reproduced from the mentioned reference.[320]

Supplementary Fig. S2.4

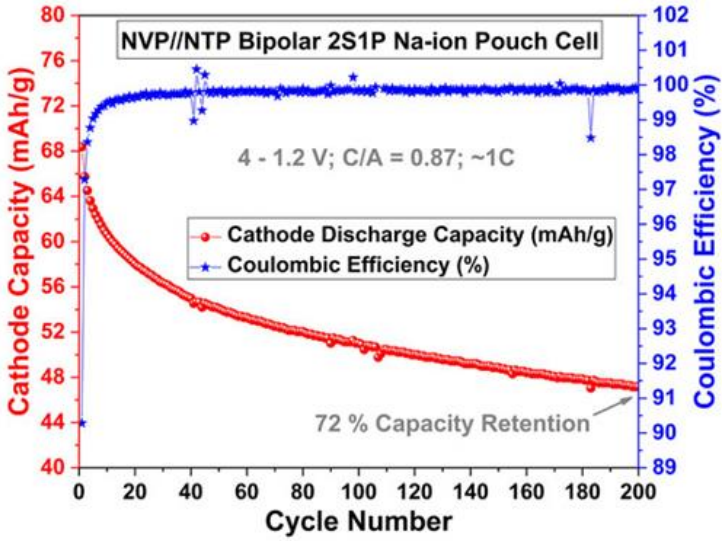

Capacity retention and coulombic efficiency over 200 cycles for the bipolar $Na_3V_2(PO_4)_3$ //$NaTi_2(PO_4)_3$ Na-ion pouch cell. Reproduced from the mentioned reference.[335]

Supplementary Fig. S2.5

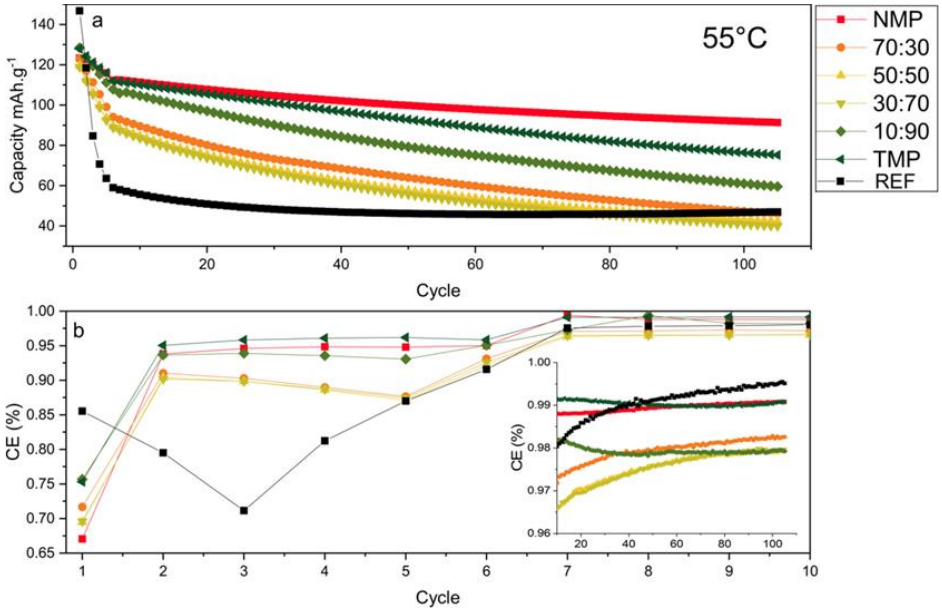

Galvanostatic cycling of full-cell sodium-ion batteries at 55 °C starting with five cycles at 0.2C followed by 100 cycles at 1C (a) and the Coulombic efficiencies for the same cells (b). Reproduced from the mentioned reference.[121]

Supplementary Fig. S2.6

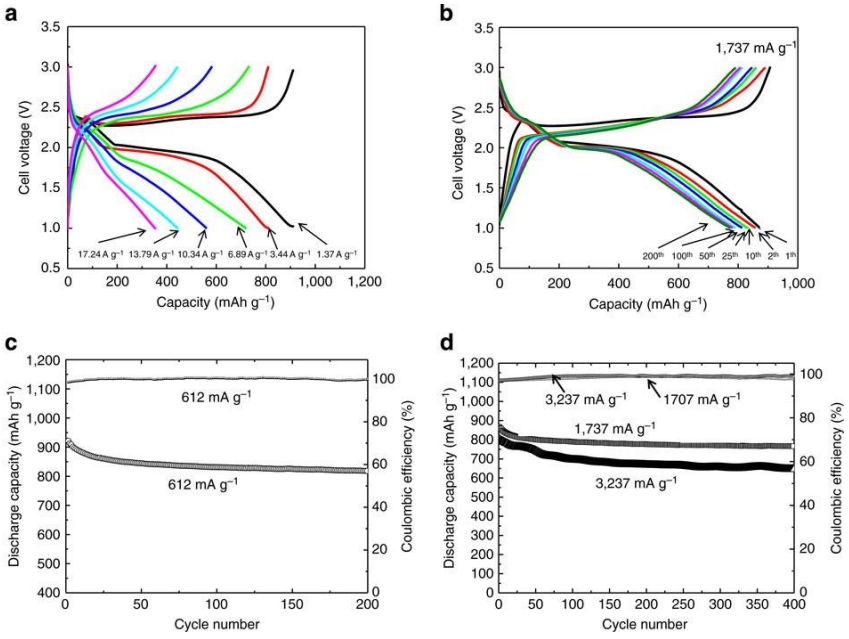

(a) Charge–discharge curves of hybrid Li–S cells at different rates. (b) Cycling ability of the hybrid Li–S cell at a rate of 1,737 mA g^{-1}. (c,d) Long-term cycling behaviour and corresponding Coulombic efficiencies of hybrid Li–S cells at different rates. Reproduced from the mentioned reference.[336]

Supplementary Fig. S2.7

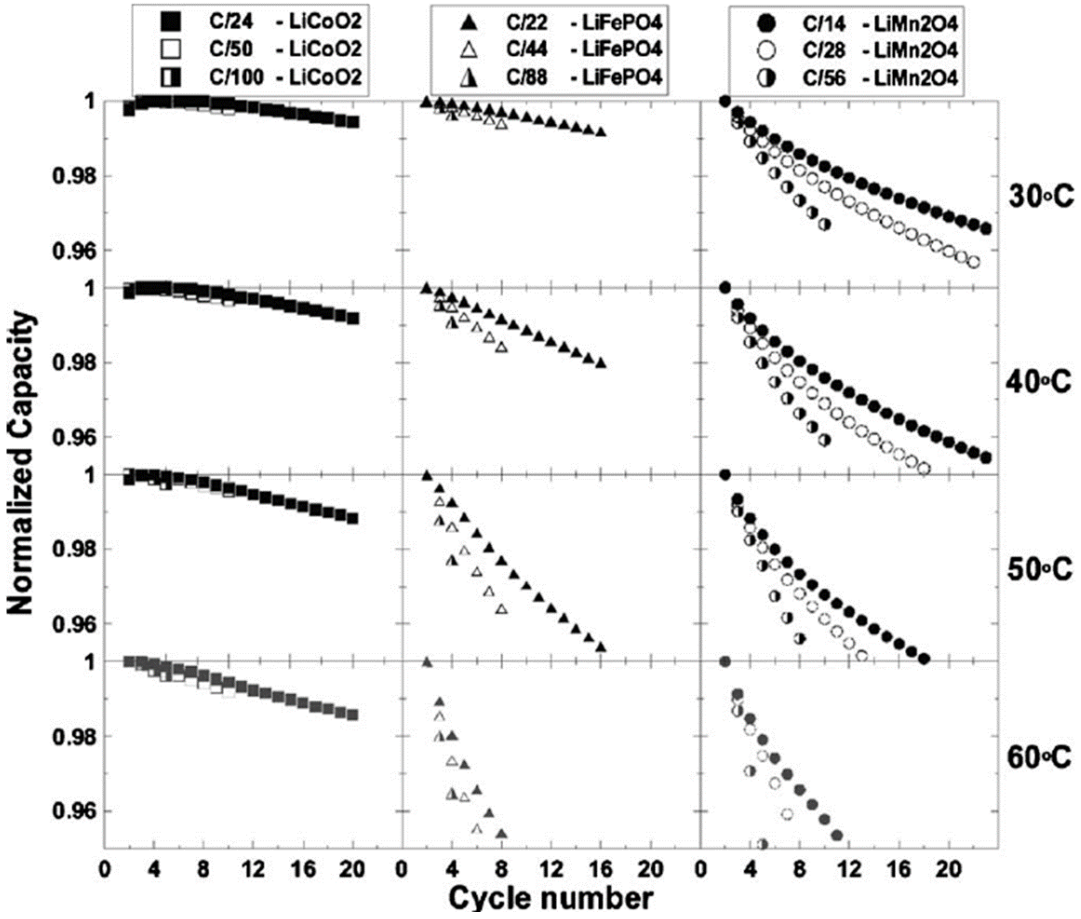

Normalized capacity vs. cycle number of the thirty six Li-ion cells charged and discharged at the C rates and temperatures indicated. Twelve each of 18650-sized $LiCoO_2$|graphite cells (2400 mAh) and $LiMn_2O_4$|graphite (1400 mAh) cells were cycled between 3.0 and 4.2 V. Twelve 26700-sized LiFePO4/graphite cells (2200 mAh) were cycled between 2.7 and 3.8 V. Reproduced from the mentioned reference.[165]

- At low C rates (C/14 to C/100) observed in these cells, increased temperature or decreased C-rate results in greater capacity loss. This indicates that parasitic reactions are exacerbated under high temperature conditions or when the cell undergoes prolonged charging periods (low C-rate).
- Despite both LCO and LMO being cycled within the same voltage window (3-4.2V), LCO exhibits greater stability than LMO across all temperatures. Furthermore, LCO cycled at higher voltage ranges demonstrates superior stability compared to LFP cycled in the lower voltage region of 2.7-3.8V.

Supplementary Fig. S2.8

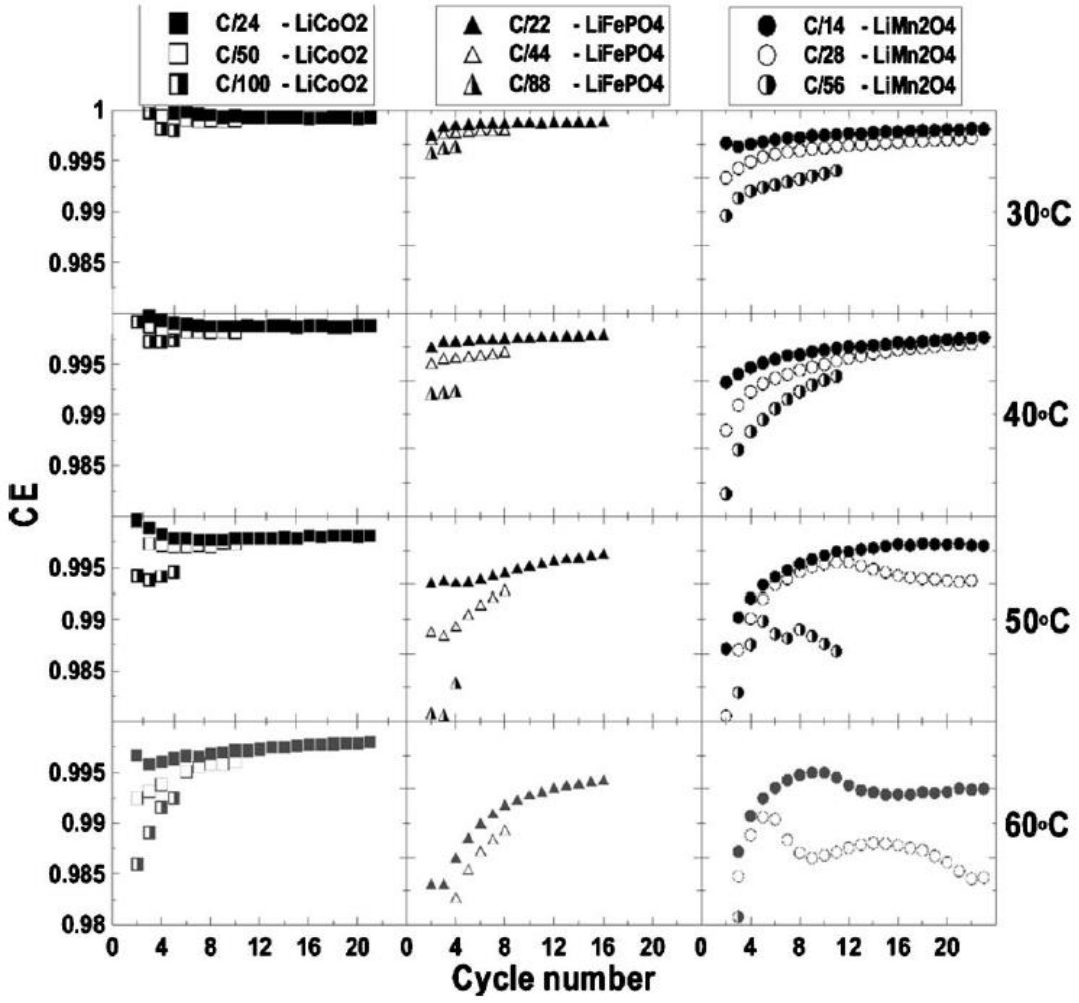

Normalized coulombic efficiency vs. cycle number of the thirty six Li-ion cells charged and discharged at the C rates and temperatures indicated. Twelve each of 18650-sized $LiCoO_2$|graphite cells (2400 mAh) and $LiMn_2O_4$|graphite (1400 mAh) cells were cycled between 3.0 and 4.2 V. Twelve 26700-sized LiFePO4/graphite cells (2200 mAh) were cycled between 2.7 and 3.8 V. Reproduced from the mentioned reference.[165]

- The same conclusions regarding aggravated degradation at high temperatures and slow C-rates, as well as the superior stability of LCO compared to LFP and LMO, can be drawn from the CE analysis. Notably, for most cells depicted, the CE initially increases over the first few cycles and then stabilizes at a certain value. This behavior is typically observed in batteries that are stable, except for LMO at 50°C and 60°C, as indicated by the CE and CR data.

Supplementary Fig. S2.9

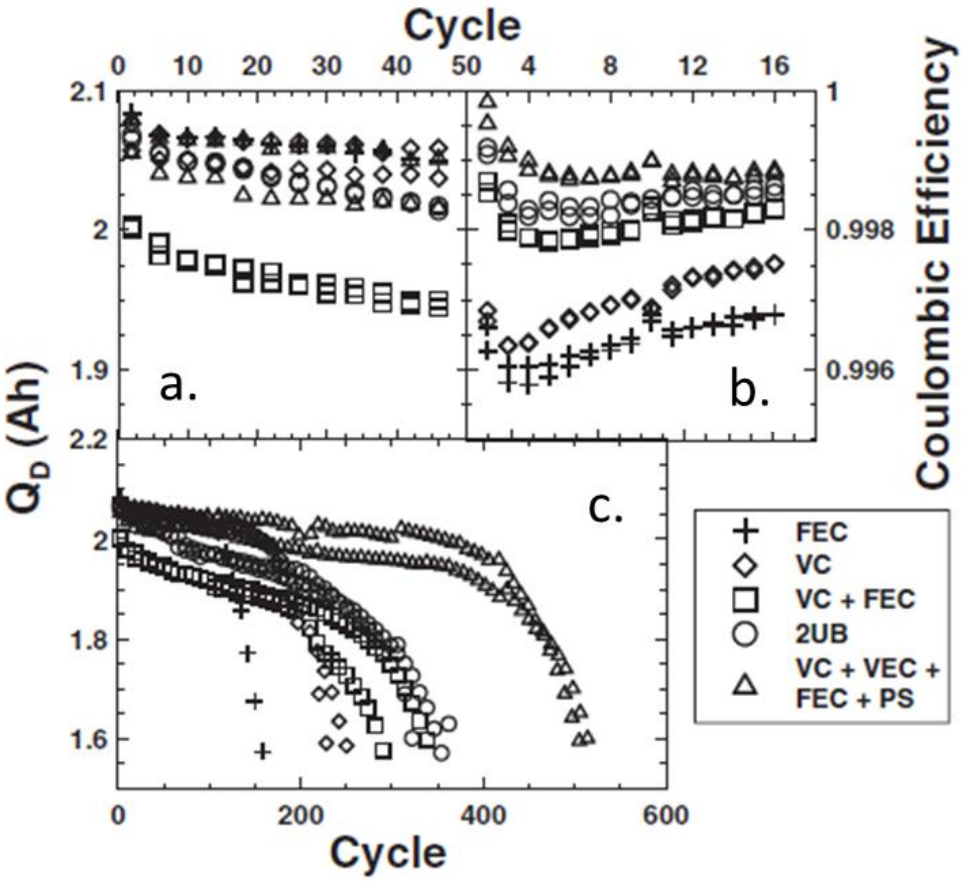

a) Effect of the CE on the capacity retention of a full cell. b) Capacity vs. cycle number for initial cycles at 1C, c) CE of 16 high precision coulometry cycles at C/20 before long cycling, d) Capacity vs. cycle number for long cycling at 1C for the same cells as b), which are NMC/graphite 18650 cells with the additives. Reproduced from the mentioned reference.[337]

- **Fig. S2.9d** illustrates the capacity retention of NMC/graphite 18650 cells with different additives, while **Fig. S2.9b** provides a zoomed-in view of the capacity for the first 50 cycles. It is noteworthy that the relative comparison of cell lifetime in **Fig. S2.9d** can be accurately predicted by analyzing the CE (**Fig. S2.9c**), even with only 20 cycles on the HPC. This prediction cannot be reliably made by solely comparing the capacity retention (CR) in **Fig. S2.9b**. These precision chargers are recently commercialized by Novonix, Biologic, and Arbin, allowing for the prediction of cell lifetime in months instead of requiring years of cell testing.

Supplementary Fig. S2.10

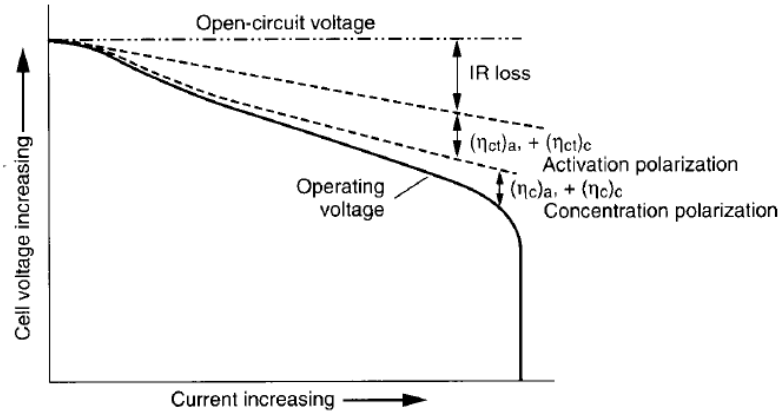

Cell polarization divided into activation polarization, concentration polarization and ohmic (IR) polarization as a function of operating current. Reproduced from the mentioned reference. [174]

$$E = E_0 - [(\eta_{ct})_a + (\eta_c)_a] - [(\eta_{ct})_c + (\eta_c)_c] - iR_i = iR$$

where E_0 = electromotive force or open-circuit voltage of cell
$(\eta_{ct})_a$, $(\eta_{ct})_c$ = activation polarization or charge-transfer overvoltage at anode and cathode
$(\eta_c)_a$, $(\eta_c)_c$ = concentration polarization at anode and cathode
i = operating current of cell on load
R_i = internal resistance of cell

Supplementary Fig. S2.11

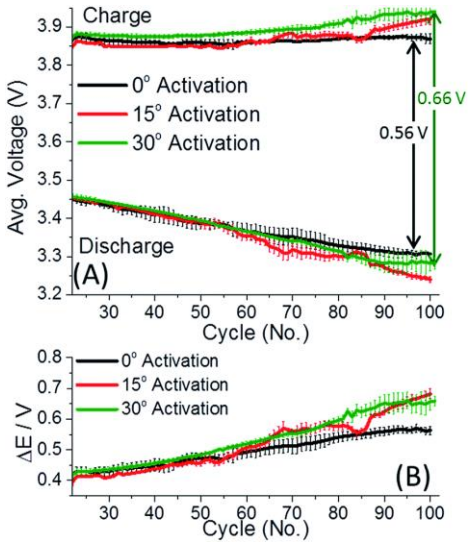

A)The average charge and discharge voltages were measured for $0.35Li_2MnO_3 \cdot 0.65Li[Mn_{0.45}Ni_{0.35}Co_{0.20}]O_2$ electrodes activated at different temperatures: 0 °C (black), 15 °C (red), and 30 °C (green). The cells were cycled at 30 °C with a C/3 rate. B) The average charge-discharge voltage difference, ΔE, was calculated for the cells described in (A). Initial

rate capability cycles were excluded for clarity as the average voltage changes with the rate. The error bars represent one standard deviation among 3-4 cells. Reproduced from the mentioned reference.[338]

Supplementary Fig. S2.12

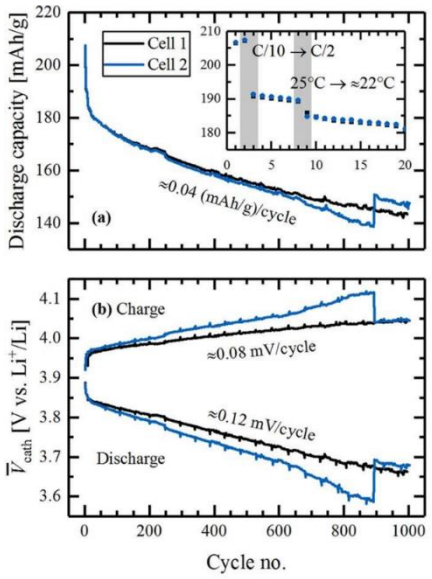

(a) Specific discharge capacity, (b) charge-averaged mean charge and discharge voltage of the NMC811-Li cell. Reproduced from the mentioned reference.[339]

Supplementary Fig. S2.13

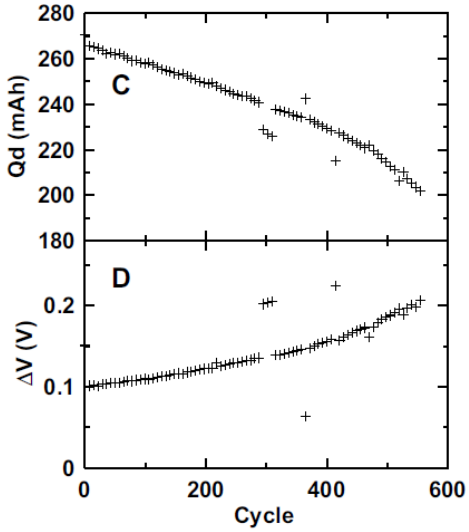

NMC532| artificial graphite pouch cells cycled with 1.2 M $LiPF_6$ in EC:EMC 3:7 electrolyte cycled in 3-4.2V with c) capacity retention and d)average charge voltage – average discharge voltage. Reproduced from the mentioned reference.[175]

Supplementary Fig. S2.14

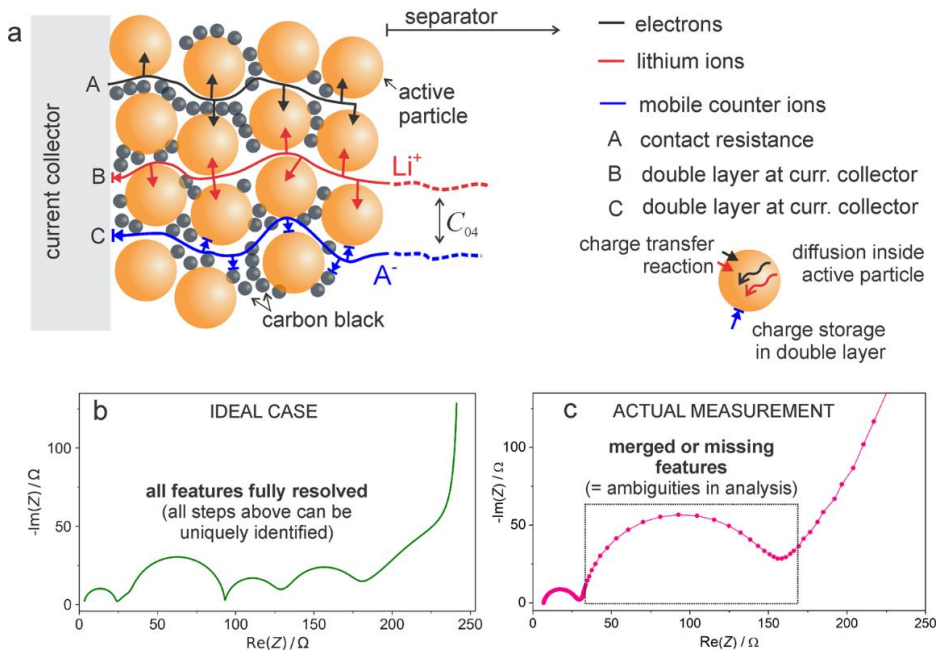

Typical processes in a lithium-ion battery electrode and their identification using EIS measurements. a) Schematics showing the movement of electrons and mobile ions in a typical Li-ion insertion positive electrode. b) Theoretical impedance response for an ideal case where each individual step shown in a can be seen as a separate feature. c) Example of a practical EIS measurement where many of the predicted features are not seen due to overlap of time constants, very small values of impedance values for certain steps or other measurement artefacts. Reproduced from the mentioned reference.[340]

- When considering EIS for batteries, it reveals a multitude of elementary processes as depicted in **Fig. S2.14**. These processes commonly involve: (i) electron transfer from the current collector to the electrode composite, (ii) electron conduction and migration through the composite electrode, (iii) ion migration across the electrode thickness, (iv) electrochemical insertion of ions and electrons into active storage particles, (v) double-layer charging at solid/liquid interfaces, (vi) coupled diffusion of active and non-active ions within the porous electrode composite, (vii) simultaneous diffusion of ions and electrons within the active storage particles, and (viii) migration and diffusion of ions in the separator.
- In the ideal scenario depicted in **Fig. S2.14b**, the number of observed features is only one less than the number of individual processes, highlighting the ability of EIS to separate complex processes into their elementary steps. However, in realistic measurements (**Fig. S2.14c**) many of these individual features overlap, posing a considerable challenge in accurately decoupling them.

Supplementary Fig. S2.15

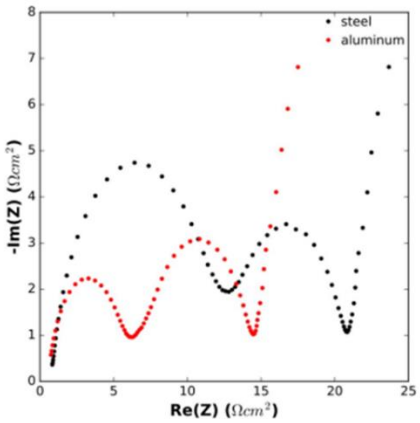

The Nyquist spectra were obtained for NMC532 positive electrode symmetric cells at 30°C. These positive electrodes were derived from an NMC532/AG pouch cell that used EC:DMC (3:7, w:w) + 1.2 M LiPF6 electrolyte and was formed and disassembled at 4.4V. The black spectra represent a symmetric cell with stainless steel hardware (can, cap, spring, and spacer), while the red spectra represent a symmetric cell with aluminum hardware (can, cap, spacers). Reproduced from the mentioned reference.[178]

Supplementary Fig. S2.16

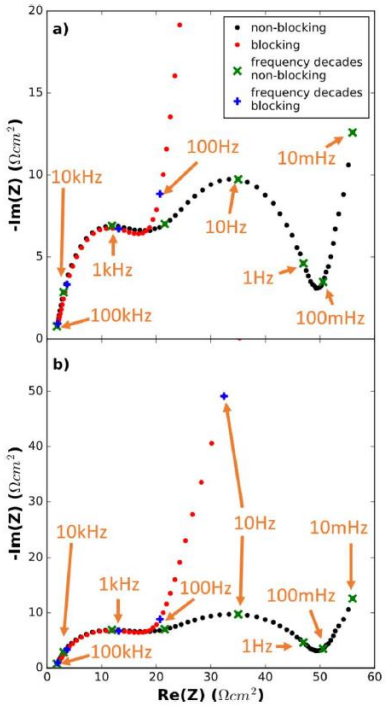

(a-b) Area-specific Nyquist plots were generated for blocking and non-blocking full coin cells at 20°C, with frequency decades labeled. These cells consisted of an NMC532 positive electrode and an artificial graphite negative electrode,

using a 1.2M LiPF6 in EC:DMC (3:7, w:w) electrolyte. The non-blocking full coin cell was constructed by utilizing electrodes from a pouch cell that had been formed to 4.2V and operated at 3.8V while blocking full cells were assembled using fresh electrodes. (a) The imaginary impedance axis is magnified to enhance clarity. (b) The scales of the real and imaginary impedance axes are equal. Reproduced from the mentioned reference.[178]

Supplementary Fig. S2.17

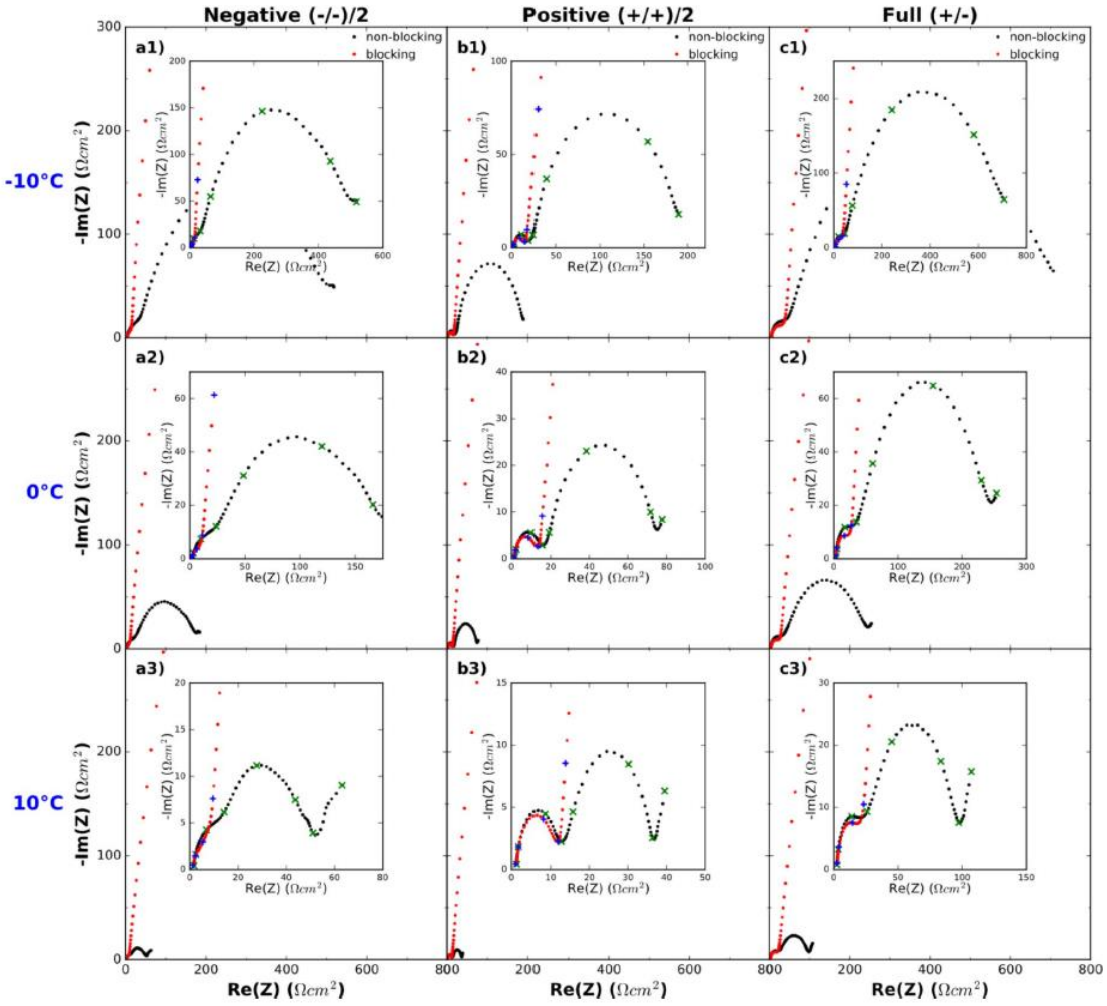

Area-specific Nyquist plots were obtained for various types of cells: blocking and non-blocking negative electrode symmetric cells (a1-a3), positive electrode symmetric cells (b1-b3), and full coin cells (c1-c3). These cells utilized an NMC532 positive electrode and an artificial graphite negative electrode with a 1.2M LiPF6 in EC:DMC (3:7, w:w) electrolyte. The non-blocking symmetric cells and full coin cell were assembled using electrodes from a pouch cell that had been formed to 4.2V and operated at 3.8V. Measurements were taken at different temperatures: (a1), (b1), and (c1) at -10°C; (a2), (b2), and (c2) at 0°C; and (a3), (b3), and (c3) at 10°C. The frequency decades are indicated

using blue "+" symbols for blocking data and green "x" symbols for non-blocking data. Reproduced from the mentioned reference.[178]

Supplementary Fig. S2.18

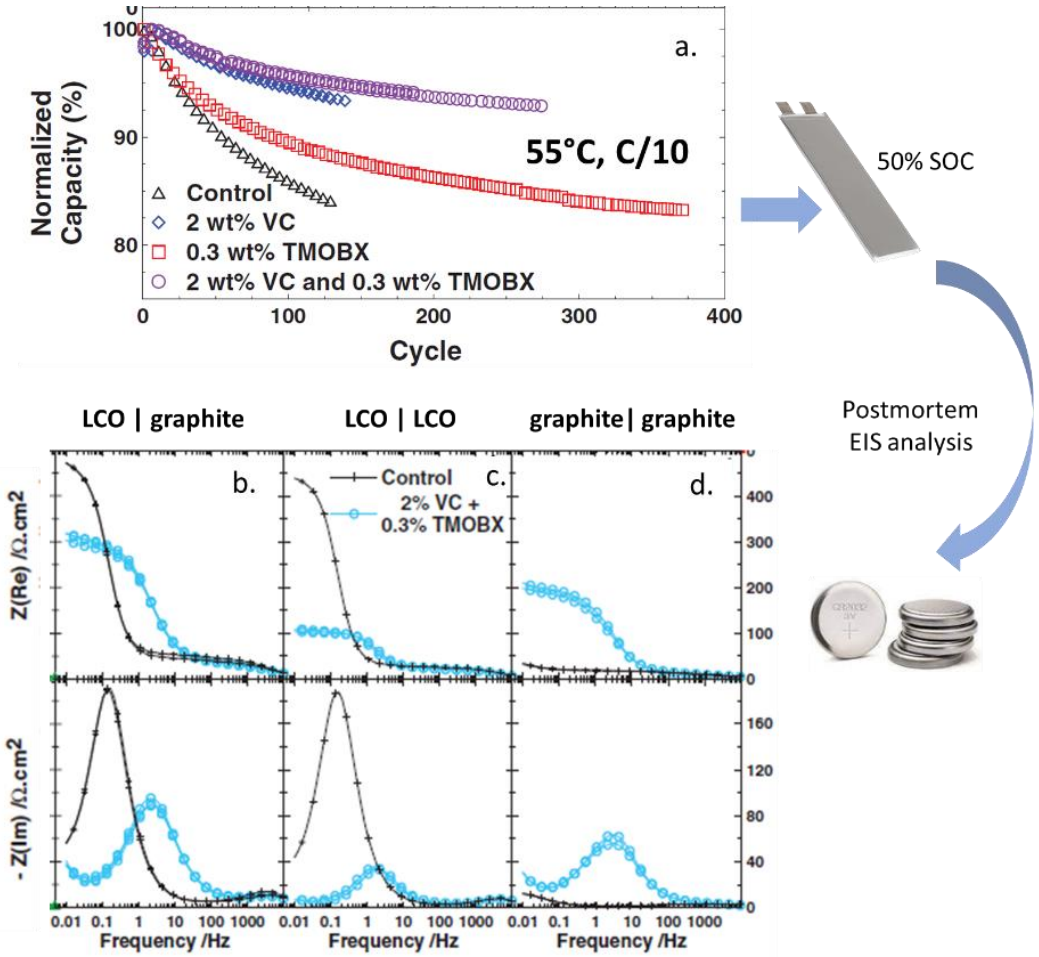

a) Long-term cycling of $LiCoO_2$|graphite cells with different electrolytes containing additives at a C/10 rate at 55°C. b)Bode plot of reassembled LCO|graphite coin cell, c)Bode plot of reassembled LCO|LCO coin cell, b)Bode plot of reassembled graphite|graphite coin cell from the recovered electrodes from the aged pouch cell at 50% SOC. Adapted and modified from ref.[180]

A case study from Dahn et. al is presented regarding identification of impact of additives for LCO|graphite pouch cell (Fig. 2.9). The introduction of VC+TMOBX, shows superior cell stability (**Fig. S2.18a**) at 55°C as compared to control electrolyte with no additives. The aged pouch cell was disassembled in 50% state-of-charge, the LCO and graphite electrodes were punched and three different kind of coin cells were assembled, namely LCO|graphite, LCO|LCO and graphite|graphite. Thus the impedance of full cell (LCO|graphite) can be effectively deconvoluted in terms of impedances of cathode (LCO|LCO) and anode (graphite|graphite).

Fig. S2.18b-d represents impedance in terms of bode plot of as-prepared coin cells for control and VC+TMBOX configurations. The impedance of the LCO|graphite cell with additives (**Fig. S2.18b**) is lower compared to the control, indicating reduced degradation at a temperature of 55°C. This improvement can be attributed to the substantial degradation of the LCO electrode observed in the absence of additives, resulting in significant impedance development (**Fig. S2.18c**). In contrast, the graphite symmetric cells exhibit higher impedance (**Fig. S2.18d**) with additives compared to the control, which is attributed to the formation of a passivating film during cell formation rather than cell degradation, as discussed by the authors in the paper.

Supplementary Fig. S2.19

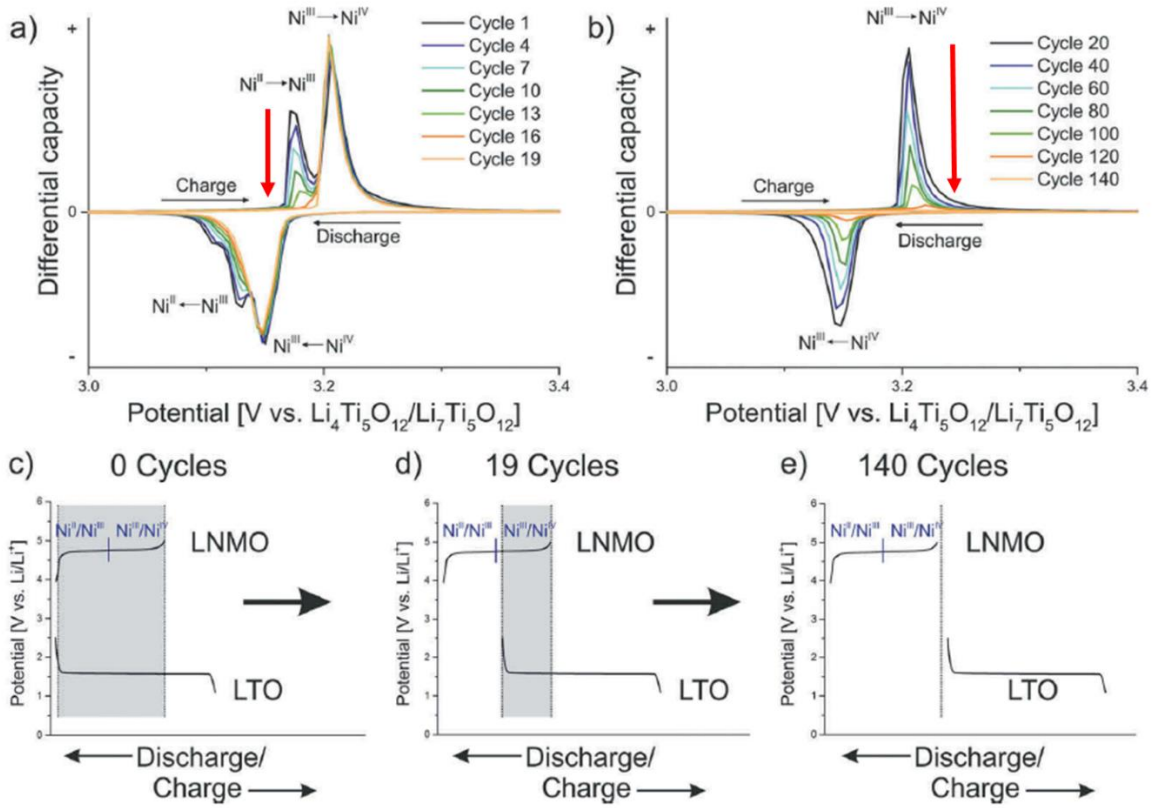

LTO degradation spotted using DCA for LNMO|LTO full cell. (a) First 20 cycles of the cell; (b) the following 120 cycles; (c–e) the corresponding shift of the voltage characteristics of the electrodes to each other. The blue line separates the regions of the two-phase transformations of the LNMO. The gray area between the dashed lines marks the amount of lithium left in the cell. Reproduced from the mentioned reference.[195]

As peaks in DCA indicate electrochemical processes, they can be tracked to study cell degradation. **Fig. S2.19a-b** shows the DCA profiles of LNMO| $Li_4Ti_5O_{12}$ (LTO) for cycle 1 to 19 and cycle 20 to 140, respectively. In the initial 19 cycles (**Fig. S2.19a**), the $Ni^{II/III}$ peak diminishes while the $Ni^{III/IV}$ peak remains relatively constant, leading to

capacity loss. Subsequently, the DCA profiles from cycles 20-140 show a continuous decrease in the $Ni^{III/IV}$ peak (**Fig. S2.19b**). Notably, the DCA profiles of the LNMO half-cell exhibit stability over 300 cycles (**Fig. S2.19b**), indicating the robustness of the LNMO material. Hence, the observed capacity loss cannot be attributed to the degradation of LNMO, as both the peaks in DCA profiles should decrease in initial cycles and not only one of them.

To explain the observed peak variations, the V-Q profiles of LNMO and LTO electrodes are shifted with respect to each other, as illustrated in **Fig. S2.19c-e.** The overlapping region, highlighted by the gray area, provides the full cell curves. During the first 19 cycles, LTO shifts to the right (**Fig. S2.19c-d**) relative to the LNMO electrode, resulting in the decrease and disappearance of the $Ni^{II/III}$ peak. As cycling progresses, the LTO further shifts (**Fig. S2.19d-e**), leading to the diminishing of $Ni^{III/IV}$ peak and complete loss of overlap between LNMO and LTO. This phenomenon of electrode shifting with respect to each other is known as electrode slippage, which, in this case, is caused by the continuous loss of Li inventory from the LTO electrode due to parasitic reactions.

Supplementary Fig. S2.20

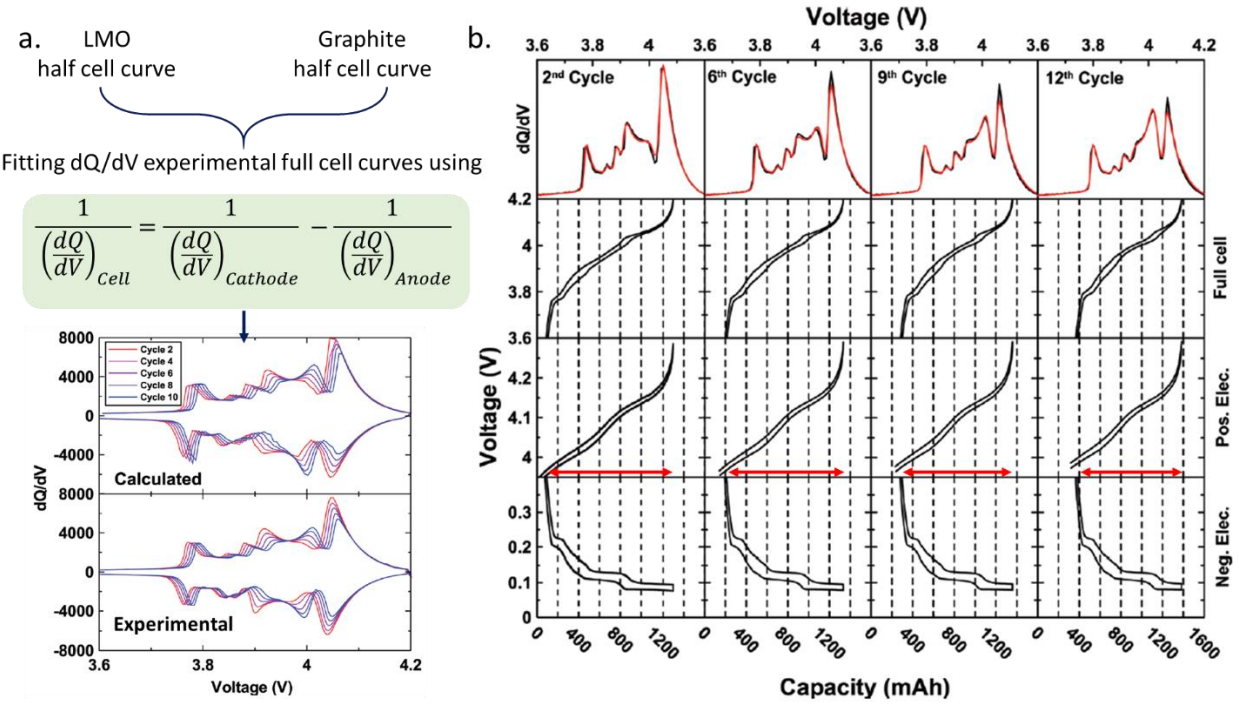

a) Method to fit the experimental dQ/dV curves of LMO|graphite full cell with the combination of LMO and graphite half-cell curves. b) (Top row) Experimental dQ/dV vs. V data for the $LiMn_2O_4$/graphite cell (red) and the calculated fit (black) for the indicated cycles. (Bottom three Rows) The voltage curves of the full cell and its positive and negative electrodes, respectively, calculated from the dQ/dV fit. Adapted and modified from reference.[196]

In another case study by Dahn et al., a LMO|graphite cell is investigated and presented in Figure 2.12. The experimental dQ/dV profile of the full cell is fitted using combinations of LMO and graphite half-cell curves, as

depicted in **Fig. S2.20**. By analyzing the fitted data, the deconvoluted V-Q profiles of the full cell, LMO, and graphite for selected cycles are shown in **Fig. S2.20b**. The decreasing area under the dQ/dV curve indicates capacity loss (**Fig. S2.20b**, top panel). Additionally, the deconvoluted curves reveal that the capacity of the graphite electrode remains unchanged, while the capacity of the LMO electrode is reduced (as indicated by the red arrow in **Fig. S2.20b**) at a rate of 0.5% per cycle. Therefore, the authors assert that cell degradation is primarily attributed to the degradation of the LMO active material and the corresponding loss of capacity.

Supplementary Fig. S2.21

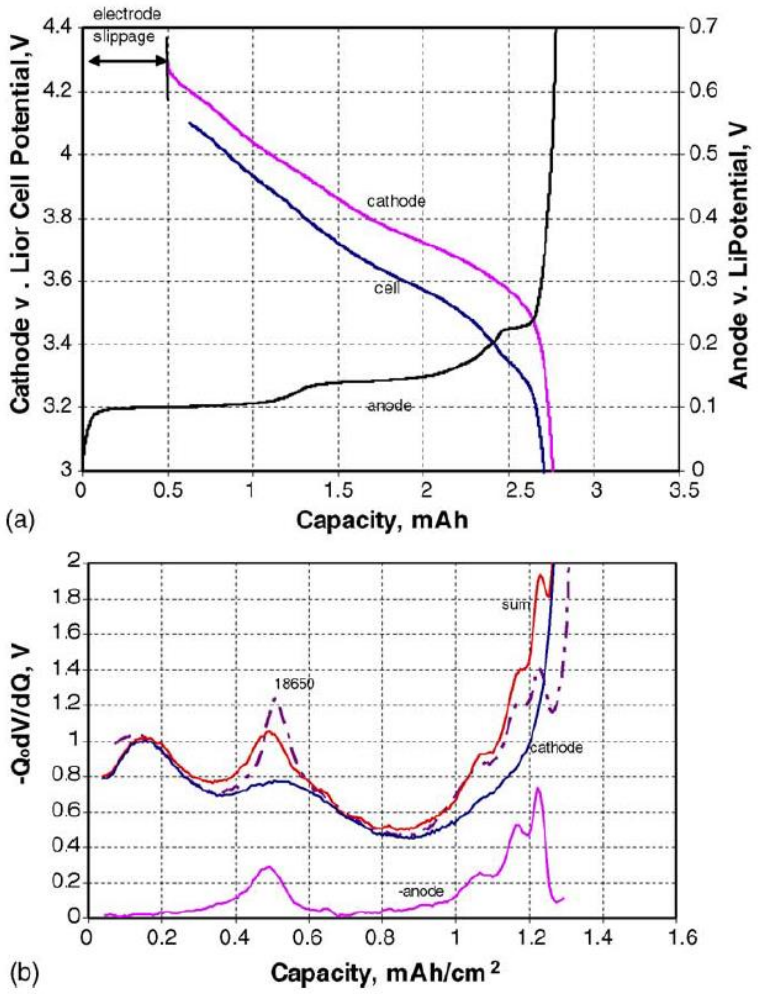

(a) Effect of electrode slippage on cell voltage vs. capacity curve. The amount of electrode slippage is 0.31 mAh cm^{-2}. The calculated cell capacity is 2.08 mAh. (b) $-Q0dV/dQ$ vs. capacity from the data in a. Reproduced from the mentioned reference.[189]

Supplementary Fig. S2.22

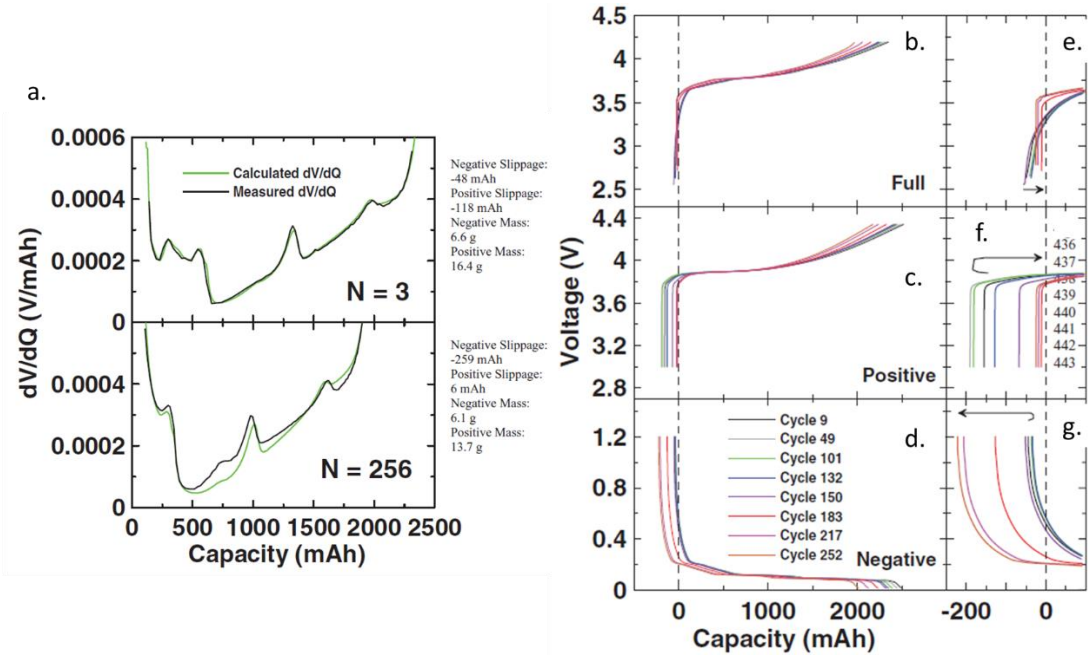

a) Measured and calculated dV/dQ vs.Q for a graphite/$LiCoO_2$ 18650- size cell at cycle 3 and at cycle 256. The cell was cycled at a rate of C/24 at 55°C for about 15 months. b) Calculated voltage versus relative capacity for a full graphite/$LiCoO_2$ cell at various cycles. c) V vs. Q for the positive electrode of the same cell as determined by the dV/dQ fitting. d) V vs. Q for the negative electrode of the same cell as determined by the dV/dQ fitting. Q = 0 represents the fully discharged state of the cell at each cycle. e–g) show expanded views near Q = 0. Reproduced from the mentioned reference.[185]

For instance, **Fig. S2.21** shows dV/dQ (V/mAh) vs. Q (mAh) for a commercial graphite/$LiCoO_2$ 18650 cell at the third cycle (**Fig. S2.21a**) and after 256 cycles (**Fig. S2.21b**). The experimental curve was fitted using the half-cell reference curves represented by green curves in **Fig. S2.21**, note the electrode slippage and mass losses parameters. The deconvoluted V-Q profiles extracted out of fitting LCO and graphite electrodes are presented in **Fig. S2.21 b-g**. LCO and graphite electrodes degrade at different rates leading to different electrode slippages indicated in **Fig. S2.21 e-g**. More detailed analysis and reasons of this slippages is explained in the reference.[185]

Supplementary Fig. S2.23

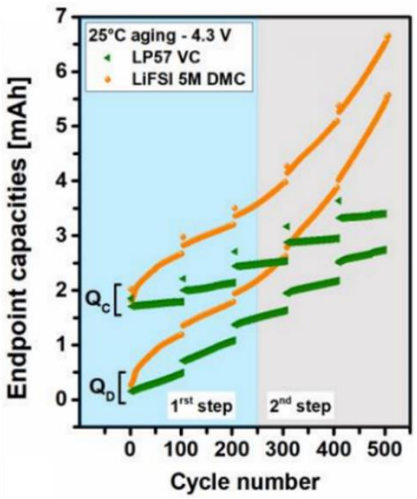

Graphite/NMC811 full cells cycled using LP57 + VC and LiFSI 5M DMC. Associated charge and discharge endpoint slippages are plotted as a function of cycle number. Reproduced from the mentioned reference.[202]

Supplementary Fig. S2.24

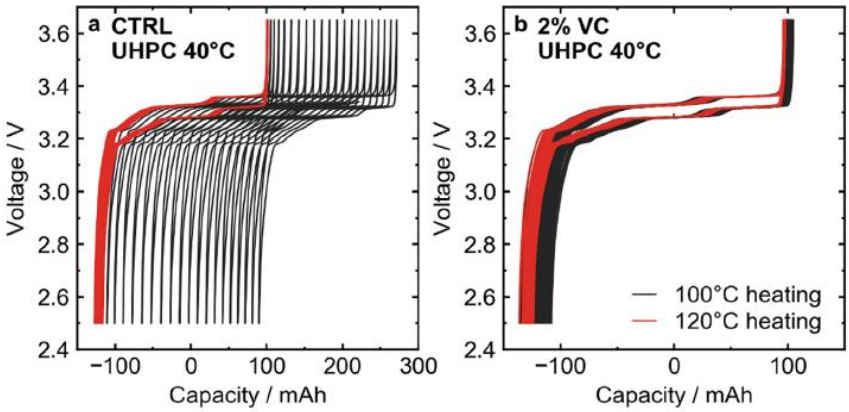

(a) Voltage-capacity curves for LFP cells with control electrolyte cycled at a rate of C/20 at 40 °C. Cells vacuum dried at 100 °C vs 120 °C are shown. (b) Voltage-capacity curves for LFP cells with the 2VC electrolyte vacuum dried at 100 °C and 120 °C. Cells were cycled at C/20 at 40 °C. Reproduced from the mentioned reference.[203]

Fig. S2.23 gives an example of LFP|graphite cell dried at 100°C (black) and 120°C (red), and cycled with control electrolyte (**part a**) and 2%VC additive (**part b**). **Fig. S2.23a** shows huge charge endpoint slippage for cell dried at 100°C (and not for 120°C) indicating the electrolyte oxidation caused by presence of water. With the VC additive there is no significant charge endpoint slippage (**Fig. S2.23b**) for cells dried at 100°C or 120°C. Authors indicated that the charge endpoint slippage was caused by formation of lithium alkoxides in presence of trace water and VC can suppress formation of these alkoxides.

S-3 Supplementary Information for Chapter 3

o Methods

Synthesis of $Na_3V_2(PO_4)_2F_3$ with different carbon coating: The $Na_3V_2(PO_4)_2F_3$ (NVPF) was synthesized using two-step solid-state reaction as described previously.[108,341] The first step involves the synthesis of VPO_4, and the second step consists of the heating stoichiometric amount of VPO_4 and NaF. Agar-agar was used as a carbon source.

Cell assembly and electrochemical tests: The $Na_3V_2(PO_4)_2F_3$ (NVPF) sample containing ~5% carbon coating is used throughout the studies except for studies on 18650 cells where the NVPF containing either 3 - 7% carbon coating were used. The NVPF and HC electrodes coated (one side) on Al foil for coin cell experiments, as well as the dry 18650 cells without electrolyte for prototype cell assembly, were received from TIAMAT Energy, Amiens. NVPF and HC mass loading was roughly ~12 $mg.cm^{-2}$ and ~6 $mg.cm^{-2}$, respectively. Active material: PVDF binder: conductive carbon for NVPF and HC was 94:3:3. The electrochemical tests on $Na_3V_2(PO_4)_2F_3$ (NVPF) were carried out in either Na-metal half-cell using Na metal as a counter (negative) electrode, or Na-ion full cell where hard carbon casted on aluminum foil was used as the negative electrode. Either 2032 coin type cells or 18650 cylindrical type cells (exclusively for full cell analyses) were used for the study. The electrolyte used is 1M $NaPF_6$ in Ethylene carbonate (EC)-Propylene carbonate (PC) – Dimethyl Carbonate (DMC) in 1:1:2 volume ratio, with or without electrolyte additives. The electrolyte additives used are 3 wt. % succinonitrile (SN), 1 wt. % vinylene carbonate (VC), 0.5 wt. % sodium oxalatodifluoroborate (NaODFB) and 0.5 wt.% tri-methylsilylphosphite (TMSPi). A mixture of 0.7M $NaPF_6$+ 0.3M NaTFSI is used as an electrolyte salt for some selected experiments.

Coin cell assembly was carried out in an argon-filled glove box using a glass fiber separator, whereas 18650 cells were filled with electrolyte and sealed in a dry room. For analyzing the electrochemical performance of the $Na_1V_2(PO_4)_2F_3$ samples after treatment with different electrolytes, Na-metal half cells were assembled with 1M $NaPF_6$ in PC as electrolyte. Three-electrode cyclic voltammetry tests were performed with glassy carbon as the working electrode, Pt wire as the counter electrode, and Ag/Ag^+ organic reference electrode (calibrated against Na metal). Aged electrolyte for cyclic voltammetry (CV) was recovered as explained in the leaching procedure section next or by washing the NVPF recovered from 18650 after current interruption device (CID) break (mentioned as 'green electrolyte' as the prepared electrolyte was greenish due to the presence of dissolved vanadium in it). All electrochemical measurements were carried out using a Biologic battery cycler/potentistat-galvanostat, at a specific cycling rate and temperature as specified in the main text.

Leaching procedure: Firstly, 300 mg of $Na_3V_2(PO_4)_2F_3$ powder (90% active mass-10% carbon black Super P) was charged in a homemade big cell to the $Na_1V_2(PO_4)_2F_3$ composition using 1M $NaPF_6$ in PC electrolyte. The powder was recovered from the cell and washed several times with DMC before drying in the glovebox antechamber. For leaching, either a solvent mixture (EC – PC- DMC) or the electrolytes containing 1M salt from $NaPF_6$, $NaClO_4$, $NaBF_4$, NaFSI, and NaTFSI in EC-PC-DMC (1:1:1 by volume) were used. All the salts were dried overnight in a Büchi oven under vacuum at 80 °C before transferring into the glove box. All the solvents were dried over molecular sieves till the water content of less than 10 ppm, as measured by Karl-Fischer titration. Secondly, the electrolyte or solvent (3 mL) was mixed with $Na_1V_2(PO_4)_2F_3$ (20 mg) in a 15 mL polypropylene vial and sealed in an aluminum bag inside an argon-filled glovebox. The aluminum bag was then

transferred to a 55 °C oven for 21 days of leaching. After leaching, the Al bags were transferred to an argon-filled glovebox, and the samples were recovered. The leached NVPF powder was separated from the electrolyte by centrifugation and washed several times with DMC before drying under vacuum. The recovered electrolyte was filtered using a 0.2 µm polypropylene syringe filter (VWR international) to ensure the removal of any NVPF particles in the recovered electrolyte for analyses. The separated solid (leached NVPF) and the liquid (aged electrolyte) were used for further characterization.

Quantifying vanadium dissolution using ICP-MS: For the 2032 coin cell mode, HC electrodes and the separator touching the HC electrodes were recovered after the specified charging/storage procedure. HC + separator was digested in 10.000 mL of 2 wt. % nitric acid (Suprapur, 65 % HNO_3, Merck, vanadium content ≤ 0.5 ppb), and solutions were sonicated and rested overnight. Solutions were filtered with polypropylene 0.2 µm PP syringe filters and diluted with 2 wt. % nitric acid solution until final vanadium concentrations between 1 ppb to 1 ppm were reached. The vanadium amount was quantified using inductively coupled plasma mass spectroscopy (ICP-MS, Nexion 2000, Perkin Elmer). The calibration was obtained from three diluted vanadium standard solutions (TraceCERT, 1 $mg.L^{-1}$ V in nitric acid, Sigma-Aldrich). For the aged electrolyte obtained in the leaching procedure section, the 200.00 µL of electrolyte was diluted until final vanadium concentrations between 1 ppb and 1 ppm were obtained and measured with ICP-MS.

X-ray diffraction (XRD): Synchrotron XRD patterns (λ = 0.4589 Å) were collected via the mail-in service of the 11-BM beamline at the Advanced Photon Source at Argonne National Laboratory. The leached and reference NVPF powders were sealed in glass capillaries and kept inside the kapton holder. The Rietveld refinement of the synchrotron XRD pattern (for solvent leached

NVPF) was performed using the FullProf program.[342] *Operando* X-ray measurements were taken by a BRUKER D8 Advance diffractometer with Cu Kα radiation ($\lambda K\alpha_1$ = 1.54056 Å, $\lambda K\alpha_2$ = 1.54439 Å) and a Lynxeye XE 583 detector. The *operando* XRD analyses were conducted using a homemade airtight XRD cell equipped with a beryllium window.

Transmission electron microscopy (TEM): Samples for transmission electron microscopy (TEM) were prepared in an Ar-filled glove box by grinding the leached NVPF powder in an agate mortar in dimethyl carbonate and depositing drops of suspension onto a copper TEM grid with a holey carbon support layer. The sample was transported to the TEM column with a Gatan vacuum transfer holder avoiding contact with air and moisture. High angle annular dark field scanning transmission electron microscopy (HAADF-STEM) images, energy-dispersive X-ray (EDX) spectra, STEM-EDX maps, electron energy loss spectra (EELS) and STEM-EELS maps were collected with a probe-corrected Titan Themis Z electron microscope operated at 200 kV equipped with a Super-X EDX detector and a Gatan Quantum ER965 spectrometer. The energy resolution, measured from the full width at half maximum of the zero-loss peak, was 0.175 eV.

Scanning Electron Microscopy (SEM): SEM images of the NVPF with different carbon coating were obtained on an FEI Magellan scanning electron microscope equipped with an Oxford Instruments energy dispersive X-ray spectroscopy (EDX) detector. EDX analyses of the NVPF particles were carried out using an acceleration voltage of 20 kV.

Fourier-Transform Infrared (FTIR) Spectroscopy: The leached NVPF powders were discharged to 2 V (0% state of charge) vs. Na metal for FTIR measurement. FTIR spectra were recorded on a Nicolet iS5 FTIR spectrometer, mounted with a diamond Attenuated Total Reflectance accessory

(iD1 ATR). All the spectra were taken using 16 scans with a 4 cm^{-1} resolution from 2000 to 400 cm^{-1}. The background correction is performed by measuring the ambient atmosphere under the same conditions as for the leached NVPF.

Mass Spectroscopy (MS): Mass spectra were recorded for the gas inside the pouch bags collected during the leaching process of Na_1VPF with NaTFSI or $NaPF_6$ for 21 days at 55 °C. The pouch bags with samples containing polypropylene tubes were bulged up due to gassing after 21 days of storage at 55 °C. A needle was pierced to the pouch and the gas was transported to the mass spectrometer via a gastight syringe. The gas samples were then injected into an ExQ gas analysis system (Hiden Analytical, USA) composed of a HAL (Hiden Analytical) series quadrupole mass spectrometer, an ultra-high vacuum (UHV) mass spectrometer vacuum chamber, a vacuum pumping system and a QIC series capillary inlet. The partial pressures are eventually determined for each gas based on their mass to charge ratio (m/z), after ionization in the ionization source of the MS.

Nuclear magnetic resonance (NMR) spectroscopy: The leached NVPF powders were discharged to 2 V (0% state of charge) vs Na metal for solid state NMR analyses. Solid-state ^{31}P and ^{23}Na NMR spectra were recorded on electrode materials with a 4.7 T (200 MHz for ^{1}H) Bruker WB spectrometer equiped with an Avance HD console and a 1.3 mm Magic Angle Spinning (MAS) double resonance ^{1}H-^{19}F/^{31}P-^{15}N probe. The rotors were filled inside an argon filled glovebox and the rotor were spinning at ν_R = 60 kHz under 100% N_2 atmosphere. The solid-state NMR spectra were recorded with a rotor synchronized Hahn echo sequence (90° – 1/ν_R – 180°- 1/ν_R – acquisition), and the chemical shift were referenced with 85% H_3PO_4 in water for ^{31}P and 1 M NaCl in water for ^{23}Na, both at 0 ppm. Full relaxation of the magnetization was achieved with a

50 ms recovery delay between each transient in both case. 1 024 000 transients were recorded for ^{31}P and 10240 for ^{23}Na.

Liquid-state spectra were recorded in the same spectrometer with a double resonance probe equiped with 10 mm inserts, tuned to ^{31}P or ^{51}V. Liquid-state spectra were recorded for all samples inside 5 mm glass tubes filled in the glove box, and sealed with parafilm. An N_2 flow of 500 L/h was sent inside the probe to shield the sample from the air. The spectra were recorded with a 90°-acquisition sequence. 102 400 transients were recorded for ^{31}P (recovery delay 5s) and 1 024 000 transients were recorded for ^{51}V (recovery delay 50 ms).

The presence of HF in the electrolyte was evaluated by ^{19}F liquid-state NMR spectra, recorded in a Bruker 7.046 T (282 MHz for ^{19}F) Advance III NMR spectrometer mounted with a 5 mm HX(F) probehead. The samples were meassured in a 5 mm glass tube equiped with a D_2O-filled inset for signal lock. The spectra were recorded with a 90° adquisition sequence, over 16 scans (5 s adquisition time each) and 10 s recovery delay, and were referenced with the expected signal of the anion (PF_6^- or $TFSI^-$ accordingly).

○ Supplementary Figures

Supplementary Fig. S3.1

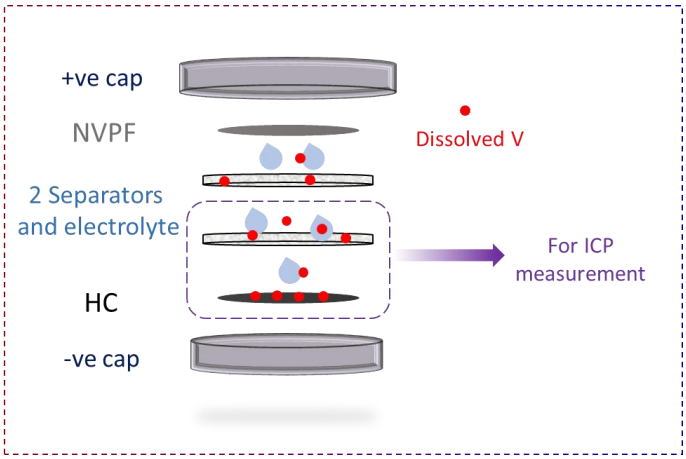

Schematic presenting the collection of HC and separator touching it from the aged cell for ICP measurements.

Supplementary Fig. S3.2

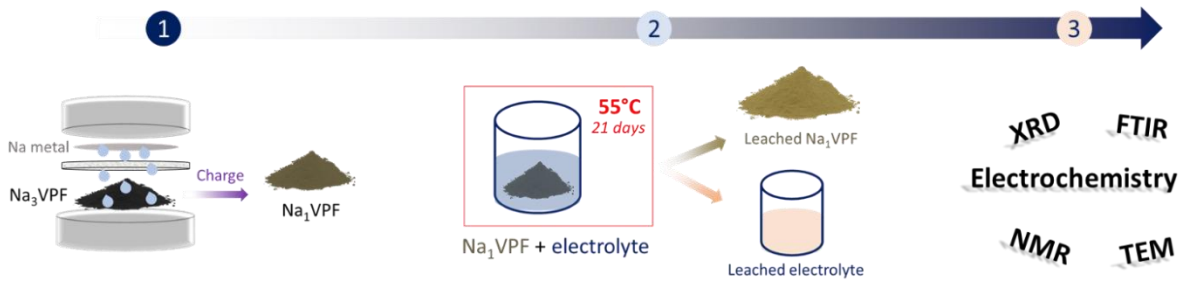

The protocol used to study the leaching of NVPF material with electrolyte/solvents is represented in the above scheme:

1. NVPF ($Na_3V_2(PO_4)_2F_3$) powder is charged to Na_1VPF ($Na_1V_2(PO_4)_2F_3$) in large quantities using 1M $NaPF_6$ in PC electrolyte.

2. 3 mL of the desired electrolyte is mixed with Na_1VPF (~20 mg) in a 15 mL polypropylene vial.

3. The vial is sealed in an aluminum bag inside an argon-filled glovebox.

4. The aluminum bag is transferred to a 55 °C oven and stored for 21 days with periodic shaking every 1-2 days to ensure continuous contact between NVPF particles and electrolyte.

5. After 21 days, the aluminum bag is transferred back to the argon-filled glovebox, and the samples are recovered.

6. The NVPF powder is separated from the electrolyte through centrifugation.

7. The recovered electrolyte is filtered using a 0.2 µm polypropylene syringe filter to ensure the absence of NVPF particles in the electrolyte.

8. The leached Na_1VPF and aged electrolyte are utilized for various electrochemical and chemical characterizations as depicted in the figure.

9. The experiment is performed twice, and the ICP values of V dissolution show good reproducibility, indicating the reliability of the protocol.

Supplementary Fig. S3.3

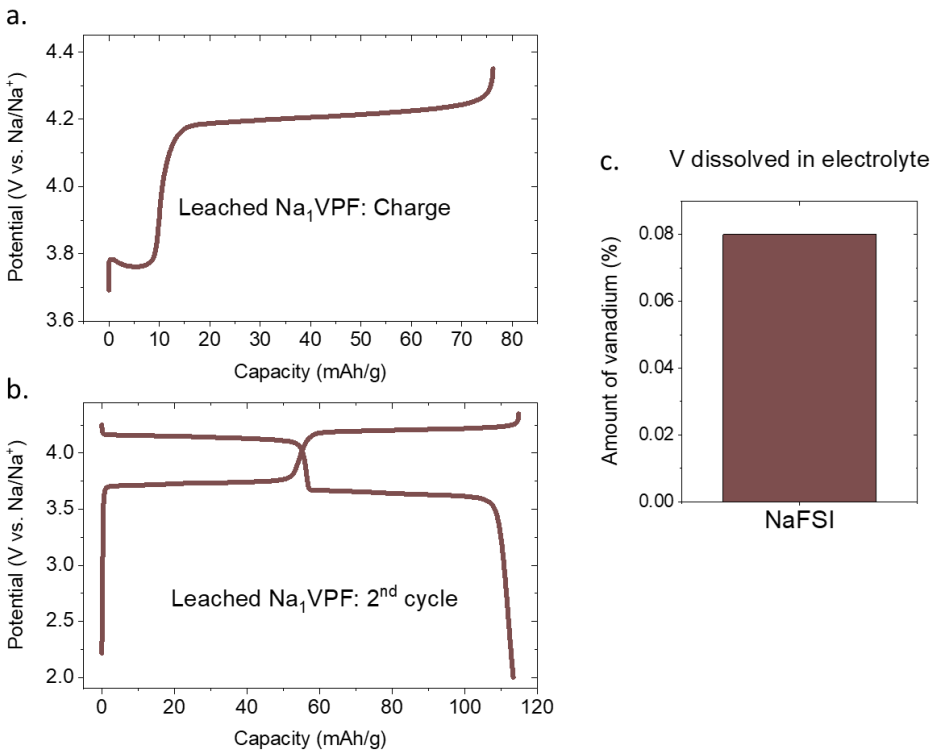

The electrochemical performance and vanadium dissolution of Na_1VPF with 1M NaFSI in EC-PC-DMC for 1 week at 55 °C were examined. The charge of the recovered FSI-NVPF material is depicted in Figure (a), while Figure (b) illustrates the second cycle of FSI-NVPF. It is observed that there is negligible capacity loss in the NVPF material as a consequence of leaching. The vanadium dissolution was analyzed in the recovered electrolyte, and the results are presented in Figure (c). The findings indicate that the vanadium dissolution in the FSI-NVPF system is comparable to that observed for TFSI-NVPF. These results suggest that the leaching behavior and electrochemical performance of Na_1VPF with NaFSI are similar to those observed with NaTFSI.

Supplementary Fig. S3.4

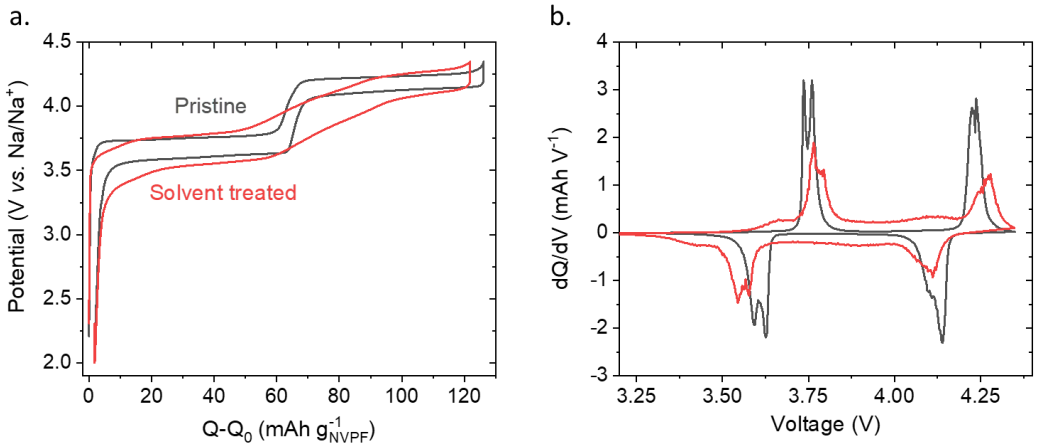

Second cycle charge-discharge curves of pristine NVPF and solvent-treated NVPF (SL-NVPF) in half-cell mode with Na metal as the counter and reference electrode. The electrolyte used was 1M $NaPF_6$ dissolved in PC, and the voltage range was set between 2 to 4.35 V with a C/5 rate. (a) The electrochemical curves reveal a distinct difference between pristine NVPF and solvent-leached NVPF, with the latter exhibiting a sloppy profile compared to the former. (b) The corresponding dQ/dV plot further highlights the deviation in the electrochemical behavior between pristine NVPF and solvent-treated NVPF, confirming the observed differences in the charge-discharge curves.

Supplementary Fig. S3.5

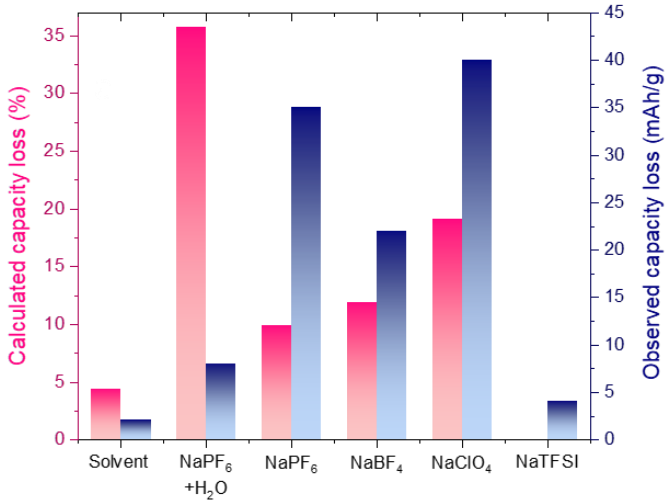

A comparison was made between the observed capacity loss, taken from **Fig. 3.3b** in the main manuscript, and the calculated capacity loss resulting from the measured vanadium loss using ICP-MS from **Fig. 3.2e**. The absence of an apparent relation between the calculated and observed capacity loss suggests the presence of a complicated degradation phenomenon that is specific to the salt used.

Supplementary Fig. S3.6

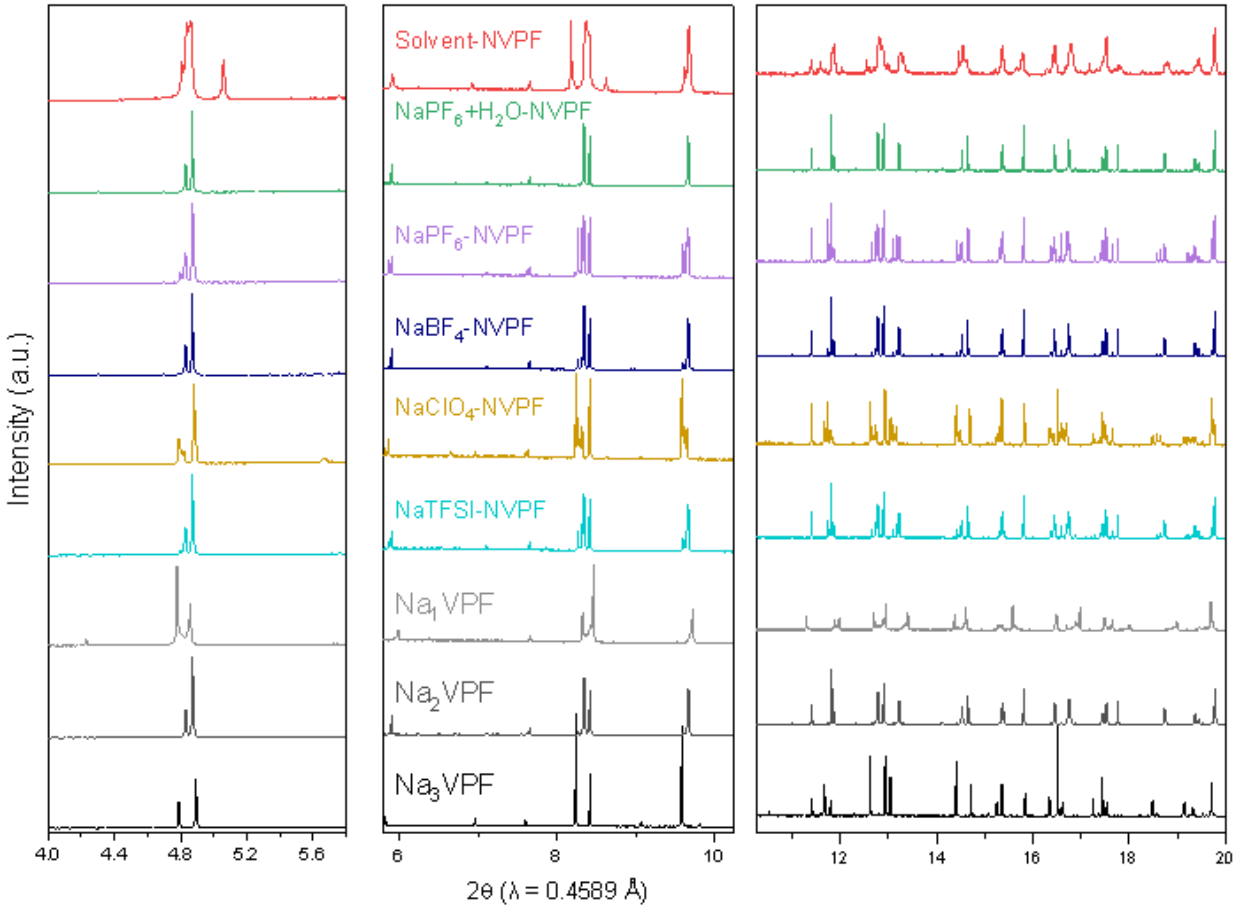

The 11BM synchrotron powder XRD pattern (Cu Kα = 0.4589 Å) for recovered Na_1VPF powders after leaching treatment in the mentioned electrolyte at 55°C for 21 days. The XRD patterns of the unleached samples namely $Na_1V_2(PO_4)_2F_3$, $Na_2V_2(PO_4)_2F_3$ and $Na_3V_2(PO_4)_2F_3$ are presented for comparison.

Supplementary Fig. S3.7

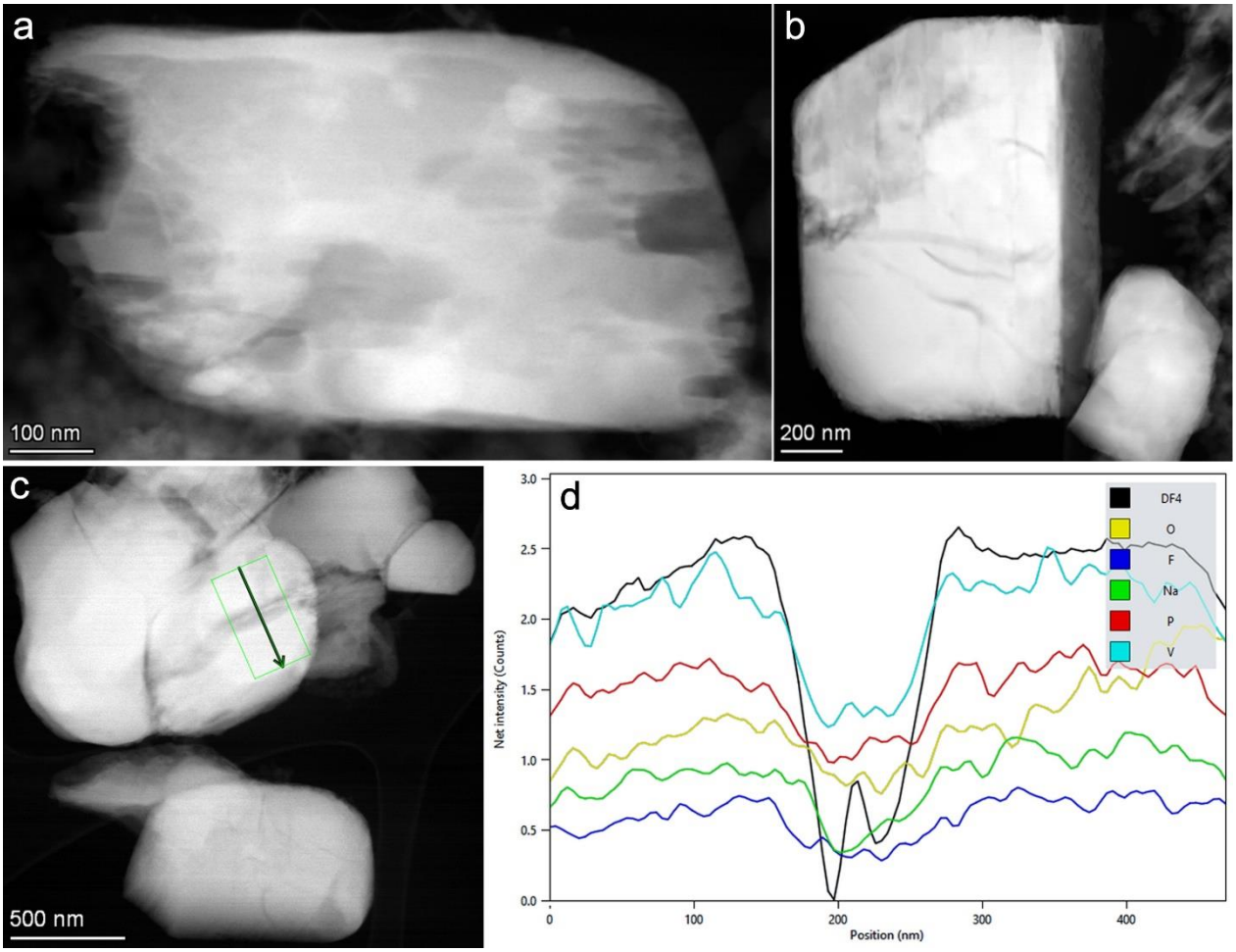

(a,b,c) HAADF-STEM images of crystallites in the SL-NVPF sample demonstrating numerous pits and cracks (look darker). (d) HAADF intensity and EDX signals profiles across a selected pit (green arrow in the image (c)). Drastic decrease of both HAADF and EDX signals indicates a loss of material.

Supplementary Fig. S3.8

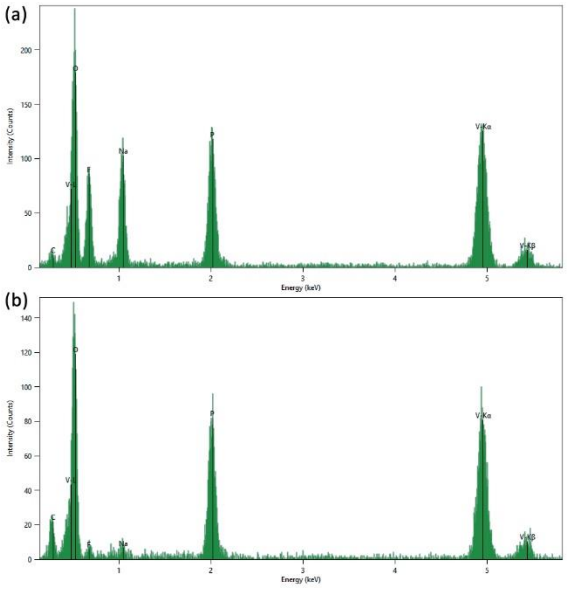

EDX spectra of the SL-NVPF crystal integrated over the areas of the core (a) and shell (b). Note distinctly different Na content. The V/P ratio is the same in both areas.

Supplementary Fig. S3.9

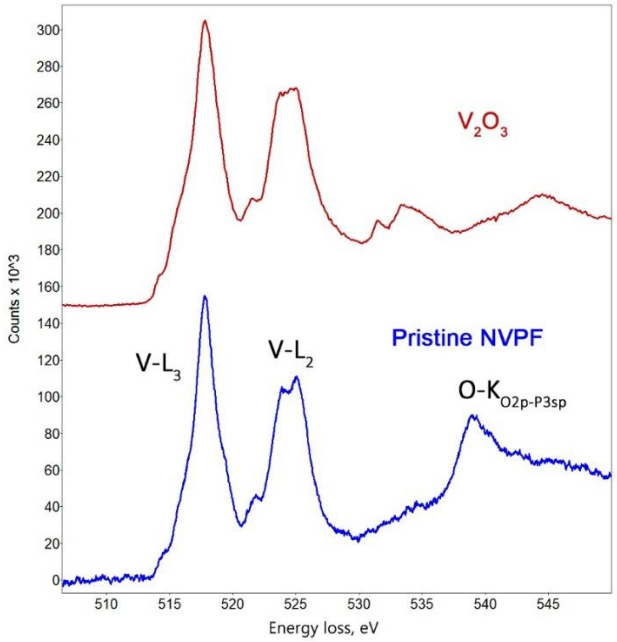

EELS spectra of the pristine NVPF sample and the reference V_2O_3 oxide demonstrating V^{3+} oxidation state in NVPF.

Supplementary Fig. S3.10

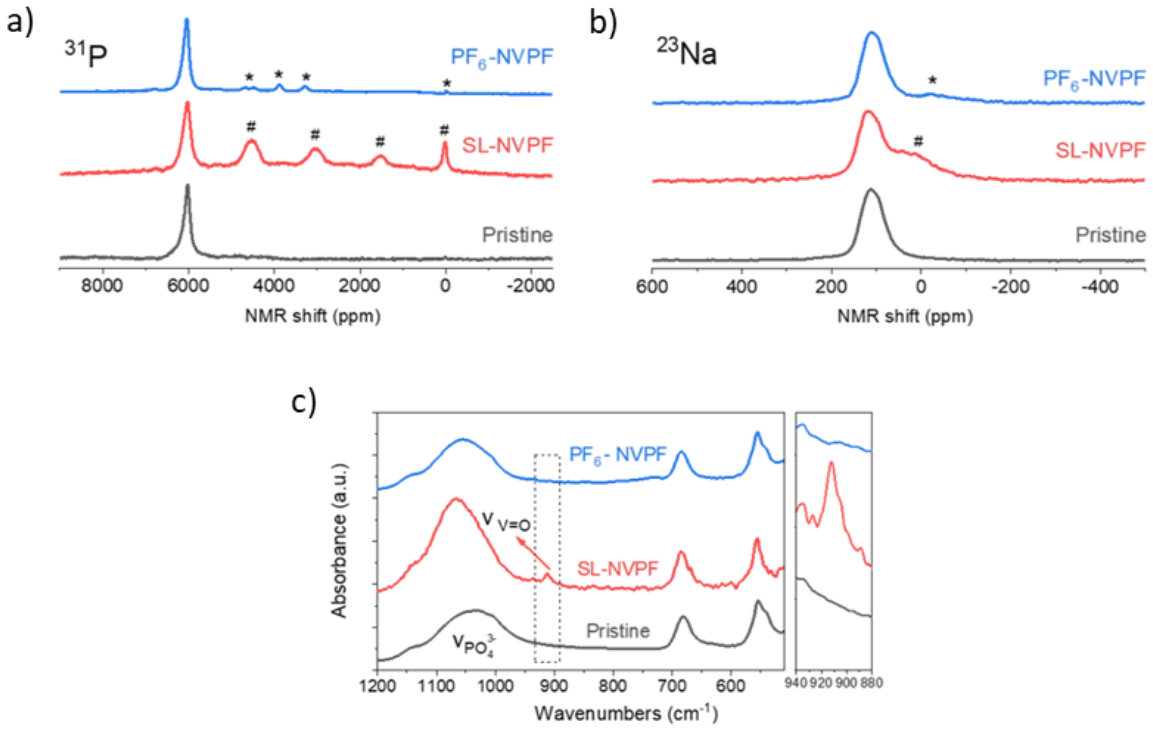

The PF_6- and SL-NVPF was discharged to 2V and compared with pristine NVPF using NMR and IR spectroscopy measurements. Markers on the NMR curves indicate the changes as compared to pristine sample. (a) ^{31}P NMR spectrum of PF_6- , SL- and pristine NVPF in the discharged state. Peaks marked by * for PF_6-NVPF show presence of another phase than NVPF. The peaks appeared at # for SL-NVPF are indication of vanadyl (V=O) type bond[106] (b) ^{23}Na NMR spectrum of PF_6- , SL- and pristine NVPF in the discharged state. SL-NVPF shows broad hump (#) indicating the disorder in the Na position (c) Infrared spectrum of PF_6- , SL- and pristine NVPF in the discharged state. The zoomed area of the marked region is presented for better visualization. The peak appearing at ~912 cm^{-1} for SL-NVPF corresponds to vanadyl (V=O) type bond. [107]

Supplementary Fig. S3.11

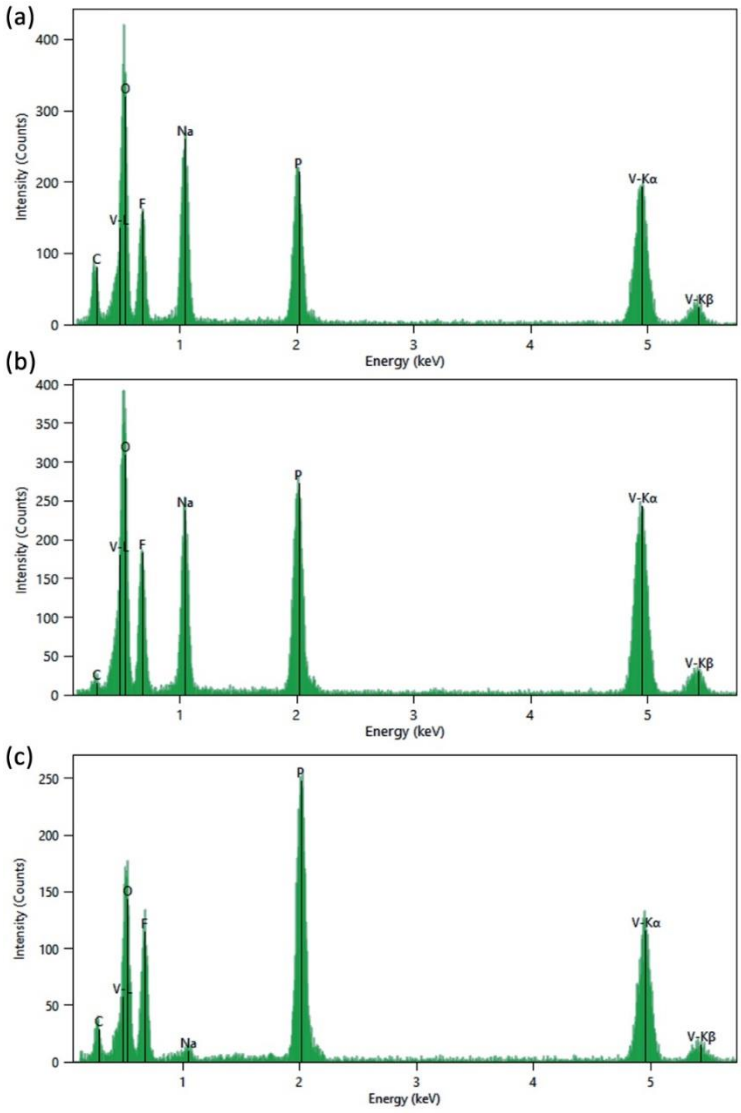

Typical EDX spectra from the Na-rich (a), Na-poor (b) crystallites and V-depleted shell (c) in the PF_6-NVPF sample.

Supplementary Fig. S3.12

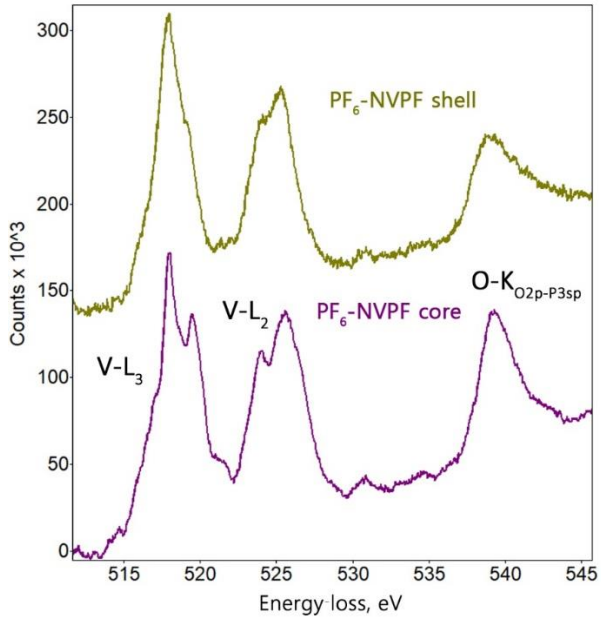

EELS spectra of the core and shell areas of the PF_6-NVPF sample. Note weaker V^{5+} signal at ~519.6 eV in the shell.

Supplementary Fig. S3.13

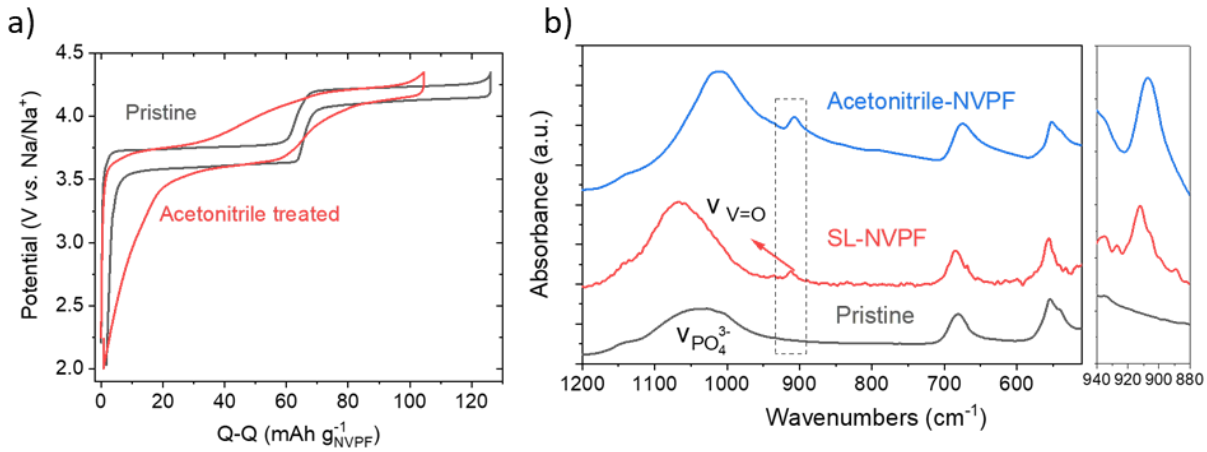

(a) The second cycle charge-discharge curve of pristine NVPF and acetonitrile treated NVPF in half cell mode with Na metal as counter and reference electrode with 1M $NaPF_6$ dissolved in PC between 2-4.35 V at C/5 rate. The acetonitrile leached NVPF showed a sloppy profile similar to solvent leached profile in **Supplementary Fig. S3.4**. (b) IR spectrum of acetonitrile leached NVPF and solvent leached NVPF in a discharged state and pristine NVPF for comparison. Zoomed in part is presented for better visualization of vanadyl (V=O) peak at ~912 cm^{-1} appearing after treatment with carbonate solvents (SL) or acetonitrile.

Supplementary Fig. S3.14

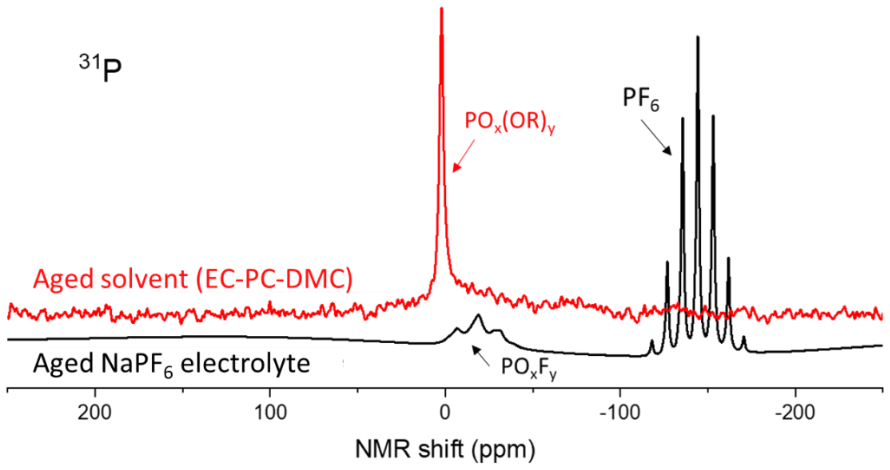

^{31}P NMR spectrum of $NaPF_6$ electrolyte and EC-PC-DMC solvent after reacting with Na_1VPF for 21 days at 55°C. The ^{31}P spectrum of Aged $NaPF_6$ electrolyte shows the signal of PF_6 and fluorophosphates species PO_xF_y, which are also observed in case of electrolyte oxidation of $LiPF_6$ in Li-ion battery electrolyte. $PO_x(OR)_y$ species observed in the "Aged solvent" indicates the structural disintegration of phosphorous or phosphate from the NVPF lattice.

Supplementary Fig. S3.15

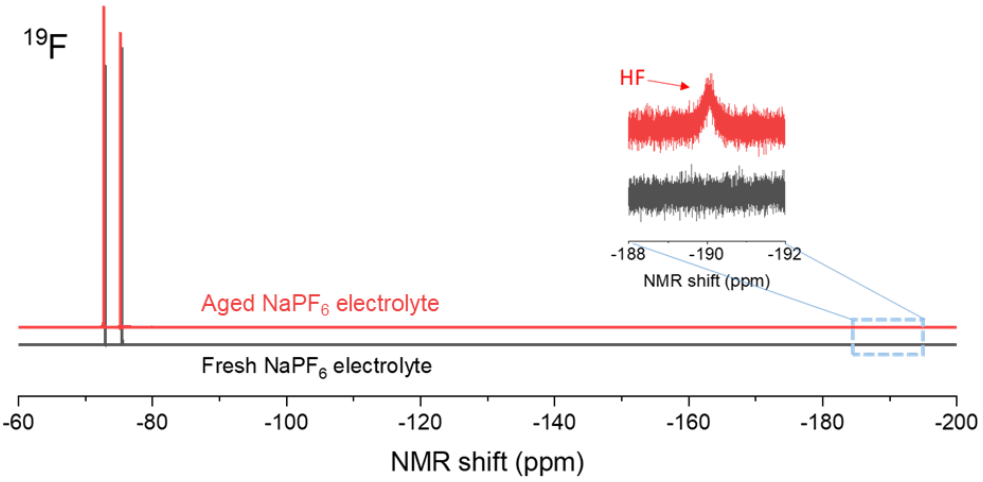

^{19}F NMR spectrum of fresh and aged (obtained after reacting fresh electrolyte with Na_1VPF for 21 days at 55 °C) $NaPF_6$ electrolyte. The peak at -190 ppm indicates the presence of the HF.

Supplementary Fig. S3.16

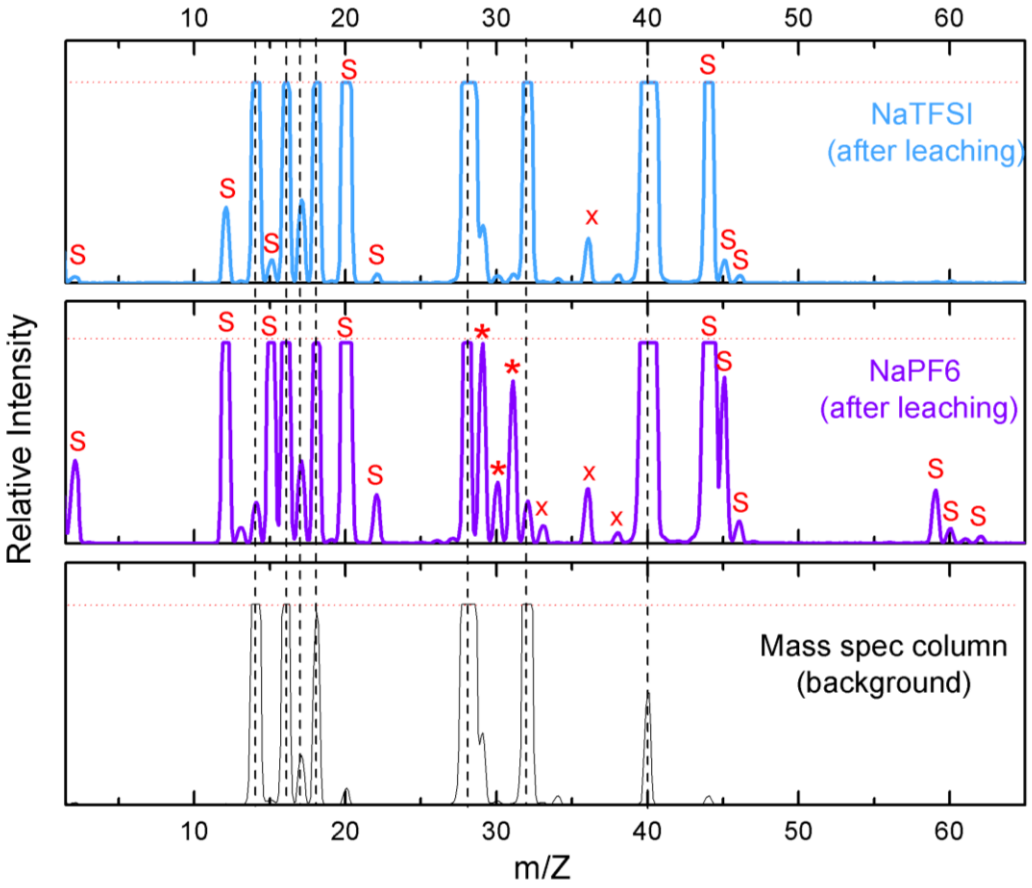

Mass spectra recorded for the gas inside the pouch bags after the leaching process of Na_1VPF with NaTFSI (top) or $NaPF_6$ (middle) for 21 days at 55°C. The pouch bags were bulged due to gassing after 21 days of storage at 55°C. A needle was pierced to the pouch and the gas was transported to the mass spectrometer via a capillary. Since the setup is not leak-proof, there is some quantity of atmospheric gases, for that purpose, the baseline spectra was collected (bottom spectra) to get atmospheric components. The black lines in the figure indicate the peaks due to the gases in column/ capillary. Due to large amount of CO_2, a detection limit is set (shown by red dotted lines in the figure) to facilitate the view of less intense peaks. The peaks due to solvent decomposition is mentioned as 'S' and the peaks that are possible only by solvent oxidation (eg. HCHO) are shown by '*'. The peaks mentioned by 'x' are unidentified peaks. The possible component for the observed ratio m/z of NaTFSI and $NaPF_6$ is presented in Supporting table S2.

Supplementary Fig. S3.17

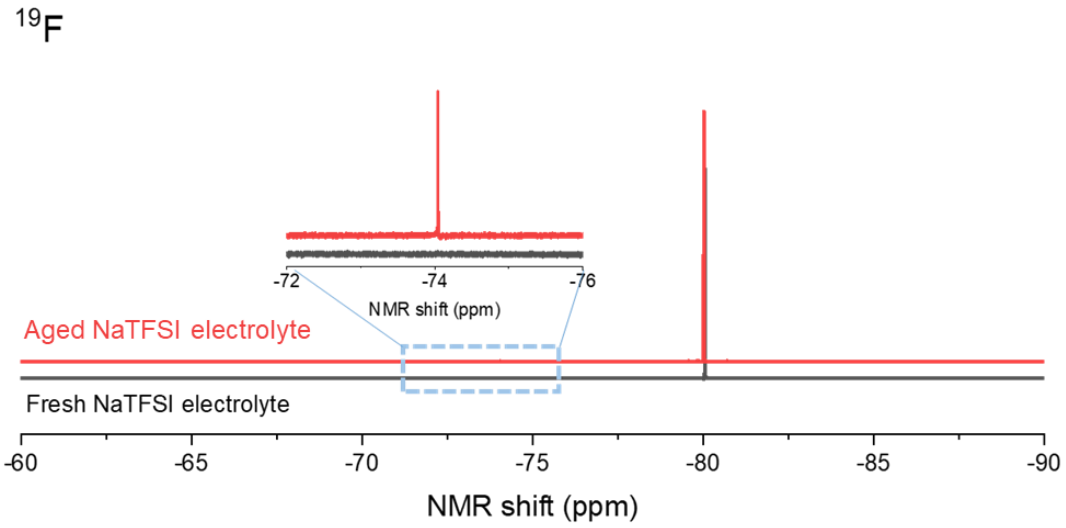

^{19}F NMR spectrum of fresh and aged (obtained after reacting fresh electrolyte with Na_1VPF for 21 days at 55 °C) NaTFSI electrolyte. The peak at -74 ppm is the result of oxidative decomposition of TFSI anion in presence of charged NVPF.

Supplementary Fig. S3.18

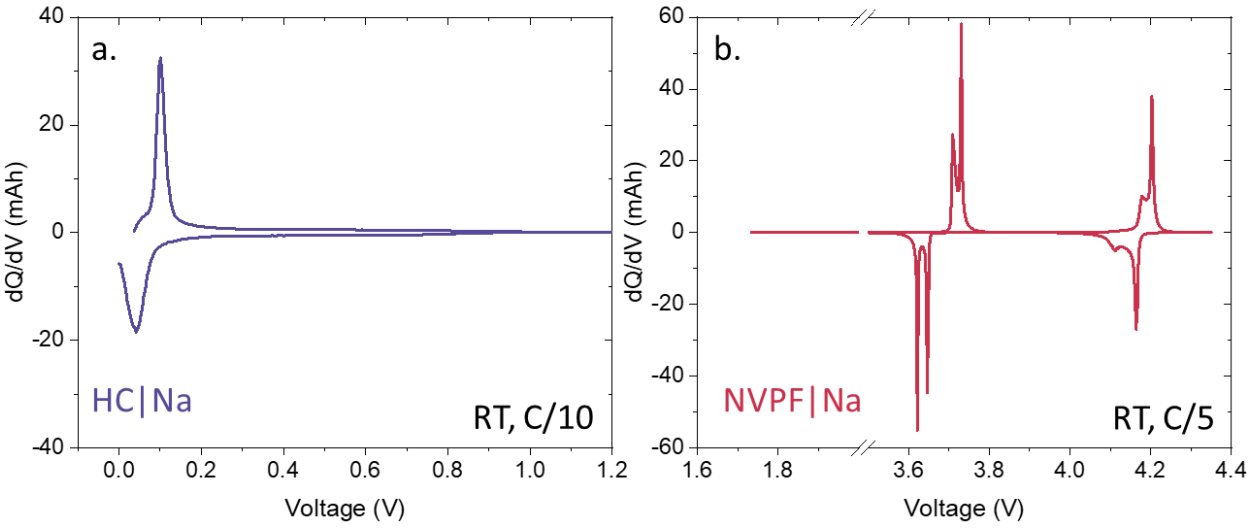

dQ/dV profile for (a) HC|Na cell cycled at C/10 rate and ambient temperature and (b) NVPF|Na half cell cycled at C/10 rate and ambient temperature.

Supplementary Fig. S3.19

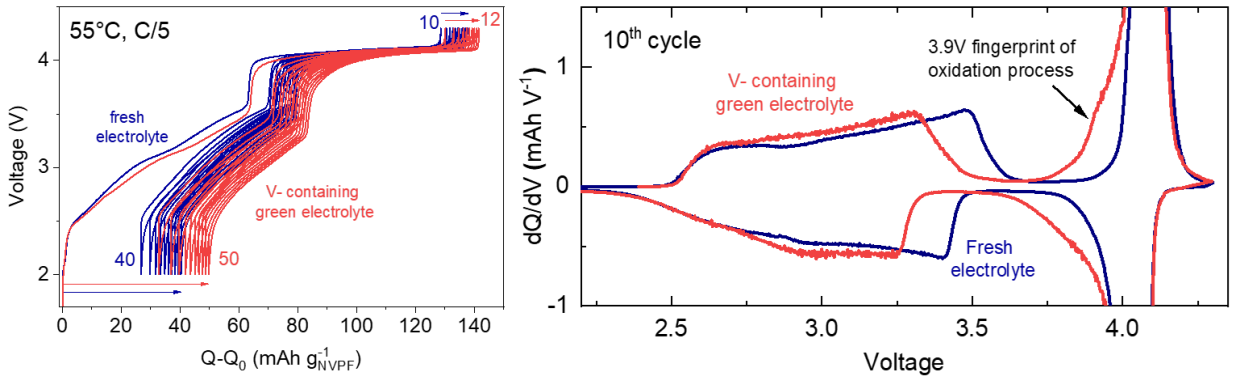

Cumulative charging profile for 10 cycles of NVPF-HC coin cell cycled with fresh (1M $NaPF_6$ in EC-PC-DMC) and vanadium containing green electrolyte. Vanadium containg green electrolyte was prepared by washing the NVPF recovered from 18650 (**Fig. 3.1**) with EC-PC-DMC and adding 1M $NaPF_6$. On the right, dQ/dV of the 10^{th} cycle with the fresh and green electrolyte indicating the green electrolyte shows the 3.9 V fingerprint.

Supplementary Fig. S3.20

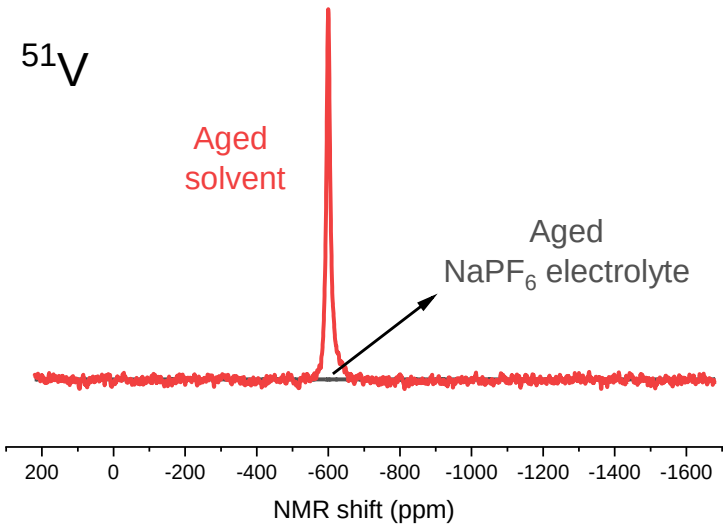

^{51}V NMR spectrum of aged $NaPF_6$ electrolyte and aged solvent (obtained after reacting with Na_1VPF for 21 days at 55°C). ^{51}V NMR is sensitive to only V^{5+}, indicating the presence of V^{5+} in leached solvent and absence of V^{5+} in leached $NaPF_6$.

Supplementary Fig. S3.21

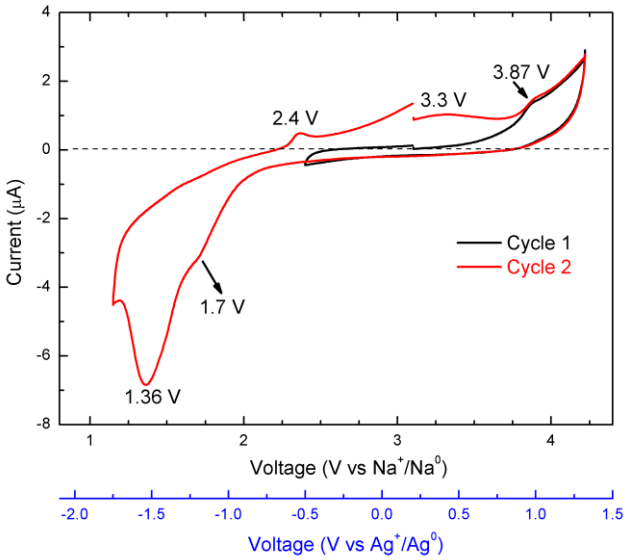

Three-electrode cyclic voltammetry of aged $NaPF_6$ electrolyte. The potential window was increased from 2.2-4.3V vs. Na^+/Na^0 in first cycle to 1-4.3 V vs. Na^+/Na^0. For cyclic voltammetry glassy carbon as working electrode, Pt wire as counter electrode and Ag/Ag^+ organic reference electrode is used.

Supplementary Fig. S3.22

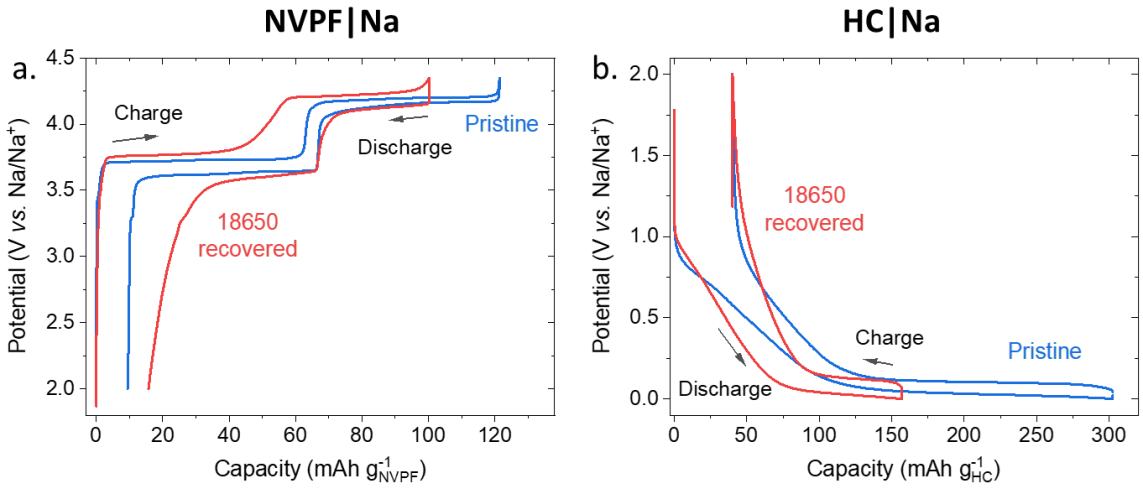

Half cell profile for the pristine and aged electrodes recovered from the 18650 shown in **Fig. 3.1.** (a) NVPF|Na cells and (b) HC|Na cells. Note that the part of the capacity loss of the aged electrodes could be from the dedweight of degraded products.

Supplementary Fig. S3.23

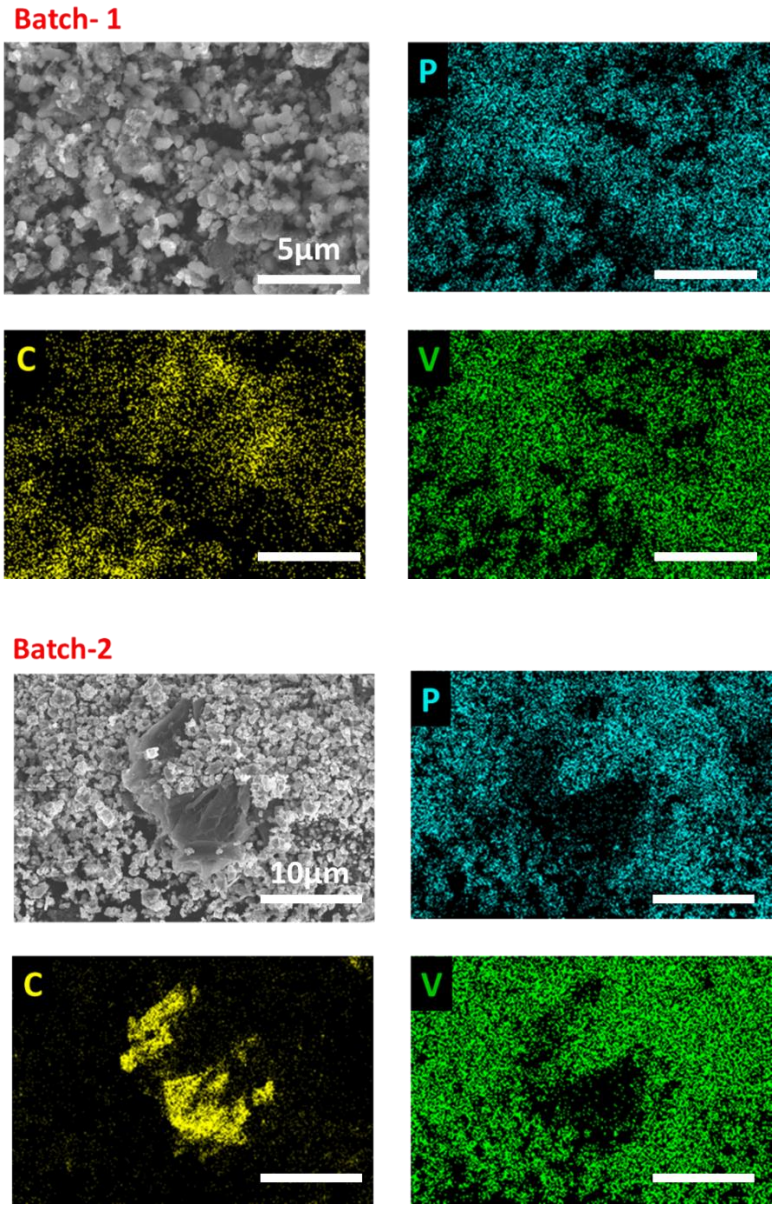

SEM and EDX mapping of phosphorous, carbon and vanadium for batch-1 and batch-2 of NVPF. Batch-1 NVPF had more carbon amount than batch-2 NVPF which is also reflected in the EDX carbon mapping represented. Additionally batch-2 NVPF had chunks of carbon with less homogenous coating.

Table S3.1

$Na_2V_2(PO_4)_2F_3$ Space group *Immm* *a* = 6.311646(6) Å, *b* = 6.318539(6) Å and *c* = 10.817618(11) Å; Vol = 431.411(2) Å^3						
Atom	Wyckoff site	x	y	z	Biso (Å^2)	Occ
P	4*j*	0	1/2	0.2501(2)	0.499(17)	1
V	4*i*	0	0	0.18007(5)	0.500(11)	1
O1	8*l*	0	0.3052(3)	0.1657(3)	1.094(19)	1
O2	8*m*	0.3054(3)	0	0.8342(3)	1.094(19)	1
F1	4*i*	0	0	0.64459(15)	1.172(19)	1
F2	2*a*	0	0	0	1.172(19)	1
Na	8*n*	0.3040(4)	0.3017(4)	0	2.19(7)	0.489(12)

Crystal structure of the PF6-H_2O-NVPF deduced from the Rietveld refinement of its synchrotron XRD pattern.

Table S3.2

m/z	Intensity from possible components
1	H^+
2	H_2^+
12	$^{12}C^+$
13	$^{13}C^+$ / $^{12}CH^+$
14	$^{14}N^+$ / $^{14}C^+$ / $^{12}CH_2^+$
15	$^{12}CH_3^+$
16	O^+
17	HO^+
18	H_2O^+
19	H_3O^+
20	$^{40}Ar^{++}$
22	CO_2^{++}
26	$C_2H_2^+$
27	$C_2H_3^+$
28	$N_2^+/C_2H_4^+/CO^+$
29	$^{14}N^{15}N^+/^{12}C^{13}CH_4^+/^{13}CO^+$ / CHO^+
30	CH_2O^+
31	CH_3O^+
32	O_2^+ / CH_4O^+
33	Fragmentation pattern from DMC ($C_3H_6O_3$)
34	Fragmentation pattern from DMC ($C_3H_6O_3$)
36	$^{36}Ar^{++}$
38	$^{38}Ar^{++}$
40	$^{40}Ar^{++}$
44	CO_2^+
45	$^{13}CO_2^+$
46	$^{14}CO_2^+$
59	$^{12}C_2H_3O_2^+$
60	$^{12}C_2H_4O_2^+$
61	$^{13}C_2H_3O_2^+$
62	$^{13}C_2H_4O_2^+$
90	$C_3H_6O_3^+$

Possible fragmentation components for the observed mass spectra (presented in **Supplementary Fig. S3.17**) recorded for the gas inside the pouch bags after the leaching process of Na1VPF with NaTFSI (top) or $NaPF_6$ (middle) for 21 days at 55°C. Apart from the baseline gases (Ar, N_2, O_2, etc. from atmosphere), the fragments possibly originate from DMC solvent, CO_2, CO, CH_4, C_2H_4, CH_2O, CH_4O, etc.

S-4 Supplementary Information for Chapter 4

o Methods

Electrolyte Preparation: All the electrolytes were prepared by dissolving one molar $NaPF_6$ (Stella, Japan) in battery grade solvents (DoDochem, China) in the Ar-filled glovebox (MBraun MB200B). The solvent mixture EC- PC- DMC in 1: 1: 1 volume ratio was dried by molecular sieves (4 Å, Sigma-Aldrich) till its water content lower than 5 ppm, confirmed by Karl-Fisher titration (Metrohm 899 coulometer). The additive NaODFB is prepared in-house as reported earlier and other additives Vinylene carbonate (TCI, Europe), Succinonitrile (Acros Organics), and Tris(trimethylsilyl) Phosphite (TCI, Europe) were purchased and used as such, except succinonitrile which is melted at 70 °C and weighed in liquid state.

Electrochemical testing of NVPF/HC coin cells: $Na_3V_2(PO_4)_2F_3$ and hard carbon coated on Al foil were received from Tiamat, France. NVPF and HC mass loading was roughly ~12 $mg.cm^{-2}$ and ~6 $mg.cm^{-2}$, respectively. Active material: PVDF binder: conductive carbon for NVPF and HC was 94:3:3. The electrodes were specially coated only on one side of the Al foil for conducting the studies in coin cells, however they are designed to have exact mass loading as in cylindrical 18650 cells. The electrode thickness, active material to conducting carbon and binder ratio, porosity etc were maintained the same as in 18650 cells. All of the electrodes were dried in a Buchi oven under vacuum (lower than 100 mbar) at 80° C for 12 h prior to being transferred into the glovebox. The electrochemical performance of NVPF/HC full cells were evaluated in 2032- type coin cells separated by two layers of glass fiber containing 150 µL of desired electrolytes. All cells were galvanostatically cycled by using MPG2 potentisostat or BCS battery cycler (Bio-Logic, France) at 55 °C, and the cycling rates were calculated with respect to NVPF (1C = 128 mA g^{-1}).

Sensing and Electrochemical testing of NVPF/HC cylindrical 18650 cells: Hermetically sealed NVPF/HC cylindrical 18650 cells without electrolyte were received from Tiamat, France. A 0.8 mm diameter hole was drilled into the negative pole of the dry, 18650 cells. The position was selected according to the welding point of the negative current collector, which was close to the center of the negative pole. This choice of the position helped in avoiding destruction of the jelly roll and

in preventing the strain interaction between the FBG sensors and the jelly roll. All of the 18650 cells were dried in Buchi oven under vacuum at 80 °C for 12 h prior to being transferred into the glovebox. The 18650 cells were then filled with 5.5 mL of desired electrolyte inside the glovebox. Then the FBG sensors were inserted into the central void of the jelly roll through the drilled hole using a needle. The interface between the needle containing the FBG sensor and the 18650 cell was subsequently sealed with an epoxy that was cured for 24 h; all processes were performed inside the glove box whose O_2 and H_2O content was maintained less than 0.1 ppm. Cells were cycled using BCS battery cycler (Bio-Logic, France) by keeping the cells inside an oven at 55 °C, and the cycling rates were calculated on the basis of NVPF material (1C = 128 mA g^{-1}). Sensors were connected to FBGuard1550 (Safibra) or LUNA Si255 (Micron Optics) interrogator via optical fibres. The sampling period of the interrogator was set to 1 s. According to the mentioned specifications, wavelength accurcy of the interrogators is 1pm. The FBGs were purchased from SAMYON and calibrated before use.

Calibration of FBG sensors: The temperature calibration of the FBG sensors was conducted in the temperature ovens (IPP110, Memmert) after being inserted into the 18650 cells, from 55 °C to 45 °C in 5°C increments. The thermal rate constant, k_T, was then linearly fitted according to the equation, $\Delta\lambda_B = k_T \Delta T$ with $\Delta\lambda_B$ and ΔT being the Bragg wavelength shift and the temperature change, respectively.

Calibration of optical sensing calorimetry: According to the zero-dimensional thermal model (see **Fig. S4.2a** in the Supporting Information), the heat generation rate of the cell, $\dot{Q}$, can be calculated by

$$\dot{Q} = MC_P \frac{dT}{dt} + \dot{q} \quad (1)$$

where M is the mass of the cell, C_P is cell's specific heat capacity, T is the spatially average temperature of the cell, and t is the time, and $\dot{q}$ is the heat dissipation rate of the cell to the environment. T is estimated according to the geometry, the internal and the surface temperatures of the cell, see the details of the previous study[244]. The thermal model also gives

$$\dot{q} = \frac{T_{surface} - T_{ambient}}{R_{out}} \quad (2)$$

where $T_{surface}$ and $T_{ambient}$ are the temperatures at the surface of the cell and the ambient environment, respectively, and R_{out} is the equivalent thermal resistance between the cell's surface and the ambient. To calculate the $\dot{Q}$ in real time, we determined the intrinsic parameters (MC_P and R_{out}) by applying an alternative galvanostatic pulse at a frequency of 2 Hz to the cell for producing known $\dot{Q}$ (see **Fig. S4.2b** in the Supporting Information), zoomed view of the pulse is presented on the right part of **Fig. S4.2b** (in the Supporting Information). Namely, because the sum of the reversible entropy terms over a cycle is zero, we calculated $\dot{Q}$ by the equation, $\dot{Q} = \oint_{Cycle} IV$, where the voltage (*V*) and the current (*I*) were recorded by the potentiostat. Together with the temporal temperature data, R_{out} can be determined during the steady state (when $\frac{dT}{dt} = 0$ and thus $\dot{Q} = \dot{q}$, see **Fig. S4.2c** in the Supporting Information) by $R_{out} = \frac{T_{surface} - T_{ambient}}{\dot{q}}$ from Equation (2). In addition, MC_P was then calculated in the transient state (**Fig. S4.2c** in the Supporting Information) by linearly fitting $\dot{Q} - \dot{q} = MC_P \frac{dT}{dt}$ from Equation (1), where $\dot{q}$ was computed by the determined R_{out} and Equation (2). Afterwards, we could derive $\dot{Q}$ under any electrochemical conditions according to Equations (1) and (2) by the operando temperature data and the pre-determined MC_P and R_{out}.

Operando pressure monitoring via optical sensors: In order to examine the operando pressure accumulation in different electrolyte formulae, we simultaneously inserted a FBG in a single-ring suspended microstructured optical fiber (MOF-FBG) with a high pressure sensitivity ($k_{P,MOF}$) of -2.7 pm bar^{-1} and a FBG in a single-mode fiber (SMF-FBG) with a low pressure sensitivity ($k_{P,SMF}$) of -0.3 pm bar^{-1} into the 18650, see more details in our previous work[244]. Due to the remarkable pressure sensitivity of MOF-FBG, the pressure change (ΔP) can be calculated as follows[244].

$$\Delta P = \frac{k_{T,SMF}\Delta\lambda_{B,MOF} - k_{T,MOF}\Delta\lambda_{B,SMF}}{k_{T,SMF}k_{P,MOF} - k_{T,MOF}k_{P,SMF}} \quad (3)$$

where $k_{T,SMF}$ and $k_{T,MOF}$ are the thermal rate constants of SMF-FBG and MOF-FBG, respectively, and $\Delta\lambda_{B,SMF}$ and $\Delta\lambda_{B,MOF}$ are the Bragg wavelength shifts of SMF-FBG and MOF-FBG, respectively

Electrochemical testing of NVPF and HC symmetric cell: Two NVPF-HC full cells with the same electrolyte were assembled in CR-2032 type coin cells inside an Ar-filled glovebox. Both the cells were cycled for one cycle to complete the formation of the cell. Then one of the two cells was charged to 4.3 V (constant current CC mode) and kept at 4.3 V (constant voltage CV mode) for 12 hours, another cell was kept at 2 V (CC- CV). Both the cells were removed from the cycler at the same time and then decrimped inside the glovebox. The NVPF and HC electrodes removed from cell discharged to 2 V is used as +ve NVPF ($Na\sim_3V_2(PO_4)_2F_3$) and -ve HC (de-sodiated HC). Similarly, NVPF and HC removed from cell charged to 4.3 V is used as -ve NVPF ($Na\sim_1V_2(PO_4)_2F_3$) and +ve HC (sodiated HC). The +ve NVPF/-ve NVPF and +ve HC/-ve HC symmetric cells were assembled using the aforementioned electrode with the electrolyte formulation which was used in full cells to get these electrodes. The cells were cycled at room temperature at C/5 rate. All cells were duplicated and the results were compared only when the reproducibility was assured.

Online electrochemical mass spectrometry: Slurries comprising either 90 wt% of NVPF, 5 wt% of conductive carbon SC65, and 5 wt% of PVdF binder, or 80 wt% of HC, 10 wt% of conductive carbon SC65, and 10 wt% of PVdF binder were cast on an Al mesh and subsequently punched into electrode discs of 13 mm in diameter. In-house designed OEMS full cells were assembled in an Ar-filled glovebox with both H_2O and O_2 contents less than 0.1 ppm, using an NVPF disc as cathode, one piece of Whatman GF/D glassfibre as separator, an HC disc as anode, and 150 µL of Na-based electrolyte. The cells were cycled between 1.8 – 4.3 V inside a temperature chamber at 55 °C using a current density of 12.8 mA g^{-1}. H_2, CO_2, and C_2H_4 amounts were quantitatively measured by a quadrupole mass spectrometer (Pfeiffer, Switzerland), where the technical details can be found elsewhere[267].

○ Supplementary Figures

Supplementary Fig. S4.1

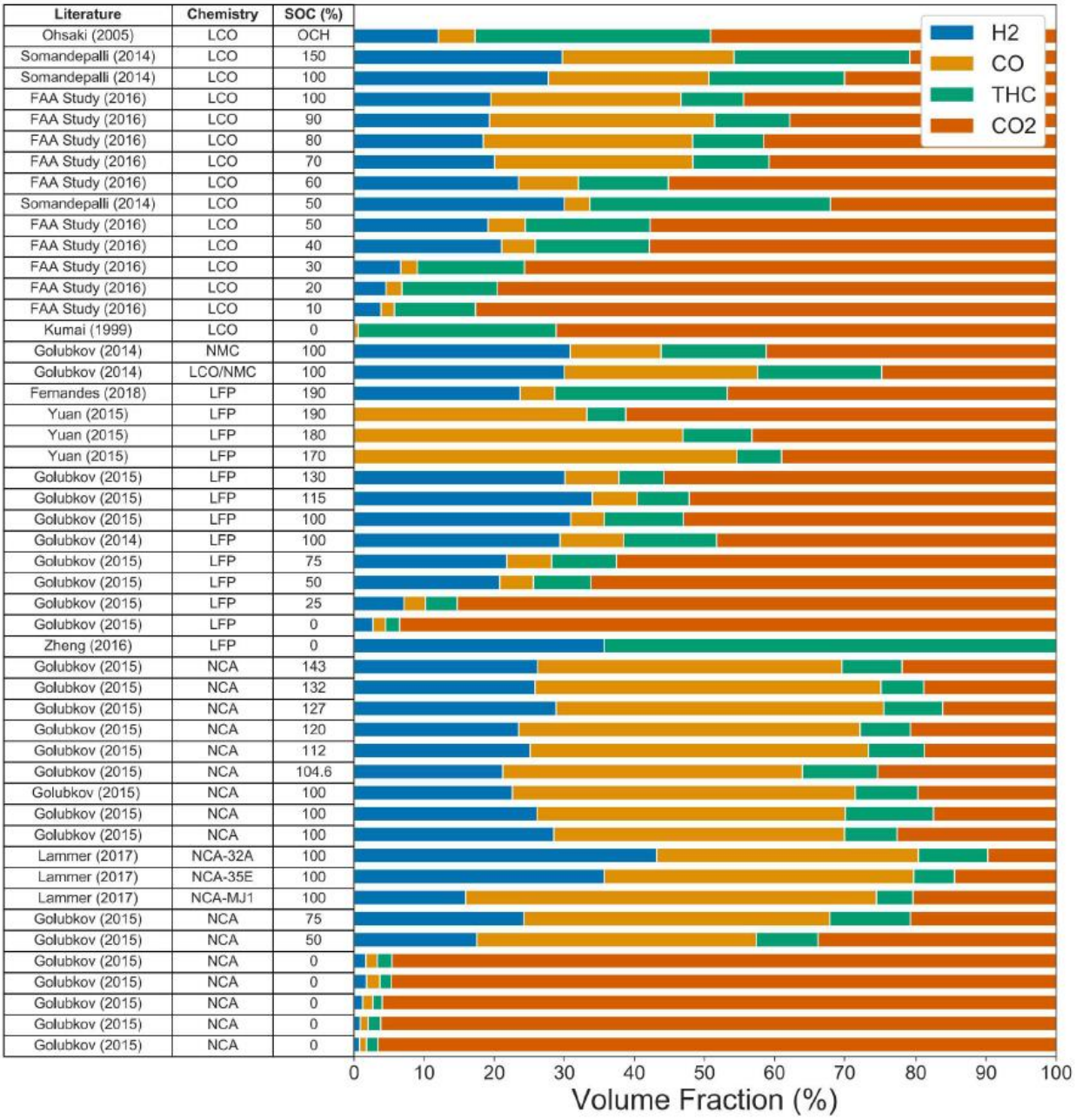

Literature	Chemistry	SOC (%)
Ohsaki (2005)	LCO	OCH
Somandepalli (2014)	LCO	150
Somandepalli (2014)	LCO	100
FAA Study (2016)	LCO	100
FAA Study (2016)	LCO	90
FAA Study (2016)	LCO	80
FAA Study (2016)	LCO	70
FAA Study (2016)	LCO	60
Somandepalli (2014)	LCO	50
FAA Study (2016)	LCO	50
FAA Study (2016)	LCO	40
FAA Study (2016)	LCO	30
FAA Study (2016)	LCO	20
FAA Study (2016)	LCO	10
Kumai (1999)	LCO	0
Golubkov (2014)	NMC	100
Golubkov (2014)	LCO/NMC	100
Fernandes (2018)	LFP	190
Yuan (2015)	LFP	190
Yuan (2015)	LFP	180
Yuan (2015)	LFP	170
Golubkov (2015)	LFP	130
Golubkov (2015)	LFP	115
Golubkov (2015)	LFP	100
Golubkov (2014)	LFP	100
Golubkov (2015)	LFP	75
Golubkov (2015)	LFP	50
Golubkov (2015)	LFP	25
Golubkov (2015)	LFP	0
Zheng (2016)	LFP	0
Golubkov (2015)	NCA	143
Golubkov (2015)	NCA	132
Golubkov (2015)	NCA	127
Golubkov (2015)	NCA	120
Golubkov (2015)	NCA	112
Golubkov (2015)	NCA	104.6
Golubkov (2015)	NCA	100
Golubkov (2015)	NCA	100
Golubkov (2015)	NCA	100
Lammer (2017)	NCA-32A	100
Lammer (2017)	NCA-35E	100
Lammer (2017)	NCA-MJ1	100
Golubkov (2015)	NCA	75
Golubkov (2015)	NCA	50
Golubkov (2015)	NCA	0
Golubkov (2015)	NCA	0
Golubkov (2015)	NCA	0
Golubkov (2015)	NCA	0
Golubkov (2015)	NCA	0

Battery Vent Gas Species Compositions from Literature with main gases as H_2, CO, CO_2 and the hydrocarbons.

Supplementary Fig. S4.2

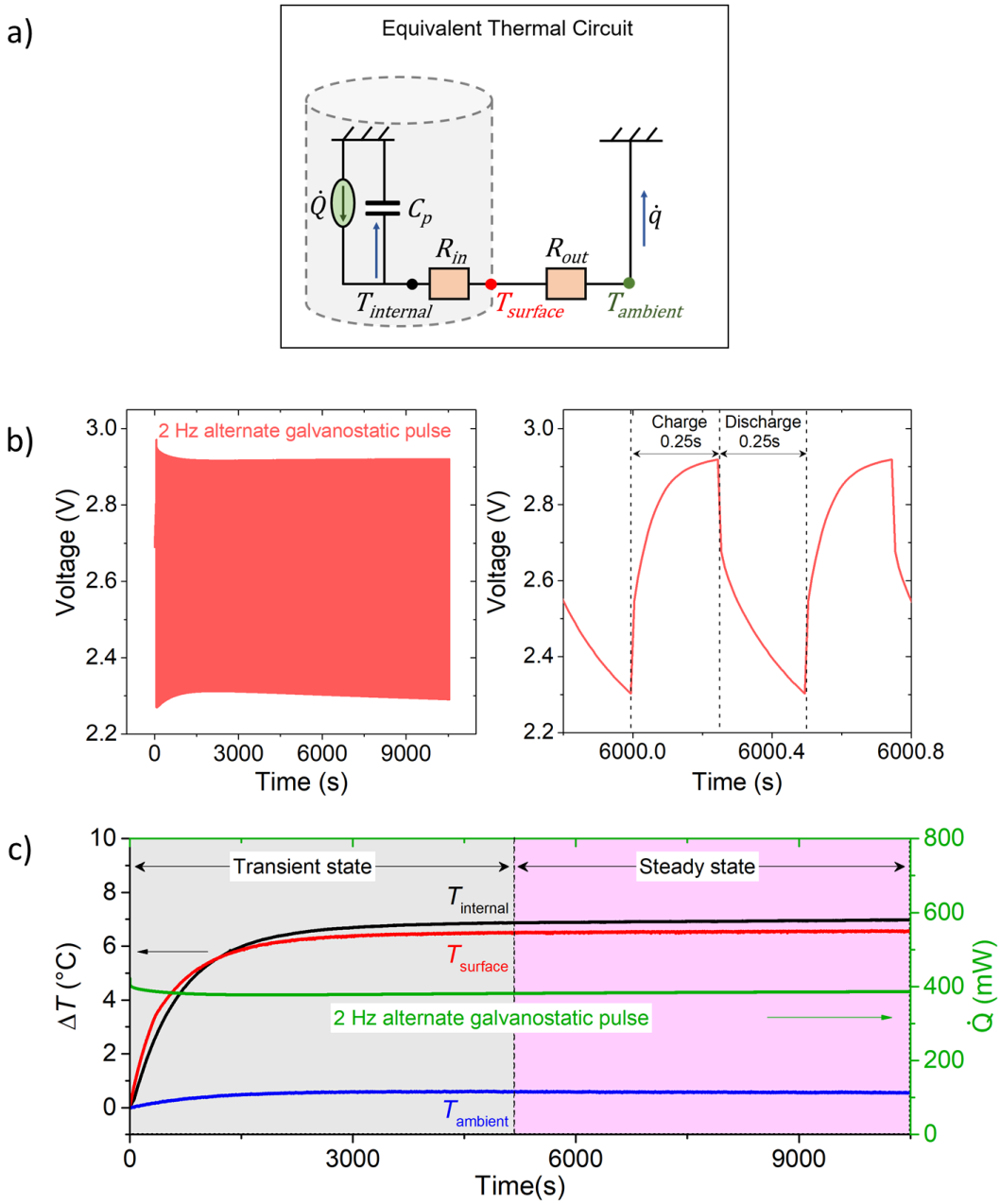

a) Thermal equivalent circuit for zero dimensional thermal model used for sensing calorimetry. b) The voltage *vs.* time behavior of NVPF/HC cylindrical 18650 cell during the alternative galvanostatic pulse at a frequency of 2 Hz is shown for the complete data (b, left) and for one full cycle (b, right). Applied current gives the rate of heat generation ($\dot{Q}$) and is calculated as $\dot{Q} = \oint_{Cycle} IV$. c) Thermal response corresponding to the applied galvanostatic pulse for ambient, surface and internal sensors. Temperature response is divided into transient state and steady state. R_{out} is determined from steady state and then MC_P (~38 J K^{-1}) is calculated from the transient state (See *Calibration of optical sensing calorimetry* in Experimental Procedure for details).

Supplementary Fig. S4.3

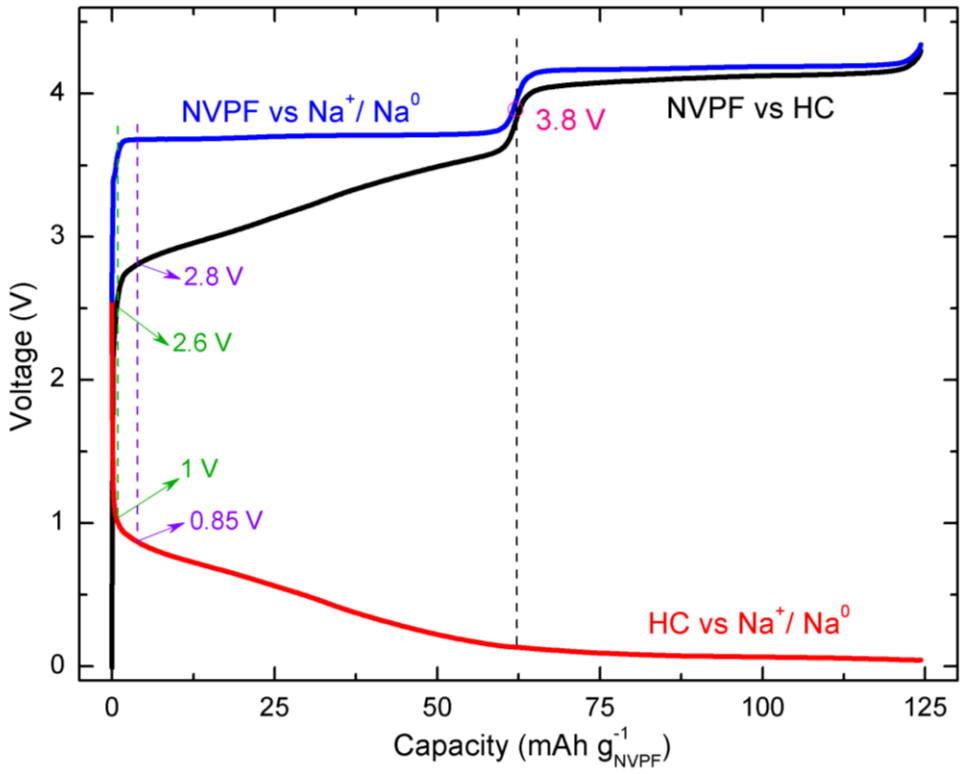

The three electrode cycling data of NVPF/HC cell where the cell was cycled using NVPF and HC as positive and negative electrodes respectively while a piece of sodium metal is used as the reference electrode. The black curve shows the potential evolution of the NVPF/HC cell as a function of capacity whereas blue and red curves represent the corresponding potential of individual electrodes (NVPF and HC) measured against sodium metal. For example, 2.6 V and 2.8 V in the NVPF/HC full cell nearly corresponds to 1 V and 0.85 V of HC versus Na. Similarly, the 3.8 V in NVPF/HC cell corresponds to 1 sodium removal from NVPF. The capacity is measured with respect to the active material weight of NVPF.

Supplementary Fig. S4.4

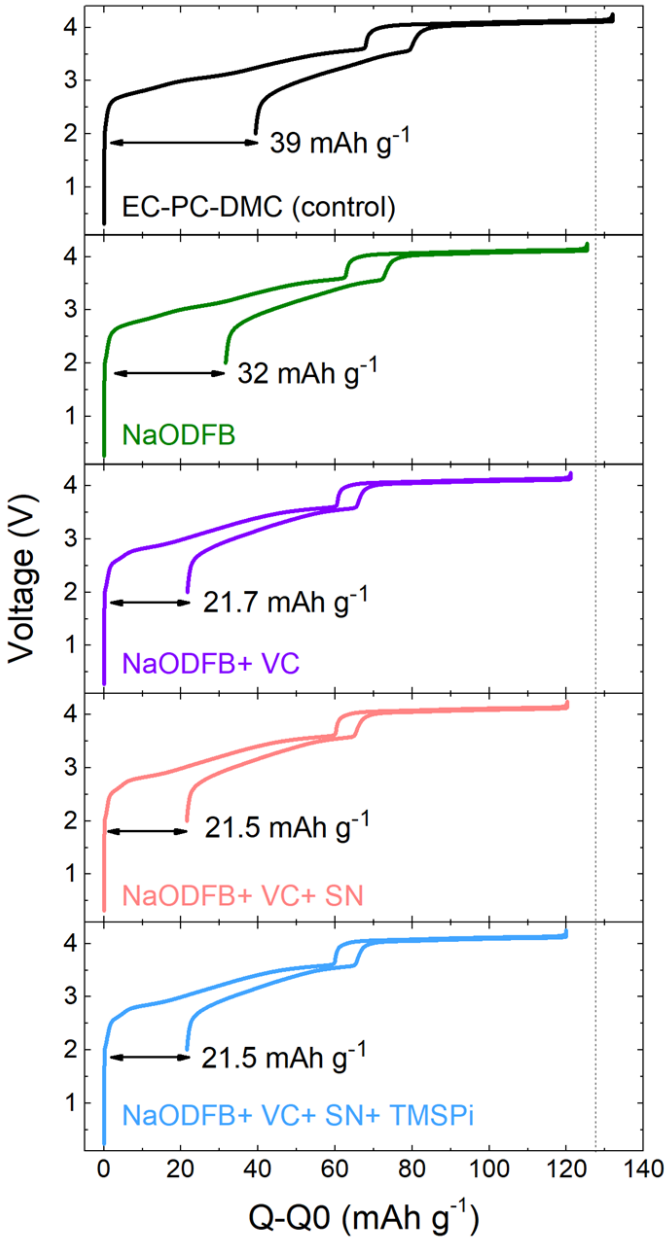

The 1st cycle data of NVPF/HC cylindrical 18650 cells used for the sensing studies. Minimum 2 cells were assembled for each electrolyte formulation and the cells are kept in 55 °C oven and cycled at C/10 rate. The electrolyte studied are the control electrolyte (1 M $NaPF_6$ in EC- PC- DMC 1: 1: 1 by volume) with no additive or having additives namely 0.5 wt% NaODFB, 0.5 wt% NaODFB+ 3 wt% VC, 0.5 wt% NaODFB+ 3 wt% VC+ 3 wt% SN and 0.5 wt% NaODFB+ 3 wt% VC+ 3 wt% SN+ 0.2 wt% TMSPi respectively. The mentioned additive combinations are blended in control electrolyte and named using the additives present in that specific electrolyte formulation. The first cycle irreversible capacities are mentioned in the figures. The dotted line in the figure indicates the theoretical capacity limit of the cell.

Supplementary Fig. S4.5

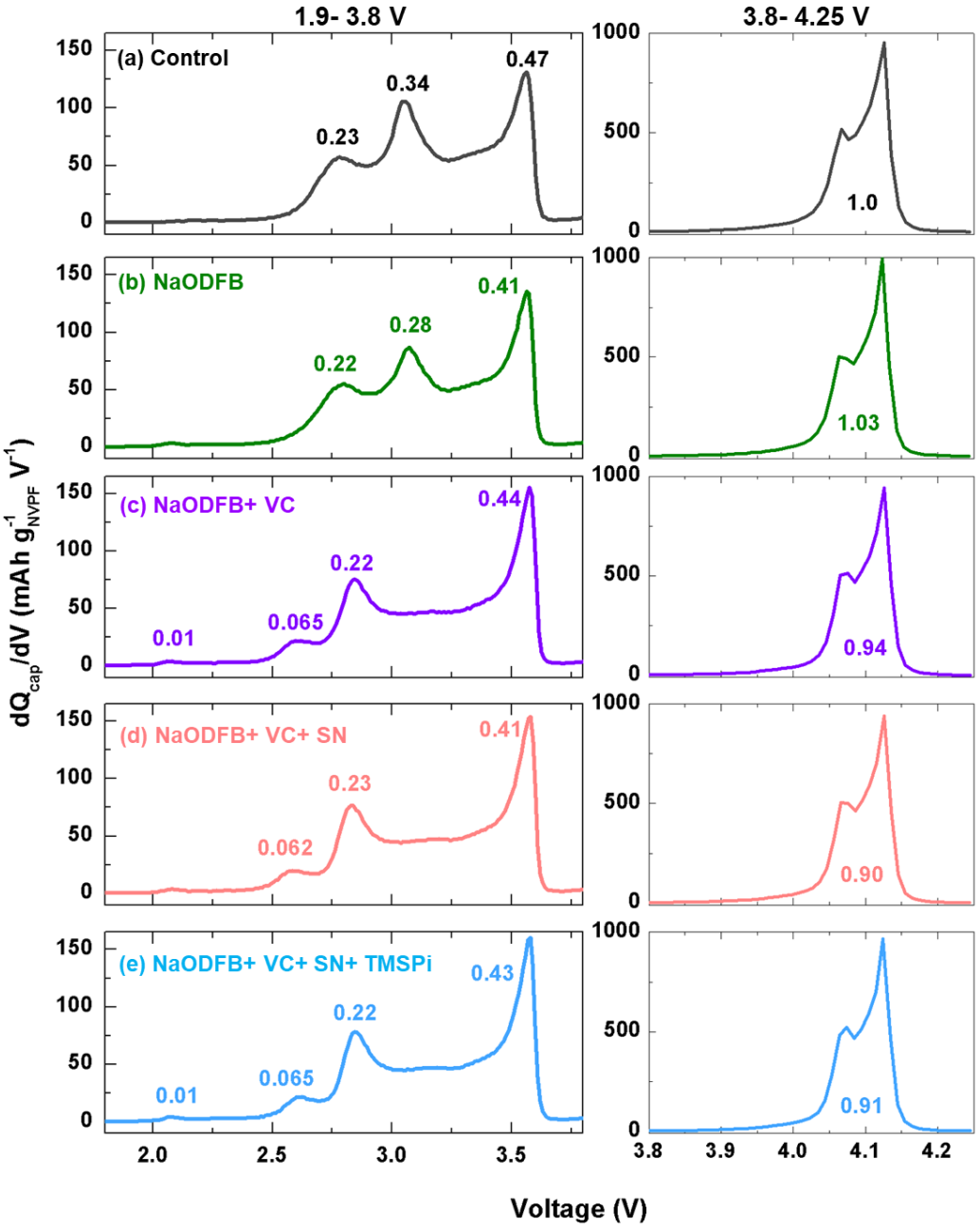

Capacity derivative dQ_{cap}/dV *vs.* voltage (V) plots for the 1st charge of the NVPF/HC cylindrical 18650 cells. The voltage region from OCV- 3.8 V are shown in left and 3.8- 4.25 V in right. The electrolyte studied are the control electrolyte (1 M $NaPF_6$ in EC- PC- DMC 1: 1: 1 by volume) with no additive or having additives namely 0.5 wt% NaODFB, 0.5 wt% NaODFB+ 3 wt% VC, 0.5 wt% NaODFB+ 3 wt% VC+ 3 wt% SN and 0.5 wt% NaODFB+ 3 wt% VC+ 3 wt% SN+ 0.2 wt% TMSPi respectively. Amount of e^- involved in the reaction corresponding to a particular peak is presented in the figure and is calculated with respect to NVPF.

Supplementary Fig. S4.6

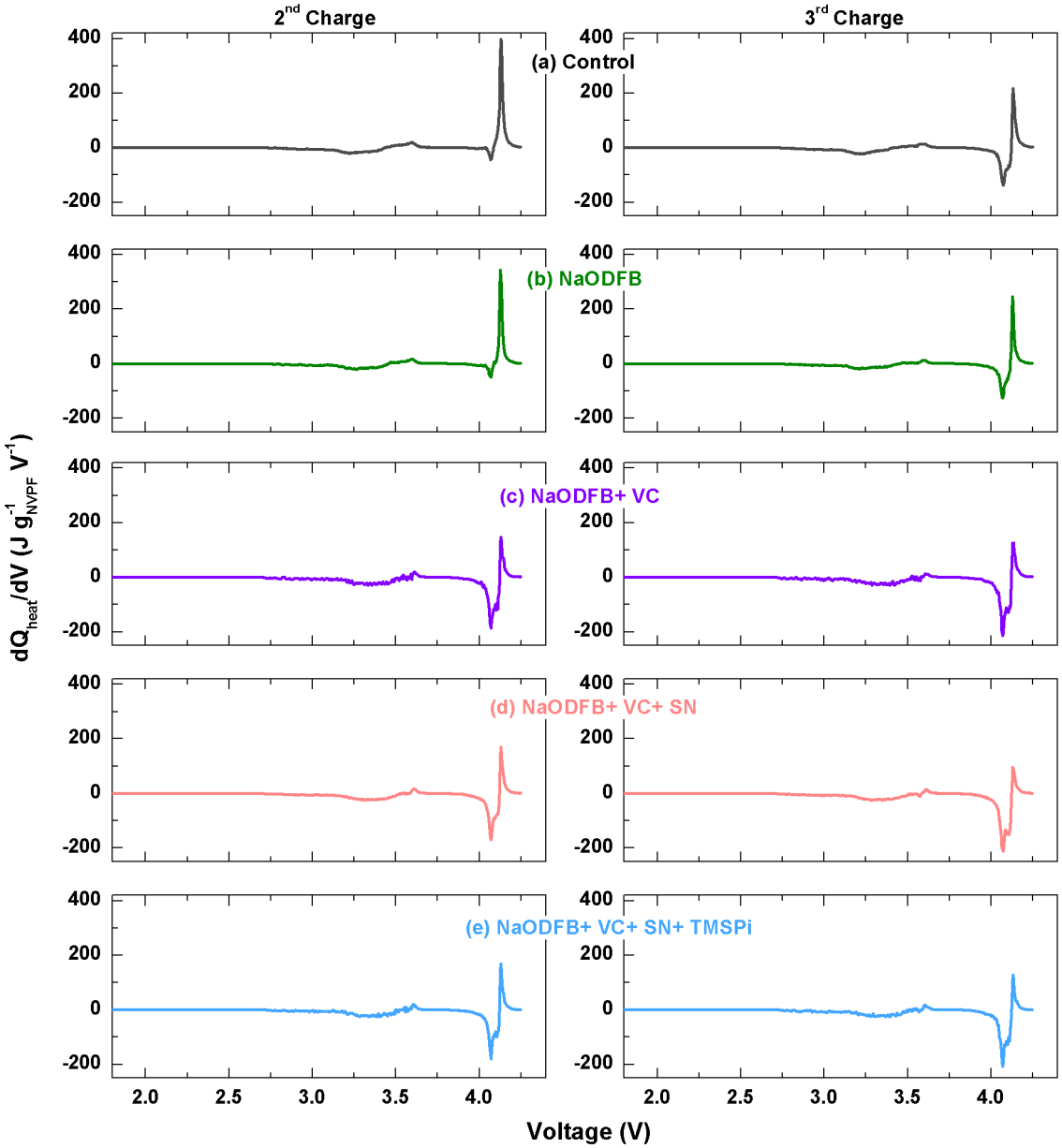

Derivative heat dQ_{heat}/dV *vs.* voltage (V) plots for the 2nd and 3rd charge of the NVPF/HC cylindrical 18650 cells cycled at C/10 in 55°C oven. The electrolyte studied are the control electrolyte (1 M $NaPF_6$ in EC- PC- DMC 1: 1: 1 by volume) with no additive or having additives namely 0.5 wt% NaODFB, 0.5 wt% NaODFB+ 3 wt% VC, 0.5 wt% NaODFB+ 3 wt% VC+ 3 wt% SN and 0.5 wt% NaODFB+ 3 wt% VC+ 3 wt% SN+ 0.2 wt% TMSPi respectively. A clear evolution in exothermic heat was observed in moving from 2nd charge to 3rd charge, especially above 3.8 V; however the evolutions are minimum in (c), (d) and (e) indicating faster stabilisation of positive electrode in these electrolytes. (The data were derived from same cells whose first charges were shown in supporting **Fig. S4.4** and **S4.5**.

Supplementary Fig. S4.7

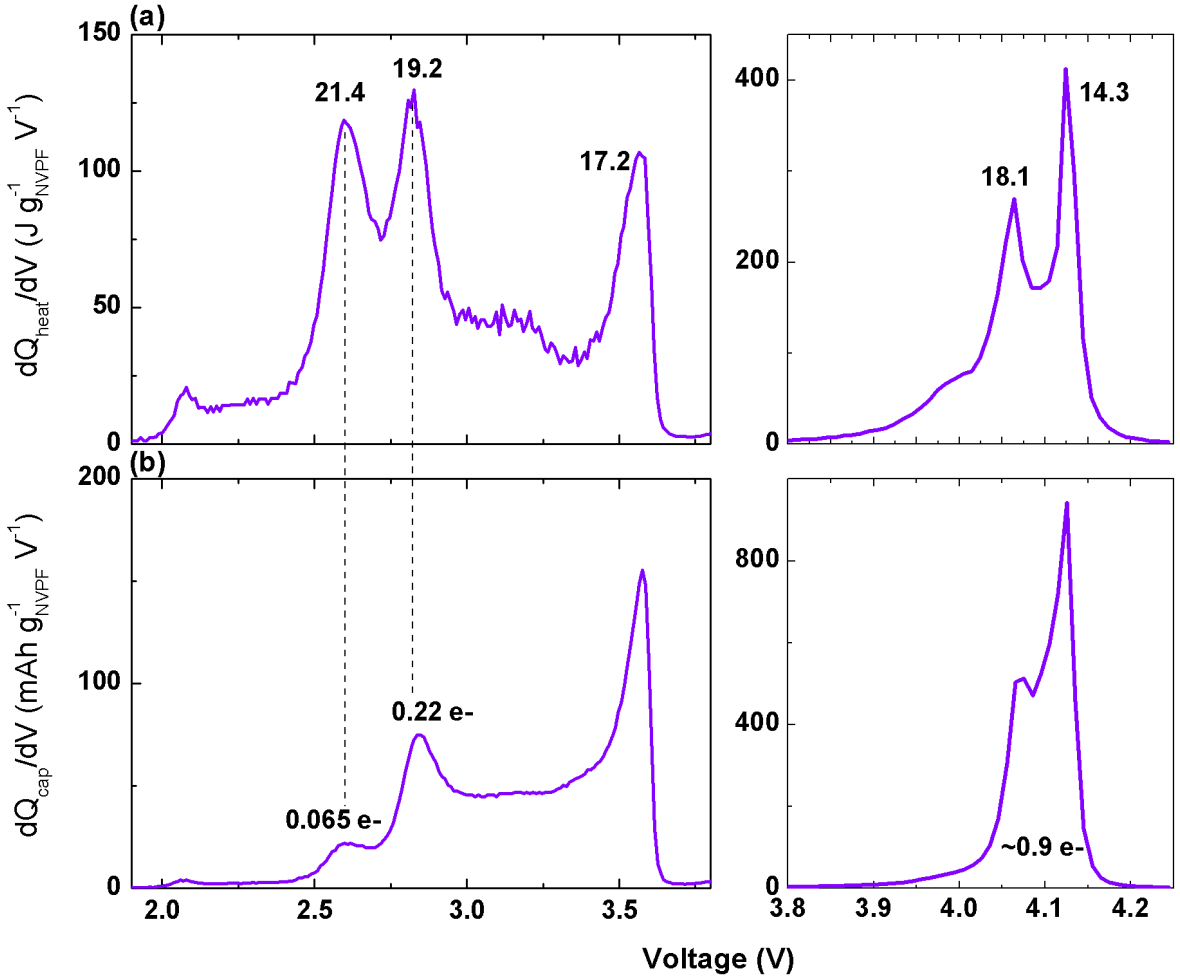

Comparison of derivative heat (dQ_{heat}/dV) with derivative capacity (dQ_{cap}/dV) as a function of potential (V) for the NVPF/HC cylindrical 18650 cells using 1M $NaPF_6$ in EC- PC- DMC (1: 1: 1 by volume) with additives NaODFB+ VC. The cells were cycled at 55°C using C/10 rate. The total heats (in joules per gram of NVPF) for each exothermic peak were measured by integrating the total area under the peak and are mentioned in (a). Similarly, the corresponding electrons involved were measured from the capacity obtained in that voltage region and converting them to ΔNa, hence electrons (e^-). The heat evolution peaks at 2.6 V and 2.8 V have almost similar area but the corresponding e^- involved at 2.6 V are less than that at 2.8 V, indicating the process at 2.6 V is highly exothermic chemical/ electrochemical reaction.

Supplementary Fig. S4.8

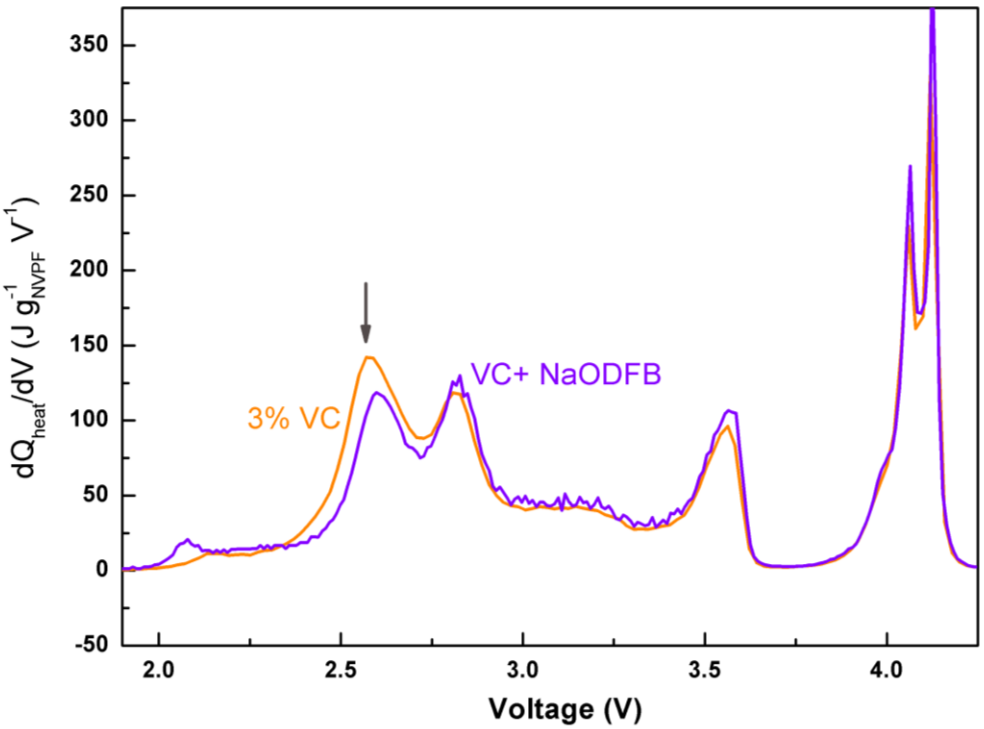

The heat derivatives dQ_{heat}/dV *vs.* V of NVPF/ HC cylindrical 18650 cells cycled at 55 °C. The data from two different electrolyte formulations were compared in which one electrolyte was 1 M $NaPF_6$ in EC-PC-DMC (1 :1: 1 by volume) with solely 3 wt% VC as additive and the other one had 0.5 wt% NaODFB+ 3%VC. In short, both electrolytes differ only by presence or absence of NaODFB additive. Relatively lesser heat was observed at 2.6 V process when VC is used together with NaODFB indicating the possible suppression of VC reduction by the addition of NaODFB.

Supplementary Fig. S4.9

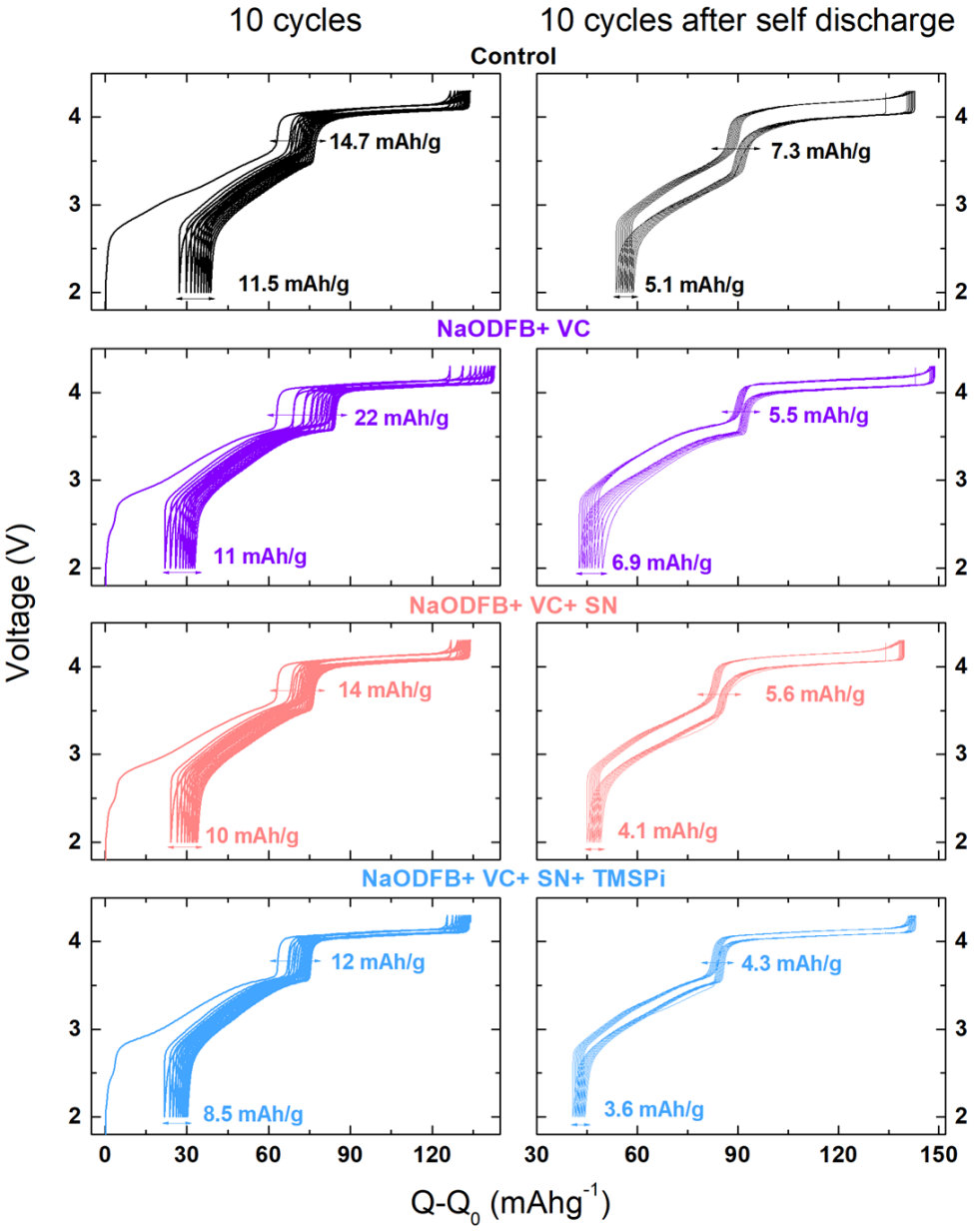

Voltage *vs.* capacity ($Q-Q_0$) of NVPF/HC coin cells cycled with different electrolyte formulations at 55 °C. The cells were cycled for 10 cycles at C/5 rate and allowed to rest during the 11th charge at 4.3 V (100 % SOC) for 1 week. The cycling curves for the initial 10 cycles and the next 10 cycles after self- discharge tests were cumulated in left and right. The consolidated parameters such as capacity loss and change in polarisation during self-discharge, capacity retention are reported in Figure 3. Capacity losses happening at end of discharge and at around 50% SOC are marked in the Figure. Feature at 50 % SOC is the signature of NVPF and changes in that feature is directly correlated to the slippage of NVPF. The least capacity loss was observed with electrolyte containing 4 additives NaODFB+ VC+ SN+ TMSPi.

Supplementary Fig. S4.10

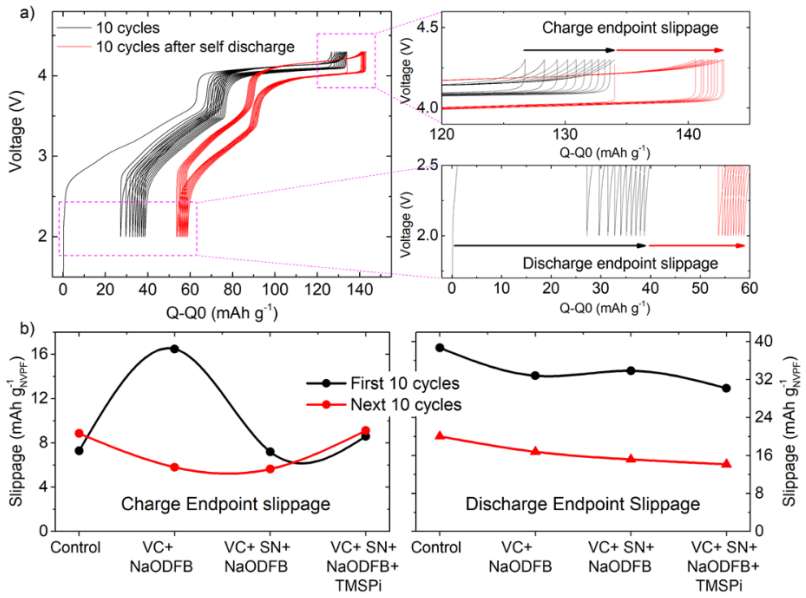

The end point slippage capacity in charge and discharge are measured as shown in Figure S10(a). The values for 10 cycles were calculated together to minimize the experimental error. The values thus calculated before and after self-discharge for various cells using different electrolyte formulations were consolidated in Figure S10(b). Highest end point slippage in charge is observed with electrolyte containing NaODFB+ VC specifying its poor oxidative stability. Such end point slippage is reduced with the addition of SN and TMSPi. Still, a small increase in both charge and discharge end point slippage capacity is observed with NaODFB+ VC+ SN+ TMSPi than that of the electrolyte without TMSPi (NaODFB+ VC+ SN). It could be related to the oxidation of TMSPi or its reduction product in the positive electrode.

Supplementary Fig. S4.11

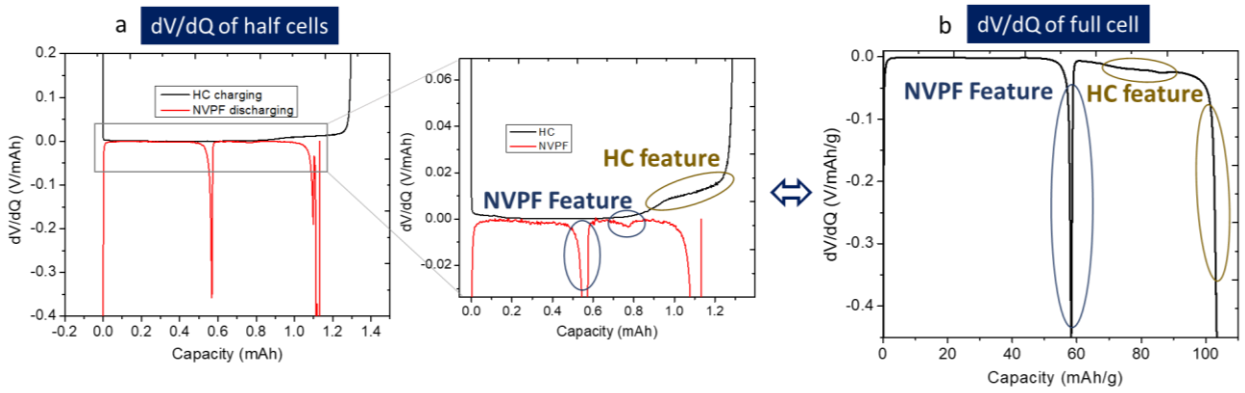

a) The dV/dQ for the NVPF discharge and HC charge for the half cells with the features marked for NVPF and HC. b) dV/dQ for the discharge of NVPF|HC full cells with the features marked for NVPF and HC respectively.

Supplementary Fig. S4.12

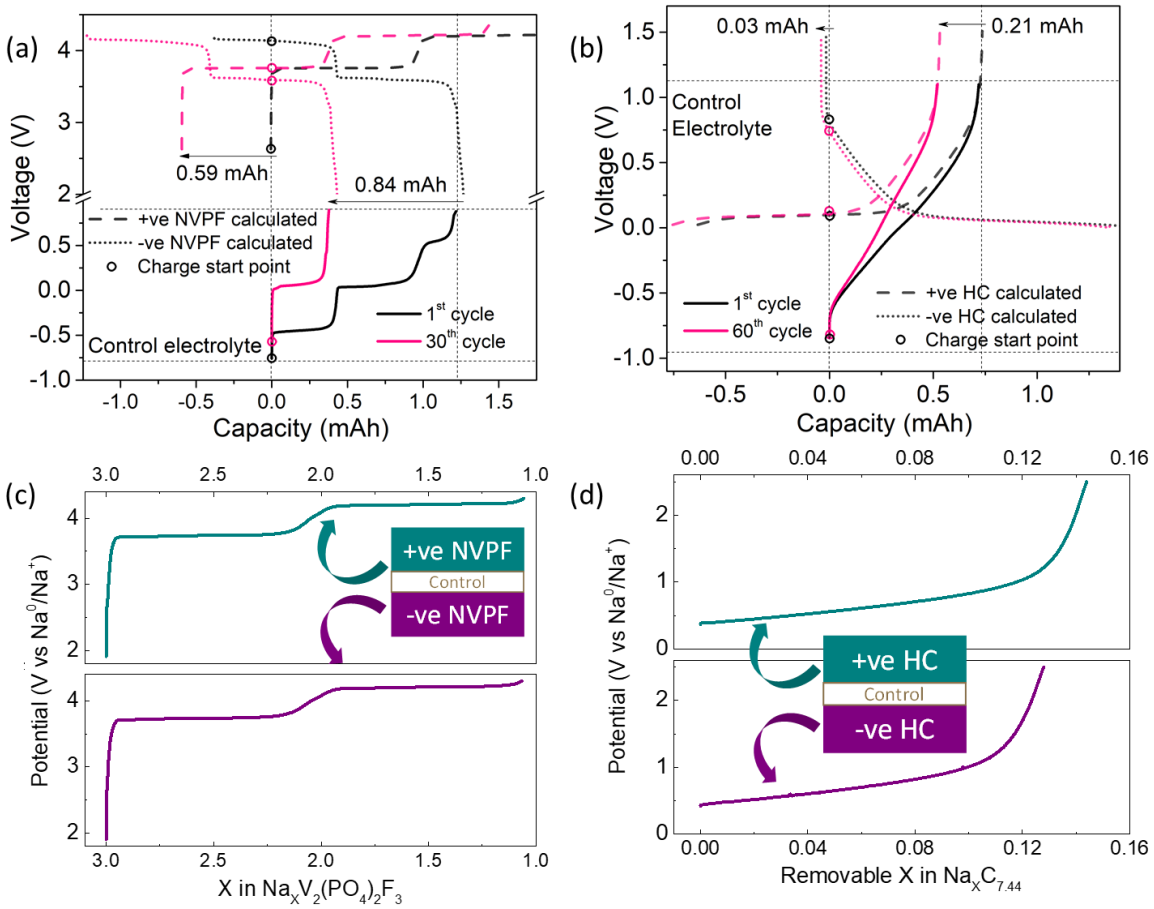

(a) The 1st and 30th cycle of NVPF symmetric cells with control electrolyte and the fitted +ve NVPF (dahshed) and –ve NVPF (dotted) curves. Electrode slippage at –ve NVPF(0.84 mAh) and +ve NVPF(0.59 mAh) is indicated. After 100 cycles, NVPF symmetric cell was decrimped and +ve NVPF/Na and –ve NVPF/Na half cells were prepared and sodium was extrated from NVPF, (c) shows the half cell curves. To our surprise both the NVPF had almost 3 sodium.(b) The 1st and 30th cycle of HC symmetric cells with control electrolyte and the fitted +ve HC (dashed) and –ve HC (dotted) curves. In this case slippage of +ve HC (0.21 mAh) is significantly higher than the -ve HC (0.03 mAh). After 100 cycles, HC symmetric cell was decrimped and +ve HC/Na and –ve HC/Na half cells were prepared and sodium was extrated from HC, (d) shows the half cell curves. Total Na^+ in the HC electrodes is 0.27 (where x=1 corrosponds to 300mAh/g of capacity for $Na_xC_{7.44}$). Note that the +ve NVPF is the one with more Na and –ve NVPF is the one with less Na. +ve HC is the one with more Na and –ve HC is the one with less Na.

Supplementary Fig. S4.13

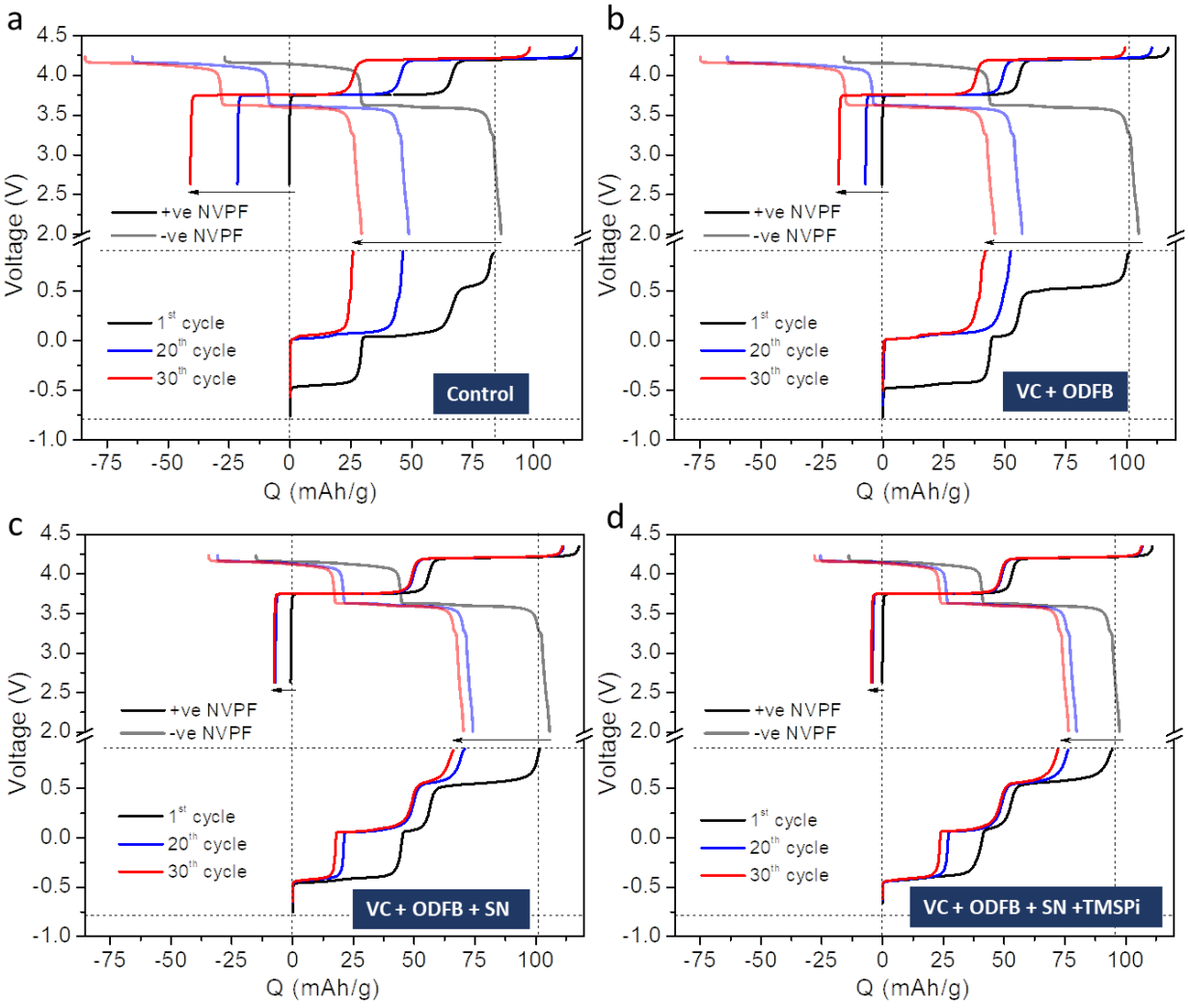

Deconvoluted electrode curves, namely +ve NVPF (with more Na content) and –ve NVPF (for less Na content) are extracted from the dV/dQ fitting of charging curves of NVPF symmetric cells. a) Control electrolyte. b)NaODFB+VC. c)NaODFB+VC+SN and d) NaODFB+VC+SN+TMSPi electrolyte. Note that the +ve NVPF is the one with more Na and –ve NVPF is the one with less Na. +ve HC is the one with more Na and –ve HC is the one with less Na.

Supporting Notes.

Note S4.1. To make symmetric cells, both the NVPF and HC electrodes are sodiated or desodiated as per the requirement (explained in Experimental Procedure), in NVPF/ HC full cells using the electrolyte formulation under study. The cells are decrimped and the electrodes recovered and used without washing the formed SEI/CEI. The desodiated NVPF (-ve NVPF) in **Fig 4.9c** doesn't start with composition $Na_1V_2(PO_4)_2F_3$, but with slightly more sodium. Similarly, Sodiated HC starts with the less sodium than it was sodiated (**Fig 4.9d**). After many experimental trials, it was observed that it was impossible to avoid this behavior entirely. The possible reason of this behaviour could be the process of decrimping the cell and assembling it again with fresh electrolyte. Since sodiated HC and desodiated NVPF materials are highly reactive they will try to lose and gain sodium, respectively.

Note S4.2. In **Fig. S4.12a** the slippage at –ve electrode is 0.84 mAh which is more than the slippage at +ve electrode, 0.59mAh. Refereing to the starting point of fitted curves, –ve NVPF and +ve NVPF slippage is attributed to the gain and loss of Na^+ respectively, considering there is no mass loss. The same behaviour of –ve NMC slippage more than +ve NMC slippage can be observed in NMC symmetric cells. This indicates that there is increase in the total sodium content in the electrode.To confirm this, after 100 cycles, NVPF symmetric cell was decrimped and +ve NVPF/Na and –ve NVPF/Na half cells were prepared and sodium was extrated from NVPF(shown in **Fig. S4.12c**), to our surprise both the NVPF had almost 3 sodium. This indicates gain of sodium from electrolyte, which happens with simultaneous oxidation of electrolyte. Since both NVPF electrodes are at high voltage, the possibility of electrolyte reduction is negligible, hence the only dominant mechanism of degradation is electrolyte oxidation. This eliminates the cross talk caused by the reaction of reduced and oxidized species on cathode and anode electrode respectively. From the slippage of the individual electrode curves, it is established that the additive which decreases the extent of electrolyte oxidation decreases the slippage in the electrode and hence stabilizes symmetric cell capacity.

Note S4.3. In **Fig. S4.12b** the slippage of +ve HC (0.21 mAh) is significantly higher than the -ve HC (0.03 mAh). Referring to the starting point of fitted curves, it is evident that slippage at +ve HC and –ve HC stems from Na^+ loss and Na^+ gain, respectively, considering there is no mass loss. To confirm this, after 100 cycles, HC symmetric cell was decrimped and +ve HC/Na and –ve HC/Na half cells were prepared and sodium was extrated from HC (shown in **Fig. S4.12d**). Total extracted Na^+ in the HC electrodes is 0.27 (where x=1 corrosponds to 300mAh/g of capacity for $Na_xC_{7.44}$). The initial Na^+ amount after sodiation of HC for symmetric cells was 0.63(calculated from the capacity obtained in the first cycle of symmetric cell). This indicates loss of sodium to electrolyte with simultaneous electrolyte reduction and SEI growth. Since both HC electrodes are at low voltage, so the possibility of electrolyte oxidation is negligible.

S-5 Supplementary Information for Chapter 5

Methods

Ionic conductivity measurements: Bulk ionic conductivity of the electrolyte solutions was measured using a Mettler Toledo S230 conductivity meter. For accurate measurements, the conductivity meter was calibrated using a known standard solution of conductivity 12.88 mS cm^{-1} at 25 °C. 5mL of the electrolyte was taken in a 15ml polypropylene centrifuge tube and was then placed in a thermostatic bath. Conductivity was measured at -10, 0, 10, 25, 40 and 55 °C respectively. At each temperature step, a constant temperature was maintained for at least 2 hours to allow the electrolyte temperature to equilibrate with the bath temperature. Measurement was performed twice to confirm the reproducibility of the data.

Electrochemical full cells testing: $Na_3V_2(PO_4)_2F_3$ and HC coated on Al foil were received from TIAMAT, France. The electrodes were coated on one side of the foil with keeping the mass loading the same as commercial 18650 cells. NVPF and HC mass loading was roughly ~12 $mg.cm^{-2}$ and ~6 $mg.cm^{-2}$, respectively. Active material: PVDF binder: conductive carbon for NVPF and HC was 94:3:3. The electrode thickness, active material to conducting carbon and binder ratio, porosity, etc. were maintained the same as in 18650 cells. Before assembling the coin cells, electrodes of 12.7mm diameter were punched and dried in a Buchi oven under vacuum (lower than 100 mbar) at 80 °C for 12 h. The electrochemical performance of NVPF/HC full cells was evaluated in 2032-type coin cells separated by two layers of glass fiber containing 150 µL of desired electrolytes. All cells were galvanostatically cycled using MPG2 potentiostat or BCS battery cycler (Bio-Logic, France), and the cycling rates were calculated with respect to NVPF (1C = 128 mA g^{-1}). For electrolyte preparation, classic organic solvents were used throughout the thesis namely ethylene carbonate (EC), propylene carbonate (PC) and dimethyl carbonate (DMC) containing water amount less than 10ppm. The Control electrolyte throughout is 1M $NaPF_6$ in EC-PC-DMC (1:1:2 by vol %). Electrolyte with Additives (or Add) contains 0.5% NaODFB, 3% VC, 3% SN and 0.2% TMSPi. When MA/EA is added, the mentioned x% represents that x% of solvent was replaced with MA/EA. Two cells were assembled for each experiment to confirm the reproducibility of the data.

Electrochemical Impedance Spectroscopy (EIS) measurements: A BioLogic MPG2 cycler was used to measure electrochemical impedance spectra of the full coin cells. The spectra were collected over a frequency range of 20 kHz to 10 mHz with six points per decade with a perturbation amplitude of 10 mV. Spectra were collected at 10°C, 25°C, 40°C, and 55°C. Two cells were assembled for each experiment to confirm the reproducibility of the impedance data. Electrodes of 12.7mm diameter (and of 1.267 cm^2 area) were used for impedance measurements.

○ Supplementary Figures

Supplementary Fig. S5.1

	Ionic Conductivity (mS/cm)		
Temperature (°C)	*Control*	*20%MA + Control*	*20%EA + Control*
-10	4.95	7.07	5.72
0	6.68	8.76	8.05
10	8.67	10.36	9.89
25	11.61	13.65	12.75
40	14.52	16.56	15.42
55	17.29	19.55	18.02

Ionic conductivity values of the electrolyte blends Control (1M $NaPF_6$ in EC-PC-DMC 1:1:2 by vol %), 20%MA + Control (1M $NaPF_6$ in EC-PC-DMC-MA 1:1:2:1 by vol %) and 20%EA + Control (1M $NaPF_6$ in EC-PC-DMC-EA 1:1:2:1 by vol %) measured at -10°C, 0°C, 10°C, 25°C, 40°C and 55°C.

Supplementary Fig. S5.2

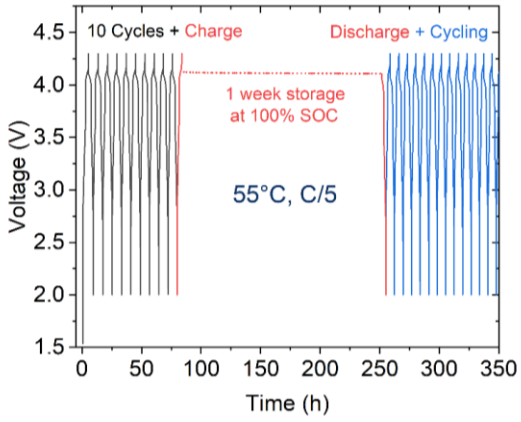

Cycling protocol at 55°C and C/5 rate that is used to rapidly screen the electrolyte blends. It starts with 10 normal cycles (in black color). The 11th cycle (in red color) consists of charge to 4.3V (100%SOC), storage for 1 week in charged state and then discharge. Then further cycling continues (in blue color). Continuous cycling gives information only about cycle life of a battery and not the calendar life. The self-discharge during the storage cycle (11th cycle)

gives indication about the calendar life of the cell. This is rather an important factor since in real life applications, battery stays in both storage state (when it is not (dis)charging) and cycling state.

Supplementary Fig. S5.3

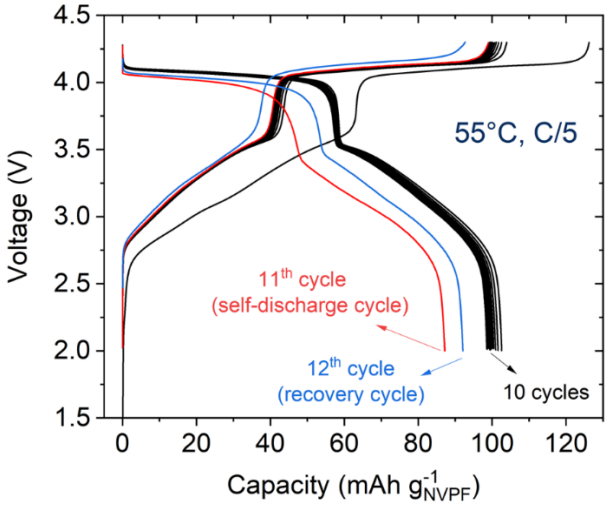

$$\text{Self-discharge}(\%) = \frac{Q^{d}_{11}}{Q^{d}_{10}} * 100$$

$$\text{Recovery}(\%) = \frac{Q^{d}_{12}}{Q^{d}_{10}} * 100$$

The representative voltage vs. capacity data of (first 12 cycles with self-discharge test) NVPF/HC coin cell using the protocol mentioned in **Fig. S5.2**. It is evident that huge amount of capacity is lost due to the parasitic reactions during storage at 100% SOC (4.3 V) causing self-discharge of the cell and capacity loss in the 11th cycle. This can be formalized in terms of Self-discharge (%), which is ($Q_{discharge-11th}$/ $Q_{discharge-10th}$) x 100. Some of the lost capacity is recovered as seen from increase in capacity in recovery cycle (12th cycle). This recovered capacity is formalized as Recovery (%), which is ($Q_{discharge-12}$/ $Q_{discharge-10}$) x100.

Supplementary Fig. S5.4

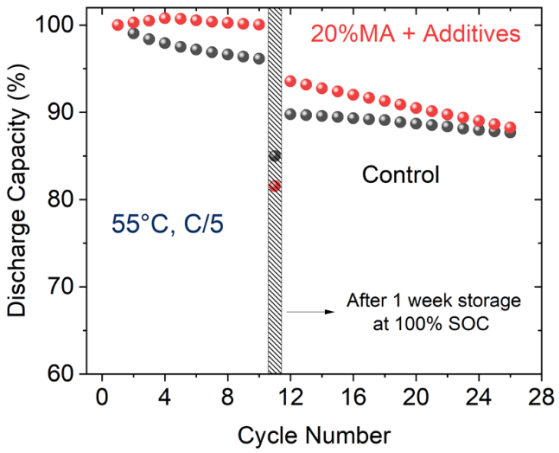

The percentage discharge capacity vs. cycle number for NVPF/HC cells using 1M $NaPF_6$ in EC: PC: DMC (1:1:2 by volume) as a control electrolyte and 20%MA +Additives (1M $NaPF_6$ in EC:PC:DMC:MA (1:1:2:1 by volume) and 3%VC, 0.5%NaODFB, 0.2% TMSPi and 3%SN). Control electrolyte seems to be stabilized after self-discharge but electrolyte

containing MA is degrading with more slope in discharge capacity vs. cycle number plot. This could be attributed to high amount of MA (20% of solvent) in the electrolyte and high temperature 55°C.

Supplementary Fig. S5.5

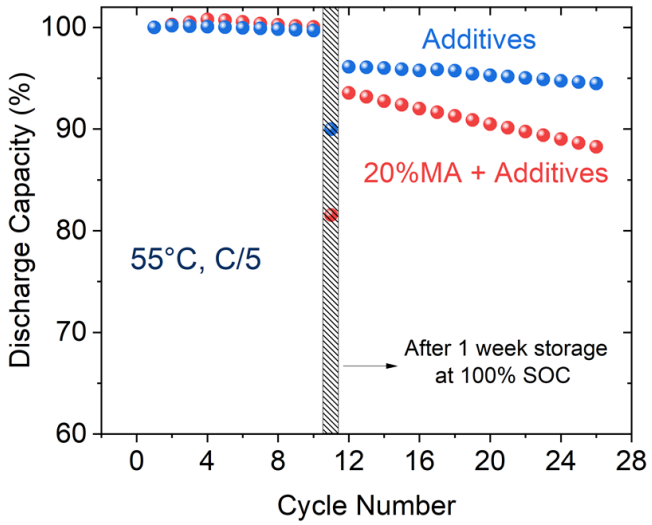

The percentage discharge capacity vs. cycle number for NVPF/HC cells using Additives electrolyte (1M $NaPF_6$ in EC:PC:DMC (1:1:2 by volume) and 3%VC, 0.5%NaODFB, 0.2% TMSPi and 3%SN) and 20%MA +Additives (1M $NaPF_6$ in EC:PC:DMC:MA (1:1:2:1 by volume) and 3%VC, 0.5%NaODFB, 0.2% TMSPi and 3%SN). Here the capacity retention for both the electrolytes seems similar for first 10 cycles but the electrolyte without MA has low self-discharge and recovery during storage cycle as well as better retention after that. It can be inferred that optimized additives helps in improving the stability of the MA containing electrolyte but they do not stop parasitic reactions caused by MA completely.

Supplementary Fig. S5.6

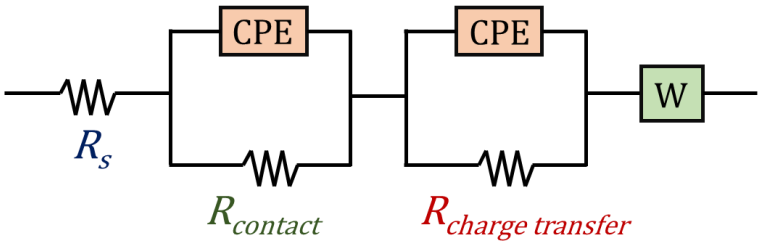

R_s = *Electronic resistance* in the electrode and *Ionic resistance* in the electrolyte

$R_{contact}$ = *All the contacts in the coin cell including* contacts between *electrode material* and *current collector*

$R_{charge\ transfer}$ = *Desolvation of Na^+, charge transfer of Na^+ across SEI and into the electrode particle*

CPE = Constant phase element (imperfect capacitor)

W = Warburg element for linear diffusion in solids

The equivalent circuit model is used to fit the NVPF/HC coin cell impedance. R_s (solution resistance) that represents the electronic resistance in the electrodes and ionic resistance in the electrolyte. $R_{contact}$ corresponds to all the contacts in the coin cell and CPE parallel to it represents constant phase element (from imperfect capacitive effects) from all the interfaces like electrode film and current collector etc. Desolvation of Na^+ and its travel across CEI/SEI into the electrode particle is denoted as $R_{charge\ transfer}$ and the CPE parallel to it is from the double layer capacitance at the electrode interface.

Supplementary Fig. S5.7

	25°C			*10°C*		
Electrolyte	**R_s (Ω)**	**$R_{contact}$ (Ω)**	**$R_{charge\text{-}transfer}$ (Ω)**	**R_s (Ω)**	**$R_{contact}$ (Ω)**	**$R_{charge\text{-}transfer}$ (Ω)**
Control	-	-	-	15.69	88.96	14.4
Additives	12.45	53.28	12.93	17.19	56.94	75.28
4%MA + Additives	11.36	55.39	9.15	15.99	60.72	42.24
20%MA + Additives	6.91	54.83	7.04	9.441	61.07	33.45

Values of the solution resistance (R_s), contact resistance ($R_{contact}$) and charge transfer resistance ($R_{charge\ transfer}$) fitted using model described in **Fig. S5.6**. for the impedance data presented in **Fig. 5.7**.

Supplementary Fig. S5.8

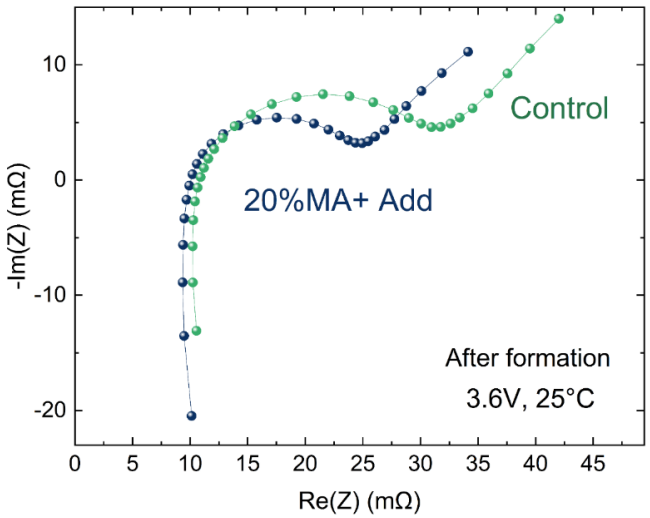

Impedance taken at 50% SOC or 3.6 V of the cell at 25 °C for the 18650 type NVPF/HC cell were filled with homemade electrolyte blends Control (1M $NaPF_6$ in EC:PC:DMC:MA , 1:1:2:1 by volume) and 20% MA+Additives (1M $NaPF_6$ in EC:PC:DMC:MA (1:1:2:1 by volume) and 3% VC, 0.5% NaODFB, 0.2% TMSPi and 3% SN). and cycled at 25°C and C/2:D/2 rates.

Supplementary Fig. S5.9

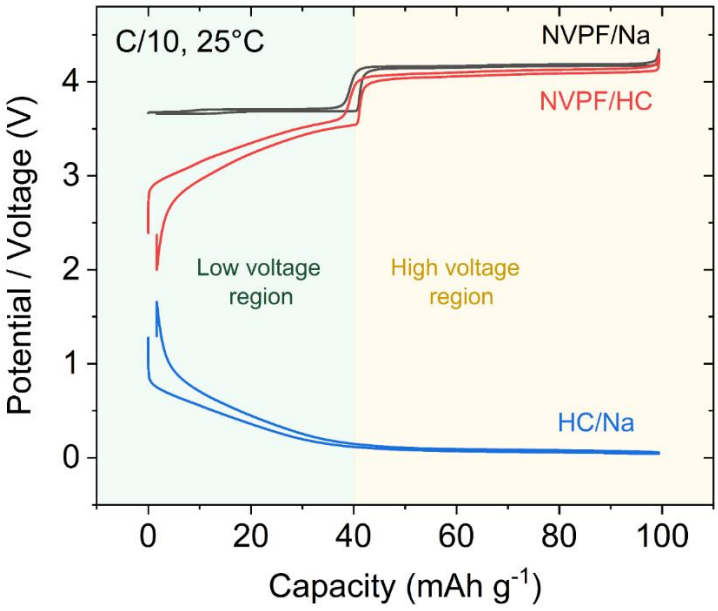

Voltage curves of NVPF and HC in three-electrode configuration at C/10 and 25°C. The NVPF electrode (black line) exhibited very less polarization throughout the cycling. In contrast, the HC showed (blue line) higher polarization in

the initial stages of sodiation (mentioned low voltage region in figure as the full cell potential is low at this region). As a result, the NVPF-HC full cell (red line) polarization is higher in low voltage region than high voltage region and it is mainly contributed from the voltage hysteresis of HC. Even at very low rates, the hysteresis cannot be completely removed and it is reported to be thermodynamic hysteresis[343,344] of the electrode materials. This thermodynamic hysteresis can be calculated by going at very slow C rates (C/100 or C/500) and known as zero-current voltage gap. In the present study, for comparing the role of different electrolyte formulations in determining the rate capability of the cells, the thermodynamic hysteresis of electrode materials were maintained constant by using NVPF and HC electrodes derived same batch of raw materials and processed in the same way with similar mass loading, porosity etc.

Supplementary Fig. S5.10

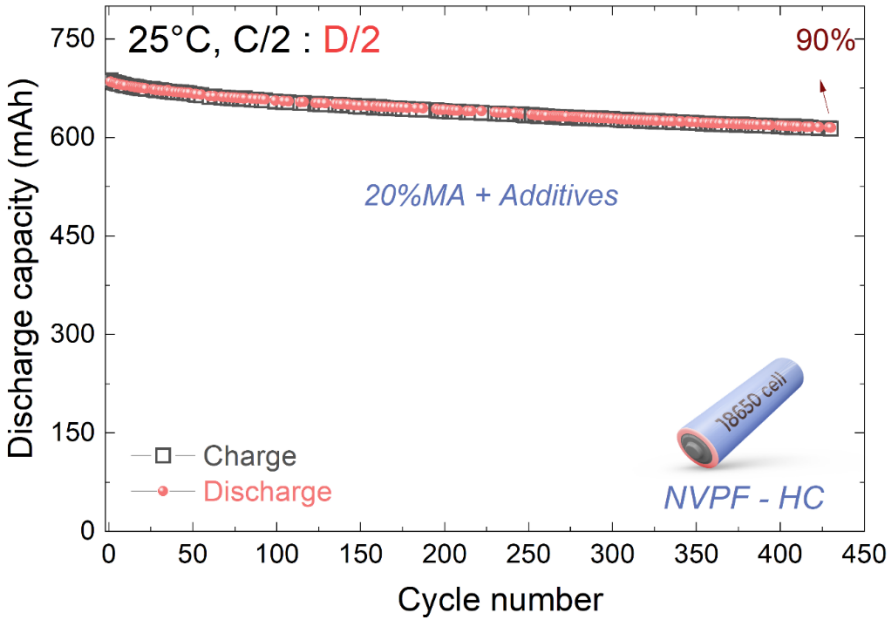

Discharge capacity vs. cycle number for 18650 type NVPF/HC cell were filled with homemade electrolyte 20% MA+Additives (1M $NaPF_6$ in EC:PC:DMC:MA (1:1:2:1 by volume) and 3% VC, 0.5% NaODFB, 0.2% TMSPi and 3% SN). The cell was cycled at cycled at 25°C using C/2:D/2 rate after the formation cycle.

S-6 Supplementary Information for Chapter 6

○ Methods

Electrochemical analyses: All electrochemical tests were carried out using either MPG2 potentiostat or BCS battery cycler (Bio-Logic, France). Four different cell configurations are used in the manuscript to compare Li- and Na-ion cells. The mainly studied cell configurations are, (i) $LiNi_{0.8}Mn_{0.1}Co_{0.1}O_2$ // 1M $LiPF_6$ in ethylene carbonate (EC)-dimethyl carbonate (DMC) (1:1) // Graphite, (ii) $LiFePO_4$ // 1M $LiPF_6$ in EC-DMC (1:1) // Graphite, (iii) $Na_3V_2(PO_4)_2F_3$ // 1M $NaPF_6$ in EC-propylene carbonate (PC)-DMC (1:1:1) // Hard carbon and (iv) O3 $NaNi_{0.45}Zn_{0.05}Mn_{0.35}Ti_{0.15}O_2$ // 1M $NaPF_6$ in EC-PC-DMC (1:1:1) // Hard carbon. In all these configurations, the active material is mixed with conducting carbon and coated on Cu (graphite) or Al (all other materials) foil using polyvinylidene fluoride (PVDF) binder. The active material masses for positive and negative electrodes were balanced considering their practical capacities with the negative to positive (n/p) ratio of 1.1. The electrodes are punched into 11 mm diameter for studies in Swagelok type cells and 12.7 mm diameter for 2032 coin cells. The electrodes are dried at 100°C in a vacuum and transferred to argon filled glove box where the cell assemblies were carried out. The electrolytes were homemade by dissolving the dry $LiPF_6$/ $NaPF_6$ in mentioned solvent(s). The solvents used in this study are battery grade EC, PC, DMC etc, purchased from E-lyte, Germany. The solvents were dried over molecular sieves and tested for water content using Karlfisher titration. The water content was always less than 10ppm in the used solvents.

Two types of cell designs were used. (i) *Three electrode cells:* Swagelok type three electrode cells were used for the analyses. Lithium metal is used as a reference electrode for Li-ion cells and $Na_3V_2(PO_4)_3$ charged to 3.4V (50% state of charge) is used as a reference electrode for Na-ion cells. Tests were carried out at either C/10 or C/5 rates at 25 °C.

(ii) *Full cells testing: The Li (Na)-ion cells assembled using* insertion electrodes for both positive and negative electrodes (vs. Li(Na)- metal as a negative electrode in Li(Na)-half cell) are termed as full cells throughout the text. The long cycle performance of different electrodes with or without 0V hold was measured in coin type 2032- cells. The dried electrodes were separated by two layers of glass fiber containing 150 µL of desired electrolytes.

Electrochemical Impedance Spectroscopy (EIS) measurements: The impedance spectra were collected in coin cells, over a frequency range of 20 kHz to 10 mHz with six points per decade and a perturbation amplitude of 10 mV. Two cells were assembled for each experiment to confirm the reproducibility of the impedance data and measurements were done at 25°C.

X-ray photoelectron spectroscopy analyses: X-ray photoemission spectroscopy (XPS) measurements were carried out with a THERMO Escalab spectrometer, using focused monochromatic Al Kα radiation (hν = 1486.6 eV) and equipped with an argon-filled glove box. The HC samples were cycled using the prescribed condition and removed at 2V, washed using dry DMC and sealed in argon. The samples were preserved from moisture and air at all times from their preparation to their analysis. Peaks were recorded with a constant pass energy of 20 eV. The pressure in the analysis chamber was around 5×10^{-8} mbar. The binding energy scale was calibrated using the C 1s peak at 285.0 eV from the hydrocarbon contamination present at the surface of the sample. The spectra were fitted using a minimum number of components. Several spectra were recorded at different times to check that the samples were not subjected to degradation during the X-ray irradiation.

Operando optical calorimetric analyses: Hermetically sealed NVPF/HC cylindrical 18650 cells without electrolyte were received from Tiamat, France. A 0.8 mm diameter hole was drilled into the negative pole of the dry, 18650 cells. The position was selected according to the welding point of the negative current collector, which was close to the centre of the negative pole. This choice of position helped in avoiding the destruction of the jelly roll and in preventing the strain interaction between the TFBG sensors and the jelly roll. All of the 18650 cells were dried in a Buchi oven under vacuum at 80 °C for 12 h prior to being transferred into the glovebox. The 18650 cells were then filled with 5.5 mL of the desired electrolyte inside the glovebox. Then the FBG sensors were inserted into the central void of the jelly roll through the drilled hole using a needle. The interface between the needle containing the TFBG sensor and the 18650 cell was subsequently sealed with an epoxy that was cured for 24 h; all processes were performed inside the glove box whose O_2 and H_2O content was maintained at less than 0.1 ppm. Cells were cycled using BCS battery cycler (Bio-Logic, France) by keeping the cells inside an oven at 55 °C, and the cycling rates were calculated on the basis of NVPF material (1C = 128 mA g^{-1}). Sensors were

connected to FBGuard1550 (Safibra) or LUNA Si255 (Micron Optics) interrogator via optical fibers. The sampling period of the interrogator was set to 1 s. According to the mentioned specifications, the wavelength accuracy of the interrogators is 1 pm. The FBGs were purchased from SAMYON and calibrated before use. The temperature calibration of the FBG sensors was conducted as reported previously.[244,252,253]

○ Supplementary Figures

Supplementary Fig. S6.1

The separator removed from the NMC811-Li-graphite three electrode cell after a single 0V hold for 24 hours. The reddish regions in the separator is due to dissolved Cu from the current collector.

Supplementary Fig. S6.2

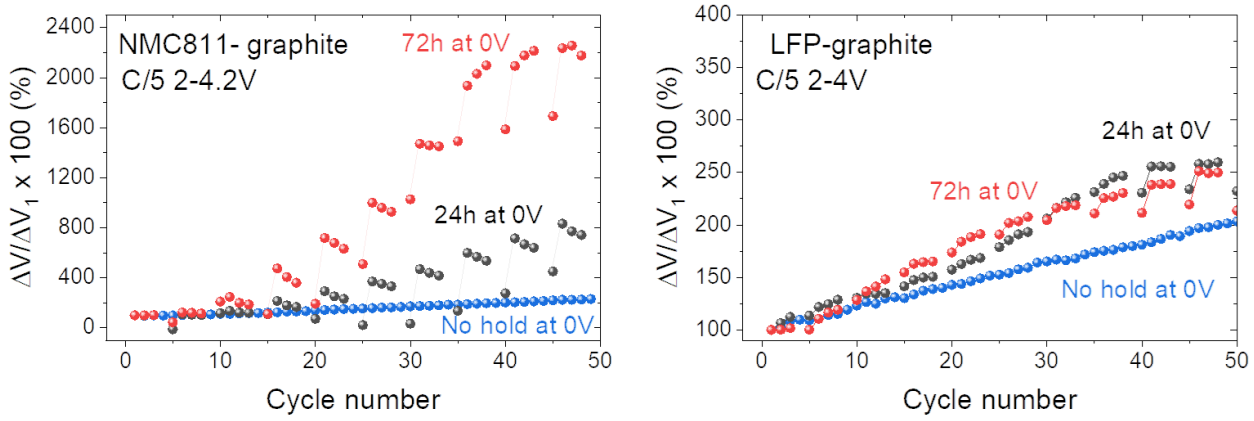

Normalized polarization evolution as a function of cycle number for the (a) NMC811-graphite and (b) LFP-graphite cells with the continuous cycling and with the 0V hold protocol (described in Supplementary Figure S2). Huge polarization increase in NMC811-graphite cells after two 0V holds represent the rapid cell degradation. On the contrary the LFP-graphite cells show comparatively slower increase in polarization upon cycling with 0V hold.

Supplementary Fig. S6.3

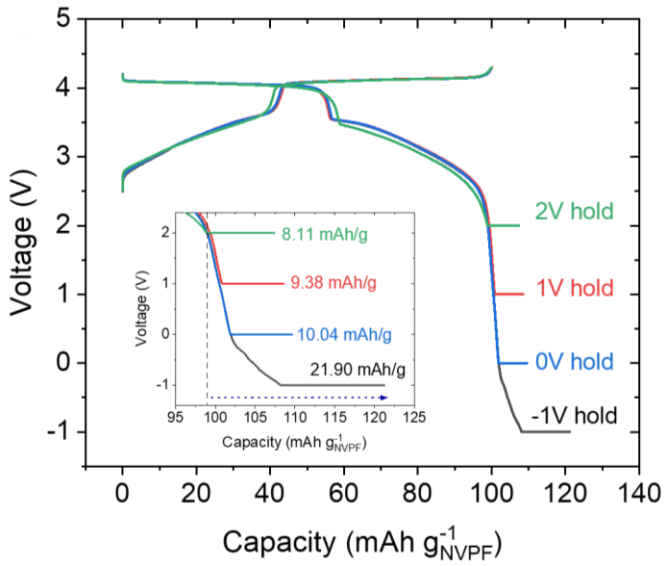

Charging profile of the NVPF-HC cells containing 1M $NaPF_6$ in EC-PC-DMC (1:1:1 by volume) electrolyte which undergone constant voltage hold at lower cut-off voltages of 2V, 1V, 0V and -1V for 24h. An increase in discharge capacity is observed by reducing the potential from 2V to 1V and so on, indicating more Na^+ (more capacity) is extracted from HC+SEI to insert into NVPF.

Supplementary Fig. S6.4

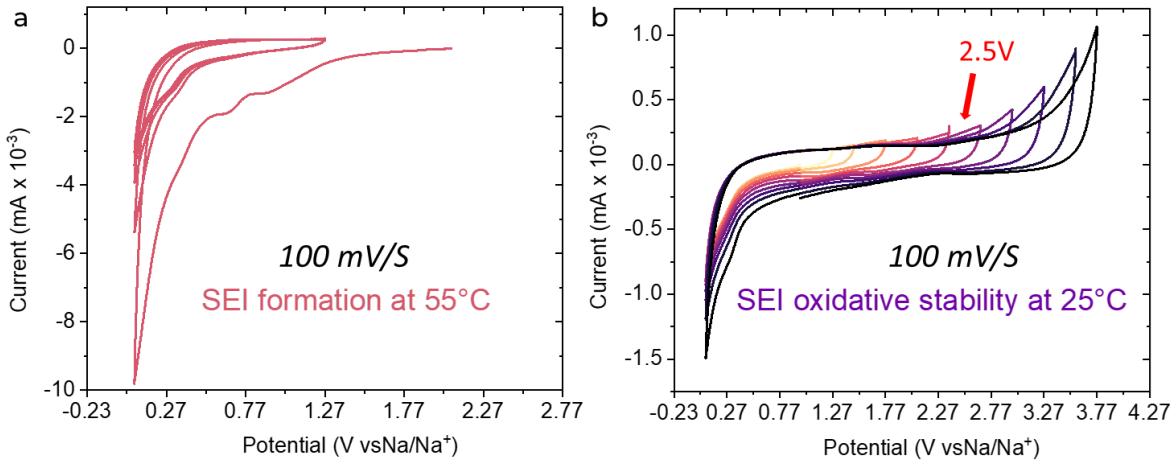

The cyclic voltammetry experiments were carried out in three electrode cell as explained earlier.[123] A beaker type cell was used with glassy carbon and platinum as working and counter electrode, respectively, with a non-aqueous Ag/Ag^+ reference electrode (silver wire immersed in an acetonitrile/0.1 M tetrabutylammonium perchlorate/0.01 M $AgNO_3$ solution). The electrolyte used is 1M $NaPF_6$ in EC-PC-DMC (1: 1: 1 by volume). a) Five formation cycles at 55°C to form stable interphase on the glassy carbon surface (SEI) and (b) subsequent CV with increasing upper cut-off

voltage from 1.30V to 3.77V *vs.* Na/Na^+ with 0.5V incremental step to analyze the oxidative stability of formed interphase. The oxidation current onsets at around 2.5V *vs.* Na/Na^+ indicating the formed SEI is not stable towards oxidation for the potential above 2.5V.

Supplementary Fig. S6.5

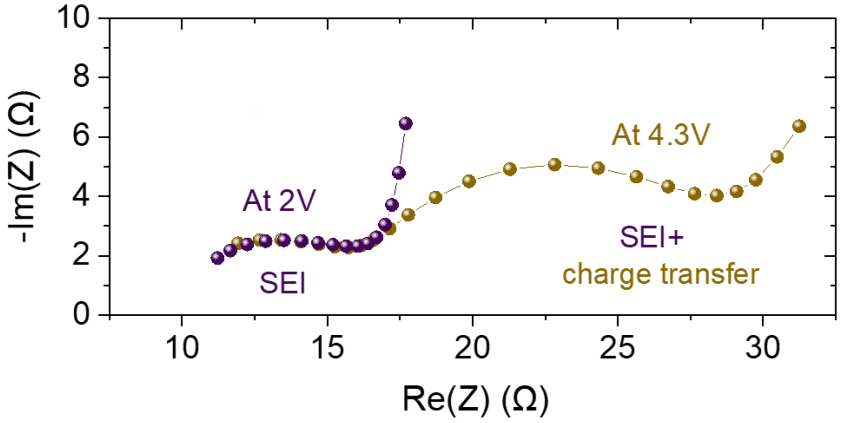

Impedance spectra taken at 2V and 4.3V of NVPF-HC cells with control electrolyte. The impedance taken at 2V shows one semi-circle and is considered as blocking condition without any significant faradic contributions. On the contrary, impedance taken at 4.3V shows two semi-circle with the low frequency semi-circle corresponding to the faradic charge transfer contribution.

Supplementary Fig. S6.6

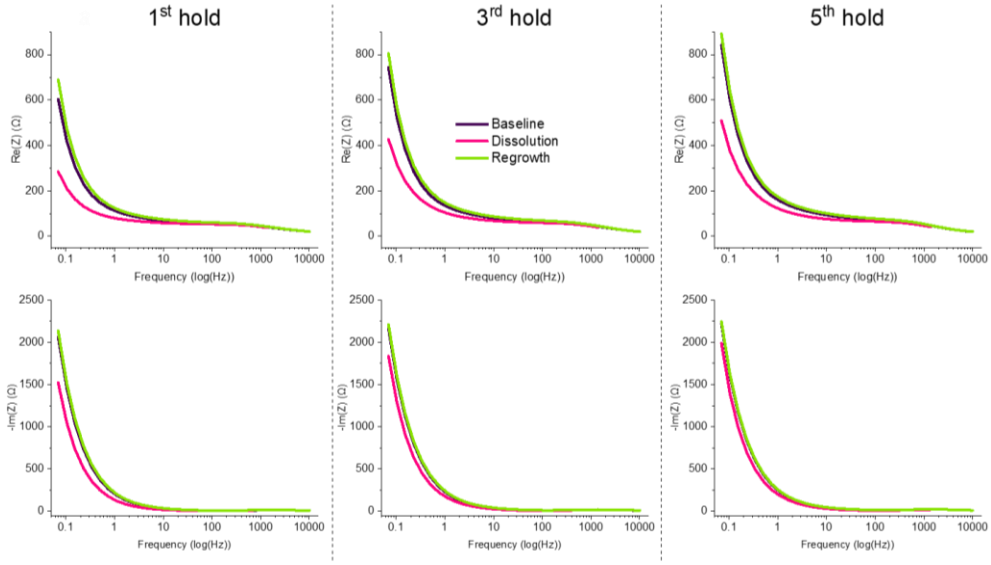

Bode plot in terms of real or imaginary impedance as a function of frequency in logarithmic scale for 1st, 3rd and 5th 0V hold. Corresponding Nyquist impedance plot are shown in Figure 3 of the main manuscript. Drop in the real and

imaginary impedance after the 0V hold (dissolution) and increase after the next cycle (regrowth) as compared to baseline impedance is evident from the bode plot.

Supplementary Fig. S6.7

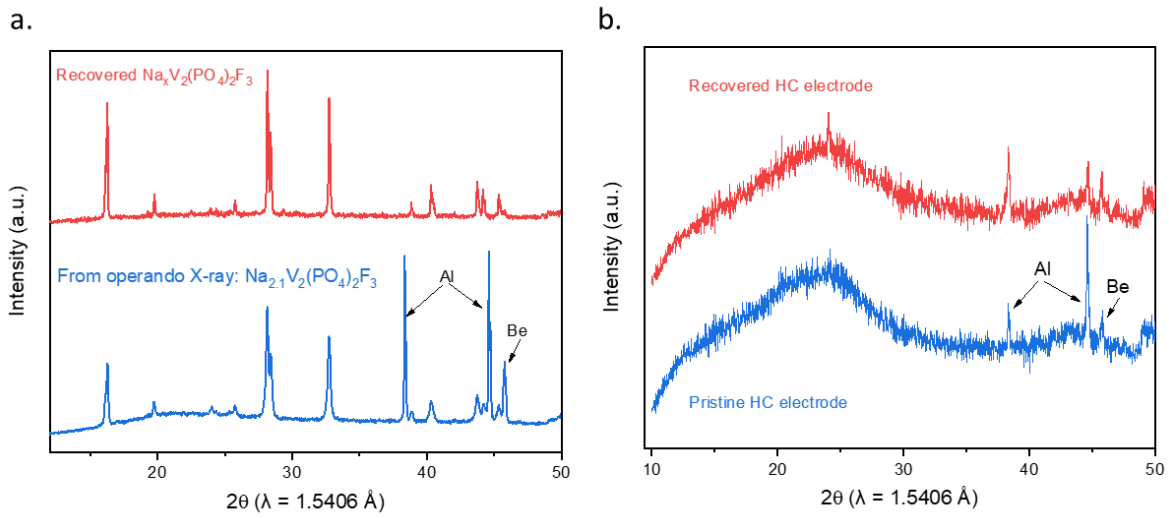

XRD pattern taken in the air tight beryllium cell of the cycled electrodes of NVPF and HC. The 'recovered' represents the material cycled in NVPF-HC cell with repeated discharge to 0V and holding for 72h. The cells were cycled using 1M $NaPF_6$ in EC-PC-DMC electrolyte and cycled for more than 100 cycles. (a) XRD pattern of recovered NVPF matches with the $Na_{2.1}V_2(PO_4)_2F_3$ (obtained from operando XRD). It is the consequence of the sodium inventory loss from the SEI formation and dissolution processes during the 0V. (b) XRD pattern of recovered HC and pristine HC are closely similar. There is no significant difference observed with XRD of the material for both NVPF and HC.

Supplementary Fig. S6.8

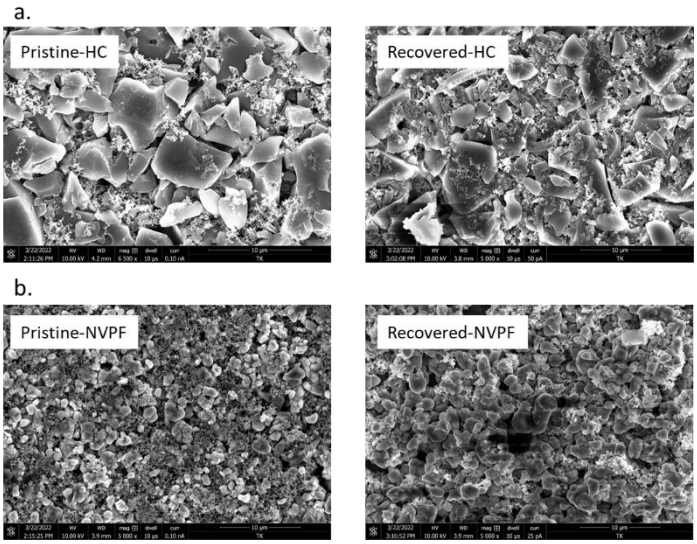

SEM images comparing the fresh and cycled electrodes of NVPF and HC. The 'pristine' represents the as coated electrode film and the 'recovered' represents the material cycled in NVPF-HC cell with repeated discharge to 0V and holding for 72h. The cells were cycled using 1M $NaPF_6$ in EC-PC-DMC electrolyte and cycled for more than 100 cycles. There is no visible appearance of the particle breaking in the cycled electrodes of both HC and NVPF.

Supplementary Fig. S6.9

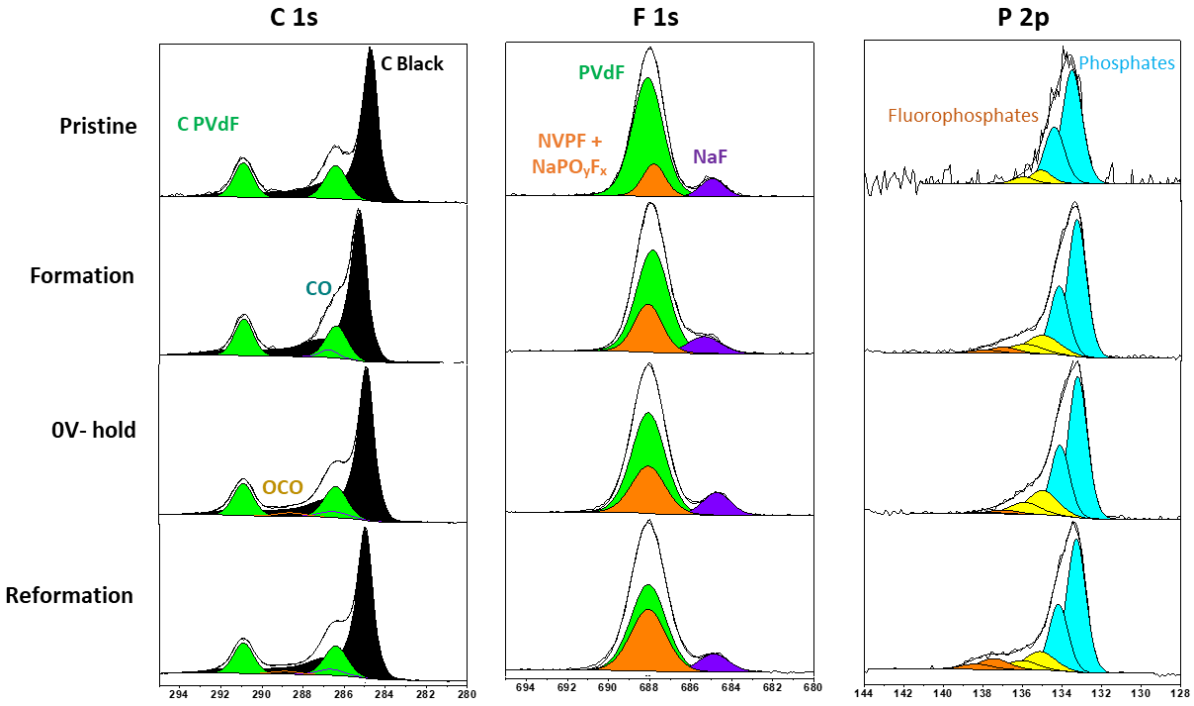

XPS analyses of the NVPF electrodes recovered at different states of NVPF-HC cell cycling as per the points mentioned in Figure 4(a) cycled with control electrolyte. The C1s, F1s and P2p for all the electrodes are cumulated below. The

NaF peaks in the F 1s of pristine NVPF correspond to the residual impurity in the NVPF during the synthesis. Since the formation step, a thin deposited surface is created containing organic (CO, OCO) and inorganic ($NaPO_yF_x$) species. The evolution during the following steps of cycling is very weak indicating significantly less/no change in the CEI.

Supplementary Fig. S6.10

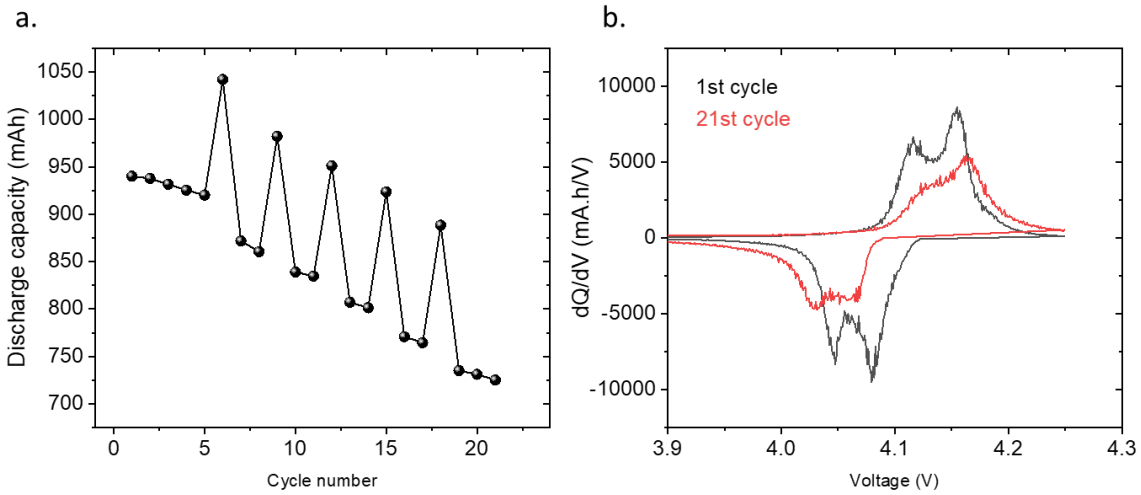

(a) Capacity retention plot for cylindrical 18650 NVPF-HC cell with control electrolyte used for the optical sensing experiment presented in Figure 6 of the main manuscript. (b) Corresponding dQ/dV vs. V of the 1st and 21st cycle shows the peak shifted to right as a result of polarization but absence of any sodium plating.

Supplementary Fig. S6.11

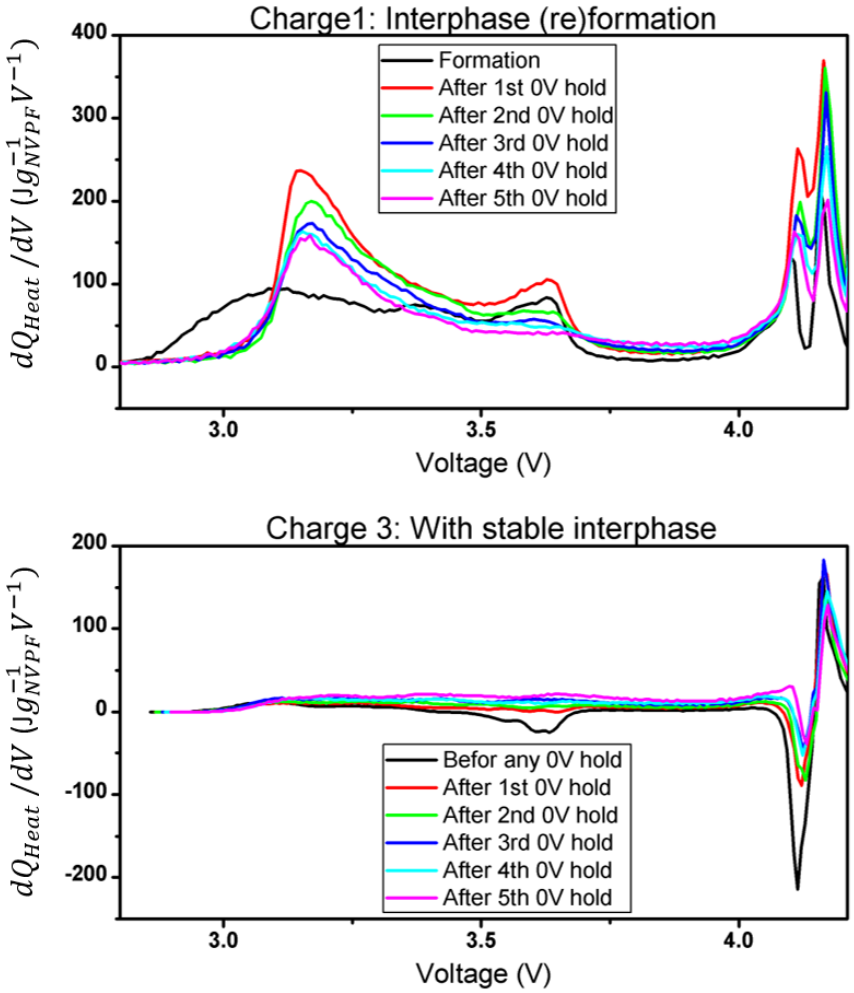

Heat derivative of the charge cycles after 2nd, 3rd and 4th 0V hold process. The heat evolution after each 0V hold (charge 1) indicates the SEI reformation and the process is exothermic. In the charge 3 after each 0V hold, the heat evolution is reduced indicating the stabilization of interphases.

Supplementary Fig. S6.12

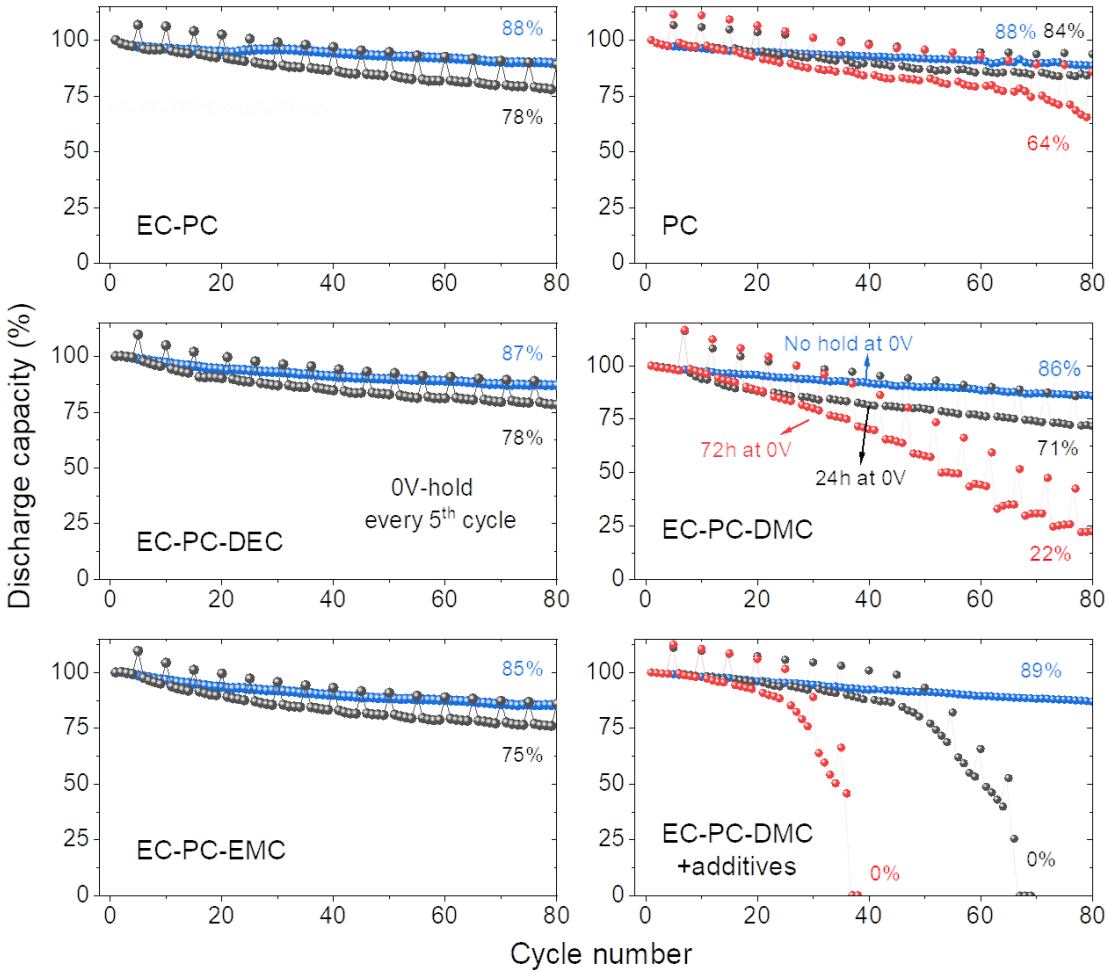

Capacity retention plots of NVPF-HC cells cycled using electrolyte formulations that contain different solvent(s) as mentioned in the figure. EC: Ethylene carbonate, PC: propylene carbonate, DEC: Diethyl carbonate, DMC: Dimethyl carbonate, EMC: Ethyl methyl carbonate. Additives namely NaODFB, VC, SN and TMSPi are used in only one set of experiments (mentioned EC-PC-DMC+ additives). The cells were cycled between 2- 4.25 V at C/5 rate and only for 0V hold cycles, the cells were pushed to 0V. The data is used to derive the information in **Fig. 6.9** of the **Chapter 6**.

Supplementary Fig. S6.13

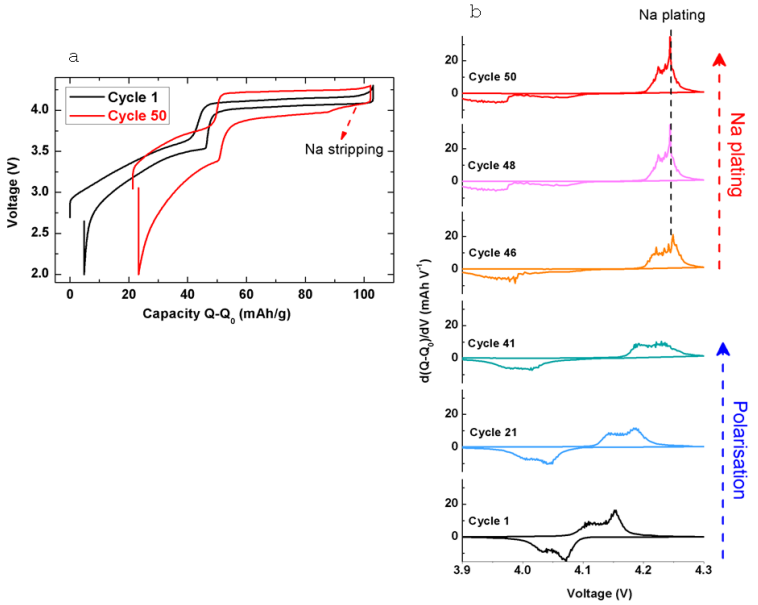

(a) Cycling profile of NVPF-HC coin cell cycled with electrolytes containing additives (0.5% NaODFB+ 3% VC+ 3% SN+ 0.2% TMSPi) with repeated 0V hold (24h) for each 5 cycles. The cell polarization increases that leads to sodium plating which is visible as sharp peak around ~4.22V in the derivative plot (b). The corresponding capacity retention data is used in Figure 7c of the main manuscript.

Supplementary Fig. S6.14

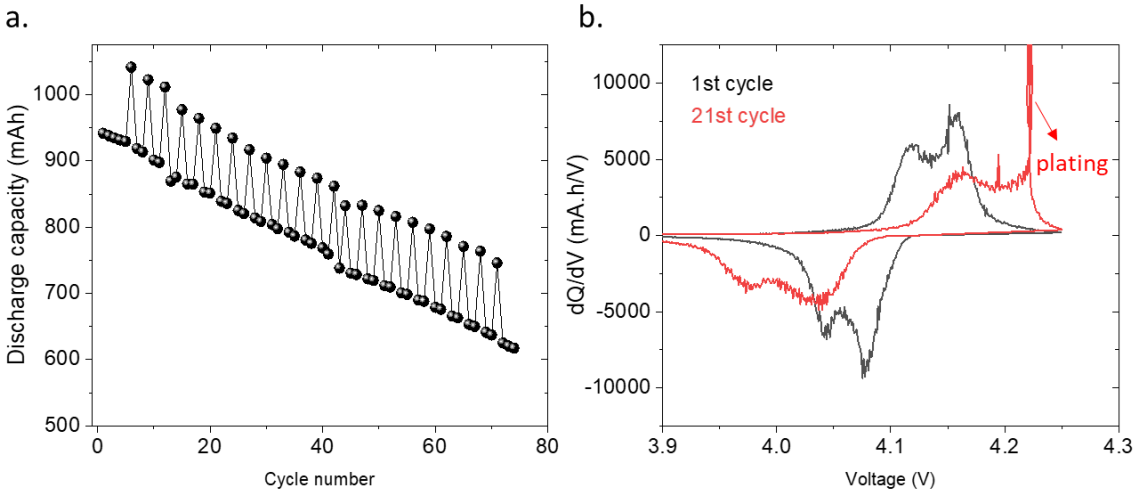

(a) Capacity retention plot for cylindrical 18650 NVPF-HC cell with electrolytes containing additives (0.5% NaODFB+ 3% VC+ 3% SN+ 0.2% TMSPi) with repeated 0V hold (24h) every 3 cycles. (b) Corresponding dQ/dV vs. V of the 1st and 21st cycle indicates that the sodium plating at the negative electrode due to repetitive holds at 0V.

Supplementary Fig. S6.15

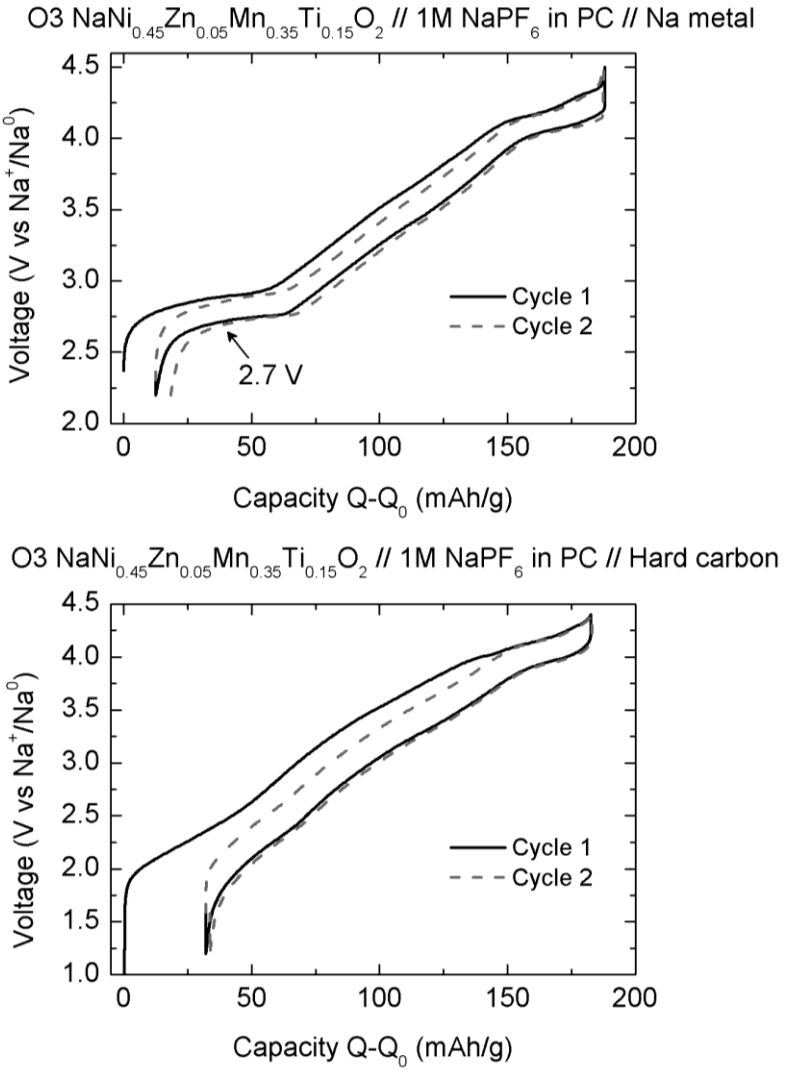

Galvanostatic charge- discharge cycles of O3 type $NaNi_{0.45}Zn_{0.05}Mn_{0.35}Ti_{0.15}O_2$ (ZNMT) in (top) Na-metal half-cell and (bottom) Na-ion full cell configuration using hard carbon as counter electrode. The cells were cycled at C/10 rate (1C= ~240 mAh/g) at room temperature. The different redox plateau and sloppy potential regions observed with this sodium layered oxide is due to the phase transitions in the material. The lowest redox of this layered oxide happens around 2.7V and it can be modified by changing the transition metal(s) stoichiometry.

Supplementary Table S6.

	Electrode material	Organic SEI	Inorganic SEI
HC-Prist	10		
HC-1	10	12.3(9)	37.4(6)
HC-2	10	8.1(7)	26.5(8)
HC-3	10	20.9(6)	46.8(8)

Quantification of SEI components obtained from XPS analyses. The C1s data is used for quantifying the organic components where the all species except the active material is used for calculation. P2p and F1s spectra are used for inorganic components quantifications. All values were normalized by normalizing the HC spectrum intensity as 10.

References

1. Executive summary – World Energy Outlook 2022 – Analysis IEA. https://www.iea.org/reports/world-energy-outlook-2022/executive-summary.

2. Climate change: A Summary of the Science | Royal Society https://royalsociety.org/topics-policy/publications/2010/climate-change-summary-science/.

3. USGCRP Climate Science Special Report (U.S. Global Change Research Program, Washington, DC).

4. The Paris Agreement | UNFCCC https://unfccc.int/process-and-meetings/the-paris-agreement.

5. AR5 Synthesis Report: Climate Change 2014 — IPCC https://www.ipcc.ch/report/ar5/syr/.

6. Arbabzadeh, M., Sioshansi, R., Johnson, J.X., and Keoleian, G.A. (2019). The role of energy storage in deep decarbonization of electricity production. Nat Commun *10*, 3413. 10.1038/s41467-019-11161-5.

7. Tarascon, J.-M., and Armand, M. (2001). Issues and challenges facing rechargeable lithium batteries. Nature *414*, 359–367. 10.1038/35104644.

8. Yoo, H.D., Markevich, E., Salitra, G., Sharon, D., and Aurbach, D. (2014). On the challenge of developing advanced technologies for electrochemical energy storage and conversion. Materials Today *17*, 110–121. 10.1016/j.mattod.2014.02.014.

9. Cano, Z.P., Banham, D., Ye, S., Hintennach, A., Lu, J., Fowler, M., and Chen, Z. (2018). Batteries and fuel cells for emerging electric vehicle markets. Nat Energy *3*, 279–289. 10.1038/s41560-018-0108-1.

10. Goodenough, J.B., and Park, K.-S. (2013). The Li-Ion Rechargeable Battery: A Perspective. J. Am. Chem. Soc. *135*, 1167–1176. 10.1021/ja3091438.

11. Buchmann, I. (2001). Batteries in a portable world : A handbook on rechargeable batteries for non-engineers. 2nd ed.

12. A Review of Lithium-Ion Battery for Electric Vehicle Applications and Beyond - ScienceDirect https://www.sciencedirect.com/science/article/pii/S1876610219308215.

13. Crabtree, G. (2019). The coming electric vehicle transformation. Science. 10.1126/science.aax0704.

14. Dunn, B., Kamath, H., and Tarascon, J.-M. (2011). Electrical Energy Storage for the Grid: A Battery of Choices. Science. 10.1126/science.1212741.

15. Larcher, D., and Tarascon, J.-M. (2015). Towards greener and more sustainable batteries for electrical energy storage. Nature Chem *7*, 19–29. 10.1038/nchem.2085.

16. A Vision for a Sustainable Battery Value Chain in 2030 World Economic Forum. https://www.weforum.org/reports/a-vision-for-a-sustainable-battery-value-chain-in-2030/.

17. Olivetti, E.A., Ceder, G., Gaustad, G.G., and Fu, X. (2017). Lithium-Ion Battery Supply Chain Considerations: Analysis of Potential Bottlenecks in Critical Metals. Joule *1*, 229–243. 10.1016/j.joule.2017.08.019.

18. Tian, Y., Zeng, G., Rutt, A., Shi, T., Kim, H., Wang, J., Koettgen, J., Sun, Y., Ouyang, B., Chen, T., et al. (2021). Promises and Challenges of Next-Generation "Beyond Li-ion" Batteries for Electric Vehicles and Grid Decarbonization. Chem. Rev. *121*, 1623–1669. 10.1021/acs.chemrev.0c00767.

19. Choi, J.W., and Aurbach, D. (2016). Promise and reality of post-lithium-ion batteries with high energy densities. Nat Rev Mater *1*, 16013. 10.1038/natrevmats.2016.13.

20. Kubota, K., Dahbi, M., Hosaka, T., Kumakura, S., and Komaba, S. (2018). Towards K-Ion and Na-Ion Batteries as "Beyond Li-Ion." The Chemical Record *18*, 459–479. 10.1002/tcr.201700057.

21. Duffner, F., Kronemeyer, N., Tübke, J., Leker, J., Winter, M., and Schmuch, R. (2021). Post-lithium-ion battery cell production and its compatibility with lithium-ion cell production infrastructure. Nat Energy *6*, 123–134. 10.1038/s41560-020-00748-8.

22. Au, H., Crespo-Ribadeneyra, M., and Titirici, M.-M. (2022). Beyond Li-ion batteries: performance, materials diversification, and sustainability. One Earth *5*, 207–211. 10.1016/j.oneear.2022.02.014.

23. Volta, A. (1997). On the electricity excited by the mere contact of conducting substances of different kinds. In a letter from Mr. Alexander Volta, F. R. S. Professor of Natural Philosophy in the University of Pavia, to the Rt. Hon. Sir Joseph Banks, Bart. K. B. P. R. S. Abstracts of the Papers Printed in the Philosophical Transactions of the Royal Society of London *1*, 27–29. 10.1098/rspl.1800.0016.

24. Barak, M. (1980). Electrochemical Power Sources: Primary and Secondary Batteries (IET).

25. Boddula, R., Inamuddin, Pothu, R., and Asiri, A.M. (2020). Rechargeable Batteries: History, Progress, and Applications (John Wiley & Sons).

26. Liu, Y., Su, M.-Y., Gu, Z.-Y., Zhang, K.-Y., Wang, X.-T., Du, M., Guo, J.-Z., and Wu, X.-L. (2022). Advanced Lithium Primary Batteries: Key Materials, Research Progresses and Challenges. The Chemical Record *22*, e202200081. 10.1002/tcr.202200081.

27. Jasinski, R. (1967). High-energy batteries. [Book with 377 publications references and 427 patent references].

28. Whittingham, M.S. (2004). Lithium Batteries and Cathode Materials. Chem. Rev. *104*, 4271–4302. 10.1021/cr020731c.

29. Ikeda, H., Ueno, D.W., Saito, T., Nakaido, S., and Tamura, H. (1977). Lithium-Manganese Dioxide Cell (2). Denki Kagaku *45*, 391–395.

30. Greatbatch, W., Lee, J.H., Mathias, W., Eldridge, M., Moser, J.R., and Schneider, A.A. (1971). The Solid-State Lithium Battery: A New Improved Chemical Power Source for Implantable Cardiac Pacemakers. IEEE Transactions on Biomedical Engineering *BME-18*, 317–324. 10.1109/TBME.1971.4502862.

31. Holmes, C. (2007). The Lithium/Iodine-Polyvinylpyridine Pacemaker Battery - 35 years of Successful Clinical Use. ECS Trans. *6*, 1. 10.1149/1.2790382.

32. Yoshino, A. (2012). The Birth of the Lithium-Ion Battery. Angewandte Chemie International Edition *51*, 5798–5800. 10.1002/anie.201105006.

33. Whittingham, M.S. (1976). Electrical Energy Storage and Intercalation Chemistry. Science *192*, 1126–1127. 10.1126/science.192.4244.1126.

34. Goodenough, J.B., Mizushima, K., and Wiseman, P.J. (1984). Electrochemical cell and method of making ion conductors for said cell.

35. Yoshino, A., Sanechika, K., and Nakajima, T. (1987). Secondary battery.

36. Thackeray, M.M., Johnson, P.J., de Picciotto, L.A., Bruce, P.G., and Goodenough, J.B. (1984). Electrochemical extraction of lithium from LiMn2O4. Materials Research Bulletin *19*, 179–187. 10.1016/0025-5408(84)90088-6.

37. Padhi, A.K., Nanjundaswamy, K.S., and Goodenough, J.B. (1997). Phospho-olivines as Positive-Electrode Materials for Rechargeable Lithium Batteries. J. Electrochem. Soc. *144*, 1188. 10.1149/1.1837571.

38. Lu, Z., and Dahn, J.R. (2005). Cathode compositions for lithium-ion batteries.

39. Ohzuku, T., and Makimura, Y. (2001). Layered Lithium Insertion Material of LiCo1/3Ni1/3Mn1/3O2 for Lithium-Ion Batteries. Chem. Lett. *30*, 642–643. 10.1246/cl.2001.642.

40. The Nobel Prize in Chemistry 2019 NobelPrize.org. https://www.nobelprize.org/prizes/chemistry/2019/summary/.

41. Parant, J.-P., Olazcuaga, R., Devalette, M., Fouassier, C., and Hagenmuller, P. (1971). Sur quelques nouvelles phases de formule NaxMnO2 (x ⩽ 1). Journal of Solid State Chemistry *3*, 1–11. 10.1016/0022-4596(71)90001-6.

42. Fouassier, C., Matejka, G., Reau, J.-M., and Hagenmuller, P. (1973). Sur de nouveaux bronzes oxygénés de formule NaχCoO2 (χ1). Le système cobalt-oxygène-sodium. Journal of Solid State Chemistry *6*, 532–537. 10.1016/S0022-4596(73)80011-8.

43. Delmas, C., Fouassier, C., and Hagenmuller, P. (1980). Structural classification and properties of the layered oxides. Physica B+C *99*, 81–85. 10.1016/0378-4363(80)90214-4.

44. Delmas, C., Braconnier, J.-J., Fouassier, C., and Hagenmuller, P. (1981). Electrochemical intercalation of sodium in NaxCoO2 bronzes. Solid State Ionics *3–4*, 165–169. 10.1016/0167-2738(81)90076-X.

45. Braconnier, J.J., Delmas, C., and Hagenmuller, P. (1982). Etude par desintercalation electrochimique des systemes NaxCrO2 et NaxNiO2. Materials Research Bulletin *17*, 993–1000. 10.1016/0025-5408(82)90124-6.

46. Maazaz, A., Delmas, C., and Hagenmuller, P. (1983). A study of the NaxTiO2 system by electrochemical deintercalation. Journal of Inclusion Phenomena *1*, 45–51. 10.1007/BF00658014.

47. Mendiboure, A., Delmas, C., and Hagenmuller, P. (1985). Electrochemical intercalation and deintercalation of NaxMnO2 bronzes. Journal of Solid State Chemistry *57*, 323–331. 10.1016/0022-4596(85)90194-X.

48. Takeda, Y., Nakahara, K., Nishijima, M., Imanishi, N., Yamamoto, O., Takano, M., and Kanno, R. (1994). Sodium deintercalation from sodium iron oxide. Materials Research Bulletin *29*, 659–666. 10.1016/0025-5408(94)90122-8.

49. Delmas, C., Braconnier, J.-J., and Hagenmuller, P. (1982). A new variety of LiCoO2 with an unusual oxygen packing obtained by exchange reaction. Materials Research Bulletin *17*, 117–123. 10.1016/0025-5408(82)90192-1.

50. Delmas, C., Olazcuaga, R., Le Flem, G., Hagenmuller, P., Cherkaoui, F., and Brochu, R. (1981). Crystal chemistry of the Na1+xZr2−xLx(PO4)3 (L = Cr, In, Yb) solid solutions. Materials Research Bulletin *16*, 285–290. 10.1016/0025-5408(81)90044-1.

51. Delmas, C., Cherkaoui, F., Nadiri, A., and Hagenmuller, P. (1987). A nasicon-type phase as intercalation electrode: NaTi2(PO4)3. Materials Research Bulletin *22*, 631–639. 10.1016/0025-5408(87)90112-7.

52. Tarascon, J.M., and Hull, G.W. (1986). Sodium intercalation into the layer oxides NaxMo2O4. Solid State Ionics *22*, 85–96. 10.1016/0167-2738(86)90062-7.

53. Kubota, K., and Komaba, S. (2015). Review—Practical Issues and Future Perspective for Na-Ion Batteries. J. Electrochem. Soc. *162*, A2538–A2550. 10.1149/2.0151514jes.

54. Yabuuchi, N., Kubota, K., Dahbi, M., and Komaba, S. (2014). Research Development on Sodium-Ion Batteries. Chem. Rev. *114*, 11636–11682. 10.1021/cr500192f.

55. Hwang, J.-Y., Myung, S.-T., and Sun, Y.-K. (2017). Sodium-ion batteries: present and future. Chem. Soc. Rev. *46*, 3529–3614. 10.1039/C6CS00776G.

56. Reddy, M.V., Mauger, A., Julien, C.M., Paolella, A., and Zaghib, K. (2020). Brief History of Early Lithium-Battery Development. Materials *13*, 1884. 10.3390/ma13081884.

57. History of the lithium-ion battery (2023). Wikipedia. https://en.wikipedia.org/w/index.php?title=History_of_the_lithium-ion_battery&oldid=1170808737.

58. Blomgren, G.E. (2017). The Development and Future of Lithium Ion Batteries. J. Electrochem. Soc. *164*, A5019–A5025. 10.1149/2.0251701jes.

59. Tarascon, J.-M. (2020). Na-ion versus Li-ion Batteries: Complementarity Rather than Competitiveness. Joule *4*, 1616–1620. 10.1016/j.joule.2020.06.003.

60. Abraham, K.M. (2020). How Comparable Are Sodium-Ion Batteries to Lithium-Ion Counterparts? ACS Energy Lett. *5*, 3544–3547. 10.1021/acsenergylett.0c02181.

61. Stevens, D.A., and Dahn, J.R. (2001). The Mechanisms of Lithium and Sodium Insertion in Carbon Materials. J. Electrochem. Soc. *148*, A803. 10.1149/1.1379565.

62. Stevens, D.A., and Dahn, J.R. (2000). High Capacity Anode Materials for Rechargeable Sodium-Ion Batteries. J. Electrochem. Soc. *147*, 1271. 10.1149/1.1393348.

63. Komaba, S., Murata, W., Ishikawa, T., Yabuuchi, N., Ozeki, T., Nakayama, T., Ogata, A., Gotoh, K., and Fujiwara, K. (2011). Electrochemical Na Insertion and Solid Electrolyte Interphase for Hard-Carbon Electrodes and Application to Na-Ion Batteries. Advanced Functional Materials *21*, 3859–3867. 10.1002/adfm.201100854.

64. Peters, J.F., Baumann, M., Binder, J.R., and Weil, M. (2021). On the environmental competitiveness of sodium-ion batteries under a full life cycle perspective – a cell-chemistry specific modelling approach. Sustainable Energy Fuels *5*, 6414–6429. 10.1039/D1SE01292D.

65. Liu, T., Zhang, Y., Chen, C., Lin, Z., Zhang, S., and Lu, J. (2019). Sustainability-inspired cell design for a fully recyclable sodium ion battery. Nat Commun *10*, 1965. 10.1038/s41467-019-09933-0.

66. Wang, C.-Y., Liu, T., Yang, X.-G., Ge, S., Stanley, N.V., Rountree, E.S., Leng, Y., and McCarthy, B.D. (2022). Fast charging of energy-dense lithium-ion batteries. Nature *611*, 485–490. 10.1038/s41586-022-05281-0.

67. Yang, X.-G., Liu, T., and Wang, C.-Y. (2021). Thermally modulated lithium iron phosphate batteries for mass-market electric vehicles. Nat Energy *6*, 176–185. 10.1038/s41560-020-00757-7.

68. Rudola, A., Sayers, R., Wright, C.J., and Barker, J. (2023). Opportunities for moderate-range electric vehicles using sustainable sodium-ion batteries. Nat Energy *8*, 215–218. 10.1038/s41560-023-01215-w.

69. Assat, G. (2018). Anionic redox for high-energy batteries. Fundamental understanding, practical challenges, and future outlook.

70. Frith, J.T., Lacey, M.J., and Ulissi, U. (2023). A non-academic perspective on the future of lithium-based batteries. Nat Commun *14*, 420. 10.1038/s41467-023-35933-2.

71. Goodenough, J.B., and Kim, Y. (2010). Challenges for Rechargeable Li Batteries. Chem. Mater. *22*, 587–603. 10.1021/cm901452z.

72. Hina launches sodium-ion battery tests in vehicles - electrive.com https://www.electrive.com/. https://www.electrive.com/2023/02/23/hina-launches-sodium-ion-battery-tests-in-vehicles/.

73. CATL's First Sodium-ion Battery to Power Chery EV Models https://www.catl.com/en/news/6013.html.

74. Pié, J.-P. (2021). Les batteries Sodium de Tiamat électrisent Plastic Omnium. GreenUnivers. https://www.greenunivers.com/2021/03/les-batteries-sodium-de-tiamat-electrisent-plastic-omnium-254322/.

75. Tournevis sans fil DEXTER Sodium 3.6vsd2-so.5 3.6 V 0.7 Ah | Leroy Merlin Leroy Merlin - Bricolage, déco, maison, jardin. https://www.leroymerlin.fr/produits/tournevis-sans-fil-dexter-sodium-3-6vsd2-so-5-3-6-v-0-7-ah-86650845.html.

76. Altris https://www.altris.se/news/scaling-up-production-of-fennac-in-2022.

77. Bard, A.J., Faulkner, L.R., and White, H.S. (2022). Electrochemical Methods: Fundamentals and Applications (John Wiley & Sons).

78. Wang, S., Peng, B., Lu, J., Jie, Y., Li, X., Pan, Y., Han, Y., Cao, R., Xu, D., and Jiao, S. (2023). Recent Progress in Rechargeable Sodium Metal Batteries: A Review. Chemistry – A European Journal *29*, e202202380. 10.1002/chem.202202380.

79. Harlow, J.E., Ma, X., Li, J., Logan, E., Liu, Y., Zhang, N., Ma, L., Glazier, S.L., Cormier, M.M.E., Genovese, M., et al. (2019). A Wide Range of Testing Results on an Excellent Lithium-Ion Cell Chemistry to be used as Benchmarks for New Battery Technologies. J. Electrochem. Soc. *166*, A3031–A3044. 10.1149/2.0981913jes.

80. Xu, K. (2004). Nonaqueous Liquid Electrolytes for Lithium-Based Rechargeable Batteries. Chem. Rev. *104*, 4303–4418. 10.1021/cr030203g.

81. Bianchini, M., Roca-Ayats, M., Hartmann, P., Brezesinski, T., and Janek, J. (2019). There and Back Again—The Journey of LiNiO2 as a Cathode Active Material. Angewandte Chemie International Edition *58*, 10434–10458. 10.1002/anie.201812472.

82. Huo, H., Xing, Y., Pecht, M., Züger, B.J., Khare, N., and Vezzini, A. (2017). Safety Requirements for Transportation of Lithium Batteries. Energies *10*, 793. 10.3390/en10060793.

83. Barai, A., Uddin, K., Chevalier, J., Chouchelamane, G.H., McGordon, A., Low, J., and Jennings, P. (2017). Transportation Safety of Lithium Iron Phosphate Batteries - A Feasibility Study of Storing at Very Low States of Charge. Sci Rep *7*, 5128. 10.1038/s41598-017-05438-2.

84. Krause, L.J., Jensen, L.D., and Dahn, J.R. (2012). Measurement of Parasitic Reactions in Li Ion Cells by Electrochemical Calorimetry. J. Electrochem. Soc. *159*, A937. 10.1149/2.021207jes.

85. Logan, E.R., Hebecker, H., Ma, X., Quinn, J., HyeJeong, Y., Kumakura, S., Paulsen, J., and Dahn, J.R. (2020). A Comparison of the Performance of Different Morphologies of $LiNi_{0.8}Mn_{0.1}Co_{0.1}O_2$ Using Isothermal Microcalorimetry, Ultra-High Precision Coulometry, and Long-Term Cycling. J. Electrochem. Soc. *167*, 060530. 10.1149/1945-7111/ab8620.

86. Tarascon, J.M. (2016). The Li-Ion Battery: 25 Years of Exciting and Enriching Experiences. Electrochem. Soc. Interface *25*, 79. 10.1149/2.F08163if.

87. Fang, L., Bahlawane, N., Sun, W., Pan, H., Xu, B.B., Yan, M., and Jiang, Y. (2021). Conversion-Alloying Anode Materials for Sodium Ion Batteries. Small *17*, 2101137. 10.1002/smll.202101137.

88. Moriwake, H., Kuwabara, A., Fisher, C.A.J., and Ikuhara, Y. (2017). Why is sodium-intercalated graphite unstable? RSC Adv. *7*, 36550–36554. 10.1039/C7RA06777A.

89. Liu, Y., Merinov, B.V., and Goddard, W.A. (2016). Origin of low sodium capacity in graphite and generally weak substrate binding of Na and Mg among alkali and alkaline earth metals. Proc. Natl. Acad. Sci. U.S.A. *113*, 3735–3739. 10.1073/pnas.1602473113.

90. Stratford, J.M., Kleppe, A.K., Keeble, D.S., Chater, P.A., Meysami, S.S., Wright, C.J., Barker, J., Titirici, M.-M., Allan, P.K., and Grey, C.P. (2021). Correlating Local Structure and Sodium Storage in Hard Carbon Anodes: Insights from Pair Distribution Function Analysis and Solid-State NMR. J. Am. Chem. Soc. *143*, 14274–14286. 10.1021/jacs.1c06058.

91. Youn, Y., Gao, B., Kamiyama, A., Kubota, K., Komaba, S., and Tateyama, Y. (2021). Nanometer-size Na cluster formation in micropore of hard carbon as origin of higher-capacity Na-ion battery. npj Comput Mater *7*, 1–8. 10.1038/s41524-021-00515-7.

92. Kamiyama, A., Kubota, K., Igarashi, D., Youn, Y., Tateyama, Y., Ando, H., Gotoh, K., and Komaba, S. (2021). MgO-Template Synthesis of Extremely High Capacity Hard Carbon for Na-Ion Battery. Angewandte Chemie International Edition *60*, 5114–5120. 10.1002/anie.202013951.

93. Hasegawa, G., Kanamori, K., Kannari, N., Ozaki, J., Nakanishi, K., and Abe, T. (2015). Hard Carbon Anodes for Na-Ion Batteries: Toward a Practical Use. ChemElectroChem *2*, 1917–1920. 10.1002/celc.201500412.

94. Sayahpour, B., Hirsh, H., Parab, S., Nguyen, L.H.B., Zhang, M., and Meng, Y.S. (2022). Perspective: Design of cathode materials for sustainable sodium-ion batteries. MRS Energy & Sustainability *9*, 183–197. 10.1557/s43581-022-00029-9.

95. Gupta, P., Pushpakanth, S., Haider, M.A., and Basu, S. (2022). Understanding the Design of Cathode Materials for Na-Ion Batteries. ACS Omega *7*, 5605–5614. 10.1021/acsomega.1c05794.

96. Delmas, C., Carlier, D., and Guignard, M. (2021). The Layered Oxides in Lithium and Sodium-Ion Batteries: A Solid-State Chemistry Approach. Advanced Energy Materials *11*, 2001201. 10.1002/aenm.202001201.

97. Mariyappan, S., Wang, Q., and Tarascon, J.M. (2018). Will Sodium Layered Oxides Ever Be Competitive for Sodium Ion Battery Applications? J. Electrochem. Soc. *165*, A3714–A3722. 10.1149/2.0201816jes.

98. You, Y., Dolocan, A., Li, W., and Manthiram, A. (2019). Understanding the Air-Exposure Degradation Chemistry at a Nanoscale of Layered Oxide Cathodes for Sodium-Ion Batteries. Nano Lett. *19*, 182–188. 10.1021/acs.nanolett.8b03637.

99. Masquelier, C., and Croguennec, L. (2013). Polyanionic (Phosphates, Silicates, Sulfates) Frameworks as Electrode Materials for Rechargeable Li (or Na) Batteries. Chem. Rev. *113*, 6552–6591. 10.1021/cr3001862.

100. Abakumov, A.M., Fedotov, S.S., Antipov, E.V., and Tarascon, J.-M. (2020). Solid state chemistry for developing better metal-ion batteries. Nat Commun *11*, 4976. 10.1038/s41467-020-18736-7.

101. Ling, J., Karuppiah, C., Krishnan, S.G., Reddy, M.V., Misnon, I.I., Ab Rahim, M.H., Yang, C.-C., and Jose, R. (2021). Phosphate Polyanion Materials as High-Voltage Lithium-Ion Battery Cathode: A Review. Energy Fuels *35*, 10428–10450. 10.1021/acs.energyfuels.1c01102.

102. Saravanan, K., Mason, C.W., Rudola, A., Wong, K.H., and Balaya, P. (2013). The First Report on Excellent Cycling Stability and Superior Rate Capability of Na3V2(PO4)3 for Sodium Ion Batteries. Advanced Energy Materials *3*, 444–450. 10.1002/aenm.201200803.

103. Barker, J., Gover, R.K.B., Burns, P., and Bryan, A.J. (2006). Hybrid-Ion: A Lithium-Ion Cell Based on a Sodium Insertion Material. Electrochem. Solid-State Lett. *9*, A190. 10.1149/1.2168288.

104. Le Meins, J.-M., Crosnier-Lopez, M.-P., Hemon-Ribaud, A., and Courbion, G. (1999). Phase Transitions in the Na3M2(PO4)2F3 Family (M=Al3+, V3+, Cr3+, Fe3+, Ga3+): Synthesis, Thermal, Structural, and Magnetic Studies. Journal of Solid State Chemistry *148*, 260–277. 10.1006/jssc.1999.8447.

105. Shakoor, R.A., Seo, D.-H., Kim, H., Park, Y.-U., Kim, J., Kim, S.-W., Gwon, H., Lee, S., and Kang, K. (2012). A combined first principles and experimental study on Na3V2(PO4)2F3 for rechargeable Na batteries. J. Mater. Chem. *22*, 20535–20541. 10.1039/C2JM33862A.

106. Broux, T., Bamine, T., Fauth, F., Simonelli, L., Olszewski, W., Marini, C., Ménétrier, M., Carlier, D., Masquelier, C., and Croguennec, L. (2016). Strong Impact of the Oxygen Content in $Na_3V_2(PO_4)_2F_{3-y}O_y$ ($0 \le y \le 0.5$) on Its Structural and Electrochemical Properties. Chem. Mater. *28*, 7683–7692. 10.1021/acs.chemmater.6b02659.

107. Nguyen, L.H.B., Broux, T., Camacho, P.S., Denux, D., Bourgeois, L., Belin, S., Iadecola, A., Fauth, F., Carlier, D., Olchowka, J., et al. (2019). Stability in water and electrochemical properties of the Na3V2(PO4)2F3 – Na3(VO)2(PO4)2F solid solution. Energy Storage Materials *20*, 324–334. 10.1016/j.ensm.2019.04.010.

108. Broux, T., Fauth, F., Hall, N., Chatillon, Y., Bianchini, M., Bamine, T., Leriche, J., Suard, E., Carlier, D., Reynier, Y., et al. (2019). High Rate Performance for Carbon-Coated $Na_3V_2(PO_4)_2F_3$ in Na-Ion Batteries. Small Methods *3*, 1800215. 10.1002/smtd.201800215.

109. Hurlbutt, K., Wheeler, S., Capone, I., and Pasta, M. (2018). Prussian Blue Analogs as Battery Materials. Joule *2*, 1950–1960. 10.1016/j.joule.2018.07.017.

110. Wang, B., Han, Y., Wang, X., Bahlawane, N., Pan, H., Yan, M., and Jiang, Y. (2018). Prussian Blue Analogs for Rechargeable Batteries. iScience *3*, 110–133. 10.1016/j.isci.2018.04.008.

111. Peng, J., Zhang, W., Liu, Q., Wang, J., Chou, S., Liu, H., and Dou, S. (2022). Prussian Blue Analogues for Sodium-Ion Batteries: Past, Present, and Future. Advanced Materials *34*, 2108384. 10.1002/adma.202108384.

112. Wu, X., Wu, C., Wei, C., Hu, L., Qian, J., Cao, Y., Ai, X., Wang, J., and Yang, H. (2016). Highly Crystallized Na2CoFe(CN)6 with Suppressed Lattice Defects as Superior Cathode Material for Sodium-Ion Batteries. ACS Appl. Mater. Interfaces *8*, 5393–5399. 10.1021/acsami.5b12620.

113. Hwang, J.-Y., Oh, S.-M., Myung, S.-T., Chung, K.Y., Belharouak, I., and Sun, Y.-K. (2015). Radially aligned hierarchical columnar structure as a cathode material for high energy density sodium-ion batteries. Nat Commun *6*, 6865. 10.1038/ncomms7865.

114. He, S., Zhao, J., Rong, X., Xu, C., Zhang, Q., Shen, X., Qi, X., Li, Y., Li, X., Niu, Y., et al. (2022). Solvent-free mechanochemical synthesis of Na-rich Prussian white cathodes for high-performance Na-ion batteries. Chemical Engineering Journal *428*, 131083. 10.1016/j.cej.2021.131083.

115. Leng, F., Tan, C.M., and Pecht, M. (2015). Effect of Temperature on the Aging rate of Li Ion Battery Operating above Room Temperature. Scientific Reports *5*, 12967. 10.1038/srep12967.

116. Handel, P., Fauler, G., Kapper, K., Schmuck, M., Stangl, C., Fischer, R., Uhlig, F., and Koller, S. (2014). Thermal aging of electrolytes used in lithium-ion batteries – An investigation of the impact of protic impurities and different housing materials. Journal of Power Sources *267*, 255–259. 10.1016/j.jpowsour.2014.05.080.

117. Ramadass, P., Haran, B., White, R., and Popov, B.N. (2002). Capacity fade of Sony 18650 cells cycled at elevated temperatures: Part I. Cycling performance. Journal of Power Sources *112*, 606–613. 10.1016/S0378-7753(02)00474-3.

118. Bodenes, L., Naturel, R., Martinez, H., Dedryvère, R., Menetrier, M., Croguennec, L., Pérès, J.-P., Tessier, C., and Fischer, F. (2013). Lithium secondary batteries working at very high temperature: Capacity fade and understanding of aging mechanisms. Journal of Power Sources *236*, 265–275. 10.1016/j.jpowsour.2013.02.067.

119. Waldmann, T., Wilka, M., Kasper, M., Fleischhammer, M., and Wohlfahrt-Mehrens, M. (2014). Temperature dependent ageing mechanisms in Lithium-ion batteries – A Post-Mortem study. Journal of Power Sources *262*, 129–135. 10.1016/j.jpowsour.2014.03.112.

120. Hijazi, H., Ye, Z., Zhang, L., Deshmukh, J., Johnson, M.B., Dahn, J.R., and Metzger, M. (2023). Impact of Sodium Metal Plating on Cycling Performance of Layered Oxide/Hard Carbon Sodium-ion Pouch Cells with Different Voltage Cut-offs. J. Electrochem. Soc. *170*, 070512. 10.1149/1945-7111/ace4fa.

121. Mogensen, R., Buckel, A., Colbin, S., and Younesi, R. (2021). A Wide-Temperature-Range, Low-Cost, Fluorine-Free Battery Electrolyte Based On Sodium Bis(Oxalate)Borate. Chem. Mater. *33*, 1130–1139. 10.1021/acs.chemmater.0c03570.

122. Yan, G., Reeves, K., Foix, D., Li, Z., Cometto, C., Mariyappan, S., Salanne, M., and Tarascon, J. (2019). A New Electrolyte Formulation for Securing High Temperature Cycling and Storage Performances of Na-Ion Batteries. Adv. Energy Mater. *9*, 1901431. 10.1002/aenm.201901431.

123. Cometto, C., Yan, G., Mariyappan, S., and Tarascon, J.-M. (2019). Means of Using Cyclic Voltammetry to Rapidly Design a Stable DMC-Based Electrolyte for Na-Ion Batteries. J. Electrochem. Soc. *166*, A3723–A3730. 10.1149/2.0721915jes.

124. Li, Z., Dadsetan, M., Gao, J., Zhang, S., Cai, L., Naseri, A., Jimenez-Castaneda, M.E., Filley, T., Miller, J.T., Thomson, M.J., et al. (2021). Revealing the Thermal Safety of Prussian Blue Cathode for Safer Nonaqueous Batteries. Advanced Energy Materials *11*, 2101764. 10.1002/aenm.202101764.

125. Liu, Q., Hu, Z., Chen, M., Zou, C., Jin, H., Wang, S., Chou, S.-L., Liu, Y., and Dou, S.-X. (2020). The Cathode Choice for Commercialization of Sodium-Ion Batteries: Layered Transition Metal Oxides versus Prussian Blue Analogs. Advanced Functional Materials *30*, 1909530. 10.1002/adfm.201909530.

126. A start-up for much faster batteries | CNRS (2017). https://www.cnrs.fr/en/start-much-faster-batteries.

127. Peled, E., and Menkin, S. (2017). Review—SEI: Past, Present and Future. J. Electrochem. Soc. *164*, A1703. 10.1149/2.1441707jes.

128. Peled, E., Golodnitsky, D., and Ardel, G. (1997). Advanced Model for Solid Electrolyte Interphase Electrodes in Liquid and Polymer Electrolytes. J. Electrochem. Soc. *144*, L208. 10.1149/1.1837858.

129. Peled, E. (1979). The Electrochemical Behavior of Alkali and Alkaline Earth Metals in Nonaqueous Battery Systems—The Solid Electrolyte Interphase Model. J. Electrochem. Soc. *126*, 2047. 10.1149/1.2128859.

130. Thomas, M.G.S.R., Bruce, P.G., and Goodenough, J.B. (1985). AC Impedance Analysis of Polycrystalline Insertion Electrodes: Application to Li1 − x CoO2. J. Electrochem. Soc. *132*, 1521. 10.1149/1.2114158.

131. Kanamura, K., Toriyama, S., Shiraishi, S., Ohashi, M., and Takehara, Z. (1996). Studies on electrochemical oxidation of non-aqueous electrolyte on the LiCoO2 thin film electrode. Journal of Electroanalytical Chemistry *419*, 77–84. 10.1016/S0022-0728(96)04862-0.

132. Aurbach, D., Levi, M.D., Levi, E., Teller, H., Markovsky, B., Salitra, G., Heider, U., and Heider, L. (1998). Common Electroanalytical Behavior of Li Intercalation Processes into Graphite and Transition Metal Oxides. J. Electrochem. Soc. *145*, 3024. 10.1149/1.1838758.

133. Xu, K. (2014). Electrolytes and Interphases in Li-Ion Batteries and Beyond. Chem. Rev. *114*, 11503–11618. 10.1021/cr500003w.

134. Xu, K. (2023). Interfaces and interphases in batteries. Journal of Power Sources *559*, 232652. 10.1016/j.jpowsour.2023.232652.

135. Linden, D., and Reddy, T.B. eds. (2002). Handbook of batteries 3rd ed. (McGraw-Hill).

136. Tarascon, J.M., and Guyomard, D. (1994). New electrolyte compositions stable over the 0 to 5 V voltage range and compatible with the Li1+xMn2O4/carbon Li-ion cells. Solid State Ionics *69*, 293–305. 10.1016/0167-2738(94)90418-9.

137. Fang, C., Tran, T.-N., Zhao, Y., and Liu, G. (2021). Electrolyte decomposition and solid electrolyte interphase revealed by mass spectrometry. Electrochimica Acta *399*, 139362. 10.1016/j.electacta.2021.139362.

138. Gachot, G., Ribière, P., Mathiron, D., Grugeon, S., Armand, M., Leriche, J.-B., Pilard, S., and Laruelle, S. (2011). Gas Chromatography/Mass Spectrometry As a Suitable Tool for the Li-Ion Battery Electrolyte Degradation Mechanisms Study. Anal. Chem. *83*, 478–485. 10.1021/ac101948u.

139. Gachot, G., Grugeon, S., Armand, M., Pilard, S., Guenot, P., Tarascon, J.-M., and Laruelle, S. (2008). Deciphering the multi-step degradation mechanisms of carbonate-based electrolyte in Li batteries. Journal of Power Sources *178*, 409–421. 10.1016/j.jpowsour.2007.11.110.

140. Rowden, B., and Garcia-Araez, N. (2020). A review of gas evolution in lithium ion batteries. Energy Reports *6*, 10–18. 10.1016/j.egyr.2020.02.022.

141. Baird, A.R., Archibald, E.J., Marr, K.C., and Ezekoye, O.A. (2020). Explosion hazards from lithium-ion battery vent gas. Journal of Power Sources *446*, 227257. 10.1016/j.jpowsour.2019.227257.

142. Barnes, P., Smith, K., Parrish, R., Jones, C., Skinner, P., Storch, E., White, Q., Deng, C., Karsann, D., Lau, M.L., et al. (2020). A non-aqueous sodium hexafluorophosphate-based electrolyte degradation study: Formation and mitigation of hydrofluoric acid. Journal of Power Sources *447*, 227363. 10.1016/j.jpowsour.2019.227363.

143. An, S.J., Li, J., Daniel, C., Mohanty, D., Nagpure, S., and Wood, D.L. (2016). The state of understanding of the lithium-ion-battery graphite solid electrolyte interphase (SEI) and its relationship to formation cycling. Carbon *105*, 52–76. 10.1016/j.carbon.2016.04.008.

144. von Wald Cresce, A., Borodin, O., and Xu, K. (2012). Correlating Li+ Solvation Sheath Structure with Interphasial Chemistry on Graphite. J. Phys. Chem. C *116*, 26111–26117. 10.1021/jp303610t.

145. Pan, Y., Zhang, Y., Parimalam, B.S., Nguyen, C.C., Wang, G., and Lucht, B.L. (2017). Investigation of the solid electrolyte interphase on hard carbon electrode for sodium ion batteries. Journal of Electroanalytical Chemistry *799*, 181–186. 10.1016/j.jelechem.2017.06.002.

146. Yan, G., Alves-Dalla-Corte, D., Yin, W., Madern, N., Gachot, G., and Tarascon, J.-M. (2018). Assessment of the Electrochemical Stability of Carbonate-Based Electrolytes in Na-Ion Batteries. J. Electrochem. Soc. *165*, A1222–A1230. 10.1149/2.0311807jes.

147. Eshetu, G.G., Grugeon, S., Kim, H., Jeong, S., Wu, L., Gachot, G., Laruelle, S., Armand, M., and Passerini, S. (2016). Comprehensive Insights into the Reactivity of Electrolytes Based on Sodium Ions. ChemSusChem *9*, 462–471. 10.1002/cssc.201501605.

148. Gauthier, M., Carney, T.J., Grimaud, A., Giordano, L., Pour, N., Chang, H.-H., Fenning, D.P., Lux, S.F., Paschos, O., Bauer, C., et al. (2015). Electrode–Electrolyte Interface in Li-Ion Batteries: Current Understanding and New Insights. J. Phys. Chem. Lett. *6*, 4653–4672. 10.1021/acs.jpclett.5b01727.

149. Zhang, L., Tsolakidou, C., Mariyappan, S., Tarascon, J.-M., and Trabesinger, S. (2021). Unraveling gas evolution in sodium batteries by online electrochemical mass spectrometry. Energy Storage Materials *42*, 12–21. 10.1016/j.ensm.2021.07.005.

150. Rinkel, B.L.D., Hall, D.S., Temprano, I., and Grey, C.P. (2020). Electrolyte Oxidation Pathways in Lithium-Ion Batteries. J. Am. Chem. Soc. *142*, 15058–15074. 10.1021/jacs.0c06363.

151. Pham, T.A., Kweon, K.E., Samanta, A., Lordi, V., and Pask, J.E. (2017). Solvation and Dynamics of Sodium and Potassium in Ethylene Carbonate from ab Initio Molecular Dynamics Simulations. J. Phys. Chem. C *121*, 21913–21920. 10.1021/acs.jpcc.7b06457.

152. Cresce, A.V., Russell, S.M., Borodin, O., Allen, J.A., Schroeder, M.A., Dai, M., Peng, J., Gobet, M.P., Greenbaum, S.G., Rogers, R.E., et al. (2017). Solvation behavior of carbonate-based electrolytes in sodium ion batteries. Phys. Chem. Chem. Phys. *19*, 574–586. 10.1039/C6CP07215A.

153. Hijazi, H., Desai, P., and Mariyappan, S. (2021). Non-Aqueous Electrolytes for Sodium-Ion Batteries: Challenges and Prospects Towards Commercialization. Batteries & Supercaps *4*, 881–896. 10.1002/batt.202000277.

154. Mogensen, R., Brandell, D., and Younesi, R. (2016). Solubility of the Solid Electrolyte Interphase (SEI) in Sodium Ion Batteries. ACS Energy Lett. *1*, 1173–1178. 10.1021/acsenergylett.6b00491.

155. Ma, L.A., Naylor, A.J., Nyholm, L., and Younesi, R. (2021). Strategies for Mitigating Dissolution of Solid Electrolyte Interphases in Sodium-Ion Batteries. Angewandte Chemie International Edition *60*, 4855–4863. 10.1002/anie.202013803.

156. Dose, W.M., Li, W., Temprano, I., O'Keefe, C.A., Mehdi, B.L., De Volder, M.F.L., and Grey, C.P. (2022). Onset Potential for Electrolyte Oxidation and Ni-Rich Cathode Degradation in Lithium-Ion Batteries. ACS Energy Lett. *7*, 3524–3530. 10.1021/acsenergylett.2c01722.

157. Edge, J.S., O'Kane, S., Prosser, R., Kirkaldy, N.D., Patel, A.N., Hales, A., Ghosh, A., Ai, W., Chen, J., Yang, J., et al. (2021). Lithium ion battery degradation: what you need to know. Phys. Chem. Chem. Phys. *23*, 8200–8221. 10.1039/D1CP00359C.

158. Birkl, C.R., Roberts, M.R., McTurk, E., Bruce, P.G., and Howey, D.A. (2017). Degradation diagnostics for lithium ion cells. Journal of Power Sources *341*, 373–386. 10.1016/j.jpowsour.2016.12.011.

159. Kabir, M.M., and Demirocak, D.E. (2017). Degradation mechanisms in Li-ion batteries: a state-of-the-art review. International Journal of Energy Research *41*, 1963–1986. 10.1002/er.3762.

160. Narayan, R., Laberty-Robert, C., Pelta, J., Tarascon, J.-M., and Dominko, R. (2022). Self-Healing: An Emerging Technology for Next-Generation Smart Batteries. Advanced Energy Materials *12*, 2102652. 10.1002/aenm.202102652.

161. Bottom–up and top–down design (2023). Wikipedia. https://en.wikipedia.org/w/index.php?title=Bottom%E2%80%93up_and_top%E2%80%93down_design&oldid=1170565493.

162. Protocols for studying intercalation electrodes materials- I: Galvanostatic cycling/potential limitations (GCPL) GITT Battery - Application Note 1 BioLogic. https://www.biologic.net/documents/gitt-electrochemistry-battery-application-note-1/.

163. Kasnatscheew, J., Evertz, M., Streipert, B., Wagner, R., Klöpsch, R., Vortmann, B., Hahn, H., Nowak, S., Amereller, M., Gentschev, A.-C., et al. (2016). The truth about the 1st cycle Coulombic efficiency of LiNi1/3Co1/3Mn1/3O2 (NCM) cathodes. Phys. Chem. Chem. Phys. *18*, 3956–3965. 10.1039/C5CP07718D.

164. Fong, R., Sacken, U. von, and Dahn, J.R. (1990). Studies of Lithium Intercalation into Carbons Using Nonaqueous Electrochemical Cells. J. Electrochem. Soc. *137*, 2009. 10.1149/1.2086855.

165. Smith, A.J., Burns, J.C., and Dahn, J.R. (2010). A High Precision Study of the Coulombic Efficiency of Li-Ion Batteries. Electrochem. Solid-State Lett. *13*, A177. 10.1149/1.3487637.

166. Smith, A.J., Burns, J.C., Xiong, D., and Dahn, J.R. (2011). Interpreting High Precision Coulometry Results on Li-ion Cells. J. Electrochem. Soc. *158*, A1136. 10.1149/1.3625232.

167. Xu, K. (2022). Navigating the minefield of battery literature. Commun Mater *3*, 1–7. 10.1038/s43246-022-00251-5.

168. Xiao, J., Li, Q., Bi, Y., Cai, M., Dunn, B., Glossmann, T., Liu, J., Osaka, T., Sugiura, R., Wu, B., et al. (2020). Understanding and applying coulombic efficiency in lithium metal batteries. Nat Energy *5*, 561–568. 10.1038/s41560-020-0648-z.

169. Obrovac, M.N., and Chevrier, V.L. (2014). Alloy Negative Electrodes for Li-Ion Batteries. Chem. Rev. *114*, 11444–11502. 10.1021/cr500207g.

170. Tornheim, A., and O'Hanlon, D.C. (2020). What do Coulombic Efficiency and Capacity Retention Truly Measure? A Deep Dive into Cyclable Lithium Inventory, Limitation Type, and Redox Side Reactions. J. Electrochem. Soc. *167*, 110520. 10.1149/1945-7111/ab9ee8.

171. Smith, A.J., Burns, J.C., Trussler, S., and Dahn, J.R. (2010). Precision Measurements of the Coulombic Efficiency of Lithium-Ion Batteries and of Electrode Materials for Lithium-Ion Batteries. J. Electrochem. Soc. *157*, A196. 10.1149/1.3268129.

172. Bond, T.M., Burns, J.C., Stevens, D.A., Dahn, H.M., and Dahn, J.R. (2013). Improving Precision and Accuracy in Coulombic Efficiency Measurements of Li-Ion Batteries. J. Electrochem. Soc. *160*, A521–A527. 10.1149/2.014304jes.

173. Importance of Coulombic Efficiency Measurements in R&D Efforts to Obtain Long-Lived Li-Ion Batteries (2016). Electrochemical Society Interface. 10.1149/2.F07163if.

174. Broadhead, J., and Kuo, H.C. (2001). Electrochemical principles and reactions. Handbook of batteries, 2.1.

175. Harlow, J.E., Glazier, S.L., Li, J., and Dahn, J.R. (2018). Use of Asymmetric Average Charge- and Average Discharge- Voltages as an Indicator of the Onset of Unwanted Lithium Deposition in Lithium-Ion Cells. J. Electrochem. Soc. *165*, A3595. 10.1149/2.0011816jes.

176. Wang, S., Zhang, J., Gharbi, O., Vivier, V., Gao, M., and Orazem, M.E. (2021). Electrochemical impedance spectroscopy. Nat Rev Methods Primers *1*, 41. 10.1038/s43586-021-00039-w.

177. Lazanas, A.Ch., and Prodromidis, M.I. (2023). Electrochemical Impedance Spectroscopy–A Tutorial. ACS Meas. Sci. Au. 10.1021/acsmeasuresciau.2c00070.

178. Keefe, A.S., Buteau, S., Hill, I.G., and Dahn, J.R. (2019). Temperature Dependent EIS Studies Separating Charge Transfer Impedance from Contact Impedance in Lithium-Ion Symmetric Cells. J. Electrochem. Soc. *166*, A3272–A3279. 10.1149/2.0541914jes.

179. Chen, C.H., Liu, J., and Amine, K. (2001). Symmetric cell approach and impedance spectroscopy of high power lithium-ion batteries. Journal of Power Sources, 8.

180. Petibon, R., Aiken, C.P., Sinha, N.N., Burns, J.C., Ye, H., VanElzen, C.M., Jain, G., Trussler, S., and Dahn, J.R. (2013). Study of Electrolyte Additives Using Electrochemical Impedance Spectroscopy on Symmetric Cells. J. Electrochem. Soc. *160*, A117–A124. 10.1149/2.005302jes.

181. Ogihara, N., Kawauchi, S., Okuda, C., Itou, Y., Takeuchi, Y., and Ukyo, Y. (2012). Theoretical and Experimental Analysis of Porous Electrodes for Lithium-Ion Batteries by Electrochemical Impedance Spectroscopy Using a Symmetric Cell. Journal of The Electrochemical Society, 7.

182. Middlemiss, L.A., Rennie, A.J.R., Sayers, R., and West, A.R. (2020). Characterisation of batteries by electrochemical impedance spectroscopy. Energy Reports *6*, 232–241. 10.1016/j.egyr.2020.03.029.

183. Kasnatscheew, J., Placke, T., Streipert, B., Rothermel, S., Wagner, R., Meister, P., Laskovic, I.C., and Winter, M. (2017). A Tutorial into Practical Capacity and Mass Balancing of Lithium Ion Batteries. J. Electrochem. Soc. *164*, A2479–A2486. 10.1149/2.0961712jes.

184. Murray, V., Hall, D.S., and Dahn, J.R. (2019). A Guide to Full Coin Cell Making for Academic Researchers. J. Electrochem. Soc. *166*, A329–A333. 10.1149/2.1171902jes.

185. Dahn, H.M., Smith, A.J., Burns, J.C., Stevens, D.A., and Dahn, J.R. (2012). User-Friendly Differential Voltage Analysis Freeware for the Analysis of Degradation Mechanisms in Li-Ion Batteries. J. Electrochem. Soc. *159*, A1405. 10.1149/2.013209jes.

186. Dose, W.M., Xu, C., Grey, C.P., and De Volder, M.F.L. (2020). Effect of Anode Slippage on Cathode Cutoff Potential and Degradation Mechanisms in Ni-Rich Li-Ion Batteries. Cell Reports Physical Science *1*, 100253. 10.1016/j.xcrp.2020.100253.

187. Smith, A.J., Dahn, H.M., Burns, J.C., and Dahn, J.R. (2012). Long-Term Low-Rate Cycling of LiCoO2/Graphite Li-Ion Cells at 55°C. J. Electrochem. Soc. *159*, A705. 10.1149/2.056206jes.

188. Keil, P., and Jossen, A. (2017). Calendar Aging of NCA Lithium-Ion Batteries Investigated by Differential Voltage Analysis and Coulomb Tracking. J. Electrochem. Soc. *164*, A6066–A6074. 10.1149/2.0091701jes.

189. Bloom, I., Jansen, A.N., Abraham, D.P., Knuth, J., Jones, S.A., Battaglia, V.S., and Henriksen, G.L. (2005). Differential voltage analyses of high-power, lithium-ion cells: 1. Technique and application. Journal of Power Sources *139*, 295–303. 10.1016/j.jpowsour.2004.07.021.

190. Dubarry, M., and Anseán, D. (2022). Best practices for incremental capacity analysis. Frontiers in Energy Research *10*.

191. Dubarry, M., and Beck, D. (2021). Analysis of Synthetic Voltage vs. Capacity Datasets for Big Data Li-ion Diagnosis and Prognosis. Energies *14*, 2371. 10.3390/en14092371.

192. Dubarry, M., and Beck, D. (2020). Big data training data for artificial intelligence-based Li-ion diagnosis and prognosis. Journal of Power Sources *479*, 228806. 10.1016/j.jpowsour.2020.228806.

193. Dubarry, M., and Liaw, B.Y. (2009). Identify capacity fading mechanism in a commercial LiFePO4 cell. Journal of Power Sources *194*, 541–549. 10.1016/j.jpowsour.2009.05.036.

194. Dubarry, M., Svoboda, V., Hwu, R., and Yann Liaw, B. (2006). Incremental Capacity Analysis and Close-to-Equilibrium OCV Measurements to Quantify Capacity Fade in Commercial Rechargeable Lithium Batteries. Electrochem. Solid-State Lett. *9*, A454. 10.1149/1.2221767.

195. Jehnichen, P., Wedlich, K., and Korte, C. (2019). Degradation of high-voltage cathodes for advanced lithium-ion batteries – differential capacity study on differently balanced cells. Science and Technology of Advanced Materials *20*, 1–9. 10.1080/14686996.2018.1550625.

196. Smith, A.J., Burns, J.C., and Dahn, J.R. (2011). High-Precision Differential Capacity Analysis of LiMn $_2$ O $_4$ /graphite Cells. Electrochem. Solid-State Lett. *14*, A39–A41. 10.1149/1.3543569.

197. Fath, J.P., Dragicevic, D., Bittel, L., Nuhic, A., Sieg, J., Hahn, S., Alsheimer, L., Spier, B., and Wetzel, T. (2019). Quantification of aging mechanisms and inhomogeneity in cycled lithium-ion cells by differential voltage analysis. Journal of Energy Storage *25*, 100813. 10.1016/j.est.2019.100813.

198. Honkura, K., Honbo, H., Koishikawa, Y., and Horiba, T. (2008). State Analysis of Lithium-Ion Batteries Using Discharge Curves. ECS Trans. *13*, 61–73. 10.1149/1.3018750.

199. Olson, J.Z., López, C.M., and Dickinson, E.J.F. (2023). Differential Analysis of Galvanostatic Cycle Data from Li-Ion Batteries: Interpretative Insights and Graphical Heuristics. Chem. Mater. *35*, 1487–1513. 10.1021/acs.chemmater.2c01976.

200. Bloom, I., Walker, L.K., Basco, J.K., Abraham, D.P., Christophersen, J.P., and Ho, C.D. (2010). Differential voltage analyses of high-power lithium-ion cells. 4. Cells containing NMC. Journal of Power Sources *195*, 877–882. 10.1016/j.jpowsour.2009.08.019.

201. Meunier, V., Leal De Souza, M., Morcrette, M., and Grimaud, A. (2023). Design of workflows for crosstalk detection and lifetime deviation onset in Li-ion batteries. Joule *7*, 42–56. 10.1016/j.joule.2022.12.004.

202. Meunier, V., Capone, F., Dedryvère, R., and Grimaud, A. (2023). Cascading Degradations Artificially Improving the Lifetime of Li-ion Full Cells using DMC-based Highly Concentrated Electrolyte. J. Electrochem. Soc. *170*, 060551. 10.1149/1945-7111/ace031.

203. Logan, E.R., Hebecker, H., Eldesoky, A., Luscombe, A., Johnson, M.B., and Dahn, J.R. (2020). Performance and Degradation of LiFePO 4 /Graphite Cells: The Impact of Water Contamination and an Evaluation of Common Electrolyte Additives. J. Electrochem. Soc. *167*, 130543. 10.1149/1945-7111/abbbbe.

204. Elgrishi, N., Rountree, K.J., McCarthy, B.D., Rountree, E.S., Eisenhart, T.T., and Dempsey, J.L. (2018). A Practical Beginner's Guide to Cyclic Voltammetry. J. Chem. Educ. *95*, 197–206. 10.1021/acs.jchemed.7b00361.

205. Pérez-Villar, S., Lanz, P., Schneider, H., and Novák, P. (2013). Characterization of a model solid electrolyte interphase/carbon interface by combined in situ Raman/Fourier transform infrared microscopy. Electrochimica Acta *106*, 506–515. 10.1016/j.electacta.2013.05.124.

206. Zampardi, G., Mantia, F.L., and Schuhmann, W. (2015). Determination of the formation and range of stability of the SEI on glassy carbon by local electrochemistry. RSC Adv. *5*, 31166–31171. 10.1039/C5RA02940F.

207. Tang, M., Lu, S., and Newman, J. (2012). Experimental and Theoretical Investigation of Solid-Electrolyte-Interphase Formation Mechanisms on Glassy Carbon. J. Electrochem. Soc. *159*, A1775. 10.1149/2.025211jes.

208. Burns, J.C., Krause, L.J., Le, D.-B., Jensen, L.D., Smith, A.J., Xiong, D., and Dahn, J.R. (2011). Introducing Symmetric Li-Ion Cells as a Tool to Study Cell Degradation Mechanisms. J. Electrochem. Soc. *158*, A1417. 10.1149/2.084112jes.

209. Shen, C., Xiong, D., Ellis, L.D., Gering, K.L., Huang, L., and Dahn, J.R. (2017). Using the Charge-Discharge Cycling of Positive Electrode Symmetric Cells to Find Electrolyte/Electrode Combinations with Minimum Reactivity. J. Electrochem. Soc. *164*, A3349. 10.1149/2.1711713jes.

210. Liu, Y., Ma, L., and Dahn, J.R. (2021). Designing Positive/Positive and Negative/Negative Symmetric Cells with Electrodes Operating in the Same Potential Ranges as Electrodes in a Full Li-Ion Cell. J. Electrochem. Soc. *168*, 080537. 10.1149/1945-7111/ac1eb7.

211. Waldmann, T., Iturrondobeitia, A., Kasper, M., Ghanbari, N., Aguesse, F., Bekaert, E., Daniel, L., Genies, S., Gordon, I.J., Löble, M.W., et al. (2016). Review—Post-Mortem Analysis of Aged Lithium-Ion Batteries: Disassembly Methodology and Physico-Chemical Analysis Techniques. J. Electrochem. Soc. *163*, A2149–A2164. 10.1149/2.1211609jes.

212. Waldmann, T., Ghanbari, N., Kasper, M., and Wohlfahrt-Mehrens, M. (2015). Correlations between Electrochemical Data and Results from Post-Mortem Analysis of Aged Lithium-Ion Batteries. J. Electrochem. Soc. *162*, A1500. 10.1149/2.0411508jes.

213. Ponrouch, A., Marchante, E., Courty, M., Tarascon, J.-M., and Palacín, M.R. (2012). In search of an optimized electrolyte for Na-ion batteries. Energy Environ. Sci. *5*, 8572. 10.1039/c2ee22258b.

214. Ponrouch, A., Dedryvère, R., Monti, D., Demet, A.E., Ateba Mba, J.M., Croguennec, L., Masquelier, C., Johansson, P., and Palacín, M.R. (2013). Towards high energy density sodium ion batteries through electrolyte optimization. Energy Environ. Sci. *6*, 2361. 10.1039/c3ee41379a.

215. Westman, K., Dugas, R., Jankowski, P., Wieczorek, W., Gachot, G., Morcrette, M., Irisarri, E., Ponrouch, A., Palacín, M.R., Tarascon, J.-M., et al. (2018). Diglyme Based Electrolytes for Sodium-Ion Batteries. ACS Appl. Energy Mater. *1*, 2671–2680. 10.1021/acsaem.8b00360.

216. Yan, G., Dugas, R., and Tarascon, J.-M. (2018). The NVPF /Carbon Na-Ion Battery: Its Performance Understanding as Deduced from Differential Voltage Analysis. J. Electrochem. Soc. *165*, A220–A227. 10.1149/2.0831802jes.

217. Amatucci, G., Du Pasquier, A., Blyr, A., Zheng, T., and Tarascon, J.-M. (1999). The elevated temperature performance of the LiMn2O4/C system: failure and solutions. Electrochimica Acta *45*, 255–271. 10.1016/S0013-4686(99)00209-1.

218. Amatucci, G.G., Schmutz, C.N., Blyr, A., Sigala, C., Gozdz, A.S., Larcher, D., and Tarascon, J.M. (1997). Materials' effects on the elevated and room temperature performance of CLiMn2O4 Li-ion batteries. Journal of Power Sources *69*, 11–25. 10.1016/S0378-7753(97)02542-1.

219. Cambaz, M.A., Vinayan, B.P., Pervez, S.A., Johnsen, R.E., Geßwein, H., Guda, A.A., Rusalev, Y.V., Kinyanjui, M.K., Kaiser, U., and Fichtner, M. (2019). Suppressing Dissolution of Vanadium from Cation-Disordered $Li_{2-x}VO_2F$ via a Concentrated Electrolyte Approach. Chem. Mater. *31*, 7941–7950. 10.1021/acs.chemmater.9b02074.

220. Zhan, C., Wu, T., Lu, J., and Amine, K. (2018). Dissolution, migration, and deposition of transition metal ions in Li-ion batteries exemplified by Mn-based cathodes – a critical review. Energy Environ. Sci. *11*, 243–257. 10.1039/C7EE03122J.

221. Zhou, G., Sun, X., Li, Q.-H., Wang, X., Zhang, J.-N., Yang, W., Yu, X., Xiao, R., and Li, H. (2020). Mn Ion Dissolution Mechanism for Lithium-Ion Battery with $LiMn_2O_4$ Cathode: *In Situ* Ultraviolet–Visible Spectroscopy and *Ab Initio* Molecular Dynamics Simulations. J. Phys. Chem. Lett. *11*, 3051–3057. 10.1021/acs.jpclett.0c00936.

222. Meunier, V., Souza, M.L.D., Morcrette, M., and Grimaud, A. (2022). Electrochemical Protocols to Assess the Effects of Dissolved Transition Metal in Graphite/LiNiO2 Cells Performance. J. Electrochem. Soc. *169*, 070506. 10.1149/1945-7111/ac7e7a.

223. Amine, K., Liu, J., and Belharouak, I. (2005). High-temperature storage and cycling of C-LiFePO4/graphite Li-ion cells. Electrochemistry Communications *7*, 669–673. 10.1016/j.elecom.2005.04.018.

224. Koltypin, M., Aurbach, D., Nazar, L., and Ellis, B. (2006). On the Stability of LiFePO4 Olivine Cathodes under Various Conditions (Electrolyte Solutions, Temperatures). Electrochem. Solid-State Lett. *10*, A40. 10.1149/1.2403974.

225. Hwang, J.-Y., Myung, S.-T., and Sun, Y.-K. (2018). Quaternary Transition Metal Oxide Layered Framework: O3-Type Na[Ni0.32Fe0.13Co0.15Mn0.40]O2 Cathode Material for High-Performance Sodium-Ion Batteries. J. Phys. Chem. C *122*, 13500–13507. 10.1021/acs.jpcc.7b12140.

226. Che, H., Yang, X., Wang, H., Liao, X.-Z., Zhang, S.S., Wang, C., and Ma, Z.-F. (2018). Long cycle life of sodium-ion pouch cell achieved by using multiple electrolyte additives. Journal of Power Sources *407*, 173–179. 10.1016/j.jpowsour.2018.08.025.

227. Eldesoky, A., Logan, E.R., Johnson, M.B., McFarlane, C.R.M., and Dahn, J.R. (2020). Scanning Micro X-ray Fluorescence (μ- XRF) as an Effective Tool in Quantifying Fe Dissolution in LiFePO4 Cells: Towards a Mechanistic Understanding of Fe Dissolution. J. Electrochem. Soc. *167*, 130539. 10.1149/1945-7111/abba62.

228. Dahbi, M., Ghamouss, F., Tran-Van, F., Lemordant, D., and Anouti, M. (2011). Comparative study of EC/DMC LiTFSI and LiPF6 electrolytes for electrochemical storage. Journal of Power Sources *196*, 9743–9750. 10.1016/j.jpowsour.2011.07.071.

229. Andersson, A.M., Herstedt, M., Bishop, A.G., and Edström, K. (2002). The influence of lithium salt on the interfacial reactions controlling the thermal stability of graphite anodes. Electrochimica Acta *47*, 1885–1898. 10.1016/S0013-4686(02)00044-0.

230. Dudley, J.T., Wilkinson, D.P., Thomas, G., LeVae, R., Woo, S., Blom, H., Horvath, C., Juzkow, M.W., Denis, B., Juric, P., et al. (1991). Conductivity of electrolytes for rechargeable lithium batteries. Journal of Power Sources *35*, 59–82. 10.1016/0378-7753(91)80004-H.

231. Blyr, A., Du Pasquier, A., Amatucci, G., and Tarascon, J.-M. (1997). Origin of self-discharge mechanism in LiMn2O4-based Li-ion cells: A chemical and electrochemical approach. Ionics *3*, 321–331. 10.1007/BF02375706.

232. Metzger, M., Walke, P., Solchenbach, S., Salitra, G., Aurbach, D., and Gasteiger, H.A. (2020). Evaluating the High-Voltage Stability of Conductive Carbon and Ethylene Carbonate with Various Lithium Salts. J. Electrochem. Soc. *167*, 160522. 10.1149/1945-7111/abcabd.

233. Bianchini, M., Fauth, F., Brisset, N., Weill, F., Suard, E., Masquelier, C., and Croguennec, L. (2015). Comprehensive Investigation of the $Na_3V_2(PO_4)_2F_3$–$NaV_2(PO_4)_2F_3$ System by Operando High Resolution Synchrotron X-ray Diffraction. Chem. Mater. *27*, 3009–3020. 10.1021/acs.chemmater.5b00361.

234. Burova, D., Shakhova, I., Morozova, P., Iarchuk, A., Drozhzhin, O.A., Rozova, M.G., Praneetha, S., Murugan, V., Tarascon, J.-M., and Abakumov, A.M. (2019). The rapid microwave-assisted hydrothermal synthesis of NASICON-structured Na3V2O2x(PO4)2F3−2x (0 < x ≤ 1) cathode materials for Na-ion batteries. RSC Adv. *9*, 19429–19440. 10.1039/C9RA02257K.

235. Hall, D.S., Eldesoky, A., Logan, E.R., Tonita, E.M., Ma, X., and Dahn, J.R. (2018). Exploring Classes of Co-Solvents for Fast-Charging Lithium-Ion Cells. J. Electrochem. Soc. *165*, A2365–A2373. 10.1149/2.1351810jes.

236. Borodin, O., Behl, W., and Jow, T.R. (2013). Oxidative Stability and Initial Decomposition Reactions of Carbonate, Sulfone, and Alkyl Phosphate-Based Electrolytes. J. Phys. Chem. C *117*, 8661–8682. 10.1021/jp400527c.

237. Björklund, E., Göttlinger, M., Edström, K., Brandell, D., and Younesi, R. (2019). Investigation of Dimethyl Carbonate and Propylene Carbonate Mixtures for LiNi0.6Mn0.2Co0.2O2-Li4Ti5O12 Cells. ChemElectroChem *6*, 3429–3436. 10.1002/celc.201900672.

238. Smith, A.J., and Dahn, J.R. (2012). Delta Differential Capacity Analysis. J. Electrochem. Soc. *159*, A290–A293. 10.1149/2.076203jes.

239. Jayawardana, C., Rodrigo, N., Parimalam, B., and Lucht, B.L. (2021). Role of Electrolyte Oxidation and Difluorophosphoric Acid Generation in Crossover and Capacity Fade in Lithium Ion Batteries. ACS Energy Lett. *6*, 3788–3792. 10.1021/acsenergylett.1c01657.

240. Heiskanen, S.K., Kim, J., and Lucht, B.L. (2019). Generation and Evolution of the Solid Electrolyte Interphase of Lithium-Ion Batteries. Joule *3*, 2322–2333. 10.1016/j.joule.2019.08.018.

241. Garcia, B., and Armand, M. (2004). Aluminium corrosion in room temperature molten salt. Journal of Power Sources *132*, 206–208. 10.1016/j.jpowsour.2003.12.046.

242. Larsson, F., Andersson, P., Blomqvist, P., and Mellander, B.-E. (2017). Toxic fluoride gas emissions from lithium-ion battery fires. Sci Rep *7*, 10018. 10.1038/s41598-017-09784-z.

243. Amano, K.O.A., Hahn, S.-K., Butt, N., Vorwerk, P., Gimadieva, E., Tschirschwitz, R., Rappsilber, T., and Krause, U. (2023). Composition and Explosibility of Gas Emissions from Lithium-Ion Batteries Undergoing Thermal Runaway. Batteries *9*, 300. 10.3390/batteries9060300.

244. Huang, J., Albero Blanquer, L., Bonefacino, J., Logan, E.R., Alves Dalla Corte, D., Delacourt, C., Gallant, B.M., Boles, S.T., Dahn, J.R., Tam, H.-Y., et al. (2020). Operando decoding of chemical and thermal events in commercial Na(Li)-ion cells via optical sensors. Nat Energy *5*, 674–683. 10.1038/s41560-020-0665-y.

245. Zhang, S.S. (2006). A review on electrolyte additives for lithium-ion batteries. Journal of Power Sources *162*, 1379–1394. 10.1016/j.jpowsour.2006.07.074.

246. Haregewoin, A.M., Wotango, A.S., and Hwang, B.-J. (2016). Electrolyte additives for lithium ion battery electrodes: progress and perspectives. Energy Environ. Sci. *9*, 1955–1988. 10.1039/C6EE00123H.

247. Zhao, W., Ji, Y., Zhang, Z., Lin, M., Wu, Z., Zheng, X., Li, Q., and Yang, Y. (2017). Recent advances in the research of functional electrolyte additives for lithium-ion batteries. Current Opinion in Electrochemistry *6*, 84–91. 10.1016/j.coelec.2017.10.012.

248. Xu, N., Shi, J., Liu, G., Yang, X., Zheng, J., Zhang, Z., and Yang, Y. (2021). Research progress of fluorine-containing electrolyte additives for lithium ion batteries. Journal of Power Sources Advances *7*, 100043. 10.1016/j.powera.2020.100043.

249. Ding, M.S., Xu, K., and Jow, T.R. (2000). Liquid-Solid Phase Diagrams of Binary Carbonates for Lithium Batteries. J. Electrochem. Soc. *147*, 1688. 10.1149/1.1393419.

250. Ding, M.S., Xu, K., Zhang, S., and Jow, T.R. (2001). Liquid/Solid Phase Diagrams of Binary Carbonates for Lithium Batteries Part II. J. Electrochem. Soc. *148*, A299. 10.1149/1.1353568.

251. Ding, M.S. (2004). Liquid-Solid Phase Diagrams of Ternary and Quaternary Organic Carbonates. J. Electrochem. Soc. *151*, A731. 10.1149/1.1690782.

252. Huang, J., Blanquer, L.A., Gervillié, C., and Tarascon, J.-M. (2021). Distributed Fiber Optic Sensing to Assess In-Live Temperature Imaging Inside Batteries: Rayleigh and FBGs. J. Electrochem. Soc. *168*, 060520. 10.1149/1945-7111/ac03f0.

253. Huang, J., Han, X., Liu, F., Gervillié, C., Blanquer, L.A., Guo, T., and Tarascon, J.-M. (2021). Monitoring battery electrolyte chemistry via in-operando tilted fiber Bragg grating sensors. Energy Environ. Sci. *14*, 6464–6475. 10.1039/D1EE02186A.

254. Chen, J., Huang, Z., Wang, C., Porter, S., Wang, B., Lie, W., and Liu, H.K. (2015). Sodium-difluoro(oxalato)borate (NaDFOB): a new electrolyte salt for Na-ion batteries. Chem. Commun. *51*, 9809–9812. 10.1039/C5CC02901E.

255. Zhang, X., Kostecki, R., Richardson, T.J., Pugh, J.K., and Ross, P.N. (2001). Electrochemical and Infrared Studies of the Reduction of Organic Carbonates. J. Electrochem. Soc. *148*, A1341. 10.1149/1.1415547.

256. Grugeon, S., Jankowski, P., Cailleu, D., Forestier, C., Sannier, L., Armand, M., Johansson, P., and Laruelle, S. (2019). Towards a better understanding of vinylene carbonate derived SEI-layers by synthesis of reduction compounds. Journal of Power Sources *427*, 77–84. 10.1016/j.jpowsour.2019.04.061.

257. Michan, A.L., Parimalam, Bharathy.S., Leskes, M., Kerber, R.N., Yoon, T., Grey, C.P., and Lucht, B.L. (2016). Fluoroethylene Carbonate and Vinylene Carbonate Reduction: Understanding Lithium-Ion Battery Electrolyte Additives and Solid Electrolyte Interphase Formation. Chem. Mater. *28*, 8149–8159. 10.1021/acs.chemmater.6b02282.

258. Ushirogata, K., Sodeyama, K., Okuno, Y., and Tateyama, Y. (2013). Additive Effect on Reductive Decomposition and Binding of Carbonate-Based Solvent toward Solid Electrolyte Interphase Formation in Lithium-Ion Battery. J. Am. Chem. Soc. *135*, 11967–11974. 10.1021/ja405079s.

259. Kim, G.-Y., Petibon, R., and Dahn, J.R. (2014). Effects of Succinonitrile (SN) as an Electrolyte Additive on the Impedance of $LiCoO_2$ /Graphite Pouch Cells during Cycling. J. Electrochem. Soc. *161*, A506–A512. 10.1149/2.014404jes.

260. Zhi, H., Xing, L., Zheng, X., Xu, K., and Li, W. (2017). Understanding How Nitriles Stabilize Electrolyte/Electrode Interface at High Voltage. J. Phys. Chem. Lett. *8*, 6048–6052. 10.1021/acs.jpclett.7b02734.

261. Kim, G.-Y., and Dahn, J.R. (2015). The Effect of Some Nitriles as Electrolyte Additives in Li-Ion Batteries. J. Electrochem. Soc. *162*, A437–A447. 10.1149/2.0651503jes.

262. Yim, T., Woo, S.-G., Lim, S.H., Cho, W., Song, J.H., Han, Y.-K., and Kim, Y.-J. (2015). 5V-class high-voltage batteries with over-lithiated oxide and a multi-functional additive. J. Mater. Chem. A *3*, 6157–6167. 10.1039/C4TA06531J.

263. Han, Y.-K., Yoo, J., and Yim, T. (2015). Why is tris(trimethylsilyl) phosphite effective as an additive for high-voltage lithium-ion batteries? J. Mater. Chem. A *3*, 10900–10909. 10.1039/C5TA01253H.

264. Bloom, I., Cole, B.W., Sohn, J.J., Jones, S.A., Polzin, E.G., Battaglia, V.S., Henriksen, G.L., Motloch, C., Richardson, R., Unkelhaeuser, T., et al. (2001). An accelerated calendar and cycle life study of Li-ion cells. Journal of Power Sources *101*, 238–247. 10.1016/S0378-7753(01)00783-2.

265. Wright, R.B., Motloch, C.G., Belt, J.R., Christophersen, J.P., Ho, C.D., Richardson, R.A., Bloom, I., Jones, S.A., Battaglia, V.S., Henriksen, G.L., et al. (2002). Calendar- and cycle-life studies of advanced technology development program generation 1 lithium-ion batteries. Journal of Power Sources *110*, 445–470. 10.1016/S0378-7753(02)00210-0.

266. Keil, P., Schuster, S.F., Wilhelm, J., Travi, J., Hauser, A., Karl, R.C., and Jossen, A. (2016). Calendar Aging of Lithium-Ion Batteries: I. Impact of the Graphite Anode on Capacity Fade. J. Electrochem. Soc. *163*, A1872–A1880. 10.1149/2.0411609jes.

267. He, M. (2016). Elucidating interface reactions in Li-ion batteries and supercapacitors by in situ gas analysis. 10.3929/ethz-a-010852357.

268. Eom, J.-Y., Jung, I.-H., and Lee, J.-H. (2011). Effects of vinylene carbonate on high temperature storage of high voltage Li-ion batteries. Journal of Power Sources *196*, 9810–9814. 10.1016/j.jpowsour.2011.06.095.

269. Qi, X., Tao, L., Hahn, H., Schultz, C., Gallus, D.R., Cao, X., Nowak, S., Röser, S., Li, J., Cekic-Laskovic, I., et al. (2016). Lifetime limit of tris(trimethylsilyl) phosphite as electrolyte additive for high voltage lithium ion batteries. RSC Adv. *6*, 38342–38349. 10.1039/C6RA06555D.

270. Azam, S., Meisner, Q., Aiken, C.P., Song, W., Liu, Q., Yoo, D.-J., Eldesoky, A., Zhang, Z., and Dahn, J.R. (2022). Performance of a Novel In-Situ Converted Additive for High Voltage Li-ion Pouch Cells. J. Electrochem. Soc. *169*, 100552. 10.1149/1945-7111/ac9c36.

271. Metzger, M., Strehle, B., Solchenbach, S., and Gasteiger, H.A. (2016). Origin of H2 Evolution in LIBs: H2O Reduction vs. Electrolyte Oxidation. J. Electrochem. Soc. *163*, A798. 10.1149/2.1151605jes.

272. Department of Energy Announces $19 Million for Advanced Battery and Electrification Research to Enable Extreme Fast Charging Energy.gov. https://www.energy.gov/articles/department-energy-announces-19-million-advanced-battery-and-electrification-research-enable.

273. Landesfeind, J., Hosaka, T., Graf, M., Kubota, K., Komaba, S., and Gasteiger, H.A. (2021). Comparison of Ionic Transport Properties of Non-Aqueous Lithium and Sodium Hexafluorophosphate Electrolytes. J. Electrochem. Soc. *168*, 040538. 10.1149/1945-7111/abf8d9.

274. Usiskin, R., Lu, Y., Popovic, J., Law, M., Balaya, P., Hu, Y.-S., and Maier, J. (2021). Fundamentals, status and promise of sodium-based batteries. Nat Rev Mater *6*, 1020–1035. 10.1038/s41578-021-00324-w.

275. Li, Z., Jian, Z., Wang, X., Rodríguez-Pérez, I.A., Bommier, C., and Ji, X. (2017). Hard carbon anodes of sodium-ion batteries: undervalued rate capability. Chem. Commun. *53*, 2610–2613. 10.1039/C7CC00301C.

276. Nyman, A., Zavalis, T.G., Elger, R., Behm, M., and Lindbergh, G. (2010). Analysis of the Polarization in a Li-Ion Battery Cell by Numerical Simulations. J. Electrochem. Soc. *157*, A1236. 10.1149/1.3486161.

277. Liu, Y., Zhu, Y., and Cui, Y. (2019). Challenges and opportunities towards fast-charging battery materials. Nat Energy *4*, 540–550. 10.1038/s41560-019-0405-3.

278. Zhang, S.S. (2020). Unveiling Capacity Degradation Mechanism of Li-ion Battery in Fast-charging Process. ChemElectroChem *7*, 555–560. 10.1002/celc.201902050.

279. Schindler, S., Bauer, M., Cheetamun, H., and Danzer, M.A. (2018). Fast charging of lithium-ion cells: Identification of aging-minimal current profiles using a design of experiment approach and a mechanistic degradation analysis. Journal of Energy Storage *19*, 364–378. 10.1016/j.est.2018.08.002.

280. Liu, Q., Du, C., Shen, B., Zuo, P., Cheng, X., Ma, Y., Yin, G., and Gao, Y. (2016). Understanding undesirable anode lithium plating issues in lithium-ion batteries. RSC Advances *6*, 88683–88700. 10.1039/C6RA19482F.

281. Petzl, M., Kasper, M., and Danzer, M.A. (2015). Lithium plating in a commercial lithium-ion battery – A low-temperature aging study. Journal of Power Sources *275*, 799–807. 10.1016/j.jpowsour.2014.11.065.

282. Lin, X., Khosravinia, K., Hu, X., Li, J., and Lu, W. (2021). Lithium Plating Mechanism, Detection, and Mitigation in Lithium-Ion Batteries. Progress in Energy and Combustion Science *87*, 100953. 10.1016/j.pecs.2021.100953.

283. Tomaszewska, A., Chu, Z., Feng, X., O'Kane, S., Liu, X., Chen, J., Ji, C., Endler, E., Li, R., Liu, L., et al. (2019). Lithium-ion battery fast charging: A review. eTransportation *1*, 100011. 10.1016/j.etran.2019.100011.

284. Weiss, M., Ruess, R., Kasnatscheew, J., Levartovsky, Y., Levy, N.R., Minnmann, P., Stolz, L., Waldmann, T., Wohlfahrt-Mehrens, M., Aurbach, D., et al. (2021). Fast Charging of Lithium-Ion Batteries: A Review of Materials Aspects. Advanced Energy Materials *11*, 2101126. 10.1002/aenm.202101126.

285. Zhang, S.S., Ma, L., Allen, J.L., and Read, J.A. (2021). Stabilizing Capacity Retention of Li-Ion Battery in Fast-Charge by Reducing Particle Size of Graphite. J. Electrochem. Soc. *168*, 040519. 10.1149/1945-7111/abf40c.

286. Zhang, Y., Alarco, J.A., Nerkar, J.Y., Best, A.S., Snook, G.A., and Talbot, P.C. (2019). Improving the Rate Capability of LiFePO4 Electrode by Controlling Particle Size Distribution. J. Electrochem. Soc. *166*, A4128. 10.1149/2.0621916jes.

287. Du, Z., Wood, D.L., and Belharouak, I. (2019). Enabling fast charging of high energy density Li-ion cells with high lithium ion transport electrolytes. Electrochemistry Communications *103*, 109–113. 10.1016/j.elecom.2019.04.013.

288. Zheng, J., Engelhard, M.H., Mei, D., Jiao, S., Polzin, B.J., Zhang, J.-G., and Xu, W. (2017). Electrolyte additive enabled fast charging and stable cycling lithium metal batteries. Nat Energy *2*, 1–8. 10.1038/nenergy.2017.12.

289. Plichta, E.J., and Slane, S. (1997). Conductivity of lithium imide in mixed aprotic solvents for lithium cells. Journal of Power Sources *69*, 41–45. 10.1016/S0378-7753(97)02545-7.

290. Irish, D.E., Deng, Z., and Odziemkowski, M. (1995). Raman spectroscopic and electrochemical studies of lithium battery components. Journal of Power Sources *54*, 28–33. 10.1016/0378-7753(94)02035-2.

291. Smart, M.C., Ratnakumar, B.V., Surampudi, S., Wang, Y., Zhang, X., Greenbaum, S.G., Hightower, A., Ahn, C.C., and Fultz, B. (1999). Irreversible Capacities of Graphite in Low-Temperature Electrolytes for Lithium-Ion Batteries. J. Electrochem. Soc. *146*, 3963. 10.1149/1.1392577.

292. Smart, M.C., Ratnakumar, B.V., and Surampudi, S. (2002). Use of Organic Esters as Cosolvents in Electrolytes for Lithium-Ion Batteries with Improved Low Temperature Performance. J. Electrochem. Soc. *149*, A361. 10.1149/1.1453407.

293. Ma, X., Li, J., Glazier, S.L., Ma, L., Gering, K.L., and Dahn, J.R. (2018). A study of highly conductive ester co-solvents in Li[Ni0.5Mn0.3Co0.2]O2/Graphite pouch cells. Electrochimica Acta *270*, 215–223. 10.1016/j.electacta.2018.03.006.

294. Li, J., Li, H., Ma, X., Stone, W., Glazier, S., Logan, E., Tonita, E.M., Gering, K.L., and Dahn, J.R. (2018). Methyl Acetate as a Co-Solvent in NMC532/Graphite Cells. J. Electrochem. Soc. *165*, A1027–A1037. 10.1149/2.0861805jes.

295. Mayers, M.Z., Kaminski, J.W., and Miller, T.F. (2012). Suppression of Dendrite Formation via Pulse Charging in Rechargeable Lithium Metal Batteries. J. Phys. Chem. C *116*, 26214–26221. 10.1021/jp309321w.

296. Marcicki, J., Conlisk, A.T., and Rizzoni, G. (2014). A lithium-ion battery model including electrical double layer effects. Journal of Power Sources *251*, 157–169. 10.1016/j.jpowsour.2013.11.001.

297. Chazalviel, J.-N. (1990). Electrochemical aspects of the generation of ramified metallic electrodeposits. Phys. Rev. A *42*, 7355–7367. 10.1103/PhysRevA.42.7355.

298. Cataldo, F. (2015). A REVISION OF THE GUTMANN DONOR NUMBERS OF A SERIES OF PHOSPHORAMIDES INCLUDING TEPA.

299. Matsuda, Y., Morita, M., and Kosaka, K. (1983). Conductivity of the Mixed Organic Electrolyte Containing Propylene Carbonate and 1,2-Dimethoxyethane. J. Electrochem. Soc. *130*, 101. 10.1149/1.2119630.

300. Matsuda, Y., and Satake, H. (1980). Mixed Electrolyte Solutions of Propylene Carbonate and Dimethoxyethane for High Energy Density Batteries. J. Electrochem. Soc. *127*, 877. 10.1149/1.2129774.

301. Logan, E.R., Tonita, E.M., Gering, K.L., Ma, L., Bauer, M.K.G., Li, J., Beaulieu, L.Y., and Dahn, J.R. (2018). A Study of the Transport Properties of Ethylene Carbonate-Free Li Electrolytes. J. Electrochem. Soc. *165*, A705. 10.1149/2.0981803jes.

302. Landesfeind, J., Hattendorff, J., Ehrl, A., Wall, W.A., and Gasteiger, H.A. (2016). Tortuosity Determination of Battery Electrodes and Separators by Impedance Spectroscopy. J. Electrochem. Soc. *163*, A1373. 10.1149/2.1141607jes.

303. CDGP, K.I. (2023). IATA 2023 Lithium Battery Guidance Document | ICC. ICC Compliance Center Inc - USA. https://www.thecompliancecenter.com/iata-2023-lithium-battery-guidance-document/.

304. Lithium Battery Incidents | Federal Aviation Administration https://www.faa.gov/hazmat/resources/lithium_batteries/incidents.

305. Maleki, H., and Howard, J.N. (2006). Effects of overdischarge on performance and thermal stability of a Li-ion cell. Journal of Power Sources *160*, 1395–1402. 10.1016/j.jpowsour.2006.03.043.

306. Zhao, M., Kariuki, S., Dewald, H.D., Lemke, F.R., Staniewicz, R.J., Plichta, E.J., and Marsh, R.A. (2000). Electrochemical Stability of Copper in Lithium-Ion Battery Electrolytes. J. Electrochem. Soc. *147*, 2874. 10.1149/1.1393619.

307. Fuentevilla, D., Hendricks, C., and Mansour, A. (2015). Quantifying the Impact of Overdischarge on Large Format Lithium-Ion Cells. ECS Trans. *69*, 1. 10.1149/06920.0001ecst.

308. Hendricks, C.E., Mansour, A.N., Fuentevilla, D.A., Waller, G.H., Ko, J.K., and Pecht, M.G. (2020). Copper Dissolution in Overdischarged Lithium-ion Cells: X-ray Photoelectron Spectroscopy and X-ray Absorption Fine Structure Analysis. J. Electrochem. Soc. *167*, 090501. 10.1149/1945-7111/ab697a.

309. Mikolajczak, C., Kahn, M., White, K., and Long, R.T. (2012). Lithium-Ion Batteries Hazard and Use Assessment (Springer Science & Business Media).

310. Flügel, M., Kasper, M., Pfeifer, C., Wohlfahrt-Mehrens, M., and Waldmann, T. (2021). Cu Dissolution during Over-Discharge of Li-Ion Cells to 0 V: A Post-Mortem Study. J. Electrochem. Soc. *168*, 020506. 10.1149/1945-7111/abdc5f.

311. Rudola, A., Rennie, A.J.R., Heap, R., Meysami, S.S., Lowbridge, A., Mazzali, F., Sayers, R., Wright, C.J., and Barker, J. (2021). Commercialisation of high energy density sodium-ion batteries: Faradion's journey and outlook. J. Mater. Chem. A *9*, 8279–8302. 10.1039/D1TA00376C.

312. Barker, J., and Wright, C.J. (2021). Storage and/or transportation of sodium-ion cells.

313. Rudola, A., Wright, C.J., and Barker, J. (2021). Reviewing the Safe Shipping of Lithium-Ion and Sodium-Ion Cells: A Materials Chemistry Perspective. Energy Material Advances *2021*, 1–12. 10.34133/2021/9798460.

314. Guo, R., Lu, L., Ouyang, M., and Feng, X. (2016). Mechanism of the entire overdischarge process and overdischarge-induced internal short circuit in lithium-ion batteries. Sci Rep *6*, 30248. 10.1038/srep30248.

315. Diao, W., Kim, J., Azarian, M.H., and Pecht, M. (2022). Degradation modes and mechanisms analysis of lithium-ion batteries with knee points. Electrochimica Acta *431*, 141143. 10.1016/j.electacta.2022.141143.

316. Ma, X., Harlow, J.E., Li, J., Ma, L., Hall, D.S., Buteau, S., Genovese, M., Cormier, M., and Dahn, J.R. (2019). Editors' Choice—Hindering Rollover Failure of Li[Ni $_{0.5}$ Mn $_{0.3}$ Co $_{0.2}$]O $_{2}$ /Graphite Pouch Cells during Long-Term Cycling. J. Electrochem. Soc. *166*, A711–A724. 10.1149/2.0801904jes.

317. Diao, W., Saxena, S., Han, B., and Pecht, M. (2019). Algorithm to Determine the Knee Point on Capacity Fade Curves of Lithium-Ion Cells. Energies *12*, 2910. 10.3390/en12152910.

318. Song, J., Xiao, B., Lin, Y., Xu, K., and Li, X. (2018). Interphases in Sodium-Ion Batteries. Adv. Energy Mater. *8*, 1703082. 10.1002/aenm.201703082.

319. Yan, G., Mariyappan, S., Rousse, G., Jacquet, Q., Deschamps, M., David, R., Mirvaux, B., Freeland, J.W., and Tarascon, J.-M. (2019). Higher energy and safer sodium ion batteries via an electrochemically made disordered Na3V2(PO4)2F3 material. Nat Commun *10*, 585. 10.1038/s41467-019-08359-y.

320. Mariyappan, S., Marchandier, T., Rabuel, F., Iadecola, A., Rousse, G., Morozov, A.V., Abakumov, A.M., and Tarascon, J.-M. (2020). The Role of Divalent (Zn2+/Mg2+/Cu2+) Substituents in Achieving Full Capacity of Sodium Layered Oxides for Na-Ion Battery Applications. Chem. Mater. *32*, 1657–1666. 10.1021/acs.chemmater.9b05205.

321. Sharova, V., Moretti, A., Diemant, T., Varzi, A., Behm, R.J., and Passerini, S. (2018). Comparative study of imide-based Li salts as electrolyte additives for Li-ion batteries. Journal of Power Sources *375*, 43–52. 10.1016/j.jpowsour.2017.11.045.

322. Song, Z., Wang, X., Wu, H., Feng, W., Nie, J., Yu, H., Huang, X., Armand, M., Zhang, H., and Zhou, Z. (2022). Bis(fluorosulfonyl)imide-based electrolyte for rechargeable lithium batteries: A perspective. Journal of Power Sources Advances *14*, 100088. 10.1016/j.powera.2022.100088.

323. Song, Z., Zheng, L., Cheng, P., Wang, X., Wu, H., Ma, Q., Liu, J., Feng, W., Nie, J., Yu, H., et al. (2022). Taming the chemical instability of lithium hexafluorophosphate-based electrolyte with lithium fluorosulfonimide salts. Journal of Power Sources *526*, 231105. 10.1016/j.jpowsour.2022.231105.

324. Eldesoky, A., Bauer, M., Azam, S., Zsoldos, E., Song, W., Weber, R., Hy, S., Johnson, M.B., Metzger, M., and Dahn, J.R. (2021). Impact of Graphite Materials on the Lifetime of NMC811/Graphite Pouch Cells: Part I. Material Properties, ARC Safety Tests, Gas Generation, and Room Temperature Cycling. J. Electrochem. Soc. *168*, 110543. 10.1149/1945-7111/ac39fc.

325. Eldesoky, A., Logan, E.R., Louli, A.J., Song, W., Weber, R., Hy, S., Petibon, R., Harlow, J.E., Azam, S., Zsoldos, E., et al. (2022). Impact of Graphite Materials on the Lifetime of NMC811/Graphite Pouch Cells: Part II. Long-Term Cycling, Stack Pressure Growth, Isothermal Microcalorimetry, and Lifetime Projection. J. Electrochem. Soc. *169*, 010501. 10.1149/1945-7111/ac42f1.

326. Li, J., Glazier, S.L., Nelson, K., Ma, X., Harlow, J., Paulsen, J., and Dahn, J.R. (2018). Effect of Choices of Positive Electrode Material, Electrolyte, Upper Cut-Off Voltage and Testing Temperature on the Life Time of Lithium-Ion Cells. J. Electrochem. Soc. *165*, A3195. 10.1149/2.0931813jes.

327. Shen, Z., Jin, X., Tian, J., Li, M., Yuan, Y., Zhang, S., Fang, S., Fan, X., Xu, W., Lu, H., et al. (2022). Cation-doped ZnS catalysts for polysulfide conversion in lithium–sulfur batteries. Nat Catal *5*, 555–563. 10.1038/s41929-022-00804-4.

328. Hua, W., Shang, T., Li, H., Sun, Y., Guo, Y., Xia, J., Geng, C., Hu, Z., Peng, L., Han, Z., et al. (2023). Optimizing the p charge of S in p-block metal sulfides for sulfur reduction electrocatalysis. Nat Catal *6*, 174–184. 10.1038/s41929-023-00912-9.

329. Dong, W.-D., Li, Y., Li, C.-F., Hu, Z.-Y., Hsu, L.-C., Chen, L.-H., Li, Y., Lei, A., and Su, B.-L. (2023). Atomically dispersed Co-N4C2 catalytic sites for wide-temperature Na-Se batteries. Nano Energy *105*, 108005. 10.1016/j.nanoen.2022.108005.

330. Marks, T., Trussler, S., Smith, A.J., Xiong, D., and Dahn, J.R. (2010). A Guide to Li-Ion Coin-Cell Electrode Making for Academic Researchers. J. Electrochem. Soc. *158*, A51. 10.1149/1.3515072.

331. Rudola, A., Wright, C.J., and Barker, J. (2021). Communication—Surprisingly High Fast Charge Volumetric Capacities of Hard Carbon Electrodes in Sodium-Ion Batteries. J. Electrochem. Soc. *168*, 110534. 10.1149/1945-7111/ac377a.

332. Croguennec, L., and Palacin, M.R. (2015). Recent Achievements on Inorganic Electrode Materials for Lithium-Ion Batteries. J. Am. Chem. Soc. *137*, 3140–3156. 10.1021/ja507828x.

333. Bauer, A., Song, J., Vail, S., Pan, W., Barker, J., and Lu, Y. (2018). The Scale-up and Commercialization of Nonaqueous Na-Ion Battery Technologies. Advanced Energy Materials *8*, 1702869. https://doi.org/10.1002/aenm.201702869.

334. Liu, X., Cao, Y., and Sun, J. (2022). Defect Engineering in Prussian Blue Analogs for High-Performance Sodium-Ion Batteries. Advanced Energy Materials *12*, 2202532. 10.1002/aenm.202202532.

335. Rudola, A., Wright, C.J., and Barker, J. (2022). Explorations Into the Viability of High Voltage Bipolar Na-Ion Cells Using Liquid Electrolytes. Frontiers in Energy Research *10*.

336. Huang, C., Xiao, J., Shao, Y., Zheng, J., Bennett, W.D., Lu, D., Saraf, L.V., Engelhard, M., Ji, L., Zhang, J., et al. (2014). Manipulating surface reactions in lithium–sulphur batteries using hybrid anode structures. Nat Commun *5*, 3015. 10.1038/ncomms4015.

337. Burns, J.C., Jain, G., Smith, A.J., Eberman, K.W., Scott, E., Gardner, J.P., and Dahn, J.R. (2011). Evaluation of Effects of Additives in Wound Li-Ion Cells Through High Precision Coulometry. J. Electrochem. Soc. *158*, A255. 10.1149/1.3531997.

338. Erickson, E.M., Schipper, F., Tian, R., Shin, J.-Y., Erk, C., Chesneau, F.F., Lampert, J.K., Markovsky, B., and Aurbach, D. (2017). Enhanced capacity and lower mean charge voltage of Li-rich cathodes for lithium ion batteries resulting from low-temperature electrochemical activation. RSC Adv. *7*, 7116–7121. 10.1039/C6RA25275C.

339. Friedrich, F., Strehle, B., Freiberg, A.T.S., Kleiner, K., Day, S.J., Erk, C., Piana, M., and Gasteiger, H.A. (2019). Editors' Choice—Capacity Fading Mechanisms of NCM-811 Cathodes in Lithium-Ion Batteries Studied by X-ray Diffraction and Other Diagnostics. J. Electrochem. Soc. *166*, A3760. 10.1149/2.0821915jes.

340. Gaberšček, M. (2021). Understanding Li-based battery materials via electrochemical impedance spectroscopy. Nat Commun *12*, 6513. 10.1038/s41467-021-26894-5.

341. HALL, N., BOULINEAU, S., Croguennec, L., LAUNOIS, S., Masquelier, C., and SIMONIN, L. (2017). Method for preparing a na3v2(po4)2f3 particulate material.

342. Rodríguez-Carvajal, J. (1993). Recent advances in magnetic structure determination by neutron powder diffraction. Physica B: Condensed Matter *192*, 55–69. 10.1016/0921-4526(93)90108-I.

343. Dreyer, W., Jamnik, J., Guhlke, C., Huth, R., Moškon, J., and Gaberšček, M. (2010). The thermodynamic origin of hysteresis in insertion batteries. Nature Mater *9*, 448–453. 10.1038/nmat2730.

344. Criado, A., Lavela, P., Ortiz, G., Tirado, J.L., Pérez-Vicente, C., Bahrou, N., and Edfouf, Z. (2020). Highly dispersed oleic-induced nanometric C@Na3V2(PO4)2F3 composites for efficient Na-ion batteries. Electrochimica Acta *332*, 135502. 10.1016/j.electacta.2019.135502.

Achieving Na-ion Battery Advancements Through Decoding Degradation Pathways and Electrolyte Engineering

Abstract: The growing dependence on lithium-ion batteries for energy storage necessitates the exploration of alternative chemistries due to the limited and geopolitically sensitive lithium resources. The sodium-ion battery, considered a sustainable complement with abundant sodium precursors, is swiftly progressing towards commercialization. Following a comparative analysis of critical parameters, the $Na_3V_2(PO_4)_2F_3$(NVPF)|hard carbon(HC) chemistry was selected for NVPF material's structural durability, robust power performance, and air/water stability. This thesis comprehensively navigates this technology by investigating degradation mechanisms, improving performance in lab-scale coin cells, and seamlessly transferring findings to commercial 18650 cells. At first, NVPF material instabilities were examined, with elevated temperatures causing vanadium dissolution, leading to NVPF electrode degradation, electrolyte instability, and finally, contamination of HC electrode. Imide co-salts and uniform carbon coating mitigate vanadium dissolution yet fail to suppress undesired electrolyte reactions. Hence, meticulously designed Gen-3 electrolytes with additives enhance cells' cycle and calendar life at elevated temperatures without excessive gassing. A low-viscosity methyl acetate cosolvent was infused in the electrolyte to enhance power and low-temperature performance further. The optimized electrolyte demonstrates remarkable cycle life, rate performance, extensive temperature tolerance, and safety, making it suitable for evaluation in commercial scenarios. The thesis concludes with assessing the 0V stability of sodium-ion batteries, comprehending SEI decomposition mechanisms, and proposing remedies. Lastly, future directions are outlined to propel Na-ion battery development and challenge $LiFePO_4$-based Li-ion technology.

Keywords: Sodium-ion batteries, Solid electrolyte interphase, High temperature stability, Vanadium dissolution, Electrolyte design, Gassing, Optical sensing, Low viscosity cosolvent, Fast charging, Zero volt stability

---

Réalisation des avancées des batteries Na-ion à travers le décodage des voies de dégradation et l'ingénierie des électrolytes.

Résumé: La dépendance croissante à l'égard des batteries lithium-ion pour le stockage de l'énergie nécessite l'exploration de produits chimiques alternatifs en raison des ressources limitées et géopolitiquement sensibles en lithium. La batterie sodium-ion, est considérée comme une alternative prometteuse, avec d'abondants précurseurs de sodium. Après une analyse comparative des paramètres critiques, la chimie $Na_3V_2(PO_4)_2F_3$(NVPF)|hard carbon(HC) a été sélectionnée pour cette etude, de par la durabilité structurelle du matériau NVPF, ses performances énergétiques robustes et sa stabilité air/eau. Cette thèse explore de manière exhaustive cette technologie en étudiant les mécanismes de dégradation, en améliorant les performances des piles boutons à l'échelle du laboratoire et en transférant les résultats aux cellules 18650 commerciales. Dans un premier temps, les instabilités des matériaux NVPF ont été examinées, avec des températures élevées provoquant la dissolution du vanadium, conduisant à une dégradation de l'électrode NVPF, à une instabilité de l'électrolyte et enfin à une contamination de l'électrode HC. Les co-sels d'imide et le revêtement de carbone uniforme atténuent la dissolution du vanadium mais ne parviennent pas à supprimer les réactions électrolytiques indésirables. Par conséquent, les électrolytes Gen-3 méticuleusement conçus avec des additifs améliorent le cycle et la durée de vie des cellules à des températures élevées sans dégagement gazeux excessif. Un cosolvant d'acétate de méthyle à faible viscosité a été infusé dans l'électrolyte pour améliorer encore plus la puissance et les performances à basse température. L'électrolyte optimisé présente une durée de vie, des performances en Crate, une tolérance de température étendue et une sécurité remarquables, ce qui le rend adapté à une possible commercialisation. La thèse se termine par l'évaluation de la stabilité à 0 V des batteries sodium-ion, la compréhension des mécanismes de décomposition du SEI et la proposition de solution pour y pallier. Enfin, des orientations futures sont décrites pour propulser le développement des batteries Na-ion et remettre en question la technologie Li-ion basée sur $LiFePO_4$.

Mots clés: Batteries sodium-ion, Interphase à électrolyte solide, Stabilité à haute température, Dissolution du vanadium, Conception de l'électrolyte, Dégazage, Détection optique, Cosolvant à faible viscosité, Charge rapide, Stabilité zéro volt